ΕΘΝΙΚΟ ΜΕΤΣΟΒΙΟ ΠΟΛΥΤΕΧΝΕΙΟ
ΣΧΟΛΗ ΠΟΛΙΤΙΚΩΝ ΜΗΧΑΝΙΚΩΝ
ΤΟΜΕΑΣ ΓΕΩΤΕΧΝΙΚΗΣ

ΑΡΙΘΜΗΤΙΚΗ ΔΙΕΡΕΥΝΗΣΗ ΤΗΣ ΣΕΙΣΜΙΚΗΣ ΑΠΟΚΡΙΣΗΣ ΠΑΣΣΑΛΟΥ ΥΠΟ ΚΑΘΕΣΤΩΣ ΡΕΥΣΤΟΠΟΙΗΣΗΣ ΚΑΙ ΟΡΙΖΟΝΤΙΑΣ ΜΕΤΑΤΟΠΙΣΗΣ ΤΟΥ ΕΔΑΦΟΥΣ

ΔΙΔΑΚΤΟΡΙΚΗ ΔΙΑΤΡΙΒΗ

Γιάννη Κ. Χαλούλου

Διπλωματούχου Πολιτικού Μηχανικού Ε.Μ.Π., M.Sc.

ΕΠΙΒΛΕΠΩΝ:

Γ. ΜΠΟΥΚΟΒΑΛΑΣ

Καθηγητής Ε.Μ.Π.

Αθήνα, Ιούλιος 2012

ΕΘΝΙΚΟ ΜΕΤΣΟΒΙΟ ΠΟΛΥΤΕΧΝΕΙΟ
ΣΧΟΛΗ ΠΟΛΙΤΙΚΩΝ ΜΗΧΑΝΙΚΩΝ
ΤΟΜΕΑΣ ΓΕΩΤΕΧΝΙΚΗΣ

ΑΡΙΘΜΗΤΙΚΗ ΔΙΕΡΕΥΝΗΣΗ ΤΗΣ ΣΕΙΣΜΙΚΗΣ ΑΠΟΚΡΙΣΗΣ ΠΑΣΣΑΛΟΥ ΥΠΟ ΚΑΘΕΣΤΩΣ ΡΕΥΣΤΟΠΟΙΗΣΗΣ ΚΑΙ ΟΡΙΖΟΝΤΙΑΣ ΜΕΤΑΤΟΠΙΣΗΣ ΤΟΥ ΕΔΑΦΟΥΣ

ΔΙΔΑΚΤΟΡΙΚΗ ΔΙΑΤΡΙΒΗ

Γιάννη Κ. Χαλούλου

Διπλωματούχου Πολιτικού Μηχανικού Ε.Μ.Π., M.Sc.

Η διατριβή υποβλήθηκε στη Σχολή Πολιτικών Μηχανικών του Εθνικού Μετσόβιου Πολυτεχνείου προς εκπλήρωση των προϋποθέσεων του τίτλου του Διδάκτορος Μηχανικού

ΤΡΙΜΕΛΗΣ ΣΥΜΒΟΥΛΕΥΤΙΚΗ ΕΠΙΤΡΟΠΗ:

1. Γ. ΜΠΟΥΚΟΒΑΛΑΣ, Καθηγητής Ε.Μ.Π. (Επιβλέπων)

2. Μ. ΚΑΒΒΑΔΑΣ, Αν. Καθηγητής Ε.Μ.Π.

3. ΑΧ. ΠΑΠΑΔΗΜΗΤΡΙΟΥ, Επ. Καθηγητής Παν. Θεσσαλίας

ΕΠΤΑΜΕΛΗΣ ΕΞΕΤΑΣΤΙΚΗ ΕΠΙΤΡΟΠΗ:

1. Γ. ΜΠΟΥΚΟΒΑΛΑΣ, Καθηγητής Ε.Μ.Π. (Επιβλέπων)

2. Μ. ΚΑΒΒΑΔΑΣ, Αν. Καθηγητής Ε.Μ.Π.

3. ΑΧ. ΠΑΠΑΔΗΜΗΤΡΙΟΥ, Επ. Καθηγητής Παν. Θεσσαλίας

4. Γ. ΓΚΑΖΕΤΑΣ, Καθηγητής Ε.Μ.Π.

5. Γ.ΤΣΙΑΜΠΑΟΣ, Καθηγητής Ε.Μ.Π.

6. Β. ΠΑΠΑΔΟΠΟΥΛΟΣ,Επ. Καθηγητής Ε.Μ.Π.

7. Γ. ΜΥΛΩΝΑΚΗΣ, Αν. Καθηγητής Παν. Πατρών

Αθήνα, Ιούλιος 2012

NATIONAL TECHNICAL UNIVERSITY OF ATHENS
SCHOOL OF CIVIL ENGINEERING
DEPARTMENT OF GEOTECHNICAL ENGINEERING

NUMERICAL INVESTIGATION OF PILE RESPONSE UNDER LIQUEFACTION AND GROUND LATERAL SPREADING

DOCTORAL THESIS

Yannis K. Chaloulos

Civil Engineer, N.T.U.A., M.Sc.

The thesis is submitted to the School of Civil Engineering of the National Technical University of Athens in fulfilment of the requirements for the Degree of Doctor of Philosophy

ADVISORY COMMITTEE:

1. G. BOUCKOVALAS, Professor N.T.U.A. (Supervisor)

2. M. KAVVADAS, Associate Professor N.T.U.A.

3. ACH. PAPADIMITRIOU, Assistant Professor University of Thessaly

EXAMINATION COMMITTEE:

1. G. BOUCKOVALAS, Professor N.T.U.A. (Supervisor)

2. M. KAVVADAS, Associate Professor N.T.U.A.

3. ACH. PAPADIMITRIOU, Assistant Professor University of Thessaly

4. G. GAZETAS, Professor N.T.U.A.

5. G. TSIAMBAOS, Professor N.T.U.A.

6. V. PAPADOPOULOS, Assistant Professor N.T.U.A.

7. G. MYLONAKIS, Assistant Professor University of Patras

Athens, July 2012

ΕΘΝΙΚΟ ΜΕΤΣΟΒΙΟ ΠΟΛΥΤΕΧΝΕΙΟ
ΣΧΟΛΗ ΠΟΛΙΤΙΚΩΝ ΜΗΧΑΝΙΚΩΝ
ΤΟΜΕΑΣ ΓΕΩΤΕΧΝΙΚΗΣ

ΑΡΙΘΜΗΤΙΚΗ ΔΙΕΡΕΥΝΗΣΗ ΤΗΣ ΣΕΙΣΜΙΚΗΣ ΑΠΟΚΡΙΣΗΣ ΠΑΣΣΑΛΟΥ ΥΠΟ ΚΑΘΕΣΤΩΣ ΡΕΥΣΤΟΠΟΙΗΣΗΣ ΚΑΙ ΟΡΙΖΟΝΤΙΑΣ ΜΕΤΑΤΟΠΙΣΗΣ ΤΟΥ ΕΔΑΦΟΥΣ

ΔΙΔΑΚΤΟΡΙΚΗ ΔΙΑΤΡΙΒΗ

Γιάννη Κ. Χαλούλου

Διπλωματούχου Πολιτικού Μηχανικού Ε.Μ.Π., M.Sc.

Η διατριβή υποβλήθηκε στη Σχολή Πολιτικών Μηχανικών
του Εθνικού Μετσόβιου Πολυτεχνείου
προς εκπλήρωση των προϋποθέσεων του τίτλου του Διδάκτορος Μηχανικού

ΤΡΙΜΕΛΗΣ ΣΥΜΒΟΥΛΕΥΤΙΚΗ ΕΠΙΤΡΟΠΗ:

1. Γ. ΜΠΟΥΚΟΒΑΛΑΣ, Καθηγητής Ε.Μ.Π. (Επιβλέπων)
2. Μ. ΚΑΒΒΑΔΑΣ, Αν. Καθηγητής Ε.Μ.Π.
3. ΑΧ. ΠΑΠΑΔΗΜΗΤΡΙΟΥ, Επ. Καθηγητής Παν. Θεσσαλίας

ΕΠΤΑΜΕΛΗΣ ΕΞΕΤΑΣΤΙΚΗ ΕΠΙΤΡΟΠΗ:

1. Γ. ΜΠΟΥΚΟΒΑΛΑΣ, Καθηγητής Ε.Μ.Π. (Επιβλέπων)
2. Μ. ΚΑΒΒΑΔΑΣ, Αν. Καθηγητής Ε.Μ.Π.
3. ΑΧ. ΠΑΠΑΔΗΜΗΤΡΙΟΥ, Επ. Καθηγητής Παν. Θεσσαλίας
4. Γ. ΓΚΑΖΕΤΑΣ, Καθηγητής Ε.Μ.Π.
5. Γ.ΤΣΙΑΜΠΑΟΣ, Καθηγητής Ε.Μ.Π.
6. Β. ΠΑΠΑΔΟΠΟΥΛΟΣ,Επ. Καθηγητής Ε.Μ.Π.
7. Γ. ΜΥΛΩΝΑΚΗΣ, Αν. Καθηγητής Παν. Πατρών

Αθήνα, Ιούνιος 2012

NATIONAL TECHNICAL UNIVERSITY OF ATHENS
SCHOOL OF CIVIL ENGINEERING
DEPARTMENT OF GEOTECHNICAL ENGINEERING

NUMERICAL INVESTIGATION OF PILE RESPONSE UNDER LIQUEFACTION AND GROUND LATERAL SPREADING

DOCTORAL THESIS

Yannis K. CHaloulos

Civil Engineer, N.T.U.A., M.Sc.

The thesis is submitted to the School of Civil Engineering of the National Technical University of Athens in fulfilment of the requirements for the Degree of Doctor of Philosophy

ADVISORY COMMITTEE:

1. G. BOUCKOVALAS, Professor N.T.U.A. (Supervisor)
2. M. KAVVADAS, Associate Professor N.T.U.A.
3. ACH. PAPADIMITRIOU Assistant Professor University of Thessaly

EXAMINATION COMMITTEE:

1. G. BOUCKOVALAS, Professor N.T.U.A. (Supervisor)
2. M. KAVVADAS, Associate Professor N.T.U.A.
3. ACH. PAPADIMITRIOU Assistant Professor University of Thessaly
4. G. GAZETAS, Professor N.T.U.A.
5. G. TSIAMBAOS, Professor N.T.U.A.
6. V. PAPADOPOULOS, Assistant Professor N.T.U.A.
7. G. MYLONAKIS, Assistant Professor University of Patras

Athens, July 2012

Στην οικογένεια μου

Προλεγόμενα

«Τι θες να γίνεις όταν μεγαλώσεις;», ρώτησε ο δάσκαλος τον τότε μαθητή δημοτικού Τζον Λένον. «Θέλω να γίνω ευτυχισμένος», εκείνος απάντησε. «Μου φαίνεται δεν έχεις καταλάβει την ερώτηση», συνέχισε ο δάσκαλος. «Μου φαίνεται δεν έχετε καταλάβει τη ζωή», αποκρίθηκε ο μαθητής. Δεν θυμήθηκα τυχαία σήμερα αυτό τον διάλογο, μια και είμαι σίγουρος πως η απάντηση του μαθητή θα τύχαινε εντελώς διαφορετικής αποδοχής, αν για δάσκαλο του είχε τον κ. Γιώργο Μπουκοβάλα, Καθηγητή Ε.Μ.Π. Ήταν εκείνος που πρώτος απ' όλους πίστεψε σε μένα, και με βοήθησε να ενεργοποιήσω δυνάμεις που δεν γνώριζα πως είχα. Παρακολουθούσε συνεχώς από κοντά την εξέλιξη της δουλειάς, άκουγε τους προβληματισμούς μου, και ενίοτε ξενυχτούσε με αυτούς, διέβλεπε τις ανησυχίες μου, ενώ πάντα έδινε λύσεις χάρη στην εφευρετικότητα, την μεθοδικότητα και την αγάπη του για το αντικείμενο. Πάνω απ' όλα, όμως, οφείλω να τον ευχαριστήσω για τον τρόπο σκέψης, τις αρχές, τις αξίες και το ήθος που μου μετέδωσε, και με βοήθησαν να γίνω καλύτερος άνθρωπος. Ένας πραγματικός δάσκαλος ζωής.

Θα ήθελα να ευχαριστήσω θερμά τα μέλη της Τριμελούς Συμβουλευτικής Επιτροπής, τον κ. Μιχάλη Καββαδά, αναπληρωτή καθηγητή Ε.Μ.Π. και τον κ. Αχιλλέα Παπαδημητρίου, Επίκουρο καθηγητή στο Πανεπιστήμιο Θεσσαλίας, για το ενδιαφέρον τους για την δουλειά μου, καθώς και την προθυμία τους να συνδράμουν ουσιαστικά όποτε χρειάστηκα την βοήθεια τους. Ειλικρινά ευχαριστώ και τα υπόλοιπα μέλη της Επταμελούς Εξεταστικής Επιτροπής, τους κ. Γ. Γκαζέτα και Γ. Τσιαμπάο, Καθηγητές Ε.Μ.Π., τον κ. Β. Παπαδόπουλο, Επίκουρο Καθηγητή Ε.Μ.Π. και τον κ. Γ. Μυλωνάκη, Αναπληρωτή Καθηγητή στο Πανεπιστήμιο Πατρών, για τα σχόλια, τις υποδείξεις και εν γένει την συμβολή τους στην τελική διαμόρφωση της εργασίας.

Πραγματικά μου είναι δύσκολο να βρω λόγια να ευχαριστήσω τον Διδάκτορα Δημήτρη Καραμήτρο. Είναι από τις περιπτώσεις εκείνες που η ζωή στέλνει τις λέξεις αδιάβαστες. Από τον καιρό της διπλωματικής εργασίας μέχρι τώρα, στο τέλος του διδακτορικού, ήταν αναμφίβολα ο πιο κοντινός μου άνθρωπος στον Τομέα. Ο πρώτος στον οποίο θα έλεγα τις δυσκολίες με τις οποίες ερχόμουνα αντιμέτωπος και τις ανησυχίες μου σχετικά με την πορεία της δουλειάς, αλλά και γενικότερα. Και πάντα θα έβρισκε τρόπο να μου δώσει ώθηση, να με σπρώξει προς τα εμπρός. Επιπλέον, το μοναδικό του χάρισμα να δημιουργεί ένα ευχάριστο περιβάλλον εργασίας –μουσικές, αστεία, αλκοόλ και τόσα άλλα- που μετέτρεπαν το γραφείο από χώρο εργασίας στον καλύτερο τόπο χαλάρωσης, απαραίτητη προϋπόθεση για την ενίσχυση της συνεργασίας και της δημιουργικότητας. Αναμφισβήτητα, ένα μεγάλο μέρος από το φως που βλέπω σήμερα του ανήκει.

Βέβαια η εργασία αυτή δεν θα είχε ολοκληρωθεί και χωρίς την πολύτιμη βοήθεια και των υπόλοιπων παιδιών της ερευνητικής μας ομάδας, του Αχιλλέα Παπαδημητρίου, του Γιώργου Κουρετζή (αχ…), του Κώστα Ανδριανόπουλου, του Αλέξανδρου Βαλσαμή, της Κικής Δημητριάδη, αλλά και του Νέου (Γιάννης Τσιάπας). Μπορεί η πορεία του διδακτορικού να είναι κατά κανόνα μια πορεία μοναχική, εντούτοις η ορθή χάραξη και τήρηση της βασίζεται στην ύπαρξη ικανών και ανιδιοτελών συναγωνιστών. Στο πλαίσιο αυτό νιώθω ιδιαίτερα περήφανος να είμαι μέλος μιας τόσο αξιόλογης και υγιούς ερευνητικής ομάδας, μα πάνω απ' όλα μιας τόσο δεμένης παρέας.

Επίσης, δεν μπορώ να μην γράψω δυο λόγια και για τα παιδιά που συνεργαστήκαμε στα πλαίσια των διπλωματικών εργασιών, τον Βασίλη, τον Ashkan και την Vida, οι οποίοι βοήθησαν ουσιαστικά στην εξέλιξη της δουλειάς. Αλλά και σε όλα τα παιδιά, από τα μαθήματα της Εδαφομηχανικής και της Γεωτεχνικής Σεισμικής Μηχανικής. Μου έδωσαν ορμή, μου έδωσαν ζωντάνια, τους έδωσα γνώση. Ένα όμορφο πάντρεμα κατά τη γνώμη μου.

Το μεγαλύτερο μέρος της ζωής μου τα τελευταία χρόνια το πέρασα μέσα στα γραφεία του Τομέα Γεωτεχνικής, τον οποίο πολύ γρήγορα άρχισα να νιώθω σαν το δεύτερο σπίτι μου. Και αυτό φυσικά χάρη σε όλους εκείνους τους ωραίους ανθρώπους που είχα την τύχη να γνωρίσω εκεί. Χάρη στους ανεκτίμητους εκείνους φίλους που έκαναν τις ατέλειωτες ώρες δουλειάς να μοιάζουν ξεκούραστες. Και τι να πρωτοθυμηθώ…

…τους καφέδες στο κυλικείο, τις μεσημεριανές συγκεντρώσεις για φαγητό, τα βράδια με ρακί, παξιμάδι και τόνο, τις αμπελοφιλοσοφίες, τα πρόστυχα αστεία, τις λεμονόπιτες, την προβατίνα της Τσικνοπέμπτης, το γουρουνόπουλο της Πρωτομαγιάς!

…και φυσικά τα ραδιοφωνικά βράδια της Πέμπτης, καθένα από αυτά εξίσου μεθυσμένο και φωτεινό, σαν φάρου αναλαμπή που κόβει στα δύο όλο το σκοτάδι της νυχτωμένης εβδομάδας!

Νιώθω πραγματικά ευτυχισμένος που όλο αυτό το κλίμα έχει μεταφερθεί και εκτός τομέα: στις ταβέρνες της Σταμάτας, στα Πρωτοχρονιάτικα ρεβεγιόν, στις συναυλίες του Χαρούλη, στις παραλίες των Σπετσών και στις Κυκλαδίτικες αστροφεγγιές, στα Κρητικά ρακοπουλειά... Είναι ένας από τους λόγους για τους οποίους δεν θα μετανιώσω ποτέ την απόφαση για το διδακτορικό.

Τελευταία και σημαντικότερη η Οικογένεια μου. Παρόλο που αυτή η διαδικασία με ανάγκαζε να βρίσκομαι όλο και περισσότερες ώρες μακριά από το σπίτι, το σπίτι, με έναν μαγικό τρόπο, βρισκόταν συνεχώς κοντά μου. «Εκτός από τη μάνα σου, κανείς δεν σε θυμάται», λέει ο ποιητής. Και οι ποιητές έχουν πάντα δίκιο.

Βέβαια οι ποιητές έχουν και ένα άλλο θετικό. Καταφέρνουν, με λίγες λέξεις, να περιγράψουν πολύ ιδιαίτερα συναισθήματα, σχεδόν στα όρια του ανείπωτου. Για μένα, σήμερα, έχει φροντίσει ο Μανώλης Αναγνωστάκης με την «Αφιέρωση» του:

«*Για τους ερωτευμένους που παντρεύτηκαν.*
Για το σπίτι που χτίστηκε.
Για τα παιδάκια που μεγάλωσαν.
Για τα πλοία που άραξαν.
Για τη μάχη που κερδήθηκε.
Για τον άσωτο που επέστρεψε.

Για όλα όσα τέλειωσαν χωρίς ελπίδα πια.»

Γιάννης Χαλούλος (14 Ιουλίου, 2012)

Διδακτορική Διατριβή

Αριθμητική διερεύνηση της σεισμικής απόκρισης πασσάλου υπό καθεστώς ρευστοποίησης και οριζόντιας μετατόπισης του εδάφους

Γιάννης Κ. Χαλούλος

ΕΚΤΕΝΗΣ ΠΕΡΙΛΗΨΗ

I. Περιγραφή του Προβλήματος

Η τρέχουσα πρακτική για την ανάλυση πασσάλων υπό οριζόντια φόρτιση βασίζεται συνηθέστατα στην μέθοδο της «Ελαστικής Δοκού επί μη γραμμικού Ελατηριωτού Εδάφους» (BNWF), ευρύτερα γνωστής και ως μέθοδος «p-y» (**Σχήμα 1**). Η εφαρμογή της εν λόγω μεθοδολογίας συνίσταται στις ακόλουθες τρεις (3) παραδοχές:

- Τα δομικά στοιχεία (πάσσαλος, κεφαλόδεσμος, ανωδομή) προσομοιώνονται με στοιχεία δοκού.
- Η αλληλεπίδραση εδάφους-θεμελίωσης προσομοιώνεται μέσω οριζόντιων ελατηρίων Winkler, το ένα άκρο των οποίων είναι συνδεδεμένο με την θεμελίωση και το άλλο είναι ακλόνητο.
- Τέλος, ανάλογα με τη φύση τους, τα φορτία σχεδιασμού επιβάλλονται είτε ως συγκεντρωμένες δυνάμεις και ροπές στην κεφαλή του πασσάλου (εξωτερικά φορτία), είτε ως μετατοπίσεις στα ακλόνητα άκρα των οριζόντιων ελατηρίων (κινηματικά φορτία).

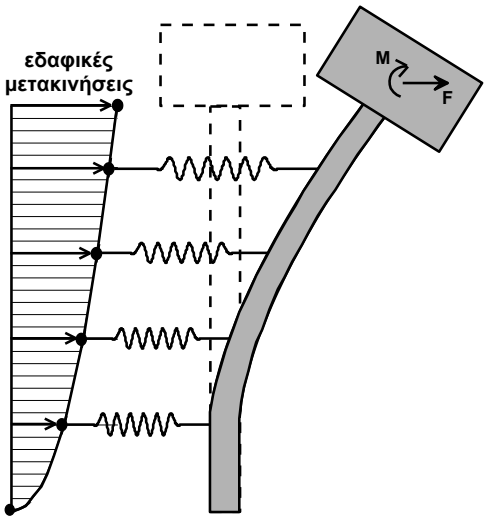

Σχήμα 1: Σχηματική απεικόνιση της μεθόδου «p-y».

Ίσως, η πλέον κρίσιμη παράμετρος στην παραπάνω μεθοδολογία είναι η περιγραφή της μη γραμμικής σχέσης δύναμης-μετατόπισης των ελατηρίων Winkler, γνωστής και ως καμπύλη p-y (**Σχήμα 2**). Για την πλήρη περιγραφή μιας τέτοιας καμπύλης, είναι ανάγκη να προσδιορισθούν τρία (3) επιμέρους στοιχεία:

- Η οριακή εδαφική αντίδραση, p_{ult} [μονάδες F/L]
- Η αρχική δυσκαμψία, K_{ini} [μονάδες F/L^2], ή ισοδύναμα ο δείκτης αρχικής δυσκαμψίας, $k_{ini}= K_{ini}/z$ [μονάδες F/L^3], όπου z δηλώνει το βάθος από την επιφάνεια του εδάφους.
- Η μαθηματική σχέση που συνδέει την δύναμη (p) με την μετατόπιση (y) του πασσάλου, για δεδομένες τιμές των σταθερών p_{ult} και k_{ini}.

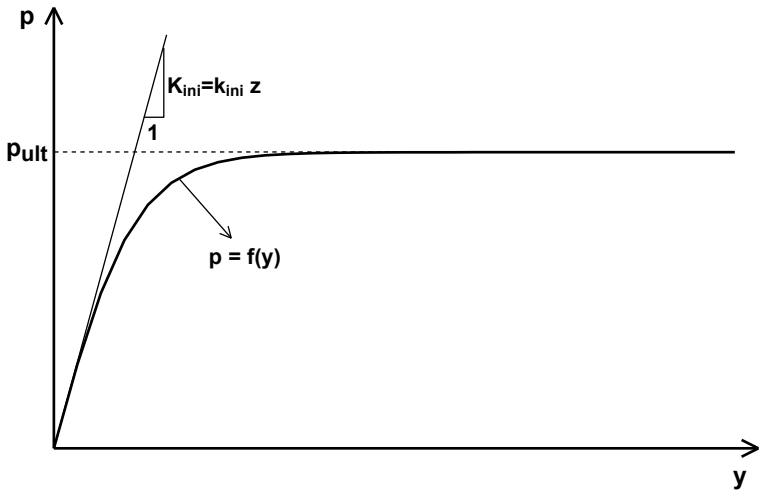

Σχήμα 2: Τυπική καμπύλη οριζόντιας εδαφικής αντίδρασης (p) – μετατόπισης (y).

Τα επιμέρους χαρακτηριστικά μιας καμπύλης p-y (οριακή αντίδραση, αρχική δυσκαμψία, μη-γραμμική μαθηματική σχέση) μεταβάλλονται τόσο ανάλογα με το είδος του εδάφους εντός του οποίου είναι κατασκευασμένος ο πάσσαλος, όσο και ανάλογα με το είδος της φόρτισης στην οποία υποβάλλεται. Οι διάφοροι συνδυασμοί φορτίσεων και εδαφών συνοψίζονται στο **Σχήμα 3**. Αναφορικά με τα εδάφη, διακρίνονται τα συνεκτικά και τα μη συνεκτικά. Τα τελευταία είναι είτε μη ρευστοποιημένα, αναφερόμενα εφεξής με τον όρο «ξηρά» εδάφη, είτε ρευστοποιημένα, αναφερόμενα εφεξής με τον όρο «ρευστοποιημένα» εδάφη. Αναφορικά με τους τύπους φόρτισης, ένας πάσσαλος μπορεί να υποβληθεί είτε σε εξωτερικά φορτία (δυνάμεις και ροπές) είτε σε κινηματικά (π.χ. λόγω πλευρικής

εδαφικής μετακίνησης). Επιπλέον, τα εξωτερικά φορτία μπορούν να είναι είτε στατικά είτε δυναμικά, ενώ τα κινηματικά παροδικά ή μόνιμα.

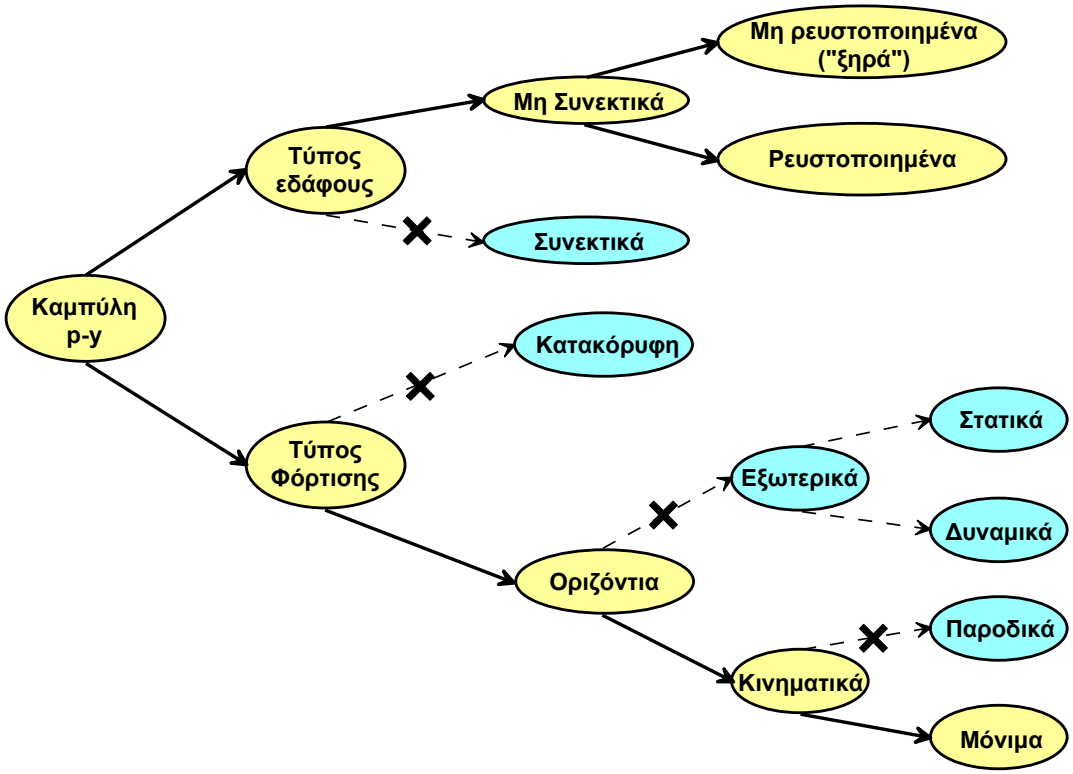

Σχήμα 3: Διαφορετικοί συνδυασμοί τύπου εδάφους και τύπου φόρτισης που επιδρούν στην απόκριση του πασσάλου και κατ' επέκταση στη μορφή των καμπυλών p-y. (Με «**X**» σημειώνονται οι περιπτώσεις εδάφους και φόρτισης οι οποίοι δεν απασχολούν την παρούσα διατριβή).

Από τους ανωτέρω δώδεκα (12) συνδυασμούς τύπου εδάφους και τύπου φόρτισης, **η παρούσα Διατριβή πραγματεύεται την περίπτωση καμπυλών p-y για πασσάλους σε «ξηρές» και «ρευστοποιημένες» άμμους, υποβαλλόμενους σε μόνιμα κινηματικά φορτία**. Ένα μικρό μέρος της Διατριβής αφιερώνεται επίσης στην περίπτωση εξωτερικών φορτίων και «ξηρών» εδαφών, κυρίως για λόγους σύγκρισης με τα αντίστοιχα ευρήματα για κινηματικά φορτία.

Στην πράξη, η περίπτωση πασσάλων σε «ξηρά» εδάφη, υποβαλλόμενων σε μόνιμες πλευρικές μετακινήσεις του εδάφους, συναντάται κυρίως κατά την λήψη μέτρων ανάσχεσης κατολισθητικών φαινομένων σε φυσικά ή τεχνητά πρανή μεγάλης σχετικά κλίσης. Αντίθετα, η περίπτωση οριζόντια φορτιζόμενων πασσάλων σε ρευστοποιημένο έδαφος, αντιμετωπίζεται ακόμη και υπό ήπιες κλίσεις του εδάφους ή μικρού ύψους τοπογραφικούς αναβαθμούς, και αποτελεί συνηθισμένη πηγή

σημαντικών βλαβών σε θεμελιώσεις πασσάλων, όπως καταδεικνύουν και οι παρακάτω φωτογραφίες (**Σχήμα 4**) από πρόσφατους ισχυρούς σεισμούς.

Σχήμα 4: Παραδείγματα αστοχίας πασσάλων λόγω ρευστοποίησης και πλευρικής εξάπλωσης του εδάφους σε πρόσφατους ισχυρούς σεισμούς.

Ο κρίσιμος ρόλος των καμπυλών p-y για τον σχεδιασμό οριζόντια φορτιζόμενων πασσάλων απετέλεσε κίνητρο για την εκπόνηση σημαντικής, σε όγκο και πρωτοτυπία, πειραματικής κυρίως έρευνας, η οποία επικεντρώθηκε αρχικά στην περίπτωση «ξηρών» άμμων [Reese et al. (1974), Murchison and O'neill (1984), Georgiadis et al. (1992), Det Norske Veritas (1980), Broms (1964), Prasad and Chari (1999), Fleming et al. (1992), Brinch-Hansen (1961)] και ακολούθως στην περίπτωση «ρευστοποιημένων» άμμων υπό πλευρική εξάπλωση [Brandenberg et al. (2005), Abdoun et al. (2003), Gonzalez et al. (2009), Suzuki and Tokimatsu (2009), Cubrinovski and Ishihara (2007), Haigh (2002)].

Αποτέλεσμα των προσπαθειών αυτών ήταν η διερεύνηση των μηχανισμών που ελέγχουν την αλληλεπίδραση πασσάλου-εδάφους, καθώς και η διατύπωση εμπειρικών σχέσεων για τις καμπύλες p-y, τόσο σε «ξηρές» όσο και σε ρευστοποιημένες άμμους. Ωστόσο, παρά την πληθώρα των σχετικών δημοσιεύσεων, η

μελέτη της βιβλιογραφίας κατέδειξε ότι υπάρχουν αρκετές ακόμη αβεβαιότητες που θα πρέπει να διερευνηθούν.

Συγκεκριμένα, για την περίπτωση «ξηρών» άμμων:

(α) Οι διάφορες εμπειρικές καμπύλες p-y αποκλίνουν σημαντικά μεταξύ τους. Ενδεικτικά, στο **Σχήμα 5** συγκρίνονται οι καμπύλες p-y που προβλέπονται από έξι (6) διαφορετικές μεθοδολογίες. Παρατηρείται ότι οι διάφορες προβλέψεις διαφοροποιούνται σημαντικά τόσο ως προς το σχήμα της καμπύλης, όσο και ως προς την εκτίμηση της αρχικής δυσκαμψίας και οριακής εδαφικής αντίδρασης, γεγονός που δημιουργεί εύλογα ερωτηματικά ως προς την αξιοπιστία τους.

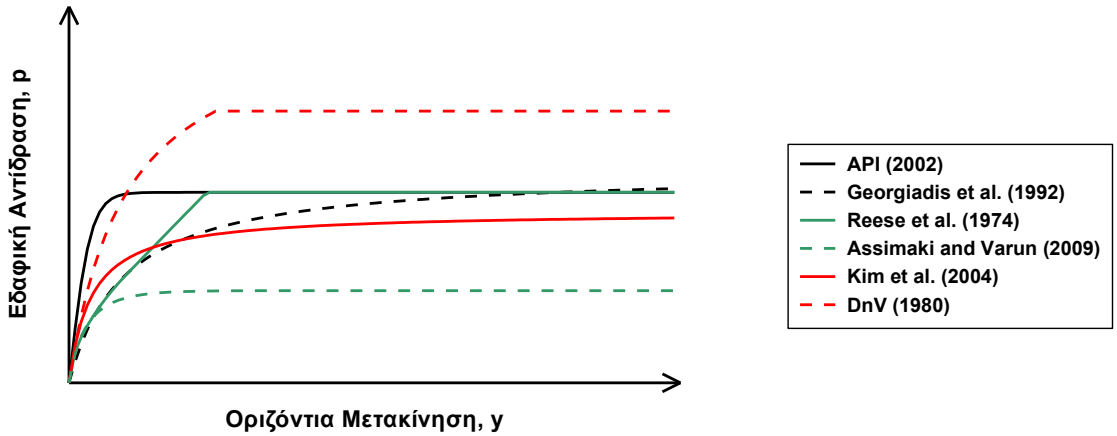

Σχήμα 5: Σύγκριση προτεινόμενων καμπύλων p-y για «ξηρή άμμο».

(β) Στην πλειονότητά τους, οι υπάρχουσες μεθοδολογίες βασίζονται σε αποτελέσματα πειραματικών ερευνών, μεγάλης κλίμακας ή φυγοκεντριστή. Ως γνωστό, το κόστος των ερευνών αυτών είναι ιδιαίτερα υψηλό και επομένως οι δυνατότητες για συστηματική και σε βάθος διερεύνηση όλων των παραγόντων που μπορεί να επιδρούν στις καμπύλες p-y είναι αντικειμενικά περιορισμένες. Αυτό ίσως εξηγεί και τις σημαντικές αποκλίσεις μεταξύ των καμπυλών που φαίνονται στο **Σχήμα 5**.

(γ) Σε συνέχεια, και προς ενίσχυση του (β) ανωτέρω, η πλειονότητα των μεθοδολογιών, εκφράζει τις καμπύλες p-y συναρτήσει της σχετικής πυκνότητας του εδάφους και της διαμέτρου του πασσάλου, παρά το γεγονός ότι πρόσφατες έρευνες (π.χ. Ashour and Norris, 2000; Kim et al., 2004) καταδεικνύουν την ύπαρξη και άλλων σημαντικών παραγόντων. Για παράδειγμα, αναφέρεται ο

τρόπος κατασκευής των πασσάλων (με έμπηξη ή εκσκαφή), ο οποίος είναι ευρέως γνωστό ότι διαφοροποιεί το πεδίο των τάσεων στο περιβάλλον έδαφος, αλλά αγνοείται από όλες τις εμπειρικές σχέσεις προσδιορισμού των καμπύλων p-y. Επιπλέον, σε καμία από τις υπάρχουσες μεθοδολογίες δεν γίνεται διάκριση σε ότι αφορά τον τύπο της επιβαλλόμενης φόρτισης (εξωτερικά ή κινηματικά φορτία). Έτσι, ενώ στην πλειοψηφία τους οι μεθοδολογίες αυτές έχουν προκύψει από πειράματα φόρτισης της κεφαλής του πασσάλου χρησιμοποιούνται αδιάκριτα και στην περίπτωση επιβαλλομένων εδαφικών μετατοπίσεων.

Στην περίπτωση ρευστοποιημένων άμμων, οι προτεινόμενες καμπύλες p-y βασίζονται στις αντίστοιχες καμπύλες για «ξηρές» άμμους, με δραστική απομείωση της οριακής εδαφικής αντίδρασης ή/και της αρχικής δυσκαμψίας. Η απομείωση των καμπυλών p-y γίνεται είτε θεωρώντας εμπειρικούς μειωτικούς συντελεστές (m_p multipliers, **Σχήμα 6**), είτε με αναγωγή στην παραμένουσα αντοχή του ρευστοποιημένου εδάφους. Όπως και στην περίπτωση των «ξηρών» άμμων, οι προκύπτουσες τελικά καμπύλες p-y εξαρτώνται μόνον από τις αρχικές συνθήκες (σχετική πυκνότητα, τάση εγκιβωτισμού) καθώς και την διάμετρο του πασσάλου.

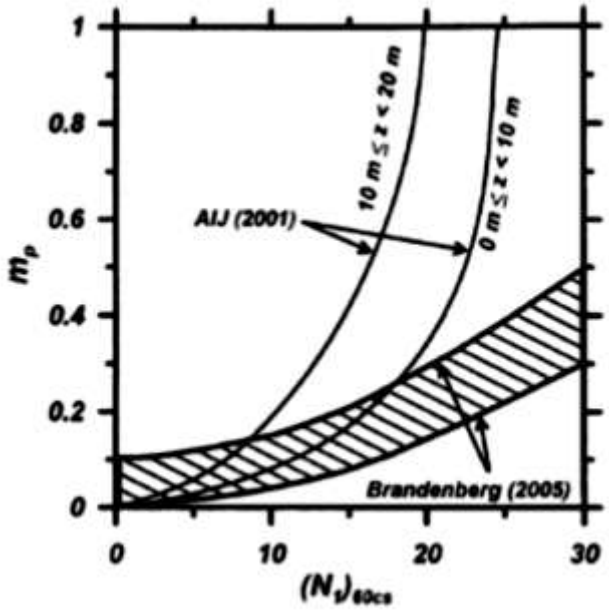

Σχήμα 6: Μειωτικός συντελεστής (m_p multiplier) για την επίδραση της ρευστοποίησης στις στατικές καμπύλες p-y.

Ωστόσο, πρόσφατα πειραματικά αποτελέσματα καταδεικνύουν την ύπαρξη και άλλων σημαντικών παραμέτρων. Για παράδειγμα, κατά τους Suzuki and Tokimatsu

(2009), Brandenberg et al. (2005) κ.α., εκτός από τις αρχικές συνθήκες και την διάμετρο του πασσάλου, η συμπεριφορά φαίνεται να εξαρτάται και από τα χαρακτηριστικά του πασσάλου (ακαμψία, τρόπος εγκατάστασης, συνθήκες στήριξης της κεφαλής) καθώς και τις συνθήκες στράγγισης (εδαφική διαπερατότητα, περίοδος διέγερσης). Επιπλέον, οι Gonzalez et al. (2009) κατέδειξαν ότι για τυπικές τιμές της διαπερατότητας του εδάφους, είναι δυνατόν να αναπτυχθούν σημαντικές αρνητικές πιέσεις πόρων σε μικρά βάθη στην περιοχή γύρω από τον πάσσαλο, ως αποτέλεσμα της έντονης διαστολικότητας που αναπτύσσεται λόγω ροής του ρευστοποιημένου εδάφους γύρω από τον πάσσαλο. Το φαινόμενο αυτό, δεν λαμβάνεται υπόψη στις υπάρχουσες μεθοδολογίες, παρά το γεγονός ότι προκαλεί αύξηση (και όχι απομείωση) των εδαφικών ωθήσεων σε σχέση με το «ξηρό» έδαφος, και επομένως επιβαρύνει σημαντικά την καταπόνηση του πασσάλου.

II. Σκοπός της Διατριβής

Η ανωτέρω συνοπτική περιγραφή καταδεικνύει την ύπαρξη σημαντικών αβεβαιοτήτων στις υφιστάμενες μεθοδολογίες εκτίμησης των καμπυλών p-y, τόσο για «ξηρό» όσο και για ρευστοποιημένο έδαφος, οι οποίες δεν κατέστη μέχρι σήμερα δυνατόν να διερευνηθούν αποτελεσματικά μέσω πειραματικών μεθόδων.

Στο πλαίσιο αυτό, **σκοπός της Διατριβής** είναι η συστηματική διερεύνηση των μηχανισμών που επιδρούν στις καμπύλες p-y για πασσάλους σε άμμους υπό οριζόντια φορτία λόγω μετακίνησης του εδάφους, και η διατύπωση βελτιωμένων, πολυπαραμετρικών σχέσεων υπολογισμού, συναρτήσει των χαρακτηριστικών του εδάφους, του πασσάλου και της σεισμικής διέγερσης.

Προκειμένου να παρακαμφθούν οι αντικειμενικοί περιορισμοί των πειραματικών διερευνήσεων που αναφέρθηκαν στην προηγούμενη παράγραφο, η παρούσα έρευνα βασίσθηκε σε «αριθμητικά πειράματα», δηλαδή σοφιστευμένες αριθμητικές αναλύσεις οι οποίες επιτρέπουν: την παράλληλη προσομοίωση της δυναμικής φόρτισης του εδάφους, την ανάπτυξη υπερπιέσεων πόρων, την ροή υγρού των πόρων κατά την διάρκεια της φόρτισης, καθώς και την έντονα μη γραμμική συμπεριφορά των εδαφικών στοιχείων λόγω της ανακυκλικής φόρτισης και της ρευστοποίησης που προκαλεί η σεισμική δόνηση.

Έμφαση δίνεται στην περίπτωση πασσάλων σε έδαφος υπό καθεστώς ρευστοποίησης και πλευρικής εξάπλωσης, η οποία έρχεται συχνά στην επικαιρότητα, μετά από κάθε

ισχυρό σεισμό. Προηγείται βέβαια η διερεύνηση για «ξηρό» έδαφος, δεδομένου ότι αποτελεί αφετηρία για την κατανόηση της αλληλεπίδρασης πασσάλου-εδάφους, αλλά και βάση αναφοράς για το πλέον πολύπλοκο πρόβλημα της αλληλεπίδρασης του πασσάλου με το ρευστοποιημένο έδαφος.

Αναγνωρίζοντας ότι, από την φύση τους, οι αριθμητικές αναλύσεις ανήκουν στην σφαίρα του «δυνητικού ρεαλισμού» (virtual reality), καταβλήθηκε κάθε προσπάθεια πιστοποίησης των αριθμητικών μεθόδων και των αποτελεσμάτων έναντι καλά τεκμηριωμένων πειραματικών μετρήσεων, αλλά και συσχέτισης των προτεινόμενων νέων καμπυλών p-y με υφιστάμενες, οι οποίες αποτελούν σήμερα την βάση σχεδιασμού οριζόντια φορτιζόμενων πασσάλων.

III. Επιμέρους Ερευνητικές Εργασίες

ΕΕ 1. Βιβλιογραφική Αναδρομή

Όπως προαναφέρθηκε, το πρόβλημα της οριζόντιας φόρτισης πασσάλων έχει αποτελέσει αντικείμενο εκτενούς έρευνας κατά το παρελθόν. Ως εκ τούτου, το πρώτο βήμα ήταν η μελέτη των σχετικών δημοσιεύσεων με στόχο την συγκέντρωση και κριτική αξιολόγηση:

(α) των υφιστάμενων μεθοδολογιών σχεδιασμού πασάλων υπό οριζόντια φόρτιση με την μέθοδο BNWF, σε «ξηρά» και σε ρευστοποιημένα εδάφη.

(β) των κυριοτέρων συμπερασμάτων και παρατηρήσεων αναφορικά με τους μηχανισμούς που καθορίζουν την συμπεριφορά, καθώς και τις παραμέτρους που επιδρούν σημαντικά στο πρόβλημα.

Τα συμπεράσματα της βιβλιογραφικής έρευνας συνέβαλαν στην κατανόηση των κυριοτέρων χαρακτηριστικών της αλληλεπίδρασης πασσάλου-εδάφους, και κατ' επέκταση στην οργάνωση της παραμετρικής διερεύνησης του προβλήματος μέσω αριθμητικών αναλύσεων, καθώς και στην μετέπειτα επεξεργασία των αποτελεσμάτων.

ΕΕ 2. Αριθμητική Προσομοίωση Πασσάλου σε «Ξηρό» Έδαφος

Η αριθμητική προσομοίωση ήταν στατική και αφορούσε έναν μεμονωμένο πάσσαλο που μετακινείται οριζόντια, ως άκαμπτο σώμα, εντός του εδάφους. Το έδαφος θεωρήθηκε ως απόλυτα διαπερατό ή «ξηρό». Δεδομένης της πολυπλοκότητας του εν

λόγω προβλήματος που εξετάζεται, έγινε εξ' αρχής κατανοητό ότι θα πρέπει να αξιοποιηθούν στο έπακρο οι δυνατότητες που προσφέρουν οι σύγχρονες αριθμητικές μέθοδοι ανάλυσης. Έτσι, η αριθμητική προσομοίωση βασίστηκε στις ακόλουθες επιλογές και παραδοχές:

(α) Έγινε χρήση του κώδικα πεπερασμένων διαφορών FLAC3D. Αξίζει να σημειωθεί ότι στον κώδικα αυτό εφαρμόζεται ένας μη πεπλεγμένος αλγόριθμος αριθμητικής ολοκλήρωσης, γεγονός που τον καθιστά υπολογιστικά πιο αποτελεσματικό σε έντονα μη-γραμμικά προβλήματα μεγάλων μετατοπίσεων με χρονική εξέλιξη (π.χ. ροή υγρού των πόρων, δυναμική φόρτιση). Επίσης, επιτρέπει την ενσωμάτωση από τον Χρήστη εξειδικευμένων καταστατικών προσομοιωμάτων (User-Defined-Models) για την ακριβέστερη προσομοίωση της συμπεριφοράς του εδαφικού στοιχείου.

(β) Χρησιμοποιήθηκε το καταστατικό προσομοίωμα NTUA_Sand (Papadimitriou and Bouckovalas, 2002, και Andrianopoulos et al., 2010), όπως ενσωματώθηκε στον κώδικα FLAC3D στα πλαίσια της διδακτορικής διατριβής του Δ. Καραμήτρου (2010). Το εν λόγω προσομοίωμα υιοθετεί την θεωρία «Κρίσιμης Κατάστασης των Εδαφών» με αποτέλεσμα η επίδραση της αρχικής κατάστασης (σχετική πυκνότητα και τάση εγκιβωτισμού) να λαμβάνεται υπόψη μόνο με μια ομάδα παραμέτρων. Επίσης, η ελαστική απόκριση εκφράζεται από τις σχέσεις των Ramberg-Osgood με αποτέλεσμα να προσομοιώνεται με ακρίβεια η υστερητική μη-γραμμικη συμπεριφορά κατά την δυναμική – ανακυκλική φόρτιση (μείωση του μέτρου διάτμησης και αύξηση της υστερητικής απόσβεσης με την επιβαλλόμενη διατμητική παραμόρφωση). Τέλος, ποσοτικοποιείται η επίδραση της αλλαγής της δομής (fabric) της άμμου, ένα φαινόμενο ιδιαίτερης σημασίας για την προσομοίωση της συσσώρευσης πλαστικών παραμορφώσεων ή/και υπερπιέσεων πόρων κατά την ανακυκλική φόρτιση (shakedown effects).

(γ) Τοποθετήθηκαν ειδικά στοιχεία διεπιφάνειας μεταξύ του πασσάλου και του περιβάλλοντος εδάφους, τα οποία επιτρέπουν την ελαστο-πλαστική ολίσθηση ή/και την αποκόλληση πασσάλου-εδάφους. Η χρήση στοιχείων διεπιφάνειας είναι αναγκαία για την ακριβή προσομοίωση των μηχανισμών παραμόρφωσης του εδάφους, ειδικά πλησίον της επιφάνειας του εδάφους όπου η σχετική μετακίνηση του εδάφους ως προς τον πάσσαλο αποτελεί τον κύριο μηχανισμό αλληλεπίδρασης.

(δ) Υπολογίζονται απευθείας οι καμπύλες p-y, με βάση τις ορθές και διατμητικές τάσεις στους κόμβους των στοιχείων διεπιφάνειας, μέσω ειδικής συνάρτησης γραμμένης στην παρεχόμενη από το FLAC3D γλώσσα προγραμματισμού FISH.

(ε) Όλες οι επιμέρους παραδοχές της αριθμητικής μεθοδολογίας (μέγεθος καννάβου, διακριτοποίηση, ιδιότητες στοιχείων διεπιφάνειας κ.λ.π.) αξιολογήθηκαν μέσω μιας σειράς παραμετρικών αναλύσεων ευαισθησίας, με γνώμονα την επίδραση στην προβλεπόμενη συμπεριφορά του πασσάλου.

Στο **Σχήμα 7** φαίνεται ο κάνναβος που χρησιμοποιήθηκε για τις αριθμητικές αναλύσεις, ενώ στο **Σχήμα 8** φαίνεται η παραμορφωμένη μορφή του, μετά την επιβολή οριζόντιας μετατόπισης του πασσάλου. Στα μικρά βάθη διακρίνεται ο μηχανισμός αστοχίας μορφής σφήνας, ενώ στα μεσαία και μεγάλα βάθη η αστοχία λαμβάνει χώρα μόνο στο οριζόντιο επίπεδο (αστοχία επίπεδης παραμόρφωσης). Τέλος στο **Σχήμα 9** παρουσιάζονται αριθμητικές καμπύλες p-y.

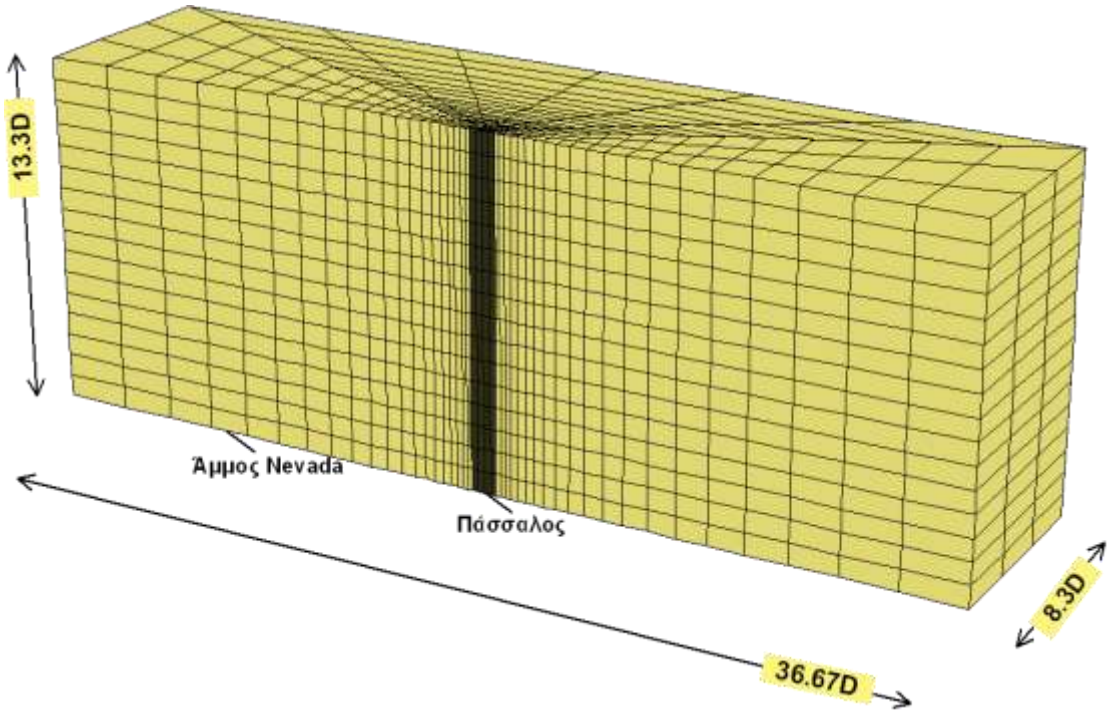

Σχήμα 7: Κάνναβος προσομοίωσης πασσάλου σε «ξηρό» έδαφος.

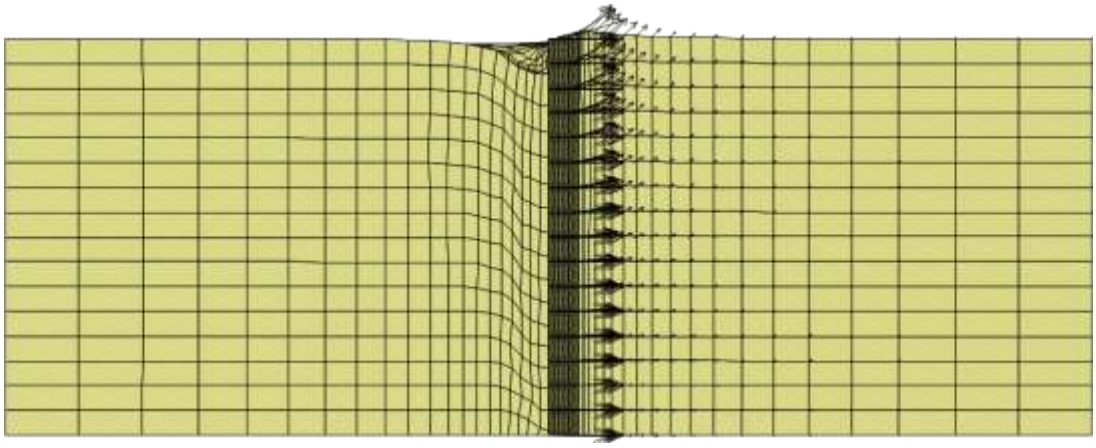

Σχήμα 8: Παραμορφωμένος κάνναβος και διανύσματα μετατόπισης μετά την επιβολή οριζόντιας κινηματικής φόρτισης. Στα μικρά βάθη διακρίνεται ο μηχανισμός αστοχίας σφήνας και στα μεσαία και μεγάλα η αστοχία επίπεδης παραμόρφωσης.

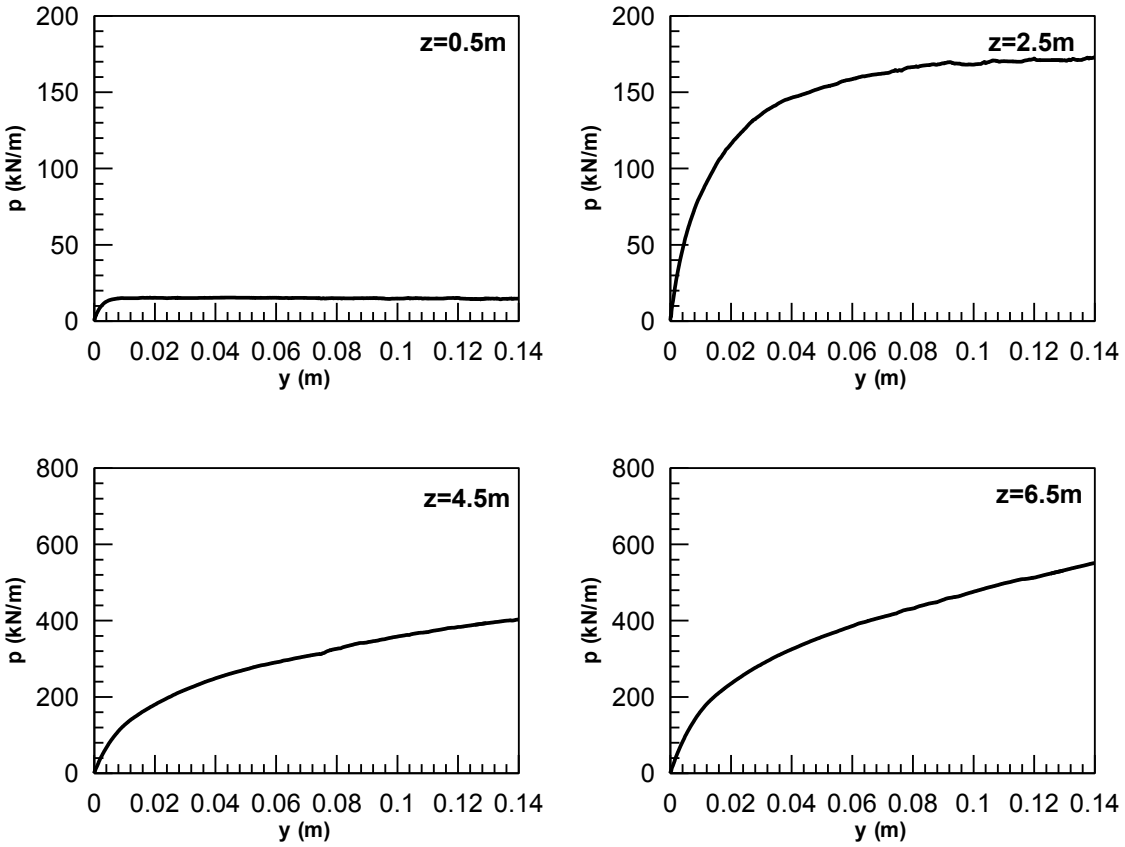

Σχήμα 9: Τυπικές αριθμητικές καμπύλες p-y για διάφορα βάθη κατά μήκος του πασσάλου.

ΕΕ 3. Αριθμητική Προσομοίωση της Εγκατάστασης Πασσάλου

Όπως προαναφέρθηκε, κατά την τοποθέτηση πασσάλων με έμπηξη, τόσο οι τάσεις όσο και οι ογκομετρικές παραμορφώσεις στο περιβάλλον έδαφος μεταβάλλονται σε σχέση με το ελεύθερο πεδίο. Από βιβλιογραφική αναδρομή προέκυψε, αρχικά, ότι ο μηχανισμός οριζόντιας εκτόπισης του εδάφους κατά την έμπηξη του πασσάλου είναι διαφορετικός ανάλογα με την απόσταση από την ελεύθερη επιφάνεια του εδάφους: ένα παθητικό πρίσμα Rankine κοντά στην επιφάνεια, και αξονο-συμμετρική διεύρυνση κυλινδρικής κοιλότητας στο υπόλοιπο μήκος του πασσάλου (πλην της αιχμής).

Κατ᾽ επέκταση των ανωτέρω, υιοθετήθηκε η αναλυτική μέθοδος του Vesic (1972) για την εκτίμηση των τάσεων λόγω διεύρυνσης κυλινδρικής κοιλότητας, και προγραμματίστηκε στην παρεχόμενη από το FLAC3D γλώσσα προγραμματισμού FISH. Με τον τρόπο αυτό οι τροποποιημένες τάσεις λόγω της εγκατάστασης του πασσάλου υπολογίζονται αναλυτικά για όλα τα εδαφικά στοιχεία, ένα βήμα πριν από την επιβολή της οριζόντιας φόρτισης. Έτσι αποφεύγεται η ανάγκη πλήρους αριθμητικής προσομοίωσης της εγκατάστασης του πασσάλου, που θα επιβάρυνε σημαντικά τον συνολικό χρόνο εκτέλεσης της ανάλυσης, μια και η αριθμητική προσομοίωση της διεύρυνσης πλευρικής κοιλότητας αυξάνει δραματικά τις απαιτήσεις όσον αφορά τις διαστάσεις του καννάβου.

Η μέθοδος του Vesic είναι απλή στον προγραμματισμό της, ενώ επιπλέον στηρίζεται σε μια σειρά παραμέτρων σαφώς καθορισμένων (ελαστικές σταθερές, γωνία τριβής, ειδικό βάρος, διάμετρος και πάχος τοιχώματος πασσάλου). Οι μόνες παράμετροι που είναι δυσχερείς ως προς την εκτίμησή τους είναι η ογκομετρική παραμόρφωση (Δ) και ο λόγος του Poisson (ν) στην πλαστική ζώνη που δημιουργείται γύρω από τον πάσσαλο. Για την βαθμονόμηση των μεγεθών αυτών εκτελέστηκαν 96 αριθμητικές αναλύσεις προσομοίωσης του φαινομένου διεύρυνσης κυλινδρικής κοιλότητας σε μια οριζόντια λωρίδα εδάφους, για διάφορες τιμές της σχετικής πυκνότητας, της τάσης εγκιβωτισμού και του μεγέθους της διεύρυνσης που προκαλεί η έμπηξη του πασσάλου (**Σχήμα 10**). Από την επεξεργασία των αποτελεσμάτων προέκυψαν εμπειρικές σχέσεις εκτίμησης των Δ και ν, που ενσωματώθηκαν στην υπορουτίνα προγραμματισμού της μεθόδου του Vesic.

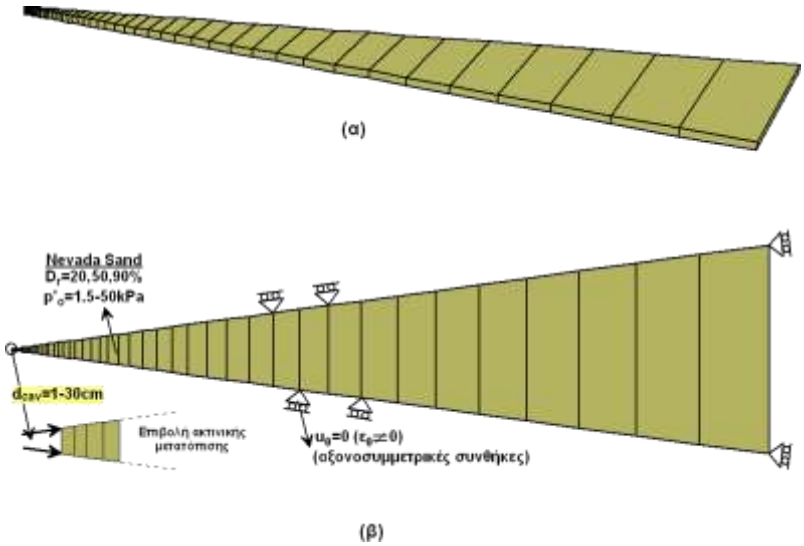

Σχήμα 10: Κάνναβος παραμετρικών αναλύσεων προσομοίωσης διεύρυνσης κυλινδρικής κοιλότητας.

Η ημι-αναλυτική αυτή διαδικασία καλύπτει το μεγαλύτερο κατά μήκος τμήμα του πασσάλου, όπου η έμπηξη αντιστοιχεί πρακτικά σε διεύρυνση κυλινδρικής κοιλότητας. Ωστόσο, όπως αναφέρθηκε νωρίτερα, κοντά στην επιφάνεια του εδάφους, η απόκριση χαρακτηρίζεται από τη δημιουργία ενός πρίσματος παθητικής ολίσθησης κατά Rankine. Η κινηματική αυτή ασυμφωνία κοντά στην επιφάνεια του εδάφους δεν χρειάσθηκε να προσομοιωθεί ξεχωριστά, δεδομένου ότι αναγνωρίζεται και διορθώνεται από το ίδιο το λογισμικό, προκειμένου να εξασφαλισθεί η συμβατότητα με τις συνοριακές συνθήκες της ελεύθερης επιφάνειας. Συγκεκριμένα, μόλις καλείται η συνάρτηση Vesic και εισάγονται οι τροποποιημένες τάσεις στο σύστημα, ο κώδικας στην προσπάθειά του να επαναφέρει ισορροπία αναπτύσσει κατακόρυφες μετακινήσεις στην επιφάνεια, οδηγώντας στο σχηματισμού του παθητικού πρίσματος και σε αντίστοιχη τροποποίηση των τάσεων εντός αυτού.

Η προτεινόμενη διαδικασία αξιολογήθηκε μέσω αναλύσεων πλήρους προσομοίωσης της εγκατάστασης του πασσάλου. Στο **Σχήμα 11** φαίνονται οι κατανομές των ακτινικών, εφαπτομενικών και κατακόρυφων τάσεων συναρτήσει της απόστασης από την διεπιφάνεια πασσάλου-εδάφους, όπως προκύπτουν από τις αναλυτικές εξισώσεις του Vesic, από την εφαρμογή της υπορουτίνας FISH και από την πλήρη προσομοίωση της εγκατάστασης του πασσάλου. Τέλος, στο **Σχήμα 12** η ημι-αναλυτική διαδικασία αξιολογείται σε επίπεδο καμπυλών p-y που είναι και το βασικό ζητούμενο της παρούσης έρευνας.

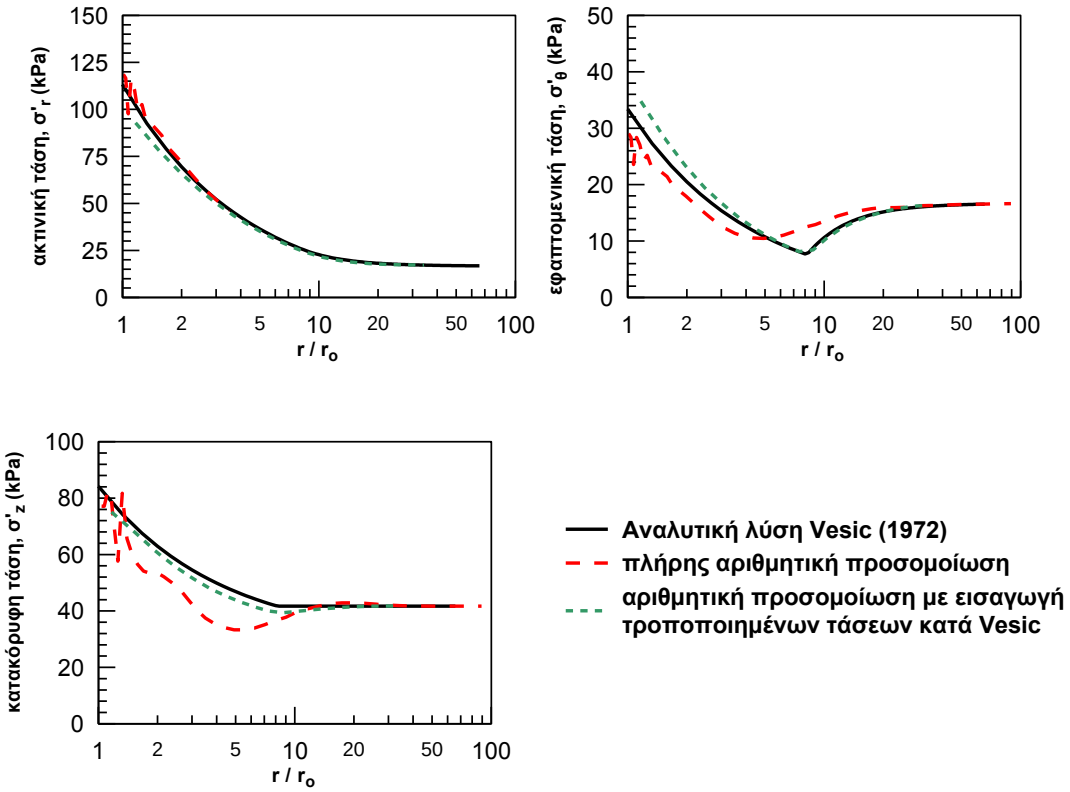

Σχήμα 11: Μεταβολή τάσεων λόγω εγκατάστασης πασσάλου εκτοπίσεως – αξιολόγηση προτεινόμενης μεθοδολογίας.

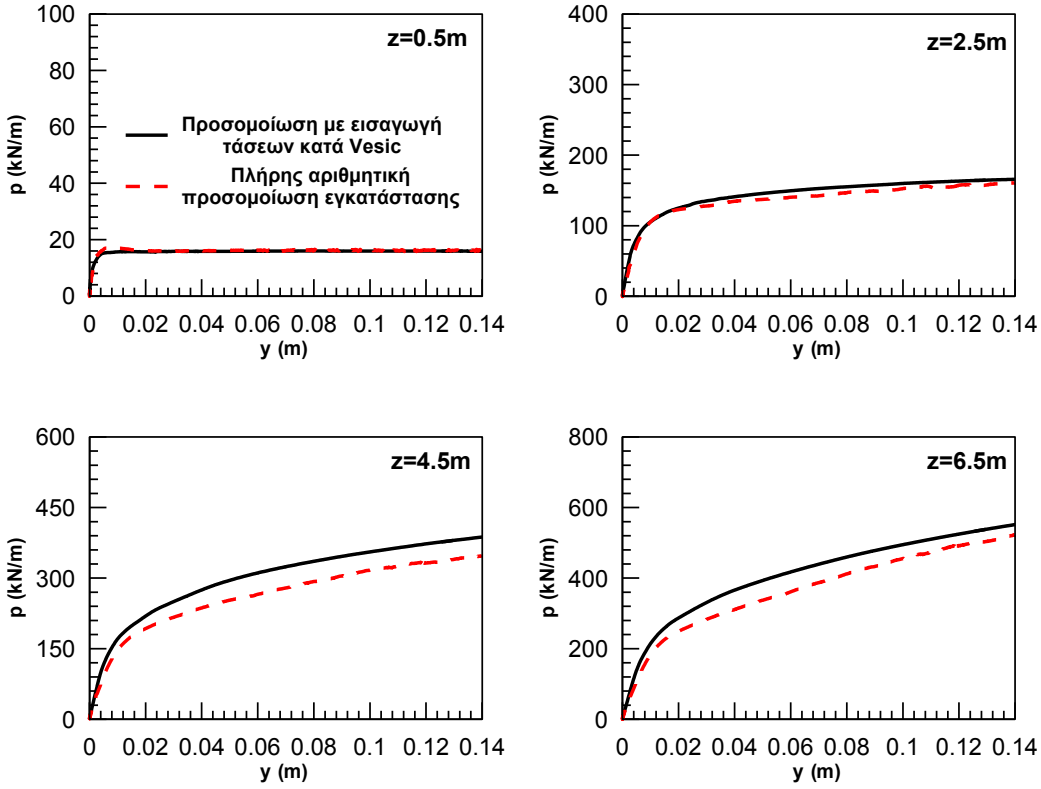

Σχήμα 12: Αξιολόγηση μεθοδολογίας προσομοίωσης εγκατάστασης πασσάλου σε όρους καμπυλών p-y.

ΕΕ 4. Παραμετρική Διερεύνηση & Βελτιωμένες Καμπύλες p-y για «Ξηρό» Έδαφος

Η ανωτέρω αριθμητική μεθοδολογία χρησιμοποιήθηκε για την παραμετρική διερεύνηση της απόκρισης πασσάλων σε «ξηρά» εδάφη υπό οριζόντια κινηματική φόρτιση. Η διερεύνηση αφορούσε την επίδραση της σχετικής πυκνότητας του εδάφους, της διαμέτρου του πασσάλου, καθώς και της μεθόδου εγκατάστασης (έμπηξη ή εκσκαφή). Επιπλέον, εκτελέστηκε ένας μικρός σχετικά αριθμός αναλύσεων που αφορούσε στη φόρτιση πασσάλου, όχι λόγω εδαφικής μετακίνησης, αλλά λόγω εξωτερικού συγκεντρωμένου φορτίου στην κεφαλή. Το σύνολο των αναλύσεων που πραγματοποιήθηκαν φαίνονται στον **Πίνακα 1**.

Πίνακας 1: Παραμετρικές Αναλύσεις κινηματικής φόρτισης πασσάλου σε «ξηρό» έδαφος.

α/α	**Σχετική Πυκνότητα (%)**	**Διάμετρος Πασσάλου (m)**	**Μέθοδος Κατασκευής**	**Τύπος Φόρτισης**
1	50	0.6	Εκσκαφή	Ομοιόμορφη πλευρική μετακίνηση
2	20	0.6	Εκσκαφή	Ομοιόμορφη πλευρική μετακίνηση
3	90	0.6	Εκσκαφή	Ομοιόμορφη πλευρική μετακίνηση
4	50	0.4	Εκσκαφή	Ομοιόμορφη πλευρική μετακίνηση
5	50	1.0	Εκσκαφή	Ομοιόμορφη πλευρική μετακίνηση
6	50	0.6	Έμπηξη (d_{cav}=1cm)*	Ομοιόμορφη πλευρική μετακίνηση
7	50	0.6	Έμπηξη (d_{cav}=10 cm)	Ομοιόμορφη πλευρική μετακίνηση
8	50	0.6	Έμπηξη (d_{cav}=30 cm)	Ομοιόμορφη πλευρική μετακίνηση
9	50	0.4	Έμπηξη (d_{cav}=1 cm)	Ομοιόμορφη πλευρική μετακίνηση
10	50	0.4	Έμπηξη (d_{cav}=13 cm)	Ομοιόμορφη πλευρική μετακίνηση
11	50	0.4	Έμπηξη (d_{cav}=20 cm)	Ομοιόμορφη πλευρική μετακίνηση
12	50	0.6	Εκσκαφή	Συγκεντρωμένη δύναμη στην κεφαλή (με ελεύθερη στροφή)
13	50	0.6	Εκσκαφή	Συγκεντρωμένη δύναμη στην κεφαλή (με δεσμευμένη στροφή)

*d_{cav}: Πάχος τοιχώματος διατομής

Στατιστική επεξεργασία των αποτελεσμάτων των παραμετρικών αναλύσεων οδήγησε ακολούθως στην διατύπωση βελτιωμένων καμπυλών p-y για μεμονωμένους πασσάλους σε «ξηρά» αμμώδη εδάφη, υποκείμενων σε οριζόντιες εδαφικές μετατοπίσεις. Οι προτεινόμενες καμπύλες p-y συγκρίθηκαν και αξιολογήθηκαν σε σχέση με τις υφιστάμενες σχέσεις που εντοπίσθηκαν στα πλαίσια της Επιμέρους Εργασίας ΕΕ 1.

ΕΕ 5. Αριθμητική Προσομοίωση Πασσάλου σε Ρευστοποιημένο Έδαφος

Η εν λόγω αριθμητική προσομοίωση ήταν δυναμική και αφορούσε ένα κεκλιμένο έδαφος που ρευστοποιείται κατά την σεισμική δόνηση, και έναν εύκαμπτο μεμονωμένο πάσσαλο που έχει πακτωθεί στην βάση του καννάβου. Το έδαφος θεωρήθηκε ως κορεσμένο με δεδομένο κάθε φορά συντελεστή διαπερατότητας. Ο κάνναβος που χρησιμοποιήθηκε για την ανάλυση φαίνεται στο **Σχήμα 13**. Πέραν των όσων στοιχείων παρέχονται ανωτέρω (Επιμέρους Εργασίες ΕΕ 2 και ΕΕ 3) σχετικά με την αριθμητική προσομοίωση σε «ξηρό» έδαφος, οι αναλύσεις για ρευστοποιημένο έδαφος έλαβαν επιπλέον υπόψη τα ακόλουθα:

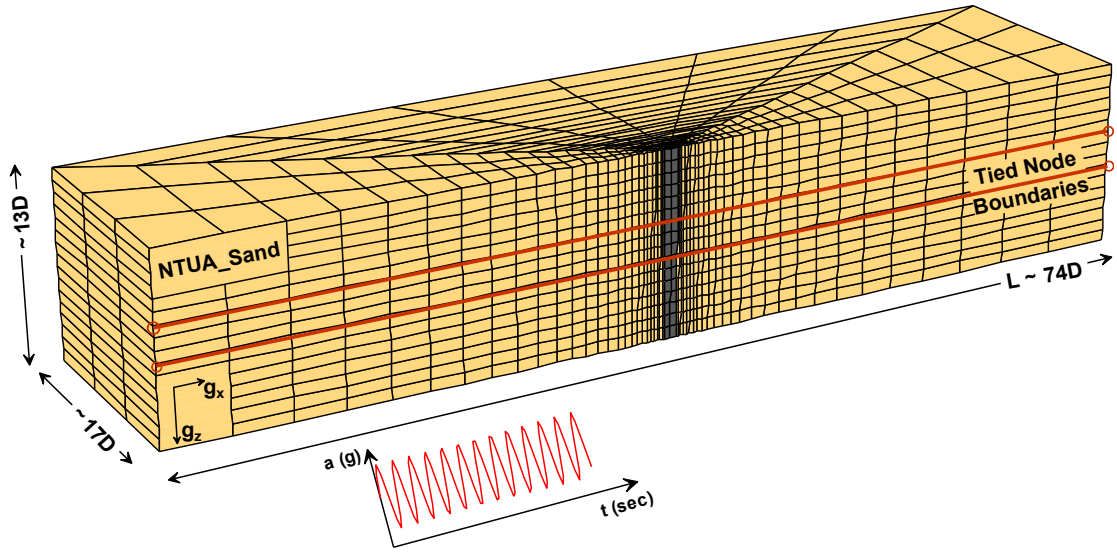

Σχήμα 13: Κάνναβος αναλύσεων μεμονωμένου πασσάλου σε ρευστοποιημένο έδαφος υπό πλευρική εξάπλωση

(α) Ενεργοποιήθηκε η δυνατότητα που παρέχει ο κώδικας FLAC3D για σύζευξη της δυναμικής ανάλυσης ενεργών τάσεων με ανάλυση υδατικής ροής. Επιπλέον διερευνήθηκαν τρία (3) σενάρια αναφορικά με την τιμή της διαπερατότητας του ρευστοποιημένου εδάφους:

- Διαπερατότητα υπό στατικές συνθήκες (Arulmoli et al., 1992)
- Διαπερατότητα υπό δυναμικές συνθήκες (Liu and Dobry, 1997)
- Διαπερατότητα διαρκώς μεταβαλλόμενη κατά τη φόρτιση συναρτήσει του λόγου υπερπιέσεων πόρων (Shahir et al., 2012).

(β) Τα συμβατικά πλευρικά σύνορα «συζευγμένων κόμβων» (tied nodes), τα οποία χρησιμοποιούνται στην περίπτωση σεισμικής φόρτισης εδαφών με οριζόντια στρωματογραφία και οριζόντια ελεύθερη επιφάνεια τροποποιήθηκαν

προκειμένου να λάβουν υπόψη την κλίση του φυσικού εδάφους, όπως εξηγείται λεπτομερέστερα στην επόμενη ενότητα.

(γ) Και σε αυτή την περίπτωση, όλες οι επιμέρους παραδοχές της αριθμητικής μεθοδολογίας (μέγεθος καννάβου, διακριτοποίηση, ιδιότητες στοιχείων διεπιφάνειας κ.λ.π.) αξιολογήθηκαν μέσω μιας σειράς παραμετρικών αναλύσεων ευαισθησίας. Επιπλέον, πριν από την παραμετρική διερεύνηση της κινηματικής αλληλεπίδρασης εδάφους-πασσάλου, η ποσοτική και ποιοτική ακρίβεια των αριθμητικών αναλύσεων αξιολογήθηκε έναντι αποτελεσμάτων από πρόσφατα πειράματα φυγοκεντριστή (Gonzalez et al. 2009).

Ενδεικτικά, στο **Σχήμα 14** συγκρίνονται οι καμπύλες p-y όπως προέκυψαν από τα εν λόγω πειράματα και τις αντίστοιχες αριθμητικές αναλύσεις, ενώ στο **Σχήμα 15** συγκρίνονται οι ισοκαμπύλες του λόγου υπερπιέσεων πόρων στο τέλος της διέγερσης. Πέραν της αξιοσημείωτης συμφωνίας μεταξύ αριθμητικών και πειραματικών αποτελεσμάτων, διαπιστώνεται πως η αριθμητική μεθοδολογία μπορεί να προβλέψει με ακρίβεια τα κύρια χαρακτηριστικά της δυναμικής απόκρισης πασσάλων υπό καθεστώς πλευρικής εξάπλωσης, όπως έχουν κατά καιρούς παρατηρηθεί σε πειραματικές δοκιμές φυγοκεντριστή και σεισμικής τράπεζας.

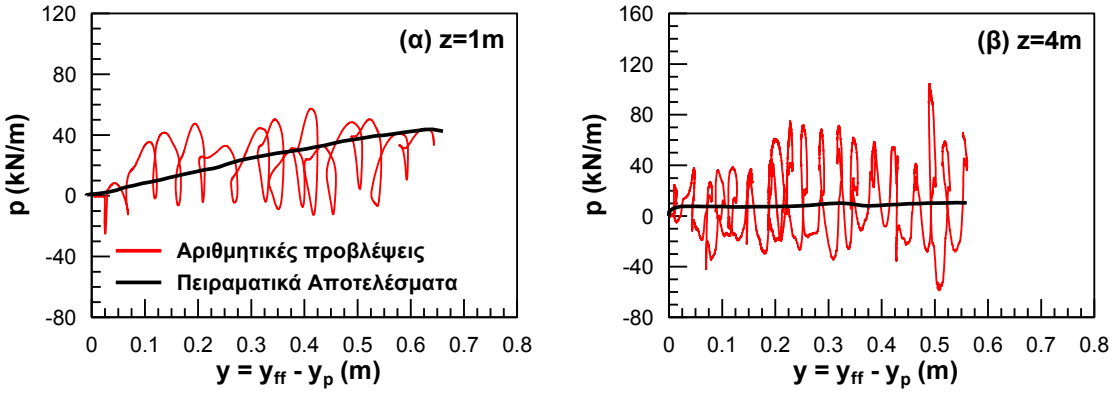

Σχήμα 14: Αξιολόγηση της Αριθμητικής Μεθοδολογίας: Σύγκριση πειραματικών και αριθμητικών καμπυλών p-y σε βάθος (α) z=1m και (β) z=4m από την επιφάνεια.

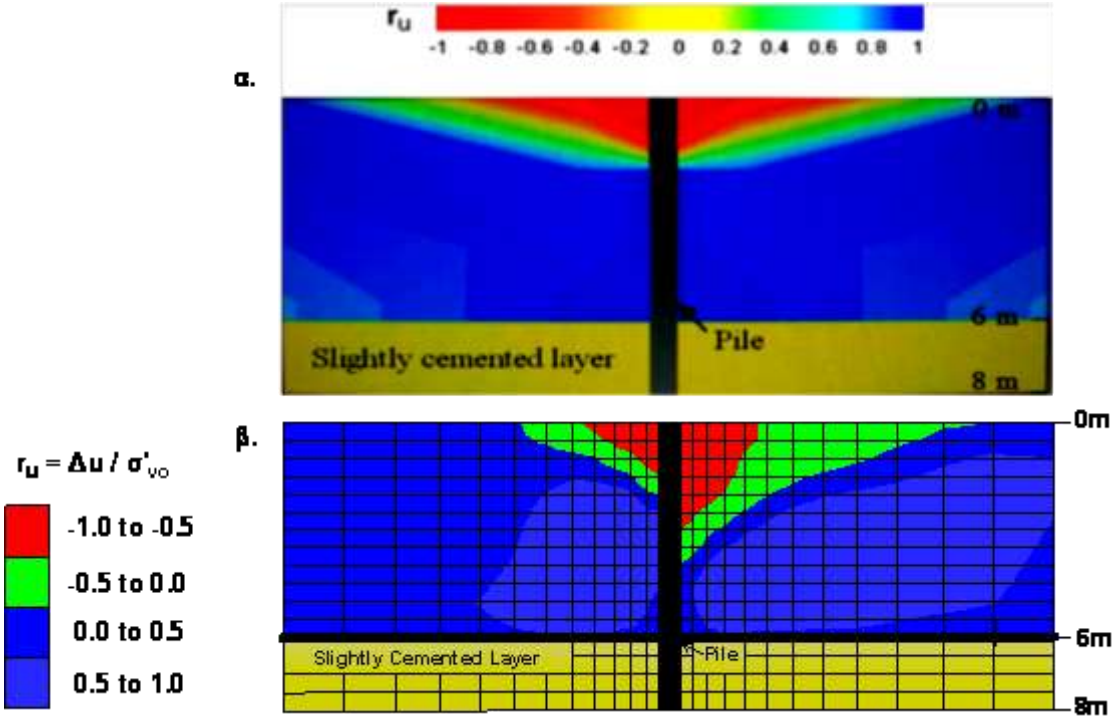

Σχήμα 15: Αξιολόγηση της Αριθμητικής Μεθοδολογίας: Ισοκαμπύλες λόγου υπερπιέσεων πόρων στο τέλος της διέγερσης (α) Πειραματικά αποτελέσματα (β) Αριθμητικές προβλέψεις

ΕΕ 6. <u>Ανάπτυξη Συνόρων Ελεύθερου Πεδίου για Προσομοίωση της Οριζόντιας Εξάπλωσης Κεκλιμένου Εδάφους</u>

Όπως προλογήθηκε, στα πλαίσια της Επιμέρους Εργασίας ΕΕ 5, μια σημαντική καινοτομία που έπρεπε να εισαχθεί στην αριθμητική ανάλυση για ρευστοποιημένο έδαφος, ήταν η ανάπτυξη μιας νέας μορφής συνοριακών συνθηκών ελεύθερου πεδίου για κεκλιμένο έδαφος. Ως αφετηρία για τη νέα μορφή συνόρων χρησιμοποιήθηκε η προγενέστερη και ευρέως διαδεδομένη συνθήκη συνοριακών συνθηκών για οριζόντια διαμορφωμένα εδάφη, κατά την οποία επιβάλλονται ίσες μετακινήσεις για κόμβους των πλευρικών συνόρων με το ίδιο υψόμετρο (tied nodes).

Η ιδιαιτερότητα των αναλύσεων για κεκλιμένο έδαφος προκύπτει από το γεγονός ότι, για οριζόντιο υδροφόρο ορίζοντα, οι υδροστατικές πιέσεις στα κατάντη είναι μεγαλύτερες από ότι στα ανάντη. Το γεγονός αυτό, σε συνδυασμό με την απαίτηση ισορροπίας απειρομήκους πρανούς για ίσες ενεργές τάσεις στα σημεία με ίδιο βάθος από την επιφάνεια του εδάφους, έχει ως αποτέλεσμα και οι ολικές τάσεις στα κατάντη να είναι μεγαλύτερες. Ως εκ τούτου, δημιουργείται μια προς-τα-κατάντη δρώσα δύναμη που ωθεί το πρανές να μετακινηθεί με την ίδια φορά, ακόμα και υπό συνθήκες στατικής ισορροπίας. Η συμπεριφορά αυτή δεν είναι βεβαίως συμβατή με

τις κινηματικές συνθήκες απειρομήκους πρανούς, και έχει ως αποτέλεσμα την ανομοιόμορφη κατανομή των αρχικών τάσεων και των μετατοπίσεων του καννάβου. Η τροποποίηση που επιβλήθηκε στις συνθήκες πλευρικών συνόρων βασίζεται στην επιβολή σε κάθε ζεύγος συζευγμένων κόμβων μιας προς-τα-ανάντη σταθερής δύναμης, η οποία υπολογίζεται κατάλληλα, συναρτήσει της διαφοράς των πιέσεων πόρων στα άκρα του καννάβου. Στο **Σχήμα 16** φαίνονται οι κατανομές διατμητικών τάσεων κατά τη φάση στατικής ισορροπίας του μοντέλου με την συμβατική και την τροποποιημένη θεώρηση.

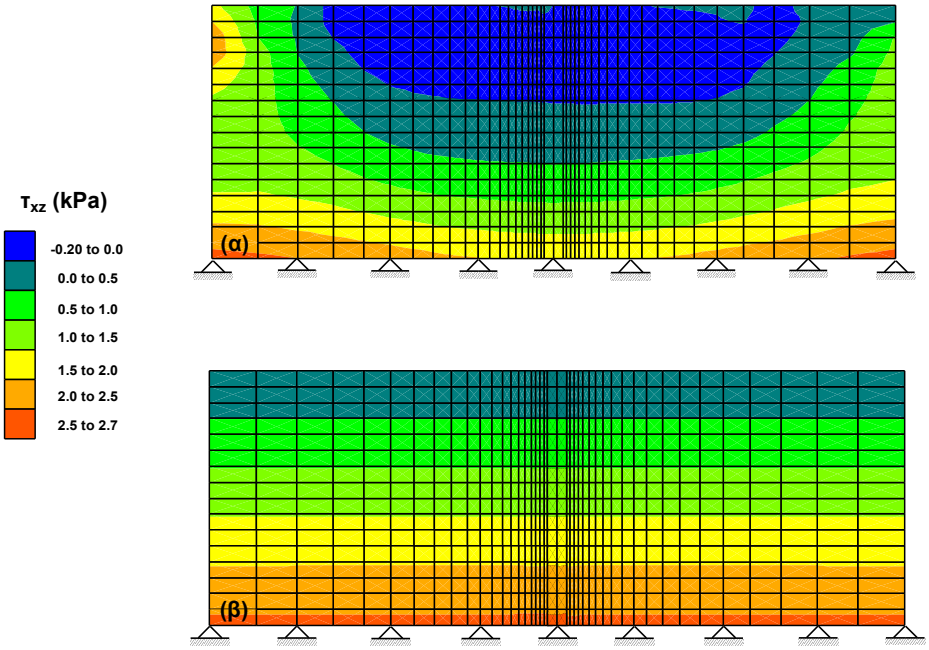

Σχήμα 16: Κατανομές διατμητικών τάσεων στο τέλος της στατικής ισορροπίας με (α) Συμβατικές (typical tied nodes – laminar box) (β) Τροποποιημένες συνοριακές συνθήκες (modified tied nodes –free field).

ΕΕ 7. <u>Παραμετρική Διερεύνηση & Βελτιωμένες Καμπύλες p-y για Ρευστοποιημένο Έδαφος</u>

Στην περίπτωση ρευστοποιημένου εδάφους, η παραμετρική διερεύνηση αφορούσε στην επίδραση επί των καμπυλών p-y των χαρακτηριστικών:

(α) του εδάφους [σχετική πυκνότητα (D_r), διαπερατότητα (k)],

(β) του πασσάλου [διάμετρος (D), δυσκαμψία (EI), συνθήκες στήριξης κεφαλής, μέθοδος κατασκευής], και

(γ) της σεισμικής δόνησης [περίοδος διέγερσης (T)].

Πίνακας 2: Παραμετρικές Αναλύσεις κινηματικής αλληλεπίδρασης πασσάλου σε ρευστοποιημένο έδαφος υπό καθεστώς πλευρικής εξάπλωσης

α/α	Ιδιότητες Εδάφους		Ιδιότητες Πασσάλου				Ιδιότητες Διέγερσης
	k (m/sec)	D_r (%)	D(m)	EI (kNm²)	Συνθήκες Στήριξης Κεφαλής	Μέθοδος Κατασκευής	T (sec)
1	6.1e-5	50	0.60	1300000	Ελεύθερη	Εκσκαφή	0.30
2	6.1e-5	35	0.60	1300000	Ελεύθερη	Εκσκαφή	0.30
3	6.1e-5	70	0.60	1300000	Ελεύθερη	Εκσκαφή	0.30
4	1.8e-5	50	0.60	1300000	Ελεύθερη	Εκσκαφή	0.30
5	1.8e-4	50	0.60	1300000	Ελεύθερη	Εκσκαφή	0.30
6	6.1e-4	50	0.60	1300000	Ελεύθερη	Εκσκαφή	0.30
7	1.8e-3	50	0.60	1300000	Ελεύθερη	Εκσκαφή	0.30
8	6.1e-5	50	0.40	1300000	Ελεύθερη	Εκσκαφή	0.30
9	6.1e-5	50	1.0	1300000	Ελεύθερη	Εκσκαφή	0.30
10	6.1e-5	50	0.60	250000	Ελεύθερη	Εκσκαφή	0.30
11	6.1e-5	50	0.60	325000	Ελεύθερη	Εκσκαφή	0.30
12	6.1e-5	50	1.0	2000000	Ελεύθερη	Εκσκαφή	0.30
13	6.1e-5	50	1.0	9750000	Ελεύθερη	Εκσκαφή	0.30
14	6.1e-5	50	1.0	1300000	Ελεύθερη	Έμπηξη*	0.30
15	6.1e-5	50	1.0	1300000	Ακλόνητη	Εκσκαφή	0.30
16	6.1e-5	50	1.0	1300000	Άστρεπτη	Εκσκαφή	0.30
17	6.1e-5	50	1.0	1300000	Ελεύθερη	Εκσκαφή	0.20
18	6.1e-5	50	1.0	1300000	Ελεύθερη	Εκσκαφή	0.50

*θεωρήθηκε πάχος διατομής ίσο με την ακτίνα του πασσάλου

Πραγματοποιήθηκαν δεκαοχτώ (18) συνολικά αναλύσεις, για τις τιμές των βασικών παραμέτρων που συνοψίζονται στον **Πίνακα 2**, και για κάθε μία ανάλυση, υπολογίσθηκαν οι μέσες καμπύλες p-y σε οχτώ (8) διαφορετικά βάθη κατά μήκος του πασσάλου. Έτσι, υπολογίστηκαν τελικώς 144 διαφορετικές καμπύλες p-y.

Η επεξεργασία των ανωτέρω αποτελεσμάτων οδήγησε αρχικά στον εντοπισμό των βασικών μηχανισμών που διέπουν την αλληλεπίδραση πασσάλου-εδάφους, και ακολούθως στην διατύπωση πολύ-παραμετρικών αναλυτικών σχέσεων για τον υπολογισμό των καμπυλών p-y του πλευρικώς εξαπλούμενου εδάφους. Τέλος, έγινε αποτίμηση της ακρίβειας των βελτιωμένων σχέσεων, έναντι προηγούμενων εμπειρικών σχέσεων της βιβλιογραφίας, τόσο με απ' ευθείας σύγκριση των καμπυλών p-y όσο και με σύγκριση των μετατοπίσεων και των ροπών του πασσάλου για συνήθεις εφαρμογές πρακτικού ενδιαφέροντος.

IV. Αποτελέσματα, Συμπεράσματα & Προτάσεις

IV.1. Κινηματική Αλληλεπίδραση Πασσάλου-Εδάφους σε «Ξηρό» Έδαφος

Όπως προαναφέρθηκε, η απόκριση πασσάλου σε «ξηρό» έδαφος, λόγω ομοιόμορφης οριζόντιας εδαφικής μετακίνησης, εξετάστηκε μέσω μιας σειράς παραμετρικών αναλύσεων που λαμβάνουν υπόψη την επίδραση της σχετικής πυκνότητας, της διαμέτρου και του τρόπου εγκατάστασης του πασσάλου. Παράλληλα εκτελέστηκε και ένας μικρός αριθμός αναλύσεων για την περίπτωση εξωτερικής φόρτισης λόγω συγκεντρωμένου φορτίου στην κεφαλή. Τα κύρια συμπεράσματα που προέκυψαν από την εν λόγω διερεύνηση είναι τα ακόλουθα:

Αλληλεπίδραση Πασσάλου – Εδάφους & Μορφή της Καμπύλης p-y

1. Διαπιστώθηκε η ύπαρξη ενός κρίσιμου βάθους $(z/D)_{cr}$, το οποίο οριοθετεί δύο (2) διαφορετικούς μηχανισμούς απόκρισης. Για βάθη μικρότερα από το $(z/D)_{cr}$, το έδαφος αστοχεί μέσω ενός μηχανισμού σφήνας, ενώ για μεγαλύτερα βάθη από το κρίσιμο ο μηχανισμός είναι επίπεδης αστοχίας.
2. Η μορφή της καμπύλης p-y μπορεί να περιγραφεί με ακρίβεια από μια υπερβολική σχέση της μορφής:

$$p = \frac{y}{\frac{1}{k_{ini} z} + \frac{y}{p_{ult}}} \tag{1}$$

3. Ο δείκτης αρχικής δυσκαμψίας, k_{ini}, δεν παραμένει σταθερός με το βάθος όπως προβλέπουν οι περισσότερες υπάρχουσες μεθοδολογίες (**Σχήμα 17α**). Συγκεκριμένα, για βάθη μικρότερα από το κρίσιμο ο δείκτης k_{ini}, μειώνεται σημαντικά με το βάθος, ενώ για βάθη μεγαλύτερα παραμένει πρακτικά σταθερός. Στα μικρά βάθη, και για άμμους μέσης πυκνότητας, οι τιμές του k_{ini} προσεγγίζονται καλύτερα από τις συστάσεις των Reese et al. (1974) ή API (2002), ενώ στα μεγάλα βάθη οι τιμές του k_{ini} είναι πιο κοντά στις συστάσεις του Terzaghi (1955). Η μεταβολή του k_{ini} με το βάθος μπορεί να περιγραφεί από την παρακάτω σχέση:

$$k_{ini,z} = k_{ini,0}\left(1 - \frac{z/D}{1 + z/D}\right) \tag{2}$$

όπου $k_{ini,0}$ η τιμή του δείκτη στην επιφάνεια του εδάφους.

4. Η οριακή εδαφική αντίδραση (p_{ult}), αδιαστατοποιημένη ως προς τη διάμετρο του πασσάλου (D) και την ενεργό κατακόρυφη τάση (σ'_{vo}), $p_{ult}/\sigma'_{vo}D$, αυξάνεται γραμμικά με το βάθος για βάθη μικρότερα του κρίσιμου, ενώ παραμένει πρακτικά σταθερή για μεγαλύτερα βάθη (**Σχήμα 17β**). Η μεταβολή του $p_{ult}/\sigma'_{vo}D$ με το βάθος προσεγγίζεται καλύτερα από την αναλυτική μεθοδολογία του Hansen (1961).

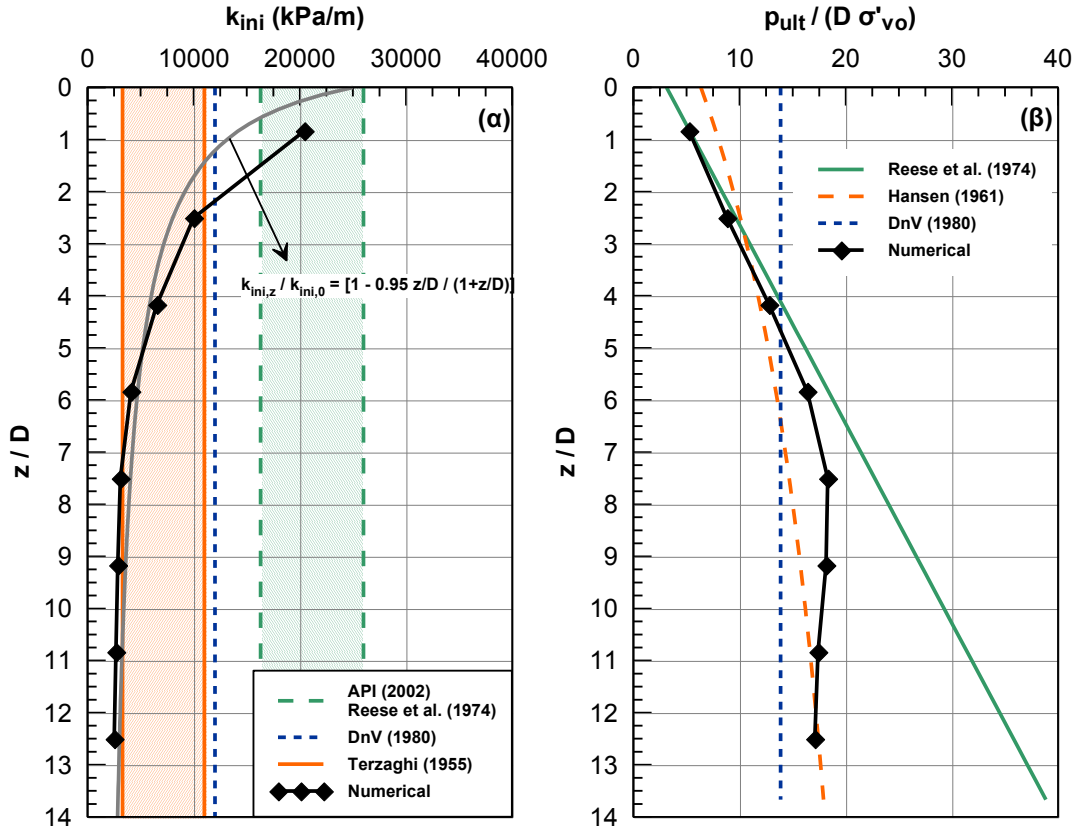

Σχήμα 17: Τυπική μεταβολή (α) δείκτη αρχικής δυσκαμψίας, k_{ini}, και (β) αδιαστατοποιημένης οριακής αντίδρασης, $p_{ult}/D\sigma'_{vo}$ με το βάθος για πασσάλους σε μη ρευστοποιημένα εδάφη υπό οριζόντια κινηματική φόρτιση (D_r=50%, D=0.60m).

Επίδραση Σχετικής Πυκνότητας, D_r

5. Αύξηση της Σχετικής Πυκνότητας προκαλεί αύξηση του κρίσιμου βάθους, $(z/D)_{cr}$, αλλαγής του μηχανισμού αστοχίας.
6. Ο δείκτης αρχικής δυσκαμψίας, k_{ini}, αυξάνεται ομοιόμορφα και ανεξαρτήτως βάθους με το D_r. Η σχετική επίδραση της σχετικής πυκνότητας στο k_{ini}, προβλέπεται καλύτερα από την μεθοδολογία DnV (1980).

7. Η οριακή εδαφική αντίδραση αυξάνεται με την σχετική πυκνότητα του εδάφους. Ωστόσο καμία από τις υπάρχουσες μεθοδολογίες δεν προβλέπει ικανοποιητικά την σχετική επίδραση, με εξαίρεση τις μεθοδολογίες των Hansen (1961) και DnV (1980) για τις οποίες η απόκλιση είναι μικρότερη.

Επίδραση Διαμέτρου Πασσάλου, D

8. Το κρίσιμο βάθος, $(z/D)_{cr}$, αλλαγής του μηχανισμού αστοχίας μειώνεται με την αύξηση της διαμέτρου.
9. Ο δείκτης αρχικής δυσκαμψίας, k_{ini}, αυξάνεται με τη διάμετρο για βάθη μικρότερα του κρίσιμου, ενώ παραμένει αμετάβλητος για βάθη μεγαλύτερα του κρίσιμου. Καμία από τις υπάρχουσες μεθοδολογίες δεν προβλέπει μεταβολή του k_{ini} με τη διάμετρο.
10. Η οριακή εδαφική αντίδραση, $p_{ult}/\sigma'_{vo}D$, δεν επηρεάζεται από την διάμετρο για βάθη μικρότερα του κρίσιμου, ενώ μικραίνει όσο αυξάνει η διάμετρος για μεγαλύτερα βάθη. Η σχετική επίδραση προβλέπεται ικανοποιητικά από όλες τις αναλυτικές μεθοδολογίες.

Επίδραση Μεθόδου Εγκατάστασης Πασσάλου

11. Η μέθοδος εγκατάστασης δεν επηρεάζει την τιμή της οριακής εδαφικής αντίδρασης, $p_{ult}/\sigma'_{vo}D$.
12. Η τιμή του δείκτη αρχικής δυσκαμψίας μεταβάλλεται, ωστόσο, σημαντικά, και μπορεί να περιγραφεί από την ακόλουθη σχέση:

$$\frac{k_{ini,d_{cav}}}{k_{ini,d_{cav=0}}} = 1 + 3\sqrt{\frac{d_{cav}}{D}} \tag{3}$$

όπου, d_{cav} το πάχος του τοιχώματος του πασσάλου, ενώ $k_{ini,dcav}$ και $k_{ini,dcav=0}$, οι τιμές του δείκτη αρχικής δυσκαμψίας για την περίπτωση πασσάλου εκτοπίσεως και πασσάλου εκσκαφής αντίστοιχα.

Αναλυτική Μεθοδολογία Εκτίμησης καμπυλών p-y σε «ξηρό» έδαφος

13. Με βάση τις παραπάνω διαπιστώσεις και με κατάλληλη στατιστική επεξεργασία αναπτύχθηκε η παρακάτω μεθοδολογία αναλυτικής εκτίμησης των καμπυλών p-y για πάσσαλο σε «ξηρό» έδαφος υπό οριζόντια κινηματική φόρτιση:

- Σχήμα Καμπύλης

$$p = \frac{y}{\frac{1}{k_{ini} z} + \frac{y}{p_{ult}}} \tag{4}$$

- Δείκτης Αρχικής Δυσκαμψίας, k_{ini}

$$k_{ini} = k_{ini,0} \cdot \left(1 - \frac{z/D}{1 + z/D}\right) \cdot \left(\frac{D}{0.6m}\right)^{-0.35} \cdot \left(1 + 3\sqrt{\frac{d_{cav}}{D}}\right) \tag{5}$$

όπου:

$k_{ini,0}$: Δείκτης αρχικής δυσκαμψίας στην επιφάνεια του εδάφους (**Πίνακας 3**)

z: Βάθος από την επιφάνεια του εδάφους

D: Διάμετρος πασσάλου

d_{cav}: Πάχος τοιχώματος διατομής πασσάλου (για πασσάλους εκτόπισης)

Πίνακας 3: Μεταβολή δείκτη αρχικής δυσκαμψίας στην επιφάνεια του εδάφους συναρτήσει της σχετικής πυκνότητας

Σχετική Πυκνότητα	**Χαλαρές Άμμοι**	**Άμμοι Μέσης Πυκνότητας**	**Πυκνές Άμμοι**
$k_{ini,0}$ (kPa/m)	18000	30000	45000

- Οριακή εδαφική αντίδραση, p_{ult}

$$\frac{p_{ult}}{\sigma'_{vo} D} = \begin{cases} Reese\,et\,al\,(1974) - API\,(2002), & z/D < z/D_{cr} \\ \sigma\tau\alpha\theta\varepsilon\rho\acute{o} & , \; z/D > z/D_{cr} \end{cases} \tag{6}$$

Όπου ο όρος $(z/D)_{cr}$ αντιστοιχεί στο βάθος αλλαγής του μηχανισμού αστοχίας και μπορεί να υπολογιστεί ως εξής:

$$z/D_{cr} = (6-7) \cdot \left(\frac{D_r}{50\%}\right) \cdot \left(\frac{D}{0.6m}\right)^{-0.64} \tag{7}$$

Τέλος, υπενθυμίζεται ότι η αντοχή κατά API (2002) υπολογίζεται ως εξής:

$$\frac{p_{ult}}{\sigma'_{vo} D} = \min \begin{cases} C_1 \cdot z/D + C_2 \\ C_3 \end{cases} \tag{8}$$

Όπου C_1, C_2 και C_3 συντελεστές συναρτήσει της γωνίας τριβής του εδάφους:

$$C_1 = 0.115 \cdot 10^{0.0405 \cdot \varphi}$$
$$C_2 = 0.571 \cdot 10^{0.022 \cdot \varphi} \quad (9)$$
$$C_3 = 0.646 \cdot 10^{0.0555 \cdot \varphi}$$

Τέλος, οι αναλυτικές προβλέψεις συγκρίνονται στο **Σχήμα 18** με τις αντίστοιχες αριθμητικές σε όρους δείκτη αρχικής δυσκαμψίας (k_{ini}) και οριακής εδαφικής αντίδρασης (p_{ult}).

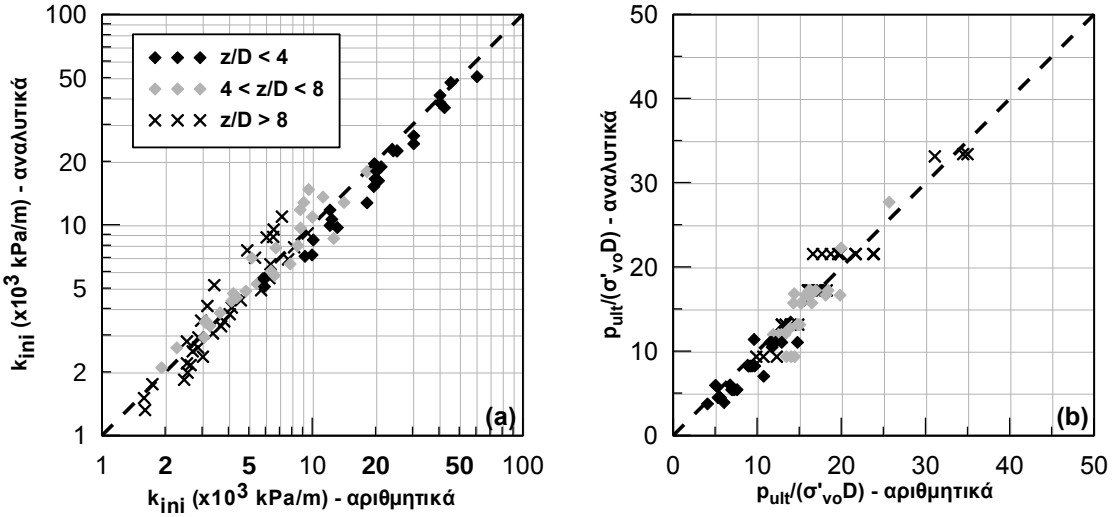

Σχήμα 18: Σύγκριση αναλυτικών και αριθμητικών προβλέψεων για (α) τον δείκτη αρχικής δυσκαμψίας και (β) την οριακή εδαφική αντίδραση

Επίδραση Τύπου Φόρτισης

14. Η επιβολή εξωτερικού φορτίου στην κεφαλή του πασσάλου προκαλεί μείωση του κρίσιμου βάθους κατά το οποίο λαμβάνει χώρα αλλαγή του μηχανισμού αστοχίας.
15. Η επιβολή συγκεντρωμένης δύναμης στην κεφαλή, σε σχέση με την ομοιόμορφη πλευρική μετακίνηση, οδηγεί σε ανάπτυξη πρόσθετων διατμητικών δυνάμεων κοντά στην επιφάνεια του εδάφους.
16. Έτσι, στα μικρά βάθη, αυξάνεται σημαντικά τόσο η τιμή του δείκτη αρχικής δυσκαμψίας, όσο και η οριακή εδαφική αντίδραση. Αντίθετα στα μεγάλα βάθη, που η αστοχία έχει τη μορφή επίπεδης παραμόρφωσης, η επίδραση είναι πρακτικά αμελητέα.

17. Η επίδραση της πρόσθετης διάτμησης στην οριακή αντίδραση λαμβάνεται υπόψη στις υπάρχουσες μεθοδολογίες μέσω του εμπειρικού συντελεστή A (Reese et al. 1974, Georgiadis et al. 1992). Οι προτεινόμενες τιμές του A προβλέπουν ικανοποιητικά την επίδραση κοντά στην επιφάνεια του εδάφους, ωστόσο υποεκτιμούν το βάθος στο οποίο η διάτμηση δεν επιδρά στην αντοχή, με αποτέλεσμα να προβλέπουν μειωμένες τιμές του λόγου $p_{ult}/\sigma'_{vo}D$ στα μεσαία βάθη.

V.2. Κινηματική Αλληλεπίδραση Πασσάλου-Εδάφους σε Ρευστοποιημένο Έδαφος υπό Καθεστώς Πλευρικής Εξάπλωσης.

Η απόκριση του πασσάλου σε έδαφος υπό καθεστώς πλευρικής εξάπλωσης εξετάστηκε μέσω μιας σειράς παραμετρικών αναλύσεων που αφορούσαν στις ιδιότητες του εδάφους (σχετική πυκνότητα, διαπερατότητα), του πασσάλου (διάμετρος, ακαμψία, μέθοδος εγκατάστασης, συνθήκες στήριξης της κεφαλής) και της διέγερσης (περίοδος). Έμφαση δόθηκε στους μηχανισμούς αλληλεπίδρασης πασσάλου-εδάφους, και κυρίως στην οριακή εδαφική πίεση. Όπως προαναφέρθηκε σημαντικό στοιχείο στην ανάλυση ήταν η εισαγωγή στην αριθμητική μεθοδολογία ενός νέου τύπου συνοριακών συνθηκών που λαμβάνει υπόψη την κεκλιμένη γεωμετρία του προβλήματος. Στο πλαίσιο της ανωτέρω διερεύνησης διαπιστώθηκαν τα εξής:

Επίδραση Πλευρικών Συνόρων στην Σεισμική Απόκριση Πασσάλου και Εδάφους

1. Η απόκριση του συστήματος με τις δύο (2) εναλλακτικές θεωρήσεις (typical vs. modified tied nodes) φαίνεται: (α) στο **Σχήμα 19**, όπου παρουσιάζεται η μορφή του παραμορφωμένου καννάβου και οι κατανομές των οριζόντιων μετακινήσεων στο τέλος της διέγερσης, και (β) στο **Σχήμα 20**, όπου συγκρίνονται οι κατανομές των οριζόντιων μετακινήσεων στο τέλος της διέγερσης τόσο κατά μήκος του πασσάλου όσο και στο ελεύθερο πεδίο.

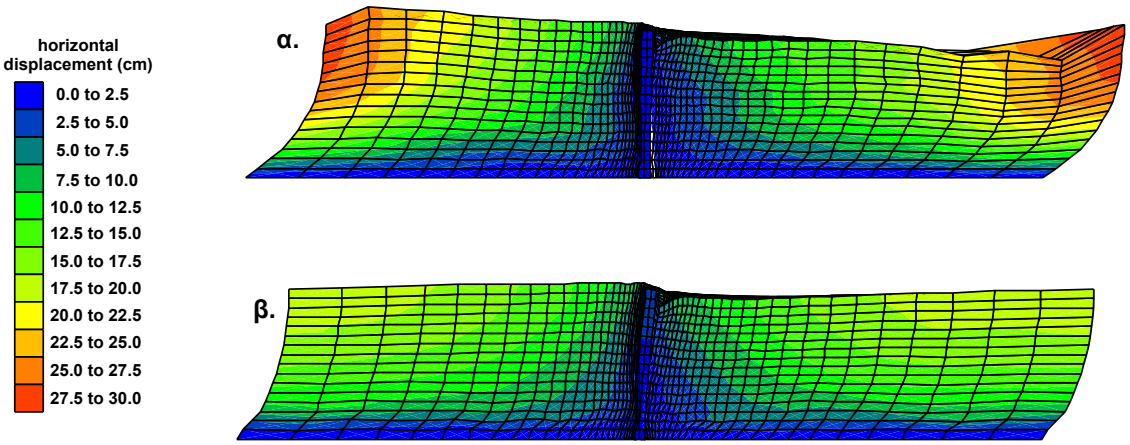

Σχήμα 19: Κατανομή οριζόντιων μετακινήσεων και μορφή παραμορφωμένου καννάβου στο τέλος της διέγερσης με (α) Συμβατικές (typical tied nodes – laminar box) (β) Τροποποιημένες συνοριακές συνθήκες (modified tied nodes –free field).

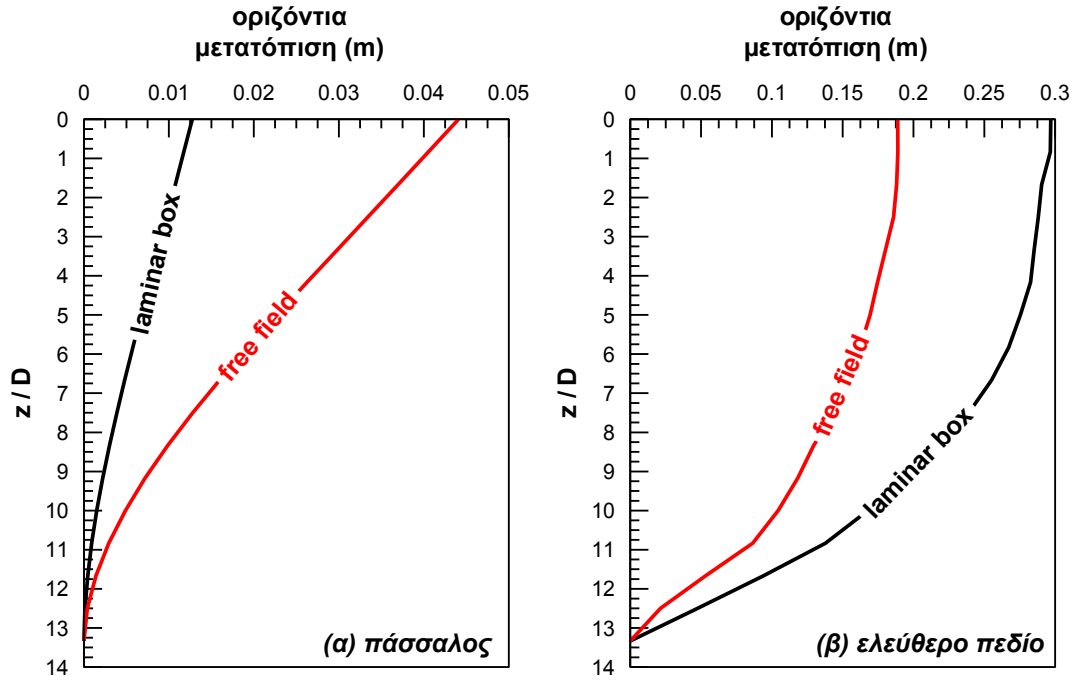

Σχήμα 20: Σύγκριση οριζόντιων μετακινήσεων στο τέλος της διέγερσης (α) στον πάσσαλο και (β) στο ελεύθερο πεδίο με βάση τη συμβατική και την τροποποιημένη μορφή συνοριακών συνθηκών κινηματικά όμοιων ακραίων κόμβων (typical vs. modified tied nodes)

Από την σύγκριση προκύπτει πως η εφαρμογή του νέου τύπου συνοριακών συνθηκών υπερτερεί δεδομένου ότι:

- επιτυγχάνει την ακριβή προσομοίωση των μηχανισμών απόκρισης όπως έχουν παρατηρηθεί στο πεδίο, τόσο κατά την στατική ισορροπία, όσο και κατά τη δυναμική φόρτιση.
- Η συμβατική θεώρηση υποεκτιμά σημαντικά τις μετακινήσεις του πασσάλου, με αποτέλεσμα ενδεχόμενη χρήση της να οδηγεί σε μη συντηρητική εκτίμηση της απόκρισης.

Επιπλέον, η σημαντική διαφοροποίηση που παρατηρείται ανάμεσα στην προσομοίωση εύκαμπτου δοχείου (laminar box with typical tied nodes) και συνθηκών ελεύθερου πεδίου (modified tied nodes) γεννά ερωτηματικά όσον αφορά την αξιοπιστία των πειραματικών δοκιμών σε σεισμική τράπεζα ή φυγοκεντριστή με χρήση εύκαμπτων δοχείων.

Μηχανισμοί Αλληλεπίδρασης Πασσάλου – Εδάφους

2. Η ανηγμένη οριακή αντίδραση του ρευστοποιημένου εδάφους ($p_{ult}/\sigma'_{vo}D$) εξαρτάται μονοσήμαντα από τον λόγο υπερπιέσεων πόρων στην περιοχή γύρω από τον πάσσαλο ($r_{u,pile}$). Συγκεκριμένα, όπως φαίνεται στο **Σχήμα 21β** έντονα αρνητικές τιμές του λόγου υπερπιέσεων πόρων μπορούν να αναπτυχθούν σε μικρά βάθη γύρω από τον πάσσαλο, ως αποτέλεσμα της διαστολικότητας που προκαλείται λόγω ροής του ρευστοποιημένου εδάφους γύρω από τον πάσσαλο. Οι τιμές του λόγου υπερπιέσεων αυξάνουν αλγεβρικά με το βάθος, ενώ σε μεγάλα βάθη, όπου η σχετική μετατόπιση πασσάλου-εδάφους είναι μικρή, λαμβάνουν τιμές περίπου ίσες με τη μονάδα. Αντίστοιχα, όπως φαίνεται και στο **Σχήμα 21α,** οι εδαφικές πιέσεις λαμβάνουν μεγάλες τιμές κοντά στην επιφάνεια και μειώνονται με το βάθος.

3. Συσχετίζοντας τα αποτελέσματα του συνόλου των παραμετρικών αναλύσεων (**Σχήμα 22**), προκύπτει ότι η μονοσήμαντη σχέση μεταξύ των $p_{ult}/\sigma'_{vo}D$ και $r_{u,pile}$ μπορεί να εκφραστεί μαθηματικά ως εξής:

$$\frac{p_{ult}}{\sigma'_{vo} D} = 5.0 \cdot (1 - r_{u,pile})^{1.75} \qquad (10)$$

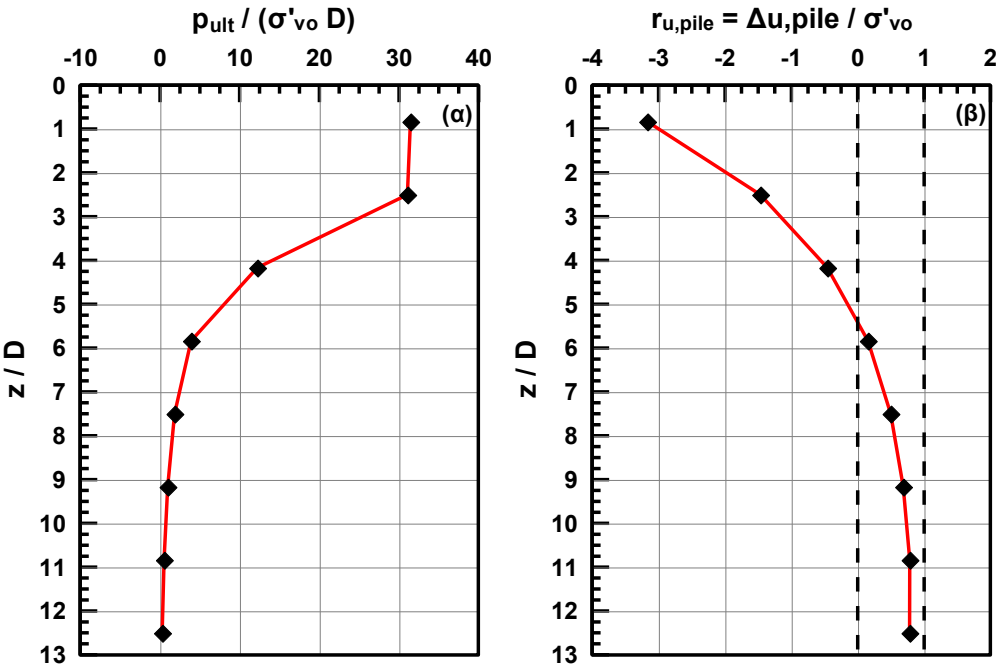

Σχήμα 21: Μεταβολή με το βάθος (α) της αδιαστατοποιημένης οριακής πίεσης και (β) του λόγου υπερπιέσεων πόρων γύρω από τον πάσσαλο.

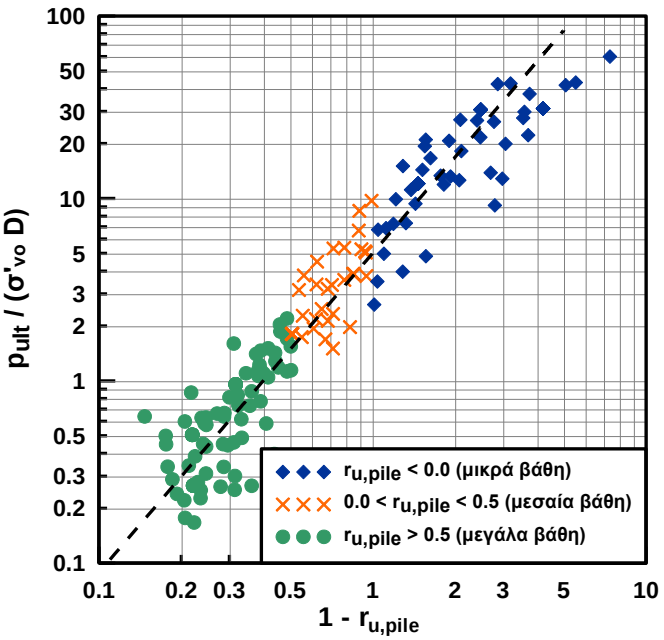

Σχήμα 22: Αδιαστατοποιημένη οριακή πίεση, $p_{ult}/\sigma'_{vo}D$, συναρτήσει του λόγου υπερπιέσεων πόρων γύρω από τον πάσσαλο, $r_{u,pile}$.

4. Ο λόγος υπερπιέσεων πόρων γύρω από τον πάσσαλο δεν συμπίπτει με τον αντίστοιχο στο ελεύθερο πεδίο ($r_{u,ff} \approx 1.0$), αλλά επηρεάζεται από τρεις (3) τουλάχιστον σύνθετους μηχανισμούς:

(α) Αρχικές συνθήκες (τάση εγκιβωτισμού και σχετική πυκνότητα)

(β) Συνθήκες στράγγισης

(γ) Μέγεθος επιβαλλόμενης διατμητικής παραμόρφωσης λόγω σχετικής μετατόπισης πασσάλου-εδάφους.

Ως εκ τούτου η σχέση (10), παρόλο που τεκμηριώνει την εξάρτηση της οριακής πίεσης από τον λόγο υπερπιέσεων πόρων γύρω από τον πάσσαλο, είναι μικρής πρακτικής αξίας μια και η πρόβλεψη του $r_{u,pile}$ είναι δύσκολη στην πράξη.

Βελτιωμένες Σχέσεις Υπολογισμού Καμπυλών p-y

5. Κατ' επέκταση του (4) ανωτέρω, η οριακή αντοχή του ρευστοποιημένου εδάφους συσχετίστηκε απευθείας με τα χαρακτηριστικά του εδάφους (σχετική πυκνότητα, D_r; Διαπερατότητα, k), του πασσάλου (Διάμετρος, D; Δυσκαμψία, EI) και της διέγερσης (Περίοδος, T), με αποτέλεσμα να προκύψουν οι παρακάτω εμπειρικές σχέσεις υπολογισμού:

$$\frac{p_{ult}}{\sigma'_{vo} D} = A\left(\frac{\sigma'_{vo}}{p_a}\right)^{-B} \le C \tag{11}$$

όπου A, B και C υπολογίζονται ως εξής:

$$A = 0.0013 \cdot D_r \cdot e^{5.2D} \cdot T^{1.2} \tag{12}$$

$$B = 27 \cdot D_r^{-0.6} \cdot e^{1.6D} \cdot \mathrm{e}^{-4.4e-8 \cdot EI} \cdot e^{-2.5T} \cdot e^{-212k} \tag{13}$$

$$C = 0.9 \cdot D_r^{-0.8} \cdot \min\left[EI \cdot 10^{-5}{}^{0.6}, 24 \cdot EI \cdot 10^{-4}{}^{-0.7} \right] \cdot \left(\frac{k \cdot T}{D}\right)^{-0.5} \tag{14}$$

Για την περίπτωση εμηγνυόμενων πασσάλων και πασσάλων με κινηματικούς περιορισμούς στην κεφαλή, οι τιμές των A, B και C μεταβάλλονται ως εξής:

$$\begin{aligned} A_{fixed-head} &= A_{no-rotation} = A_{free-head} \\ A_{driven} &= A_{drilled} \end{aligned} \tag{15}$$

$$\begin{aligned} B_{fixed-head} &= B_{no-rotation} = B_{free-head} \\ B_{driven} &= 0.86 \cdot B_{drilled} \end{aligned} \tag{16}$$

$$C_{fixed-head} = 0.5 \cdot C_{free-head}$$
$$C_{no-rotation} = C_{free-head} \quad (17)$$
$$C_{driven} = 0.67 \cdot C_{drilled}$$

6. Από πλευράς φυσικής σημασίας, η παράμετρος Α εκφράζει την αντοχή σε μεγάλα βάθη και άρα σε περιοχές όπου ο λόγος υπερπιέσεων είναι κοντά στη μονάδα. Επομένως, η τιμή της σχετίζεται, κυρίως, με τους μηχανισμούς που καθορίζουν την παραμένουσα αντοχή του ρευστοποιημένου εδάφους. Αντίθετα, η παράμετρος C εκφράζει την αντοχή σε μικρά βάθη, δηλαδή σε περιοχές με έντονη διαστολικότητα. Επομένως η τιμή της συνδέεται με τους μηχανισμούς που επιδρούν στην ανάπτυξη αρνητικών πιέσεων πόρων, που περιγράφηκαν παραπάνω.

7. Η ακρίβεια της προτεινόμενης συσχέτισης αξιολογείται στο **Σχήμα 23** και στο **Σχήμα 24** όπου φαίνεται η σύγκριση μεταξύ αριθμητικών και αναλυτικών προβλέψεων, καθώς και το σχετικό σφάλμα αντίστοιχα. Η συμφωνία είναι αρκετά ικανοποιητική, ενώ το σχετικό σφάλμα δεν ξεπερνά το 50% για το 95% περίπου των δεδομένων.

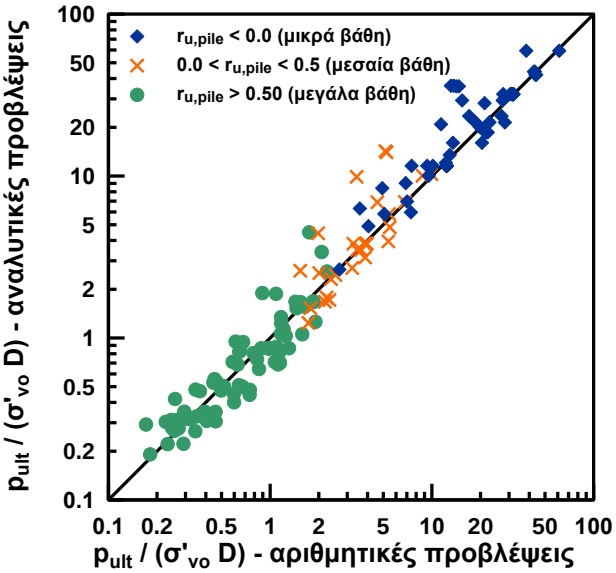

Σχήμα 23: Σύγκριση μεταξύ αναλυτικών και αριθμητικών προβλέψεων της οριακής αντίδρασης του εδάφους.

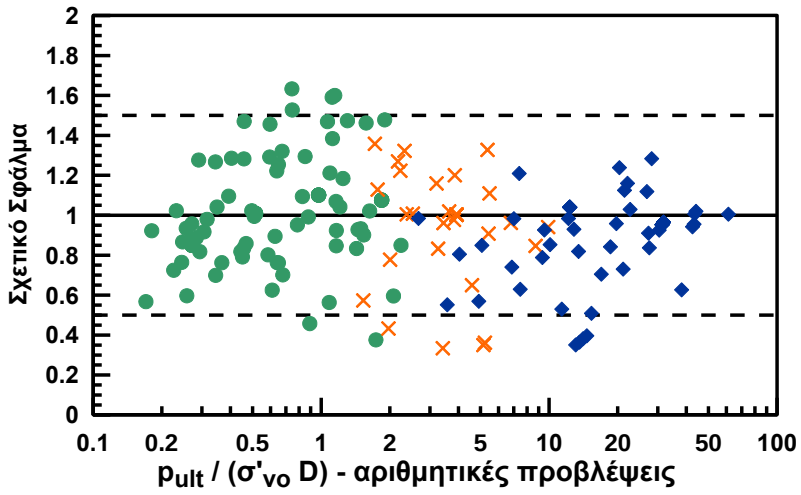

Σχήμα 24: Εκτίμηση σχετικού σφάλματος προτεινόμενων αναλυτικών σχέσεων για την οριακή αντίδραση του εδάφους.

Σύγκριση με Υφιστάμενες Σχέσεις Υπολογισμού Καμπυλών p-y

8. Οι προβλέψεις των προτεινόμενων σχέσεων συγκρίθηκαν με τις μεθοδολογίες των Cubrinovski and Ishihara (2007), Brandenberg et al. (2007) και Suzuki and Tokimatsu (2009). Στις εν λόγω μεθοδολογίες η οριακή αντίδραση του εδάφους περιγράφεται από τις παρακάτω εξισώσεις:

Cubrinovski and Ishihara (2007)

$$\frac{p_{ult}}{D} = S_{u,res} \tag{18}$$

$$s_{u,res} = 0.14 \cdot \left[N_{1\ 60-cs} \right]^2 \tag{19}$$

όπου D η διάμετρος του πασσάλου, $S_{u,res}$ η παραμένουσα αντοχή του ρευστοποιημένου εδάφους και $(N_1)_{60\text{-}cs}$, ο αριθμός κρούσεων SPT.

Brandenberg et al. (2007)

$$\frac{p_{ult}}{D} = m_p \cdot \min \begin{cases} \left[C_1 \ z/D \ + C_2 \right] \cdot \sigma'_{vo} \\ C_3 \cdot \sigma'_{vo} \end{cases} \tag{20}$$

όπου z το βάθος από την επιφάνεια του εδάφους, C_1, C_2 και C_3 εμπειρικοί συντελεστές που εξαρτώνται από τη γωνία τριβής του εδάφους και m_p μειωτικός συντελεστής που λαμβάνει υπόψη την ρευστοποίηση, και προκύπτει συναρτήσει του αριθμού κρούσεων SPT (**Σχήμα 6**).

Suzuki and Tokimatsu (2009)

$$\frac{p_{ult}}{D} = \beta \cdot \ 3K_p \ \cdot \sigma'_{vo} \tag{21}$$

όπου K_p συντελεστής παθητικών ωθήσεων και β μειωτικός συντελεστής για την επίδραση της ρευστοποίησης κατά τους Ιαπωνικούς Κανονισμούς Κτιριακών Θεμελιώσεων (AIJ, 2001), που δίνεται συναρτήσει του διορθωμένου αριθμού κρούσεων SPT (**Σχήμα 6**).

Παρατηρείται ότι οι υφιστάμενες μεθοδολογίες εξαρτούν την οριακή αντίδραση των ρευστοποιημένων εδαφών αποκλειστικά από τις αρχικές συνθήκες (σχετική πυκνότητα και κατακόρυφη ενεργό τάση) καθώς και την διάμετρο του πασσάλου. Πρακτικά αυτό σημαίνει ότι δεν λαμβάνονται υπόψη οι μηχανισμοί που σχετίζονται με την ανάπτυξη αρνητικών πιέσεων πόρων, και συνεπώς υψηλών ωθήσεων, στα μικρά βάθη.

9. Στο **Σχήμα 25** οι προτεινόμενες σχέσεις συγκρίνονται με τις υφιστάμενες σε όρους επιβαλλόμενων οριακών εδαφικών ωθήσεων, για την περίπτωση ενός τυπικού πασσάλου σκυροδέματος με D=0.6m, EI=190000kNm^2, σε άμμο με D_r=50% και διαπερατότητα k=3.05 x 10^{-3} m/s (αμμοχάλικο) και k=6.1 x 10^{-5} m/s (ιλυώδης άμμος). Από τη σύγκριση παρατηρούνται τα ακόλουθα:

   (α) Για περιπτώσεις όπου δεν αναμένεται έντονη διαστολική συμπεριφορά (μεγάλα βάθη, μεγάλη διαπερατότητα) οι προτεινόμενες σχέσεις συγκρίνονται ικανοποιητικά με τις υφιστάμενες.

   (β) Αντίθετα, για περιπτώσεις όπου η συμπεριφορά αναμένεται να είναι έντονα διαστολική (μικρά βάθη, μικρή διαπερατότητα), οι υπάρχουσες μεθοδολογίες υποεκτιμούν σημαντικά το μέγεθος των επιβαλλόμενων ωθήσεων.

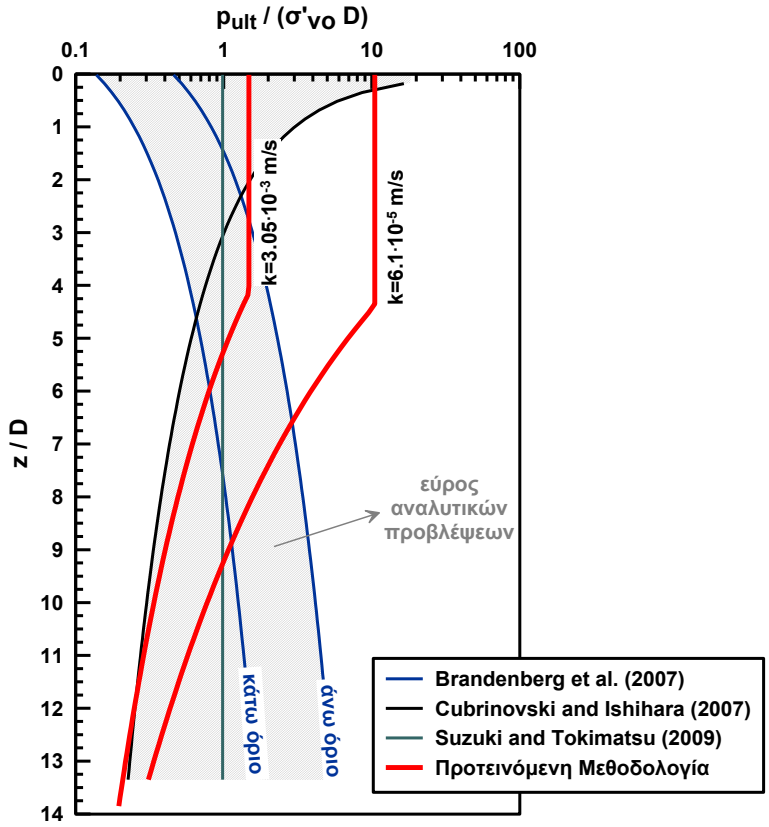

Σχήμα 25: Σύγκριση οριακών εδαφικών πιέσεων μεταξύ της προτεινόμενης και των υφιστάμενων μεθοδολογιών σχεδιασμού, για συντελεστή διαπερατότητας $k=3.05 \times 10^{-3}$ m/s (με περιορισμένα φαινόμενα διαστολικότητας) και $k=6.10 \times 10^{-5}$ m/s (με έντονα φαινόμενα διαστολικότητας).

10. Τέλος, προκειμένου να αξιολογηθεί η επίδραση των παραπάνω διαφορών στις τιμές του $p_{ult}/\sigma'_{vo}D$ στην καταπόνηση του πασσάλου, εκτελέστηκαν ψευδο-στατικές αναλύσεις με τη μέθοδο p-y και με χρήση του προγράμματος πεπερασμένων στοιχείων ANSYS. Στο **Σχήμα 26** συγκρίνονται οι μετακινήσεις και οι καμπτικές ροπές του πασσάλου σύμφωνα με τις υφιστάμενες και την προτεινόμενη μεθοδολογία. Παρατηρείται πως στην περίπτωση της μικρής σχετικά διαπερατότητας, η έντονη διαστολικότητα οδηγεί σε δραματική αύξηση τόσο των μετακινήσεων όσο και των καμπτικών ροπών του πασσάλου, η οποία δεν είναι δυνατόν να προβλεφθεί από τις υφιστάμενες σχέσεις για τις καμπύλες p-y.

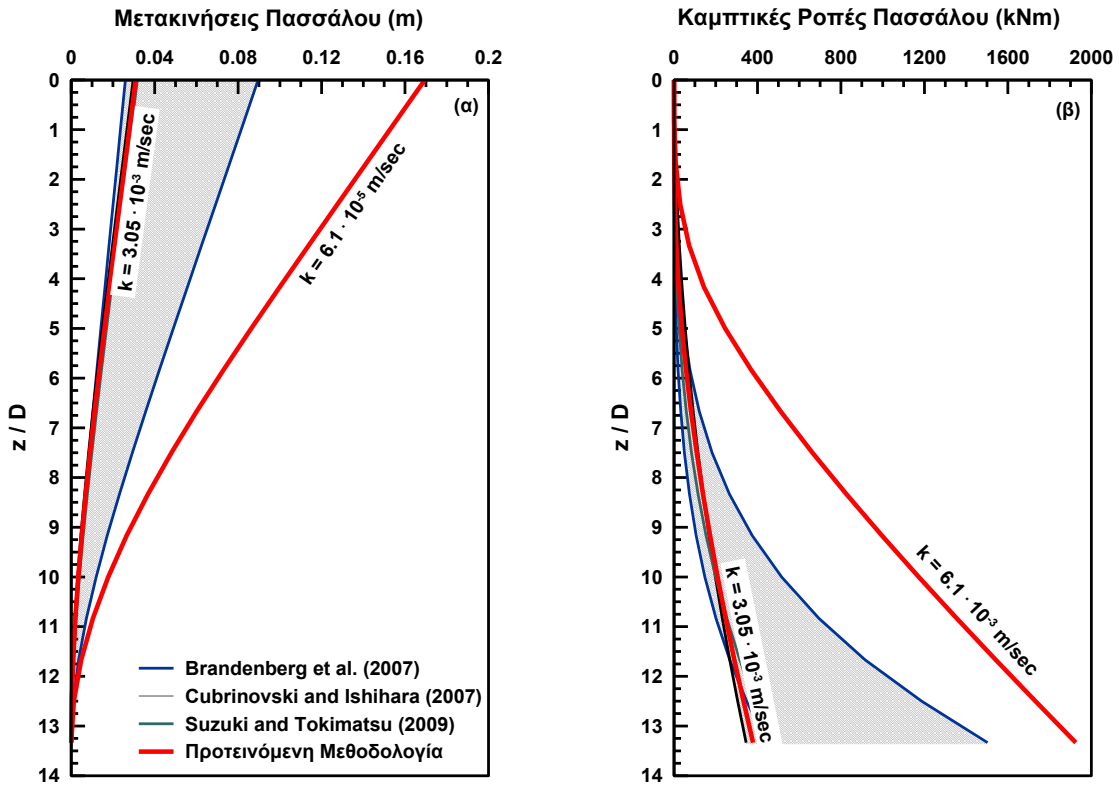

Σχήμα 26: Σύγκριση (α) μετακινήσεων και (β) καμπτικών ροπών πασσάλου μεταξύ της προτεινόμενης και των υφιστάμενων μεθοδολογιών σχεδιασμού, για διαπερατότητα k=3.05 x 10^{-3} m/s (με περιορισμένα φαινόμενα διαστολικότητας) και k=6.10 x 10^{-5} m/s (με έντονα φαινόμενα διαστολικότητας).

Table of Contents

1. Introduction 7

1.1 Problem description 7

1.2 Scope of work 12

1.3 Preview of Thesis contents 13

2. The p-y method 17

2.1 General 17

2.2 P-y curves for static analysis 21

2.2.1 Reese et al. (1974) 21

2.2.2 Murchison and O'Neill (1984) – API (2002) 28

2.2.3 Georgiadis et al. (1992) 31

2.2.4 Det Norske Veritas (DnV) (1980) 33

2.2.5 Non-unified methodologies 36

2.2.6 Comparison and observations between various recommendations for p-y curves in nonliquefied sand 44

2.3 P-y curves for dynamic analysis 49

2.3.1 Modeling of soil hysteretic response 49

2.3.2 Modeling of soil radiation damping 53

2.3.3 Modeling of gap between soil and pile 55

2.4 P-y curves for liquefaction related problems 57

2.5 Additional considerations on p-y method and pile design 71

2.5.1 Analysis of pile groups 71

2.5.2 Estimation of kinematic loads ... 75
2.5.3 Critical loading cycle and superposition of kinematic and inertial loads ... 79
2.5.4 Pile analysis with the Limit Equilibrium Method (LEM) ... 82
2.5.5 Estimation of Inertia Loads ... 87
2.5.6 Loads transmitted to pile cap ... 88
2.5.7 Load transfer behavior of the non-liquefied crust ... 92
2.5.8 P-y relations for soft and stiff clays ... 95

2.6 Guidelines for the design of piles in liquefied and laterally spreading soil 98

2.7 Concluding Remarks ... 102
2.7.1 Piles in nonliquefied soils ... 102
2.7.2 Piles in liquefied soils ... 103

3. Numerical Simulation of p-y curves in non-liquefied sands ... 107

3.1 General ... 107

3.2 Basic Aspects of the Numerical Methodology for Static Problems ... 107
3.2.1 The Explicit Finite Difference Method ... 108
3.2.2 Numerical Scheme for Static Problems ... 109

3.3 The physical problem: Layout and Parameter Selection ... 115

3.4 Numerical Simulation ... 120

3.5 Discretization effects ... 123

3.6 Interface Formulation and Selection of Interface Properties ... 125

3.7 Deformation Mechanism ... 131

3.8 Typical shape of p-y Curves ... 135

3.9 Boundary Effects ... 143

3.10 Effect of the "large-strain" mode of computations ... 145

3.11 Conclusions ... 147

4. Numerical Simulation of Pile Installation Effects ... 149

4.1 General ... 149

4.2 Mechanisms of pile installation effects ... 149

4.3 Analytical solution for the expansion of a cavity (Vesic, 1972) 156
4.3.1 Basic equations and assumptions 156
4.3.2 Evaluation of stresses 160
4.3.3 Insight on the effect of Δ 164
4.4 Numerical simulation of cylindrical cavity expansion 166
4.5 Typical Results 170
4.6 Analytical Evaluation of Average Volumetric Strain, Δ 175
4.7 Analytical Evaluation of Poisson's ratio in the plastic zone 181
4.8 Implementation of Vesic's method to FLAC3D 183
4.9 Numerical Verification of the semi-analytical procedure 186
4.10 Conclusions 193

5. Parametric Investigation of p-y curves for Piles in Nonliquefied Sand 195
5.1 General 195
5.2 Analyses data and interpretation of results 195
5.3 Typical Results from the baseline analysis 198
5.4 Effect of Relative Density, D_r 200
5.5 Effect of Pile Diameter, D 208
5.6 Effect of Pile Installation 216
5.7 Effect of loading type 221
5.8 Conclusions 229
5.8.1 Shape of p-y curves 230
5.8.2 Typical response characteristics for k_{ini} and p_{ult} 231
5.8.3 Effect of Relative Density, D_r 232
5.8.4 Effect of Pile diameter, D 232
5.8.5 Effect of pile installation 233
5.8.6 Effect of type of loading 234
5.9 Analytical estimation of p-y curves in nonliquefied soils 235

6. Numerical Simulation of Piles in Laterally Spreading Soils 239

6.1 General ... 239

6.2 Problem Statement and Basic Input Parameters ... 239

6.3 Stage 1: Generation of the proper stress field for the infinite slope ... 241

6.3.1 Analytical computation of static stress field ... 241

6.3.2 Numerical generation of static stress field ... 249

6.4 Stage 2: Pile installation ... 264

6.5 Stage 3: Seismic Shaking ... 265

6.6 Comparative evaluation of the modified tied nodes formulation ... 266

6.6.1 Lateral spreading of uniform sand layer ... 266

6.6.2 Single pile in laterally spreading soil ... 272

6.7 Concluding Remarks ... 276

7. Numerical Methodology Verification ... 279

7.1 General ... 279

7.2 Description of the Centrifuge Test ... 280

7.3 Numerical Simulation of metulose saturated model (1x1-v) ... 290

7.3.1 Numerical model description ... 290

7.3.2 Rotational Stiffness of Cemented Sand, K_r ... 299

7.3.3 Soil acceleration ... 301

7.3.4 Pore pressures in the free-field (P1-P4) ... 305

7.3.5 Pore pressures in the near field and close to the pile (P5-P12) ... 309

7.3.6 Free field soil displacements ... 317

7.3.7 Pile head displacements ... 328

7.3.8 P-y curves ... 330

7.3.9 Pile Bending Moments ... 335

7.4 Numerical Simulation of water saturated model (1x1-w) ... 339

7.5 Free Field vs. Laminar Box Simulation ... 345

7.6 Concluding Remarks ... 355

8. Parametric Investigation of the p-y Pile Response in Laterally Spreading Soils ... 361

8.1 General ... 361

8.2 Outline of parametric analyses ... 362

8.3 Mesh size verification ... 364

8.4 Typical numerical predictions ... 366

8.4.1 Near and far field Soil Acceleration ... 366

8.4.2 Development of Excess Pore Pressures ... 368

8.4.3 Soil and Pile Lateral Displacements ... 371

8.4.4 Development of soil reaction ... 372

8.4.5 P-y curves ... 374

8.5 Evaluation of liquefied soil subgrade reaction ... 376

8.5.1 Interpretation of numerical p-y predictions ... 376

8.5.2 Mechanisms affecting the Ultimate p-y Resistance ... 379

8.5.3 Simplified Pile-Soil Interaction Model ... 384

8.6 Concluding Remarks ... 388

9. Analytical Calculation of Ultimate Soil Resistance in Laterally Spreading Soils ... 391

9.1 Identification of main problem parameters ... 391

9.2 Empirical relations in terms of pile, soil and excitation characteristics ... 392

9.3 Soil resistance in terms of relative soil-pile displacement ... 404

9.4 Comparison against existing empirical relations ... 407

9.4.1 Overview of existing empirical relations ... 407

9.4.2 Comparison of proposed and existing empirical relations ... 414

10. Conclusions ... 421

10.1 Summary of main points ... 421

10.2 Recommendations for future research ... 424

11. References ... 427

1

Introduction

1.1 Problem description

There is no doubt that piles are among the most widely used types of foundation. Their use is unavoidable in a very large number of projects, such as bridge abutments, slope stabilization, heavy buildings, presence of surface soft or liquefiable layers, special buildings that require minimization of settlements, e.t.c. Focusing on the case of piles subjected to horizontal loads current design practice is largely based on the "Beam on Nonlinear Winkler Foundation" (BNWF) method, alternatively known as the p-y method (**Figure 1.1**).

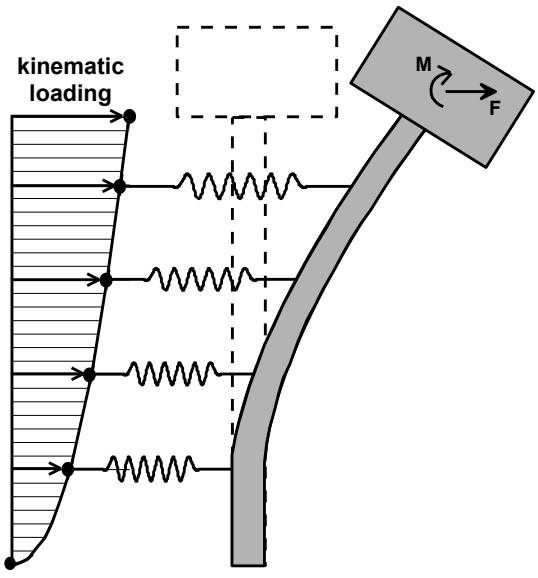

Figure 1.1: Layout of the "Beam on Nonlinear Winkler Foundation" (BNWF) or p-y method.

The formulation of this method is based on the following three (3) assumptions:

- Structural elements (pile, pile cap, superstructure) are modeled as beam elements.
- Soil-foundation interaction is modeled by means of lateral p-y springs. One end of the springs is attached to the pile foundation while the other remains fixed.
- Finally, kinematic loads are applied at the fixed end of the springs, while external loads (forces, moments) are applied at the superstructure, the pile cap or the pile head.

Possibly, the most uncertain parameter involved in the above formulation, is the determination of the non-linear force-displacement relationship for the Winkler springs, widely known as the "p-y curves". In a typical BNWF analysis, the characteristics of the p-y curves are modified based on both the soil type in which the pile is built, as well, as on the type of loading at which the pile is subjected. The various scenarios are schematically illustrated in **Figure 1.2**. As far as soil types are concerned, we can distinguish between cohesive and cohesionless soils. The latter can be either non-liquefied, hereafter referred as "dry sands" or liquefied, hereafter referred as "liquefied sands".

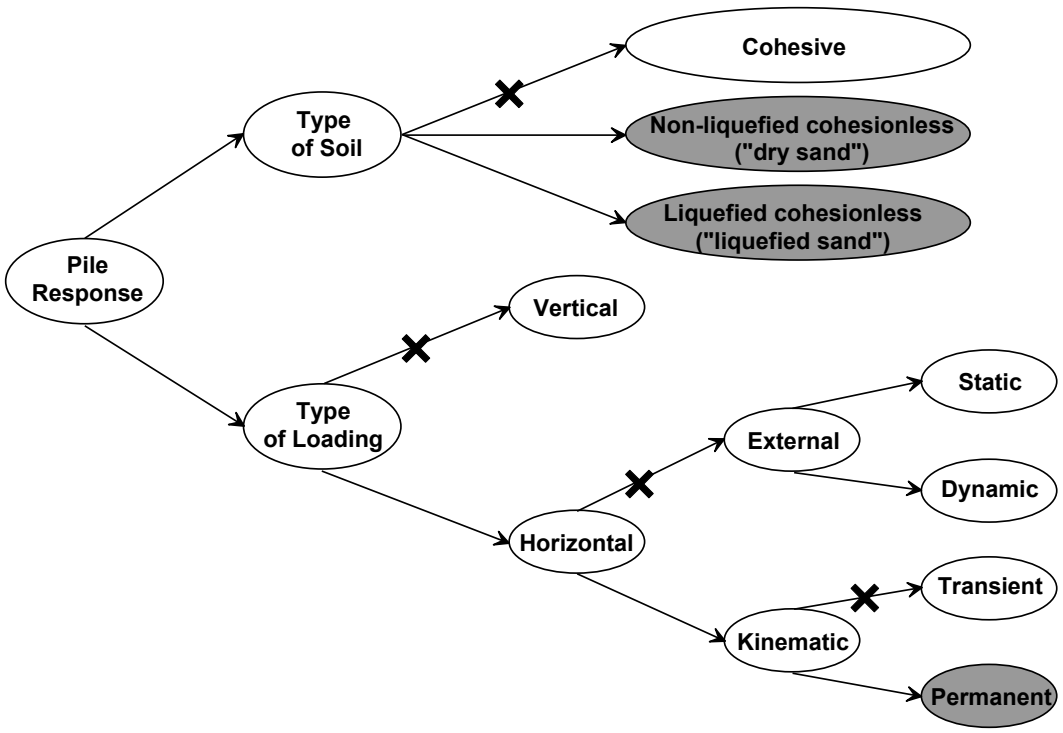

Figure 1.2: Different combinations of soil type and loading type, affecting pile response (X is placed on paths which are not explored in this thesis).

As for the different types of loads imposed on the pile, these can be either kinematic (caused by lateral ground displacement) or external (forces and moments applied at the pile head by the superstructure). Furthermore, external loads can be either static or dynamic, while kinematic loads can be either transient or permanent. From the above twelve (12) different soil and loading type combinations, **the present Thesis deals with the case of p-y curves for piles in "dry" and in "liquefied" sand, subjected to kinematic loads caused by permanent ground displacement.** Also, and only for the case of "dry sands", the case of external static loads is also considered, but only on a very limited extent.

In practice, piles in "dry sand" undergoing permanent ground displacements can be encountered in slope stabilization problems, under static or seismic loading. The problem of piles in "liquefied" sand subjected to lateral ground displacements, is typical in Geotechnical Earthquake Engineering, commonly known as liquefaction – induced lateral spreading, and has been encountered in almost all recent strong earthquakes (e.g. **Figure 1.3**).

Figure 1.3: Pile failure due to liquefaction-induced lateral spreading from the Chile, 2010, M=8.8 and the Christchurch, New Zealand, 2011, M=6.3 earthquakes.

Given the importance of p-y curves on the design of the pile, it is no surprise that a large number of research studies, mainly experimental, have been dedicated to this topic, and have given valuable insight to the parameters that affect the p-y curves. In addition, they have led to the development of various empirical methodologies for their analytical estimation, so that they can be easily implemented to design practice.

However, the extensive literature survey that was performed as part of the present study has revealed that there are still grey areas which need to be investigated, while there are cases where application of the existing methodologies may lead to unconservative design. More specifically, for the case of "dry sands":

a. The various analytical methodologies may vary widely with regard to the basic elements of the proposed p-y curves (i.e. the nonlinear shape of the curve, the initial subgrade modulus and the ultimate soil resistance), raising justified concerns to the engineer who is called to choose among them. For instance, **Figure 1.4** compares seven (7) of the different p-y curves proposed in the literature so that the Reader himself may appreciate the aforementioned differences.

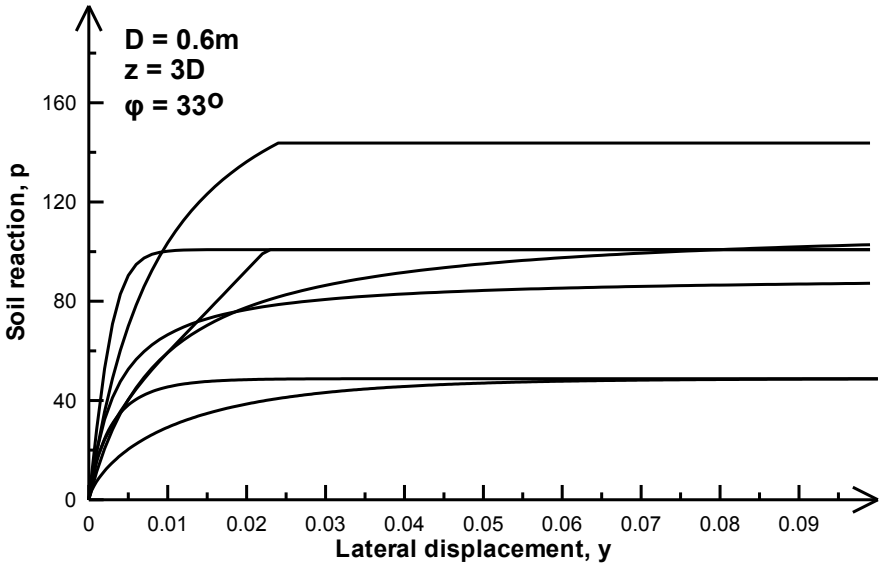

Figure 1.4: P-y curves for "dry sands" at a depth z=3D, for a D=0.6m diameter pile built in sand with φ=33°.

b. The majority of the above methods are based on results from experimental studies, and consequently apply to a small value range of the associated problem parameters.

c. Finally, existing methods correlate the p-y curves only with the relative density of the soil and the diameter of the pile. However, recent studies (e.g. Ashour and Norris, 2000; Kim et al., 2004) indicate that other parameters may also affect the response, such as the stiffness of the pile, the kinematic constraints applied to the pile head, and the method of pile installation.

Furthermore, for the case of "liquefied sand", recent experimental data raise the following concerns:

a. Existing methodologies for estimating the liquefied p-y response are based on the corresponding relations for "dry sands" after properly reducing the ultimate resistance and the initial subgrade modulus. Modification of the curves for "dry sands" is performed either by applying appropriate reduction factors (e.g. Brandenberg et al., 2007) or by considering empirical relations for the residual strength of liquefied soil (e.g. Cubrinovski and Ishihara, 2007). In both cases, the pursued reduction of the p-y curves is related only to the relative density of the sand.
b. Contrary to the above, recent experimental data (e.g. Suzuki and Tokimatsu, 2009) indicate the influence of additional parameters like soil permeability, excitation characteristics, as well, as pile properties (bending stiffness, installation, head constraint, e.t.c.). Along the same direction, Gonzalez et al. (2009) have shown that significant negative excess pore pressures may develop near the pile head, for values of soil permeability commonly encountered in the field, thus increasing instead of decreasing the soil pressures compared to the nonliquefied case.
c. Finally, the experimentally verified p-y curves for the "liquefied" soil, similarly to the ones for "dry" soil, apply only to a limited value range of the associated parameters. Note, that this limitation is more severe than for dry sands because the problem of piles in laterally spreading liquefied soil is much more complicated and is affected by a larger number of pile, soil and excitation parameters.

1.2 Scope of work

The discussion above reveals that the problem under consideration deserves further investigation. Nevertheless pursuing further this challenge by experimental means is technically and financially cumbersome since the number of parameters involved is large and does not favor a systematic parametric investigation. However, recent advances in numerical (Finite Elements, Finite Differences) methods, along with the development of sophisticated constitutive models which capture soil response even under extreme conditions (e.g. earthquake – induced liquefaction), allow researchers to simulate with realism even the most complicated boundary value problems in Geotechnical Engineering and overcome this limitation. Hence, it was decided to continue the investigation of p-y response of piles undergoing ground displacements through a series of "numerical experiments", i.e. advanced numerical analyses which take consistently into account dynamic loading, excess pore pressure build up and drainage, as well as non-linear soil response.

In this context, **the scope of the present Thesis** is, (a) to develop a three-dimensional numerical methodology for the simulation of piles in "dry" and "liquefied" sands, undergoing kinematic loads due to permanent ground displacement, and (b) consequently apply it in order to investigate the mechanisms that govern the pile response and develop upgraded p-y relationships in terms of the basic soil, pile and excitation parameters.

The following four (4) main steps will be undertaken in order to achieve these objectives:

Step 1: Extensive literature survey in order to collect and evaluate existing studies on the lateral response of piles in cohesionless soils. The survey should focus on existing analytical methodologies, as well as gaining insight on the phenomenon through experimental observations from centrifuge and shaking table tests.

Step 2: Simulate the **effects of pile installation** on the stress and volume state of the soil surrounding the pile, in order to differentiate driven from excavated piles during the subsequent p-y response evaluation.

Step 3: Evaluation of the **p-y response** of drilled and driven piles in "dry sands", based on 3-D numerical simulation and extensive parametric investigation. Note that, investigation mainly focuses on the case of **kinematic loads due to permanent**

ground displacement, while, only a small amount of analyses is performed to explore the effects of **external static loading**.

Step 4: Evaluation of the **p-y response** of drilled and driven piles in "liquefied sands", **under earthquake-induced lateral spreading,** similarly based on 3-D numerical simulation and extensive parametric investigation.

Note that Steps 3 and 4 led to a set of new p-y relationships for single piles subjected to lateral soil pressures, following a multi-variable statistical analysis of the parametric numerical predictions and a thorough verification against experimental results and existing empirical relations.

1.3 Preview of Thesis contents

In Chapter 2 of the Thesis, an extensive literature survey is performed focusing on two (2) main topics:

- Description of existing analytical methodologies for the design of piles in cohesionless soils under lateral loading and,
- Overview of main experimental findings and observations in order to identify mechanisms as well as the basic parameters that govern the p-y response of the soil.

Ultimately, the conclusions from the literature investigation will be used as a guide for the setup of the numerical analyses program.

In Chapter 3 of the thesis, the 3-dimensional numerical model developed for the simulation of pile lateral loading in "dry sands" is thoroughly described. Furthermore results from sensitivity analyses are presented which verify the accuracy of the various assumptions incorporated in the analyses (e.g. mesh size and discretization, interface element properties, e.t.c). Emphasis is placed on the ability of the constitutive model to capture basic response patterns, as identified in the literature, and also produce realistic p-y curves.

In Chapter 4 the basic mechanisms that govern soil response during pile installation are investigated. Following a literature survey, a procedure is described for the semi-analytical computation of soil stresses after pile installation. The methodology draws upon the implementation in the numerical code of Vesic's analytical equations for the problem of cylindrical expansion of cavities. In order to calibrate Vesic's parameters, a series of numerical analyses is performed which deal with the drained cavity

expansion within horizontal soil slices. Finally, pile driving is fully simulated numerically, in order to validate the semi-analytical procedure proposed.

In Chapter 5 an extensive parametric investigation of pile response in "dry sands" is performed. Emphasis is placed on the case where the pile is subjected to kinematic loading due to permanent ground displacement, while the effect of the soil Relative Density, pile diameter and pile type (drilled and driven) is considered. Results of the parametric analyses are properly processed in order to evaluate existing methodologies as well as provide new design recommendations. In a second level, the case of piles subjected to external static loading is considered, through a limited number of analyses, aiming at identifying the differences between the two (2) types of loading in qualitative terms.

In Chapter 6 the numerical model developed for the case of piles in "liquefied sand" is presented. The simulation focuses on the case where the pile is subjected to large kinematic loads as a result of ground lateral spreading. Emphasis is placed on critical components of the analysis that can affect the response like properties of interface elements, water flow and soil permeability, as well as boundary conditions. An innovative procedure had to be developed with regard to the later, in order to take consistently into account the inclined geometry of the problem when reproducing free field conditions during initial consolidation and subsequent seismic shaking.

In Chapter 7 the numerical methodology is calibrated with respect to the well-documented centrifuge tests by Gonzalez et al. (2009) which explore pile response undergoing lateral spreading loads. Numerical results are compared with the experimental measurements in order to verify the numerical model. Special emphasis is given to the selection of an appropriate permeability coefficient for the liquefied state of the sand.

In Chapter 8 an extensive parametric investigation is performed focusing on single pile response in laterally spreading ground. The analyses explore the effect of various parameters regarding soil characteristics (relative density, permeability coefficient), pile characteristics (diameter, bending stiffness, pile head constraint, installation method), as well as excitation characteristics (period). The numerical results are used to identify the mechanisms and the parameters that govern the p-y response. Special emphasis is given to dilation of the soil surrounding the upper part of the pile and the associated effects on the ultimate resistance of the liquefied sand.

Finally, in Chapter 9 the results of the parametric analyses are further processed, and multi-variable analytical relationships are established for the estimation of the ultimate resistance and the p-y response of laterally spreading soils. Furthermore, the proposed relationships are compared to existing ones which overlook dilation effects. The response (deflection and bending moment) of a typical pile is computed in order to evaluate the consequences on pile design from omitting possible dilation effects.

2

The p-y method

2.1 General

The present chapter deals with current design practice of foundations subjected to kinematic (transient and permanent) and external (static and dynamic) lateral loads with emphasis on the BNWF (Beam on Nonlinear Winkler Foundation) method, also known as the *p-y method*. The three (3) major assumptions of the method, which is illustrated in **Figure 2.1**, are the following:

- Structural elements (pile, pile cap, superstructure) are modeled as beam elements.
- Soil-foundation interaction is modeled by means of lateral (p-y), axial (t-z) and tip-bearing (q-z) springs (*static p-y*). For dynamic problems, formulation should include both springs and dashpots to account for radiation and viscous damping (*dynamic p-y*). Springs are attached to the foundation on one side and are fixed on the other.
- External loads are either applied as imposed displacements on the fixed-end of the springs (kinematic loads) or as concentrated forces and moments acting on the center mass of the superstructure and pile cap (external loads).

In the fully coupled dynamic p-y analysis (**Figure 2.1**) ground motion is applied at the fixed-end of the springs and inertial and kinematic response is estimated simultaneously accounting for interaction effects. Additionally, two (2) more simplified approaches to analyze dynamic problems are common in literature:

- *Uncoupled Dynamic p-y Analysis*: Simulation again includes springs and dashpots, but inertial and kinematic effects are estimated separately. The former by keeping the springs and dashpots fixed and applying inertial loads on the cap and

structure (**Figure 2.2a**), and the latter by applying input motion at the fixed-end of the springs and assuming that the cap and the superstructure are mash-less (**Figure 2.2b**). The response of the pile is obtained by superposition of the results from each analysis.

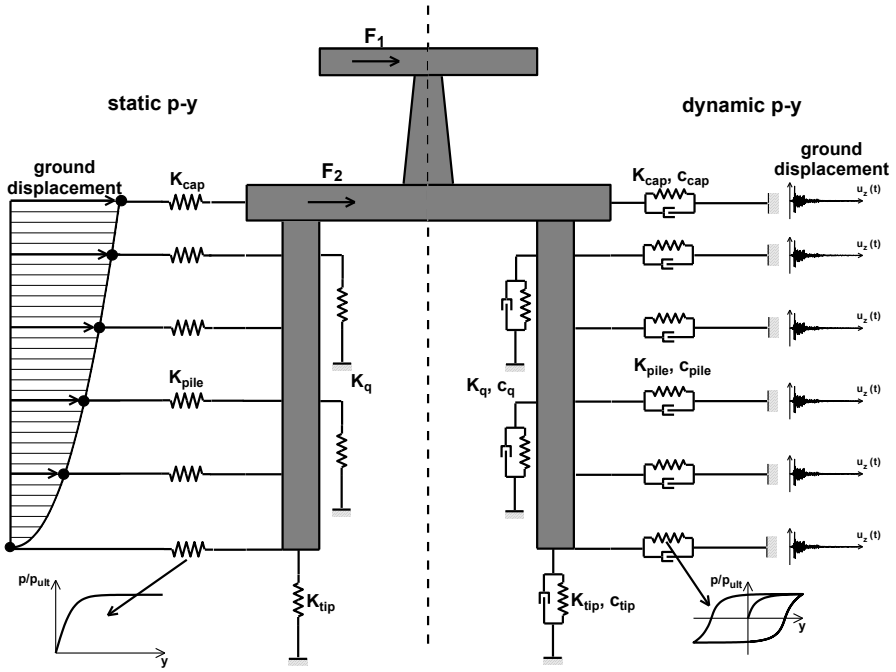

Figure 2.1: Layout of the static and dynamic p-y method

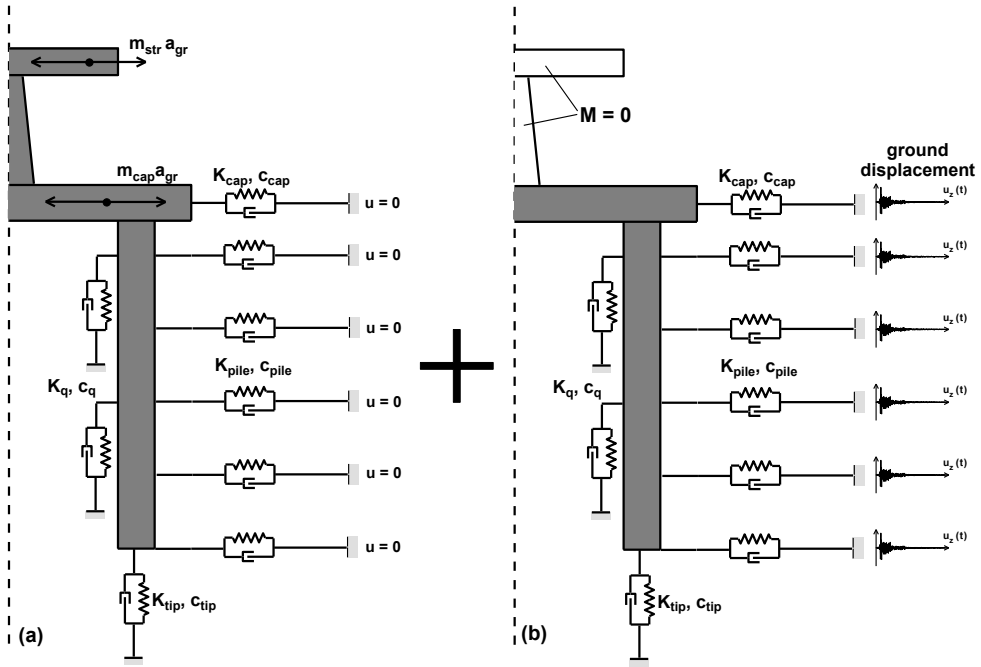

Figure 2.2: Layout of the uncoupled dynamic p-y method.

- *Pseudo-Static p-y analysis*: According to this over-simplifying approach the dynamic nature of the problem is ignored by assuming that external loads are applied statically (as concentrated forces) in the superstructure, and the kinematic as imposed permanent displacements at the fixed-ends of the springs (**Figure 2.1a**).

Finally, special treatment is required for the case where piles are built in slightly inclined soil formations prone to liquefaction (loose, saturated cohesionless soils). If lateral spreading takes place, following severe earthquake loading, then pile is subjected to large lateral displacements, which are composed of a transient and a permanent component. The former are a result of earthquake shaking and cease as loading ends, while the latter are progressively accumulated as soil spreads laterally.

Hence, pile response can be obtained by performing two (2) p-y analyses, one dynamic, by imposing the transient displacements, and one static by applying the permanent. This procedure is schematically illustrated in **Figure 2.3(a) and (b)**.

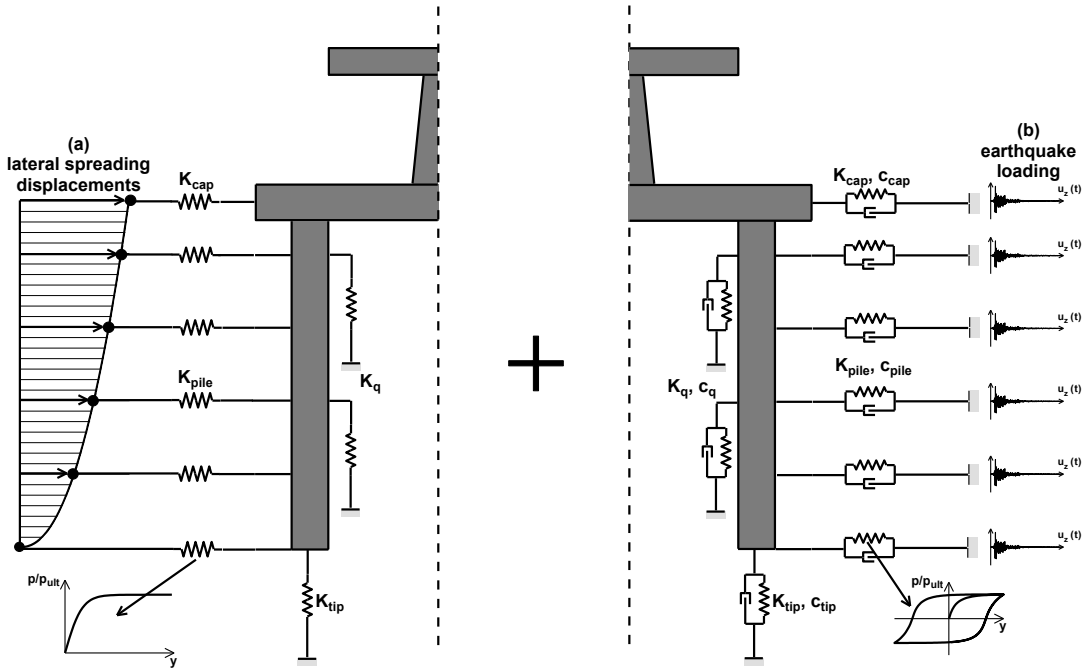

Figure 2.3: (a) Static and (b) Dynamic p-y analysis for problems involving lateral spreading displacements

Prior to performing an analysis with the p-y method knowledge with regard to the following issues is required:

- Determination of foundation and superstructure geometric and inertial characteristics.
- Estimation of applied loads (forces and displacements)
- Selection of an appropriate force/deformation law for the springs and dashpots to properly simulate soil response.

The latter is an issue that has been thoroughly investigated by many researchers during the past years, but still certain points remain unclear. **Figure 2.4**, which shows various p-y relationships for piles built in nonliquefied sand, is indicative of the uncertainties still governing the topic. The pile has a diameter of D=0.6m, the friction angle of the sand is 33^o and curves are drawn for a depth z=3D=1.8m. It is obvious that predictions vary significantly for each method, in terms of all the parameters that control a p-y curve (ultimate soil resistance, initial stiffness and non-linear shape).

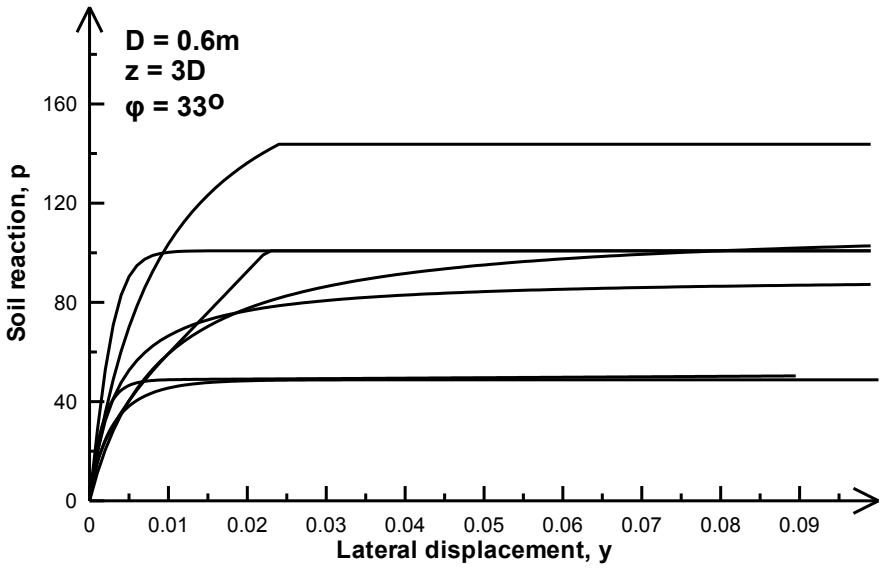

Figure 2.4: Various p-y curves in cohesionless soils

The following sections discuss in detail the various parameters involved in a p-y analysis. Findings and observations from recent studies, including centrifuge and shaking table tests, as well as numerical analyses, are also presented. Emphasis is

placed on parameters and mechanisms that govern p-y response of cohesionless soils.

2.2 P-y curves for static analysis

P-y curves for static problems should be developed to capture soil response under monotonic loading. In general, formulation of a p-y curve requires estimation of three (3) quantities, graphically illustrated in **Figure 2.5**:

- Ultimate Soil Resistance (p_{ult})
- Initial subgrade modulus (K_{ini}), usually expressed in terms of the subgrade modulus coefficient $k_{ini}= K_{ini} / z$, where z is the depth.
- Analytical expression (usually in terms of k_{ini} and p_{ult}) to describe the non-linear shape of the curve.

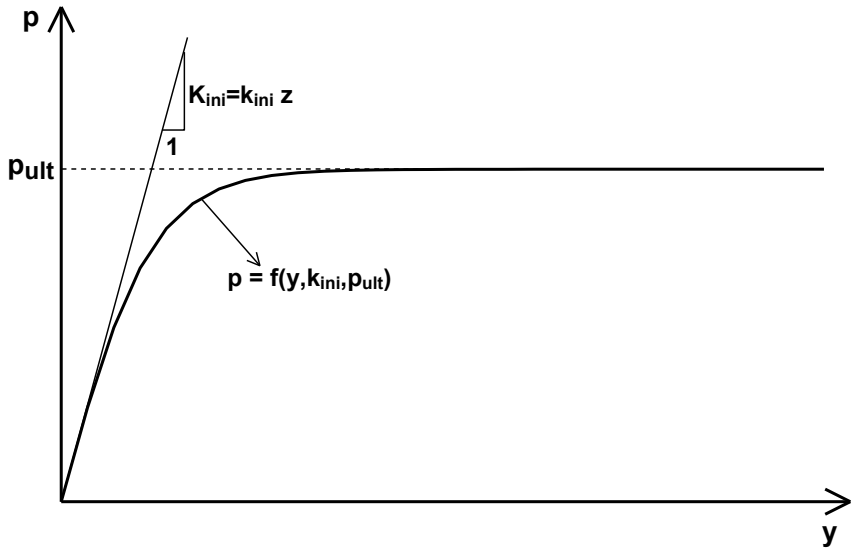

Figure 2.5: Quantities required to define a p-y curve

In the following, a series of analytical methods, developed by various researchers throughout the years, for developing p-y curves in sand will be presented. Finally, a comparison between the different methods will attempt to explain possible differences between them and reveal issues that might need further investigation.

2.2.1 Reese et al. (1974)

The relationships proposed by Reese et al. (1974) were developed based on full scale experiments carried out in Mustang Island in Texas, as described by Cox et al. (1974).

The layout of the test and the characteristics of the piles are shown in **Figure 2.6**. In total, two (2) open-ended steel piles with a diameter of 0.61m and a wall thickness of 9.5mm were used (Piles 1 and 2 in **Figure 2.6**), resulting in a pile stiffness of $E_p I_p = 168000 kNm^2$. The embedded length of each pile was 21m, corresponding to a slenderness ratio of L/D=34.4, and the distance between the two piles was 7.5m. The load cell was installed between the two piles, while a total of 34 strain gauges were bonded directly to the inside of the piles. To evaluate soil properties, two (2) boreholes were made prior to installation. After processing of the data, the relative density of the soil was estimated at approximately 90% and the friction angle at 39°.

In total, seven (7) tests were performed, two (2) static and five (5) cyclic, by applying a horizontal displacement at the head of the pile. Interpolation of test results led to the following analytical expressions in terms of Ultimate Soil Resistance, Non linear shape and Initial stiffness.

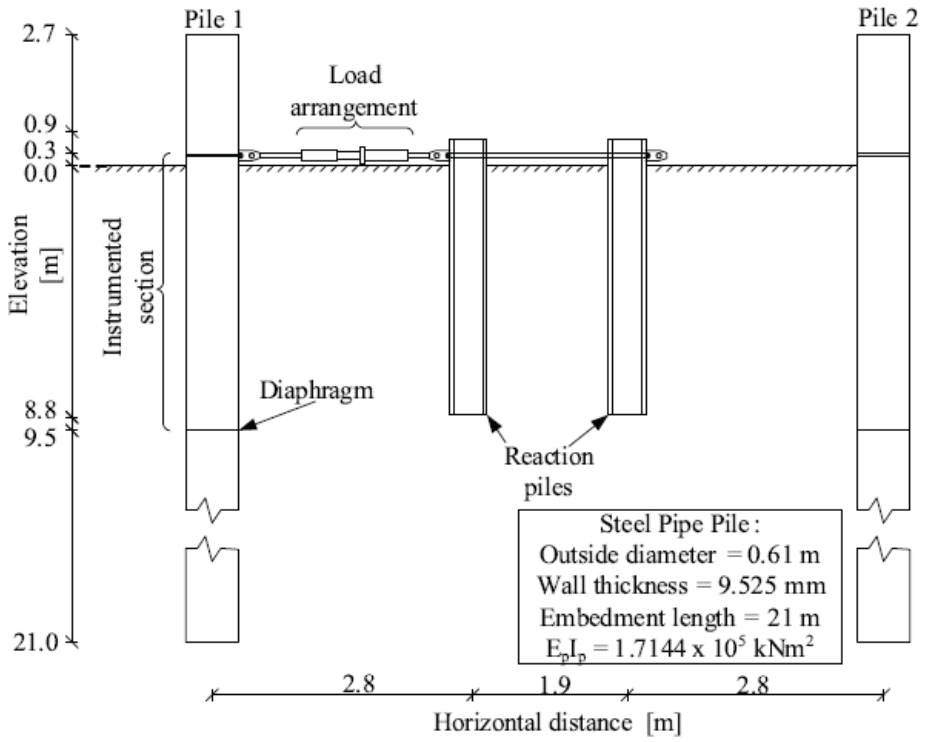

Figure 2.6: Layout of the tests in Mustang Island, Texas (Cox et al. 1974)

Ultimate Soil Resistance (p_{ult})

The researchers concluded that there are two possible failure mechanisms that can be developed, one for shallow and one for large depths. For shallow depths, it is assumed that a wedge, that extends to ground surface, will form in front of the pile, as illustrated in **Figure 2.7a** . The ultimate resistance per unit length (p_{cs}) can be estimated by the following expression:

$$p_{cs} = \gamma' z\left[\frac{K_o z \tan\varphi_{tr}\sin\beta}{\tan(\beta-\varphi_{tr})\cos\delta} + \frac{\tan\beta}{\tan(\beta-\varphi_{tr})}D + z\tan\beta\tan\alpha\right] + \gamma' z\left[K_o z\tan\beta\tan\varphi_{tr}\sin\beta - \tan\alpha - K_a D\right] \quad (2.1)$$

For large depths, a horizontal plane strain failure mechanism, like the one shown in **Figure 2.7b** is adopted. The authors, however, note that the principal horizontal stress at the back of the pile should be equal or larger to the minimum active Rankine pressure; otherwise the soil will fail by slumping. This type of failure is expressed analytically by the following equation:

$$p_{cd} = K_a D\gamma' z\left(\tan^8\beta - 1\right) + K_o D\gamma' z\tan\varphi\tan^4\beta \quad (2.2)$$

where:

γ': buoyant unit weight of the soil

z: Depth at which p_{cs} is calculated

D: Pile diameter

K_o: coefficient of horizontal earth pressure at rest

K_a: coefficient of active earth pressure

φ_{tr}: internal angle of friction based on triaxial tests

With respect to the above parameters, Reese et al. (1974) make the following assumptions:

$$\alpha = \varphi_{tr}/2 \quad (2.3)$$

$$K_a = \tan^2(45 - \varphi_{tr}/2) \quad (2.4)$$

$$\beta = 45 + \varphi_{tr}/2 \quad (2.5)$$

$$K_o = 0.40 \tag{2.6}$$

The previous formulation indicates that ultimate resistance is calculated based on Rankine's theory which is valid only if the pile surface is assumed smooth. Furthermore equation (2.6) assumes that horizontal stresses are not affected by neither the friction angle of the soil or the installation method of the pile.

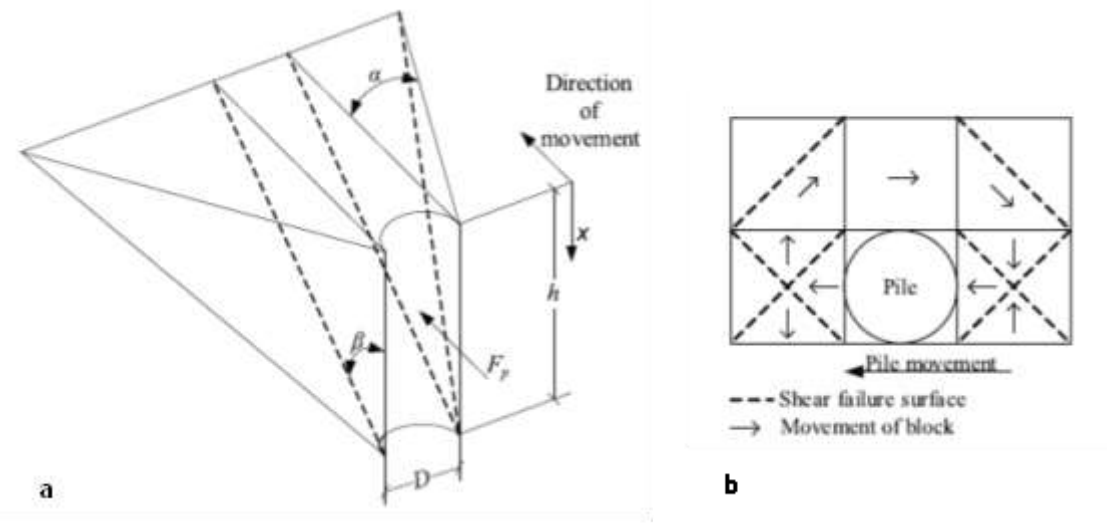

Figure 2.7: a) Wedged shaped and b) Horizontal plane strain failure mechanism (Reese et al. 1974)

It was observed that the analytical predictions from equations (2.1) and (2.2) did not fit well with the experimental data, especially for shallow depths and for the case where the pile was subjected to static loading. As a result the authors introduced the empirical coefficient A, whose variation with depth and type of loading, is shown in **Figure 2.8a**. This discrepancy can be attributed to the fact that the proposed failure mechanisms do not account for the shearing force between soil layers, whose effects are more pronounced in shallow depths and for static loads. Given this modification, the ultimate load per unit length (p_{ult}) can now be calculated as follows:

$$p_{ult} = Ap_c \tag{2.7}$$

where p_c is the minimum between p_{cs} and p_{cd}.

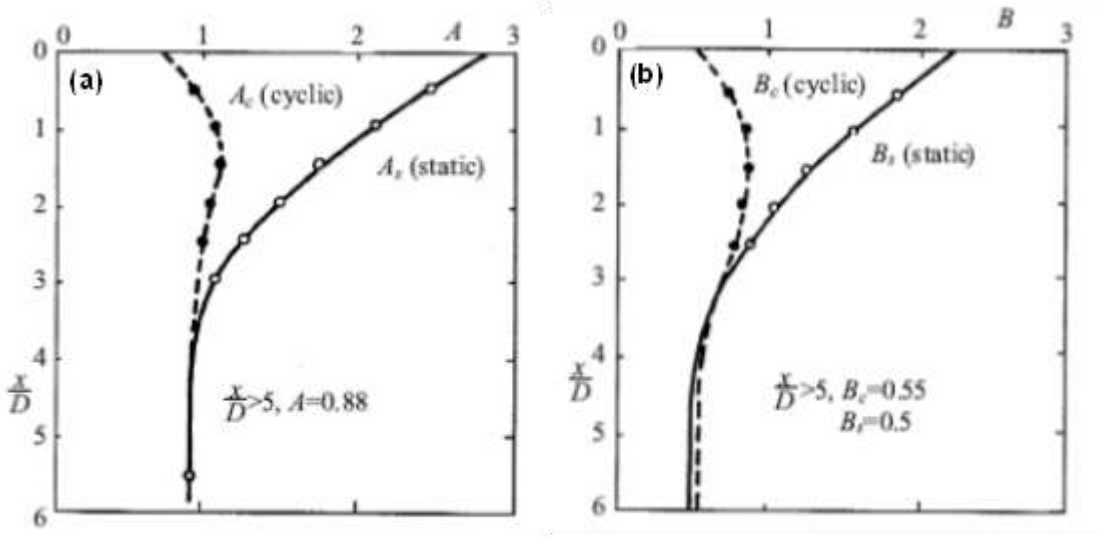

Figure 2.8: Values of nondimensional coefficients A and B for soil resistance versus depth

The following observations should be taken into account with regard to the ultimate soil resistance expression developed by Reese et al. (1974):

- The method, for shallow depths, assumes no friction between the pile and soil, leading to the formation of a Rankine failure mode. However, since the assumption of a perfectly smooth wall is over-simplifying, in reality a combination of the Rankine and Prandtl (mode for perfectly rough walls) failure surfaces will develop. Rankine's and Prandtl's failure surfaces are shown in **Figure 2.9a** and **Figure 2.9b** respectively.

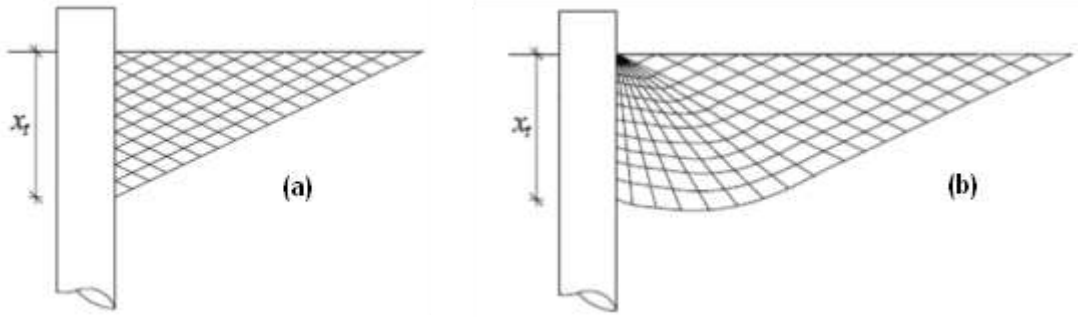

Figure 2.9: Failure modes for (a) smooth (Rankine) and (b) rough (Prandtl) surfaces (after Brodbaek et al. 2009)

- Furthermore the failure mechanism adopted disregards deformations that may occur beneath the point of zero deflection. This might be a common case for piles with high bending stiffness.
- Finally, the solutions are derived for the 2-dimensional case, while estimation of angle α, which defines the spread of the wedge, is based solely on the friction angle of the soil. However, Reese et al. (1974), in their work identify that the void ratio and type of loading also affect the value of angle α.

Initial Subgrade Modulus, K_{ini}

As for the initial subgrade modulus, it is assumed that it varies linearly with depth:

$$K_{ini} = k_{ini} z \tag{2.8}$$

Reese et al. (1974) suggest that k_{ini} depends on the relative density of the sand and whether the soil is above or below the water table and propose the values shown in **Table 2.1**.

Table 2.1: Representative values for k_{ini} for sand below and above the water table (Reese et al. 1974)

Relative Density	Loose	Medium	Dense
k_{ini} (kN/m³) - below the water table	5400	16300	34000
k_{ini} (kN/m³) - above the water table	6800	24400	61000

Nonlinear shape of p-y curve

The p-y curve is formulated by two (2) linear segments interpolated by a parabola as illustrated in **Figure 2.10** and described in the following step-by-step procedure (Reese and Van Impe, 2001):

- Obtain values for the friction angle φ_{tx}, the soil unit weight γ and pile diameter D.
- Select a depth at which the p-y curve is desired
- Calculate p_{ult} based on equations (2.1), (2.2) and (2.7).
- Establish y_u as 3D/80.
- Establish y_m as D/60 and calculate p_m by the following equation:

$$p_m = Bp_c \tag{2.9}$$

where B, shown in **Figure 2.8b**, is an empirical coefficient depending on the non-dimensional depth and type of loading.

- Establish the initial straight-line portion of the curve, using the appropriate value of k_{ini} from **Table 2.1**:

$$p = k_{ini} z \; y \tag{2.10}$$

- Establish the parabolic section of the p-y curve:

$$p = \bar{C} y^{1/m} \tag{2.11}$$

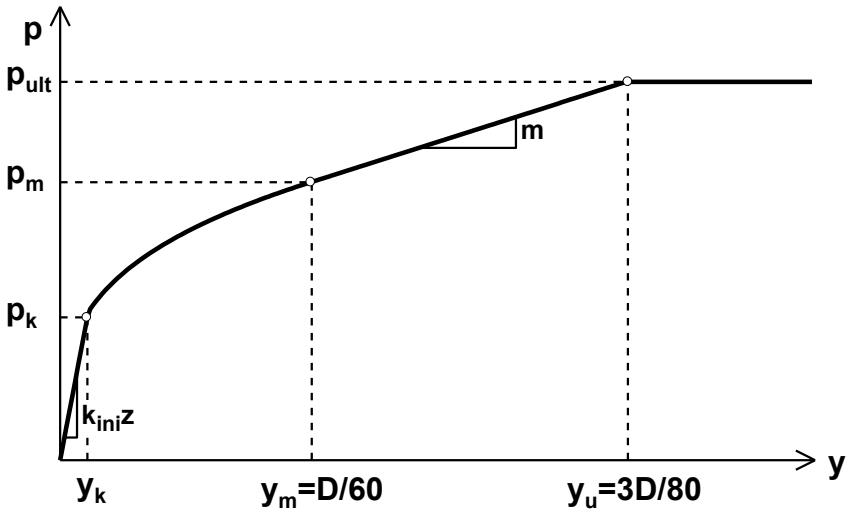

Figure 2.10: Characteristic shape of p-y curve for static and cyclic loading in sand (Reesse et al. 1974)

- Fit the parabola between points k and m as follows:
  - Get the slope of the line between m and u by:

$$m = \frac{p_{ult} - p_m}{y_u - y_m} \tag{2.12}$$

  - Obtain the power of the parabolic section:

$$n = \frac{p_m}{m y_m} \tag{2.13}$$

- Obtain coefficient $\bar{C}$ as follows:

$$\bar{C} = \frac{p_m}{y_m^{1/n}} \tag{2.14}$$

- Determine point k as follows:

$$y_k = \left(\frac{\bar{C}}{k_{ini} z} \right)^{n/m-1} \tag{2.15}$$

2.2.2 Murchison and O'Neill (1984) – API (2002)

Murchison and O'Neill (1984) proposed a slightly modified procedure for developing p-y curves in sands based on the work by Reese et al. (1974). It should be noted that their recommendations are included in the design regulations published by the American Petroleum Institute (API, 1993; API, 2002) and guide the design of pile supported structures in the United States and elsewhere. The proposed modifications are summarized in the following, in terms of ultimate soil resistance, initial subgrade modulus and nonlinear shape of the p-y curve:

Ultimate Soil Resistance (p_{ult})

The authors adopt the failure mechanisms proposed by Reese et al. (1974), but introduce the following approximations to their expressions:

$$p_{cs} = C_1 z + C_2 D \ \gamma' z \tag{2.16}$$

$$p_{cd} = C_3 D \gamma' z \tag{2.17}$$

where p_{cs} and p_{cd} correspond to the wedge-shaped and the horizontal plane strain failure mode respectively. C_1, C_2 and C_3 are dimensionless functions of the relative density or peak friction angle, and can be evaluated by the chart of **Figure 2.11** or by the following approximations proposed by **Stewart (2000)**:

$$C_1 = 0.115 \cdot 10^{0.0405\varphi_p} \tag{2.18}$$

$$C_2 = 0.571 \cdot 10^{0.022\varphi_p} \tag{2.19}$$

$$C_3 = 0.646 \cdot 10^{0.0555\varphi_p} \tag{2.20}$$

where φ_P is the friction angle of the soil.

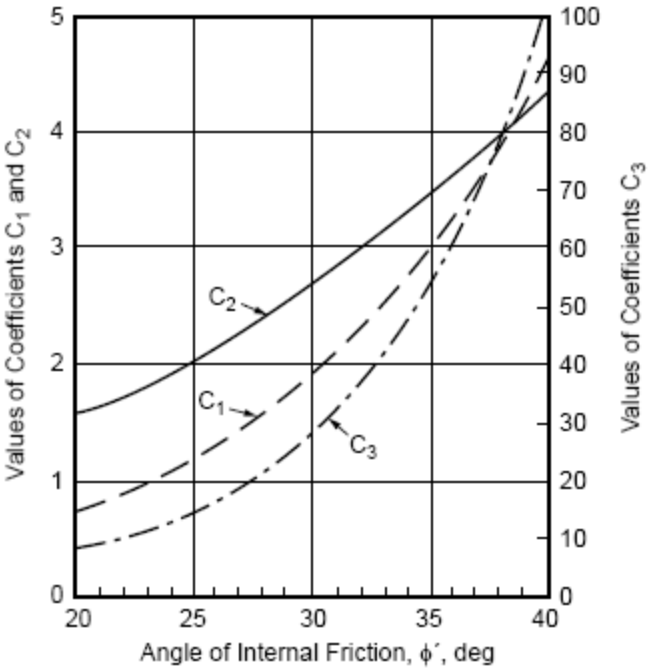

Figure 2.11: Coefficients C_1, C_2 and C_3 as function of angle of internal friction (API, 2002)

It should be noted that if the exact solution for p_c, proposed by Reese et al. (1974), is desired the following expressions for C_1, C_2 and C_3 should be used:

$$C_1 = \frac{K_o \tan\varphi \sin\beta}{\tan(\beta-\varphi)\cos\alpha} + \frac{\tan^2\beta \tan\alpha}{\tan(\beta-\varphi)} + K_o \tan\beta\,[\tan\varphi \sin\beta - \tan\alpha] \tag{2.21}$$

$$C_2 = \frac{\tan\beta}{\tan(\beta-\varphi)} - K_\alpha \tag{2.22}$$

$$C_3 = K_o \tan\varphi \tan^4\varphi + K_\alpha \tan^8\beta - 1 \tag{2.23}$$

As for the empirical coefficient A [see eq. (2.7)], the authors suggest the following analytical expression instead of the values in **Figure 2.8a**:

$$A = \begin{cases} 3 - 0.8\dfrac{z}{D} \geq 0.9 & \text{for static loading} \\ 0.9 & \text{for dynamic loading} \end{cases} \tag{2.24}$$

Initial Subgrade Modulus, K_{ini}

Similarly to what is suggested by Reese et al. (1974), initial subgrade modulus is assumed to vary linearly with depth, as described in equation (2.8). However, evaluation of the gradient k_{ini} of the initial modulus is performed by the chart in **Figure 2.12** as a function of either the Relative Density or the friction angle of the soil. It can be observed that the proposed chart corresponds to values of Relative Density of up to 80%, and thus it should be used with caution for very dense soils.

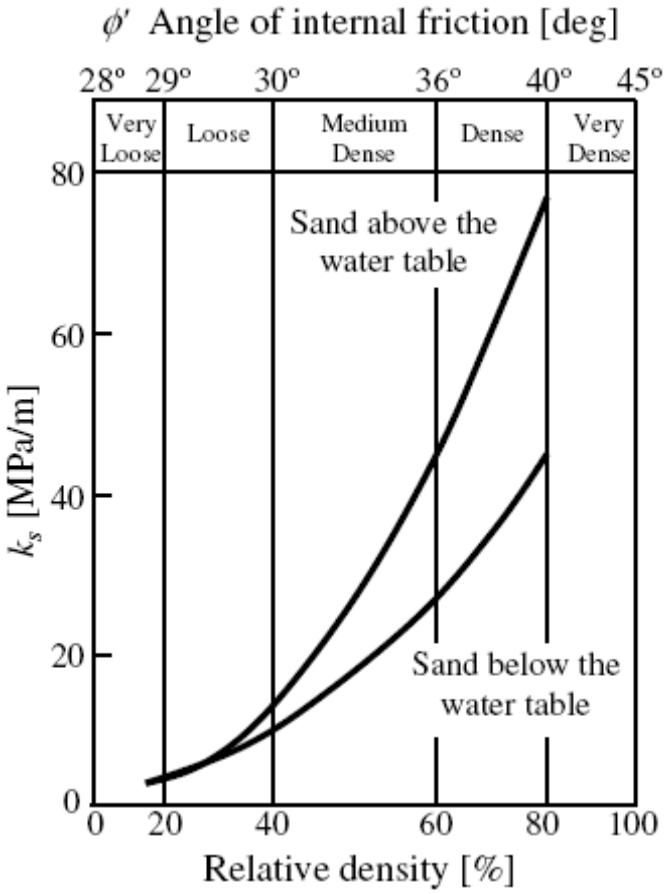

Figure 2.12: Gradient k_{ini} of initial subgrade modulus of soil as a function of Relative Density or internal friction angle of the soil (API, 2002)

Nonlinear shape of p-y curve

Murchison and O'Neill (1984) assume that the non linear response of the soil can be expressed by the following hyperbolic function:

$$p = p_{ult} \tanh\left(\frac{k_{ini} z y}{p_{ult}} \right) \tag{2.25}$$

Differentiation of this expression with respect to horizontal displacement y, for y approaching zero, yields:

$$\left.\frac{dp}{dy}\right|_{y=0} = p_{ult} \left. \frac{\frac{k_{ini} z}{p_{ult}}}{\cosh^2\left(\frac{k_{ini} z y}{p_{ult}} \right)} \right|_{y=0} = k_{ini} z = K_{ini} \tag{2.26}$$

which reflects the linear variation of the initial subgrade modulus with depth, discussed previously.

2.2.3 Georgiadis et al. (1992)

Georgiadis et al. (1992) proposed a new relationship to describe the p-y response of cohesionless soils based on the results of a centrifuge experiment program. The program involved lateral loading of three (3) open-ended steel pipes installed in dry sand. The layout of the test is shown in **Figure 2.13**, while the pile characteristics are summarized in **Table 2.2**. The sand was compacted to a relative density of 60%, corresponding to a unit weight of 16.3kN/m^3 and an angle of internal friction of 36^o (determined by triaxial tests).

The piles were pulled laterally through a steel cable adjusted to a gear box motor unit. The applied load was measured by a 2.5 kN load cell, and pile displacements were measured at two different elevations along the length of the pile above the soil surface. Based on these measurements horizontal displacements at ground surface were evaluated taking into account the applied load and the flexural stiffness of the pile. Finally, numerous strain gauges were installed on each pile to evaluate the bending moment profile with depth. Interpolation of the results led to the following suggestions with respect to the p-y response of cohesionless soils.

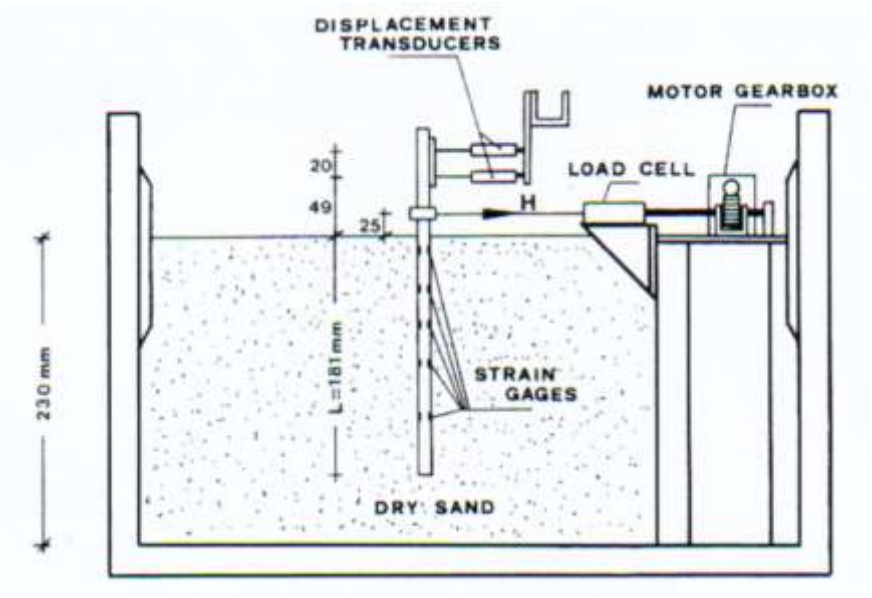

Figure 2.13: Experimental layout (Georgiadis et al. 1992)

Table 2.2: Characteristics of the three piles used in the experiment (Georgiadis et al. 1992)

	Pile P_1	Pile P_2	Pile P_3
Outside Diameter D (m)	1.092	1.224	1.229
Wall thickness t (mm)	44.45	17.25	15.25
Length L (m)	9.05	9.05	9.05
Young Modulus (kN/m^2)	1.928 x 10^8	1.928 x 10^8	1.928 x 10^8
Flexural Stiffness EI (MN m^2)	3878.5	2495.0	2066.0

Ultimate Soil Resistance (p_{ult})

The authors adopt the analytical model, initially proposed by Reese et al. (1974), described in equations (2.1) and (2.2). However, they propose a modified expression for the empirical facto A, which is described as:

$$A = 2 - \frac{z/D}{3} \geq 1 \qquad (2.27)$$

The proposed values are slightly smaller than the ones predicted by the **Figure 2.8** or equation (2.24), however the authors note that results are not very sensitive to the values of the parameter A.

Initial Subgrade Modulus, K_{ini}

This study also adopts the assumption that initial subgrade modulus varies linearly with depth [see equation (2.8)]. However the authors suggest, for the gradient of initial modulus (k_{ini}), the use of the values proposed by Terzaghi (1955), shown in **Table 2.3**. These values are significantly smaller compared to the ones proposed by Reese et al. (1974) and Murchison and O'Neill (1984) in **Table 2.1** and **Figure 2.12** respectively.

Table 2.3: Gradient of initial subgrade modulus, k_{ini} (Terzaghi, 1955)

Relative Density	Loose	Medium	Dense
k_{ini} (kN/m^3)	1100 - 3300	3300 - 11000	11000 - 23400

Nonlinear shape of p-y curve

Description of the non linear soil response is performed by the following hyperbolic function, originally proposed by **Kodner (1963)**:

$$p = \frac{y}{\frac{1}{k_{ini} z} + \frac{y}{p_{ult}}} \tag{2.28}$$

Again differentiation with respect to y, for $y \to 0$ yields

$$\left.\frac{dp}{dy}\right|_{y=0} = \left.\frac{k_{ini} p_{ult}^2 z}{k_{ini}^2 y^2 z^2 + 2 k_{ini} p_{ult} z y + p_{ult}^2}\right|_{y=0} = k_{ini} z = K_{ini} \tag{2.29}$$

indicating the linear variation of K_{ini} with depth.

2.2.4 Det Norske Veritas (DnV) (1980)

The Norwegian classification society Det Norske Veritas (DnV) developed in 1980 a methodology to construct p-y curves based on empirical methods as well as a few full-scale tests. It should be noted that DnV' s expressions were developed for piles supporting offshore structures and undergoing severe cyclic wave loads. These piles have large diameters, typically ranging between 1.0 and 1.5m, and hence are stiffer compared to the ones used in typical geotechnical projects. DnV's recommendations are summarized in the following:

Ultimate Soil Resistance (p_{ult})

For static loading, p_{ult} can be calculated as:

$$p_{ult} = 4K_p\sigma_v D \tag{2.30}$$

For cyclic loading p_{ult} is given by:

$$p_{ult} = 3K_p\sigma_v D, \text{ for depths } z > 2D \tag{2.31}$$

$$p_{ult} = 3\frac{z}{2D}K_p\sigma_v D, \text{ for depths } z \le 2D \tag{2.32}$$

where:

$$K_p = \frac{1+\sin\varphi}{1-\sin\varphi} \text{ (Passive Pressure Coefficient)} \tag{2.33}$$

σ'_v: effective overburden pressure

φ: characteristic angle of shearing resistance

z: depth

D: Pile diameter

Friction angle should be estimated from representative laboratory test. In the guidelines it is also noted that expressions (2.30), (2.31) and (2.32) might underestimate soil resistance, especially for large depths. However, the above conservative expressions were adopted, given that few tests results were available.

Initial Subgrade Modulus, K_{ini}

Estimation of the initial subgrade modulus follows the logic of all previous methodologies that assume linear variation with depth and dependence on the Relative Density of the soil. However, as shown in **Table 2.4**, values of the subgrade modulus coefficient, k_{ini}, are modified, being closer to Terzaghi and significantly smaller than Reese or API.

Table 2.4: Estimation of initial subgrade modulus coefficient (DnV, 1980)

Relative Density	Loose	Medium	Dense
k_{ini} (kN/m3)	5000	12000	18000

Nonlinear shape of p-y curve

Similarly to the method of Georgiadis et al. (1992), the nonlinear shape of the curve is simulated using equation (2.28) proposed by Kodner (1963). However, the authors aiming to achieve a more stiff response, multiply ultimate soil resistance with a coefficient factor $\alpha > 1$. Thus, the asymptote of the hyperbola is not the $p = p_{ult}$ line, but the $p = a \cdot p_{ult}$. The mathematical expression of the curve, which is also drawn in **Figure 2.14**, has the following form:

$$p = \frac{y}{\frac{1}{k_{ini} z} + \frac{y}{a \cdot p_{ult}}} \tag{2.34}$$

in which the coefficient factor α is given by:

$$a = \frac{1}{1 - \frac{p_{ult}}{\beta k_{ini} z D}} \tag{2.35}$$

where β=0.04. Equation (2.34) for α is valid for $\beta D > p_{ult} / k_{ini} z$, while for $\beta D \le p_{ult} / k_{ini} z$ the hyperbola can be replaced by a straight line.

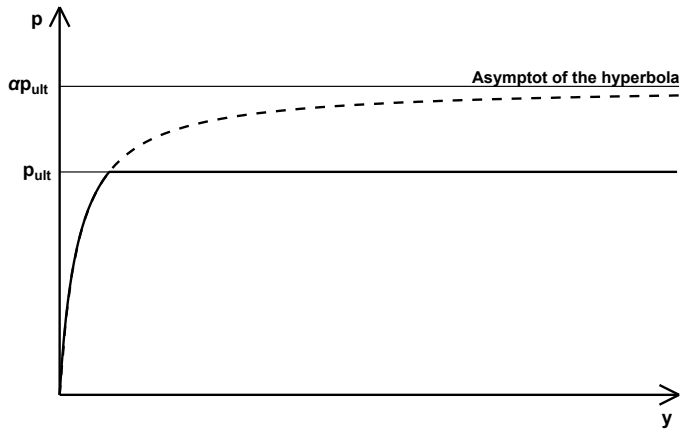

Figure 2.14: Construction of the p-y curve according to DnV recommendations (1980)

2.2.5 Non-unified methodologies

The methodologies described so far provide guidance to estimate all three (3) components of a p-y curve (p_{ult}, k_{ini}, shape). Apart from these methods, which constitute a unified framework, there are a number of studies that provide estimates for the ultimate soil resistance or the initial subgrade modulus. These estimates, which will be described in the following, can be used either to evaluate predictions of unified methodologies or to develop a new framework.

2.2.5.1 Estimation of ultimate soil resistance, p_{ult}, based on passive earth pressure theory

Most of these methods are used to analyze short piles, i.e. piles that move as rigid bodies, a very common case for piles subjected to kinematic loads due to lateral ground displacement. For piles undergoing horizontal forces applied to their heads, **Broms (1964a, 1964b)** has developed the following criterion to classify a pile as short:

$$\frac{L}{T} \leq 2 \tag{2.36}$$

where L is the pile length and T an index to estimate the relative soil-pile stiffness, defined as:

$$T = \left[\frac{E_p I_p}{k_{ini}} \right]^{1/5} \tag{2.37}$$

where:

E_pI_p: Stiffness of the pile

k_{ini}: coefficient of subgrade modulus

Depending on the fixity conditions of its head, a short pile can deform according to two (2) mechanisms, which are shown in **Figure 2.15a** and **Figure 2.15b** for free-head and fixed-head piles respectively.

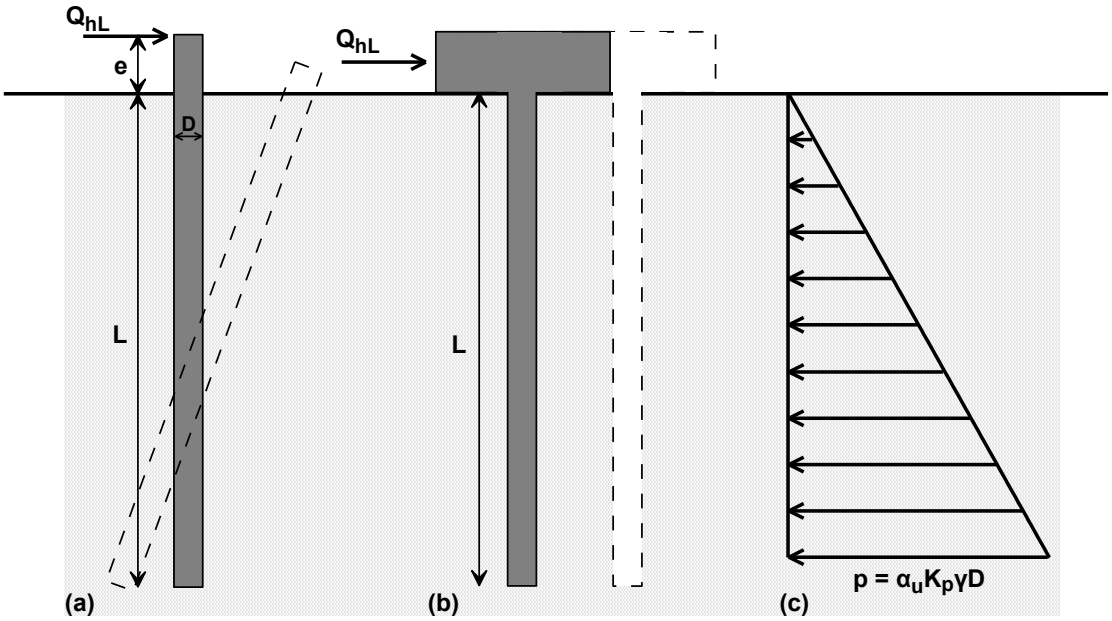

Figure 2.15: Mode of failure for (a) free-head and (b) fixed-head short piles and (c) distribution of soil reaction

Calculation of ultimate soil resistance is based on the following assumptions:

- Effect of active earth pressures, developed at the back of the pile, is ignored.
- Passive earth pressures developed in front of the pile are significantly larger compared to Rankine theory due to the shearing resistance on the vertical sides of the failure wedge in the soil. This is taken into account by incorporating a coefficient α_u (**Figure 2.15c**) in the calculation of passive pressures, according to the following equation:

$$p = \alpha_u K_p \gamma z D \tag{2.38}$$

where:

p: Soil reaction per unit length

α_u: Shape factor for passive pressures due to 3-D effects

K_p: Passive earth pressure coefficient

γ: Unit weight of soil

D: Pile diameter

Bransby (1996) suggests that the value of α_u depends on the type of lateral loading, namely, active-pile-loading and passive-pile-loading, shown in **Figure 2.16a** and **Figure 2.16b** respectively. In active piles a horizontal force is applied at the head of

the pile and passive pressures develop at the front of the pile. On the other hand, loading of passive piles is the result of lateral ground displacement and development of passive pressures at their back. In other words, earth pressures act as resisting forces for active piles, and as driving forces in passive piles.

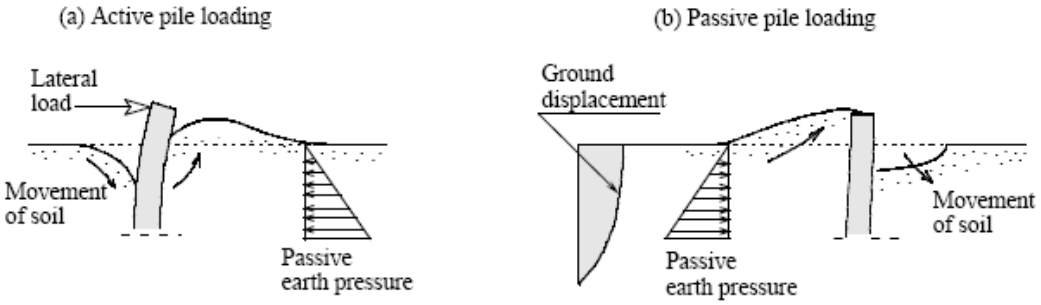

Figure 2.16: Schematic illustration for (a) active and (b) passive lateral pile loading (Cubrinovski et al., 2005)

Estimation of the shape factor α_u is based on experimental tests. **Figure 2.17** summarizes test results from various researchers (Broms, 1964; Meyerhof et al., 1981; Poulos et al., 1995; Prasad and Chari, 1999; **Cubrinovsky et al., 2005**), which indicate that α_u ranges between 3 and 7, with the lower bound corresponding to active piles and the upper to passive. **Table 2.5** summarizes several recommendations for calculation of ultimate soil resistance in sand.

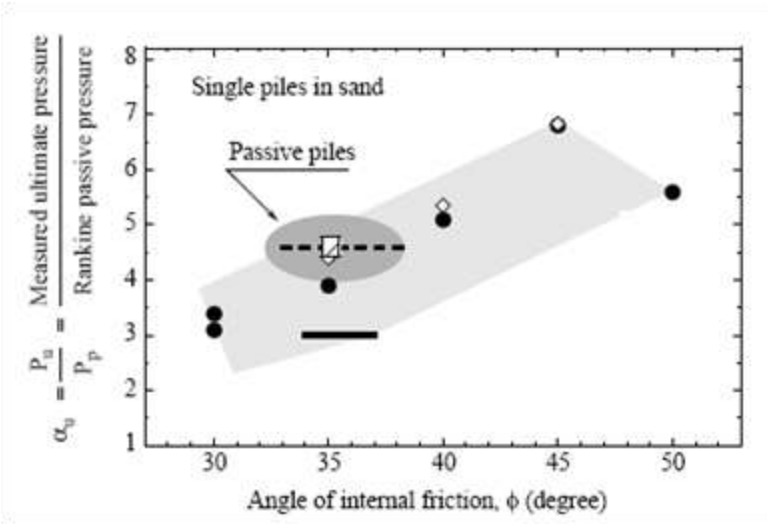

Figure 2.17: Shape factor for passive pressure based on experimental tests on single piles in sand (Cubrinovski et al., 2005)

Table 2.5: Summary of recommendations for calculation of p_{ult} based on passive earth pressure theory

α/α	**$p_{ult}/(\sigma_{vo}D)$**	**Reference**
1	3 K_p	Broms (1964a, 1964b)
2	4.5 K_p	Cubrinovski et al. (2005)
3	$10^{(1.3\tan\varphi+0.3)}$	Prasad and Chari (1999)
4	K_p^2	Fleming et al. (1992)

2.2.5.2 Brinch – Hansen's method for p_{ult}

Brinch-Hansen (1961) developed a more sophisticated method for short piles, based on experimental tests on wooden piles in sand. In his analysis Brinch-Hansen distinguishes three (3) types of soil response, for small, moderate and large depths, and develops equations to estimate soil resistance for each case.

For *small depths* ($z \to 0$), the author assumes that ordinary active and passive earth pressures act on the pile, and hence soil resistance is calculated as:

$$p = K_q \sigma_{vo} D \tag{2.39}$$

where K_q is the difference between passive and active coefficients, given by the following equation:

$$K_{q\ z=0} = K_p - K_a = e^{0.5\pi+\varphi\ \tan\varphi}\cos\varphi\tan(45+\varphi/2) - \\ - e^{-\ 0.5\pi+\varphi\ \tan\varphi}\cos\varphi\tan(45-\varphi/2) \tag{2.40}$$

where φ is the friction angle of the soil.

For *moderate depths*, the Passive Rankine case is considered, i.e. a wedge with a $45+\frac{\varphi}{2}$ slope with respect to the vertical. Assuming that the wedge is bounded by two (2) vertical planes running along the two (2) sides of the pile (the vertical distance between the planes is equal to the pile diameter, D), and that in these planes the shearing forces that develop correspond to a normal pressure equal to the earth pressure at rest ($K_o\sigma_{vo}$), then force equilibrium gives the following expression for soil reaction due to passive earth pressures at depth z:

$$p_p = \gamma z K_p \left[1+\frac{z}{D}\frac{K_o\sin\varphi}{\sin\ 45+\varphi/2}\right] D \tag{2.41}$$

If active pressures acting at the back of the pile are included in the formulation, the above expression yields:

$$p = \gamma z K_q \left[1 + \frac{z}{D} \frac{K_o \sin\varphi}{\sin\ 45+\varphi/2} \right] D \qquad (2.42) \quad .$$

Finally, for *large depths* $z \to \infty$, it is assumed that rupture lines do not have a $45+\varphi/2$ inclination, but they are horizontal. For this case, the author uses his formula for the bearing capacity of strip foundations (**Brinch Hansen, 1961**):

$$p_u = cN_c d_c + \ q + \gamma D \ \ N_q d_q + \frac{1}{2}\gamma B N_\gamma d_\gamma \qquad (2.43)$$

where:

c: Cohesion of soil

q: Overburden pressure

γ: Unit weight of soil

D: Depth of foundation

N_c, N_q, N_γ: Bearing Capacity factors

d_c, d_q, d_γ: Depth factors

Since failure takes place horizontally, the γ-term, which represents increase of soil strength with depth, should be left out, yielding:

$$p_u = cN_c d_c + qN_q d_q \qquad (2.44)$$

However, factors N_c and N_q, d_c and d_q are interrelated according to the following equations:

$$N_c = \ N_q - 1 \ \frac{1}{\tan\varphi} \qquad (2.45)$$

$$d_q = d_c - \frac{d_c - 1}{N_q} \qquad (2.46)$$

Applying equations (2.45) and (2.46) into (2.44) yields:

$$p_u = \ c + q\tan\varphi \ \ N_c d_c + q \tag{2.47}$$

For piles in sand c=0. In addition, the effective vertical pressure, q, is substituted by the horizontal pressure at rest, $\sigma_{ho}=K_o\sigma_{vo}$. This pressure is obviously applied at the back of the pile as well, and hence the second term in the right side of equation (2.47) should be left out in order to calculate the net ultimate soil resistance:

$$p_u = K_o\sigma_{vo}\tan\varphi N_c d_c = \sigma_{vo}K_q \tag{2.48}$$

where:

$$K_{q\ \ z\to\infty} = K_o\tan\varphi N_c d_c \tag{2.49}$$

Brinch Hansen makes the following recommendations for K_o, N_c and d_c:

$$K_o = 1-\tan\varphi \tag{2.50}$$

$$N_c = \left[e^{\pi\tan\varphi}\tan^2\ \ 45+\varphi/2\ \ -1\right]\cot\varphi \tag{2.51}$$

$$d_c = 1+0.35\left[\frac{B}{D}+\frac{0.6}{1+7\tan^4\varphi}\right] \tag{2.52}$$

However, it is rational to assume that the depth of the foundation, i.e. the width of the soil behind the pile, is infinite, $D\to\infty$. Thus equation (2.52) becomes:

$$d_c = 1.58+4.09\tan^4\varphi \tag{2.53}$$

Therefore, the ultimate soil resistance for a pile of diameter D, at a depth z, in a soil with a friction angle φ, is calculated by:

$$p = \gamma z K_q D \tag{2.54}$$

Where K_q, K_o, N_c and d_c are estimated from equations (2.49), (2.50), (2.51) and (2.53).

Finally, in order to simplify the calculations, Brinch Hansen introduced the following formula for K_q, which is valid for all depths:

$$K_q = \frac{K_{q\ z=0} + K_{q\ z\to\infty} \cdot \alpha_q \frac{z}{D}}{1+\alpha_q \frac{z}{D}} \tag{2.55}$$

where:

$$\alpha_q = \frac{K_{q\ z=0}}{K_{q\ z\to\infty} - K_{q\ z=0}} \cdot \frac{K_o \sin\varphi}{\sin\ 45+\varphi/2} \tag{2.56}$$

The above empirical formula yields the same results with equations (2.40) and (2.49) for small and very large depths, while variation with depth is expressed with the brackets in (2.42), satisfying the moderate depth criterion.

2.2.5.3 Japanese regulations for the estimation of initial subgrade modulus

According to **Japanese Design Specifications (JRA, 2002; RTRI, 1999; AIJ, 2001)** soil reaction, p, is related to pile deflection, y, with the following expression:

$$p = k_h D y \tag{2.57}$$

where k_h is the coefficient of subgrade reaction and D the diameter of the pile. It should be noted that in Japanese specifications k_h is not normalized with depth, as shown in equation (2.8), but with respect to pile diameter D:

$$K_h = k_h D \tag{2.58}$$

where K_h is the modulus of subgrade reaction. Therefore, for Japanese recommendations to be compared with values of k_{ini} presented earlier, one should multiply the proposed values with the ratio of pile diameter to depth, as follows:

$$k_{ini} = k_h \frac{D}{z} \tag{2.59}$$

In ***JRA*** *(Specifications for Highway Bridges)* k_h can be calculated by the following equations:

$$k_h = k_{ho}\ \ B_H / 0.3^{\ -3/4}\ \ (\mathrm{kN/m^3}) \tag{2.60}$$

$$B_H = \sqrt{D/\beta} \tag{2.61}$$

$$\beta = \left(k_h D / 4EI\right)^{1/4} \tag{2.62}$$

$$k_{ho} = \alpha E_0 / 0.3 \ (\mathrm{kN/m^3}) \tag{2.63}$$

$$E_0 = 2800N \ (\mathrm{kN/m^2}) \tag{2.64}$$

where:

B_H: normalized width of pile (m)

D: Pile diameter (m)

β: Characteristic value

EI: Bending rigidity of pile ($\mathrm{kNm^2}$)

α: constant value (α=2 for E_0 evaluated from N-value)

E_0: Young's modulus ($\mathrm{kN/m^2}$)

N: SPT N-value

In ***RTRI*** *(Design Standards for Railway Facilities)* k_h is estimated as follows:

$$k_h = f_{rk} \ 0.6\alpha E_0 D^{-3/4} \tag{2.65}$$

$$E_0 = 2500N \ (\mathrm{kN/m^2}) \tag{2.66}$$

where

f_{rk}: resisting factor of soil (=1.0)

α: constant value (=2 for E_0 evaluated from N-value)

D: Pile diameter (m)

E_0: Young's modulus ($\mathrm{kN/m^2}$)

Finally, in ***AIJ*** *(Recommendations for Design of Building Foundations)* k_h is evaluated as follows:

$$k_h = \alpha\xi E_0 B^{-3/4} \ (\mathrm{kN/m^3}) \tag{2.67}$$

$$E_0 = 700N \ (\mathrm{kN/m^2}) \tag{2.68}$$

where

y: lateral displacement of pile (cm)

α: constant value (α=80 for E_0 evaluating from N-value in sandy soil)

ξ: constant for group piles (1.0 for single pile)

E_0: Young's modulus (kN/m²)

B: Width of pile (cm)

2.2.6 Comparison and observations between various recommendations for p-y curves in nonliquefied sand

The different methodologies presented above are used in this section to simulate the response of a pile with length L=16m, diameter D=0.6m, built in a uniform sand deposit with Relative Density D_r=50%, friction angle φ=33° and unit weight γ=9.81kN/m³. Predictions are compared in terms of ultimate soil resistance, coefficient of initial subgrade modulus and nonlinear shape. Comparison reveals significant variations among the predictions of each methodology

Ultimate Soil Resistance

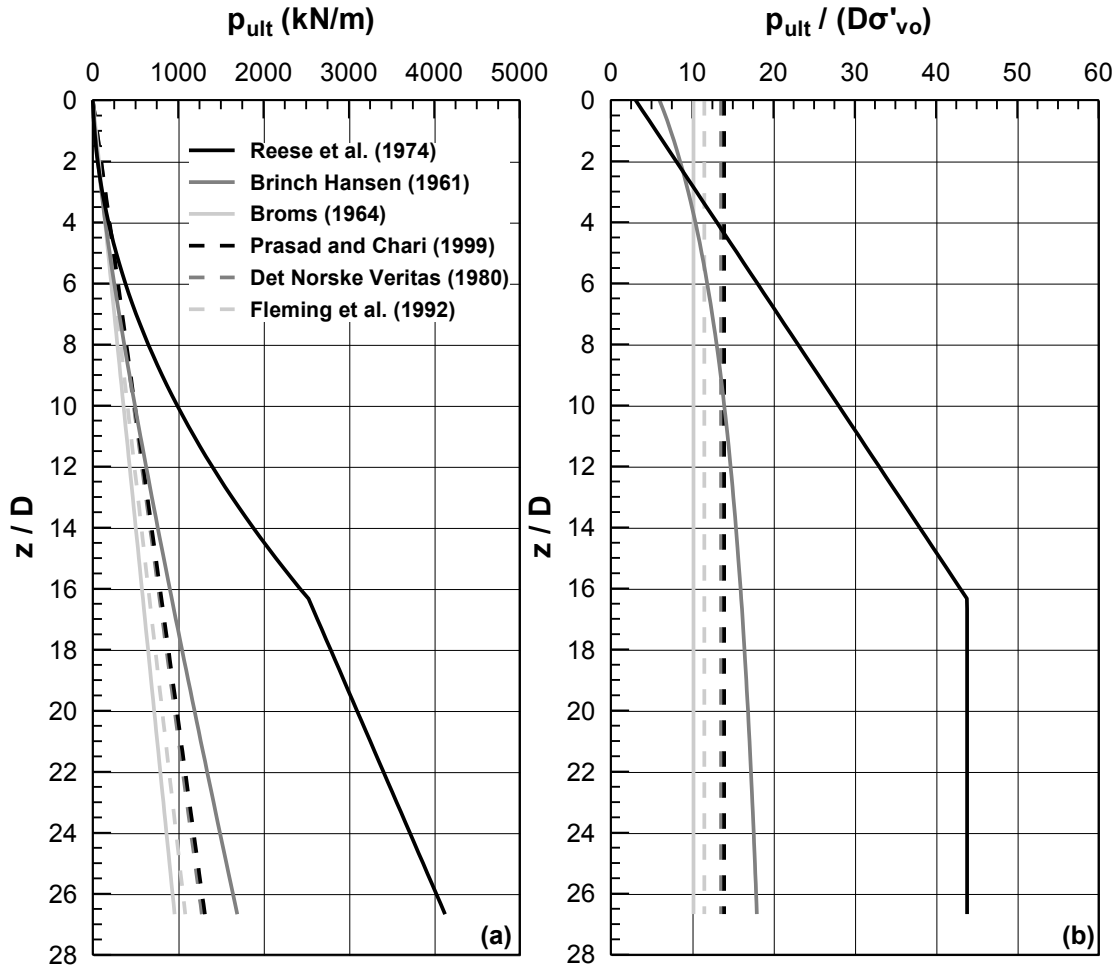

Figure 2.18: Variation of (a) p_{ult} and (b) normalized p_{ult} with depth as predicted by various analytical methodologies

The variation of ultimate soil resistance with normalized depth is shown in **Figure 2.18a**. In order to make the comparison more clear (especially for small depths), p_{ult} is normalized with vertical effective stress and pile diameter, and plotted in **Figure 2.18b**. Based on this figure, the following can be observed:

- For methods based on the passive earth pressure theory (Broms, DnV, Prasad and Chari, Fleming et al.), the ratio of p_{ult} remains constant with depth and equal to $a_u K_p$. Any differences among these methodologies arise from different suggestions for the value of a_u.
- Brinch-Hansen's formula predicts a small non-linear increase of p_{ult} with depth, starting from values that are slightly smaller compared to passive pressure theory and become slightly larger as depth increases. In any case, his predictions remain close to the passive pressure theory, but his model is more sophisticated, given that it incorporates different failure mechanisms depending on the depth of interest.
- Finally, Resse's methodology gives a linear transition, according to the wedge-type failure, until a depth of about sixteen (16) diameters. At that point, the plane strain failure mechanism becomes critical and variation with depth remains constant. Compared to the other two (2) methods, Reese's approach gives slightly smaller values of p_{ult} for small depths ($z/D < 4$). However, as depth increases, p_{ult} increases significantly reaching values which are 4÷5 times larger compared to the other methods.

Initial Subgrade Modulus

Variation of coefficient of initial subgrade modulus and initial subgrade modulus with depth are shown in **Figure 2.19a** and **Figure 2.19b** respectively. It can be observed that the methods by API and Reese recommend a very similar range, with values of k_{ini} between 15000 and 25000 kN/m^3. On the other hand Terzaghi (1955) suggests significantly smaller values that range between 3000 and 11000 kN/m^3. Finally DnV's recommendations rest approximately upon the upper bound of Terzaghi's estimates.

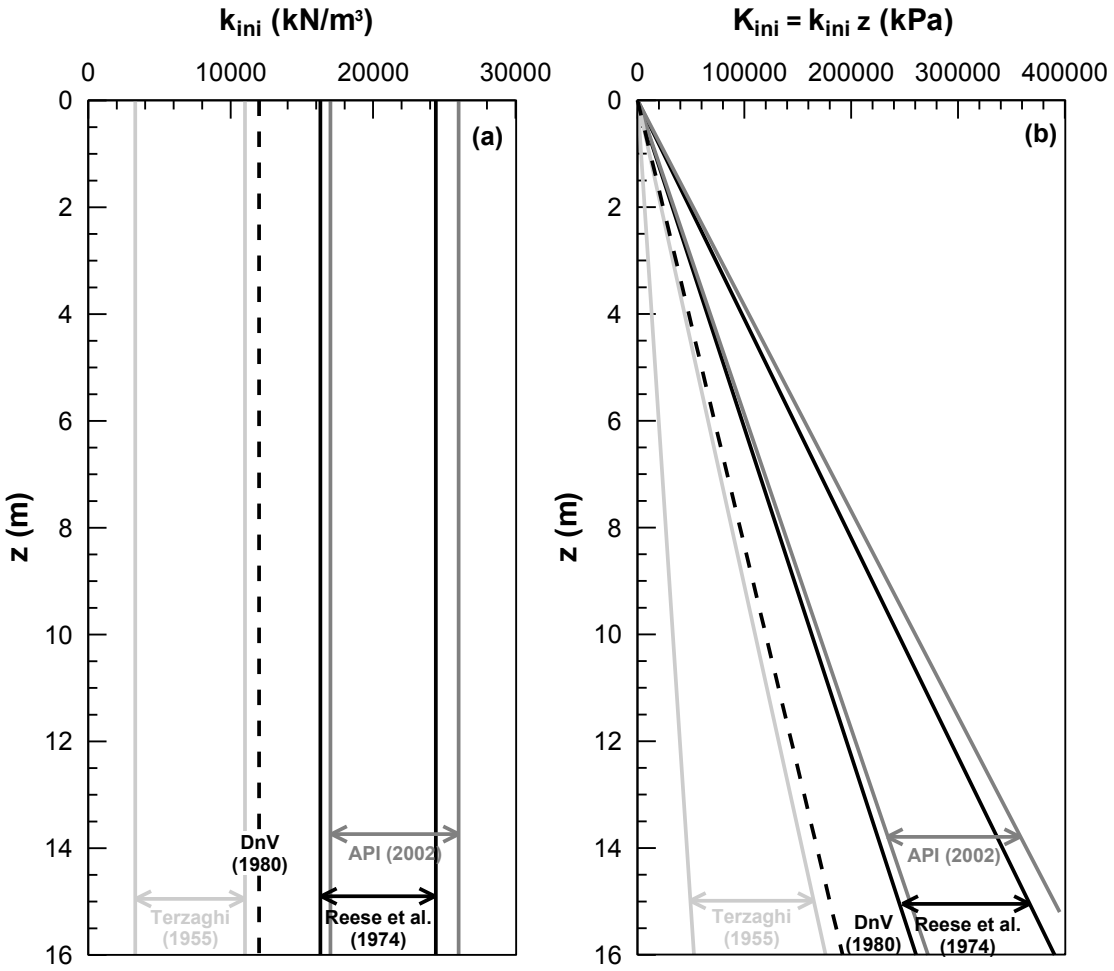

Figure 2.19: Variation of (a) coefficient of initial subgrade modulus and (b) initial subgrade modulus with depth

Nonlinear shape

Mathematical expressions (2.25), (2.28) and (2.34) adopted in API's, Georgiadis' and DnV's methods respectively, are compared in **Figure 2.20**. Note that all three expressions were applied by using as input the same values for both p_{ult} and k_{ini}. It can be observed that API reaches ultimate resistance more rapidly, resulting in an overall much stiffer response compared to Georgiadis, while DnV is somewhere in-between.

The above example makes clear that existing methodologies do not provide a generally accepted framework for estimation of soil p-y response. Therefore application of a specific method may lead to different estimation of soil response and hence, different pile design. In addition the above methodologies were developed based on a certain number of field tests and therefore reflect a limited set of field

conditions. As a result, any generalization and application of the methods for a broader range of parameters should be verified through a systematic parametric investigation. Also, it is suggested that characteristics of p-y curves (capacity, stiffness, shape) depend solely on the Relative Density of the soil and the diameter of the pile.

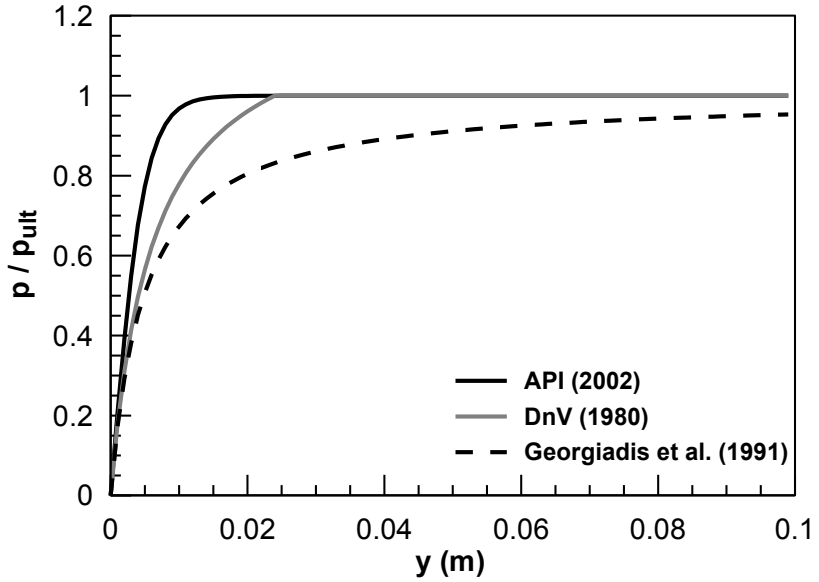

Figure 2.20: Comparison between different analytical expression for the prediction of the nonlinear shape of the p-y curve (for the same k_{ini} and p_{ult})

Ashour and Norris (2000) explored the influence of other factors based on a semi-empirical model that they developed, which was verified against well-established p-y relationships (Matlock 1970, Reese et al. 1974). The model is based on the assumption that the mechanism of failure behind the pile is wedge-shaped. **Figure 2.1** shows the effect of pile stiffness on p-y response for sands and clays. It is observed that stiff piles exhibit higher soil resistance. The effect is more pronounced for dense sands and stiff clays, but less significant for loose sands and soft clays. Similar trends are observed when other pile characteristics, such as the fixity conditions of the pile head, the pile cross-section and the depth of the embedment, are examined.

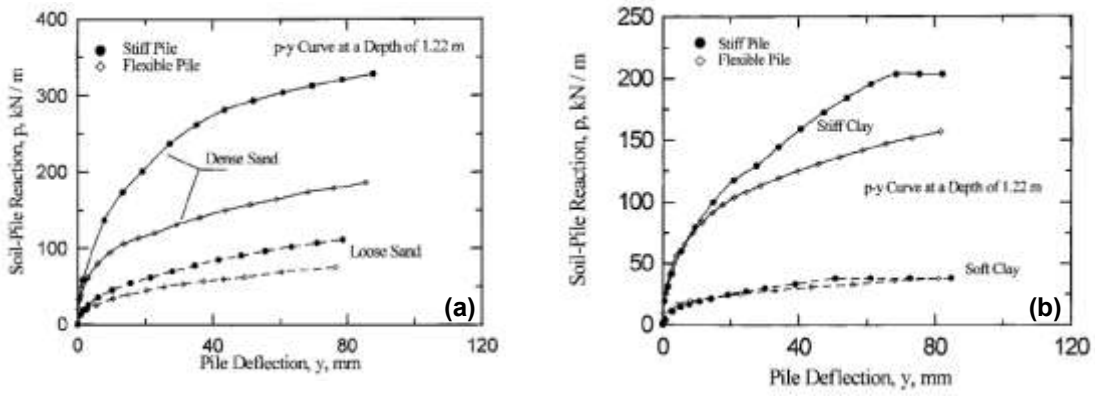

Figure 2.21: Effect of pile stiffness on p-y response for (a) sands and (b) clays (Ashour and Norris, 2001).

In addition, none of the existing methods clarifies whether it can be used for both drilled and driven piles. All the methods described above were developed based on tests on driven open-ended piles and hence, their applicability on drilled shafts is questioned. It is furthermore well established that pile driving modifies significantly the stress and volumetric state of the surrounding soil, and therefore it is reasonable to expect effect on the p-y response of the soil. **Kim et al. (2004)** performed a series of field tests on both driven and pre-installed piles. Load-displacement curves, shown in **Figure 2.22**, reveal that pile installation indeed affects p-y response of the soil.

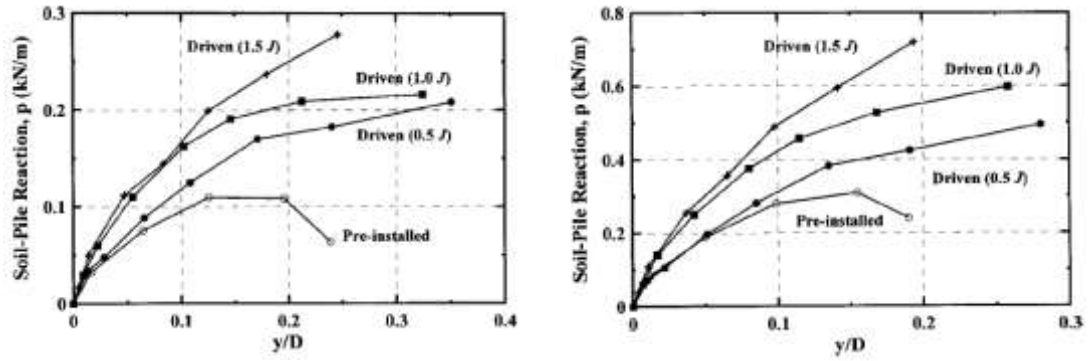

Figure 2.22: Effect of pile installation on p-y response of the soil (after Kim et al., 2004)

In any case, and especially for large-scale projects, it is recommended to develop p-y curves experimentally based on full-scale tests at the site of the project.

2.3 P-y curves for dynamic analysis

In dynamic p-y analyses, simulation of soil-pile interaction requires description of three (3) elements to capture three (3) phenomena:

- Springs that simulate the hysteretic response of the soil under dynamic loading
- Dashpots to simulate radiation and viscous damping. The former is a result of energy dissipation due to wave propagation from the pile to the soil.
- Spring to simulate the behavior of the gap, which can develop between the pile and the soil.

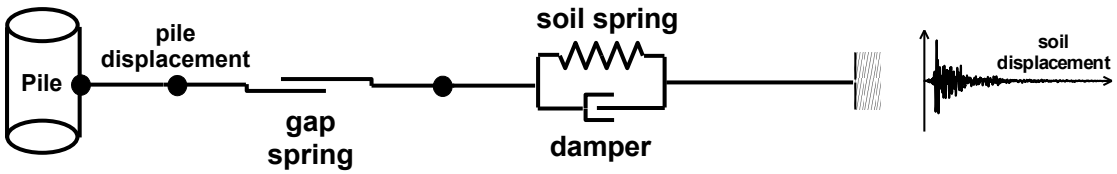

Figure 2.23: Layout and components of a typical macroelement used in dynamic p-y analyses

The layout of a typical macroelement containing all the three (3) components described above is shown in **Figure 2.23**. In the following, various recommendations related to the components of the macroelement will be discussed based on findings from the literature.

2.3.1 Modeling of soil hysteretic response

For the modeling of the hysteretic soil response under dynamic loading, many researchers use the model developed by **Bouc (1971)** and extended by **Wen (1976)**, commonly referred as the Bouc-Wen model. The equation of motion for the macroelement can be written as:

$$m\ddot{y}\ t\ + c\dot{y}_r\ t\ + F_s\ t\ = f\ t \tag{2.69}$$

where:

m: Mass of the pile

c: Damping coefficient

y(t): Absolute pile displacement

y_r(t): Soil-pile relative displacement

$F_s(t)$: Restoring force due to the reaction of the spring

$f(t)$: Excitation force due to soil displacement at the free-field

According to the Bouc-Wen model, the restoring or hysteretic spring force can be expressed by the following equation:

$$p_s\ t\ = \alpha K_{ini} y_r + \ 1-\alpha\ \ p_y \zeta \tag{2.70}$$

where,

p_s: Subgrade reaction on a pile segment of unit length

y_r: Soil-Pile relative displacement defining the reaction of the spring

K_{ini}: Initial stiffness of the hysteretic spring

p_y: Characteristic value related to the initialization of significant yielding

α: Parameter that controls the post-yielding stiffness

ζ: hysteretic dimensionless quantity

The hysteretic parameter ζ is governed by the following equation:

$$y_{r,0}\,\dot{\zeta} + \gamma |\,\dot{y}_r\,| \zeta \left|\zeta\right|^{n-1} + \beta\,\dot{y}_r \left|\zeta\right|^n - A\,\dot{y} = 0 \tag{2.71}$$

In the above equation **Constantinou and Adnane (1984)** showed that, when A=1, K_{ini} in equation (2.70) becomes the initial modulus of subgrade reaction and α is equal to the ratio of post-yielding to initial stiffness. By eliminating the time variable in (2.71), parameter ζ can be expressed as:

$$d\zeta = \frac{dy_r}{y_{r,0}}\ 1-\left|\zeta\right|^n \left[\ \beta + \gamma sign\ \ dy_r \zeta\ \right] \tag{2.72}$$

where

$y_{r,0}$: value of the relative displacement that initiates yielding at the spring and

n, β and γ: Dimensionless parameters that, along with α, control the shape of the hysteretic loop.

Parameters n and α govern the transition from the linear elastic to the nonlinear part of the curve, as well as the post-yielding response of the soil. For large values of n, the pre-yielding part of the curve remain linear, and for α=0, the post-yielding

response is perfectly plastic. The effect of parameters n and α is illustrated in **Figure 2.24**.

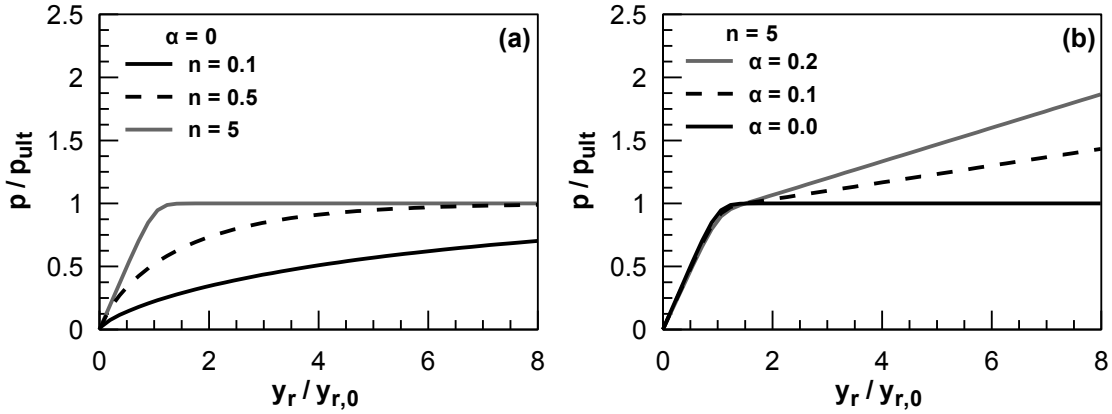

Figure 2.24: Influence of parameters (a) α and (b) n on the shape of the initial (virgin) circle of the Bouc-Wen hysteretic spring model.

Furthermore, parameters β and γ control the stiffness upon reversal. It should be noted that it is a convenient assumption to assume that $\beta+\gamma=1$, which leads to $|\zeta|\leq 1$ (**Badoni and Makris, 1995**). The effect of β and γ is illustrated in **Figure 2.25**. It can be observed that large values of β and small values of γ correspond to approximately elastic response, while small values of β and large values of γ cause the unloading stiffness to be almost twice as the initial.

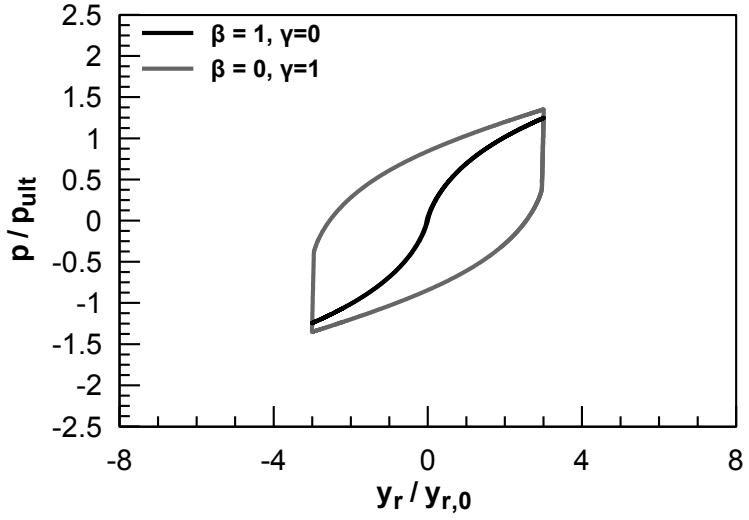

Figure 2.25: Effect of parameters β and γ on the post-yielding stiffness of the Bouc-Wen hysteretic spring model.

Parameter calibration is performed through comparison with experimental data or analytical expressions like the ones described in the previous section. A common approach by many researchers (**Badoni and Makris, 1996; Gerolymos et al., 2005; Assimaki and Varun, 2009**) is the use of Brom's method to estimate p_y [see equation (2.38) and **Table 2.5**], and the use of the following formula, proposed by **Gazetas and Dobry (1984)** to estimate initial stiffness:

$$K_{ini} = 1.2E_s \tag{2.73}$$

where E_s is the young's modulus of the soil. Finally parameters n and α are calibrated so as to fit the shape of the analytical or experimental curve in consideration.

Boulanger et al. (1999) developed a model in which the elastic and the plastic component of the soil spring are separated. This is done to improve the modeling of radiation damping, as it will be discussed later. The plastic spring has an initial range of rigid behavior between $-C_r p_{ult} \le p \le C_r p_{ult}$ where C_r is the ratio of p/p_{ult} when plastic yielding first occurs in virgin loading. Beyond the rigid range loading of the spring is described by:

$$p = p_{ult} - \left(p_{ult} - p_0\right)\left[\frac{cy_{50}}{cy_{50} + \left|y - y_0\right|}\right]^n \tag{2.74}$$

where

p_{ult}: ultimate resistance of the p-y element in the current loading direction
p_0: pressure at the start of the current plastic loading cycle
y_0: displacement at the start of the current plastic loading cycle
c: constant to control the tangent modulus at the start of plastic yielding
n: exponent to control the sharpness of the curve
y_{50}: displacement corresponding to 50% of p_{ult}

This model has also been adopted by **Tokimatsu and Suzuki (2009)** in analyses they performed to simulate shaking table tests.

In their analyses Boulanger et al. calibrated their parameters to match the backbone curve included in API's rules, discussed earlier in chapter 2.2.2. However, for the initial stiffness, API's recommendations as well as the assumption for linear variation

with depth is not adopted. The authors make use of Vesic's (1961) elastic theory for beams resting on isotropic elastic solids, with G_{max} according to site response analyses and assuming a ratio of G/G_{max} equal to 25%.

2.3.2 Modeling of soil radiation damping

The term radiation damping is used to express the energy that is absorbed by the soil and is carried away from the pile by waves that are generated as a result of the interaction between the pile and the soil. The magnitude of radiation damping depends on the frequency of excitation, the geometry of the soil-foundation system and the stress-strain characteristics of the soil (Gazetas and Dobry, 1984).

The force resulting from the dashpot is proportional to the relative velocity between the pile and the soil and can be expressed as follows:

$$p_d = c_r \, \dot{y} \, D \tag{2.75}$$

Where p_d is the force carried by the dashpot, $\dot{y}$ is the relative velocity between the pile and the soil and c_h is the dashpot coefficient.

Berger et al. **(1975)** proposed the following expression for the dashpot coefficient assuming that oscillation of the pile generates P waves in the direction of shaking and SH waves travelling in the direction perpendicular to shaking (**Figure 2.26a**):

$$c_r = 2B\rho_s V_s \left(1 + \frac{V_p}{V_s}\right) \tag{2.76}$$

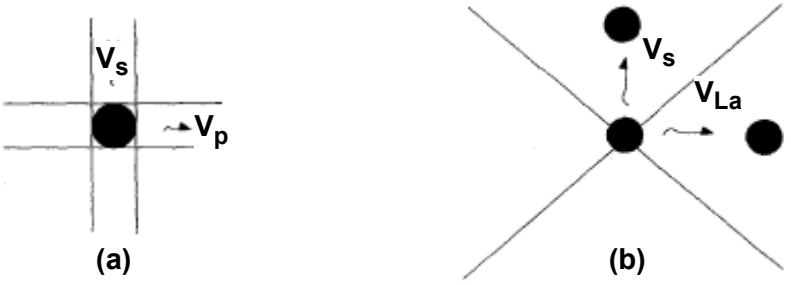

Figure 2.26: Horizontal propagation of waves away from a vibrating pile for (a) Berger et al. (1975) and (b) Gazetas and Dobry (1984) model (after Tabesh and Poulos, 2001)

Furthermore, **Kaynia (1998)**, based on Berger's recommendations, proposed the value $5\rho_s V_s$ for the dashpot coefficient, by matching results from FEM models and pile analyses with the p-y method.

Gazetas and Dobry (1984) assume that radiated S waves propagate with velocity V_s in two quarter planes and compression-extension waves propagate with the so-called Lysmer's analog "wave velocity", V_{La}, given by equation (2.77), in the other two (**Figure 2.26b**).

$$V_{La} = \frac{3.4}{\pi\ 1-\nu} V_s \tag{2.77}$$

Furthermore they correlate the damping coefficient with the diameter of the pile (B), the density of the soil (ρ_s), shear wave velocity (V_s) and the frequency of the excitation motion (ω):

$$c_r = 2\left[1+\frac{3.4}{\pi\ 1-\nu}\right]^{1.25}\left(\frac{\pi}{4}\right)^{0.75}\left(\frac{\omega B}{V_s}\right)^{-0.25}\rho V_s B \tag{2.78}$$

The correlation is shown in **Figure 2.27** for two different values of the Poisson's ratio, v=0.25 and 0.40.

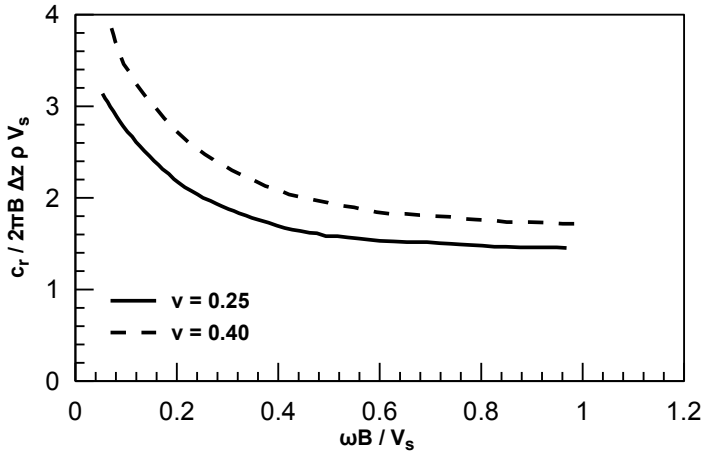

Figure 2.27: Radiation Damping Coefficient of a pile (Dobry and Gazetas, 1984)

The expressions by Gazetas and Dobry have been adopted by many researchers (Badoni and Makris, 1995; Boulanger et al. 1999; Gerolymos et al., 2005; Assimaki and

Varun, 2009). However, **Badoni and Makris (1996)** note that for large pile deflections the proposed correlation leads to large estimates of the damping force. Therefore they propose a limiting value for F_d expressed by the following formula:

$$F_d = c_r \omega y \le c_r \omega y_o \tag{2.79}$$

where y_o is the value of pile deflection at which yielding initiates at the spring.

The above formula takes advantage of the fact that, for harmonic excitations, velocity $\dot{y}$ is proportional to ωy . In other words the dashpot should connect in parallel only with the elastic component of the p-y spring, while the plastic component should be in series with the elastic spring-dashpot system. This formulation, which was also proposed by **Boulanger et al. (1999)**, is shown schematically in **Figure 2.28**.

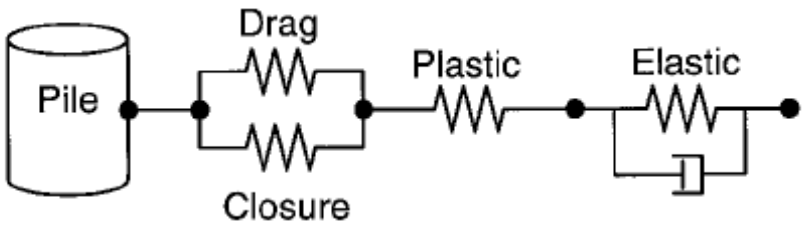

Figure 2.28: Macroelement formulation for dynamic p-y analysis in which the elastic and plastic spring components are separated to avoid large dashpot reactions (Boulanger et al. 1999)

Finally, **Tabesh and Poulos (2001)** note that both Dobry's and Berger's correlations described above give similar results, with the modification proposed by Kaynia being slightly conservative. They also stress out that extreme care should be taken with regard to radiation damping in pile analysis, because soil layers are not horizontally infinite, soil is not completely elastic and its behavior changes seasonally with changes in water level, nearby excavations etc.

2.3.3 Modeling of gap between soil and pile

Following **Matlock's et al. (1978)** suggestions, Boulanger et al. (1999) assume that the gap affects the response by means of a drag force acting on the sides of the pile, as the latter moves within the gap. This residual resistance is defined in terms of soil ultimate resistance p_{ult} with the aid of a parameter C_d:

$$C_d = p_{res,gap} / p_{ult} \tag{2.80}$$

Based on back-calculated curves from the experiments conducted by **Wilson (1998)**, the authors assigned to C_d a value equal to 0.3. In the dynamic p-y analysis the gap behavior is modeled by adding two (2) springs in the macroelement as shown in **Figure 2.28**. It can be observed that apart from the drag spring, simulating the response of the gap, the authors also used in parallel connection a closure spring in order to make the transition in load-displacement behavior, as the gap opens and closes, more smooth.

Gerolymos et al. (2005) simulates the gap formation by multiplying the hysteretic parameter ζ (section 2.3.1) with a function h_p, which represents the gap behavior and has the following form:

$$h_p\ \zeta\ = 1 - \zeta_0 \exp\left[-\left(\frac{y_0 \zeta}{\delta \Delta\ y} \right)^2 \right] \tag{2.81}$$

Hence, equation (2.72), for the hysteretic parameter takes the following form:

$$d\zeta = \frac{h_p\ \zeta}{y_{r,0}}\ 1 - |\zeta|^n \left[\beta + \gamma sign\ \ dy_r \zeta\ \right] \tag{2.82}$$

where:

δ: Parameter that controls the gap growth during cyclic (repeated) loading

ζ_0: Parameter that determines the drag resistance within the gap. Takes values between 0 and 1, with large values corresponding to negligible drag resistance

Δ (y): Maximum attained displacement when y is positive and minimum attained displacement when y is negative.

The formulation assumes that separation will take place when the net tensile stress, p/D, at a specific point of the soil-pile interface becomes larger than the difference between the earth pressure at rest σ'_{ho} and the active earth pressure, σ'_{ha}:

$$p / D > \sigma'_{ho} - \sigma'_{ha} \tag{2.83}$$

It should be noted that the formation of the gap is a phenomenon pronounced in clayey soils and negligible in sands. However, its simulation is included herein to make the presentation more comprehensive.

Overall, from the above analysis it is clear that the essential mathematical models have been developed to simulate the effects of dynamic loading on the response of the soil (hysteretic response, radiation damping and gap formation). However, calibration of these models depends in a great amount on p-y curves for nonliquefied soils, and therefore dynamic p-y analyses enclose all the uncertainties discussed previously related to static p-y analyses.

2.4 P-y curves for liquefaction related problems

Liquefaction and lateral spreading can drastically alter the response of the pile compared to the non-liquefaction case. Specifically, pore pressure build-up causes soil softening and reduction of ultimate soil resistance, which results in a different interaction mechanism between the pile and the liquefied soil and hence modification of the characteristics (stiffness, nonlinear shape and capacity) of the p-y springs.

In practice, degradation of soil resistance is simulated by applying a reduction multiplier on p-y curves for firm soil. This coefficient is called m_p-multiplier and is usually estimated through empirical charts (Brandenberg, 2005; AIJ, 2001; Dobry et al., 1995; Han et al. 2007; Cubrinovski et al., 2005), which associate m_p with various parameters (Relative Density, excess pore pressure ratio, soil-pile relative displacement etc). Recent studies (Haigh, 2002; Gonzalez et al., 2009; Tokimatsu and Suzuki, 2009; Boulanger et al., 2007), however, have shown that development of subgrade reaction in liquefied soils is a much more complicated phenomenon and the m_p approach might be over-simplifying. In addition, the various recommendations for m_p give different results, while others are hard to apply (for example it is hard to estimate pore pressure build-up). The present section aims to present existing methods for estimating subgrade reaction, as well as main findings from experimental and numerical investigation of the problem.

One of the first attempts to estimate the reduction multiplier was done by **Dobry et al. (1995).** The authors correlated the degradation factor with the pore pressure ratio in the free field based on centrifuge data in medium dense sand (D_r=40%). The

correlation is illustrated in **Figure 2.29a** and shows that m_p decreases linearly with r_u until it reaches the value of 0.10 for complete liquefaction.

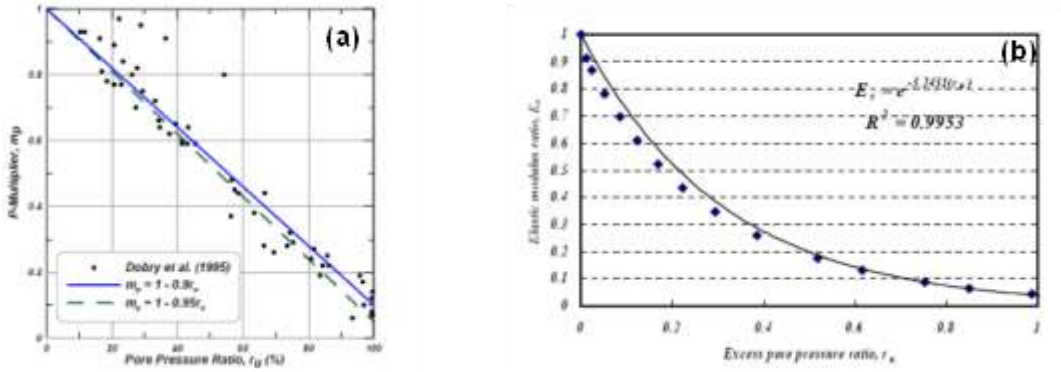

Figure 2.29: Degradation factor m_p as a function of excess pore pressure ratio in the free field (a) Dobry et al. (1995) (b) Han et al. (2007)

Similarly to Dobry's approach **Han et al. (2007),** based on combined results from shaking table tests and numerical analyses, also correlated the degradation factor with the pore pressure ratio. The relationship is shown in **Figure 2.29b** and can be described from the following function:

$$m_p = e^{-3.2431\, r_u} \tag{2.84}$$

The exponential form of the relationship results in lower values for m_p, compared to Dobry's. The main drawback of the above correlations is the fact that they do not incorporate effects of pore-pressure build-up in the area surrounding the pile, which is a paramount factor affecting development of soil resistance.

Wilson et al. (1999) conducted tests in the centrifuge facilities of UC Davis on level ground profiles of uniform sand, for different pile and structure characteristics, different input motions and different soil properties. Back-calculation of p-y response showed that the resistance was larger for models of higher relative density, while resistance was practically negligible for very loose models. Furthermore when relative displacement exceeded previous maximum values hardening occurred, indicating p-y dependence on strain history. However, as shaking evolved soil resistance decreased, resulting in an overall softening p-y response. The authors attributed degradation both to pore pressure build-up and to the fact that towards

the end of shaking displacements rarely exceeded previous maxima. Finally the authors recognized that apart from the factors that affect undrained response of saturated sand (relative density, strain and strain history), subgrade reaction is also affected by rate effects and drainage conditions.

Brandenberg et al. (2005) conducted centrifuge tests on piles in liquefied gently-sloping ground. Back-calculation of soil resistance showed large transient values of subgrade load due to transient drops of excess pore pressure, as a result of soil dilation. These drops, which are commonly referred in the literature as dilation spikes, were different for seismic motions of different frequency content, indicating the presence of loading rate effects. Finally, for flexible piles, liquefied soil provided a resisting force, as pile displacement exceeded that of the soil.

Based on the results of these tests, Brandenberg (2005) and Brandenberg et al. (2007) proposed the chart shown in **Figure 2.30** for estimating m_p. Despite the fact that the tests showed clear dependence of subgrade reaction on frequency content and pile stiffness, the multiplier was only related to the relative density of the soil. Recommendations are also compared in the same figure with AIJ (2001) guidelines, showing good agreement for small values of $(N_1)_{60}$, while m_p is much smaller than AIJ as $(N_1)_{60}$ increases.

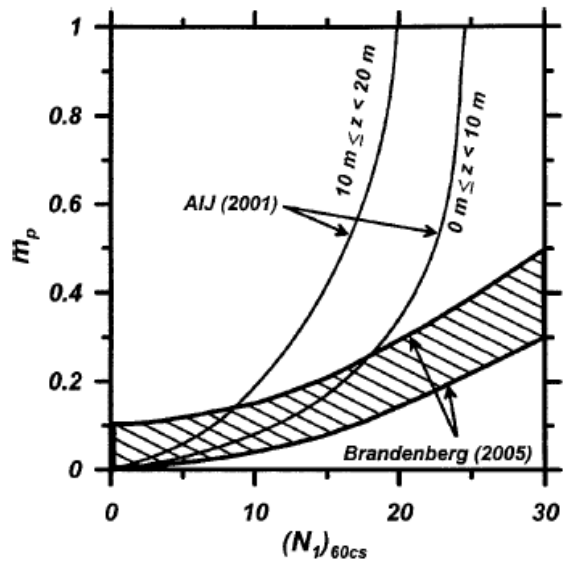

Figure 2.30: Degradation factor m_p as a function of Relative Density [D_r or $(N_1)_{60cs}$] (Brandenberg et al. 2007)

For cases where partial liquefaction is expected (i.e. r_u less than unity) the authors suggest that m_p can be approximated with linear regression:

$$m_p = 1 - r_u \left(1 - m_{p,liq}\right) \tag{2.85}$$

where m_p is the interpolated value, $m_{p,liq}$ is the value for complete liquefaction, and r_u the excess pore pressure ratio in the free field.

Finally, it should be noted that the correlation suggested by Brandenberg et al. (2007) was derived based on back-analysis of centrifuge tests with the p-y method using the p-y curves included in the API (1993) recommendations for sands (section 2.2.2). Therefore the use of the proposed correlation with other curves is not recommended.

Cubrinovski et al. (2007) back-calculated subgrade loads from shaking table tests, simulating lateral spreading conditions, of both stiff and flexible piles built in liquefied soil overlaid by a non-liquefiable crust. Analysis of test results led to the chart shown in **Figure 2.31a** for the estimation of a reduction factor for the initial stiffness called β. It can be seen that β is related to the relative displacement between the pile and the soil. Also, for small relative displacements data produce a large scatter, while the scatter is insignificant for large displacements. This observation is indicative of p-y dependence on pile stiffness, as small and large relative displacements are typical for flexible and stiff piles respectively.

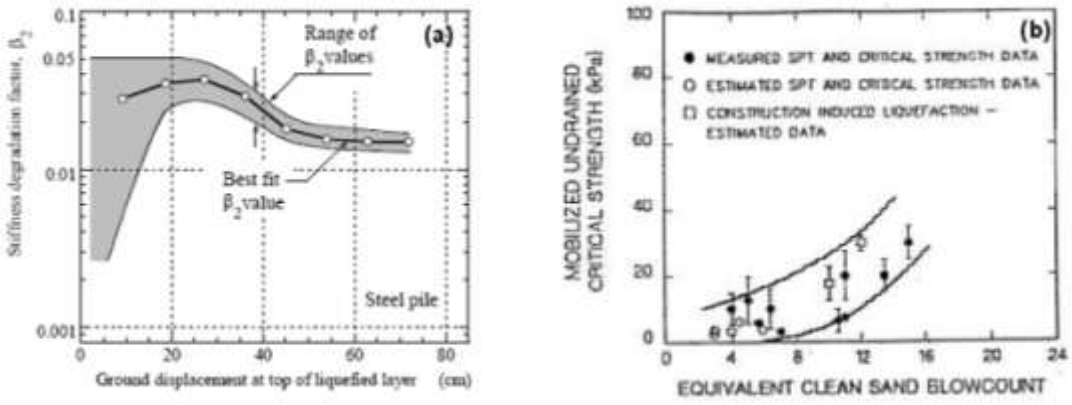

Figure 2.31: (a) Stiffness degradation factor β as a function of ground displacement (Cubrinovski et al. 2005) (b) Undrained residual shear strength (Seed and Harder, 1990)

The proposed correlation was developed by assuming a linear p-y response for the non-liquefied soil, with initial stiffness for the nonliquefied case estimated through the expressions proposed by AIJ (2001) and JRA (2002). In a later study (Cubrinovski and Ishihara, 2007), the authors recommend the use of a bilinear curve with the upper limit defined through empirical correlations for the undrained shear strength of sand, like the one shown in **Figure 2.31b** (Seed and Harder, 1990).

Tokimatsu and Suzuki (2004), **Suzuki et al. (2005) and Tokimatsu and Suzuki (2009)** investigated, through shaking table tests on level and inclined ground, the mechanisms that govern subgrade reaction in liquefied soils. Tests included soil profiles with and without crust, as well as stiff and flexible piles. The authors concluded that the response is governed by pore pressure changes and soil dilation around the pile and this fact differentiates the behavior compared to dry soils, where subgrade reaction is induced by compression of the soil due to pile oscillation. For level ground profiles, the subgrade reaction mechanism is illustrated in **Figure 2.32a**. On the extension side, combined effects of dilation (because of large relative displacement) and unloading, result in large subgrade loads which pull the pile. On the compression side, though, dilation effects are offset due to increase in normal stress, with negligible development of subgrade loads.

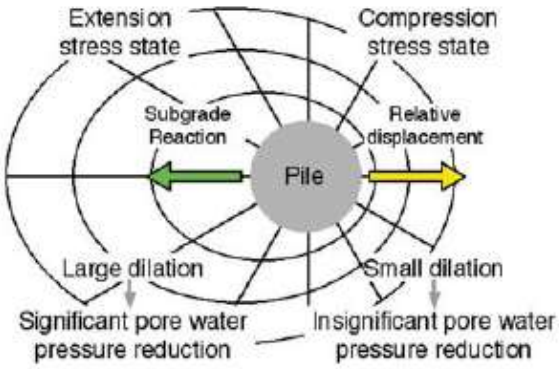

Figure 2.32: Development of subgrade reaction in level ground profiles (Tokimatsu and Suzuki, 2009)

For inclined ground, the mechanism is illustrated in **Figure 2.33** for downstream (parallel to soil inclination) and upstream movement of the soil. For the first case dilation effects are pronounced in the extension side as for level ground profiles. For upstream (opposite to soil inclination) movement, however, dilation is small in both

sides of the pile, due to accumulated downslope displacement, which causes relative displacement to decrease.

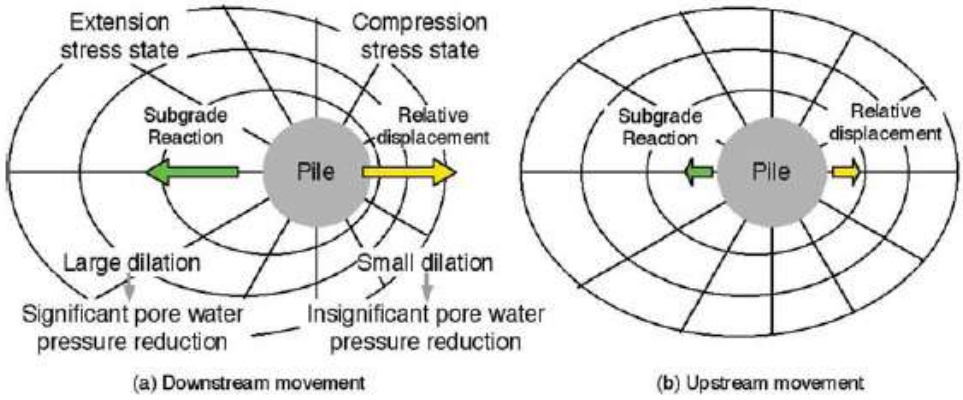

Figure 2.33: Development of subgrade reaction in inclined ground for (a) downstream and (b) upstream movement (Tokimatsu and Suzuki, 2009)

Back-calculated p-y curves showed an overall softening response, with transient hardening characteristics. Transient variations (as a result of large dilation) were of larger extent for denser soils and for stiff piles, indicating p-y dependence on relative density and pile stiffness. Typical results, including subgrade reaction and pore pressure build-up, are shown in **Figure 2.34**.

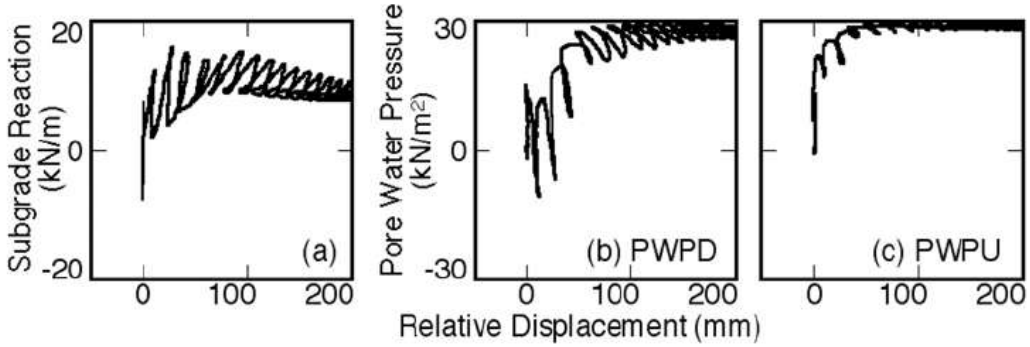

Figure 2.34: Back-Calculated p-y curves and pore pressure build-up on either side of the pile (Tokimatsu and Suzuki, 2009)

Finally, the authors recommend the use of AIJ (2001) specifications for the estimation of both the subgrade reaction coefficient for firm soil (k_h), described in equation (2.67), and the degradation factor (β_1) for liquefied soil, shown in **Figure 2.35b**.

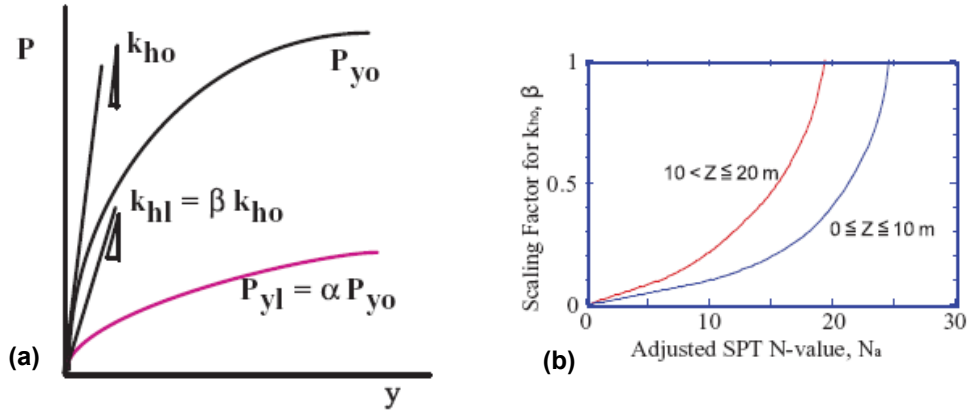

Figure 2.35: (a) Evaluation of degraded p-y curve for liquefied soil and (b) estimation of degradation factor (Tokimatsu and Suzuki, 2009)

Ultimate soil resistance can be estimated as follows:

$$p_{yl} = \alpha_1 p_{yo} \tag{2.86}$$

in which p_{yl} is the resistance of the liquefied soil, α_1 an empirical coefficient tentatively equal to β_1 and p_{yo} the ultimate lateral resistance estimated based on Brom's theory (section 2.2.5.1) as follows:

$$p_{yo} = 3k_p\sigma'_{vo} \tag{2.87}$$

where σ'_{vo} is the initial effective stress and k_p is the Rankine passive earth pressure coefficient. The estimation of degraded p-y curve from the original curve for non-liquefied soil is illustrated in **Figure 2.35a**.

Dungca et al. (2006) studied the effects of soil permeability and loading rate on subgrade reaction loads. It was observed that soil resistance increased as the ratio of lateral loading rate over hydraulic conductivity increased. Indicative results are shown in **Figure 2.36** supporting the idea that permeability and rate effects should be jointly evaluated.

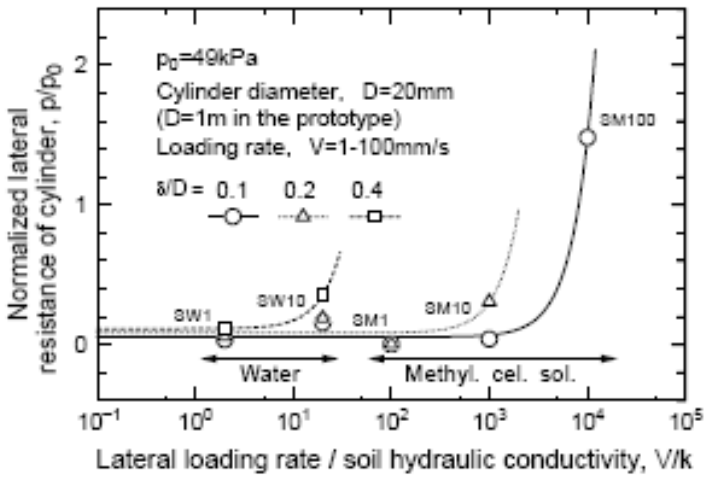

Figure 2.36: Relationship between lateral resistance and ratio of loading rate over soil conductivity (Dungca et al. (2005)

Similar trends were also observed by **Uzuoka et al. (2005)**. The authors studied parametrically rate effects by conducting numerical analyses. Analyses were performed using a Finite Element Model for spatial discretization of the equilibrium equation, while a Finite Difference Model was used for pore water pressure. Soil response was simulated with a new constitutive model that captures liquefaction effects by incorporating the concept of minimum effective stress. Parameters that were examined included pile diameter, degree of liquefaction, permeability and loading rate. The authors correlated soil resistance with a dimensionless time factor parameter T* defined as:

$$T^* = \frac{kK}{\gamma_w D v} \tag{2.88}$$

where k is the soil permeability, K is the bulk modulus, D is the diameter of the pile and v the velocity of the pile. Correlations between soil resistance and time factor are shown in **Figure 2.37a** for pile displacement d=0.25m and **Figure 2.37b** for d=0.125 and 0.25m. It can be observed that the time factor concept can capture the effects of all the parameters examined, but the relation depends on the level of pile displacement.

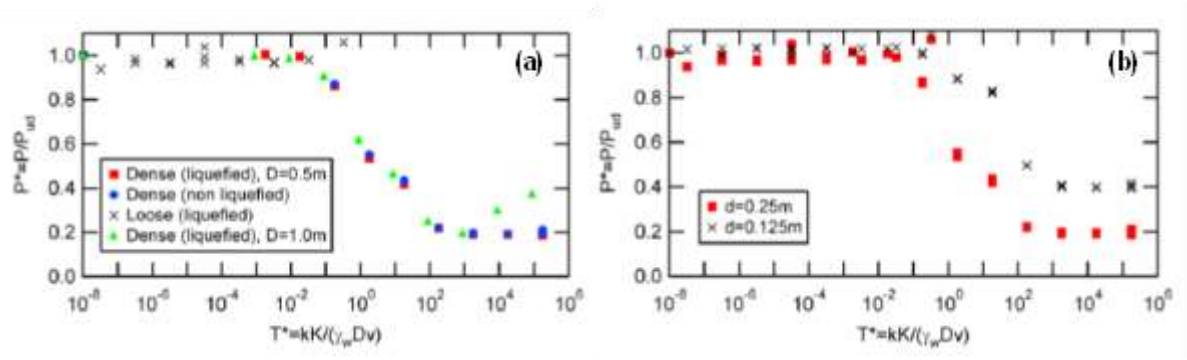

Figure 2.37: Relation between soil resistance and time factor for displacement of pile (a) d=0.25m and (b) d=0.125 and 0.25m

Gonzalez et al. (2009) also examined the effects of soil permeability by conducting centrifuge experiments on one-layer models of end-bearing single piles and pile groups subjected to lateral spreading. Two series of tests were performed, one using water and another using a viscous material as pore fluid. For the low-permeability material, it was observed that an inverted conical zone of non-liquefied soil was formed near the ground surface, as pore fluid could not travel fast enough to offset negative pore pressure increments caused by dilation and lateral stress reduction.

The authors concluded that formation of this non-liquefied zone results in much larger loads on the pile, as subgrade reaction is imposed on a much larger area. Back-calculation of p-y response, which is shown in **Figure 2.38a** and **Figure 2.38b** for the high and low permeability model respectively, supports this hypothesis. In any case, this study suggests that soil permeability is a critical factor and its effects should be investigated more thoroughly.

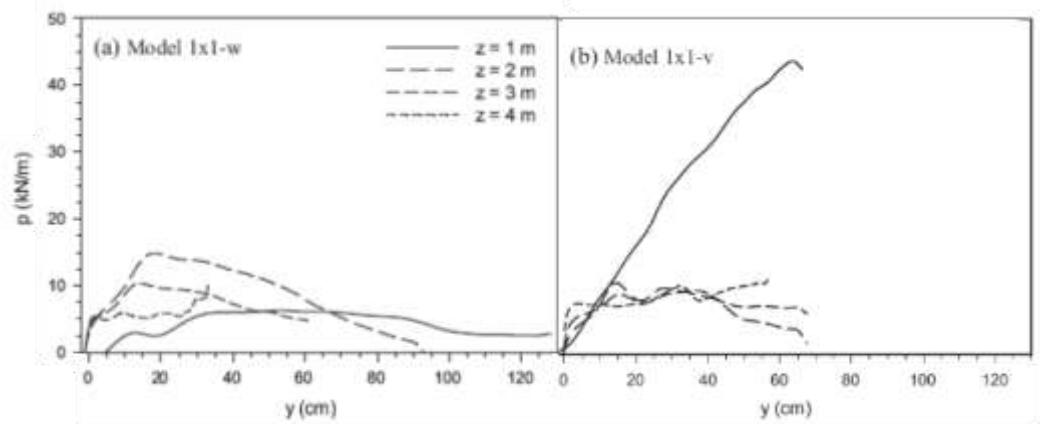

Figure 2.38: Back-calculated p-y curves for (a) high and (b) low permeability material (Gonzalez et al. 2009)

Rollins et al. (2005) developed an analytical expression to describe p-y response of liquefied sand based on field tests in Treasure Island, California. The expression proposed is graphically illustrated in **Figure 2.39** and is given by the following equation:

$$p = A \ By^{\ C} \tag{2.89}$$

where

$$A = 3 \cdot 10^{-7} \ \ z+1^{\ 6.05} \tag{2.90}$$

$$B = 2.80 \ \ z+1^{\ 0.11} \tag{2.91}$$

$$C = 2.85 \ \ z+1^{\ -0.41} \tag{2.92}$$

and p the soil pressure (kN/m), y horizontal deflection (mm) and z the depth (m). According to the authors, the use of this expression should be limited to conditions similar to that of the tests, namely, effective vertical stress less than 15kPa, lateral displacement less than 150mm, depth of soil less than 6m and sands with initial relative density around 50%. The diameter of the piles in all tests was 0.324m. In a more recent study (Rollins et al., 2007) the following expression was proposed to account for pile diameter effects:

$$p_d = 3.81 \ln D + 5.6 \tag{2.93}$$

where p_d is a multiplier for the pile load and D is the pile diameter (m).

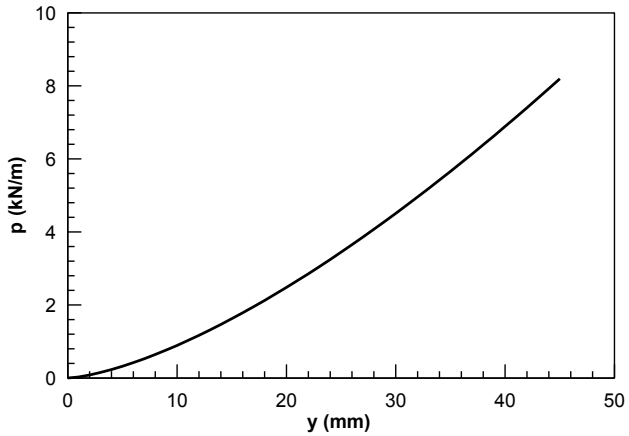

Figure 2.39: Load-deflection curve for liquefied soils (Rollins et al., 2005)

It is evident that the proposed relation predicts hardening response for the soil. This type of response is typical for each separate cycle of loading (especially for the early ones), but it cannot envelope the overall behavior, which is characterized by a softening behavior. In other words, the proposed correlation captures the transient response but not the residual.

Goh and O'Rourke (1999) performed numerical analyses to investigate the response of a pile being displaced through a cohesive material, using the finite difference code FLAC. The assumption regarding the response of the soil is shown in **Figure 2.40a**. Namely, undrained shear strength is assumed to decrease linearly with plastic deviatoric strain, until it reaches a residual value. Resulting p-y curves, which are shown in **Figure 2.40b**, are a function of peak strength, residual strength, as well as the displacements at which these are achieved.

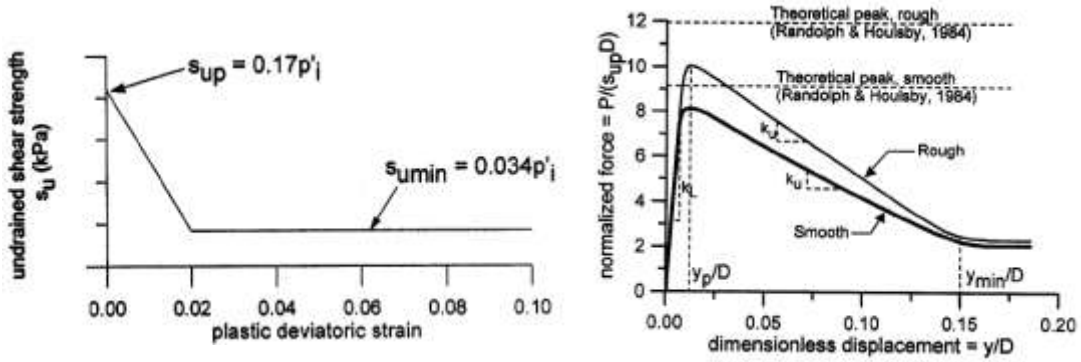

Figure 2.40: Stress-strain behavior and associated p-y curves (Goh and O'Rourke, 1999)

The proposed relation has the advantage that it can be easily calibrated, as it depends only on four (4) parameters. However, the specific curves can only capture the static or residual response of the soil, neglecting the cyclic component. For this limitation the authors denote that the cyclic effect is only one third of the maximum bending moment, and thus the response is controlled by the static component. In addition, the softening response suggested by the curves is only attributed to the increased relative displacement, while effects of liquefaction and pore pressure build-up, which significantly affect the behavior, are not considered (Haigh, 2002).

Ashour and Norris (2003) extended their semi-empirical model (section 2.2.6) to account for undrained loading and pore-pressure build-up in the far and in the near

field. Application of the methodology requires knowledge of seismic excitation characteristics, as well as soil and pile properties. Excess pore pressure prediction is based on the analytical expression proposed by De Alba et al. (1976). Typical p-y curves based on the Ashour and Norris methodology are shown in **Figure 2.41**.

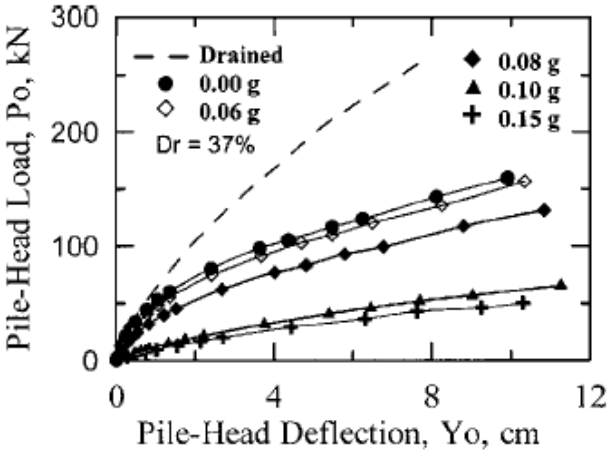

Figure 2.41: P-y curves for different earthquake levels based on the semi-empirical model of Ashour and Norris, 2003.

Liyanapathirana and Poulos (2005) calculate coefficients of subgrade reaction by integrating Mindlin's equation. Integration is performed using the minimum shear modulus corresponding to the minimum effective vertical stress for the specific site and earthquake characteristics. Minimum effective stress is estimated through free-field site response analysis that takes into account pore pressure build-up. The same analysis provides an estimate of the lateral displacements that should be applied at the fix-end of the springs.

As far as radiation damping is concerned, the authors make use of the formula $5\rho_s V_s$ developed by Kanya (1998) and described in section 2.3.2. It is realized that the specific formula was developed for firm soils and does not account for pore pressure generation.

Lin et al. (2007), based on the Bouc-Wen model**,** simulate pore-pressure build-up by applying the coefficient factor that accounts for pore pressure generation proposed by Kagawa et al. (1997). Thus, equation (2.70) for soil reaction (assuming α=0) takes the following form:

$$p_s\ t\ =\ 1-u^{\ \alpha}\ p_y\zeta \tag{2.94}$$

Where u is the excess pore pressure ratio and α a parameter. For the estimation of ultimate soil resistance, the authors make use of the passive pressure theory (section 2.2.5.1). It is worth noting that the relation predicts zero resistance for complete liquefaction (u=1).

Similarly, effects of radiation damping are incorporated by applying a coefficient factor to the relationship (2.78), to account for pore pressure build-up. The coefficient factor is expressed as follows:

$$\beta=\left[\ 1-u^{\ 1/4}+\frac{V_L u}{V_s+V_P}\right] \tag{`2.95}$$

where V_P is the velocity of pressure and V_L the viscous velocity of the liquefied soil.

Assimaki and Varun (2009), introduced in the Bouc-wen macroelement they developed (whose major assumptions are disussed in sections 2.3.1 and 2.3.2), a pore pressure generator which is connected in series with the macroelement. The layout of the macroelement is shown in **Figure 2.42**. Pore pressure generation is assumed to be proportional to the total amount of shear work done, based on the concept of Towhata and Ishihara (1985) and Iai (1991).

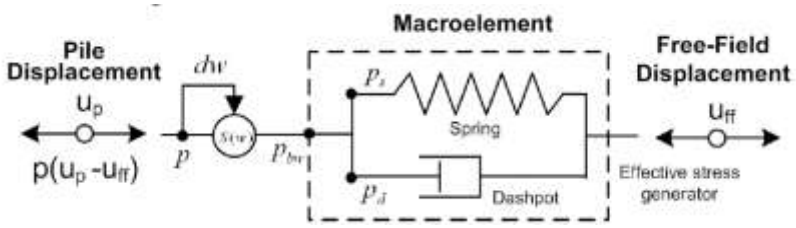

Figure 2.42: Macroelement formulation based on the Assimaki and Varun (2009) approach

Additionally, they included in their analyses viscous damping effects by introducing the coefficient c_v. According to the authors viscous damping is caused by movement of fluid between soil particles. Hence equation (2.75) for the dashpot force becomes:

$$p_d\ =\ c_r+c_v\ \ \dot{y}\,D \tag{2.96}$$

Schematic representation of both the spring and dashpot behavior are shown in **Figure 2.43**.

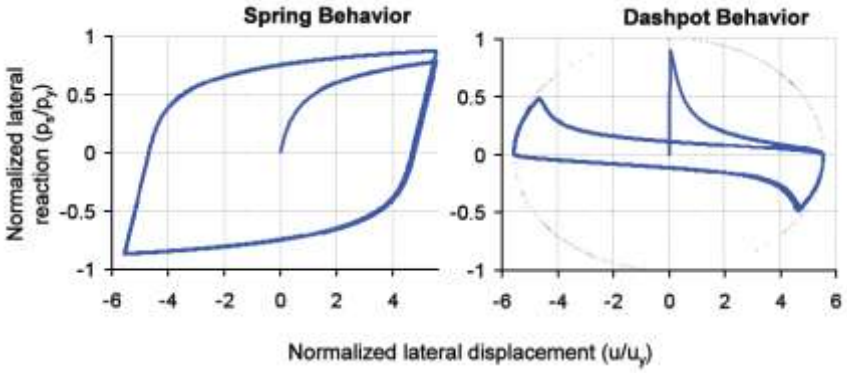

Figure 2.43: Spring and dashpot behavior for the macroelement model proposed by Assimaki and Varun (2009)

As far as *damping* is concerned, the radiation damping approach might not reflect the real dashpot response. For example, **Ueng et al. (2009)** conducted shaking table tests in which they measured the damping ratio. Test results, which are shown in **Figure 2.44**, indicate that damping ratio also depends on the stiffness of the pile, apart from the frequency of the input motion. Thus, further investigation is required to understand the mechanisms that govern dashpot behavior in liquefied soils, as well as explore practical methods to include these mechanisms in the design process.

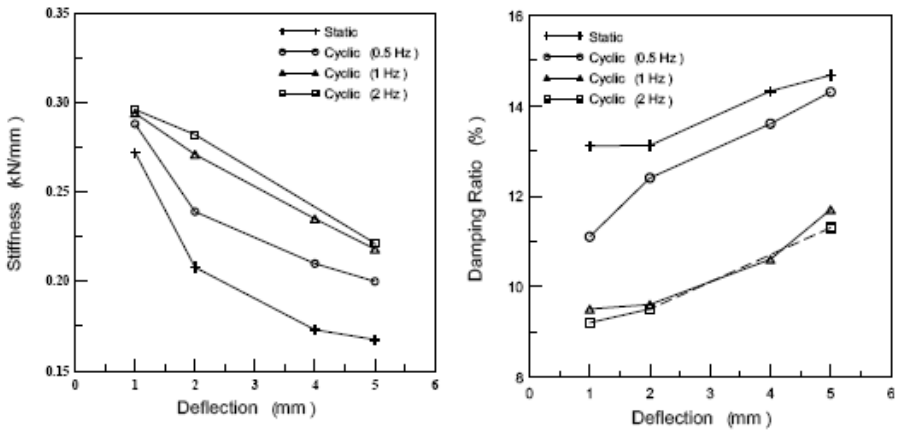

Figure 2.44: Relation between pile stiffness, damping ratio and pile deflection for various frequencies (Ueng et al., 2009)

2.5 Additional considerations on p-y method and pile design

Without doubt, the most critical parameter affecting a p-y analysis is the estimation of the response of the soil. However, there is a series of additional concerns that the engineer involved in the design of a pile against lateral loading has to deal with. The present section attempts to address some of these issues with reference to recent findings from the literature.

2.5.1 Analysis of pile groups

Mokwa (1999), based on experimental data from previous studies, proposed the use of an empirical coefficient, f_m, to account for stiffness reduction of p-y springs due to group effects. This coefficient, which is a function of pile spacing and position of the pile in the group, is multiplied with the modulus of subgrade reaction as it is estimated for the single pile. The chart proposed by Mokwa is shown in **Figure 2.45** and is derived from lateral load tests on piles built in loose and dense sands as well as soft and stiff clays.

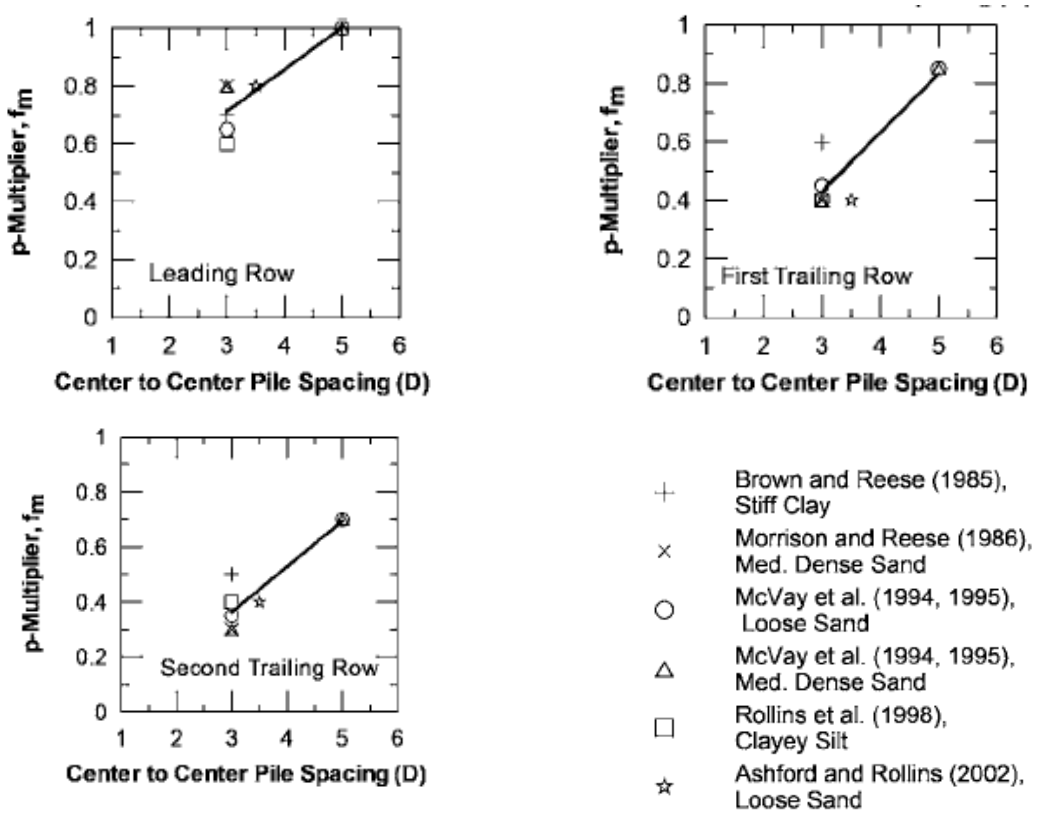

Figure 2.45: Estimation of f_m multiplier based on pile spacing and pile location I n the group (Mokwa 1999)

Pile groups are generally analyzed as single piles. Namely, an "equivalent" single pile is considered whose stiffness is equal to the number of piles times the stiffness of a single pile of the group. For the p-y springs it is rational to assume that the strength and the stiffness of the springs attached to the "equivalent" pile are equal to those of a single pile times the number of piles (Brandenberg et al. 2007).

Pile groups in liquefiable soil

The "equivalent pile" type of analysis involves the assumption that all piles in the group will respond in the same way. This might not be the case for groups in liquefied and laterally spreading soils (non-uniform development of ground displacements and excess pore pressures, e.t.c) resulting in different loading conditions and response characteristics for each pile in the group.

Tokimatsu and Suzuki (2009) investigated the response of pile groups in the E-defense shaking table. It was observed that for pile spacing larger than three (3) diameters liquefied soil flowed around piles and therefore group effects were cancelled. This critical pile spacing is larger for groups in liquefied sand than in dry soils as a result of the larger strain level. For smaller distances between the piles it was observed that the outside piles of the group developed larger bending moments and displacements. The authors attributed this response to the fact that dilation effects were more pronounced to the outside piles of the group. Furthermore, apart from pile interaction, response is different within the group because of spatial variation of lateral spreading displacements, which results in different loading conditions for each pile.

Cubrinovski and Ishihara (2006) proposed a simplified procedure to account for spatial variation in lateral spreading displacements. In a first step mean displacement of the pile group is evaluated by analyzing a single pile subjected to the average lateral ground displacement of the group. Finally, each pile of the group is analyzed for its particular deformation pattern which depends on its position in the group. In a later study (Cubrinovski and Ishihara, 2007), the authors also suggest that interaction of pile groups and spreading soil also affects the magnitude of lateral displacements and the stiffness of liquefied soil compared to the case of a single pile. Experimental data in liquefied soils for pile spacing less than 2.5 to 3 diameters show

that as the number of piles in the group increases, soil pressure decreases (**Figure 2.46**). However further investigation is required, as the data are scarce.

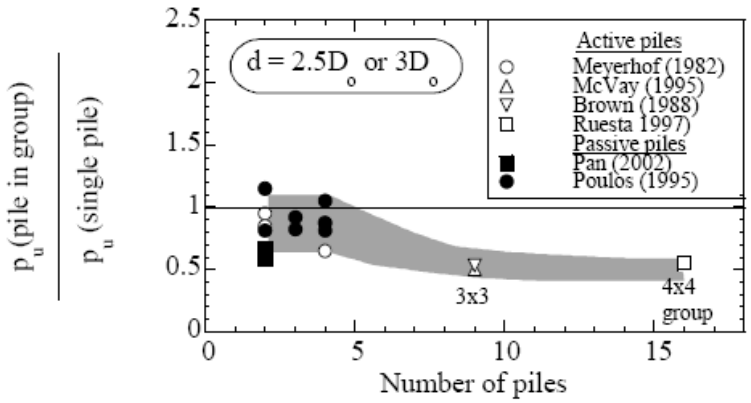

Figure 2.46: Pile group effects on the ultimate lateral soil pressure (Cubrinovski and Ishihara, 2007)

Abdoun et al. (2003) also observed, through centrifuge experiments, that piles in a group develop lower bending moment compared to single piles. They attributed this response to frame effects i.e. contribution to moment resistance from the axial forces to the piles in a group (Dobry and Gazetas, 1988) that can be expressed by the following equation:

$$\sum M_{i,\max} + \sum F_i x_i = M_e \tag{2.97}$$

Where M_e is the external moment, $M_{i,max}$ the moment developed in each pile, F_i the axial force of the pile and x_i the distance of the pile from the neutral horizontal axis of the group. Obviously the term $F_i x_i$ expresses the contribution of the axial forces.

Imamura et al. (2004) studied the response of pile rows, perpendicular to lateral flow. It was observed that the lateral force imposed on the pile depends on the number of piles in the row and on the distance between the piles expressed as the ratio of pile diameter (D) over center to center distance (L), called the pile proximity ratio (η):

$$\eta = \frac{D}{L} \tag{2.98}$$

Namely, single and double layer models were examined, and it was found that as the number of piles increases and as pile proximity ratio increases (i.e. distance between piles decreases), the lateral force decreases (**Figure 2.47** and **Figure 2.48**).

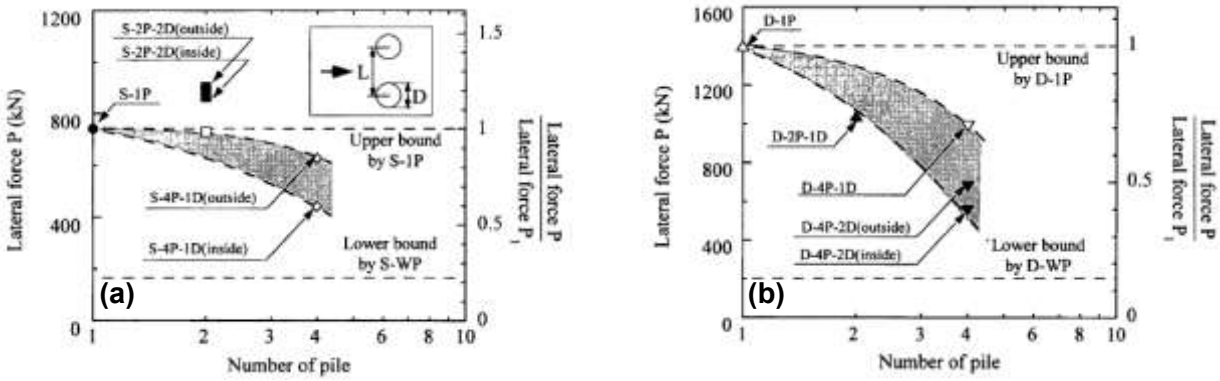

Figure 2.47: Effect of number of piles on the lateral load imposed on pile rows for (a) single and (b) double-layer models (Imamura et al. 2004)

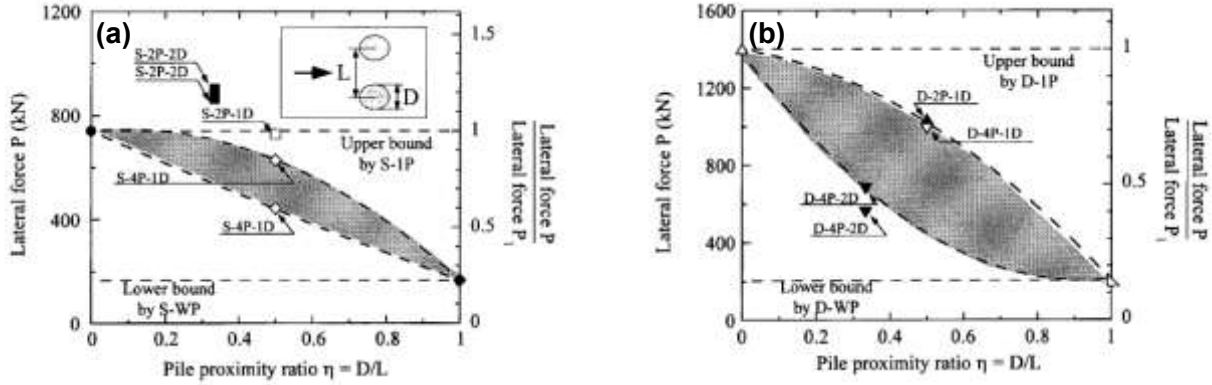

Figure 2.48: Effect of center-to-center pile distance on the lateral load imposed on pile rows for (a) single and (b) double-layer models (Imamura et al. 2004)

Finally, based on a simple analytical model the authors produced design charts that correlate the lateral force imposed on a pile with the number of piles and the pile proximity ratio. **Figure 2.49** shows the analytical solutions for single and double layered models along with the experimental results.

In any case all researchers agree on the existence of a critical pile-to-pile distance after which group effects are cancelled as soil flows around the piles (Brandenberg et al., 2005; Rollins et al., 2007; Abdoun et al., 2003; Pamuk and Zimmie, 2007). Based on a limited number of data (Tokimatsu and Suzuki, 2009; Towhata et al., 2006;

Imamura et al., 2004) this distance is estimated to three (3) times the diameter of the pile, but further investigation is needed as data are very scarce and do not account for all the factors that influence the problem.

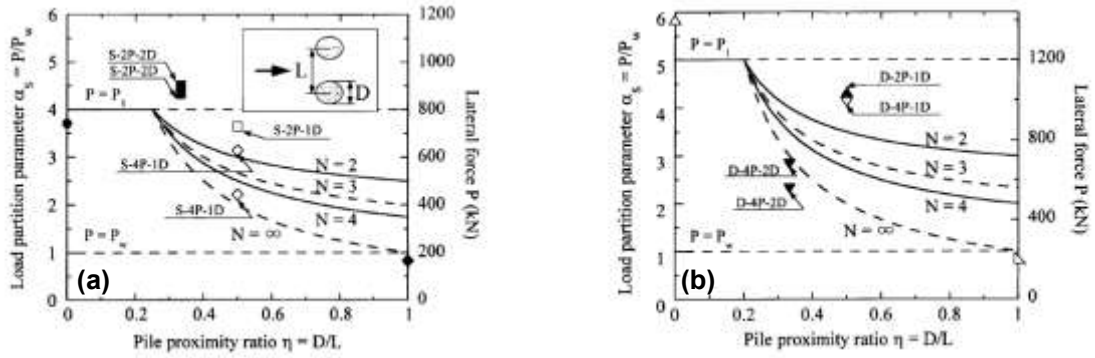

Figure 2.49: Analytical predictions vs. experimental results of lateral forces on pile rows for (a) single and (b) double-layer models (Imamura et al. 2004)

2.5.2 Estimation of kinematic loads

For the non-liquefaction case, it is common practice for horizontal ground displacements to be considered negligible and thus kinematic loads from surrounding soil are usually not included in the analysis (Boulanger et al., 2007; Tokimatsu and Suzuki, 2009, Abdoun and Dobry, 2002). However, when the soil profile consists of soft clays or loose sands lateral displacements may become significant and hence kinematic loads may affect the response of the pile.

For the liquefaction case, evaluation of kinematic loads includes estimation of both cyclic or transient loads, as well as permanent ground displacements (for inclined soils subjected to lateral spreading). *Cyclic or Transient Ground Displacements* can produce large kinematic loads mainly for level ground conditions, but for sloping grounds as well, especially before liquefaction or in the opposite direction of the spreading soil. Most commonly they are evaluated by integration of a shear strain profile with depth. **Tokimatsu and Asaka (1998)** proposed the chart shown in **Figure 2.50a** to estimate cyclic shear strain vs. depth as a function of Cyclic Stress Ratio (CSR) and adjusted SPT value. Following, horizontal ground displacement profile can be evaluated by integration, assuming that γ_c develops in the same horizontal direction:

$$y_g(z) = \int \gamma_c(z)dz \tag{2.99}$$

Lateral spreading or permanent ground displacements can be estimated in a number of ways, including integration of permanent shear strains, sliding block theory, empirical relationships and coupled dynamic 1-D and 2-D analyses (Liyanapathirana and Poulos, 2005; Lin et al. 2007).

Similarly to cyclic displacements Tokimatsu and Asaka (1998) developed the chart shown in **Figure 2.50b**, for estimation of permanent shear strains. Horizontal deformation profile near a waterfront can then be evaluated as follows:

- Estimate a ground displacement profile [$y_g(0,z)$] at the waterfront through equation (2.99) using γ_{max} from **Figure 2.50b** instead of γ_c:

$$y_g(0,z) = \int \gamma_{max}(z)dz \tag{2.100}$$

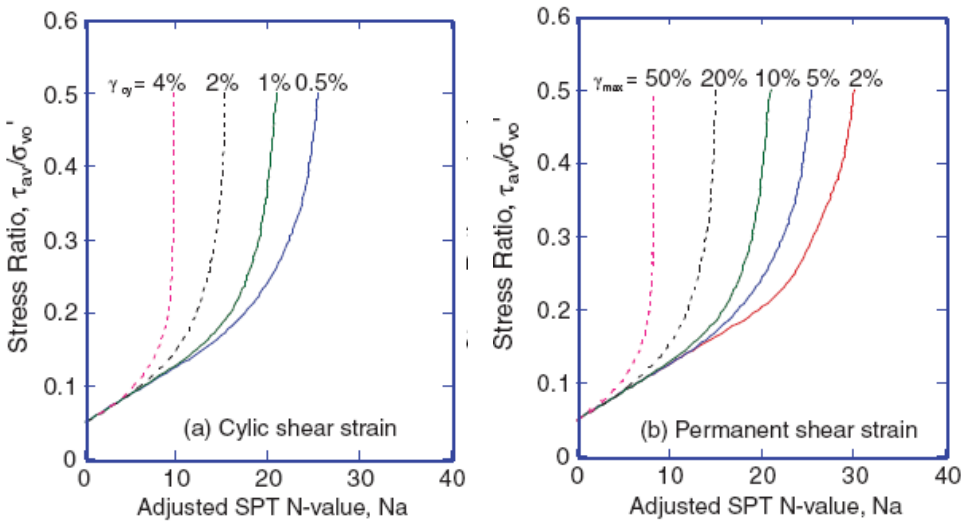

Figure 2.50: Estimation of (a) Cyclic and (b) Permanent Shear Strain in liquefied and laterally spreading ground (Tokimatsu and Asaka, 1998)

- Horizontal displacement at the ground surface and at a distance x from the waterfront, $y_g(x,0)$, is calculated through the following equation:

$$y_g\ x,0\ =\ 1/2\ ^{\frac{x}{10y_g\ 0,0}}\ y_g\ \ 0,0 \tag{2.101}$$

where $y_g(0,0)$ is the maximum horizontal displacement at the waterfront at the ground surface (x=0, z=0), as evaluated in the previous step.

- Deformation profile at any distance x and at any depth z can then be estimated as follows:

$$y_g(x,z) = y_g(x,0)\,\frac{y_g(0,z)}{y_g(0,0)} \tag{2.102}$$

In the same context, **Shamoto et al. (1998)** proposed the charts shown in **Figure 2.51** to estimate permanent shear strain $[(\gamma_r)_{max}]$ in gently sloping ground. Again, the displacement profile can be evaluated by integration:

$$D_H = 0.16\int_0^H \gamma_{r\ \max}\, dz \tag{2.103}$$

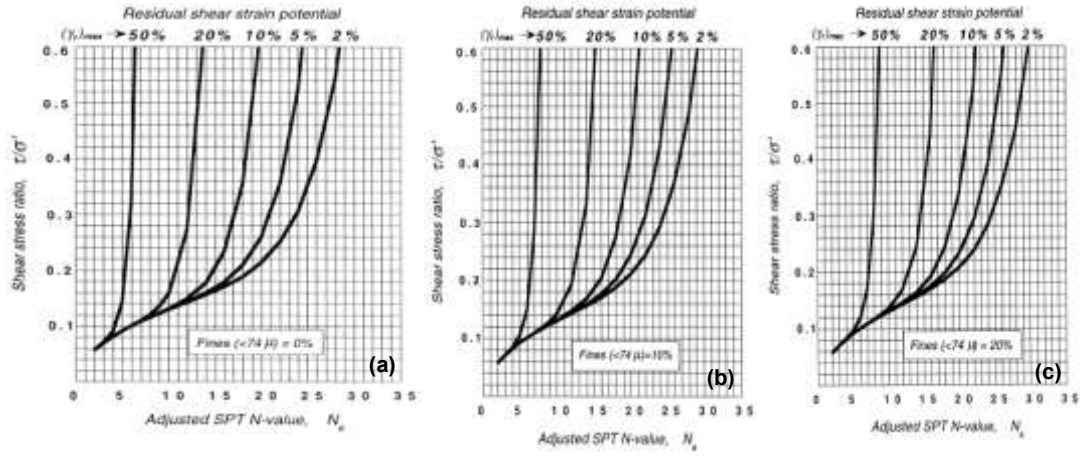

Figure 2.51: Evaluation of shear strain potential $(\gamma_r)_{max}$ in terms of the corrected SPT blow count $N_{1,60}$ and the shear stress ratio τ/σ'_{vo}, imposed by the earthquake for (a) clean sand (b) silty sands with FS=10% and FC=20%

However, common practice for evaluation of lateral spreading displacements is the use of empirical relationships. These relationships can be divided in two categories: the ones that make use of "seismological" parameters (Earthquake magnitude, epicentral distance e.t.c.) and those that make use of "engineering parameters" (soil properties base acceleration e.t.c.).

An example of the first category is the relationship by **Youd et al. (2002)** who analyzed several case studies and proposed the following correlation:

$$\log D_H = -16.213 + 1.532M - 1.406\log R^* - 0.012R + 0.338\log S + \\ + 0.540\log T_{15} + 3.413\log\ (100 - F_{15}\ ) - 0.795\log\ D_{5015} + 0.1mm \quad (2.104)$$

where

M: Moment magnitude of the earthquake

R (km): Nearest horizontal or map distance, between the site and the seismic energy source

$R^* = R_o + R$ where $R_o = 10^{\,0.89M - 5.64}$ (km)

T_{15}: Cumulative thickness of saturated granular layers with corrected blow count $(N_1)_{60}$ less than 15 (m)

F_{15}: Average fines content for granular materials included within T_{15} (mm)

D_{5015}: Average mean grain size for granular materials included within T_{15} (mm)

S (%): Ground inclination

An example of the second category is the following relationship by **Hamada (1999)**, based on the compilation of several case studies:

$$D_H = \frac{0.0125\ \ H^{\ 0.5}\theta}{\overline{N}^{0.88}} \sum \alpha_i^{0.48} t_i \quad (2.105)$$

where

H(m): Thickness of the liquefied soil layer

θ(%): Ground inclination

$\overline{N}$: Average corrected SPT blow count for the liquefied layer

α_i (gal): Mean horizontal acceleration in the I part of the acceleration time history

t_i (sec): Time length of the I part of the acceleration time history

Most recently, **Valsamis e al. (2010),** based on an extensive numerical parametric study of the problem, proposed the following equation:

$$D_h = 38.6\left[\frac{\alpha_{\max}\tan i}{N_{1\ 60}}\right]^{0.5} H_{liq}^{tot} T_d\ \ 1-FC\ ^{3.5}\left(\frac{\alpha_{mean}}{a_{\max}}\right)^{0.5} \qquad (2.106)$$

where

α_{max}: Maximum base acceleration

i: Ground surface inclination

H_{liq}^{tot}: Cumulative thickness of liquefiable soil layers

T_d: Duration of strong motion excitation

FC: Fines content

α_{mean}: Mean value of the applied acceleration, irrespective of the direction

He also studied the accuracy of eleven (11) empirical relationships based on results of numerical analyses and case histories and concluded that best predictions were obtained with the relationships proposed by Hamada (1999), Youd et al. (2002) and Shamoto (1998). In any case, prediction of lateral displacements with any of the methods described above contains uncertainties, which in turn arise from uncertainties in the evaluation of the various field parameters. Hence, application of more than one methodologies and pile analysis for a range of predictions is suggested.

As far as variation with depth is concerned, numerical data (Valsamis 2008) suggest that it can be better approximated assuming a sinusoidal distribution. However, other experimental results (Boulanger et al. 2007) have shown that for relatively stiff piles the response is not sensitive to displacements variation and therefore, for simplicity reasons, a linear variation can also be assumed.

2.5.3 Critical loading cycle and superposition of kinematic and inertial loads

When analyzing a dynamic problem with the pseudo-static p-y method, a critical question is raised with regard to the combination of inertial and kinematic loads that one should consider in the analysis, given that the former and the latter do not necessarily occur at the same time.

Tokimatsu et al. **(2005)** studied the response of pile supported structures in dry sand under seismic loading and concluded the following (**Figure 2.52**):

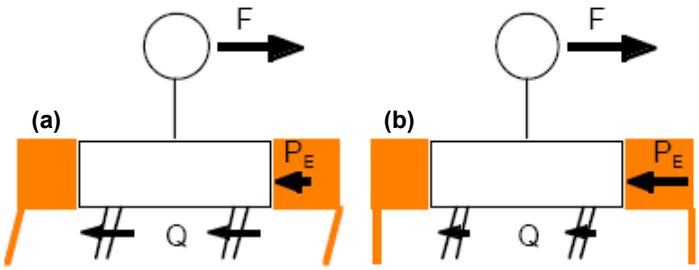

Figure 2.52: Effect of soil-structure inertia characteristics on pile response (a) $T_{str}<T_s$ (b) $T_{str}>T_s$ (Tokimatsu et al. 2005)

- If the natural period of the structure is less than that of the soil ($T_{str}<T_s$) then the inertia loads are in phase with kinematic loads leading to large stresses to piles
- If the natural period is larger than that of the structure ($T_{str}>T_s$), then inertia and kinematic loads are out of phase resulting in smaller stresses to the pile.

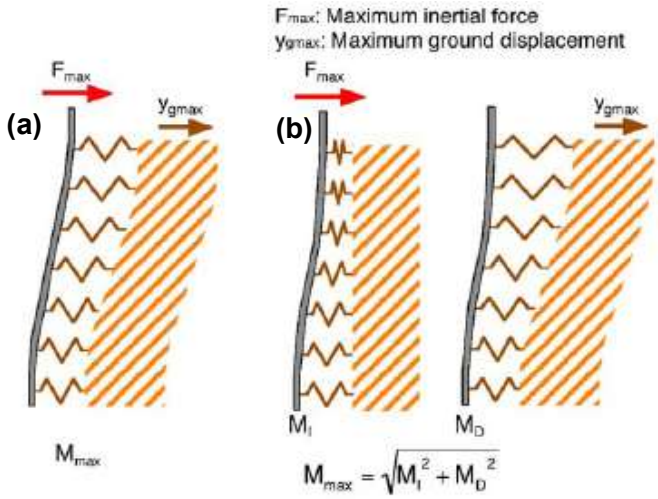

Figure 2.53: Combination of Inertia and Kinematic loads for (a) $T_{str}<T_s$ (b) $T_{str}>T_s$ (Tokimatsu et al. 2005)

As far as liquefaction is concerned, **Figure 2.54** shows the response of a pile in terms of bending moment and head displacement in one of the centrifuge tests conducted by Abdoun et al. (2003). In the same figure development of lateral spreading deformation is also illustrated. It is observed that bending moment reaches a local maximum and then decreases as shaking progresses. However, this maximum is

reached before ultimate lateral displacement is accumulated. This type of behavior has also been observed by other researchers (He et al., 2007; Sesov et al., 2005; Cubrinovski et al., 2004). As a result in order to analyze this problem pseudo-statically, a fraction of ground displacement as well as of peak inertial loads should be considered.

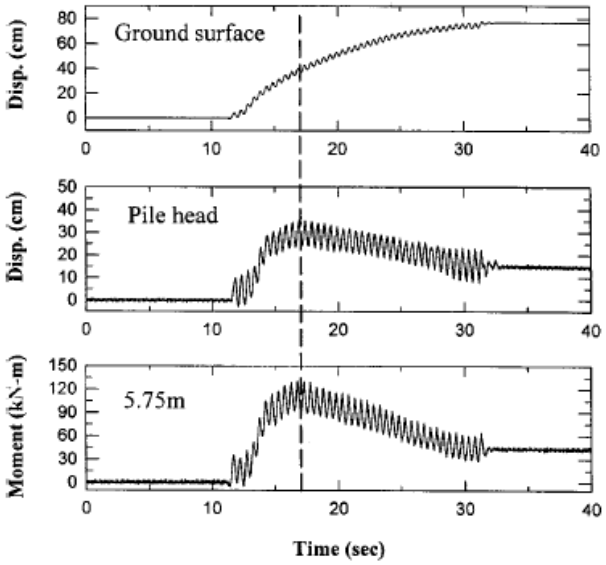

Figure 2.54: Pile bending moment and head displacement compared to free field displacement (Abdoun et al. 2003)

Boulanger et al. (2007) support these observations. Their analyses also demonstrate that different combinations of soil and pile properties, as well as input motion characteristics, lead to different critical combinations between inertial loads and ground displacements. The authors propose the use of the coefficient factors described in section 2.4 along with the maximum ground displacement, since it is very difficult, if not impossible, to evaluate development of lateral spreading displacements with time.

As for the direction of inertial loads, the approach proposed by Tokimatsu and Suzuki (2005) and was presented previously, can be adopted. These observations were further confirmed by Finite Element analysis by Boulanger et al. (2007). Furthermore, it should be noted that in most cases, due to soil softening caused by liquefaction, the natural period of the soil is expected to be larger than that of the

structure, and hence analysis can be performed assuming that inertial loads are in phase with ground displacements.

At this point it should be noted that application of inertial loads in the same direction with ground displacements does not necessarily mean that resulting kinematic loads will be in phase with inertial loads. Actually, Brandenberg et al. (2005) observed that for flexible piles liquefied soil was pushing the pile upwards. The direction of soil pressures (not displacements) depends on the relative soil-pile displacement, which in turn is a function of pile stiffness, magnitude of ground displacement and inertial loads, as well as characteristics of the crust (if present). This type of behavior, which can significantly affect the response of the pile, can be captured by the pseudo-static p-y analysis, since soil pressure is an output for the analysis.

2.5.4 Pile analysis with the Limit Equilibrium Method (LEM)

In this type of analysis, soil-foundation interaction is ignored and p-y springs are replaced with limit pressures acting directly on the pile. **Abdoun et al. (2003)** conducted experiments at the centrifuge facilities of the Rensselaer Polytechnic Institute (RPI) and concluded that for soil profiles where a non-liquefiable crust is not present at the top and for floating piles (with or without crust) pile response is determined by the loads imposed by the liquefied soil. On the other hand, for end-bearing piles response is controlled by the loads imposed from the crust. For each one of the two cases **Dobry et al. (2003)** developed analytical methods to evaluate pile response.

Case I: Pile response is controlled by loads imposed by the liquefied layer

Figure 2.55 shows the free-body diagram for the evaluation of the maximum bending moment (M_{max}). **Figure 2.55a** and **Figure 2.55b** correspond to a single pile model without and with pile cap respectively. In the same figure H_p is the embedded pile length, d the pile diameter, A_c the area of the cap and p_l the pressure applied by the liquefied soil, which is assumed to be constant. M_{max} is then given by the following equation, which is independent of the rotational fixity at the base expressed by the rotation spring k_r:

$$M_{\max} = 0.5A_P H_P + A_C H_C \quad p_l \tag{2.107}$$

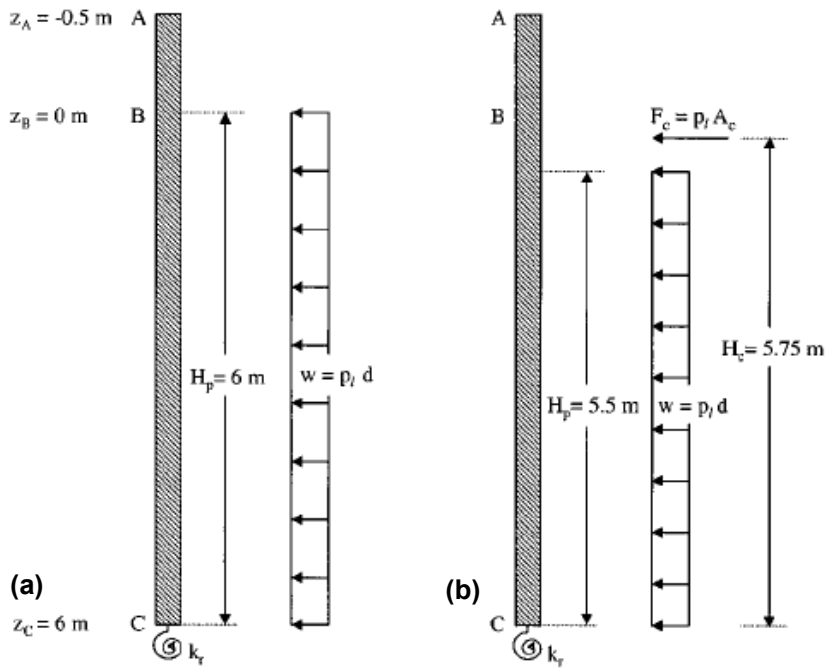

Figure 2.55: Free body diagrams for limit equilibrium analysis (a) without and (b) with cap (M_{max} controlled by loads imposed from liquefied sand) (Dobry et al. 2003)

The authors back-calculated the pressure imposed by the liquefied sand based on the experimental results and concluded that an average value of p_l=10.3 kPa can estimate with sufficient accuracy the response of the pile in each test.

Haigh (2002) conducted centrifuge experiments in which he measured peak and residual lateral soil pressures applied to the pile. He found that the former were of magnitude 50 to 110 kPa, while the latter of 8 to 24 kPa, comparable to the value suggested by Dobry et al. (2003). However, it was observed that peak bending moment was better predicted with the use of the residual pressure. The author attributed this behavior to dynamic attenuation effects due to pile response or inaccuracy in the assumption of linear soil pressure variation with depth that was adopted. Finally, He et al. (2006) conducted shaking table experiments to evaluate limit pressure imposed by liquefied soil and concluded that ultimate pressure ranges between twenty 20 to 40 kPa, much higher than the recommendations presented earlier.

Pamuk and Zimmie (2007) extended Dobry's methodology for pile groups based on centrifuge tests of floating pile groups in two-layer soil profiles, a non-liquefiable

crust over liquefiable sand. As expected, according to Abdoun et al. (2003), pile response was controlled by the loads imposed by the sand. Pile distance was 4d, where d is the diameter of the pile, and it was observed that soil did not fully liquefy inside the group, thus increasing the area at which lateral pressures were imposed.

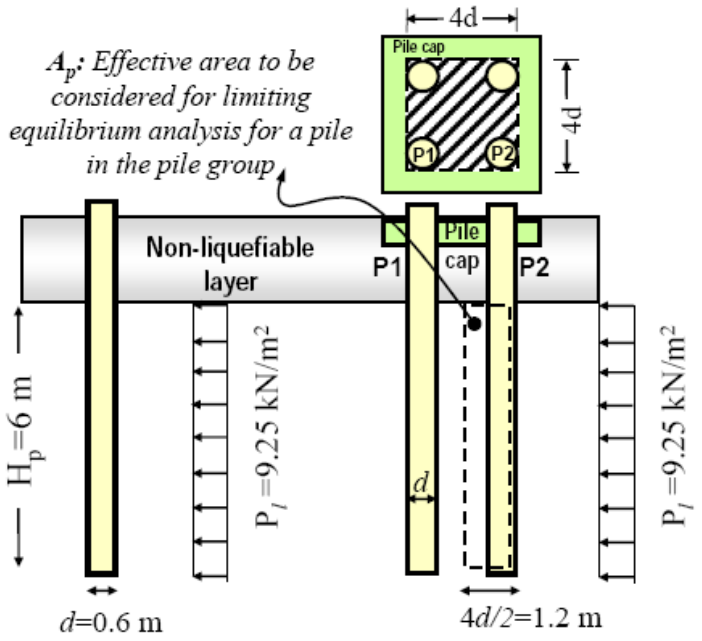

Figure 2.56: Free body diagrams of the liquefied layer for single pile and pile group limit equilibrium analysis (Pamuk and Zimmie, 2007)

Therefore bending moment can be estimated from an equation similar to (2.107) assuming a larger pile area:

$$M = A_p p_l H_p / 2 \tag{2.108}$$

where p_l is the lateral soil pressure, H_p is the length of the pile in the liquefied soil and A_p is the pile area subjected to liquefied soil pressure, as shown in **Figure 2.56**:

$$A_p = H_p \ \ 4d / 2 \tag{2.109}$$

Case II: Pile response is controlled by loads imposed by the crust

Figure 2.57 shows the free-body diagram used to evaluate the response of the pile. Free-body diagram 1 (FBD1) corresponds to the part of the pile in the non-liquefiable crust, FBD2 to the part inside the sand and finally FBD3 is used to determine the

rotation (θ_B) at the tip of the pile. For the crust in FBD1 it is assumed that the direction of loading changes at point C due to soil failure, as the pile pierced into the soil. The passive parameter p_0 was estimated through well-established p-y relations for clays. For the liquefied layer it was assumed that bending moment varies linearly between points A and B. Static equilibrium yields the following system of three (3) equations:

$$M_A / p_0 h^3 = \alpha^2 - 2/3\ \alpha^3 - 1/6 \tag{2.110}$$

$$H_A / p_0 h^2 = 0.5 - \alpha^2 \tag{2.111}$$

$$M_B / p_0 h^3 = H_A / p_0 h^2 \quad L/h \ - M_A / p_0 h^3 \tag{2.112}$$

where $\alpha = z_{ps} / h$. The three (3) equations are not sufficient to solve for the four (4) unknowns (M_A, M_B, H_A and z_{ps}). For moderate values of D_H it can be assumed, based on test observations, that

$$M_A = M_B = M_{A\ \max} \tag{2.113}$$

Hence, equations (2.110) to (2.113) can be reduced to the following relation:

$$3\left(1+\frac{2}{L/h}\right)\frac{M_{A\ \max}}{p_0 h^3} = 1 - 2\left[0.5 - \frac{2}{L/h}\frac{M_{A\ \max}}{p_0 h^3}\right]^{1.5} \tag{2.114}$$

which, for $L/h \geq 2$ can be approximated by the simple expression:

$$M_{A\ \max} \approx p_0 h^3 / \left[10.23 + 6/\ L/h\ \right] \tag{2.115}$$

The above expression indicates that bending moment can be evaluated through geometric characteristics (L, h) and the passive parameter p_0 for the crust. However, for larger displacements the assumption of equation (2.113) is not valid. For this case, the fourth equation required is obtained through FBD2 and FBD3 by calculating the horizontal displacement at point A (D_{pA}) and assuming that it is equal to horizontal displacement of the soil. The additional expression is the following:

$$\frac{EI}{p_0 h^3 L^2} D_H = \frac{1}{3}\frac{H_A}{p_0 h^2}\frac{L}{h} - \frac{1}{2}\frac{M_A}{p_0 h^3} + \frac{EI}{p_0 h^3 L}\frac{M_B}{k_r} \tag{2.116}$$

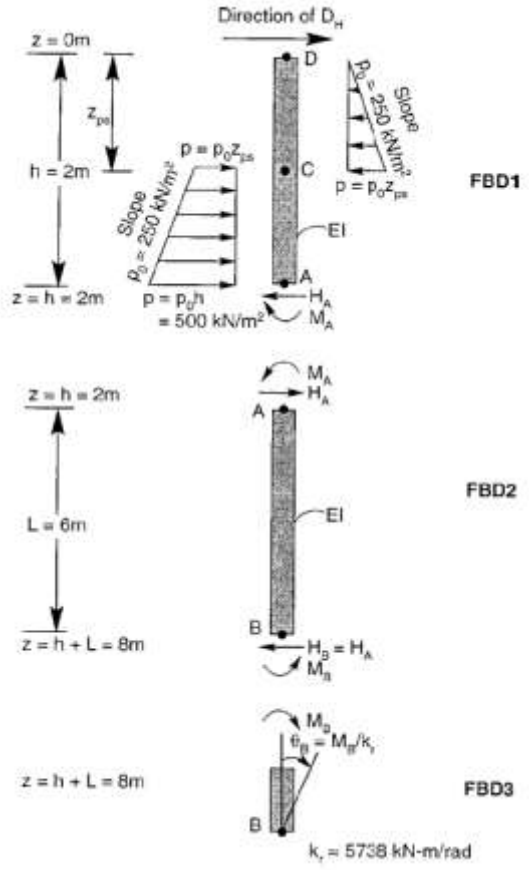

Figure 2.57: Free body diagram for limit equilibrium analysis (M_{max} controlled by loads imposed by the crust) (Dobry et al. 2003)

Both versions of the proposed methodology were used to evaluate the response of a floating and an end-bearing pile in the 1964 earthquake with satisfactory results.

It should be stressed out that the methodology proposed by the authors, as well as any LEM, underlies the assumption that lateral displacements will be large enough to mobilize full resistance of the soil. This, however, might not be the case for real earthquake events, and as a result, application of the methodology will lead to overconservative results. In addition, it is obvious that Limit Equilibrium Methods cannot capture phasing effects given that direction of kinematic loading is an input in the analysis. As a result, design is mostly performed with the p-y method.

2.5.5 Estimation of Inertia Loads

Inertia forces from the superstructure include lateral forces and bending moments. They can be determined, initially, through dynamic elastic analyses or through the acceleration response spectrum of the specific site of the project. However, a certain number of iterations may be required to account for soil-pile-structure interaction. Piles are usually designed to remain in the elastic region (subsurface damage is difficult to assess and repair), while plastic deformations are allowed for the superstructure.

For cases where liquefaction has occurred, soil softening, as a result of pore pressure build-up, affects the motion that is transmitted to the ground surface and therefore the inertia loads from the superstructure. **Boulanger et al. (2007)** studied parametrically the effects of liquefaction on inertia loads through Finite Element tests and proposed the use of two (2) coefficient factors as shown in the following expression:

$$I_{cc\_liq} = C_{cc} C_{liq} I_{\max\_nonliq} \tag{2.117}$$

where I_{max_nonliq} is the inertial load without liquefaction and can be estimated as described previously, I_{cc_liq} is the inertial load with liquefaction, C_{liq} is the ratio of maximum inertial load with liquefaction over without liquefaction and C_{cc} is the fraction of the maximum inertial load with liquefaction at the critical loading cycle. It was found that C_{cc} did not vary significantly, while C_{liq} depended on the frequency content of the input motion. Typical values of C_{cc} and C_{liq} are shown in **Table 2.6**, however further research and more data are required.

Table 2.6: Inertial Coefficients for p-y analyses in liquefied soils (Boulanger et al. 2007)

Motion ($Sa_{T=1s}$/ZPA*)	Pile Cap		Superstructure	
	C_{liq}	C_{cc}	C_{liq}	C_{cc}
Long Period (1.7-2.4)	1.40	0.85	0.75	0.65
Medium Period (0.5-1.6)	0.75	0.85	0.55	0.65

Short Period (≤0.4)	0.35	0.85	0.45	0.65

*ZPA: Zero Period Acceleration

2.5.6 Loads transmitted to pile cap

Loads transmitted to pile caps include active and passive forces on both sides of the cap, friction forces at the base and the sides of the cap as well as the inertia force of the cap. Friction forces are usually neglected in design. However, as it will be discussed later in this chapter, this might lead to conservative results, especially when the cap is subjected to lateral spreading loads. Pile cap inertia force can be estimated from 1-dimensional site response analysis. It should be noted that for most cases pile caps are less massive than the supporting structures leading to significantly lower inertia forces which are usually neglected in design. Active and passive forces can be calculated as follows:

$$P_A = \frac{1}{2} K_{EA} \gamma H^2 B \tag{2.118}$$

and

$$P_P = \frac{1}{2} K_{EP} \gamma H^2 B \tag{2.119}$$

in which γ is the unit weight, H is the height of the cap, B is the width of the cap and K_{EA}, K_{EP} are the active and passive seismic earth pressure coefficients respectively, that account for both wall friction and inertia effects. Well established pseudo-static methods can be used to evaluate K_{EA} and K_{EP} (Mononobe-Okabe, Steedman-Zeng (1990) etc.). Special attention is given below to the method of **Zhang et al. (1998)** which is less known and cannot be found in handbooks and seismic codes:

$$K_{EA} = \frac{2\cos^2(\varphi - i)}{\cos^2(\varphi - i)(1+R) + \cos i \cos(\delta_{mob} + i)(1-R) I_{E.1}} \tag{2.120}$$

$$K_{EP} = 1 + \frac{1}{2}(R-1)\left[\frac{\cos^2(\varphi - i)}{\cos i \cos(\delta_{mob} + i) I_{E.2}} - 1\right] \tag{2.121}$$

$$\begin{pmatrix} I_{E.1} \\ I_{E.2} \end{pmatrix} = \left[1 \pm \sqrt{\frac{\sin\ (\varphi + \delta_{mob})\ \sin\ (\varphi - i)}{\cos\ (\delta_{mob} + i)}} \right]^2 \tag{2.122}$$

$$\tan i = k_i \tag{2.123}$$

$$R = \max\left[-1, -\left(\frac{|\Delta_r|}{\Delta_a} \right)^{0.5} \right] \text{(Active Side)} \tag{2.124}$$

$$R = \min\left[3, 3\left(\frac{|\Delta_r|}{\Delta_p} \right)^{0.5} \right] \text{(Passive Side)} \tag{2.125}$$

$$\delta_{mob} = \frac{1}{2}\ (1 - R)\ \delta_a \text{(Active Side)} \tag{2.126}$$

$$\delta_{mob} = \frac{1}{2}\ (R - 1)\ \delta_p \text{(Passive Side)} \tag{2.127}$$

in which φ is the internal friction angle, I is the angle of seismic coefficient in horizontal direction, R is lateral strain constraint, Δ_r is the relative displacement between soil and foundation, δ the friction angle of the surface of the foundation, δ_a and δ_p are the friction angles of sand at the active and passive states and Δ_a and Δ_p are reference relative displacements at active and passive states, expressed as:

$$\Delta_a = aH \tag{2.128}$$

$$\Delta_p = bH \tag{2.129}$$

in which a=0.001-0.005 and b=0.05-1. The variation of seismic earth pressure coefficient versus relative displacement for both active and passive loading conditions is shown in **Figure 2.58**.

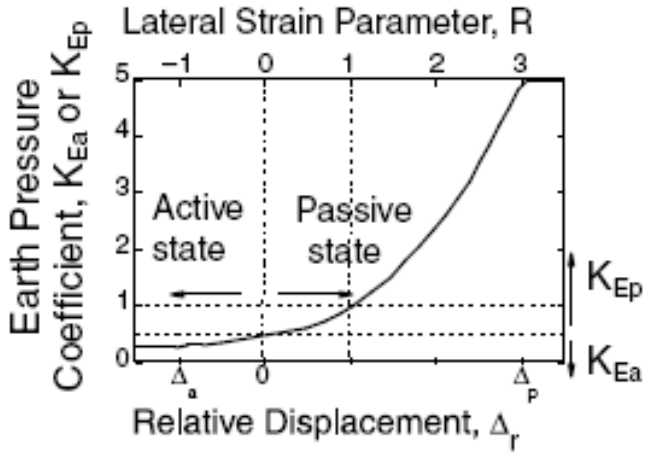

Figure 2.58: Relation of relative displacement and seismic earth pressure coefficient (Tokimatsu and Suzuki, 2009)

Alternatively, soil-pile cap interaction can be described through p-y curves developed for piles (like the ones described in sections 2.2 and 2.5.8), using as input the width of the pile cap instead of the pile diameter (**Juirnarongrit and Ashford, 2006**).

Another issue involved in the simulation of the pile cap response is the rotational constraint that should be applied at its head. In common practice it is usually assumed that no rotation occurs. However, some rotation might take place as a result of pile differential vertical displacement (Juirnarongrit and Ashford 2006). Rotation can be modeled by incorporating in the analysis a rotational spring whose characteristics (stiffness and capacity) can be estimated through the procedure proposed by Mokwa (1999) and Mokwa and Duncan (2003). As shown in **Figure 2.59** the authors propose the use of a bilinear M-θ (moment-rotation angle) model, defined by the ultimate restraining moment (M_{ult}) and rotation angle (θ_{ult}) for which $M=M_{ult}$:

$$M_{ult} = \sum_{i=1}^{N} Q_{si} + Q_{Ei} \quad X_i \tag{2.130}$$

where N is the number of piles in the group, Q_{si} the ultimate skin resistance, Q_{Ei} the ultimate bearing resistance and X_i the moment arm. In addition θ_{ult} depends on the type of the pile and can be calculated as follows:

$$\theta_{ult} = \tan^{-1}\left(\frac{2\Delta_{ult}}{S}\right) \text{(skin friction piles)} \tag{2.131}$$

$$\theta_{ult} = \tan^{-1}\left(\frac{\Delta_{ult}}{S}\right) \text{(end bearing piles)} \tag{2.132}$$

where S is the pile spacing and Δ_{ult} the relative displacement between the soil and the pile required to fully mobilize the skin friction.

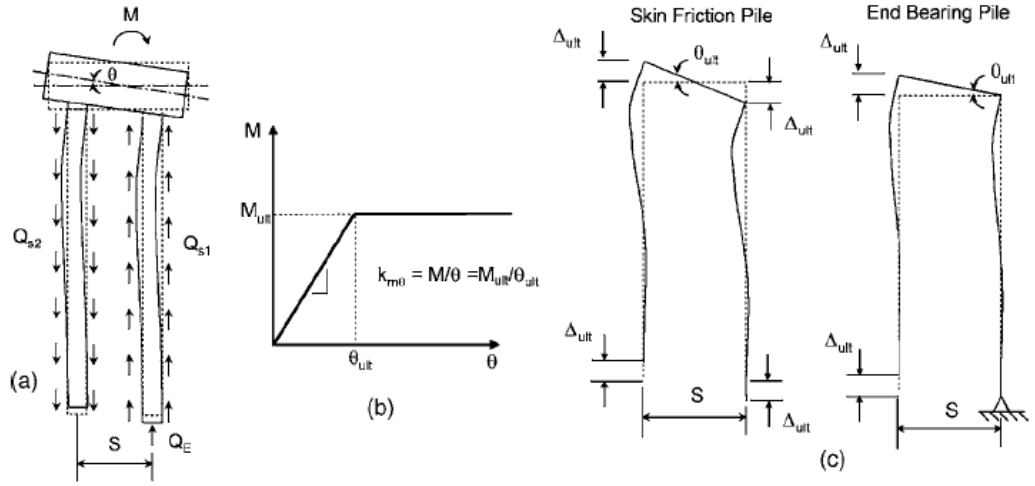

Figure 2.59: Conceptual model for estimating pile group rotational restraint: (a) pile cap restraint rotational model (b) assumed bilinear relationship between M and θ (c) schematic diagrams for estimating ultimate pile cap rotation (Mokwa and Duncan 2003)

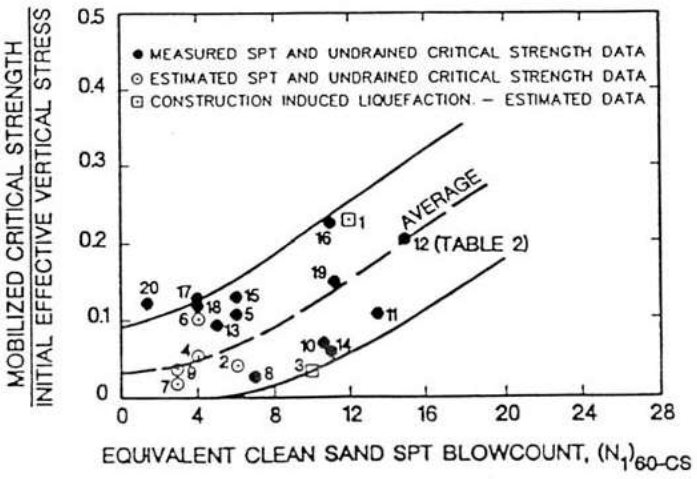

Figure 2.60: Estimation of residual strength of liquefied sand based on the equivalent SPT blowcount (after Seed et al., 2003)

For liquefaction related problems, the same procedures as above can be applied, by taking into account the residual strength of the liquefied sand. The latter is most commonly correlated to the equivalent SPT blowcount, as shown in **Figure 2.60** from the correlation proposed by **Seed et al. (2003)**. The special case where the sand is underlain by a non liquefiable crust will be analyzed separately, as the presence of the crust influences not only the loads applied to the cap, but also the response mechanism of the system.

2.5.7 Load transfer behavior of the non-liquefied crust

As discussed in the previous section loads transmitted to the pile cap include passive and active loads, side and base friction along the sides of pile cap, with the latter usually neglected in design. The same approach is adopted by several researchers (Tokimatsu and Suzuki 2009, Juirnarogrit and Ashford 2006), for cases where the non-liquefied crust is underlain by liquefied sand. However, load transfer behavior can change both in terms of ultimate pressure applied, as well as displacement required for fully mobilization of this ultimate pressure.

Brandenberg et al. (2005, 2007) thoroughly studied the behavior of non-liquefied crusts undergoing lateral spreading displacements through centrifuge experiments. It was observed that there are two possible mechanisms of interaction between the crust, the piles and the cap, as shown in **Figure 2.61**. In the first case (**Figure 2.61a**) crust has failed in passive mode and hence flows around the piles below the cap. Therefore the forces acting on the cap include passive force as well as base and side friction along the sides of the crust. Passive forces can be calculated according to equation (2.119), while friction forces can be estimated as a function of undrained shear strength of the crust by applying adhesion coefficients:

$$F_s = \alpha s_u \tag{2.133}$$

where α is the adhesion coefficient (e.g. Randolph and Murphy 1985) and s_u the undrained shear strength of the crust. Finally, forces acting on single piles can be calculated through p-y relations for clays like the ones presented in section 2.5.8.

In the second case, shown in **Figure 2.61b**, the crust hasn't failed and therefore is trapped between the piles under the cap. Hence, the analysis should be performed by considering an 'equivalent cap' which is extended along the whole depth of the

crust. As a result only passive and friction forces, acting on each side of the 'equivalent cap', should be included in the analysis. As far as active forces are concerned, the authors suggest that they should be neglected in the analysis, as they observed gaps between the pile cap and the active side of the crust.

The authors back-calculated ultimate forces based on the concept described above and compared them to the measured ones. It was found that friction forces, which are usually ignored in the design, contribute significantly to the total load imposed by the crust. They also recommended the use of the static p-y curves proposed by Matlock (1970) as the cyclic curves were found unconservative.

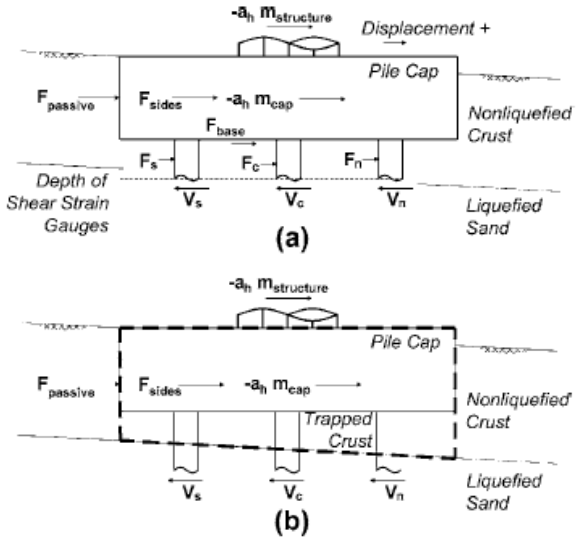

Figure 2.61: Interaction mechanism between crust and pile groups (a) crust flows around the piles (b) crust is trapped between the piles (Brandenberg et al. 2007)

The experiments also revealed that the crust exhibits a totally different load transfer behavior under lateral spreading conditions (or in general when it is underlain by a weak layer like liquefied sand) compared to static loading. Namely the displacement required for the ultimate load to be fully mobilized is much larger compared to static loading. In a first level this softening behavior can be attributed to the cyclic degradation of the clay due to previous loading. Furthermore, liquefaction causes distribution of stresses to a much larger distance inside the crust, as liquefied sand can sustain only a small portion of the lateral stress. As a result larger displacements

develop in the crust and hence larger relative displacements are required to reach a certain load level.

Based on the above observations the authors developed analytical solutions to describe load transfer behavior for two (2) cases: (a) crust displacements remain small (cyclic phase before liquefaction), while pile cap pushes the soil as a result of large inertia loads (structural loading model) (b) pile cap is subjected to large kinematic loads from the laterally spreading crust (lateral spreading model). **Figures Figure 2.62** through **Figure 2.64** show typical curves derived from the analytical models developed for variations of the different parameters involved in the calculations (strength, geometry and seismic motion characteristics).

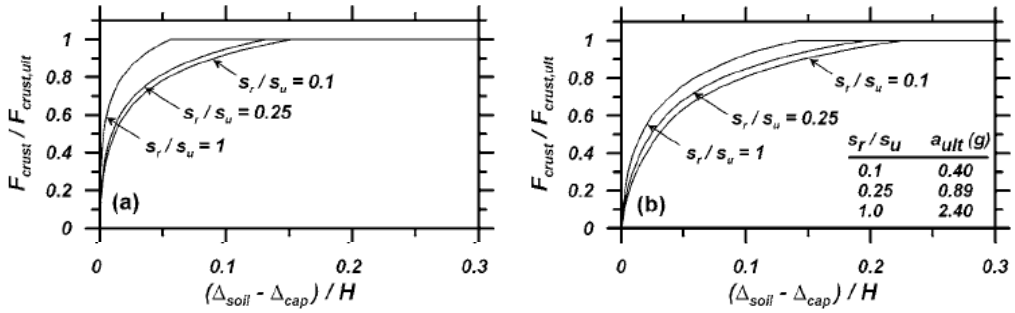

Figure 2.62: Influence of ratio of residual strength (s_r) to crust undrained shear strength (s_u) on load transfer relation for (a) structural loading (b) lateral spreading (Brandenberg et al. 2007)

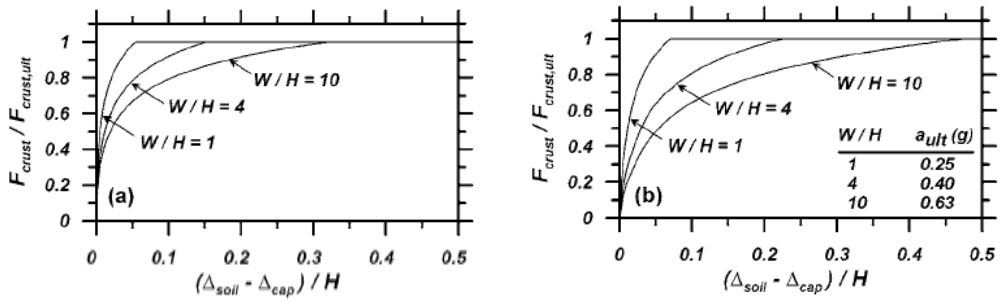

Figure 2.63: Influence of ratio of pile cap width (W) to layer thickness (L) on load transfer relation for (a) structural loading (b) lateral spreading (Brandenberg et al. 2007)

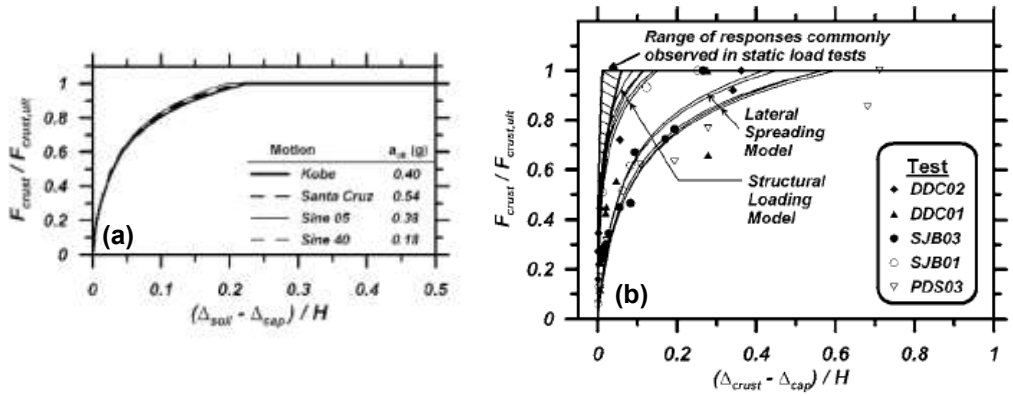

Figure 2.64: (a) Influence of ground motion on load transfer relation for lateral spreading (b) overall comparison of analytical load transfer relations with centrifuge data (Brandenberg et al. 2007)

Cubrinovski et al. (2005) also investigated the behavior of non-liquefied crusts through shaking table tests. As described earlier, in section 2.2.5.1, they recommend the use of the passive pressure theory for the estimation of ultimate resistance, along with a coefficient factor equal 4.5 to account for shear forces developed at the sides of the wedge failure.

With regard to load transfer response, the authors observed that indeed a larger displacement is required to develop full passive resistance. This observation is also supported by Rollins and Sparks (2002) who compiled data from different tests and found that required deflection for ultimate resistance depends on relative density and on the existence of a weak layer (i.e. a layer of liquefied sand) below the crust. Furthermore it was observed that, for flexible piles, soil resistance might not be fully mobilized, because of small relative displacements (flexible piles follow the movement of the soil).

Finally **Yang and Jeremic (2002)** conducted numerical analyses to study the effect of soil layering for piles under lateral loading. It was observed that in a zone near the interface ultimate soil resistance might be reduced. According to the authors this zone covers a distance of approximately three (3) pile diameters.

2.5.8 P-y relations for soft and stiff clays

Matlock (1970) performed lateral load tests to steel pipes driven in *soft and medium clays* to study their response in both monotonic and cycling loading. It was observed that for cyclic loading the resistance of the soil was significantly reduced. Reese et al.

(1989) attributed this response to the erosion and remolding of the soil around the pile because of its subjection to repeated strains of large magnitude. For static loading the p-y expression proposed by Matlock (1970) has the following form:

$$p = 0.5 p_u \left(\frac{y}{y_{50}} \right)^{1/3}, \text{ for } y / y_{50} \le 8 \qquad (2.134)$$

$$p = p_u, \text{ for } y / y_{50} > 8 \qquad (2.135)$$

where

p: lateral resistance of soil

p_u: ultimate soil resistance

y: pile deflection

y_{50}: pile deflection when p is 50% of p_{ult}

The quantity y_{50} is defined as follows:

$$y_{50} = 2.5 \varepsilon_{50} B \qquad (2.136)$$

where

B: Pile diameter

ε_{50}: axial strain in an undrained triaxial compression test corresponding to a shear stress equal to 0.5 times the maximum undrained shear strength

Table 2.7 shows representative values for ε_{50}. Matlock (1970) in his work defines the ultimate soil resistance, $p_{ult,}$ as follows:

$$p_u = \left(3 + \frac{\sigma'_v}{s_u} + J \frac{z}{B} \right), \text{ for } z < z_{cr} \qquad (2.137)$$

$$p_u = 9 s_u B, \text{ for } z \ge z_{cr} \qquad (2.138)$$

where

σ'_v: effective overburden pressure

s_u: undrained shear strength of the soil

J: empirical parameter

z_{cr}: limiting depth defining the zone within which the limit unit resistance of laterally loaded piles is reduced due to proximity of the free surface

The empirical parameter J was estimated by Matlock (based on his experiments) to 0.5 for soft clays and 0.25 for medium clays. The limiting depth, z_{cr}, can be calculated as follows:

$$z_{cr} = \frac{6B}{B\frac{\gamma_b}{s_u} + J} \geq 2.5B \tag{2.139}$$

where γ_b is the buoyant unit weight of the soil. As discussed earlier p-y response is different for cyclic loading and can be described by the following equations:

$$p = 0.5 p_u \left(\frac{y}{y_{50}}\right)^{1/3}, \text{ for } \quad y / y_{50} \leq 3 \tag{2.140}$$

Then, if $z \geq z_{cr}$:

$$p = 0.5\, p_u \;\; 3^{\;1/3} = 0.72\, p_u \tag{2.141}$$

Otherwise if $z < z_{cr}$:

$$p = 0.72\, p_u \;\; z / z_{cr} \;\; , \text{for } \; y / y_{50} \geq 15 \tag{2.142}$$

For $3 \leq y / y_{50} \leq 15$ it is rational to assume that p decreases linearly. Matlock's relationships, for both static and cyclic loading, are shown in **Figure 2.65**.

Table 2.7: Representative values of ε_{50} for clays (Reese et al. *2005)*

Consistency of Clay	**Undrained Shear Strength (kPa)**	**ε_{50}**
Very soft	>12	0.02
Soft	12-24	0.02
Medium	24-48	0.01
Stiff	48-96	0.006
Very Stiff	96-192	0.005
Hard	>192	0.004

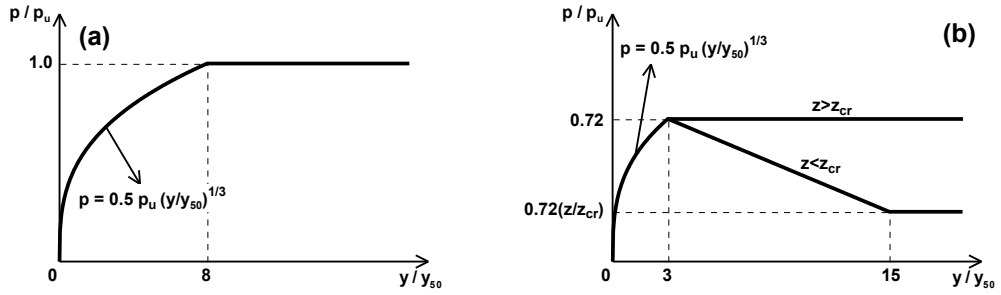

Figure 2.65: P-y curves for soft and medium clays under (a) static and (b) cyclic loading (Matlock (1970)

For *stiff clays* Dunnavant and O'Neill (1989) have proposed the following expression:

$$p = \begin{cases} 1.02\,p_u \tanh\left[0.537\left(\dfrac{y}{y_{50}}\right)^{0.7}\right] & \text{for } y < y_{50} \\ p_u & \text{for } y > y_{50} \end{cases} \qquad (2.143)$$

2.6 Guidelines for the design of piles in liquefied and laterally spreading soil

		Highway Bridges (JRA)	Railway Facilities (RTRI)	Building Foundations (AIJ)
Liquefaction	Inertia force	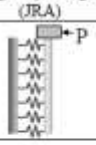	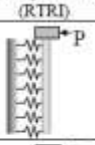	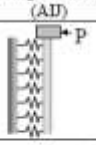
	Ground movement force	Not consider	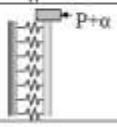	
	Subgrade reaction	Reduce with • FL-value • Depth • Liquefaction strength • Earthquake Level	Reduce with • FL-value • Depth	Reduce with • Na-value • Depth
Lateral spreading	Inertia force	Not consider	Not consider	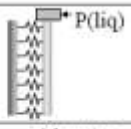
	Ground movement force	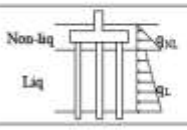	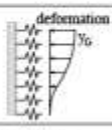	
	Subgrade reaction		Liq layer:1/1000 Non-liq layer:No reduction	Same as liquefaction

Figure 2.66: Japanese specifications for pile design in liquefied ground and for lateral spreading conditions (Uchida and Tokimatsu, 2006)

From the existing design regulations, only Japanese guidelines address the problem of pile design in laterally spreading soils. Japanese Design Codes treat the influence of liquefaction on piles differently for Highway Bridges (JRA), Railway Facilities (RTRI) and Building Foundations (AIJ). Design recommendations for level and gently sloping ground are summarized in **Figure 2.66**.

Specifications for Highway Bridges (JRA, 2002)

For level ground conditions design is performed with the p-y method. Subgrade reaction coefficient is calculated according to equations (2.60) through (2.64) and reduced with depth, liquefaction strength, earthquake level and factor of safety against liquefaction, as shown in **Table 2.8**. Kinematic loading from cyclic ground displacements is not included in the analysis.

Table 2.8: Reduction factor for Highway Bridges (JRA, 2002)

F_L	Depth	Liquefaction Strength			
		R≤0.3		0.3<R	
		Level 1	Level 2	Level 1	Level 2
$F_L \leq 1/3$	0≤x≤10	1/6	0	1/3	1/6
	10<x≤20	2/3	1/3	2/3	1/3
$1/3 < F_L \leq 2/3$	0≤x≤10	2/3	1/3	1	2/3
	10<x≤20	1	2/3	1	2/3
$2/3 < F_L \leq 1$	0≤x≤10	1	2/3	1	1
	10<x≤20	1	1	1	1

For lateral spreading conditions analysis follows the Limit Equilibrium approach. Inertia loads are neglected, while full passive earth pressure and 30% of passive earth pressure are applied from the crust and the liquefied layer respectively.

Haigh and Madabhushi (2006) evaluated the predictions of JRA based on the results of centrifuge experiments. Comparison in terms of bending moments and soil pressures are shown in **Figure 2.67**. The comparison shows that JRA predictions are unconservative by a factor of two (2) for bending moments and by a factor of up to five (5) for lateral pressures. Similar conclusions were also drawn by Brandenberg et al. (2005), based on lateral load measurements in centrifuge tests.

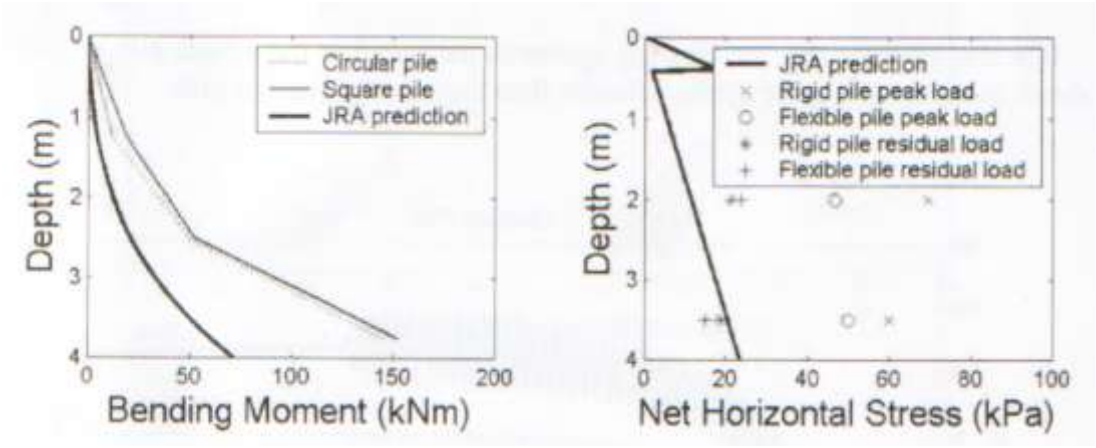

Figure 2.67: Comparison between JRA predictions and centrifuge results (Haigh and Madabhushi, 2006)

Design Standard for Railway Facilities (RTRI, 1999)

For level ground conditions analysis is performed with the p-y method. Subgrade reaction is calculated according to equations (2.65) and (2.66), and is reduced according to **Figure 2.68a** as a function of FL and depth. Kinematic loading is applied as additional inertial force.

On the other hand, for lateral spreading conditions, inertia loads are neglected and kinematic loads are included as imposed displacements. Modulus of subgrade reaction is reduced to 1/1000 for the liquefied layer, while no reduction factor is applied for the non-liquefied crust.

Recommendations for Design of Building Foundations (AIJ, 2001)

For level ground conditions design is performed with the p-y method. Subgrade reaction is estimated from equations (2.67) and (2.68), and reduced according to **Figure 2.68b** as a function of the corrected SPT value and depth. Cyclic strains are evaluated according to **Figure 2.50a** and equation (2.99).

For lateral spreading conditions permanent ground displacements are calculated according to **Figure 2.50b** and the procedure described in equations (2.100) through (2.102). Reduction of subgrade reduction is the same as for the level ground case.

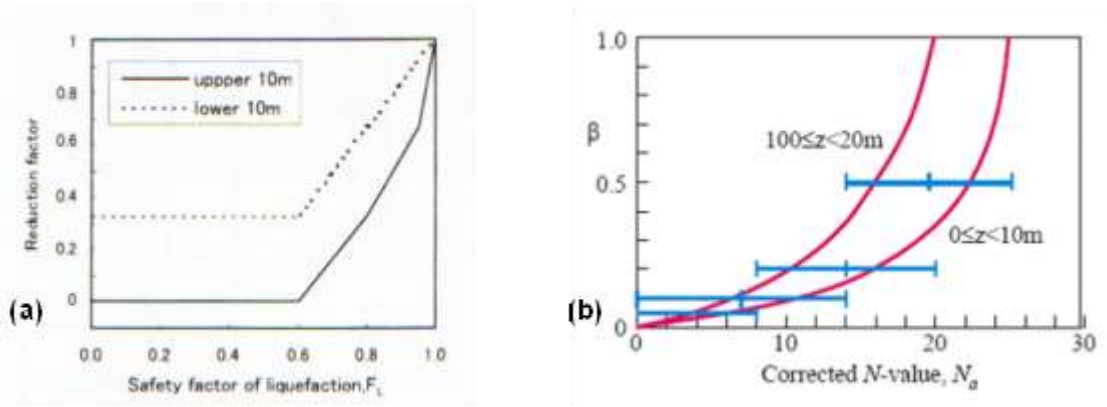

Figure 2.68: Reduction factor for (a) Railway Facilities (RTRI) and (b) Building Foundations (AIJ) (Uchida and Tokimatsu, 2006)

2.7 Concluding Remarks

Based on the preceding analysis, certain critical questions are raised with regard to pile design under both static and dynamic lateral loads.

2.7.1 Piles in nonliquefied soils

1) What is the most appropriate method to evaluate p-y response of nonliquefied sands?

The example presented in section 2.2.6 revealed that existing methodologies yield design values that vary significantly with each other in all three (3) components of a p-y curve (ultimate soil resistance, coefficient of initial subgrade modulus, non-linear shape), and hence, raising concerns with regard to which method can ensure a safe design of the pile foundation.

2) What are the limitations of the existing p-y methodologies?

- Current methods were developed based on field tests, performed for a very narrow range of values for the various parameters involved. Therefore any generalization and application of the methods for a broader range of parameters should be further investigated.
- Estimation of ultimate soil resistance employs simplifying and perhaps unrealistic assumptions (2-D analysis, no side friction, no soil dilation, no pile deformation beneath the point of zero deflection), whose validity should be investigated.

3) How does pile-soil interaction affect the response?

- Pile inertial characteristics, which affect pile-soil interaction, are not included in any of the methodologies. However, recent studies (**Ashour and Norris, 2000**), have shown that pile properties can modify drastically the p-y response of the same sand.
- All tests performed to develop analytical relationships involved piles subjected to lateral loads on their heads. Therefore, they do not take into account the effect of loading type or kinematic constraints at the head, which might influence the response, as discussed in paragraph 2.2.5.

4) Does pile installation affect the response?

- Finally, methodologies do not clarify for what types of piles (driven or drilled) are developed, and in general effects of pile installation are neglected in all analyses. However, it is well established that installation of driven piles affects in

a large amount both the stress and volumetric field around the pile. Therefore it is reasonable to expect difference in the response between displacement and non-displacement piles.

The above discussion reveals that the body of research with respect to p-y response of nonliquefied cohesionless soils is not yet sufficient. More investigation is needed with regard to the effect of both the parameters already included in p-y methodologies, but in a more systematic sense, and also of parameters so far neglected in the analysis but probably influential in the response (type of loading, pile inertia, pile installation).

However, field testing cannot allow for a systematic and parametric investigation of the problem, since soil properties are pre-defined, and also the number of tests that can be performed is limited, making it impossible to simulate different types of piles and loading conditions. These handicaps can be overcome with the use of advanced numerical methodologies verified against well-established full scale and centrifuge experiments.

2.7.2 Piles in liquefied soils

Mechanisms affecting the response of piles in liquefied soils have been thoroughly investigated both experimentally and numerically, while research is still in progress in many universities around the globe. Most of the problem's aspects have been well understood, while useful observations and recommendations lay the ground for efficient and safe design of piles in liquefied soils both in level ground and under lateral spreading conditions using the p-y method. However, uncertainties still remain, especially with regard to the response of liquefied soil. As a result the project engineer will be asked to give answer to critical questions, which may affect the design significantly. Namely:

1) What is the actual shape and ultimate capacity of liquefied p-y curves?

Major trend in current practice, recommended by many researchers (Boulanger et al., 2007; Tokimatsu and Suzuki, 2009; Cubrinovski and Ishihara, 2007), as well as design guidelines (JRA, AIJ, RTRI), is the use of p-y curves for non-liquefied soils, multiplied by a reduction factor, called the m_p multiplier. This approach leads to curves that reflect a softening (API, AIJ), linear (JRA, RTRI) or bilinear (Cubrinovski and Ishihara, 2007) response with the capacity depending on the value of the

multiplier. The latter is estimated through empirical charts (Brandenberg, 2005; AIJ, 2001, Dobry et al., 1995; Cubrinovski et al., 2005), based on various parameters (Relative density, Pore pressure ratio, Soil-pile relative displacement). However, different approaches lead to different estimations of m_p (Brandenberg 2005 and AIJ 2001), while other correlations are hard to apply (e.g. estimation of pore pressure ratio is very uncertain). In addition, studies have shown that response of liquefied soils is a very complicated phenomenon that depends on a large set of parameters, and hence correlations of m_p with one parameter are characterized as simplifying.

Others have suggested that the response is largely dilatant and recommend the use of curves with hardening characteristics (Rollins et al., 2005). In other cases the behavior of the liquefied soil is assumed to be similar with that of soft clay, and hence clay curves are used (Matlock et al., 1970), with the residual strength of the sand playing the role of the undrained shear strength. Finally, a somehow different approach has been proposed by Ashour and Norris (2003) that generates p-y curves assuming a wedge shaped failure mechanism.

As for the Limit Equilibrium Methods (LEM), uncertainty still remains on the ultimate resistance of the sand. The value of 10.3kPa proposed by Dobry et al. (2003) is comparable to JRA (2002) recommendations for a range of field conditions. However, other studies (Haigh, 2002; Brandenberg et al., 2005; He et al., 2006) showed that both Dobry's and JRA recommendations significantly underestimate the response, and much larger pressures need to be applied.

To bypass the above uncertainties, the engineer is forced to perform the design for a broad range of input parameters (especially the ones related to p-y behavior), resulting in broad ranges for the response quantities (pile bending moments and head displacements), which increase the cost of the project. It is, therefore, evident that the design can become much more efficient, if the effect of each parameter on subgrade reaction is examined more systematically and more integrated design guidelines are proposed.

2) What factors affect the subgrade reaction and how?

A large number of tests and analyses that have been carried out during the past years (citations), which have offered valuable insight on the mechanism of subgrade reaction in liquefied soils and on the parameters that affect it. Test results indicate

that subgrade reaction is largely influenced by the development of excess pore pressure, and subsequently parameters that determine p-y response include those that affect:

- Pore pressure generation and undrained response of saturated sands (relative density, strain, strain history etc.)
- Pore pressure dissipation (permeability, loading rate etc.)
- Cyclic and permanent displacements around the pile (pile stiffness, seismic motion etc.)

Evaluation of p-y response in current practice takes into account only the effects of relative density through the m_p-multiplier approach (Brandenberg, 2005; AIJ, 2001). Correlations that directly relate m_p with excess pore pressure ratio, r_u, (Dobry et al. 1995; Han et al., 1997) are hard to apply, since evaluation of r_u is very uncertain. However, recent studies, described in previous sections, have stressed out that the remaining factors can as well influence significantly the response. Loads imposed on piles varied significantly for stiff and flexible piles as observed by Haigh (2002), Cubrinovski et al. (2005), Ashour and Norris (2003). In general, flexible piles follow the movement of flowing soil, inducing small relative displacements, and thus smaller dilation. On the other hand, stiff piles cause larger dilation increasing transient subgrade reaction. However, residual resistance does not seem to be affected by pile stiffness.

In addition less permeable soils or high frequency seismic motions can lead to much higher loads as shown by Gonzalez et al. (2009), Dungca et al. (2006), Haigh (2002) and Uzuoka et al. (2005). Slower drainage conditions (low permeability materials and/or high frequency input motion) impede pore fluid migration from lower to upper levels. As a result dilation is more pronounced resulting in significantly larger loads on the pile. Rate effects have also been observed by Girard and Taylor (1994), Kutter and Voss (1995), Palmer (1999) and Towhata and Mizutani (1999).

Therefore, it is apparent that a more systematic investigation of the effects of pile stiffness and loading rate effects is needed. However, investigation of these parameters through physical model tests is a tedious task, since it is hard to simulate fluids of different permeability or piles of various inertia characteristics, and can only offer valuable insight but not systematic parametric investigation oriented to provide

design recommendations. Sophisticated numerical analyses, on the other hand, incorporating advanced constitutive models that can capture effects of pore pressure build-up and dissipation, allow the analysis of a large number of cases, providing a large set of data and thus laying the ground for further insight as well as development of design recommendations.

3) How does liquefaction influence the behavior of the dashpot?

The literature survey revealed that radiation damping is basically not included in current design of piles with the p-y method. Exceptions to this rule are the procedures proposed by Assimaki and Varun (2009), Lin et al. (2007) and Liyanapathirama and Poulos (2005). In these approaches radiation damping is simulated as in firm soils (Dobry and Gazetas, 1984; Burger et al., 1975) by applying a coefficient factor which depends on pore pressure build-up. However, this approach is not verified by numerical analyses or test results. On the contrary, results from shaking table test by Ueng et al. (2009) showed dependence of damping ratio on the stiffness of the pile, a parameter that is not included in relations for firm soils. This indicates that further investigation might uncover aspects that can affect drastically the design.

3

Numerical Simulation of p-y curves in non-liquefied sands

3.1 General

In the present chapter, the numerical model developed to simulate the problem of p-y curves in sands is thoroughly described. The model is presented by means of a baseline analysis, regarding a pile, installed in a uniform sand layer, and pushed laterally. Emphasis is placed on the model's ability to capture deformation patterns and mechanisms also reported in literature, as well as produce p-y curves to evaluate quantitatively the response of the soil. Prior to the description of the numerical simulation and demonstration of some typical results, the basic aspects of the numerical algorithm used in the analyses are presented. At this point it is assumed that the pile installation does not affect the stress and volumetric state of the surrounding soil. This assumption is roughly accurate only for excavated piles.

3.2 Basic Aspects of the Numerical Methodology for Static Problems

Numerical analyses were performed with the finite difference code FLAC3D version 3.10 (**Itasca, 2005**), while the sand response was simulated using the advanced constitutive model NTUA_Sand developed in the Geotechnical Division of the National Technical University of Athens (**Papadimitriou et al., 2002**) and implemented in the numerical codes FLAC and FLAC3D (**Andrianopoulos et al., 2010; Karamitros, 2010**). This numerical methodology has been verified against well-documented centrifuge tests (**Arulmori et al., 1992**), and has been used to investigate complicated geotechnical problems (**Valsamis et al., 2010; Karamitros, 2010**). Detailed description of the numerical methodology is beyond the scope of this thesis; however its basic characteristics need to be presented herein as they are crucial for the understanding of the numerical predictions.

3.2.1 The Explicit Finite Difference Method

FLAC3D makes use of the Finite Difference Method, whose central idea is that every derivative in the set of governing equations is replaced by an algebraic expression written in terms of the field variables (stress, displacements) at discrete points in space, while no variation of these variables within the elements needs to be specified. A typical FLAC3D calculation circle is shown in **Figure 3.1**. Starting from a given displacement state at each gridpoint the incremental strains for each zone are evaluated for a given displacement increment (velocity). Following, the new stresses at each zone are calculated based on the constitutive law adopted. Stresses are used to estimate forces at each node. If these forces are close to zero, then the system is in equilibrium or steady state flow under constant velocity. Otherwise, for non-zero nodal forces, application of equations of motion produce nodal accelerations. Each full circle of this loop is taken as one timestep.

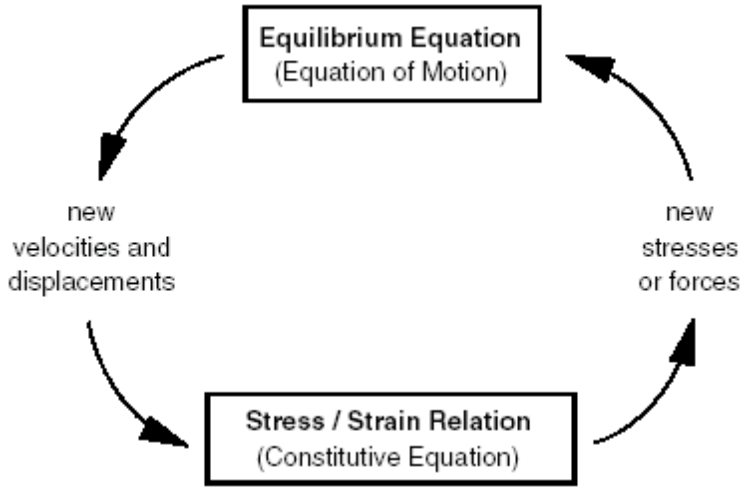

Figure 3.1: Explicit calculation sequence used in FLAC3D

The most important characteristic of the explicit finite difference method is that each box in **Figure 3.1** updates all of its grid variables (stresses and displacements) from known values that remain fixed while control is within the box. For example, the new stresses computed in the lower box are based on a set of velocities already calculated, and is assumed to be "frozen" for the operation of the box. This might seem unreasonable, since a change of stresses influences the velocities of neighboring gridpoints. However, if the integration timestep is adequately small, such that information cannot physically propagate from one element to another, then the

"frozen-velocities" assumptions can be justified. This leaves the explicit method with one disadvantage and one advantage:

- The disadvantage: a large number of computation steps will be required to complete an analysis, even if the latter involves linear materials.
- The advantage: No iteration process or matrix inversion is required, since elements do not communicate with each other during each solution step. Thus, for highly non-linear problems FLAC is expected to perform better than implicit finite element methods.

In order for the "calculation front" to move faster compared to the propagation of physical information, a critical timestep should be chosen, which is smaller than a critical value. Assuming that the pressure velocity C_p is the maximum speed at which information can propagate and that Δx is the smallest size of an element, then the critical timestep would be given by the following equation:

$$\Delta t_{crit} < \frac{\Delta x}{C_p} \tag{3.1}$$

It is obvious that a critical timestep value is estimated from equation (3.1) for each gridpoint, and the lowest of these values is adopted for the calculations throughout the grid. Furthermore, it can be shown that for a general system, consisting of solid material and arbitrary networks of interconnected masses and springs, the critical timestep is related to the smallest natural period of the system, T_{min}:

$$\Delta t_{crit} < \frac{T_{\min}}{\pi} \tag{3.2}$$

3.2.2 Numerical Scheme for Static Problems

The calculation cycle shown in **Figure 3.1** is also invoked when the static solution of a problem is desired. Equations of motion are also included in the formulation, and calculations are performed in terms of a pseudo-time, which will be defined later in the chapter. In order to demonstrate how the static response can be obtained when a load is applied dynamically, and under what circumstances convergence is faster, it is useful to examine the response of a Single Degree of Freedom (SDOF) system (**Figure 3.2a**) subjected to a dynamic force, p(t), that has finite rise time, t_r, and remains constant thereafter (**Figure 3.2b)**.

Dynamic step force p(t) can be described as follows:

$$p\ t\ = \begin{cases} p_o\ \ t/t_r & t \le t_r \\ p_o & t \ge t_r \end{cases} \tag{3.3}$$

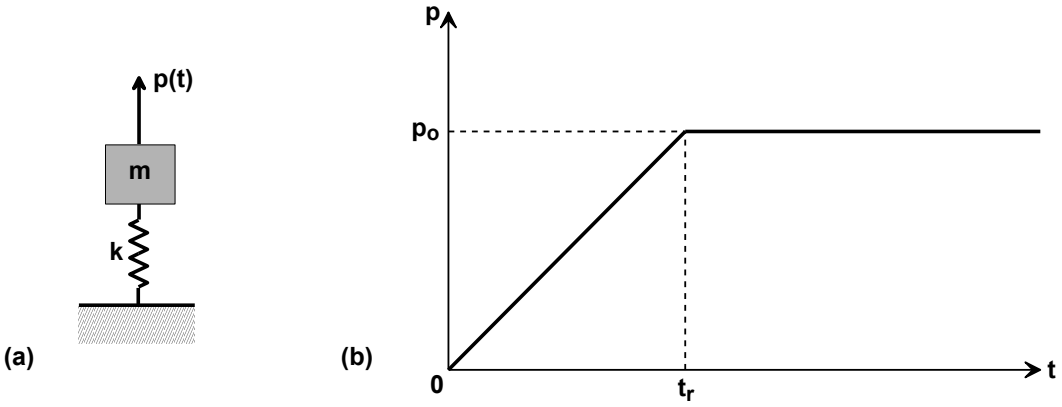

Figure 3.2: (a) SDOF system (b) step force with finite rise time

It can be shown (**Chopra, 2007**) that the displacement of the mass can be calculated as follows:

$$u\ t\ =\ u_{st}\ _o\left(\frac{t}{t_r}-\frac{\sin\omega_n t}{\omega_n t_r}\right) \text{ for } t \le t_r \tag{3.4}$$

$$u\ t\ =\ u_{st}\ _o\left\{1-\frac{1}{\omega_n t_r}\left[\sin\omega_n t-\sin\omega_n\ \ t-t_r\ \right]\right\} \text{ for } t \ge t_r \tag{3.5}$$

where $(u_{st})_o$ is the static response and ω_n is the natural frequency of the system given by:

$$u_{st}\ _o = p_o / k \tag{3.6}$$

$$\omega_n = \frac{2\pi}{T_n} = \sqrt{\frac{k}{m}} \tag{3.7}$$

The dynamic response in terms of displacement and velocity for various ratios of t_r/T is shown in **Figure 3.3**. Also plotted is the static deformation at each time instance:

$$u_{st}\ t = p\ t\ /k \tag{3.8}$$

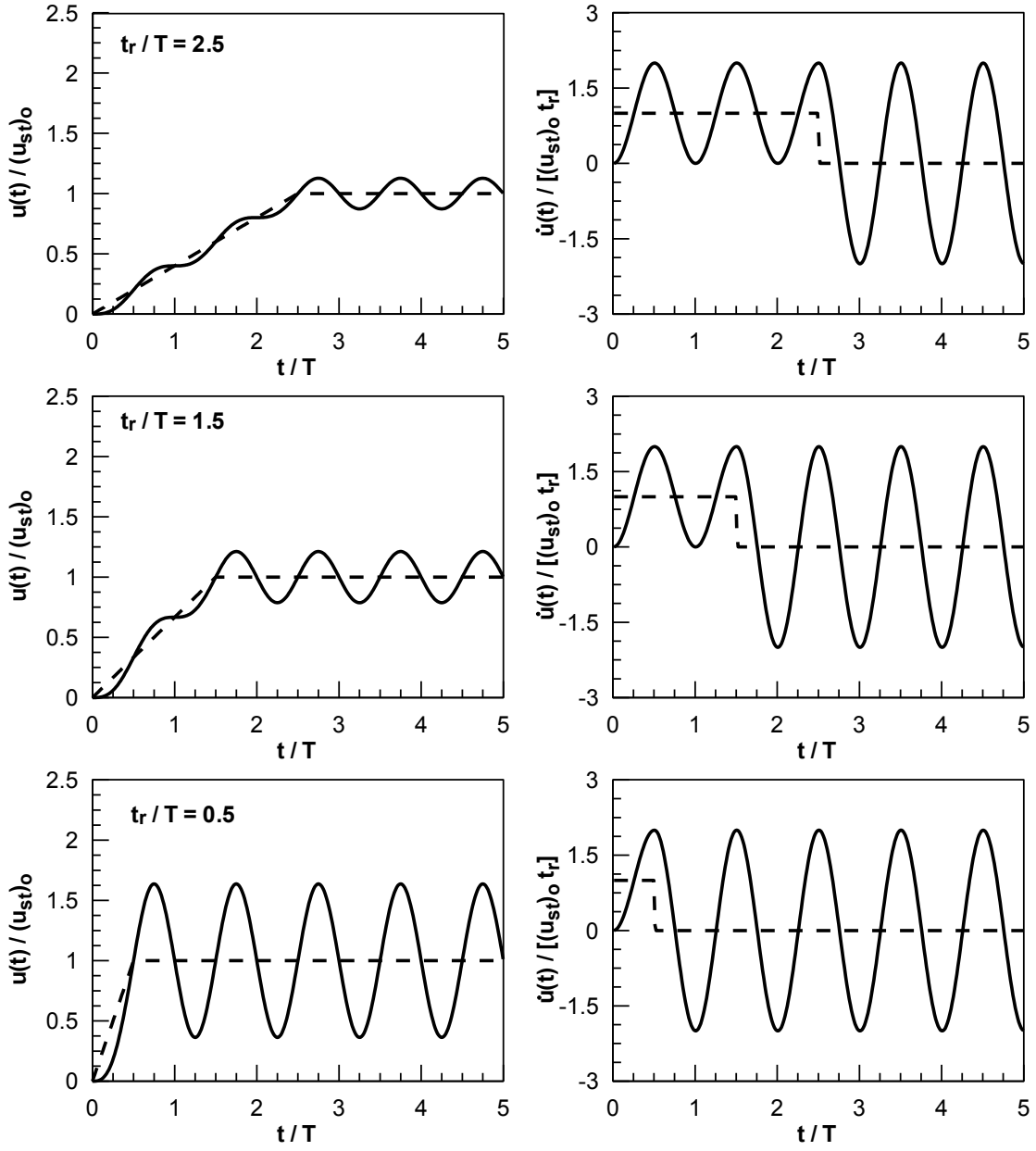

Figure 3.3: Response of undamped SDOF system to step force with finite rise time.

Based on **Figure 3.3** the following observations can be made:

- The system oscillates about the static solution during both the force-rise and the constant-force phase.
- During the initial, force-rise phase, static response is characterized by a nonzero constant velocity. As a result oscillation around the static solution results in a dynamic velocity timehistory, whose sign remains unchanged. This observation is critical for the modeling of damping, as it will be described later.
- The response is a function of the ratio t_r/T, and does not depend separately on t_r or T. Namely, dynamic effects are small for large values of t_r/T and more pronounced for small t_r/T. Hence, faster convergence is achieved either when the load is applied more slowly (less dynamically) and/or when the natural period of the system is smaller. The latter corresponds to systems with small mass or large stiffness (rigid structures are less sensitive to dynamic excitations).
- The present analysis examines structures with no damping. It is evident, however, that application of some kind of damping is necessary for the oscillation to diminish.

The basic concepts of this fundamental case are implemented in FLAC's algorithm for static problems. Consider a system at absolute equilibrium in which a constant velocity is applied somewhere in the grid, for example the lateral movement of a pile. According to the SDOF response we expect the system to start oscillating around the static solution. This is modeled in FLAC as follows (**Figure 3.1**): velocities generate new stresses, which in turn produce forces at the nodes of the grid. For the system to be in equilibrium, the sum of the forces acting at each gridpoint should be equal to zero. If not, application of equations of motion will generate the oscillation. The sum of the forces acting at the gridpoint, which is indicative of the system's instability, is called "Unbalanced Force". Values of the unbalanced force smaller than a critical value, indicate that the system is in equilibrium or in steady-state flow. In order to accelerate convergence (i.e. diminish the oscillation), FLAC3D incorporates numerical techniques, which include:

- Large damping forces (dissipation of oscillation)
- Adjustment of natural period of the system

3.2.2.1 Large damping forces

FLAC3D introduces large damping forces to the equations of motion. For static problems two (2) types of damping can be applied: local and combined.

With the *Local Damping* formulation, damping force at each gridpoint is related to the corresponding Unbalanced Force, as follows:

$$F_{d,i} = \alpha \left| F_{unbal,i} \right| \mathrm{sgn}\left(\dot{u}_i \right) \tag{3.9}$$

where:

$F_{d,i}$: Damping force at gridpoint i

$F_{unbal,i}$: Unbalanced force at gridpoint i

α: Damping constant (set to 0.8 in FLAC3D)

$\mathrm{sgn}\left(\dot{u}_i \right)$: sign (direction) of velocity at gridpoint i

The constant term α is set to 0.8 (FLAC3D default value) corresponding to a damping coefficient of 80% at each gridpoint. The direction of the damping force, based on the above formulation, is, in most cases, such that energy is dissipated. Exceptions are cases where movement includes a large steady-state component, which will cause the sign of the velocity, and hence the damping force, not to be affected by the oscillation. For example, as observed previously in the study of the SDOF system, the sign of the velocity remains unchanged during the force-rise phase (**Figure 3.3**). For this type of response, the local damping formulation would cause a damping force of constant sign, not efficient to diminish the oscillation.

For such cases (creep simulation, uniform lateral pile displacement), *combined damping* is much more efficient to use. Combined damping logic can be explained in terms of the SDOF system of **Figure 3.2a**. The dynamic response, in terms of velocity, shown in **Figure 3.3**, can be expressed as follows:

$$\dot{u}\ t\ = V \sin\ \omega t\ + \dot{u}_o \tag{3.10}$$

where

$\dot{u}_o$: superimposed steady velocity

V: Maximum Periodic Velocity

ω: Angular Frequency

Differentiating twice, and noting that $F = m\ddot{u}$, equation (3.10) yields:

$$\dot{F} = -mV\omega^2 \sin\ \omega t \tag{3.11}$$

In the above equation $\dot{F}$ is proportional to the periodic part of $\dot{u}$, without the constant $\dot{u}_o$. Hence, it can be used as an alternate to local damping as follows:

$$F_{d,i} = \alpha \left| F_{unbal,i} \right| \mathrm{sgn}\left(\dot{F}_{unbal,i} \right) \tag{3.12}$$

Note that, for periodic motions, equations (3.9) and (3.12) will produce the same damping force. However, in practice, it has been proved that this type of damping is not adequately efficient for non periodic excitations. A more efficient formulation is the combination of the two, called combined damping:

$$F_{d,i} = \alpha \left| F_{unbal,i} \right| \left[\mathrm{sgn}\left(\dot{F}_{unbal,i} \right) - \mathrm{sgn}\left(\dot{u} \right) \right] / 2 \tag{3.13}$$

Overall, it should be noted that the basic characteristic of both types of damping is that they are proportional to the Unbalanced Force, and hence they are continuously adjusted in such a way that the power absorbed by damping is a constant proportion of the rate of change of kinetic energy in the system. In addition, damping introduced with the above formulation varies spatially, reflecting more efficiently the fact that different behavior can be observed at different parts of the grid.

3.2.2.2 Adjustment of natural period of the system

For Multi Degree of Freedom Systems (MDOF) the determining criterion to obtain optimum convergence is for all parts of the system (gridpoints in the case of a FLAC3D mesh) to have the same natural period. In FLAC, this is achieved by adopting a uniform timestep value for all gridpoints equal to unity:

$$\Delta t_{gp} = 1 \tag{3.14}$$

However, as described earlier, timestep is calculated locally for each gridpoint according to equations (3.1) or (3.2), repeated here for convenience:

$$\Delta t_{gp} = \frac{T_{gp}}{\pi} = 2\sqrt{\frac{m_{gp}}{k_{gp}}} = 1 \tag{3.15}$$

where:

Δt_{gp}: Gridpoint timestep value

T_{gp}: Gridpoint natural period

m_{gp}: Gridpoint mass

k_{gp}: Gridpoint Stiffness

Therefore, FLAC, in order to satisfy the criterion for optimum convergence, readjusts the mass of each gridpoint according to equation (3.15), so that the local timestep is equal to unity. This procedure is called "Mass Scaling", and results in "apparent" nodal masses larger than the actual (the ones that correspond to the density of the neighboring zones). Obviously, for systems containing stiff elements, mass readjustment will be larger, and hence dynamic effects will be more pronounced, since mass is included in the equation of motion. For these intense dynamic phenomena to be dissipated, the load should be applied in a much slower rate, i.e. lower velocity. Again this type of simulation is compatible to the dynamics of the SDOF. Large mass scaling increases the natural period of the system, and decreases the ratio t_r/T, intensifying the dynamic effects (**Figure 3.3**). Therefore, in order to diminish the oscillation the ratio t_r/T should increase. This can be only achieved by increasing t_r, i.e. by applying the load in a much slower rate.

3.3 The physical problem: Layout and Parameter Selection

The layout of the problem simulated, as well as the basic soil and pile properties, is shown in **Figure 3.4**. The pile is 16m in length, 0.6m in diameter and has a Young's modulus of 27000 MPa, which results in a flexural stiffness of EI=172000kNm^2. Pile diameter and stiffness were selected so as to resemble the two (2) piles used by Cox et al. (1974) in the Mustang Island experiments. In addition, the length of 16m for the pile was selected so as to be able to observe the change in the failure mode from

wedge-shaped to plane strain, which according to Reese et al. (1974) occurs at the depth of 10m, for the specific sand and pile properties.

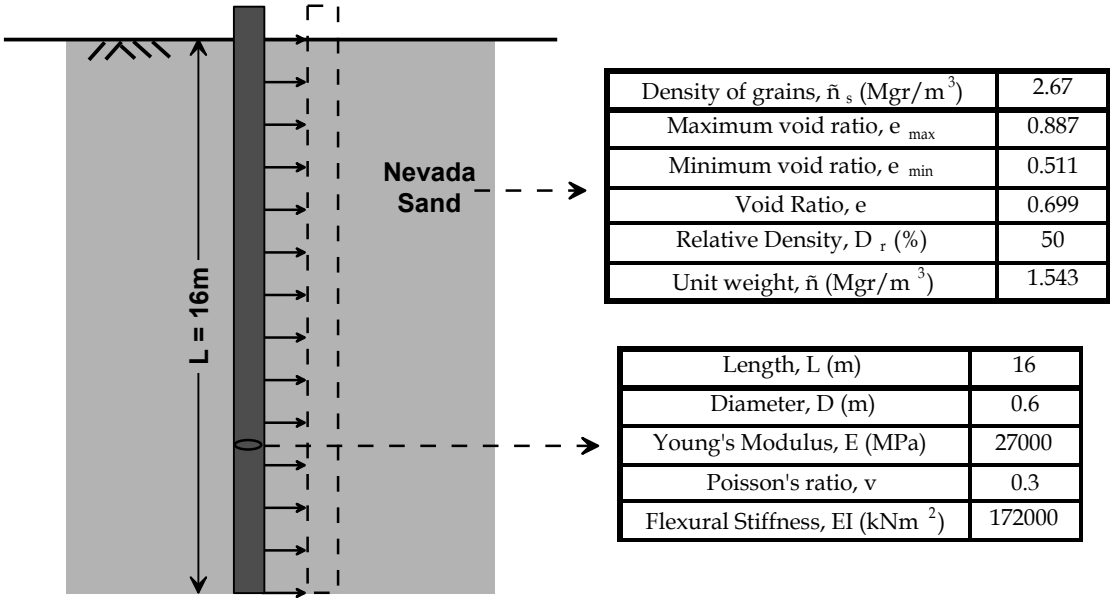

Density of grains, ñ $_s$ (Mgr/m ^{3})	2.67
Maximum void ratio, e $_{max}$	0.887
Minimum void ratio, e $_{min}$	0.511
Void Ratio, e	0.699
Relative Density, D $_r$ (%)	50
Unit weight, ñ (Mgr/m ^{3})	1.543

Length, L (m)	16
Diameter, D (m)	0.6
Young's Modulus, E (MPa)	27000
Poisson's ratio, v	0.3
Flexural Stiffness, EI (kNm ^{2})	172000

Figure 3.4: Layout of the problem and basic soil and pile characteristics

The pile is subjected to a uniform with depth horizontal displacement. This type of loading was preferred compared to the most common case of head displacement, for different reasons:

- P-y curves for the whole length of the pile can be produced. For the case of head loading, lateral displacements become very small in only a few diameters depth, and, hence, soil response at large depths cannot be evaluated.
- The long-term goal of this thesis is the p-y response of liquefied soils and soils undergoing lateral spreading displacements. In that context, the uniform displacement logic is closer to the kinematic loading caused by the earthquake.
- The effect of pile inertia is eliminated since pile does not undergo bending loading.

However, later in the thesis, analyses of head displacement will also be presented as part of a broader parametric investigation.

The soil consists of a homogeneous layer of Nevada Sand with a Relative Density of D_r=50% (e=0.699). Variation of maximum shear modulus, G_{max}, with depth is shown

in **Figure 3.5a,** in which G_{max} is estimated using **Hardin's (1972)** equation, which is adopted by the constitutive model used in the analyses:

$$G_{max} = \frac{180 p_a}{0.3 + 0.7e^2} \sqrt{\frac{p}{p_a}} \tag{3.16}$$

where:

e: void ratio

p: average effective confining stress

p_a: atmospheric pressure

For the numerical results to be compared with analytical solutions, each value of the relative density should be associated with a value of soil friction angle. Reese et al. (1974) suggest that the latter should be estimated through triaxial compression tests (TXC). For this purpose numerical TXC tests were performed in specimens of different relative density and confining stress, which were selected so as to reflect the volumetric and stress states of the problem examined. In total 48 such tests were performed, for three (3) values of the Relative Density and sixteen (16) values of the confining stress, corresponding to a depth from zero (0) to sixteen (16) meters. The results are summarized in **Figure 3.5b**. The friction angle is shown as a function of depth, instead of the vertical effective stress, in order to link in a more direct way test results to in-situ soil conditions.

As expected, soil strength increases with Relative Density and decreases with confining stress, as a result of more contractive response. However, for the stress range of interest, the effects of confining stress are not very significant. Therefore, it was decided to adopt constant values of φ=31^o, 33^o and 37^o for relative densities of D_r=20%, 50% and 90% respectively.

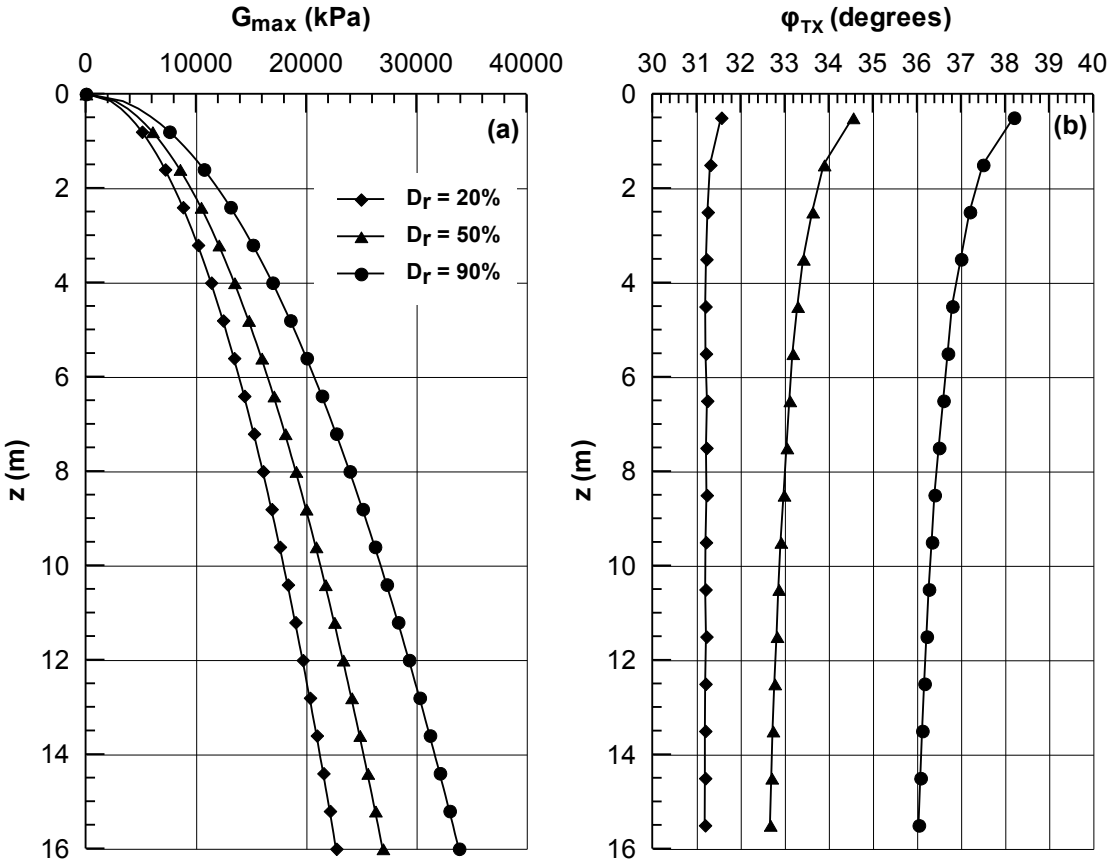

Figure 3.5: Variation of (a) maximum shear modulus (G_{max}) and (b) friction angle (φ) with depth

Another issue that should be considered in the numerical simulation is the modification of soil characteristics as a result of pile installation. The latter affects the surrounding soil in two ways (depending on pile type and installation method):

- An interface is created between the soil and the pile defined by means of an interface friction angle δ.
- The volumetric and stress field is modified, as pile-driving might compress the surrounding soil and significantly increase horizontal stresses. These changes are usually expressed in terms of a larger coefficient of lateral earth pressure, $K \geq K_o$.

The effect of δ and K on the axial bearing capacity of the pile is considered in the estimation of ultimate skin friction resistance expressed by the following equation:

$$q_{sL} = K\sigma'_v \tan\delta \qquad (3.17)$$

where:

K: coefficient of lateral earth pressure

δ: interface friction angle

σ'_v: vertical effective stress

The concept of a reduced interface friction angle δ reflects the fact that shear failure that takes place at the soil-foundation interface mobilizes only part of the friction resistance that would have been mobilized if the failure had occurred in the soil. Interface friction angle is commonly related to the soil friction angle and depends on the type of pile and soil, as well as the installation method. The values of δ from various investigations (Broms, 1975; Potyondy, 1961; Kulhawy, 1983, 1991; Bowles, 1995; Salgado, 2006; NAVFAC, 1986) appear to be in the following range:

$$\delta = 0.5 \div 1.0 \ \varphi \tag{3.18}$$

where φ is the soil friction angle. In the above range, the lower limit corresponds to steel driven piles and the upper to concrete nondisplacement piles, where the interlocking of the shaft is such that shearing occurs within the soil immediately adjacent to pile. Given that little is known with regard to the effect of δ on p-y response, it is evident that further investigation is needed before selecting a definite δ value to be used in the numerical analyses.

The use of an increased lateral pressure coefficient K reflects the fact that installation of the pile causes compression of the surrounding soil and, hence, increase in horizontal stresses. The effect of pile installation on the value of K depends on the type of the pile and the installation method (nondisplacement, close-ended or open-ended piles).

For *nondisplacement piles,* it is reasonable to assume that soil conditions are not largely affected by pile installation and resemble the free field conditions (K_o conditions). However, in cases where concrete of high fluidity is used, horizontal stresses might be slightly larger compared to the free field stresses, due to small water compressibility (Fleming et al. 1992).

For *displacement piles*, the stress and the volumetric state of the surrounding soil is largely affected. The theoretical background for this topic, as well as ways to approach it numerically, will be thoroughly discussed later in the thesis, given that the basic analysis presented in this chapter simulates a nondisplacement pile.

3.4 Numerical Simulation

The layout of the numerical model is shown in **Figure 3.6**. The model consists of 7296 zones (1152 for the pile and 6144 for the sand). The grid is denser in the region around the pile and progressively becomes sparser near the boundaries. It is 16m deep and 22m x 5m wide in the x- and y- directions respectively. The top of the model is a free surface, while the base is fixed in the vertical direction. Roller boundaries are imposed to the sides of the model, at $|x| = 11\text{m}$ and y=0 and 5m. The vertical plane through the pile axis, defined by the direction of the imposed horizontal pile displacement, is a plane of symmetry for this problem.

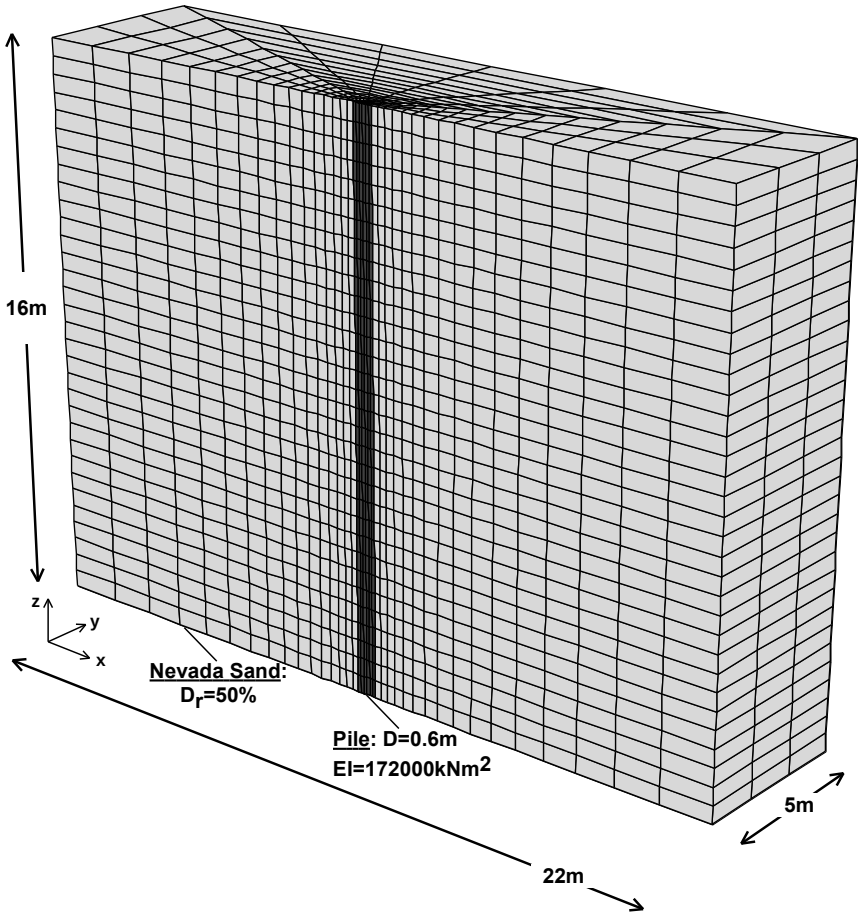

Figure 3.6: Layout of the Numerical model

A linear elastic model with the properties shown in **Figure 3.4** was adopted to simulate the response of the pile. The latter is 16m long, and has a diameter of 0.60m. Its height is divided into 32 equal segments and its cross-section is divided into 36 zones, as shown in **Figure 3.7**.

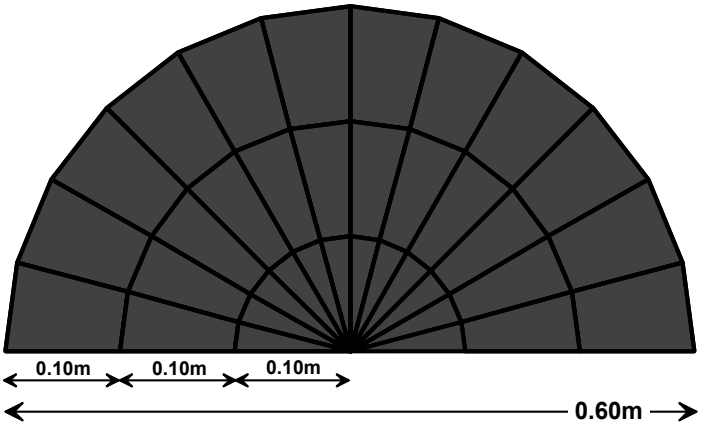

Figure 3.7: Discretization of the pile's cross-section

The advanced constitutive model mentioned earlier was used to simulate the response of the sand. The model parameters have been calibrated against tests performed on Nevada Sand (**Figure 3.4**). Note that the only soil parameter needed to be specified by the user is the void ratio. Hence, no assumptions are made with regard to critical aspects of soil response (shear strength, soil dilation, e.t.c.), giving the analysis the form of a "numerical experiment".

The skin friction between the pile and the soil is modeled by placing interface elements between the pile walls and the sand. The effect of various interface parameters, as well as main aspects of interface formulation, will be discussed later. For the basic analysis presented herein interface was assumed to have zero cohesion (c_{int}=0), a friction angle equal to half the friction angle of the soil, i.e. $\delta=\varphi/2=16.5^o$ and a normal and shear stiffness equal to 10^7 kN/m.

During lateral loading of the pile, combined damping was considered for all materials. As described in section 3.2.2, uniform displacement of a rigid body, like the pile, will result in a velocity timehistory with a significant steady-state component (see **Figure 3.3** for the initial force-rise phase). Therefore, local damping formulation cannot produce the necessary force to diminish oscillation, and hence the combined damping formulation is preferred.

Initially, the model is brought into an equilibrium stress-state under gravitational loading. K_o-conditions are established, while pile zones are treated as soil. During a second stage, pile properties (elastic model and moment inertia characteristics) are assigned to pile zones and the model is again brought into equilibrium. After

equilibrium has been accomplished, the pile is moved laterally at its entire length, by applying a uniform horizontal velocity at all pile nodes. For this purpose, pile nodes are fixed in the x-direction. The magnitude of the applied velocity is controlled in order to maintain the unbalanced force within prescribed bounds. Loading stops when pile has reached a horizontal displacement of y=0.60m, which corresponds to a nominal lateral strain of y/D=100%.

As loading progresses lateral deflection and soil reaction should be computed at various depths in order to produce p-y curves. For this purpose, a special routine was written in FLAC's inbuilt programming language FISH that calculates and stores p-y histories along the height of the pile. While lateral displacement is easy to compute, three (3) different methods were used to measure soil reaction, p:

- Through the normal and shear stress at the nodes of the interface elements
- Through the unbalanced force of the pile nodes
- Through the shear stress of pile elements

Comparison between the various methods is shown in **Figure 3.8**. The shear stress approach results in values of p, which are practically zero. This response is expected since the pile is displaced as a rigid body, and hence no bending moments are developed. For non-uniform applied displacement with depth or for application of a concentrated load at the top of the pile, this approach could estimate soil reaction correctly. The unbalanced force approach produces results which are practically identical with the interface method. For a fixed node, the unbalanced force is equivalent with the reaction of the support. Therefore, for the case where a concentrated load is applied at the top of the pile, the estimated p-y curve would include the effect of the applied load, and would not correspond to the net reaction caused by the soil. Therefore, it can be concluded that all three (3) methods can produce accurate p-y estimates; however shear stress and unbalanced force approaches are case-dependant and cannot be easily generalized. On the other hand, when interface elements are attached to the soil, they can be readily used to compute the total reaction force p for any type of loading.

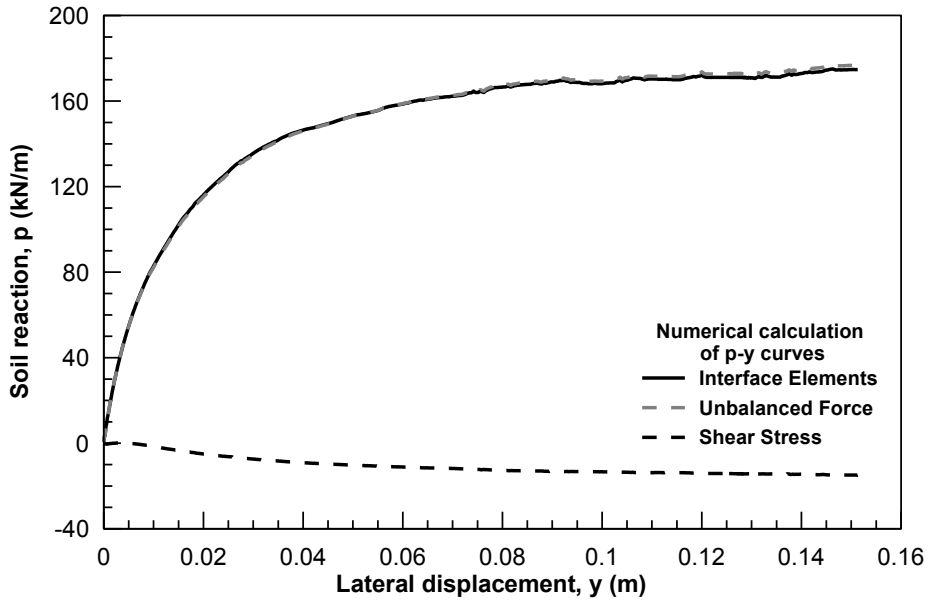

Figure 3.8: Comparison between different methods to calculate numerically p-y curves

3.5 Discretization effects

The mesh shown in **Figure 3.6** was verified in terms of discretization by examining the thickness, t_1, of the element adjacent to the pile (as mentioned earlier, zone thickness increases gradually with distance from the pile). Comparative results, in terms of p-y curves for various depths z form the soil surface, for three (3) different values of t_1, namely 0.10, 0.20 and 0.45m, are shown in **Figure 3.9**. The results indicate that the value of t_1=0.20m that was adopted minimizes discretization effects. On the contrary a more sparse mesh leads to significant deviations with regard to the prediction of soil reaction, as the t_1=0.45m analysis indicates.

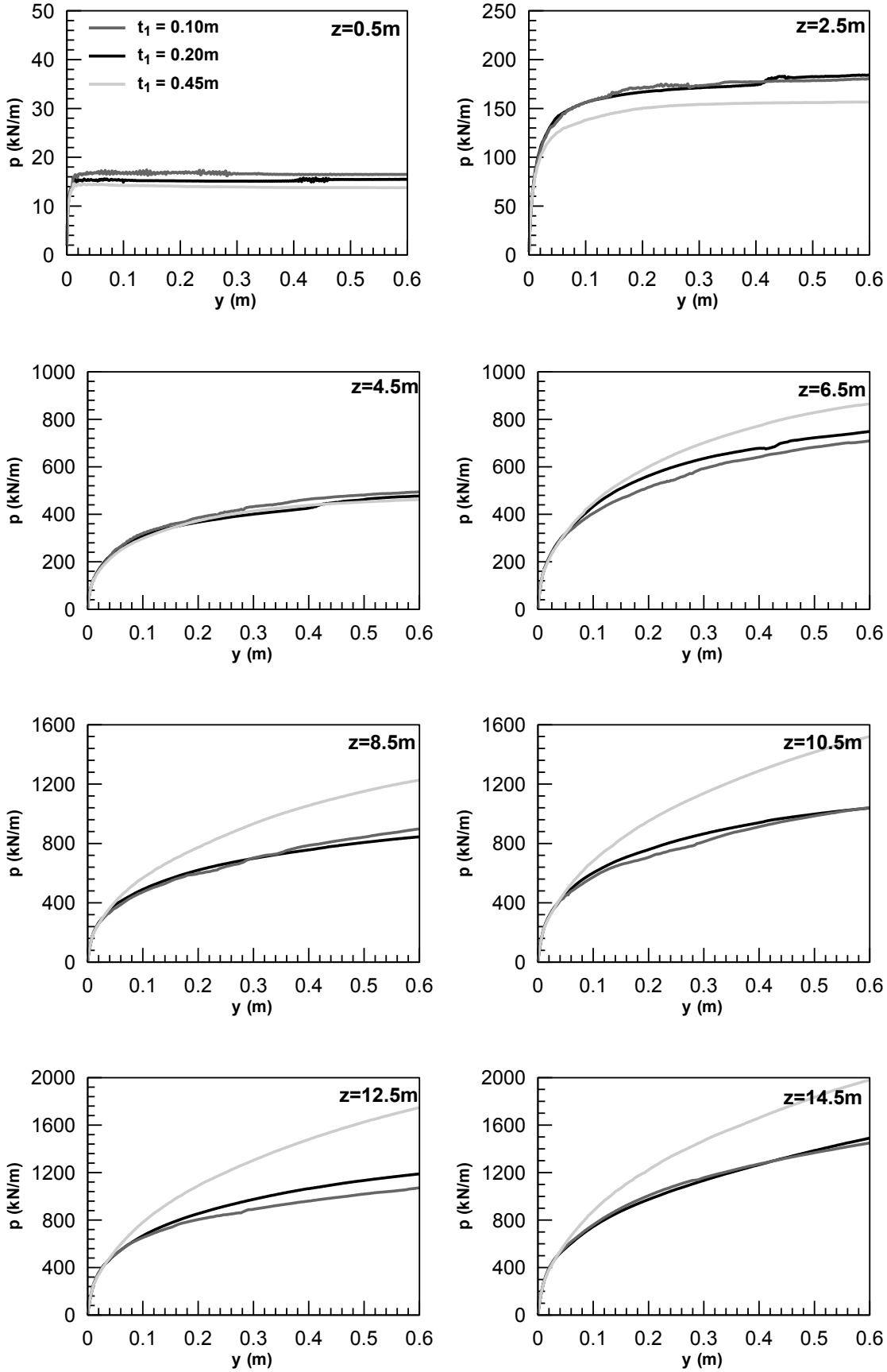

Figure 3.9: Effect of zone discretization on p-y curves for various depths from ground surface

3.6 Interface Formulation and Selection of Interface Properties

Installation of interface elements and proper calibration of their parameters is a key element in the formulation, as slip and/or separation between the soil and the pile is critical for capturing the deformation mechanisms and the overall response of the system. The formulation of a typical interface element used in a FLAC3D analysis is shown in **Figure 3.10**. The response of the interface is defined by means of the tensile and the shear strength, the dilation angle, and the stiffness.

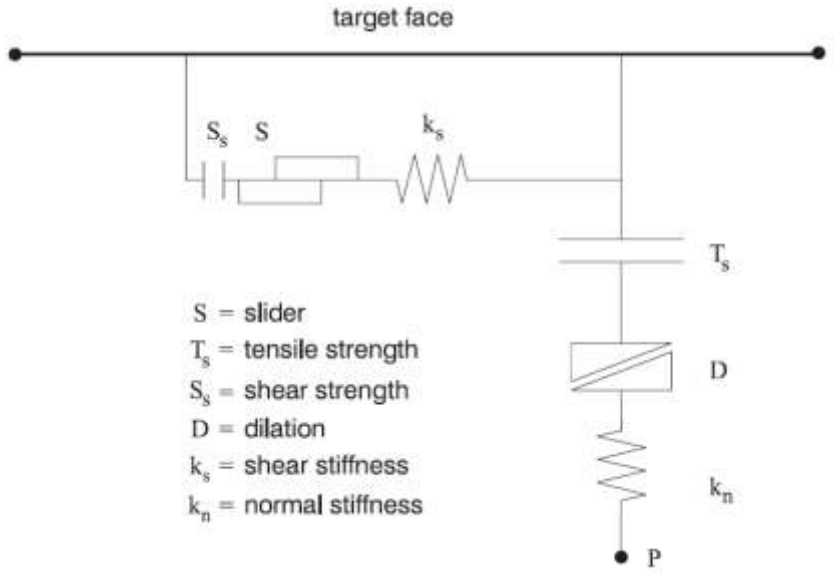

Figure 3.10: Formulation of interface element and components of interface constitutive model

Separation takes place when the normal force at the interface is tensile, and larger than the tensile strength. For the problem examined herein it is rational to assume that no tensile force can develop between the soil and the interface and hence the tensile strength of the latter was set to zero.

Slipping occurs when the shear force acting on the interface node exceeds the shear strength. From this point on, normal stress remains constant (if dilation is set to zero), leading to an elastic-perfectly plastic interface response. Shear strength is expressed in terms of a Coulomb criterion according to the following equation:

$$F_{s\max} = c_{\text{int}} A + \tan\delta \;\; F_n - pA \tag{3.19}$$

where

F_{smax}: Shear Strength of the interface

F_n: Normal force at interface node

c_{int}: Interface cohesion

δ: Interface friction

A: Representative area associated with the interface node

p: Pore pressure

For piles built in cohesionless soils, like the ones examined herein, it can be assumed that the interface has zero cohesion (c_{int}=0), while the interface friction angle δ varıes according to equation (3.18). The effect of interface friction on p-y curves was examined parametrically for δ=(0.5, 0.67 and 1.0)φ_{soil}, i.e. 16.5, 21 and 33^o, where φ_{soil} is the friction angle of the soil. All the other parameters were fixed according to the description in paragraph 3.4. **Figure 3.11** shows the comparison of p-y curves for various depths z from the ground surface. The following can be observed:

- Interface friction affects the ultimate resistance of the soil, p_{ult}, and not the initial stiffness, k_{ini}.
- The difference between 0.5φ and 0.67φ is fairly small and can be neglected.
- The difference between 0.5φ and φ is about 20% for small depths and rises to 30% for depths larger than 6.5m (z/D=11).

In view of the apparent deviations, it was decided to adopt the value δ=1/2 φ_{soil} for the rest of the analyses. This means that the results of this thesis are more representative of steel piles and not of drilled shafts, although the general conclusions are qualitatively valid for both of them.

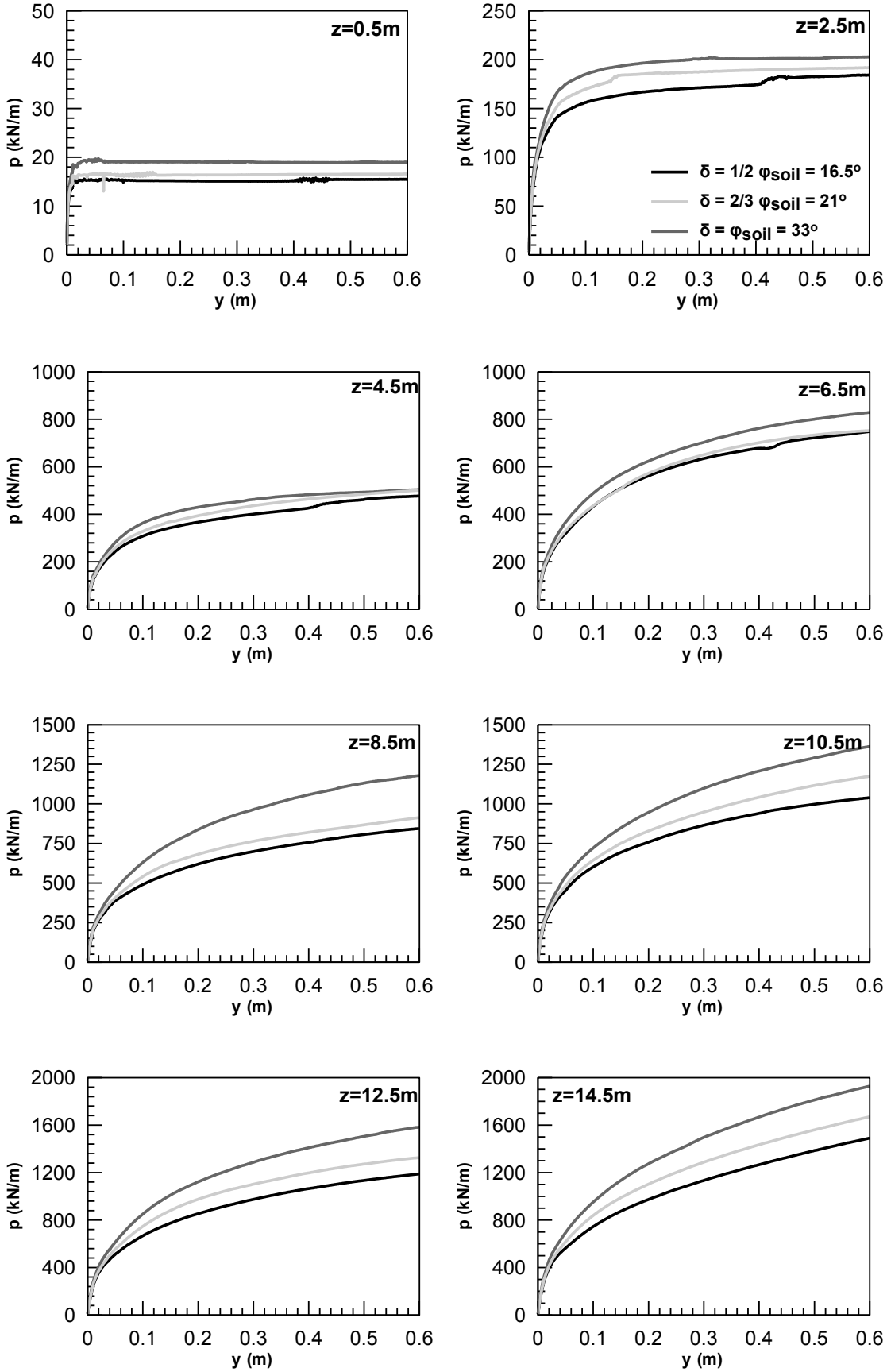

Figure 3.11: Effect of interface friction δ on p-y curves for various depths from ground surface

It should be noted that, for problems like the one simulated in this thesis, where the interface is used to provide a means for one sub-grid to slip and/or open relative to another, large values for the stiffness are desired, so that the resulting stresses are related to soil and not to interface deformation. However, as discussed in paragraph 3.2.2, FLAC3D makes use of a mass-scaling procedure to accelerate solution convergence. However, since mass scaling depends on stiffness, mass scaling is larger for large stiffness systems and instabilities more pronounced. For instance, **Figure 3.12a**, shows the adjusted nodal mass for three (3) identical systems with only differentiation in the stiffness of the interface elements. The nodal mass after scaling at the soil-pile interface is much larger for the stiff interface system, which leads to a more unstable response, as indicated in **Figure 3.12b**, which shows the variation of unbalanced force (index of instability) with lateral displacement.

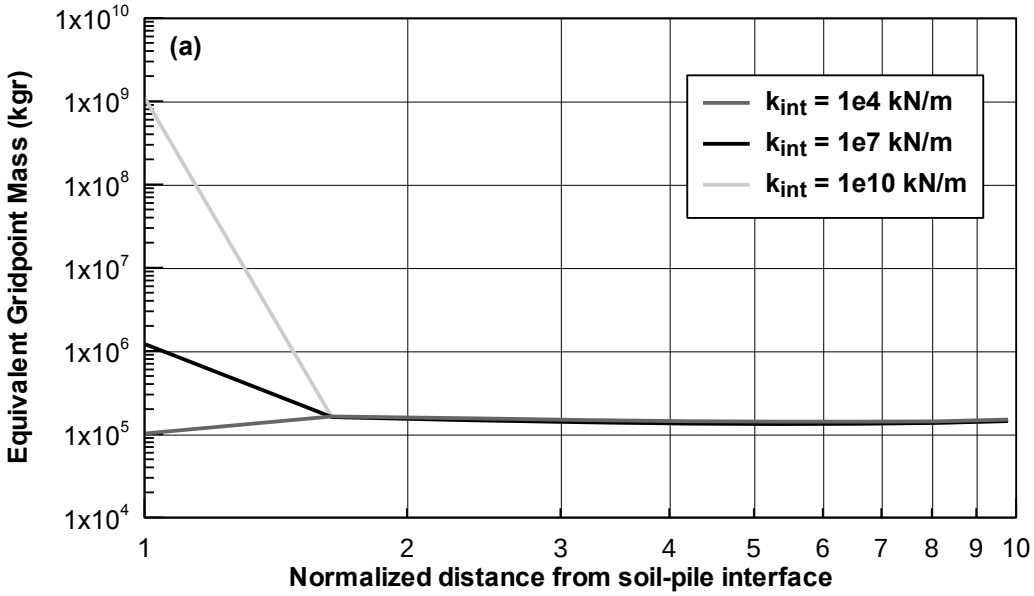

Figure 3.12a: Nodal mass readjustment and numerical instability due to interface stiffness variation

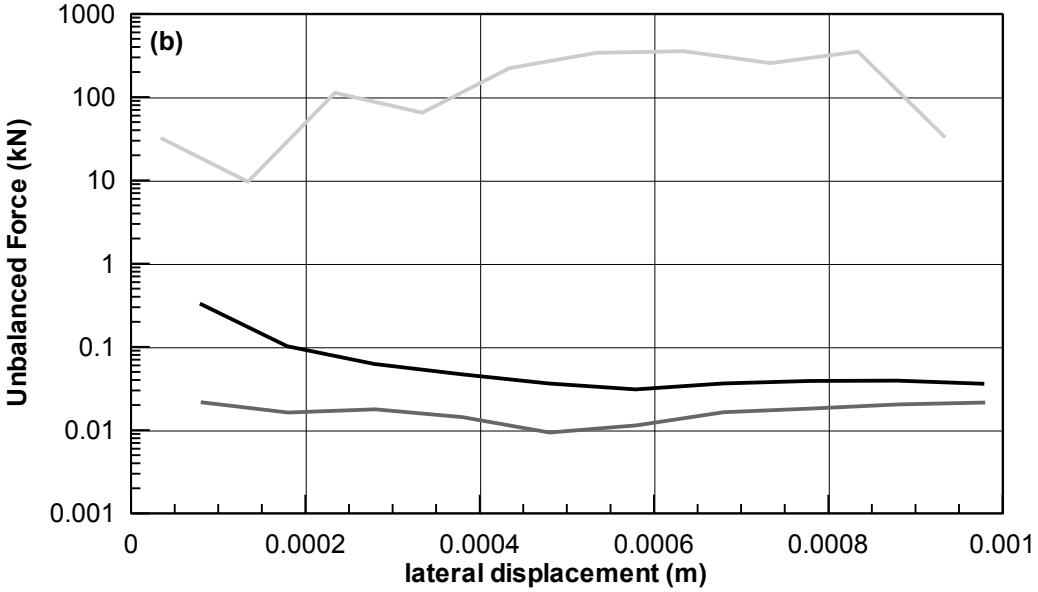

Figure 3.12b: (a) Nodal mass readjustment (b) Unbalanced force and numerical instability due to interface stiffness variation

In other words, stiffness should be large enough so that the interface is not excessively deformed and small enough so that the system does not become excessively unstable. Therefore, in order to determine an appropriate value for the interface stiffness, three (3) analyses were performed for normal and shear stiffness (k_n and k_s) equal to 10^4, 10^7 and 10^{10}kN/m. The corresponding p-y curves for various depths are compared in **Figure 3.13**.

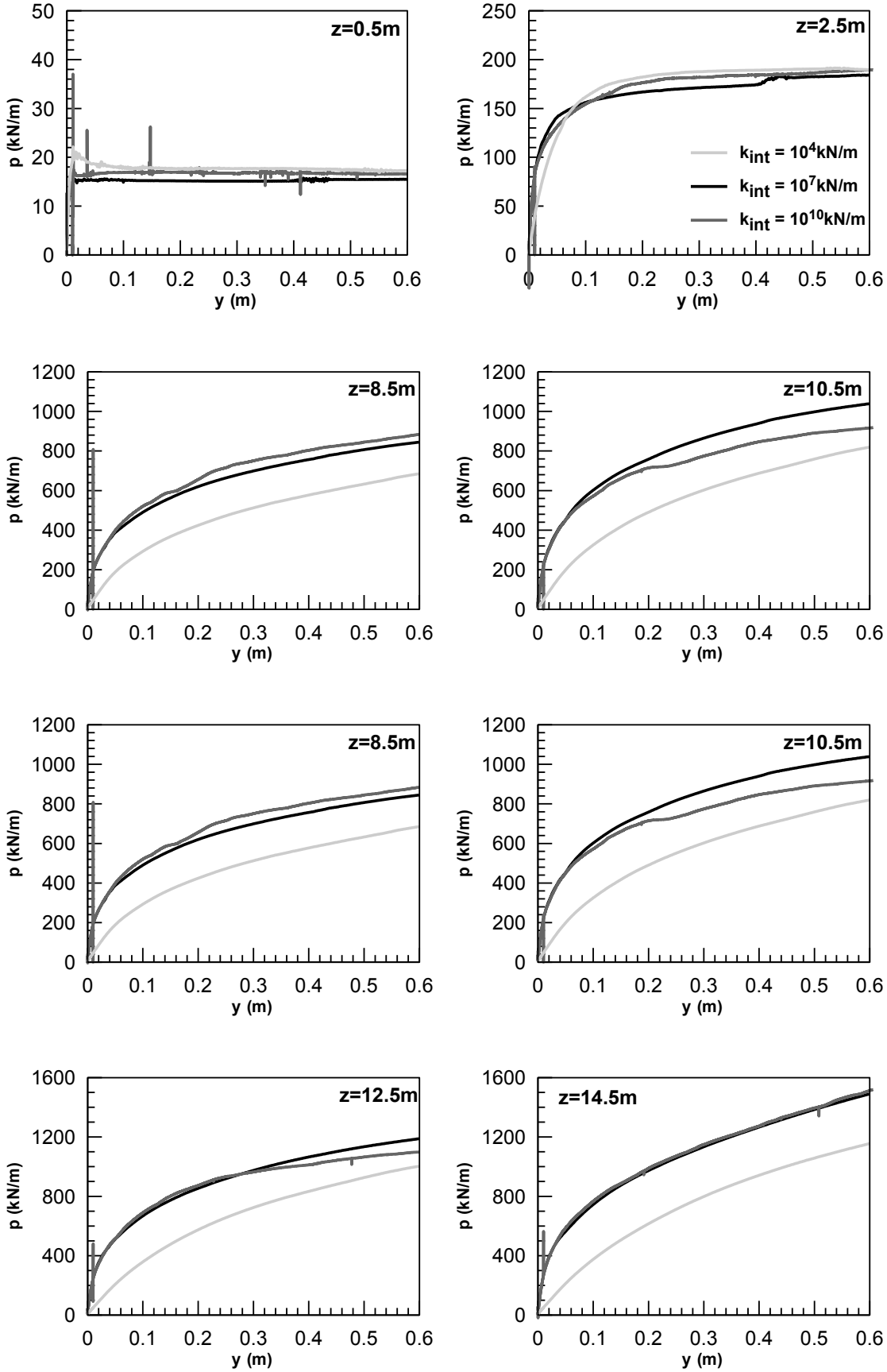

Figure 3.13: Effect of Interface Stiffness on p-y curves for various depths

This comparison reveals that for $k_n=k_s=10^4$kN/m the presence of the interface dominates the response, and the p-y curves are significantly different compared to the cases with large k_n and k_s values. In addition, interface stiffness effects are practically eliminated for the two (2) large stiffness values. However numerical instabilities are noticeable in the $k_n=k_s=10^{10}$kN/m analysis, despite the fact that imposed displacement was applied with an order of magnitude lower velocity. Therefore the value of $k_n=k_s=10^7$ kN/m was adopted for the rest of the analyses.

3.7 Deformation Mechanism

The deformed shape of the model, as well as displacement vectors are shown in **Figure 3.14** for lateral pile displacement of y=0.60m. The soil at the back of the pile fails in the active mode at the early stages of loading. However, given that cohesionless soils cannot form slopes of large inclination angles, no separation occurs and the soil follows the lateral movement of the pile, thus developing large downward displacements.

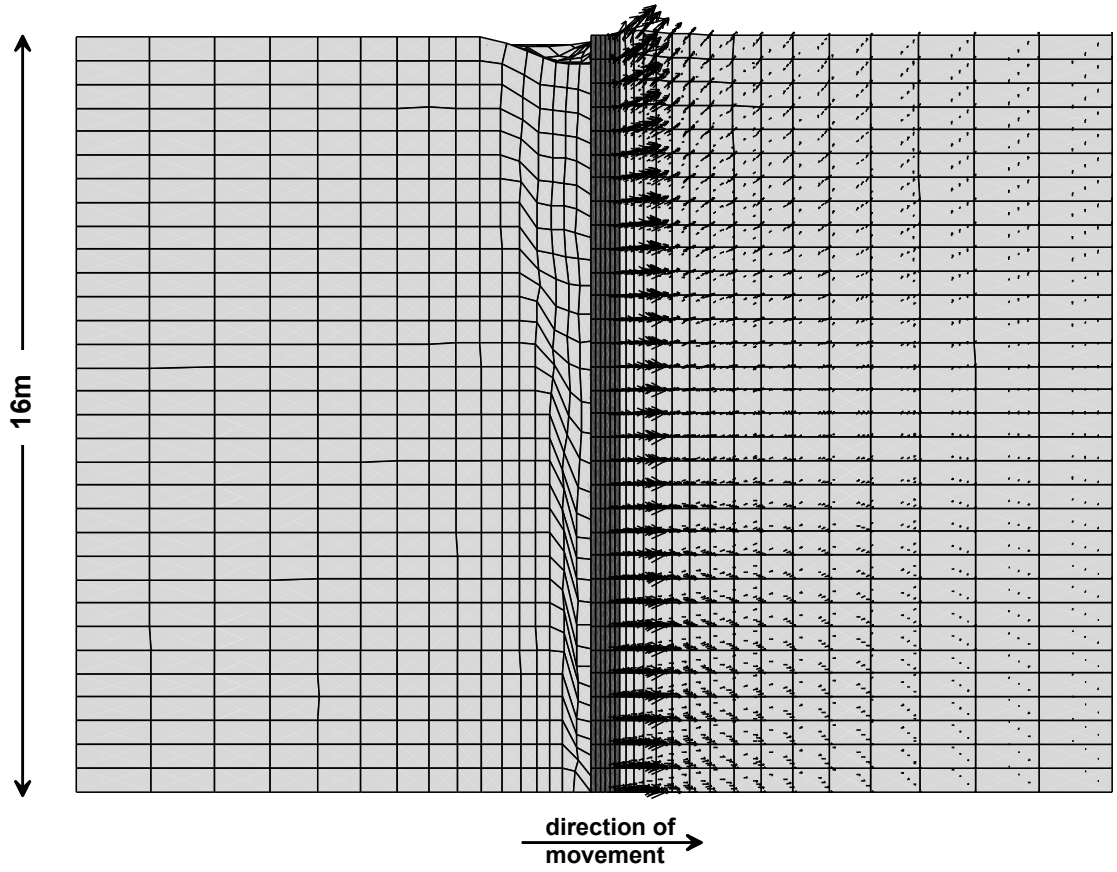

Figure 3.14: Deformed mesh and displacement vectors for lateral pile displacement y=0.60m

As for the soil in front of the pile, the response is different for small and for large depths. Namely, for small depths both horizontal and upward vertical displacements develop forming a wedge-shaped failure mechanism. Based on the deformed shape and the displacement vectors, and for the given magnitude of horizontal displacements, this type of failure extends to a depth of approximately 5÷6 meters, which corresponds to 8-10 pile diameters. For larger depths, displacement vectors are horizontal, indicating a plane strain failure mechanism.

The same conclusion can also be reached by examining the variation of vertical displacement with depth. **Figure 3.15a** shows the vertical displacement variation as a function of depth, for the gridpoint with the maximum vertical displacement at the specific depth. The values of vertical displacement are plotted for different levels of horizontal displacement, i.e. y=0.05m, 0.10m, 0.15m, 0.20m, 0.40m and 0.60m, and correspond to nominal strains ε_h=y/D=1%, 16.67%, 25%, 33.3%, 66.67% and 100% respectively. To aid the comparison, vertical displacement values are normalized with the vertical displacement at ground surface.

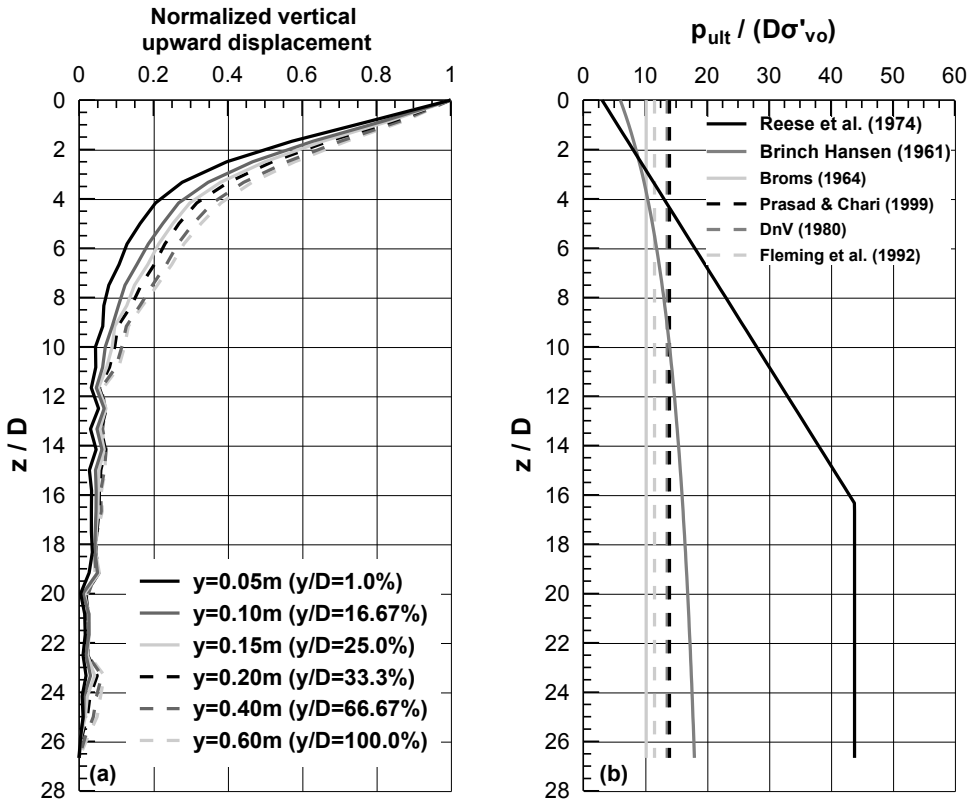

Figure 3.15: (a) Variation of vertical displacement with depth based on numerical analysis (b) Variation of normalized ultimate soil resistance with depth based on various analytical solutions

It can be observed that for strains up to 25.0% vertical displacements become very small (approximately 15% of the displacement at ground surface) for depths larger than 7-8 times the diameter of the pile. For larger strains this critical depth, which indicates modification of the failure mechanism, is approximately equal to 9-10 diameters, as also shown by the deformed mesh of **Figure 3.14**. Regardless of pile displacements, vertical ground displacements become negligible at depths larger than ten (10) pile diameters.

In other words, numerical results indicate that the plane strain mechanism becomes critical for depths well above 16m, i.e. the pile length selected for the analyses of this thesis, and consequently both mechanisms are captured. Note that the criterion based on which the specific depth was selected was to make sure that both failure mechanisms are captured. This is important because it ensures that the variation of p_{ult} with depth will be also captured correctly. Therefore, these preliminary numerical results suggest that a more shallow grid can be used allowing to capture both deformation mechanisms and significantly reduce computational time. Note that the various analytical methodologies do not provide specific recommendations on how to estimate the depth where the plane strain failure becomes critical. However, conclusions can be drawn indirectly based on the variation of normalized ultimate soil resistance with depth. The latter, for the same soil and pile characteristics as in the basic analysis, is plotted in **Figure 3.15b**. The following can be observed:

- Methods based on *Passive Earth Pressure* theory (Broms, Prasad and Chari, DnV, Fleming et al.) do not account for two (2) different failure mechanisms for the estimation of p_{ult}. The latter is calculated by accounting a Passive Rankine wedge formed in front of the pile.
- *Brinch Hansen* in his 1961 bulletin, despite the fact that he discriminates between two (2) failure mechanisms in his analysis, he ends up proposing a single relationship for the estimation of p_{ult}, suggesting that p_{ult} is not drastically affected by the deformation mechanism. This observation agrees with the passive theory methods. Note in **Figure 3.15b** the agreement between Hansen's method and passive theory methods. From the numerical analyses point of view, this suggests that variation of p_{ult} with depth can be estimated with confidence,

regardless whether the numerical model captures both failure mechanisms or not.

- On the other hand *Reese et al. (1974)* clearly mentions two (2) discrete failure mechanisms, and ends up suggesting two (2) expressions for the calculation of p_{ult}. For the specific soil and pile characteristics, the plane strain mechanism becomes critical at a depth of approximately 16.5 diameters (16.5D) or 10m, as shown in **Figure 3.15b**. This does not agree with the numerical results, which indicate that modification of soil response occurs at approximately 8-10D for ε_h<33.33%. In Reese's experiments piles failed at a lateral displacement of 50 to 80mm, which corresponds to a strain of 8.3÷13.3%, as can be concluded from the experimental p-y curves shown in **Figure 3.16**.

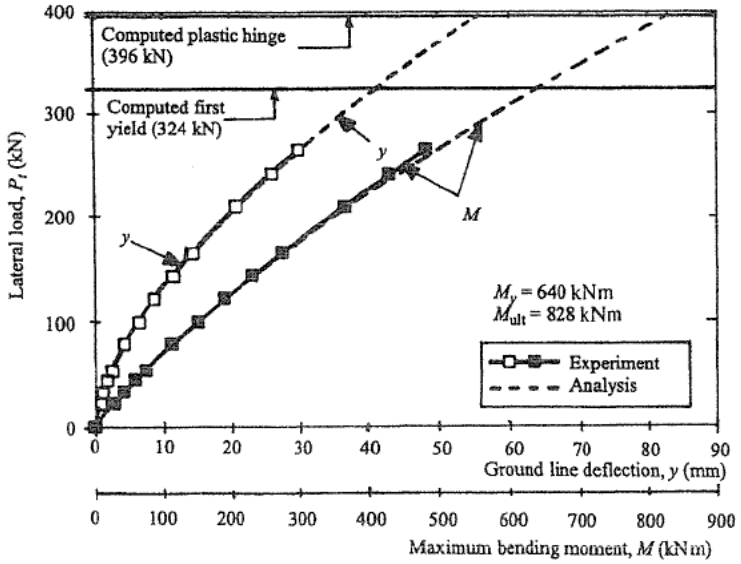

Figure 3.16: Experimental p-y curves from the Mustang Island Tests (Cox et al. 1974)

- In addition, note that the long piles in the Mustang island tests were subjected to head displacement. For long piles, this type of loading results the response demonstrated in **Figure 3.17**, where pile displacements extend to a depth of only a few pile diameters, definitely smaller than the 16.5D for which Reeses's methodology predicts transformation of the failure mechanism. In other words, it is doubtful whether Reese was able to observe in his experiments a plane strain mechanism, and hence a critical depth.

Based on the above, it is reasonable to assume that the numerical estimates of the critical depth can be considered reliable, and hence the thickness of the sand layer in the numerical model can be reduced to (7-8)D for y/D<25.0% and (9-10)D for 25.0%<y/D<100.0%.

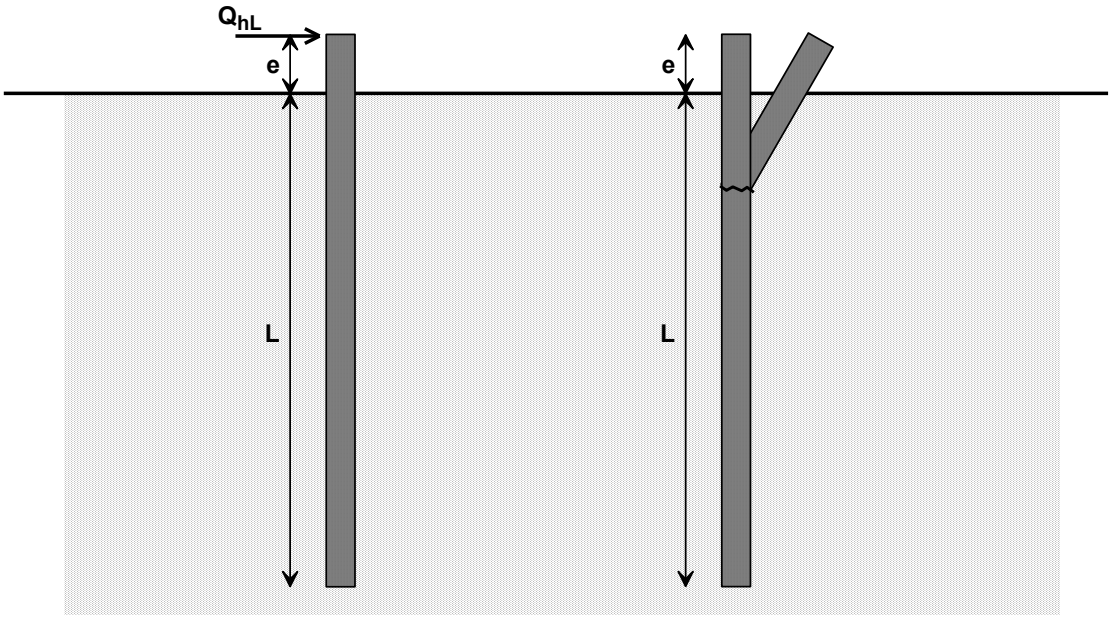

Figure 3.17: Failure mechanism of long pile subjected to lateral load at its head

3.8 Typical shape of p-y Curves

Typical p-y curves for various depths, computed by the numerical analysis, are shown in **Figure 3.18**. The results show that both soil resistance as well as initial stiffness increase with depth. Furthermore, as horizontal displacement increases, stiffness degradation occurs. For small depths (z<2.5m) p-y curves become eventually flat yielding an ultimate value for the soil resistance (p_{ult}). However, for depths larger than 4.5m, the subgrade reaction has not reached an ultimate value, despite the fact that the pile has already been pushed laterally for 0.60m, which corresponds to a lateral strain of ε_h=y/D=100%. At this point, the analysis was stopped given that larger deformation is unlikely to be encountered in practice.

The fact that the p-y curves do not reach an ultimate load p_{ult} comes in contrast with analytical methodologies, which suggest that soil reaction reaches an ultimate value for lateral strains, y/D, smaller than the ones developed in the basic analysis presented here. This contradiction raises the need for further investigation of the

numerical model's accuracy, first at the level of the constitutive model, and secondly at the level of the physical system response.

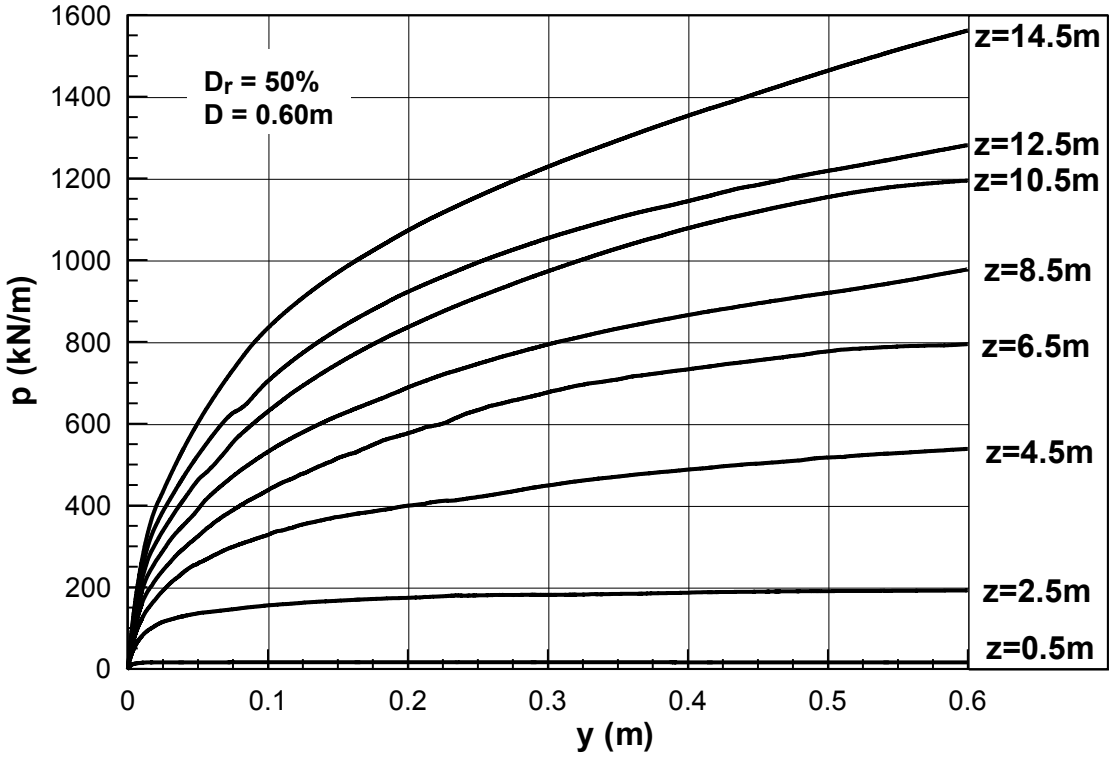

Figure 3.18: Numerical p-y curves for various depths

Constitutive model reliability.- For this purpose, the very large mesh shown in **Figure 3.19** was built, which is 120m long and 20m wide, to ensure that any boundary effects are eliminated. In addition soil response is simulated using the much simpler Mohr-Coulomb constitutive model. In order to resemble as closely as possible the in-situ soil conditions, the shear modulus was assumed to vary with depth according to equation (3.16), while a friction and dilation angle of 33^o and 5^o respectively were assigned to each soil zone. In addition, the analysis was performed with FLAC's large strain calculation option activated. After equilibrium under K_o conditions, the pile was pushed laterally until a deformation of 0.60m was reached.

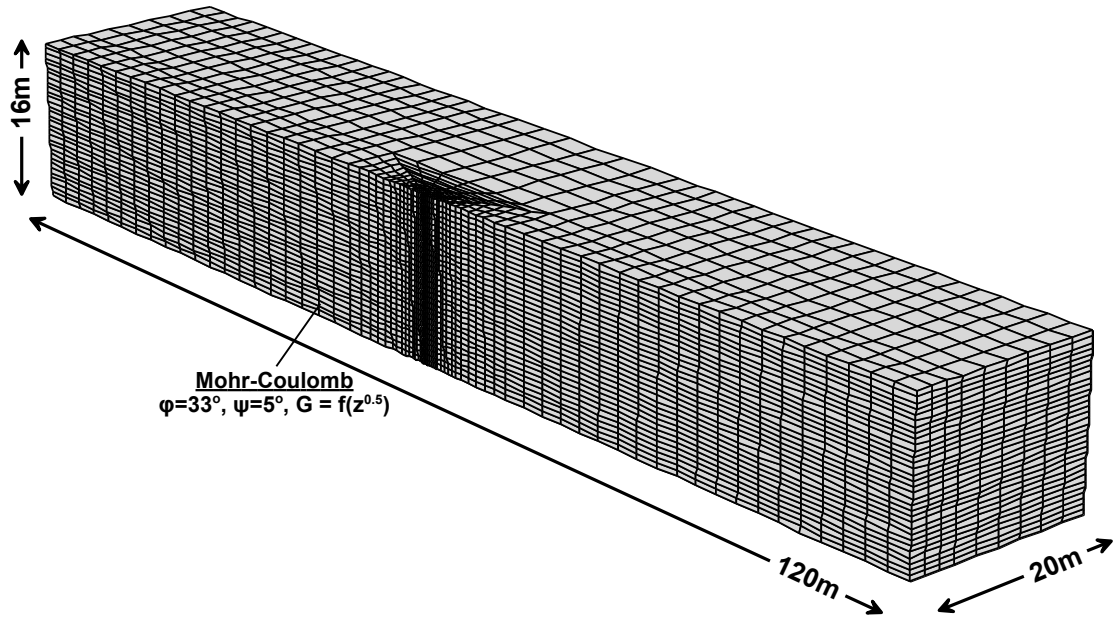

Figure 3.19: Layout of the model built to investigate p-y response at medium and large depths

The p-y curves produced from this analysis are summarized in **Figure 3.20**. It can be observed that, despite quantitative differences with the basic analysis, which are reasonable both due to the more simplified constitutive model, as well as the parameter calibration, the response is qualitatively very similar. Namely, for small depths (z<2.5m) subgrade reaction reaches an ultimate value, as in the case of the more sophisticated constitutive model. Furthermore, in the Mohr-Coulomb case, soil at small depths exhibits a slightly softening response, as soil resistance decreases after it reaches a peak value.

Similarly to the basic analysis presented previously, for depths greater than 4.5m, p-y curves exhibit a hardening response where soil resistance does not reach an ultimate value. Overall, comparison between the two (2) analyses reveals remarkable qualitative similarity, suggesting that the NTUA_Sand model used in the basic analysis should not be blamed for the predicted hardening response.

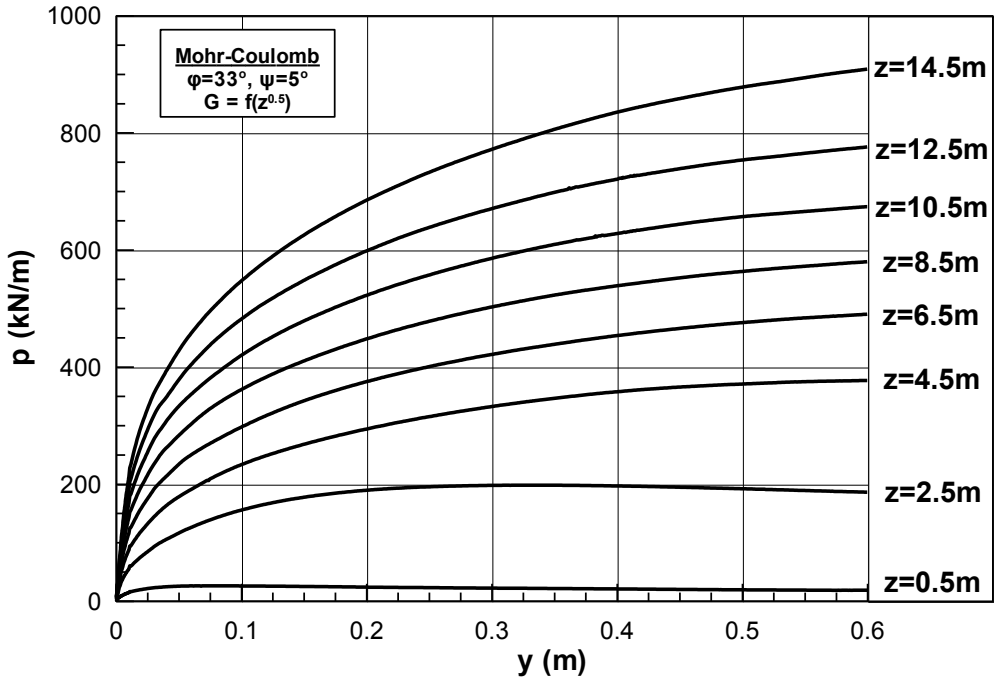

Figure 3.20: P-y curves produced by the Mohr-Coulomb analysis

Evaluation of System Response.- In a second level, an attempt to explain the observed shape of the p-y curves, was made by examining more thoroughly predicted deformation patterns, especially for large depths. **Figure 3.21** shows the deformed shape, displacement vectors and plastic points in the soil in front of the pile for the Mohr-Coulomb analysis, at a horizontal displacement of 0.60m. Dark and light colors indicate plastic and elastic response respectively. Displacement vectors as well as distribution of plastic points, denote the wedge-shaped mechanism for shallow depths (in this case up to 5 to 6 m deep), and the plane strain mechanism for larger depths.

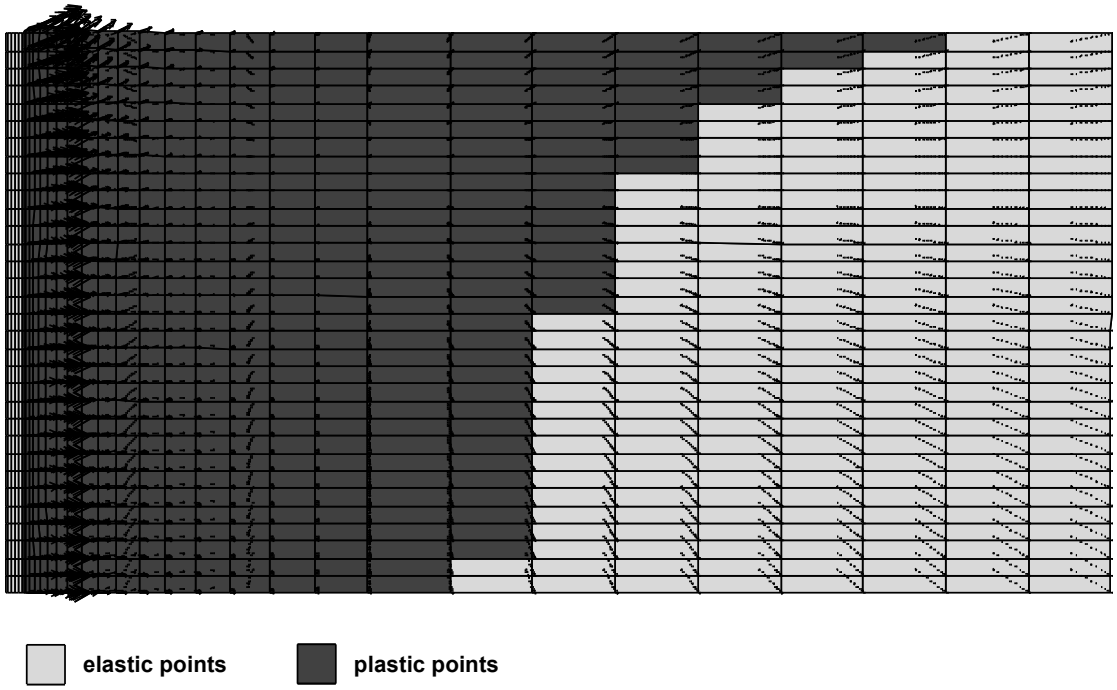

Figure 3.21: Detail of the deformed shape, plastic points and displacement in front and near the pile for the Mohr-Coulomb analysis

This latter case, is further investigated in **Figure 3.22a**, where a top view of the grid, along with displacement vectors, at a depth of 14m from surface are shown. The deformed shape in **Figure 3.22a** reveals that the soil actually has the tendency to develop a plane strain failure mechanism, as analytical methodologies suggest. However, displacement vectors denote that the elements of the row right in front of the pile (the ones marked with the dashed line in **Figure 3.22a**), are displaced only in the radial direction, indicating one-dimensional loading conditions. The same observation applies for **Figure 3.22b** where the same figure is repeated for the analysis with the NTUA_Sand model. The suggestion for one-dimensional loading conditions is further supported by observing the stress paths in the afore-mentioned elements, for the case of the analysis with the NTUA_Sand model. Note that paths are plotted both in the q-p and the e-lnp space, given that, for failure to occur, critical state should be reached in both spaces.

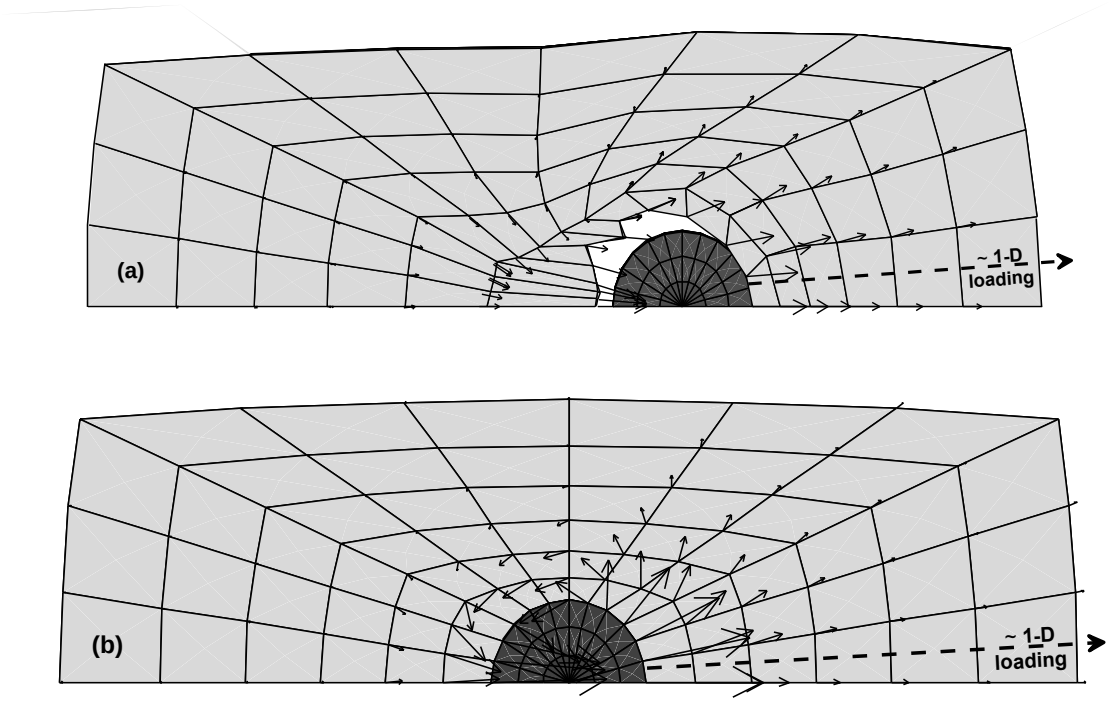

Figure 3.22: (a) Top view of the deformed mesh and displacement vectors for the Mohr-Coulomb analysis at a depth of 14m from ground surface (b) Top view and displacement vectors for the analysis with the NTUA_Sand model at a depth of 14m

Specifically **Figure 3.23a** shows the stress paths in the q-p space, where:

$$q = q' = \frac{1}{\sqrt{2}}\left[\sigma_1^{'} - \sigma_2^{'}{}^{2} + \sigma_2^{'} - \sigma_3^{'}{}^{2} + \sigma_3^{'} - \sigma_1^{'}{}^{2} \right] \tag{3.20}$$

$$p' = \frac{1}{3}\ \sigma_1^{'} + \sigma_2^{'} + \sigma_3^{'} \tag{3.21}$$

and σ_1', σ_2' and σ_3' are the maximum, intermediate and minimum effective principal stresses. Stress paths in **Figure 3.23a** are plotted for two elements, one at a distance 0.66D and another at a distance 2.40D from the pile. Also plotted in this figure are the critical state surfaces that correspond to compression and extension. As expected the stresses developed at the element closer to the pile are significantly larger. Apart from this, however, the two paths indicate the stress ratio, $\eta = q/p$, remains constant, and falls between the compression and the extension limits of the critical state surface.

Whether or not stresses actually reach the critical surface, can be observed by examining the same paths in the π-plane, shown in **Figure 3.23b**, where the values of

the critical surface for all loading paths are plotted. In this figure, the deviatoric stress ratio r is defined as follows:

$$r_{ij} = \frac{s_{ij}}{p} \tag{3.22}$$

where s_{ij} is the deviatoric stress component defined as:

$$s_{ij} = \sigma_{ij} - p\delta_{ij} \tag{3.23}$$

where δ_{ij} the delta Kronecker:

$$\delta_{ij} = \begin{Bmatrix} 1 & i = j \\ 0 & i \neq j \end{Bmatrix} \tag{3.24}$$

In the π-plane space, axes r_1, r_2 and r_3 correspond to the z-, x- and y- stress components respectively. Both paths begin from a point on the r_1-axis, which denotes K_o-conditions. The small deviation for the element close to the pile is a result of the small shear stress developed when pile properties are assigned to pile zones. As loading progress, the horizontal radial stress becomes larger than the vertical. This is reflected in the path, as it moves on the second sextant. Finally, the path indeed reaches the critical state surface and specifically at the value of η discussed in the plots of **Figure 3.23a**.

However, as mentioned earlier, in order for an element to fail, the e-lnp path should also reach the critical state. These paths, for the two (2) elements examined previously are shown in **Figure 3.23c**. Also plotted in the same figure is the location of the critical state line described by the following equation:

$$e_{cs} = e_{cs\ a} - \lambda \ln\left(\frac{p}{p_a}\right) \tag{3.25}$$

where:

p_a: Atmospheric pressure (=98.1kPa)

$(e_{cs})_a$=0.809: Void ratio at critical state for $p=p_a$

λ: Slope of Critical State Line (CSL) in the e-lnp space (λ=0.022)

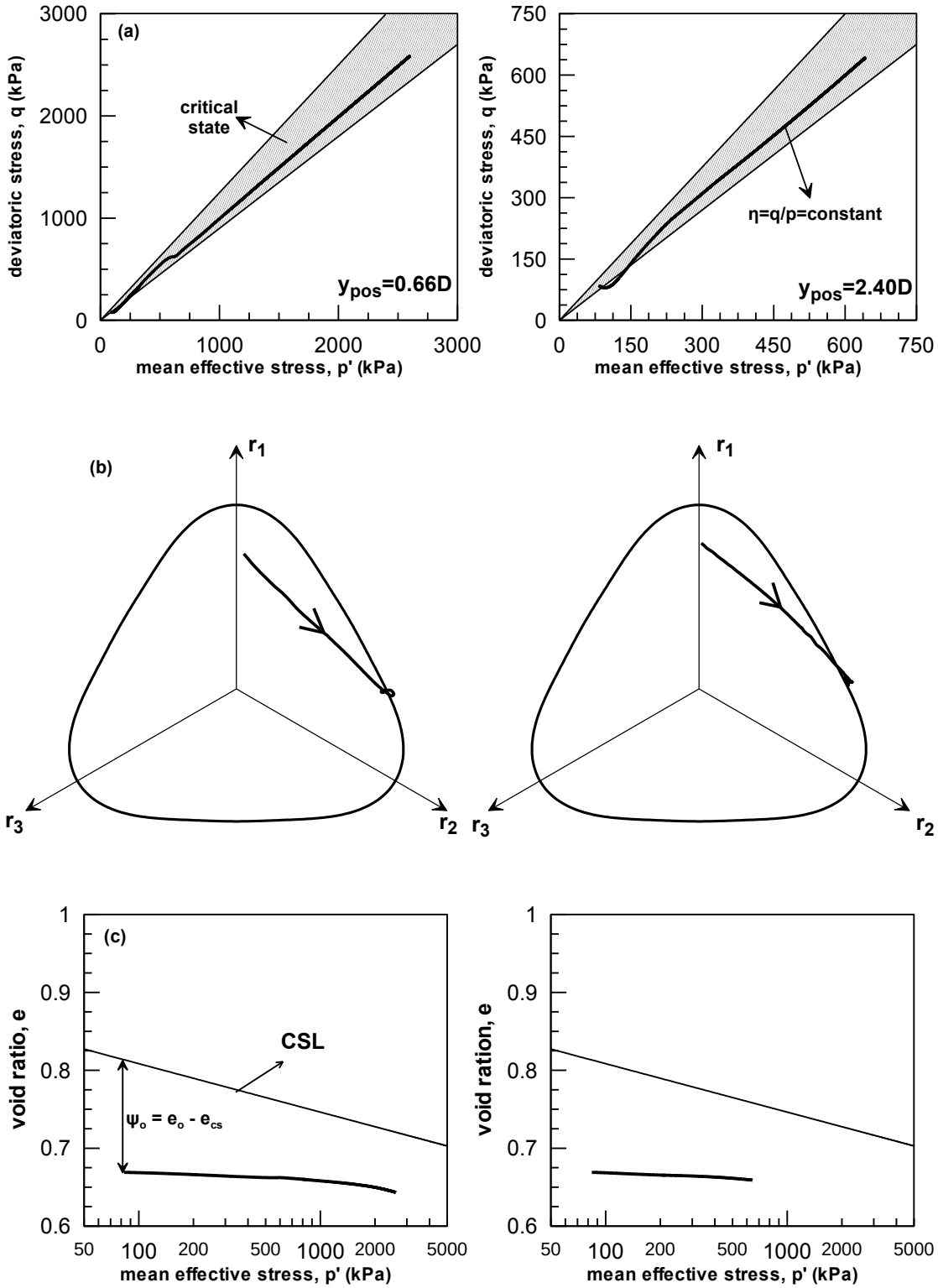

Figure 3.23: Stress paths in the (a) p-q space (b) π-plane and (c) volumetric path for two elements with distance 0.67D and 2.40D in front of the pile

Both paths indicate that both elements have a tendency to reduce their void ratio, and hence their volume. Observe that the element close to the pile follows a path which is initially horizontal and consequently tends to become parallel to the critical

state, indicating consolidation. This type of response indicates that these paths will not reach the critical state even if larger displacements are applied. Note that in the above figures, paths are plotted for a lateral displacement of up to 0.60m, while further loading is unlikely to be encountered in practice. As a result, stress in these zones will keep increasing yielding the hardening p-y response described earlier.

In conclusion.-The preceding discussion on typical results from this basic p-y analysis led to the following two (2) important conclusions:

- Modification of failure mechanism takes place in much smaller depths compared to the predictions by Reese et al. (1974).
- For medium and large depths p-y curves do not yield an ultimate value for the soil resistance.

The second point suggests that it is of no practical importance to apply large horizontal deformations of up to 60cm to the pile. The only purpose such displacements were applied was to investigate whether or not an ultimate value is reached. On the contrary, the levels of magnitude applied in the analyses should be compatible to what is encountered in practice. Hence, it was decided to apply horizontal displacements of up to 25% the pile diameter or approximately 0.15m.

For this magnitude of lateral displacement modification of failure mechanism, as the analysis in paragraph 3.7 revealed, takes place at a depth of approximately 7-8 times the diameter of the pile, approximately 4-5m. Therefore, it was decided to reduce the height of the mesh from 16m to 8m.

3.9 Boundary Effects

The new mesh adopted after reduction of the pile length is shown in **Figure 3.24**. To ensure that the lateral boundary effects are minimal, one additional analysis was performed for a mesh 44m long and 11m wide (i.e. about twice the lateral extent of the mesh in **Figure 3.24**). The predicted p-y curves for various depths are summarized in **Figure 3.25a** and **b**. Comparison reveals that the differences between the two meshes are not very important, and justify the use of the adopted mesh in **Figure 3.24** for the rest of the analyses.

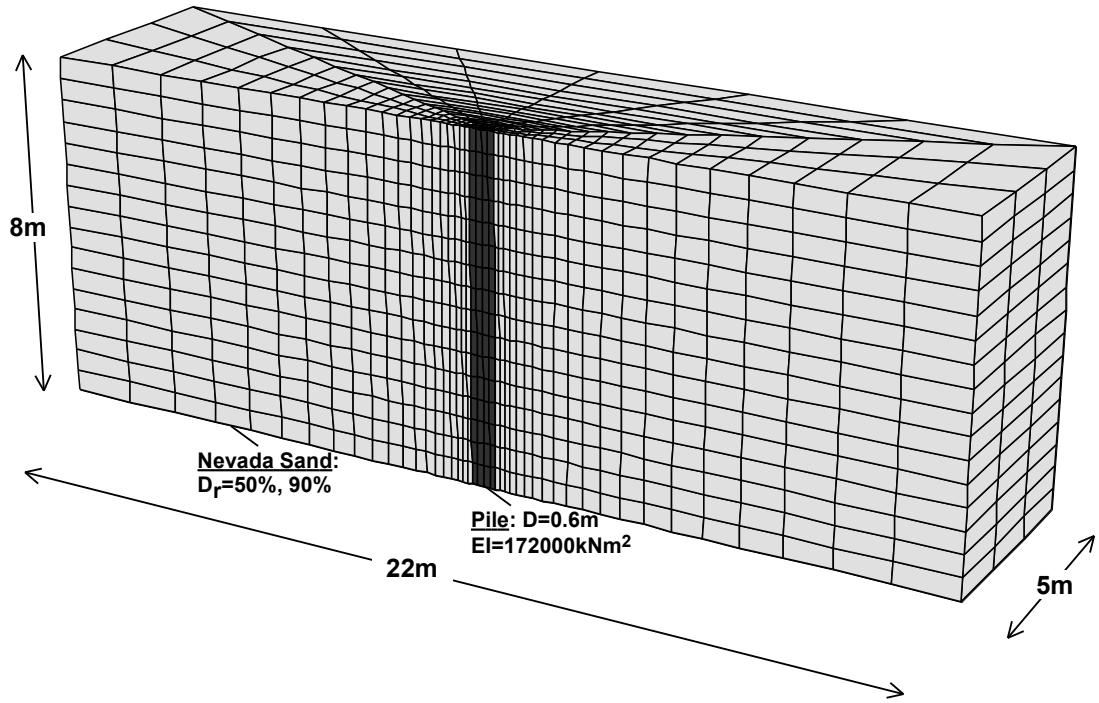

Figure 3.24: Layout of the final mesh adopted for the parametric investigation

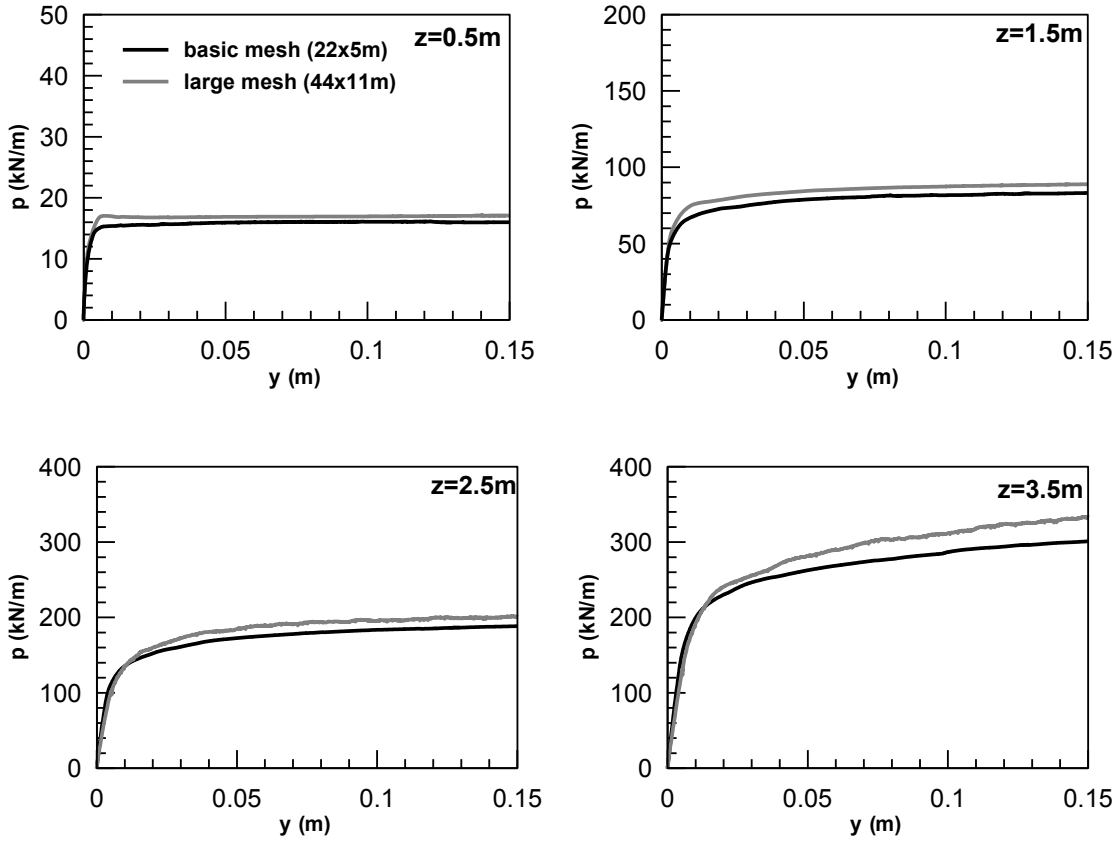

Figure 3.25a: P-y curves in small depths for the basic and a very large mesh

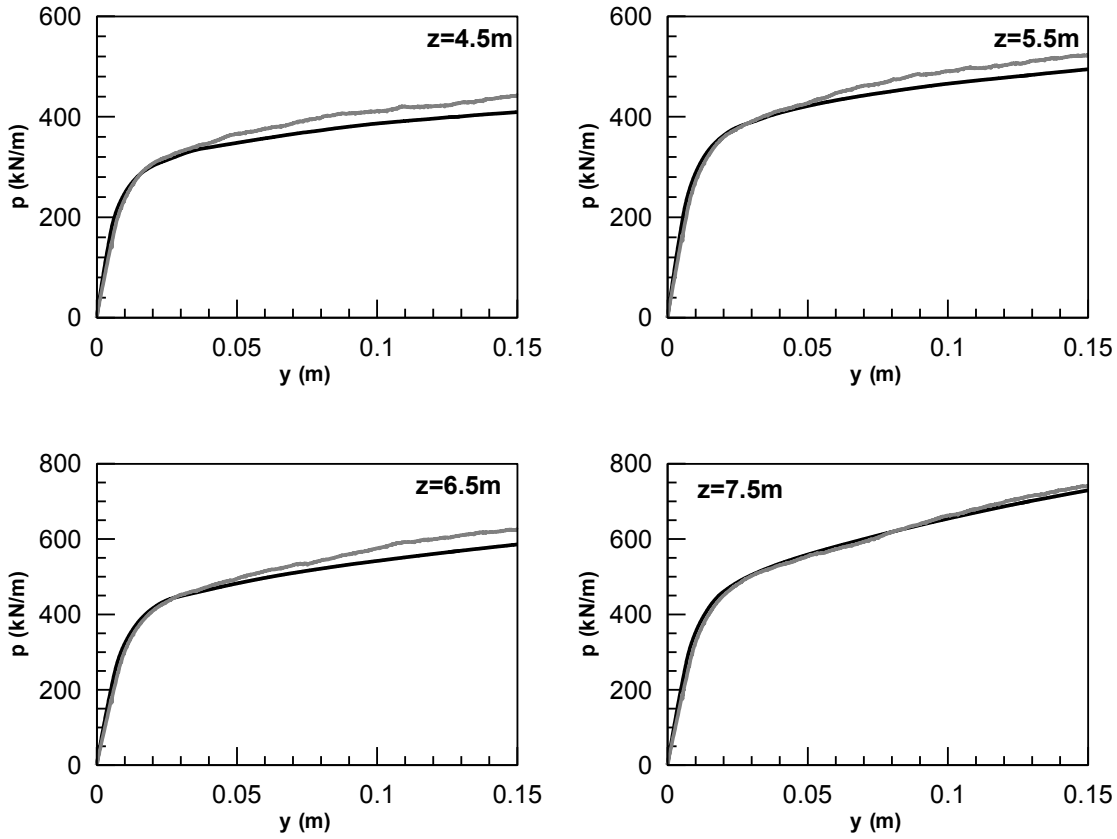

Figure 3.25b: P-y curves in large depths for the basic and a very large mesh

3.10 Effect of the "large-strain" mode of computations

The problem considered herein requires development of large lateral displacements which in turn produce large strains. Therefore, the possibility of performing the analyses by taking into account the updated coordinates of each node (i.e. "large strain" formulation), which would allow for deformation mechanisms to develop more accurately, was also considered. For this purpose, the basic analysis discussed in the previous paragraph was repeated by activating the large strain switch in FLAC. Comparison in terms of p-y curves for various depths is shown in **Figure 3.26**. It can be observed that for the specific strain magnitude the effect can be considered negligible.

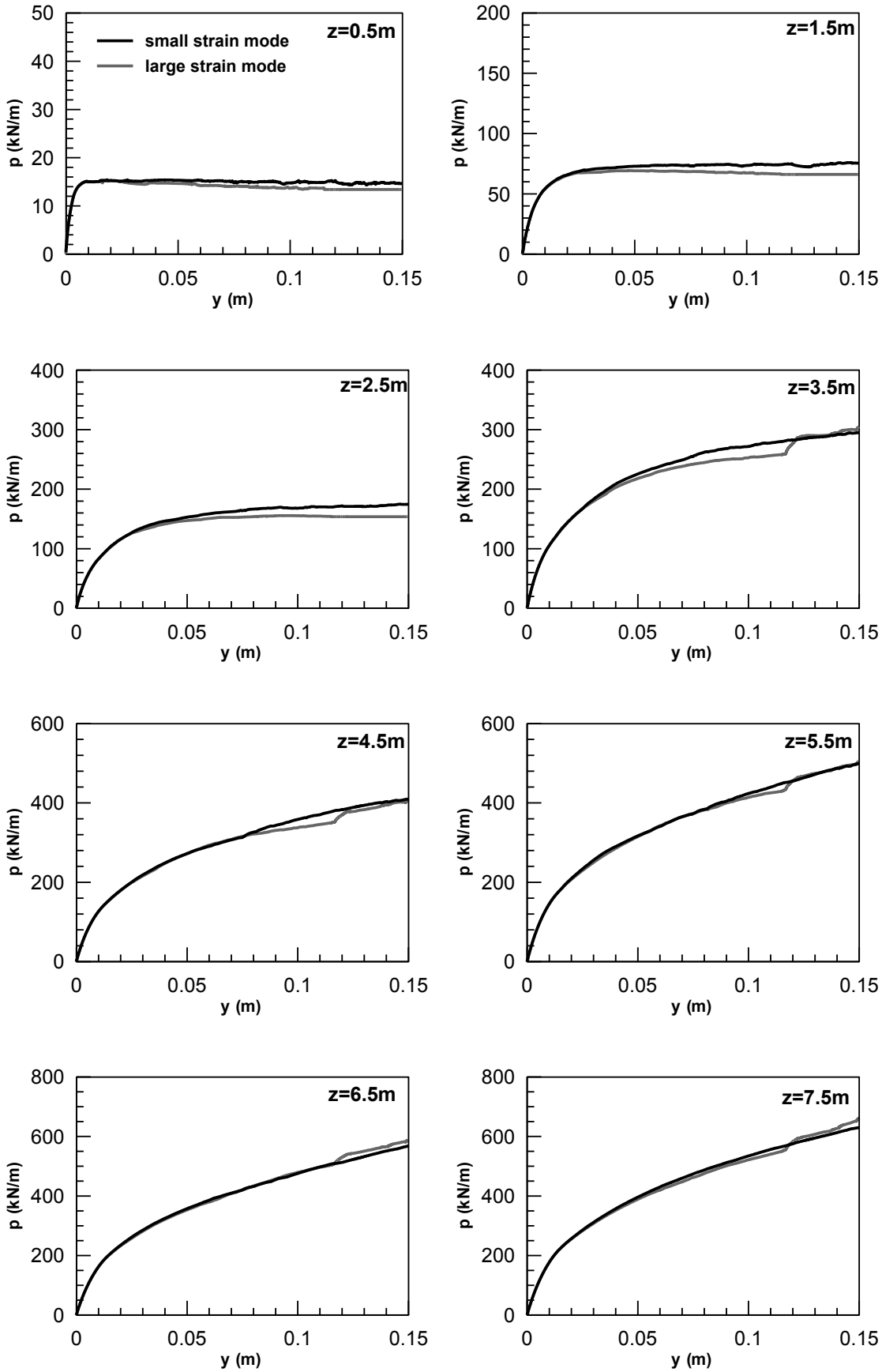

Figure 3.26: Comparison between numerical p-y curves from analyses with and without activation of the large strain mode.

3.11 Conclusions

The basic p-y analysis presented herein led to the following conclusions with regard to the numerical methodology and the response of the soil:

- The numerical model developed can capture the deformation mechanisms of the problem, as observed in field experiments and incorporated in analytical methodologies.
- A wedge-shaped failure mechanism is predicted for small depths, and a plane strain failure is predicted for large depths. However, examination of the deformed shape, as well references from the literature, denote that transition between the two (2) mechanisms takes place at significantly smaller depths than suggested in the methodology by Reese et al. (1974). To this extent it was decided to reduce the thickness of the sand layer from 16 to 8m, resulting in great benefit in terms of computational cost.
- The numerical methodology offers the ability, through in-built programming techniques, to estimate accurately the p-y response of the soil, and produce p-y curves for various depths along the pile. No need to stress out that the latter are widely used in practice for the design of deep foundations against horizontal loads.
- P-y curves at medium and large depths do not yield an ultimate value for soil resistance. Thorough examination of the kinematics of the problem revealed that this is reasonable and can be attributed to the quasi-one dimensional loading to which the elements in front of the pile are subjected. Based on this it was decided that there is no point applying large lateral displacements to the pile, causing the computational time to increase dramatically, but limit lateral displacements to what is encountered in practice. As a result analyses will be carried out for horizontal displacements of up to 25% the pile diameter or approximately 0.25*0.6=0.15m.
- Installation of interface elements and modeling of slip and/or separation is critical in order to capture the deformation mechanisms of the problem. Selection of appropriate interface properties is also important. However, for the specific sand thickness and magnitude of displacement, sensitivity analysis with regard to effect of interface friction angle revealed that influence of the latter is negligible. The differences observed in paragraph 3.6 were significant for

displacements larger than 0.15m, which is the displacement limit for the analyses of this thesis. Hence, results of this work can be applied to all types of piles.

In the following chapters, the numerical model presented herein will be used to evaluate existing p-y methodologies, and propose modifications, if needed. This will be achieved through an extensive parametric investigation, for different soil properties, pile types and geometries, as well as loading conditions.

4

Numerical Simulation of Pile Installation Effects

4.1 General

As described in Chapter 2, none of the analytical p-y methodologies accounts for pile installation effects due to the modifications in the stress and volumetric state of the surrounding soil. The aim of the present chapter is to develop a methodology which can simulate these effects. For this purpose, the basic mechanisms that govern pile installation are first analyzed, while afterwards emphasis is placed on ways to simulate these mechanisms and their outcome.

4.2 Mechanisms of pile installation effects

Pile installation effects to the soil surrounding the pile mainly depend on the type of the pile (nondisplacement, close-ended, open-ended). For *nondisplacement piles* it is rational to assume that soil conditions are not largely affected by pile installation and resemble to the free field state (K_o conditions). However, in cases where concrete of high fluidity is used, horizontal stresses might be slightly larger compared to the free field, due to small water compressibility (Fleming et al. 1992).

On the contrary, when a *close-ended* pile is driven in the ground, it should displace a volume of soil that is equal to the volume of the pile. Installation effects have been broadly studied in clays. Randolph et al. (1979) recognized three (3) distinctive deformation patterns along the pile, as shown in **Figure 4.1**. For small depths, up to about five (5) times the diameter of the pile, some heave occurs (Cooke and Price, 1973), and the displacement pattern is similar to the one generated in a Rankine's passive state. Furthermore, for the region around the tip, studies have showed (Clark and Meyerhof, 1972; Roy et al., 1975) that the displacement pattern is midway between expansion of a spherical and a cylindrical cavity.

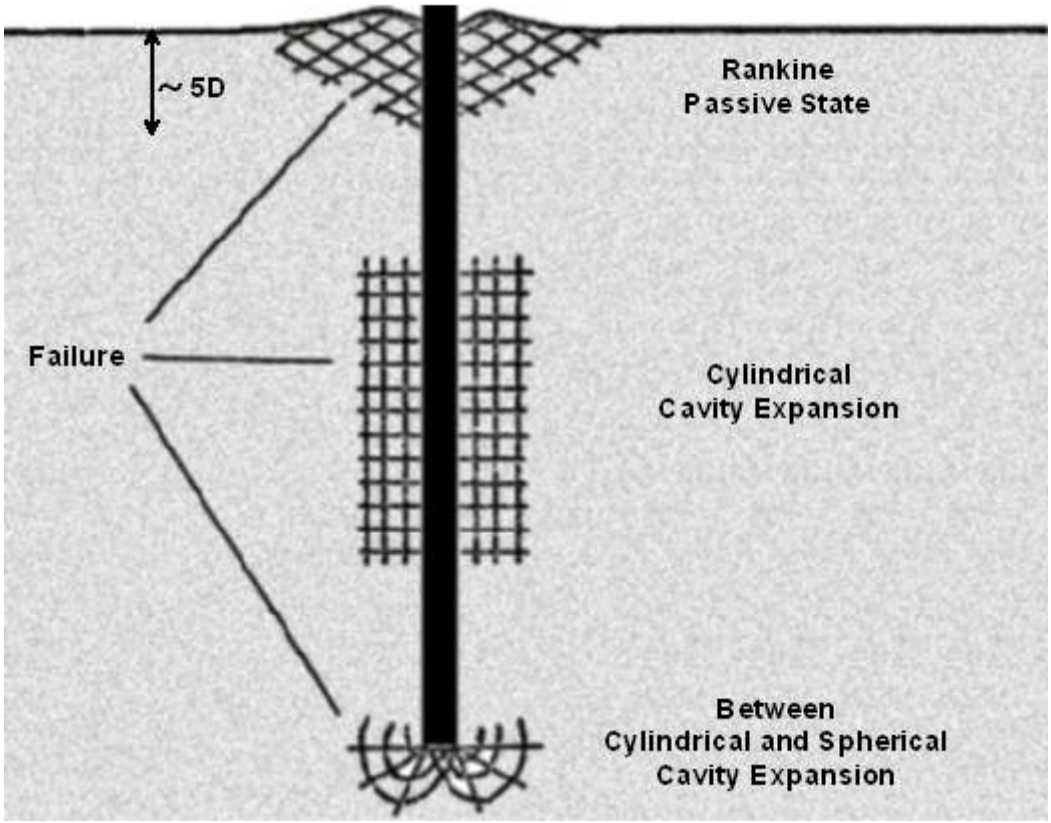

Figure 4.1: Deformation patterns during pile installation in clay after Randolph et al. (1979)

In addition a study by Randolph et al. (1979) showed that little vertical displacement takes place at any level once the tip has passed that level, while immediately after installation, when the jacking or driving force has been removed, the average shear stress down the pile shaft is likely to be small. These suggestions indicate that for the region between the tip and the top of the pile plane strain conditions occur and, thus, stresses can be predicted according to the cavity expansion theory as it will be discussed in more detail in following section of this chapter.

To support these findings, **Figure 4.2**, shows the variation of radial displacement with respect to distance from the pile, as measured in field tests and as predicted by the cavity expansion theory. The agreement between the experimental data and the theoretical predictions justifies the use of cavity expansion theory as an analytical tool to simulate pile installation. Moreover, it should be noted that similar conclusions are reported in other studies as well (Chopra and Dargush, 1992; Mabsout et al., 1999; Desai, 1978; Ersig et al., 1977; Kirby and Wroth, 1977; Soderberg, 1962; Butteroield and Banerjee, 1970).

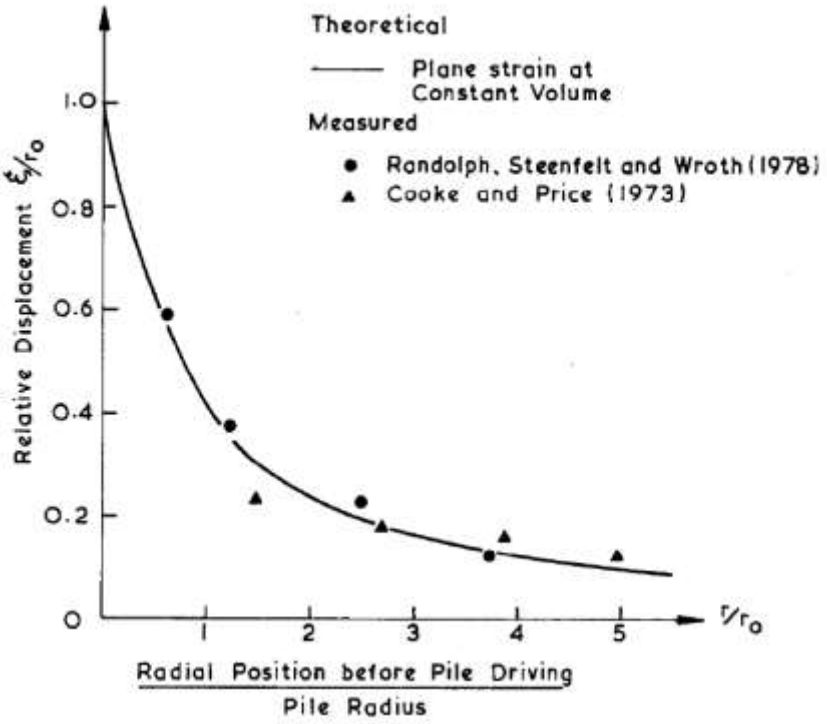

Figure 4.2: Radial displacements with distance from pile as observed in field tests and predicted by cavity expansion theory (Randolph et al., 1979)

Basu et al. (2010) studied the installation on shaft resistance for jacked piles in sand. They performed 1-D finite element numerical analyses with the model shown in **Figure 4.3**, while installation was simulated in three (3) stages, shown in **Figure 4.4**. 1-D conditions are achieved by applying tied-node boundary conditions in the vertical direction as shown in the figure.

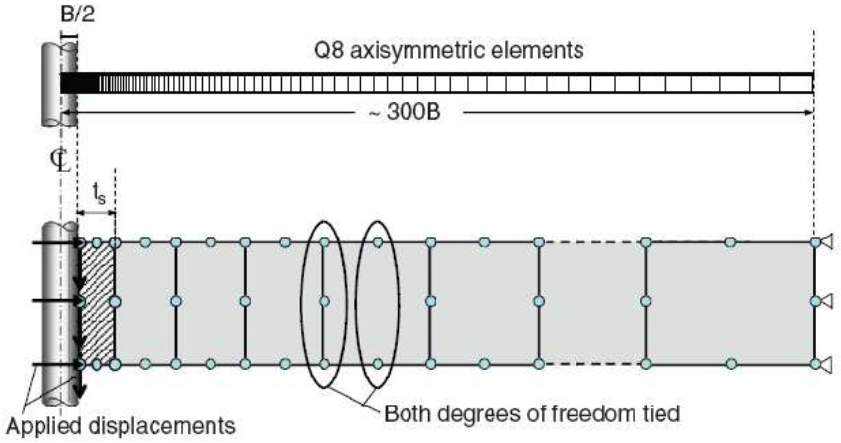

Figure 4.3: Finite element model to investigate installation effects on pile shaft resistance (Basu et al., 2010)

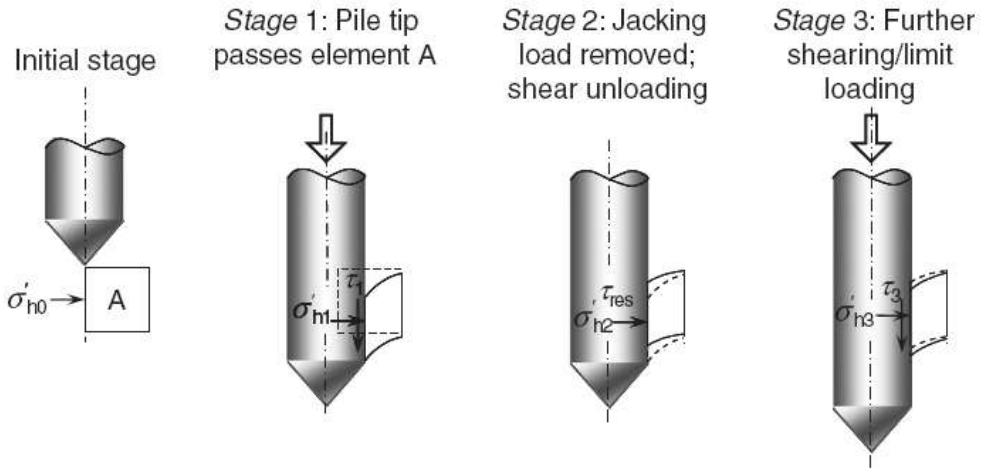

Figure 4.4: Analysis stages for the installation of jacked piles (Basu et al., 2010)

During *stage 1* the tip of the pile passes the soil element for the first time. According to the authors this penetration causes two (2) loading patterns on the element, modeled numerically in two (2) separate phases. The first phase (cavity expansion) represents the creation of a cylindrical space and stops when the cavity radius is equal to the radius of the pile. The second phase models the vertical shearing (primary shearing phase) that takes place as the tip passes from the soil element for the first time. This phase stops when the limit shaft resistance is reached. The authors also investigated the vertical shearing that occurs simultaneously with the cavity expansion phase, but concluded that does not affect significantly soil stresses (the total error introduced was about 35%).

Stage 2 represents the removal of the jacking load and causes reduction in the vertical shear stress until a residual value is reached. The latter was assumed to be equal to zero (0). Finally during *stage 3* vertical shearing is reapplied at the left boundary of the model to simulate additional jacking strokes. Stages 2 and 3 are repeated multiple times to simulate successive removals and re-applications of the jacking load, while for piles installed monotonically stage 3 is performed only once to represent application of structural load.

The authors correlated the lateral earth pressure coefficient after the first loading stage (cavity expansion and primary shearing) with Relative Density and in-situ vertical stress with the following relation:

$$\left(\frac{K}{K_o}\right)_{N=1} = 2.27\exp\left[\frac{D_r}{100}\left\{2.5 - 0.55\ln\left(\frac{\sigma'_{vo}}{p_a}\right)\right\}\right] \quad (4.1)$$

where:

K: lateral earth pressure coefficient after installation

K_o: in-situ lateral earth pressure coefficient

N: Number of successive removals and re-applications of jacking loading

D_r: Relative Density of the soil

σ'_{vo}: in-situ vertical effective stress

p_a: atmospheric pressure (=98.1kPa)

The above correlation has been drawn for various initial conditions (D_r and σ'_{vo}) in **Figure 4.5a**. It is thus shown that horizontal stresses during stage 1(cavity expansion and primary shearing) increase with relative density and decrease with confining stress, i.e. installation effects are more pronounced for soils exhibiting a more dilative response. This behavior is expected as dilative soils tend to "push back" the pile as installation progresses. On the other hand, for soils that exhibit contractive behavior large increases of K over K_o are not expected. As for the separate effects of cavity expansion and primary vertical shearing, it is noted that the latter may decrease the radial stress close to the shaft by a factor of two (2). The authors attribute this response to the fact that the direction of loading changes from horizontal to vertical, causing the soil response to switch from dilative to contractive.

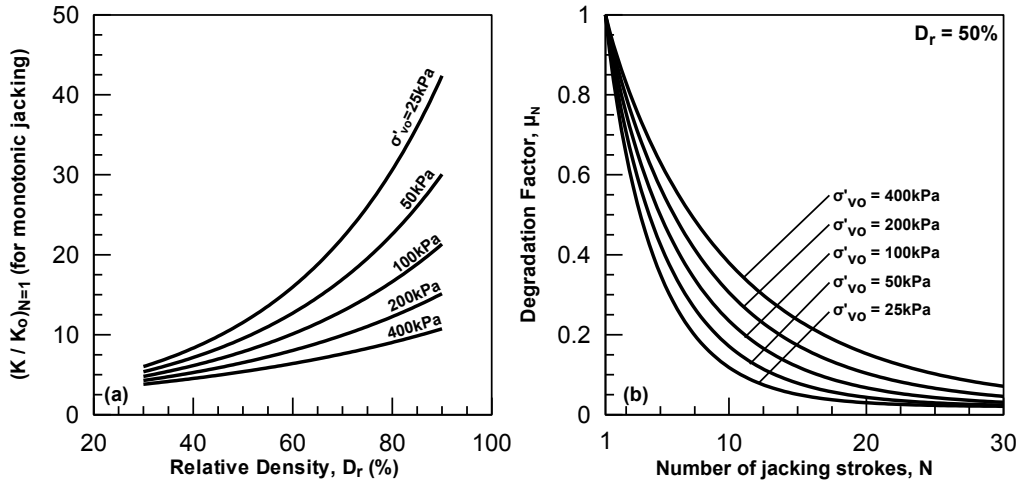

Figure 4.5: Evaluation of radial stress near the shaft for jacked piles (a) K/K_o for monotonic jacking (b) degradation factor for multiple jacking strokes (Basu et al., 2010)

Furthermore, the effects of repetitive jacking are expressed in terms of a degradation factor μ_N defined as follows:

$$\mu_N = \frac{K / K_o \;_N}{K / K_o \;_{N=1}} = 0.02 + \left(1 - 0.02\right) \exp\left\{-0.2\left(\frac{p_a}{\sigma'_{vo}}\right)^{\left[1-0.4\,D_r/100^{1.1}\right]} (N-1)\right\} \quad (4.2)$$

where N is the number of jacking strokes. The above equation has been plotted in **Figure 4.5b** for various initial vertical effective stresses (σ'_{vo}) and D_r=50%. Results show that, for small confining stresses, after only a few loading cycles, radial stresses are significantly decreased, while a larger number of loading cycles are required for larger stresses. This pronounced loss of lateral normal stress is caused by soil contraction in an annular zone around the pile. However, as the authors denote, the 1-D axisymmetric analyses performed in this study cannot capture the oblique transfer of stresses (soil arching), shown in **Figure 4.6**, which would cause soil response to alternate from contractive to dilative resulting in a much smaller decrease in radial stresses.

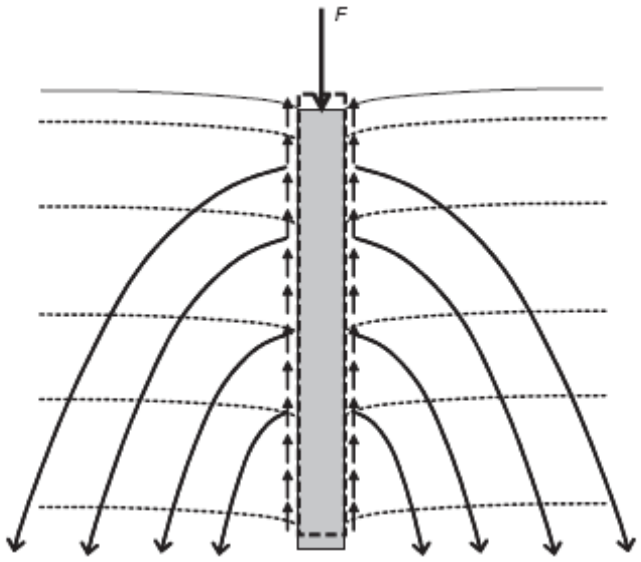

Figure 4.6: Schematic of soil arching during axial loading of a pile (Loukidis and Salgado, 2008)

Finally, *open-ended piles*, which are widely used in practice, can cause either large or small change to the stress-state of the surrounding soil and should be designed with extra caution. The level of installation effects is determined by the formation of a "soil

plug" during driving, as shown in **Figure 4.7**. The length of the plug depends on the soil properties, stress state and pile diameter (Lee et al., 2003).

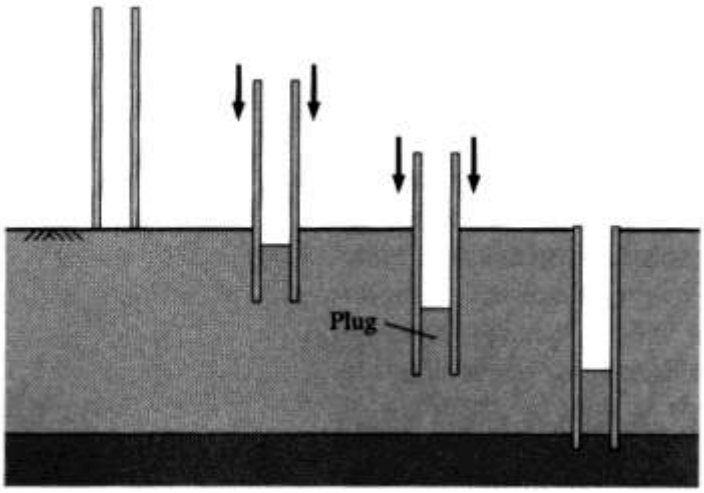

Figure 4.7: Formation of soil plug during driving of an open-ended pile (Salgado, 2006)

As driving progresses, three (3) stages can be identified:

- *Unplugged*: During this initial stage (small penetration depths), soil enters the pile at the same rate as the pile penetrates the ground. K_o conditions are practically preserved and the pile can be treated as a nondisplacement pile.
- *Partially plugged*: As driving progresses (intermediate penetration depths), soil stiffens and skin friction starts to develop between the soil and the inner side of the pile. Soil penetration is impeded, causing horizontal stresses to increase.
- *Perfectly plugged*: During this final stage (large penetration depths) soil is very stiff and large skin friction has developed between the soil plug and the pile. Soil cannot enter the pile and undergoes significant compression that generates large horizontal stresses. The pile practically behaves as close-ended.

The above analysis clearly indicates that vertical shearing that occurs during installation largely affects the stress field in the vicinity close to the pile shaft. However, in the present thesis, pile installation was modeled by only taking into account the effects of cavity expansion. This decision was based on the following:

- Cavity expansion theory has been widely used to model pile driving in clayey materials, as described earlier.
- As a result of soil arching, any effects of vertical shearing are less pronounced than discussed in the study by Basu et al. (2010).
- Taking into account that vertical shear stresses decrease inversely proportional to the radial distance, it is realized that any relevant effects are limited to area close to the pile shaft. However, the lateral response of piles is affected by a much wider region, where cavity expansion dominates the pile installation effects.

4.3 Analytical solution for the expansion of a cavity (Vesic, 1972)

The problem of the expansion of cylindrical cavities has been widely studied by many researchers (Vesic, 1972; Carter et al., 1986; Bigoni and Laudiero, 1989; Yu and Houlsby, 1991; Collins et al., 1992; Salgado and Randolph, 2001), due to its connection with a number of geotechnical problems (cone penetration and pressumeter testing, skin friction of piles, etc).

In the following, the analytical method developed by Vesic (1972) to describe stress variation around a cavity that has been expanded cylindrically is thoroughly described. The description aims to evaluate the potential of implementing the methodology into FLAC3D through a subroutine written in FLAC's built-in programming language FISH. Through the subroutine, changes caused by installation can be assigned manually in the elements of the grid prior to the p-y analysis. Hence, numerical simulation of the expansion of the cavity will not be required, and as a result computational time will not be significantly increased compared to the p-y analysis of non-displacement piles.

4.3.1 Basic equations and assumptions

The problem of cylindrical cavity is described schematically in **Figure 4.8**. As the cavity starts expanding, from an initial radius r_i to a final radius r_o, the soil around the cavity passes into a state of plastic equilibrium, forming a cylindrical plastic zone. This plastic zone expands until the pressure at the cavity wall reaches an ultimate value p_u, and the plastic zone has a radius R_p. In order to determine R_p and p_u, as

well as the variation of radial (σ'_r), and circumferential (σ'_θ) stresses around the cavity, the following assumptions are considered (Vesic, 1972; Bouckovalas, 1981):

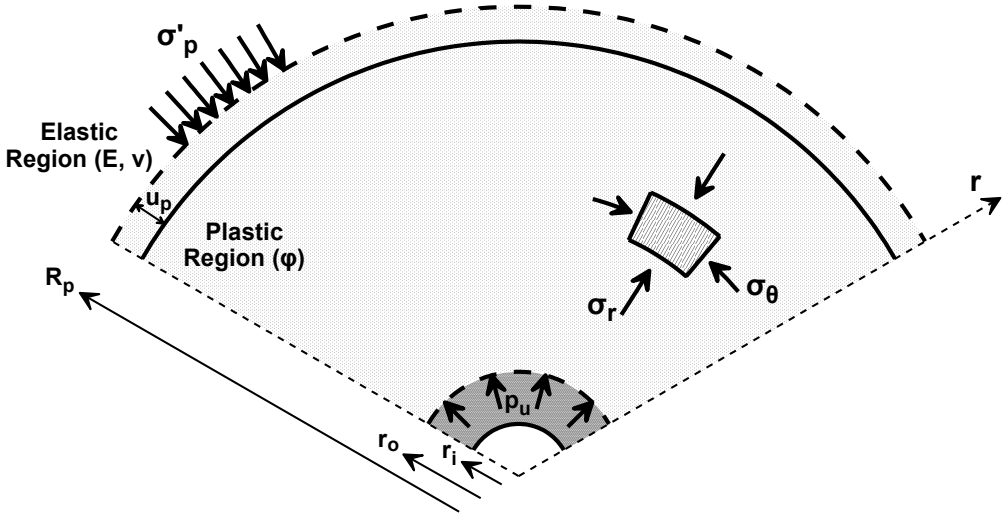

Figure 4.8: Layout and parameters involved in a cavity expansion analysis

Initial conditions prior to expansion

Stresses prior to the application of loading are geostatic, described as follows:

$$\sigma'_{ho} = K_o \sigma'_{vo} \tag{4.3}$$

where,

σ'_{ho}: horizontal effective stress prior to expansion

σ'_{vo}: vertical effective stress prior to expansion

K_o: lateral earth pressure coefficient

Equilibrium equation

The problem is axially symmetric ($\varepsilon_{r\theta}=\sigma_{r\theta}=0$) and no deformations occur in the vertical direction ($\varepsilon_{rz}=\varepsilon_{zz}=0$). Stress and strain changes occur only in the radial and circumferential direction. Therefore, the equilibrium equation, in cylindrical coordinates, is reduced to the following:

$$\frac{\partial \sigma'_r}{\partial r} + \frac{\sigma'_r - \sigma'_\theta}{r} = 0 \tag{4.4}$$

where:

σ'_r: radial stress

σ'_θ: circumferential stress

r: radial distance to the center of the cavity

Response in the plastic zone

Soil is assumed to follow an elastic-perfectly plastic stress-deformation law defined by means of the two (2) elastic parameters (E,v) and a Mohr-Coulomb failure criterion, which, for a cohesionless soil (c=0) with friction angle φ, is expressed as follows:

$$\sigma'_\theta = K_a \sigma'_r \tag{4.5}$$

where:

$$K_\alpha = \tan^2\left(45 - \frac{\varphi}{2}\right) \tag{4.6}$$

Response in the elastic zone

The nature of the problem requires that the volumetric strain in the elastic region is equal to zero. Namely, for the radial displacement, u(r) to become zero when the radial distance, r, is very large, the former should be expressed by a relation of the following form:

$$u\ r = \frac{A}{r} \text{ for } u\ r \to \infty = 0 \tag{4.7}$$

where A a constant. Based on equation (4.7), one can evaluate the radial and circumferential strain, ε_r and ε_θ respectively. Consider the slice shown in **Figure 4.9**. After application of the radial displacement u_r points a, b, c and d have moved to a', b', c' and d'. The radial and circumferential strains are calculated as follows:

$$\varepsilon_r = \frac{ab - a'b'}{dr} = \frac{u_r}{r} = \frac{\partial u_r}{\partial r} \tag{4.8}$$

$$\varepsilon_\theta = \frac{ac - a'c'}{rd\theta} = \frac{-u_r d\theta}{rd\theta} = -\frac{u_r}{r} \tag{4.9}$$

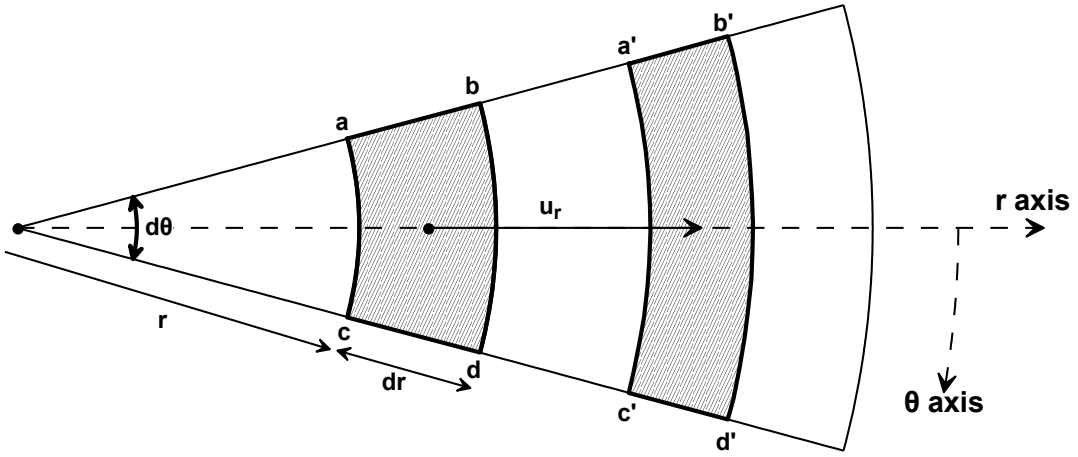

Figure 4.9: Evaluation of radial and circumferential strains in a small-strain axisymmetric problem

Note that, despite the fact that displacements along the θ axis are constrained because of axisymmetry (u_θ=0), the circumferential strain is not equal to zero $\varepsilon_\theta \neq 0$. Taking into account the variation of radial displacement from equation (4.7), equations (4.8) and (4.9) yield:

$$\varepsilon_r = \frac{\partial u_r}{\partial r} = \frac{A}{r^2} = -\frac{u_r}{r} = -\varepsilon_\theta \tag{4.10}$$

Therefore, for plane strain conditions (ε_z=0), the volumetric strain in the elastic zone is equal to:

$$\varepsilon_{vol} = \varepsilon_r + \varepsilon_\theta + \varepsilon_z = \frac{A}{r^2} - \frac{A}{r^2} = 0 \tag{4.11}$$

Application of equations of elasticity for $\varepsilon_r = -\varepsilon_\theta$ yields that any change in the radial stress ($\Delta\sigma'_r$) should be equal with the opposite of the change in circumferential stress ($\Delta\sigma'_\theta$):

$$\Delta\sigma'_r = -\Delta\sigma'_\theta \tag{4.12}$$

Conservation of volume

For a cavity expanded under undrained conditions, the initial volume of the plastic zone should be equal to the final, i.e:

$$r_o^2 - r_i^2 = R_p^2 - \left(R_p - u_p\right)^2 \tag{4.13}$$

where u_p is the radial displacement at the limit of the plastic zone (**Figure 4.8**), computed by the well-known Lame's solution:

$$u_p = \frac{1+\nu}{2E} R_p \left(\sigma'_p - \sigma'_{ho}\right) \tag{4.14}$$

with:

E, ν: Elastic parameters of the soil

σ'_p: Value of the radial stress at $r=R_p$

However, since the cavity expansion in sands occurs under drained conditions, the volume change that takes place in the plastic zone should somehow be included in the above equation. For this purpose, Vesic introduces the term Δ, which corresponds to the average volumetric strain of the plastic zone. Hence equation (4.13) becomes:

$$r_o^2 - r_i^2 = R_p^2 - \left(R_p - u_p\right)^2 + \left(R_p^2 - r_o^2\right)\Delta \tag{4.15}$$

where Δ>0 for contractive response and Δ<0 for dilative response. Note that Vesic recommends to use Δ=0 for dilative soil response.

4.3.2 Evaluation of stresses

Plastic zone ($r_o > r > R_p$)

Integration of the equilibrium equation (4.4) over the plastic zone, in combination with the Mohr-Coulomb failure criterion, yield:

$$\ln \sigma'_r = -\ln r \left(1 - K_a\right) + c \tag{4.16}$$

where c is a constant. At the cavity wall ($r=r_o$), the radial stress is equal to the limit pressure ($\sigma'_r=p_u$), so that:

$$\ln p_u = -\ln r_o \left(1 - K_a\right) + c \Rightarrow c = \ln p_u + \ln r_o \left(1 - K_a\right) \tag{4.17}$$

From equations (4.16), (4.17) and (4.5) σ'_r and σ'_θ are computed as:

$$\sigma'_r = p_u \left(\frac{r_o}{r} \right)^{1-K_a} \tag{4.18}$$

$$\sigma'_\theta = K_a p_u \left(\frac{r_o}{r} \right)^{1-K_a} \tag{4.19}$$

where p_u and R_p remain to be evaluated. For this, we consider stress equilibrium at the elastic-plastic zone interface, where $\sigma'_r=\sigma'_p$. The radial stress in the plastic side of the boundary can be obtained from equation (4.18) substituting $r=R_p$:

$$\sigma'_p = p_u \left(\frac{r_o}{R_p} \right)^{1-K_a} \tag{4.20}$$

In the elastic side of the boundary the radial and circumferential stresses are equal to:

$$\begin{aligned} \sigma'_r &= \sigma'_{ho} + \Delta\sigma'_r \\ \sigma'_\theta &= \sigma'_{ho} + \Delta\sigma'_\theta \Rightarrow \sigma'_\theta = \sigma'_{ho} - \Delta\sigma'_r \end{aligned} \tag{4.21}$$

since elasticity requires $\Delta\sigma'_r=-\Delta\sigma'_\theta$, as shown in equation (4.12). However, since we are at the plastic zone boundary, the Mohr-Coulomb failure criterion at $r=R_p$ should also be satisfied:

$$\sin\varphi = \frac{\sigma'_r - \sigma'_\theta}{\sigma'_r + \sigma'_\theta} = \frac{\sigma'_{ho} + \Delta\sigma'_r - \sigma'_{ho} - \Delta\sigma'_\theta}{\sigma'_{ho} + \Delta\sigma'_r + \sigma'_{ho} + \Delta\sigma'_\theta} \tag{4.22}$$

$$\sin\varphi = \frac{\sigma'_r - \sigma'_\theta}{\sigma'_r + \sigma'_\theta} = \frac{\sigma'_{ho} + \Delta\sigma'_r - \sigma'_{ho} + \Delta\sigma'_r}{\sigma'_{ho} + \Delta\sigma'_r + \sigma'_{ho} - \Delta\sigma' r} = \frac{\Delta\sigma'_r}{\sigma'_{ho}} = \frac{\sigma'_p - \sigma'_{ho}}{\sigma'_{ho}} \Rightarrow$$

$$\Rightarrow \sigma'_p = \sigma'_{ho}\ (1+\sin\varphi) \tag{4.23}$$

From (4.20) and (4.23), stress equilibrium at $r=R_p$ yields:

$$p_u \left(\frac{r_o}{R_p} \right)^{1-K_a} = \sigma'_{ho}\ (1+\sin\varphi) \tag{4.24}$$

Finally, combining the equations for volume conservation (4.15), radial displacement at the plastic zone boundary (4.14) and stress equilibrium (4.24) at the plastic zone boundary, we can calculate R_p and p_u as follows:

$$\begin{aligned} R_p / r_o &= \left[I_{rr} \sec\varphi \right]^{1/2} \left(1 - \frac{r_i^2}{r_o^2} + \Delta \right)^{1/2} \quad \text{(for open-ended piles)} \\ R_p / r_o &= \left[I_{rr} \sec\varphi \right]^{1/2} \quad \text{(for close-ended piles, with } r_i = 0) \end{aligned} \tag{4.25}$$

$$p_{ult} = \sigma'_{ho} \left[1 + \sin\varphi \right] \left(\frac{R_p}{r_o} \right)^{\frac{2\sin\varphi}{1+\sin\varphi}} \tag{4.26}$$

where:

$$I_{rr} = \frac{I_r}{1 + I_r \Delta \sec\varphi} \tag{4.27}$$

and

$$I_r = \frac{E}{2\left[1+\nu\right]\sigma'_{ho}\tan\varphi} = \frac{G}{\sigma'_{ho}\tan\varphi} \tag{4.28}$$

I_r is called rigidity index and represents the ratio of the shear modulus of the soil to its initial shear strength.

Elastic zone ($r > R_p$)

For $\Delta\sigma'_r = -\Delta\sigma'_\theta$, [i.e. Eq (4.12)], the equilibrium equation (4.4) becomes:

$$\frac{\partial\sigma'_r}{\partial r} = -\frac{\sigma'_r - \sigma'_\theta}{r} = -\frac{\sigma'_{ho} + \Delta\sigma'_r - \sigma'_{ho} + \Delta\sigma'_r}{r} = -\frac{2\Delta\sigma'_r}{r} = -\frac{\sigma'_r - \sigma'_{ho}}{r} \tag{4.29}$$

Integrating Eq. (4.29) and applying the boundary conditions $\sigma'_r = \sigma'_p$ for $r = R_p$, the following expressions for σ'_r and σ'_θ are finally obtained:

$$\sigma'_r = \sigma'_{ho} + \left[\sigma'_p - \sigma'_{ho} \right] \left(\frac{R_p}{r} \right)^2 \tag{4.30}$$

$$\sigma'_{\theta} = \sigma'_{ho} - \sigma'_{p} - \sigma'_{ho} \left(\frac{R_p}{r} \right)^2 \quad (4.31)$$

where σ'_p can be estimated from equation (4.20).

Note that the methodology does not provide any guidance for the vertical stresses, σ'_z. A rational approach is to use elasticity's equation for the median stress, under plane strain conditions:

$$\sigma'_z = \sigma'_{vo} + \nu \ \Delta\sigma'_r + \Delta\sigma'_{\theta} \quad (4.32)$$

For the plastic region, many researchers (Carter et al., 1986; Bigoni and Laudiero, 1989; Yu and Houlsby, 1991; Collins et al., 1992; Salgado and Randolph, 2001; Dongxue et al., 2010) suggest the value of 0.5 for Poisson's ratio, while, for the elastic zone, the $\Delta\sigma'_r$=- $\Delta\sigma'_\theta$ requirement yields:

$$\sigma'_z = \sigma'_{vo} \quad (4.33)$$

Overall, the following can be concluded with regard to the procedure suggested by Vesic to deal with the problem of cylindrical expansion of the cavity:

- The method is based on well-established assumptions with respect to soil response (Mohr-Coulomb criterion) and basic soil mechanics principles (volume conservation), and thus it is provided with a strong theoretical background which supports its credibility.
- The method provides a simple but effective tool to evaluate both radial (σ'_r) and hoop (σ'_θ) stresses around a cavity based on soil properties which are known a priori or can be easily determined (E, v, φ, γ).
- An important limitation is that not sufficient guidance is provided for the evaluation of the average volumetric strain in the plastic zone (Δ), a rather dominant parameter of the methodology, as well as the estimation of the vertical stresses in the plastic zone (σ'_z).
- The methodology is rather simple, and hence easily programmed and implemented in the numerical code.

4.3.3 Insight on the effect of Δ

Note that in Vesic's methodology the average volumetric strain Δ is considered as a known input parameter. Nevertheless, the guidance provided on how to evaluate Δ is not sufficient despite that its effect on the response is dominant. For this purpose a series of parametric analyses was carried out to explore Δ, and establish a rational approach for its evaluation.

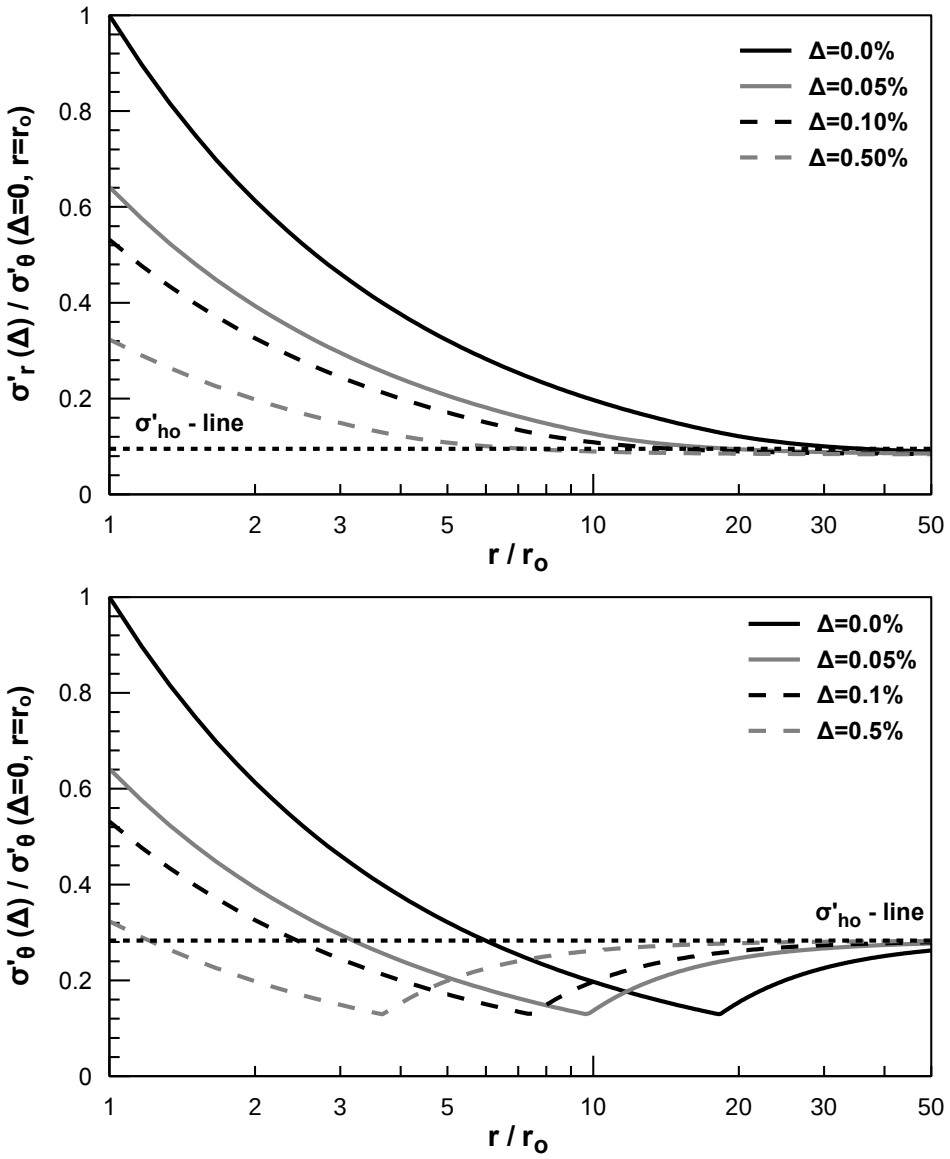

Figure 4.10: Effect of plastic zone volumetric change on σ'_r and σ'_θ.

As a first approximation, it might be assumed that no volumetric change takes place in the plastic zone, and, hence, Vesic's methodology can be applied using Δ=0 in all cases. Stress changes predicted in this way would always be larger compared to the

real ones. However, this approach could be justified only under the condition that stress overestimation is not significant. To explore this issue, Vesic's methodology was applied for various values of Δ and the results were compared in terms of σ'_r and σ'_θ as shown in **Figure 4.10**. In this figure stresses for various Δ are normalized with respect to stresses at the pile interface for Δ=0.

This comparison indicates that resulting stresses are extremely sensitive even to small variations of Δ. For example, when Δ increases from 0 to 0.05%, a rather small value, the radial stress is decreased by approximately 40%. It can be therefore concluded that assuming Δ=0 is an oversimplification that may lead to ambiguous results. Note that Vesic in his study also recognizes the pronounced effect of Δ in his methodology, stressing that Δ should be evaluated with a three-digit number precision.

In order to make recommendations with regard to the estimation of Δ, Vesic focuses on the stress paths generated in a cavity expansion problem. **Figure 4.11** shows this stress path in terms of the mean stress $p'=(\sigma'_r+\sigma'_\theta)/2$ and the deviatoric stress $q=\sigma'_r-\sigma'_\theta$. Between points 1 and 2 soil response remains elastic with the deviatoric stress constantly increasing, under constant p'. At point 2 the soil element fails and thereafter the stress path follows the failure envelope defined by K_a. Vesic argues that all elements in the plastic zone follow paths of the same shape, and all of them end somewhere in between point 2 (corresponding to $r=R_p$) and point 3 (corresponding to $r=r_o$).

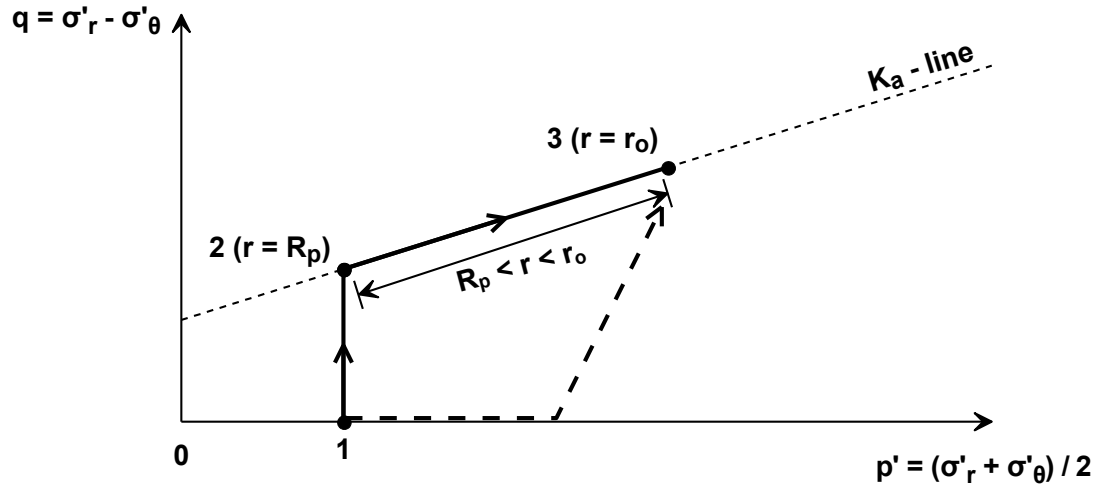

Figure 4.11: Stress path during cavity expansion as predicted by Vesic's methodology

Therefore, a laboratory test that would reproduce the path shown in **Figure 4.11** could be used to measure volumetric changes of elements subjected to cavity expansion. If multiple tests, for various pressure magnitudes (between σ'_{ho} and p_u), could be carried out, then it would be possible to estimate the volumetric strain in the plastic zone. Vesic argues that a test that captures the cavity expansion stress path is the triaxial plane strain test.

In addition, the author suggests that volumetric strains between point 1 and 3, will not differ significantly if a different path, rather than 1-2-3, was followed, as long as it has the same initial and final stress points. Hence, given the difficulties of performing triaxial plane strain tests, Vesic suggests a procedure to estimate Δ based on data from isotropic compression followed by standard triaxial tests (dotted path in **Figure 4.11**).

In any case, the above discussion reveals that the volumetric strain can only be evaluated experimentally and with rather tedious procedures, either with the triaxial plane strain test, which is not well established in literature, or with a large number of standard triaxial tests. Instead of performing these procedures numerically, and investigating their efficiency, it was decided to simulate numerically the cavity expansion problem, gain direct insight to the volumetric response of the soil and finally investigate ways of evaluating Δ analytically. The latter is a necessary step for the programming and implementation of the method in FLAC3D.

4.4 Numerical simulation of cylindrical cavity expansion

The 3-D geometry of the numerical model created to simulate cavity expansion is shown in **Figure 4.12**. In addition **Figure 4.13** shows the model in more detail form a top and a side view, along with major assumptions of the analysis (boundary conditions, load application), as well as the range of the basic input parameters. These include:

- Relative Density: D_r=20,50,90%
- Initial (in-situ) mean effective stress: p'_o=0-50kPa (z=0-8m)
- Applied radial displacement: $d_{cav} = r_o - r_i = 1,5,10,20,30cm$

  $d_{cav} / r_o = 0.03 - 1.0$

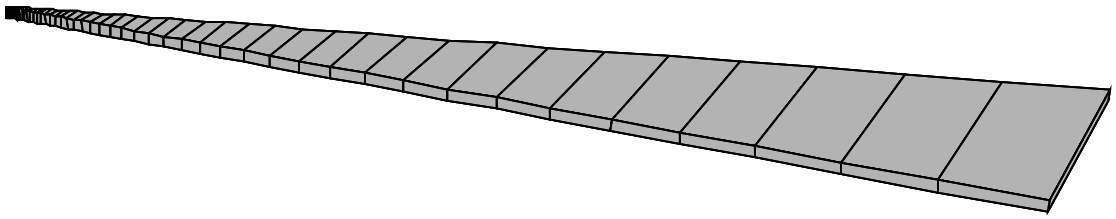

Figure 4.12: 3-D geometry of the numerical model

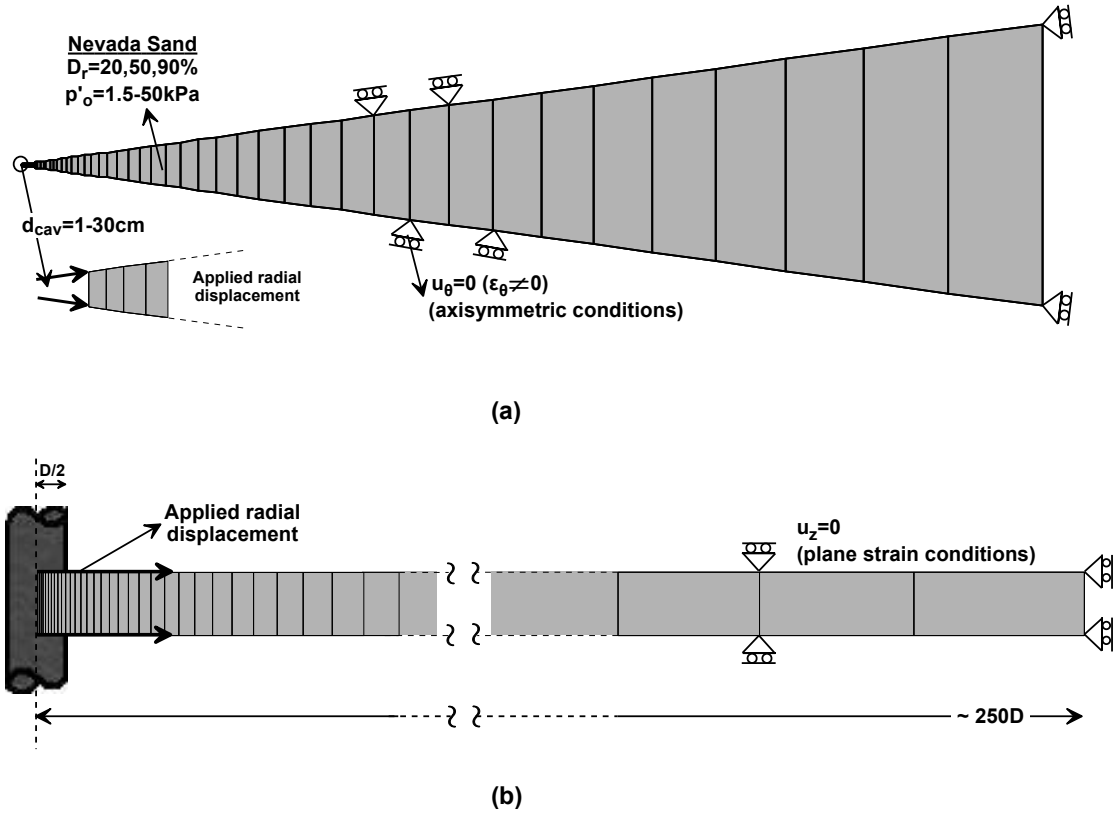

Figure 4.13: Boundary conditions, basic analysis parameters and model geometry in (a) top and (b) side view

The above parameters were selected as the ones that dominate volumetric response of the soil, while the specified ranges reflect in-situ conditions before and after installation of the 8m in length and 0.60m in diameter pile, simulated in the previous chapter. Hence, values of p'_o from 0 to 50kPa correspond to the in-situ stress field of a 8m thick sand deposit. Furthermore, variation in values of d_{cav} aims to simulate different plugging levels of open-ended piles (see paragraph 4.2). Small values correspond to approximately unplugged driving (open-ended pile), intermediate values correspond to partially plugged driving, while the value d_{cav}=30cm corresponds to perfectly plugged driving (close-ended pile).

The 3-D model is constructed by taking into account the axisymmetric and plane strain nature of the problem. Namely, a pie slice corresponding to one-sixth of a quadrant was considered. The length of the model was chosen, through parametric analyses whose results will be presented later, so as to eliminate any boundary effects. The grid is composed of a single layer of zones with constant height (h=0.50m) and variable width, that is small near the cavity wall and gradually increases with radial distance.

As for the boundaries, plane strain and axisymmetric conditions require that nodes are fixed in the vertical and circumferential direction, while they are free to move in the radial direction. Note that, as pointed out earlier, despite the fact that $u_\theta=0$, these constraints allow circumferential strains to develop $\varepsilon_\theta \neq 0$.

Soil properties are introduced in the model through the critical state constitutive model for sands NTUA_Sand (Papadimitriou and Bouckovalas, 2002; Andrianopoulos et al., 2010) discussed in the previous chapter. Model parameters are calibrated to simulate response of Nevada sand, while the only parameter that needs to be defined by the user is the void ratio. After assignment of soil properties in the zones, initial (in-situ) stresses are introduced, and the model is allowed to equilibrate. Finally, at the left boundary of the model a radial displacement is applied, as shown in **Figure 4.13**, to simulate expansion of the cavity. Since radial displacements of large amplitude were applied, leading to large radial strains, calculations were performed by activating FLAC's large strain mode.

As noted earlier, the length of the model was selected through parametric analyses, aimed to eliminate boundary effects. For this purpose a series of tests was performed for the case of d_{cav}=30cm, which will induce the larger stress changes in the soil. The other parameters were D_r=50% and p'_o=30.0kPa. Results are summarized in **Figure 4.14** in terms of radial (σ'_r) and hoop (σ'_θ) stress with radial distance normalized with the final radius of the cavity. It can be observed that a small grid significantly overestimates resulting stresses, while as size increases the error is reduced. The latter becomes negligible for a grid length equal to 250D or 150m, which was the value adopted in the analyses. It should be noted that, for smaller magnitudes of applied radial displacement, the required length is expected to be smaller compared to the case of d_{cav}=30cm. However, given the small computational effort required for

each analysis (in the order of a few minutes), it was decided to adopt the length of 150m for all analyses.

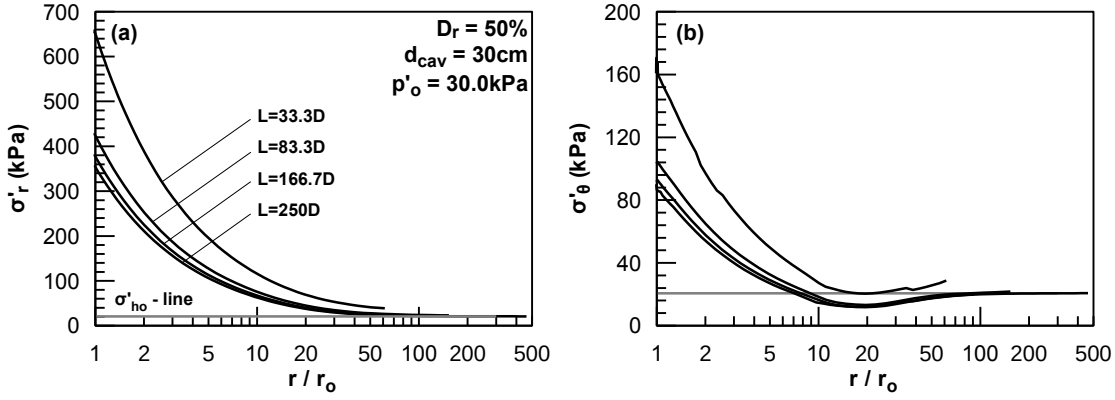

Figure 4.14: Variation of radial (σ'_r) and hoop (σ'_θ) stress with radial distance for various mesh lengths

The conclusions derived from **Figure 4.14** underline the definite need to develop a semi-analytical procedure which would allow manual implementation of the cavity expansion stresses. The alternative option would be to simulate directly pile installation by applying radial displacement at the pile-soil interface. However, based on the preceding mesh investigation this analysis would require a 300 x 150m wide grid to avoid boundary effects. Such a grid would result in an enormously large computational time, which would practically make the numerical simulation impossible.

At the end of each analysis the radial (σ'_r), the circumferential or hoop (σ'_θ) and vertical (σ'_z) stresses, as well as the volumetric strain (ε_{vol}) for each zone were computed. In addition stress and strain histories were stored for a large number of elements corresponding to different radial distances. Since analyses were performed using large-strain mode, a formula for the accumulation of strains should be adopted. Note that in FLAC strain increments (cumulative strains) are based on the geometry at the time of measurement. Since the geometry changes significantly, during a large-strain simulation, the measured strain will depend on the assumption made about the reference geometry, which constantly changes due to node update. Finally, the logarithmic strain was adopted, implemented in the analysis through a FISH subroutine and stored as an extra zone variable:

$$\varepsilon_{vol} = \int_{V_o}^{V} \frac{dV}{V} = \ln \frac{V_f}{V_o} \tag{4.34}$$

where:

V_o: Initial volume of the zone

dV/V: incremental volume change dV over a volume V

V_f: Final volume of the zone

4.5 Typical Results

Typical results from the numerical simulation of cavity expansion are shown in **Figure 4.15**, in terms of radial, hoop and vertical stress, as well as volumetric strain variation with normalized radial distance. These results correspond to an analysis with D_r=50%, p'_o=25kPa and d_{cav}=10cm. It can be observed that the radial stress at the wall of the cavity is significantly larger compared to the free-field horizontal stress, while the rate of decrease with radial distance resembles the shape of the analytical solution (e.g. **Figure 4.15a**). The circumferential stress is also increased at the edge of the cavity, but remains well below the radial. As distance increases σ'_θ is decreased and, at some point, it falls below the free-field horizontal stress until it reaches a local minimum, before it starts increasing again. In the analytical solution (**Figure 4.15b**), where the response is similar, this local minimum indicates the limit of the plastic zone, after which the volumetric strain becomes zero. This is also confirmed by the volumetric strain predictions, shown in **Figure 4.15d**, which becomes very small (essentially negligible) after $r / r_o \approx 13$ (the radius of minimum circumferential stress). **Figure 4.15c** shows that vertical stresses obtain values which are somewhere between σ'_r and σ'_θ, consistent with the plane strain assumption of the analytical scheme. However, outside the plastic zone, σ'_z gradually increases until it becomes the major principal stress and the free-field conditions are re-established.

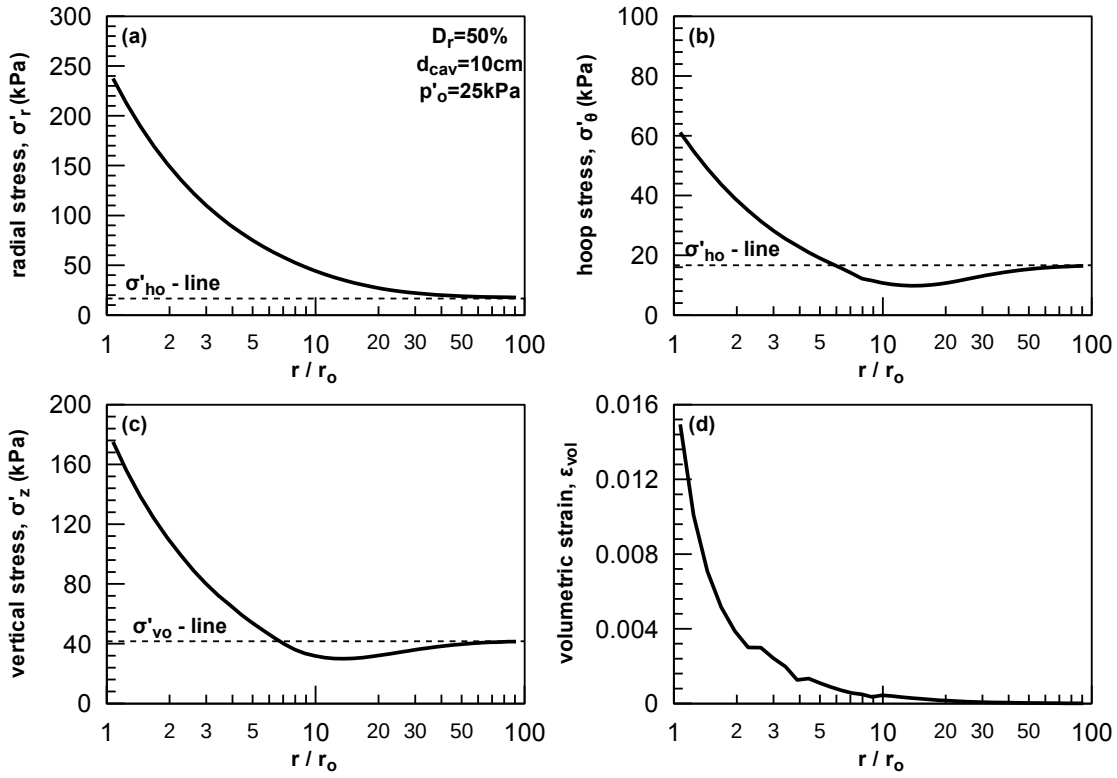

Figure 4.15: Typical results from numerical simulation of cavity expansion and (a) Radial stress (b) Circumferential stress (c) Vertical stress (d) Volumetric strain with normalized radial distance (D_r=50%, d_{cav}=10cm, p'_o=25kPa)

Figure 4.16 shows in addition stress and volumetric paths of four (4) different elements corresponding to various radial distances. Namely, **Figure 4.16a** shows the stress path in q-p/p_a, space for elements with r/r_o=1,2,7 and 20. Observe that the shape of the different paths is very similar to the one proposed by Vesic (**Figure 4.11**). Initially, the deviatoric stress, q, increases under approximately constant mean stress, p, while afterwards both p and q increase under a constant q/p ratio. Furthermore, note that all elements follow the same path and, depending on the radial distance, end up at a different p value on the same line. This is an assumption also adopted in Vesic's methodology and confirmed by the numerical analyses.

As for the volumetric response (**Figure 4.16b**), it can be observed that elements close to the cavity wall undergo large compression, which is reduced with radial distance. Finally, zones that are beyond the plastic zone, as determined from the σ'_θ-r/r_o variation, undergo essentially zero volumetric strains, as suggested by the analytical method.

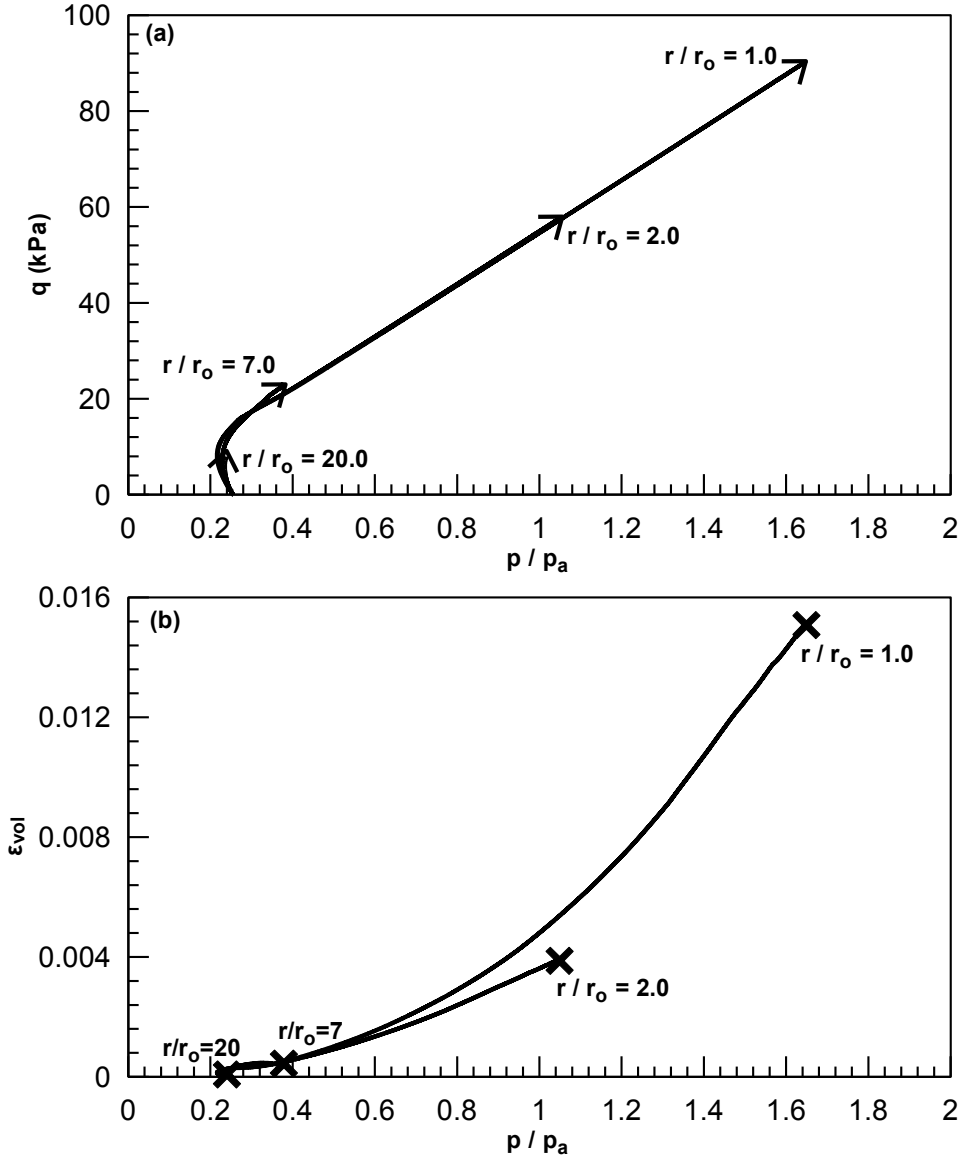

Figure 4.16: (a) Stress and (b) Volumetric paths for elements of various radial distance during cylindrical cavity expansion (D_r=50%, d_{cav}=10cm, σ'_{vo}=40kPa)

Effect of Relative Density, D_r.- The effect of relative density on the stress and volume changes induced by cavity expansion problems is shown in **Figure 4.17**. As expected, all stress components (σ'_r, σ'_θ, σ'_z) increase with relative density. In addition, from **Figure 4.17b**, it can be observed that the size of the plastic region is approximately equal to ten (10) and twenty (20) times the external radius of the cavity for D_r=20% and 90% respectively, indicating that the plastic zone also increases with D_r. Finally, in terms of volumetric response, results indicate that the D_r=20 and 50% cases exhibit contractive behavior, with the D_r=20% developing

slightly larger volumetric strains. On the contrary, the D_r=90% case causes the soil to develop negative volumetric strains, which indicate dilation.

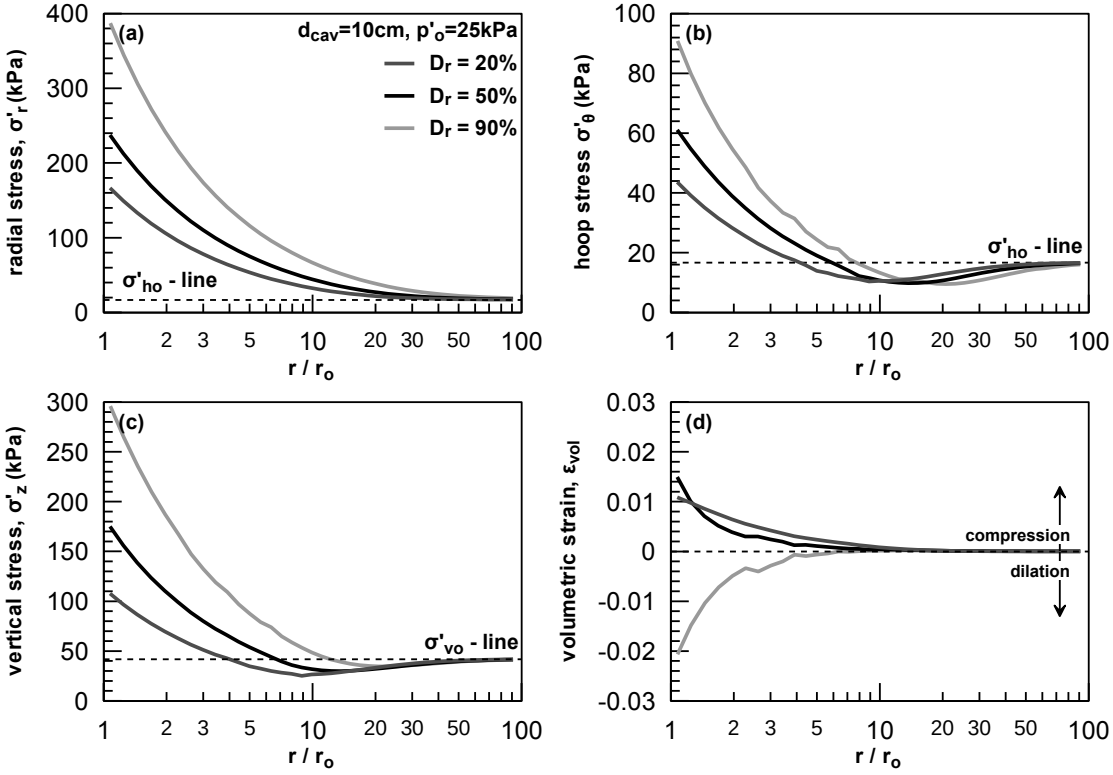

Figure 4.17: Effect of relative density on soil response after cylindrical cavity expansion (a) Radial stress (b) Circumferential stress (c) Vertical stress (d) Volumetric strain with normalized radial distance (d_{cav}=10cm, p'$_o$=25kPa)

Effect of applied radial displacement, d_{cav}/r_o.- Results from analyses of various d_{cav}/r_o ratios (**Figure 4.18**) indicate that both stresses and volumetric strains increase with applied radial displacement. In addition, the size of the plastic zone increases as the ratio d_{cav}/r_o increases. It can also be observed that the dependence between stresses and d_{cav}/r_o is exponential. Namely, note in **Figure 4.18a** that the increase in radial stress is approximately the same when d_{cav} increases from 1 to 5cm (x5 increase), with the case where d_{cav} increases from 5 to 30cm (x6 increase). This type of response is also confirmed by the analytical method, as expressed in equation (4.25), where the size of the plastic zone, and hence the resulting stresses, increases exponentially with d_{cav}/r_o. Finally, in terms of volumetric response, it is observed that as d_{cav} increases the volumetric strains developed also increase.

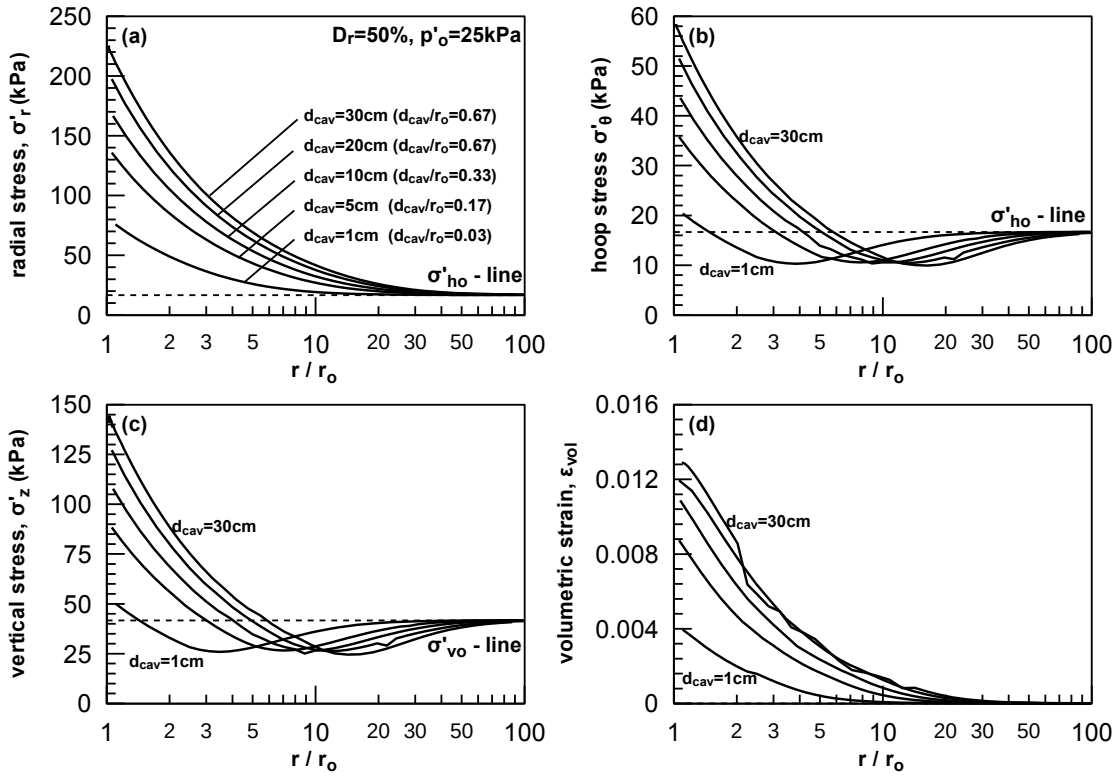

Figure 4.18: Effect of applied radial displacement on soil response after cylindrical cavity expansion (a) Radial stress (b) Circumferential stress (c) Vertical stress (d) Volumetric strain with normalized radial distance (Dr=50%, p'_o=25kPa)

Effective of in-situ stress conditions (p'_o).- In a similar fashion, **Figure 4.19** illustrates the effect of in-situ stress conditions on the response of the soil. Results point out that resulting stresses increase with initial stresses, while volumetric response is not significantly affected. To be more precise, **Figure 4.19d** indicates that larger initial pressures cause the soil to respond slightly more contractively, as suggested by the Critical State theory.

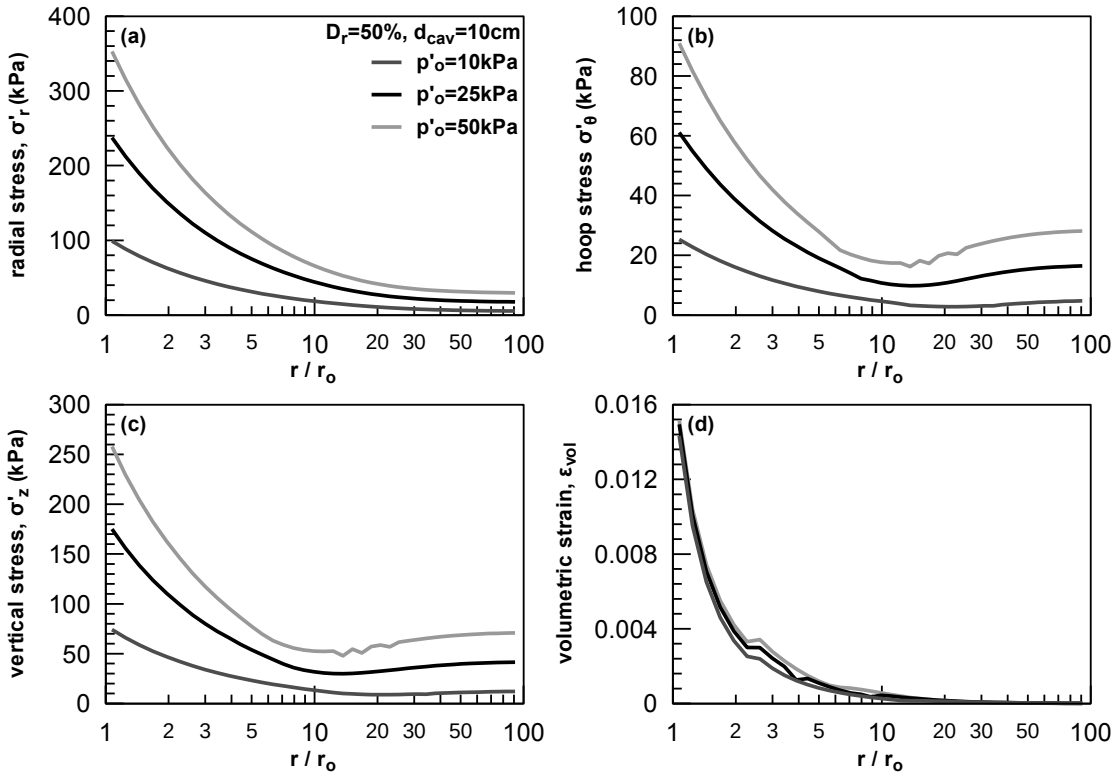

Figure 4.19: Effect of in-situ stress conditions on soil response after cylindrical cavity expansion (a) Radial stress (b) Circumferential stress (c) Vertical stress (d) Volumetric strain with normalized radial distance (Dr=50%, d_{cav}=10cm)

Overall it can be concluded that FLAC's results agree, in qualitative terms, with Vesic's solution, and confirm many of his assumptions. This observation gives more support to the idea that Vesic's approach can adequately simulate cavity expansion and consequently effects of pile installation. However, the critical issue of evaluating the average volumetric strain analytically still remains in the air, and will be addressed in the following section.

4.6 Analytical Evaluation of Average Volumetric Strain, Δ

In order to demonstrate more precisely the similarities between the numerical results and the predictions by Vesic's analytical methodology, the latter was used to predict the results of one of the analyses, and specifically the one with d_{cav}=10cm, D_r=50% and p'_o=25kPa. For this case the input values for Vesic's expressions are r_i=0.20m, r_o=0.30m, φ=33° for D_r=50% (see previous chapter for correlation between D_r and φ), while the shear modulus G was estimated according to Hardin's formula, also discussed in the previous chapter, which is adopted in the formulation of the constitutive model. As for the average volumetric strain, Δ, since there is no

analytical expression, a trial and error procedure was followed in order to obtain a value that provides optimum fit to the numerical predictions. For the case presented here that value was found equal to Δ=0.09%. As for vertical stresses, the expression from equation (4.32) was used, where the value for Poisson's ratio was estimated based on the numerical results at the wall of the cavity, and found equal to v=0.503.

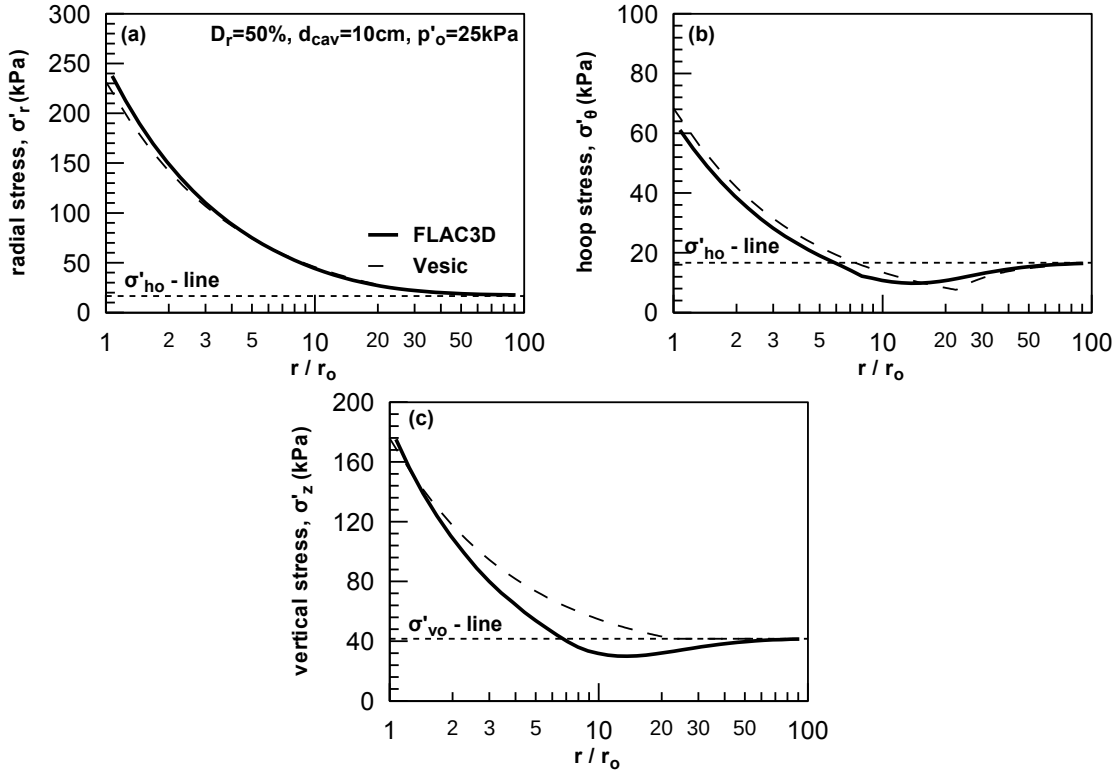

Figure 4.20: Numerical results vs. analytical predictions for Δ estimated through a trial and error procedure (a) Radial stress (b) Circumferential stress (D_r=50%, d_{cav}=10cm, p'_o=25kPa)

The comparison is shown in **Figure 4.20**, where the following can be observed:

- Radial stresses can be predicted with sufficient accuracy both in terms of maximum values as well as radial distance variations.
- Hoop stresses are captured with comparable accuracy. However the analytical method seems to slightly overestimate the size of the plastic zone. In addition, the transition from the plastic to the elastic zone is smoother for the numerical analysis. This differentiation is probably due to the fact that numerical analyses are performed with a more advanced elastoplastic model compared to the elastic-perfectly plastic model used in Vesic's method.

- Vertical stresses, finally, seem to deviate from numerical estimates mainly in terms of variation with radial distance. This response can be attributed to the fact that the analytical expressions assume that σ'_z becomes equal to the free-field vertical stress (σ'_{vo}) at the plastic zone boundary and remains constant thereafter. However, numerical results show that σ'_z falls below σ'_{vo} before the plastic zone boundary is reached and then gradually increases to reach σ'_{vo}.

The comparison in **Figure 4.20** revealed that by applying a trial and error procedure to estimate a best-fit value for Δ, Vesic's methodology can provide a quite precise analytical framework to predict the stresses induced by expansion of cylindrical cavities. Based on this observation, best-fit values for Δ were next determined for the total of 120 analyses. In all cases the observations discussed above were further confirmed. As a result, the best-fit values for Δ were collected in a database in order to derive a correlation which would allow the analytical evaluation of Δ. It was assumed that the analytical expression would be of the following product form:

$$\Delta = c \cdot f\ \ p'_o / p_a\ \cdot g\ \ d_{cav} / r_o\ \cdot w\ \ D_r \tag{4.35}$$

where c is a constant.

At first, the form of the function $g\ \ d_{cav} / r_o$ was determined based on the trends shown in **Figure 4.21**. Namely, each box in **Figure 4.21** displays the variation of the back-analyzed Δ for a specific value of the in-situ mean stress (p'_o) and for the three (3) values of the relative density (D_r) examined. Overall it can be observed that for values of d_{cav}/r_o larger than 0.2, Δ remains practically constant, while for small d_{cav}/r_o the values are slightly augmented. In any case it is rational to assume that the effect of d_{cav} on Δ can be considered negligible and can be described by a function of the following form:

$$g\ \ d_{cav} / r_o\ = a_1\ \ d_{cav} / r_o\ ^0 \tag{4.36}$$

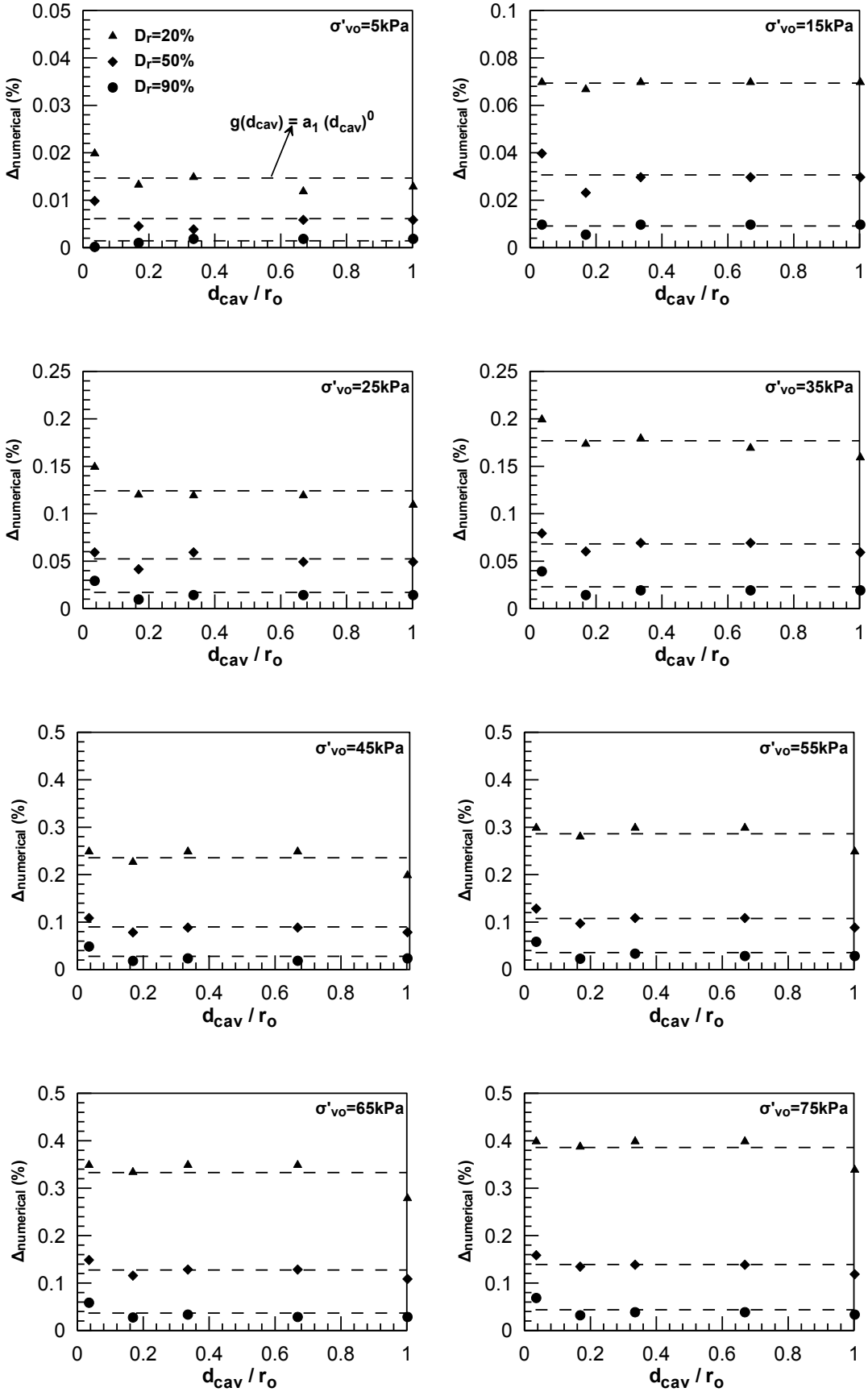

Figure 4.21: Effect of applied radial displacement (d_{cav}) on the numerically estimated Δ for various initial soil conditions (D_r, σ'_{vo})

At this point it should be noted that the back analyzed values of Δ seem to not agree with the trends observed in the numerical analyses. Namely, in **Figure 4.18d** it is clear that as the magnitude of applied displacement increases, soil contraction is more pronounced. This contradiction can be explained in terms of the formulation of the analytical method, which also does not consider d_{cav} as a parameter that affects Δ (the laboratory procedures suggested by Vesic and described in paragraph 4.3.3 do not account for d_{cav} in the evaluation of Δ). However, the undoubtable effect of d_{cav} on the volumetric response of the soil and, hence, on the resulting stresses is included indirectly in the analytical method through equation (4.25) which is used for the estimation of the size of the plastic zone. The expression in question shows that as r_o increases, or as the ratio r_i/r_o decreases (for open-ended piles), the radius of the plastic zone increases.

In order to evaluate the effect of initial stress-state, the variation of Δ is plotted in **Figure 4.22** as a function of p_o/p_a for the three (3) different values of D_r investigated, as well as all values of $d_{cav,}$. A linear increase of Δ with p_o is observed, which can be expressed analytically as follows:

$$f\left(p_o / p_a\right) = a_2 \left(p_o / p_a\right)^1 \tag{4.37}$$

where a_2 a constant depending on the relative density.

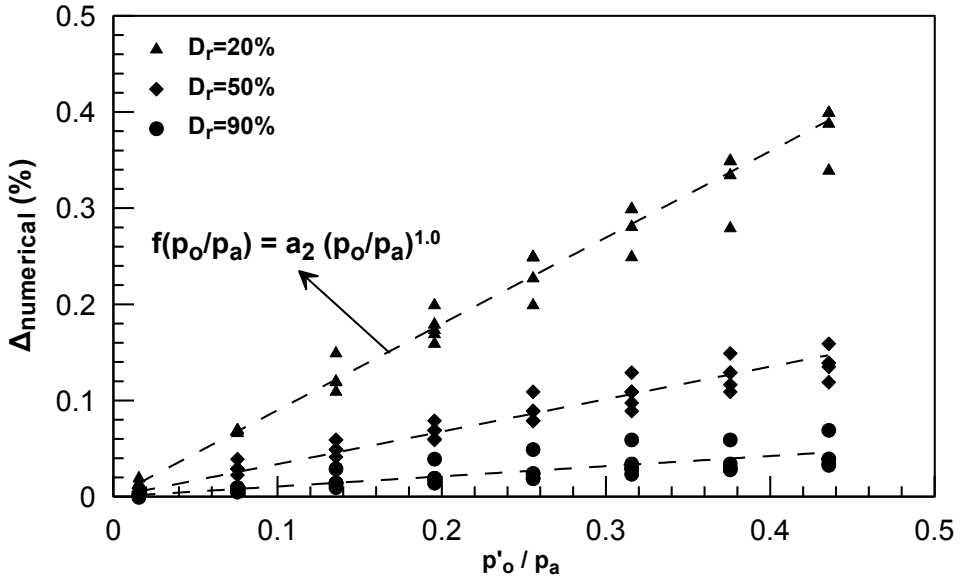

Figure 4.22: Evaluation of the effect of initial stress state on average volumetric strain, Δ

Finally, in order to determine the effect of D_r in equation (4.35), numerical values of Δ were divided with the functions $g(d_{cav}/r_o)$ and $f(p_o/p_a)$ as developed previously, and the remaining quantity was plotted against D_r, as shown in **Figure 4.23**. The correlation between Δ and D_r was found to better be described by an exponential function of the following form:

$$w\ D_r = 1.6e^{-0.03D_r}\ \% \tag{4.38}$$

Note that both the effect of p'_o and D_r on Δ, as evaluated from the back-analysis procedure, agrees with the basic principle of critical state theory, which suggests that more loose and more confined soils develop larger contractive volumetric strains.

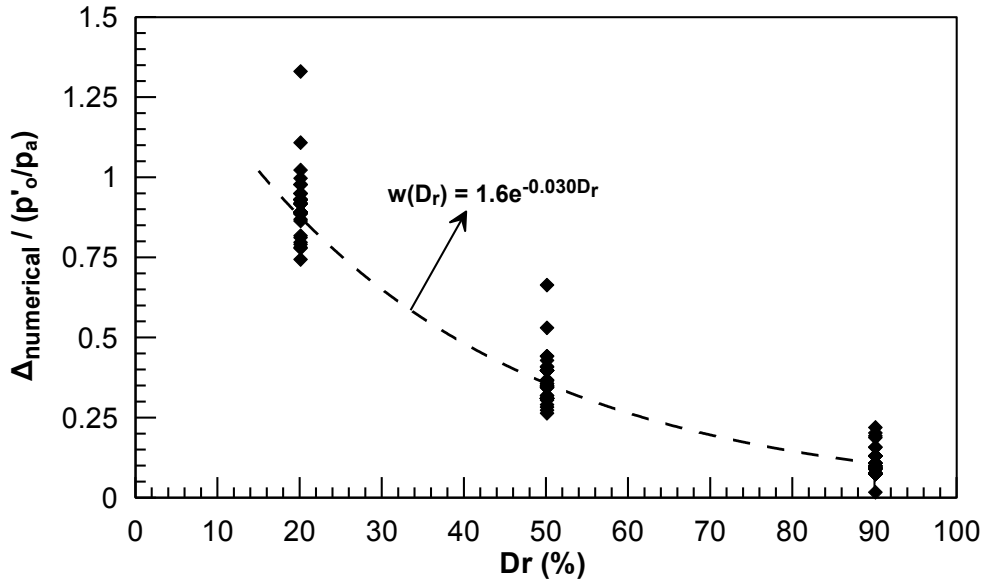

Figure 4.23: Evaluation of the effect of D_r on average volumetric strain, Δ.

Based on equations (4.36), (4.37) and (4.38), the average volumetric strain Δ can be expressed analytically according to the following relation:

$$\Delta\ \% = 1.6 \cdot \left(p_o / p_a\right) \cdot e^{-0.03D_r}\ \% \tag{4.39}$$

The above equation was used to predict analytically the average volumetric strain for each case simulated numerically, and compare it with the corresponding numerical predictions, as shown in **Figure 4.24**. The agreement is fairly consistent with only a small number of the data points exhibiting a uniform scatter that underestimates the numerical values by approximately 30%.

Note that the above equation describes the average volumetric strain in the plastic zone for expansion of cavities in Nevada sand. In order to extend the method to soils with different properties, one should perform two (2) numerical cavity expansion experiments and determine the values of the constants that appear in equation (4.39).

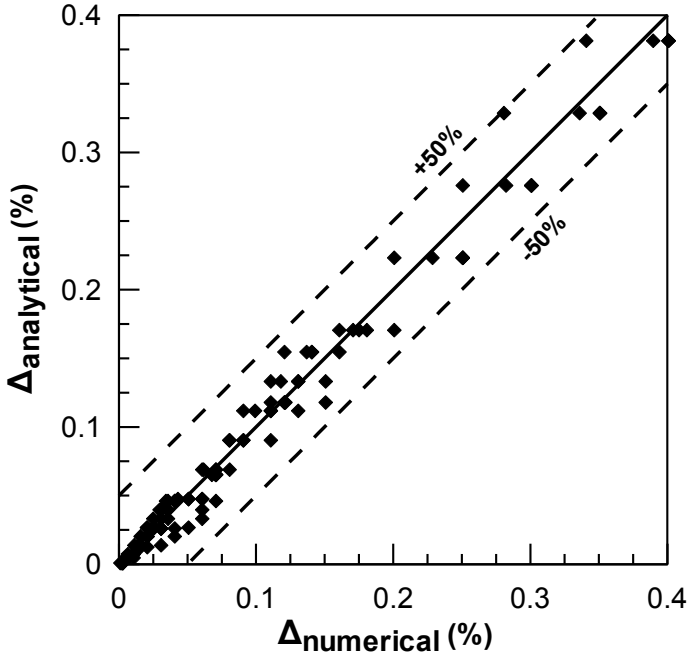

Figure 4.24: Comparison between numerical and analytical values for Δ.

4.7 Analytical Evaluation of Poisson's ratio in the plastic zone

As described at the beginning of paragraph 4.6 the numerical analyses were also used to estimate the Poisson's ratio at the wall of the cavity according to the following equation

$$v = \frac{\Delta\sigma'_z}{\Delta\sigma'_r + \Delta\sigma'_\theta} \tag{4.40}$$

derived from theory of elasticity for plane strain conditions along the z-axis. Values of v estimated numerically are plotted in **Figure 4.25** as a function of the normalized confining stress p_o/p_a. It is clear that the v=0.5 assumption, suggested by many researchers (see paragraph 4.3.2), is oversimplifying, as numerical results indicate a variation of v between 0.30 and 0.65. As a result, a statistical approach, similar to that for the evaluation of Δ, was followed, which yielded the following expression for the evaluation of v:

$$\nu = \left[1 + D_r \ \% \ /100\right] \cdot \left[0.20 + 0.13 \cdot \left(\frac{d_{cav}}{r_o}\right)^{0.16}\right] \tag{4.41}$$

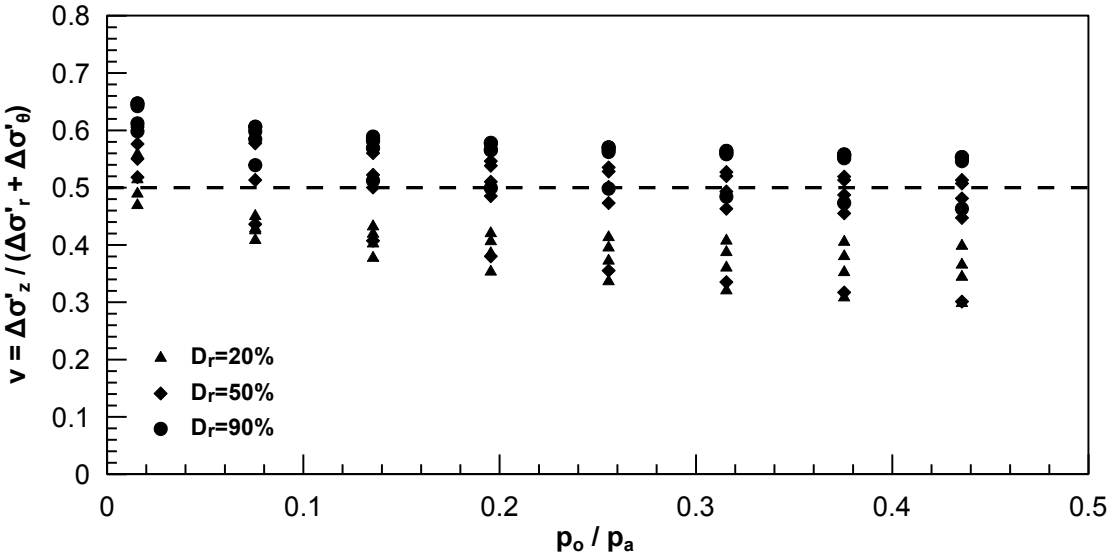

Figure 4.25: Variation of Poisson's ratio at the wall of the cavity

Based on **Figure 4.25** it can be noted that ν slightly decreases with p_o/p_a. However, for the sake of simplicity and given that σ'_z is not a dominant factor in a cavity expansion analysis, it was decided to ignore this effect of confining stress. Evaluation of the effect of the other two (2) parameters (d_{cav}/r_o and D_r) is illustrated in **Figure 4.26**. Again, in the same context of simplicity, a linear and a power relation were adopted for D_r and d_{cav}/r_o respectively, leading to the expression of equation (4.41).

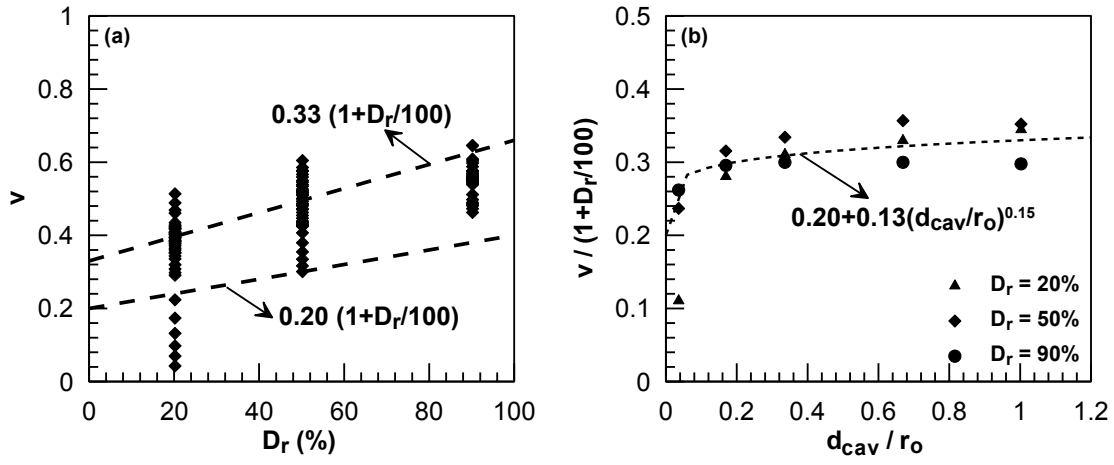

Figure 4.26: Evaluation of effect of (a) Relative Density D_r and (b) applied radial displacement d_{cav}/r_o on Poisson's ratio at the wall of the cavity

4.8 Implementation of Vesic's method to FLAC3D

Vesic's analytical procedure was programmed in FLAC's built-in programming language, FISH, so that it can be implemented in a p-y analysis of a pile. In order to use the subroutine, the user should specify the Relative Density and the friction angle of the soil, as well as the initial and the final radius of the cavity. The subroutine is invoked after free-field equilibrium has been established and prior to horizontal loading of the pile. New stresses are calculated based on the input parameters and the free-field stress-state of each zone, and new values are assigned manually at each zone in the grid. Afterwards the model is brought again to equilibrium under the new stress-state and the pile is moved laterally for estimation of the p-y response. The implementation process is illustrated schematically in **Figure 4.27** to **Figure 4.30** for a case with D_r=50% and d_{cav}=10cm. Note that the numerical model used for the p-y analysis is the same with the one described in the previous chapter.

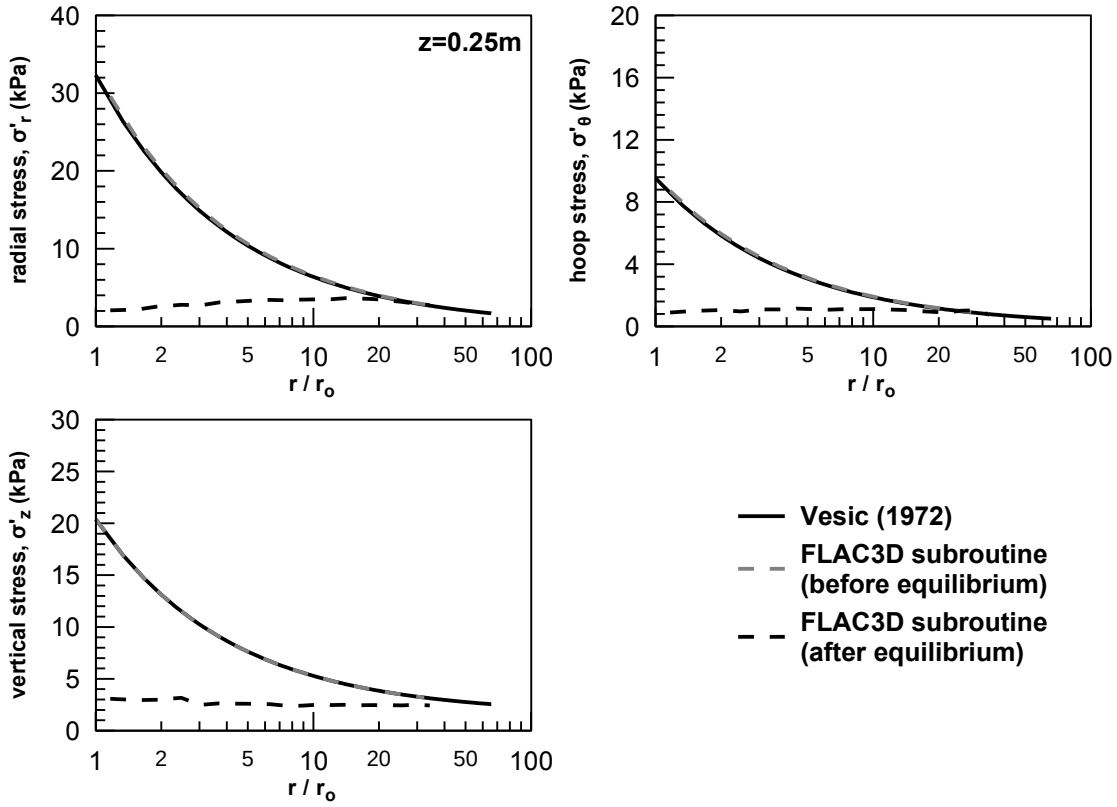

Figure 4.27: Implementation of Vesic's methodology in the numerical p-y analysis (D_r=50%, d_{cav}=10cm, z=0.25m)

Namely, **Figure 4.27** presents the stresses resulting after the implementation at a depth of z=0.25m from ground surface. The black solid line corresponds to the analytical predictions. The grey dashed line shows the stresses as calculated after the routine has been invoked and before the model is forced to equilibrate. This intermediate step ensures that the method has been correctly programmed in the subroutine. Finally, the black dashed line represents the stress state after the model has equilibrated under the new stress conditions. It can be observed that after equilibrium all stress components diverge significantly from what the cavity expansion theory predicts. This can be explained as follows:

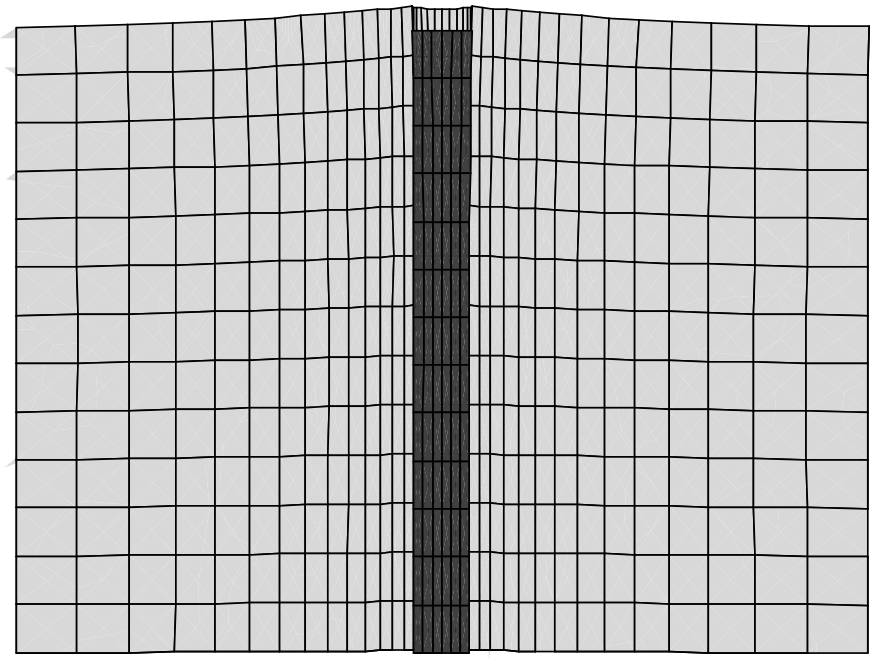

Figure 4.28: Detail of the deformed mesh after equilibrium following implementation of cavity expansion stresses – soil heaves near surface conforming to the kinematic constraints of the problem

The stresses estimated through the subroutine are based on the cavity expansion theory which assumes plane strain conditions and, hence, no vertical displacement of the soil. However, as described earlier in the chapter (paragraph 4.2), for small depths, the mechanism that better describes soil response after pile installation is that of a passive wedge with significant upward movement and not that of the expansion of a cylindrical cavity (**Figure 4.1**). In other words the stresses implemented manually do not correspond to a realistic deformation mechanism and eventually no equilibrium can be established. As a result the model is forced to develop large

upward displacements, in order to conform with the kinematic requirements of the problem, which decrease the stresses at low depths to values very close to the free-field state. Soil heave after equilibrium due to application of cavity expansion stresses is shown in **Figure 4.28**.

Similarly, **Figure 4.29** and **Figure 4.30** demonstrate the implementation process for z=4.25 and 7.25m. Again some decrease compared to the cavity expansion theory is observed (mostly for the vertical stresses), however it is now less pronounced, while for the case z=7.25m horizontal stresses are grossly equal to the analytical methodology.

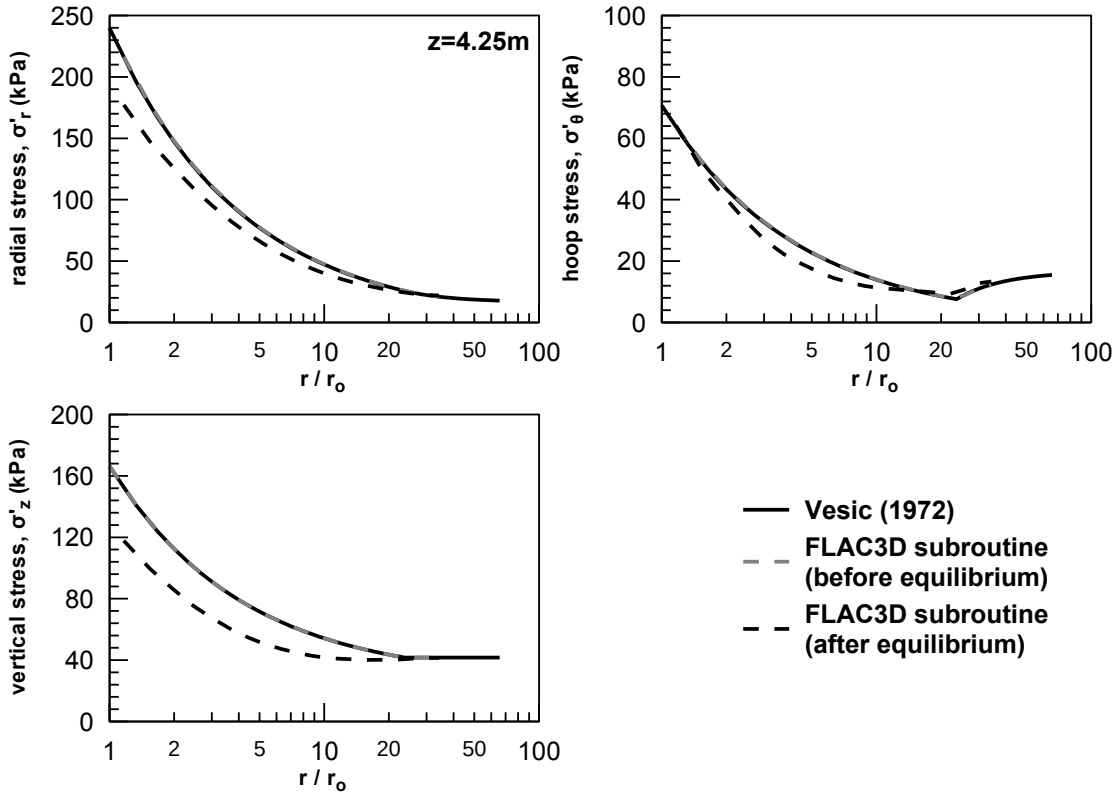

Figure 4.29: Implementation of Vesic's methodology in the numerical p-y analysis (D_r=50%, d_{cav}=10cm, z=4.25m)

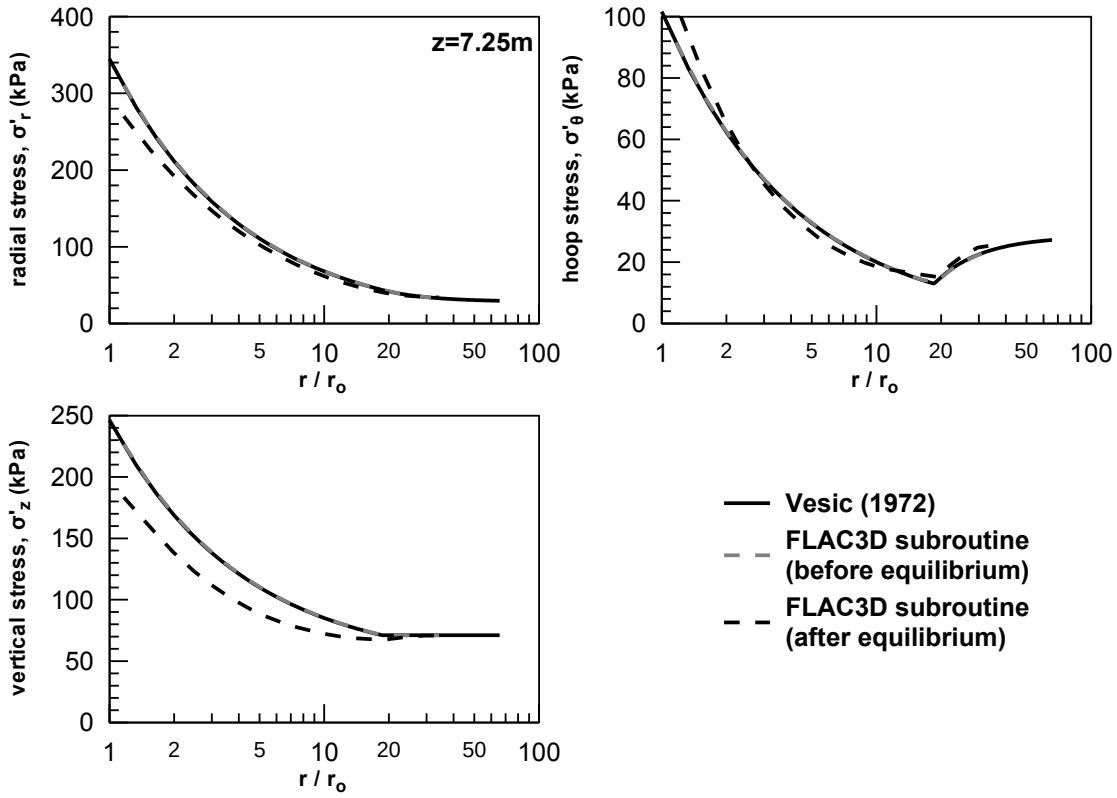

Figure 4.30: Implementation of Vesic's methodology in the numerical p-y analysis (D_r=50%, d_{cav}=10cm, z=7.25m)

4.9 Numerical Verification of the semi-analytical procedure

As described earlier, the procedure by which cavity expansion stresses are implemented manually in the model was necessary for two (2) reasons:

- Numerical simulation of soil radial displacement as a result of pile installation is avoided, resulting in significant gain in computational time
- Elimination of boundary effects in simulations of cavity expansion requires an enormously large grid size, which makes the numerical simulation impossible.

However, in order to verify the results of the proposed procedure, an analysis that simulated radial displacement of the soil as a result of installation of a 1cm thick open-ended pile, as well as subsequent lateral loading to calculate p-y curves, was performed. The case of d_{cav}=1cm, was selected since it requires the minimum computational effort. Note that completion of the analysis takes approximately a seven-day period time. The scope of the simulation is two-fold:

- Verify that the implementation using Vesic's analytical methodology yields stress values close to the results of the numerical analysis
- Ensure that the p-y curves resulting from the simplified procedure, which is the basic topic of the present thesis, do not deviate significantly compared to a full cavity expansion analysis.

The grid size requirements, as determined in **Figure 4.14**, correspond to a 30cm expansion and, hence, are overconservative for the case simulated herein. Based on a similar procedure, but for d_{cav}=1cm, the required length was specified to 50m or 83 pile diameters, which leads to a 100x50m grid. The mesh built for the full simulation of cavity expansion is shown in **Figure 4.31**. Note that apart from the size of the grid, all other parameters (interface properties, zone discretization e.t.c) were kept the same as in the p-y simulation described in the previous chapter.

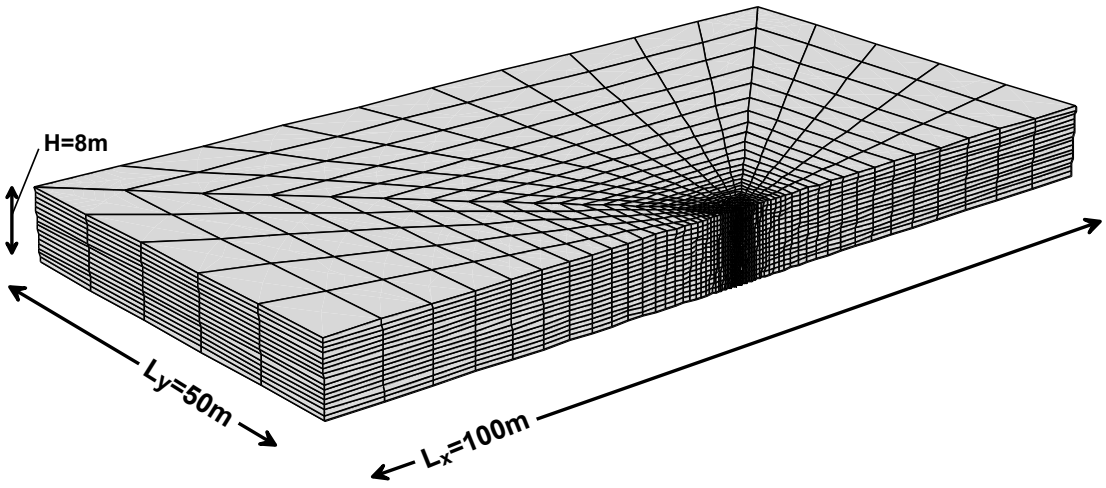

Figure 4.31: Layout of the grid used for the full simulation of soil expansion due to installation of an 1cm thickness open-ended pile.

Analysis is performed in two (2) stages, shown in **Figure 4.32**:

- Application of radial displacement d_{cav}=1cm at the soil-pile interface to simulate soil movement as a result of pile installation (**Figure 4.32a).**
- Application of uniform horizontal displacement at the pile to estimate p-y response of the soil (**Figure 4.32b**).

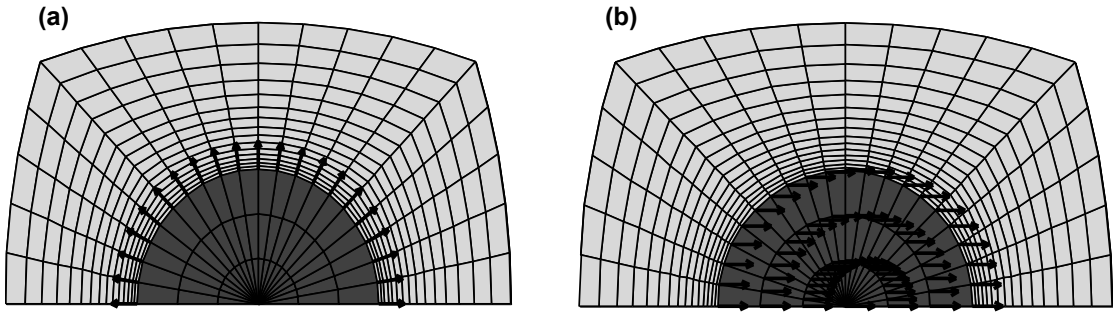

Figure 4.32: Detail of the top view of the model: (a) Application of radial displacement to simulate installation (b) Lateral loading of the pile to evaluate p-y response

Soil response after pile installation.- After the first stage of the analysis is completed, soil response is evaluated in terms of radial (σ'_r), circumferential (σ'_θ) and vertical (σ'_z) stresses, for various depths along the length of the pile. Results from the full numerical analysis of pile installation are compared with Vesic's analytical solution, as well as with the case where modified stresses are implemented manually in the model (paragraph 4.8), in **Figure 4.33** through **Figure 4.35**.

For small depths (**Figure 4.33a**), results from the numerical analysis (grey dashed line) deviate significantly from Vesic's predictions (black continuous line), while they are fairly consistent with the case of manual implementation (black dashed line). This is attributed to the soil heave that occurs near the soil surface, which is not taken into account in Vesic's theory, but it is captured during the implementation procedure (as described in the previous paragraph). However, numerical stresses appear to be larger than the manually implemented in an area very close to the pile-soil interface. This deviation is local and most probably attributed to the friction between the pile and the soil.

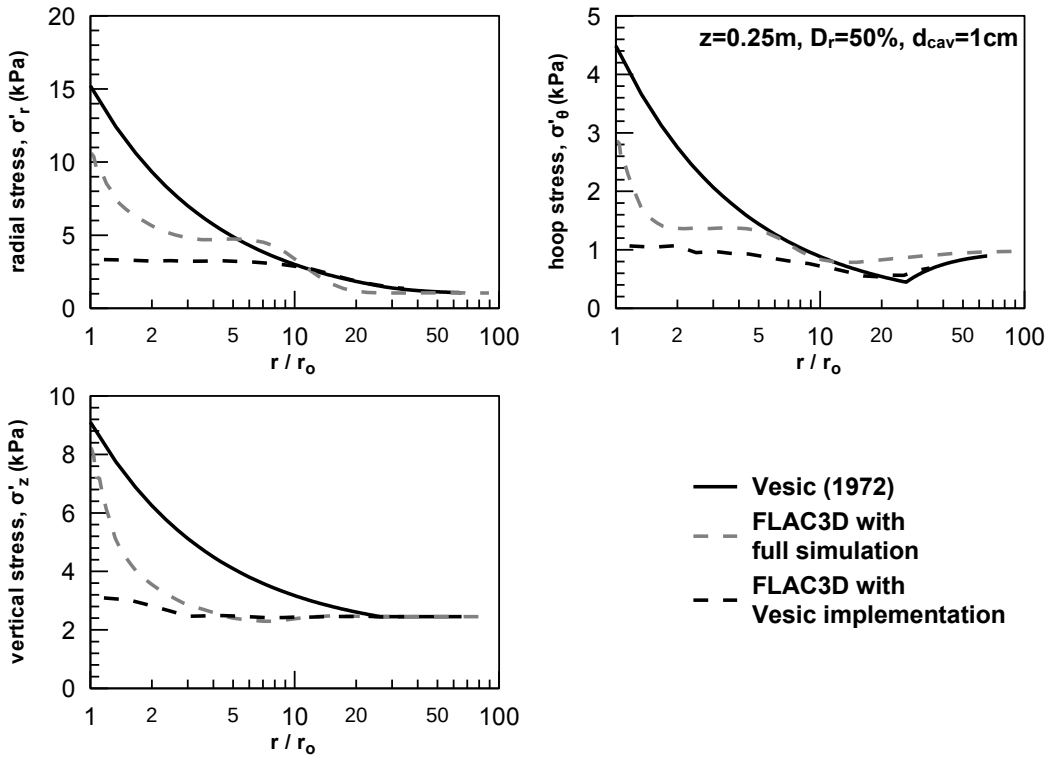

Figure 4.33: Comparison between analytical, manually implemented and numerical stresses after pile installation at depth z=0.25m (D_r=50%, d_{cav}=1cm)

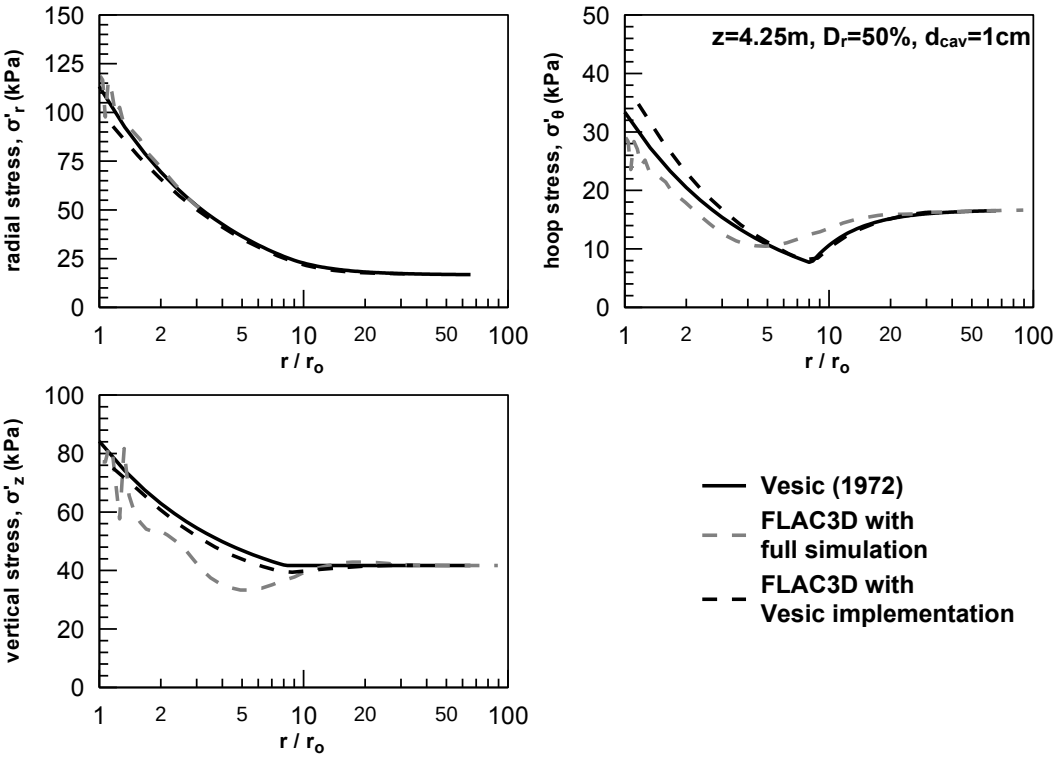

Figure 4.34: Comparison between analytical, manually implemented and numerical stresses after pile installation at depth z=4.25m (D_r=50%, d_{cav}=1cm)

For medium and large depths (z=4.25 and 7.25m), the comparison between all cases is fairly good, especially for horizontal stresses (σ'_r and σ'_θ). From the variation of hoop stresses, it is observed that the analytical method slightly overestimates the size of the plastic region, a drawback of the analytical method also observed in the pie slice cavity expansion tests (**Figure 4.20**). As for vertical stresses, the analytical method appears to capture with fair accuracy the values at the soil-pile interface, while for larger radial distances it overpredicts them. This stems from the fact that the analytical method does not account for σ'_z values lower than the in-situ, as well as changes in vertical stress outside the plastic zone. In addition, the statistical analysis performed in the previous paragraph focused on correlating the values of Poisson's ratio (and hence σ'_z) near the interface and not in large distances.

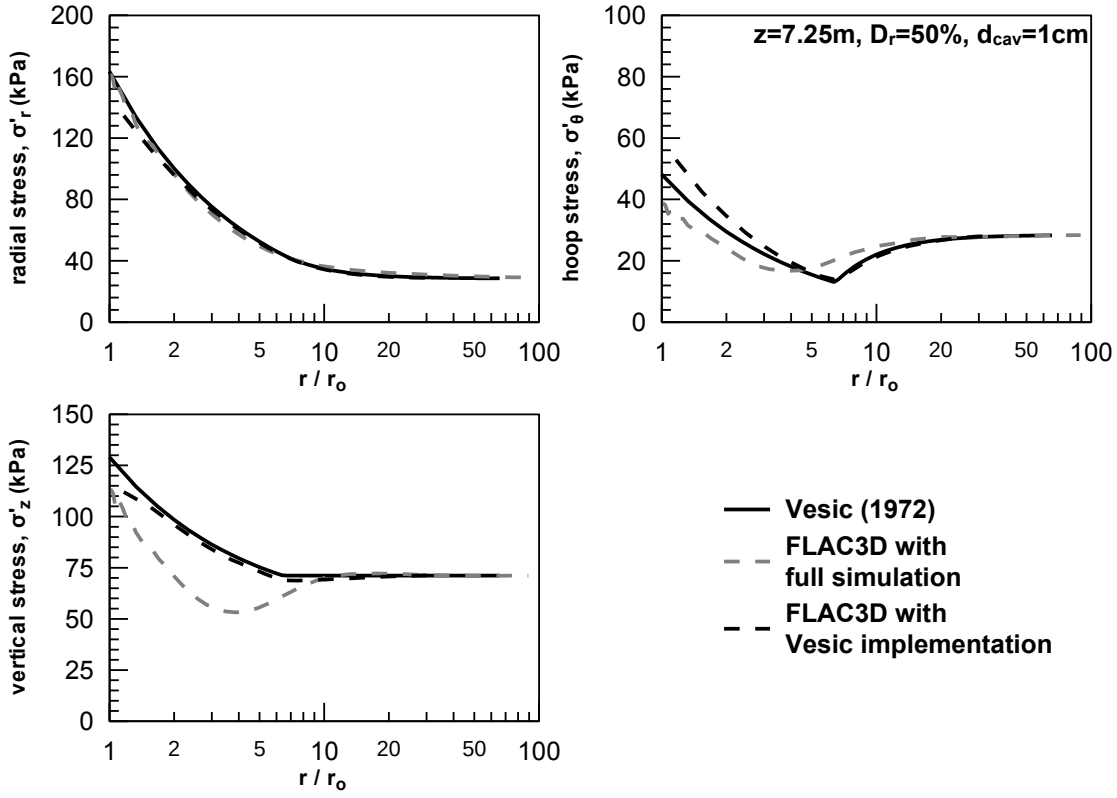

Figure 4.35: Comparison between analytical, manually implemented and numerical stresses after pile installation at depth z=7.25m (D_r=50%, d_{cav}=1cm)

Soil response after lateral pile movement.- The effect of the simulation of pile installation on predicted p-y response of the soil is illustrated in **Figure 4.36** in terms of p-y curves for various depths along the pile. The black line corresponds to the case

where Vesic's method is used to manually implement modified stresses, while the grey line corresponds to the numerical analysis where installation was simulated as applied radial displacement at the soil-pile interface. It can be observed that for small depths the two approaches yield very similar results, while, as depth increases, the analytical procedure appears to somewhat overestimate the response by approximately 10-15%. However, given the uncertainties involved in the analytical approach (accuracy of Vesic's methodology, modifications during the implementation process), as well as the difficulties in performing analyses to numerically simulate installation (extremely large computational time), this agreement can be considered satisfactory.

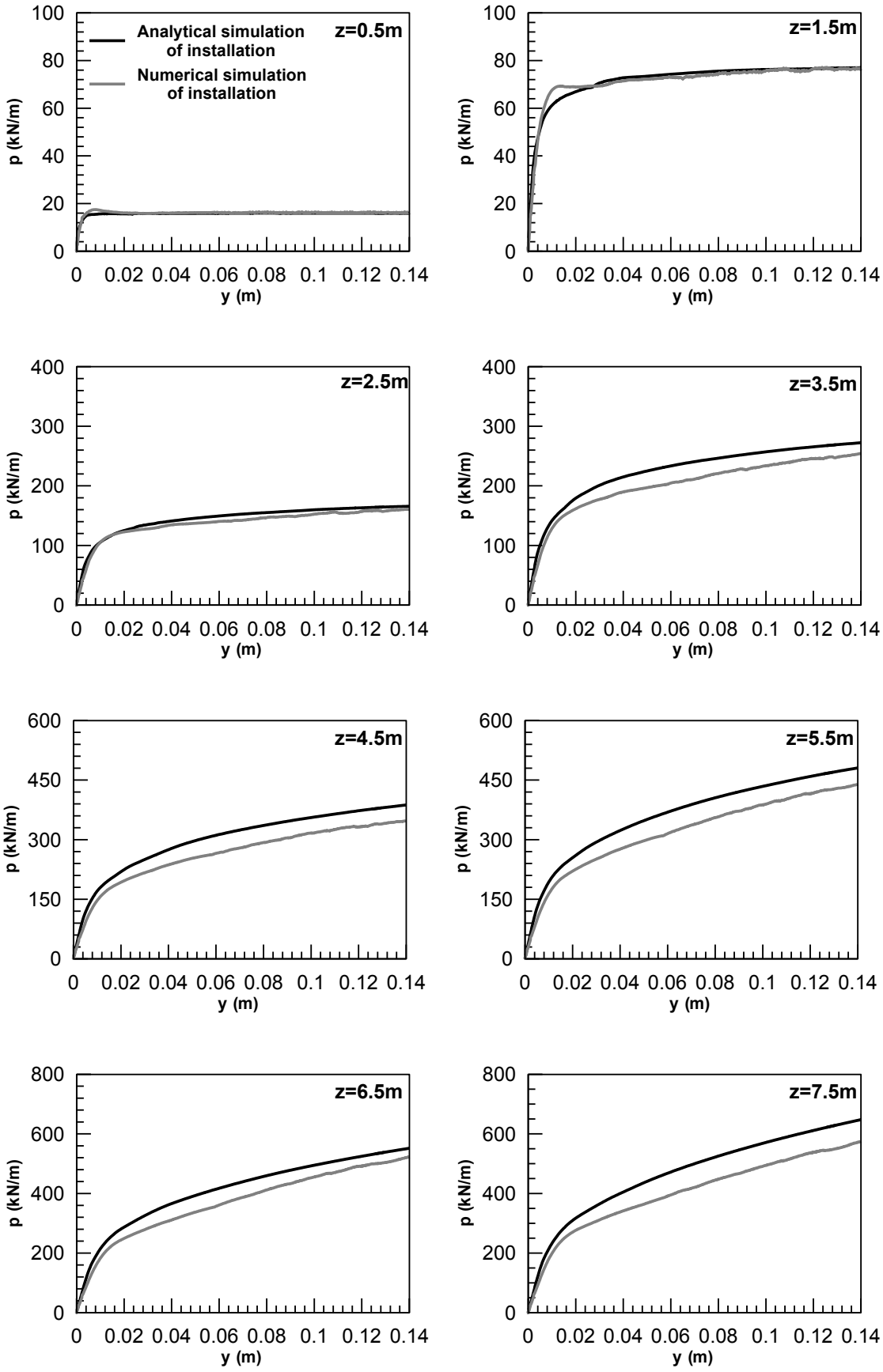

Figure 4.36: Comparison of p-y curves evaluated after analytical and numerical simulation of pile installation

4.10 Conclusions

The present chapter discussed the effects of pile installation on the stress field in the soil surrounding the pile, and ended up with a methodology by which modified stresses are manually implemented in the model prior to applying lateral displacement on the pile. In short, the following can be concluded:

- Pile installation causes the soil to displace similarly to the expansion of a cylindrical cavity, for the largest part of the pile (away from its tip and top section), while near the surface, a passive Rankine wedge is formed.
- Vesic's analytical method provides a rather simple, but quite accurate, tool to evaluate stresses around cavities, based on easily determined soil properties (E, ν, φ, γ). A major drawback of the method is the evaluation of the average volumetric strain (Δ), as well as the Poisson's ratio (ν) in the plastic zone.
- Numerical simulation of the cylindrical cavity expansion problem considering pie slices of soils revealed that Δ and ν can be analytically evaluated as follows:

$$\Delta\ \%\ = 1.6 \cdot \left(p_o / p_a \right) \cdot e^{-0.03 D_r\ \%} \tag{4.42}$$

$$\nu = \alpha \left[1 + D_r\ \%\ /100 \right] \cdot \left[0.20 + 0.13 \cdot \left(\frac{d_{cav}}{r_o} \right)^{0.16} \right] \tag{4.43}$$

where:

Δ(%): Average volumetric strain in the plastic zone
p_o: Mean effective stress prior to expansion
p_a: atmospheric pressure (=98.1kPa)
D_r(%): Relative Density of the soil
ν: Poisson's ratio at the wall of the cavity
d_{cav}: Magnitude of displacement caused by expansion
r_o: Radius of the cavity after expansion

- The simplicity of the aforementioned method allows for its programming and implementation in the FLAC3D model, prior to execution of the p-y analysis. Thus, the need to numerically simulate installation, which requires an order

of magnitude larger computational time (due to large grid size requirements), can be avoided.

- During implementation the kinematic inconsistency near the surface (cavity expansion vs. passive wedge) is identified by the code, which, in order to establish equilibrium, develops upward displacements (forming the passive wedge), that cause the stresses to decrease towards the values obtained from detailed 3D numerical analyses.
- Execution of a numerical analysis, in which installation was modeled as applied radial displacement at the soil-pile interface, revealed that implementation of modified stresses manually causes a 10-15% overestimation of the p-y response of the soil, which can be considered acceptable.

5

Parametric Investigation of p-y curves for Piles in Nonliquefied Sand

5.1 General

The numerical model for nondisplacement and displacement piles described in previous chapters is used in the following to investigate parametrically the effect of various parameters on the p-y response of piles in nonliquefiable cohesionless soils. Investigation includes the effect of soil relative density, pile diameter, installation method and type of loading, and aims at evaluating existing p-y methodologies, as well as shedding light on the uncertainties and the differences that exist among them, as described in chapter 2.

5.2 Analyses data and interpretation of results

The complete set of parametric analyses is summarized in **Table 5.1**. In total, thirteen (13) analyses were performed, for the input data and the assumptions listed below:

- Relative Density: D_r=20, 50, 90%
- Pile diameter: D=0.4, 0.6, 1.0m
- Thickness of Pile Wall (magnitude of cylindrical expansion): d_{cav}=0,1,10,30cm for D=0.6m and d_{cav}=0,1,13,20cm for D=0.4m.
- Type of loading: Uniform displacement along pile, head displacement with rotational constraint and head displacement without rotational constraint.

Table 5.1: List of parametric analyses and values of parameters investigated

α/α	D_r (%)	D (m)	d_{cav} (cm)	d_{cav}/D	Loading Type
1	50	0.6	0	0	Uniform Pile Displacement
2	20	0.6	0	0	Uniform Pile Displacement
3	90	0.6	0	0	Uniform Pile Displacement
4	50	0.4	0	0	Uniform Pile Displacement
5	50	1.0	0	0	Uniform Pile Displacement
6	50	0.6	1	0.017	Uniform Pile Displacement
7	50	0.6	10	0.170	Uniform Pile Displacement
8	50	0.6	30	0.500	Uniform Pile Displacement
9	50	0.4	1	0.025	Uniform Pile Displacement
10	50	0.4	13	0.325	Uniform Pile Displacement
11	50	0.4	20	0.500	Uniform Pile Displacement
12	50	0.6	0	0	Pile Head disp. (free rotation)
13	50	0.6	0	0	Pile Head disp. (fixed rotation)

For each one of the analyses, p-y curves were computed for various depths along the pile, while the various p-y components (k_{ini}, p_{ult}, nonlinear shape) were evaluated as follows:

- The nonlinear shape of the numerical p-y curve is assumed to be described by a hyperbola expressed as:

$$p = \frac{y}{\frac{1}{k_{ini} z} + \frac{y}{p_{ult}}} \tag{5.1}$$

Equation (5.1) can be restructured as follows:

$$\frac{y}{p} = \frac{1}{k_{ini} z} + \left(\frac{1}{p_{ult}} \right) y \tag{5.2}$$

In the y/p vs. y space, the above equation represents a straight line with slope $1/p_{ult}$ and y-intercept equal to $1/k_{ini}z$.

- Hence, the numerical data are plotted in the y/p vs. y space and k_{ini} and p_{ult} are evaluated from a straight fitting.
- Finally, for the estimated p_{ult} and k_{ini}, a hyperbola is constructed and plotted on top of the numerical p-y curve, to verify the initial assumption of a hyperbolic nonlinear shape.

The above procedure is schematically illustrated in **Figure 5.1**, for a typical analysis with D_r=50%, D=0.60m, d_{cav}=0, and depth of z=2.5m. In both figures numerical data and analytical predictions are shown with a black continuous and a grey dashed line respectively. **Figure 5.1a** demonstrates the procedure in the y/p vs. y space. Fitting of a straight line to the numerical predictions yielded k_{ini}=6500kN/m^3 and p_{ult}=188kN/m. The above values are used in **Figure 5.1b** to construct the hyperbola, which is in very good agreement with the numerical p-y curve.

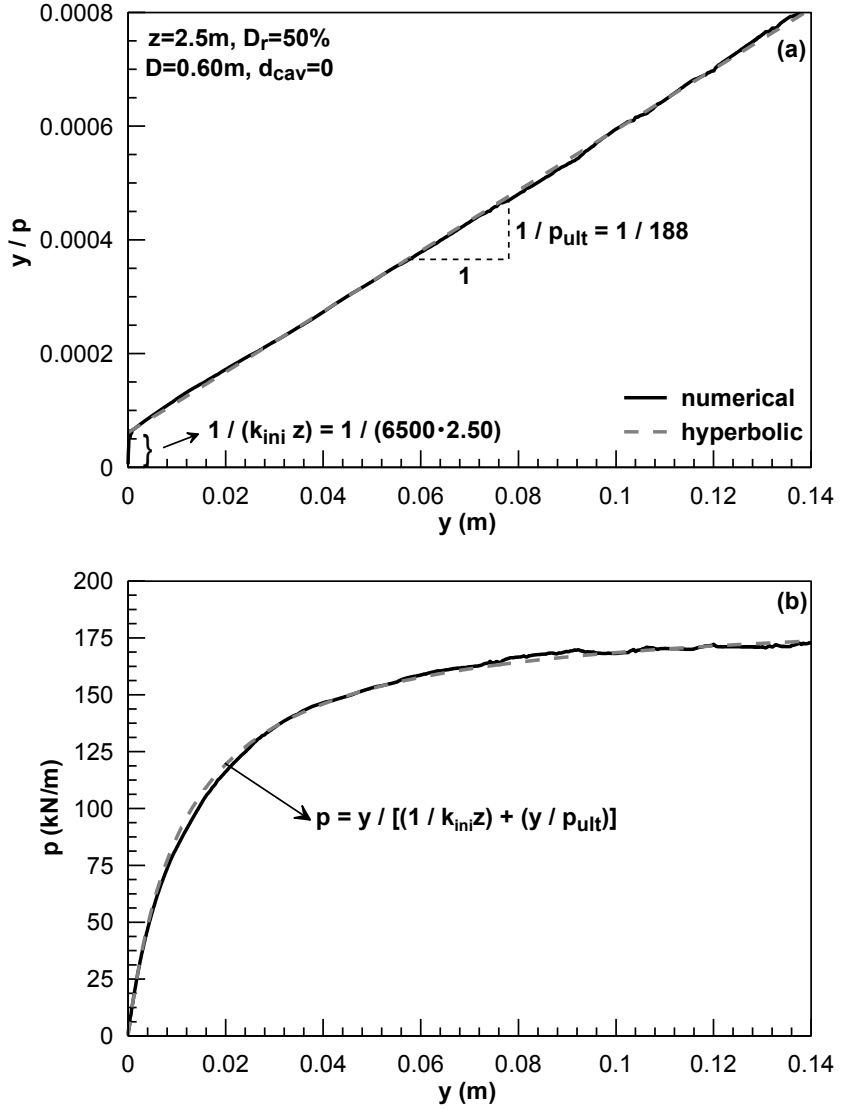

Figure 5.1: Evaluation of k_{ini} and p_{ult} by fitting a hyperbola in the numerical p-y curve (a) y/p-y and (b) p-y space.

The same procedure was repeated for every analysis and for eight (8) different depths along the length of the pile. Furthermore, values of k_{ini} and p_{ult} from each

analysis and for each depth were collected in a large database and were consequently used in the rest of the chapter to gain insight on the effect of the various parameters investigated, as well as to provide recommendations with regard to the evaluation of the p-y response of piles in sand.

5.3 Typical Results from the baseline analysis

The variation of the initial subgrade modulus coefficient k_{ini} and the ultimate soil resistance p_{ult} for the basic analysis with D_r=50%, D=0.60m and d_{cav}=0 is shown in **Figure 5.2a** and **b** respectively. Also plotted in these figures are the ranges suggested by the various analytical methodologies. Namely, for k_{ini} the values proposed by Terzaghi (1955), DnV (1980), Reese et al. (1974) and API (2002) are shown, while for p_{ult} the various lines refer to the methodologies by Reese et al. (1974), DnV (1980) and Hansen (1961). Note that recommendations from API (2002) and Reese et al. (1974) are plotted as a joint range since they yield very similar predictions. Also in **Figure 5.2b** p_{ult} is normalized against the diameter and the vertical effective stress, so that the comparison, especially for small depths, becomes more clear.

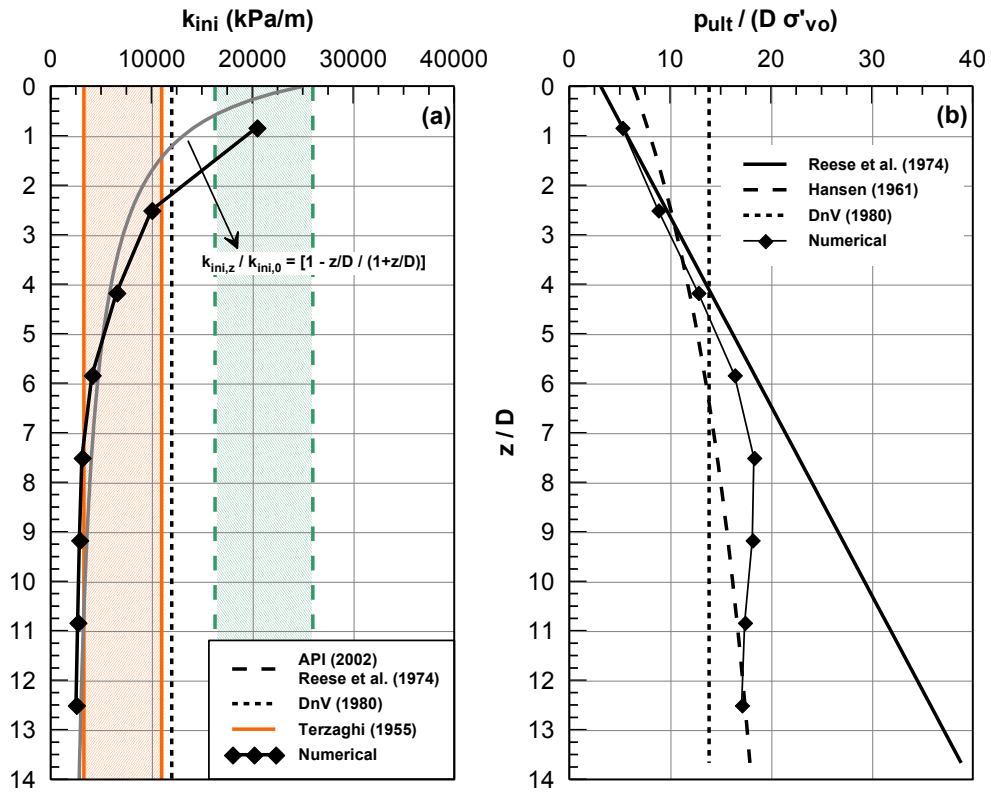

Figure 5.2: Variation of (a) coefficient of initial subgrade modulus k_{ini} and (b) ultimate soil resistance with depth from numerical analyses and analytical methodologies

Observation of the numerical results reveals that both k_{ini} and p_{ult} initially vary with depth (k_{ini} decreases and p_{ult} increases), but after a certain point they remain constant. For the case shown here, this change in the response occurs at $z/D \approx 6-7$ both for k_{ini} and p_{ult}. This depth, at which the response in terms of p_{ult} or k_{ini} changes, will be thereafter referenced as critical depth or $(z/D)_{cr}$.

Further examination of k_{ini} variation with depth leads to the following observations:

- Values of k_{ini} do not remain constant with depth, as the analytical methods suggest, but decrease.
- For depths smaller than the critical, values of k_{ini} are close to API's and Reese's recommendations, while for larger depths k_{ini} is closer to Terzaghi's recommendations.
- Variation of k_{ini} with normalized depth can be described by an equation of the following form (gray line in **Figure 5.2a**):

$$k_{ini,z} = k_{ini,0}\left(1-\frac{z/D}{1+z/D}\right) \tag{5.3}$$

where $k_{ini,0}$ is the value of the coefficient for $z \to 0$, that can be adequately approximated according to API's or Reese's recommendations.

Similarly, the following can be observed with regard to prediction of p_{ult}:

- For depths smaller than the critical $\left[z/D < z/D_{cr}\right]$ normalized p_{ult} increases linearly with depth, in good agreement with Reese's et al. (1974) analytical predictions.
- For $z/D > z/D_{cr}$ values of normalized p_{ult} remain practically constant with depth, indicating a response which is qualitative similar to what DnV, as well as the other analytical methods based on the passive pressure theory suggest (Broms, Zhang et al., Prasad and Chari e.t.c).
- Among the existing analytical methodologies, the numerical predictions for both small and large depths can be better approximated using Hansen's method.

Finally, it should be clarified that the critical depth, as defined herein, does not refer to the depth at which the mode of failure of the soil changes from wedge to plane

strain. However, for the basic analysis presented herein these two (2) depths appear to coincide, as indicated by the direction of the displacement vectors, shown in **Figure 5.3**. Namely, it can be observed from the figure that no upward displacement occurs below a depth of approximately 6-7 pile diameters below ground surface.

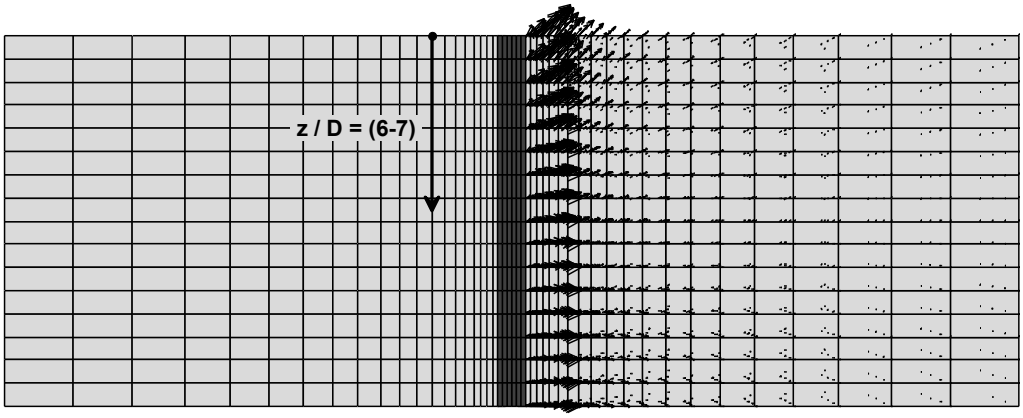

Figure 5.3: Displacement vectors for the basic analysis indicating change of failure mechanisms at z = (6-7)D

5.4 Effect of Relative Density, D_r

The effect of Relative Density on the p-y response of the soil was examined through three (3) numerical analyses for D_r=20, 50 and 90%, while the remaining parameters involved were equal to D=0.60m and d_{cav}=0. The resulting p-y curves for different depths are presented in **Figure 5.4**.

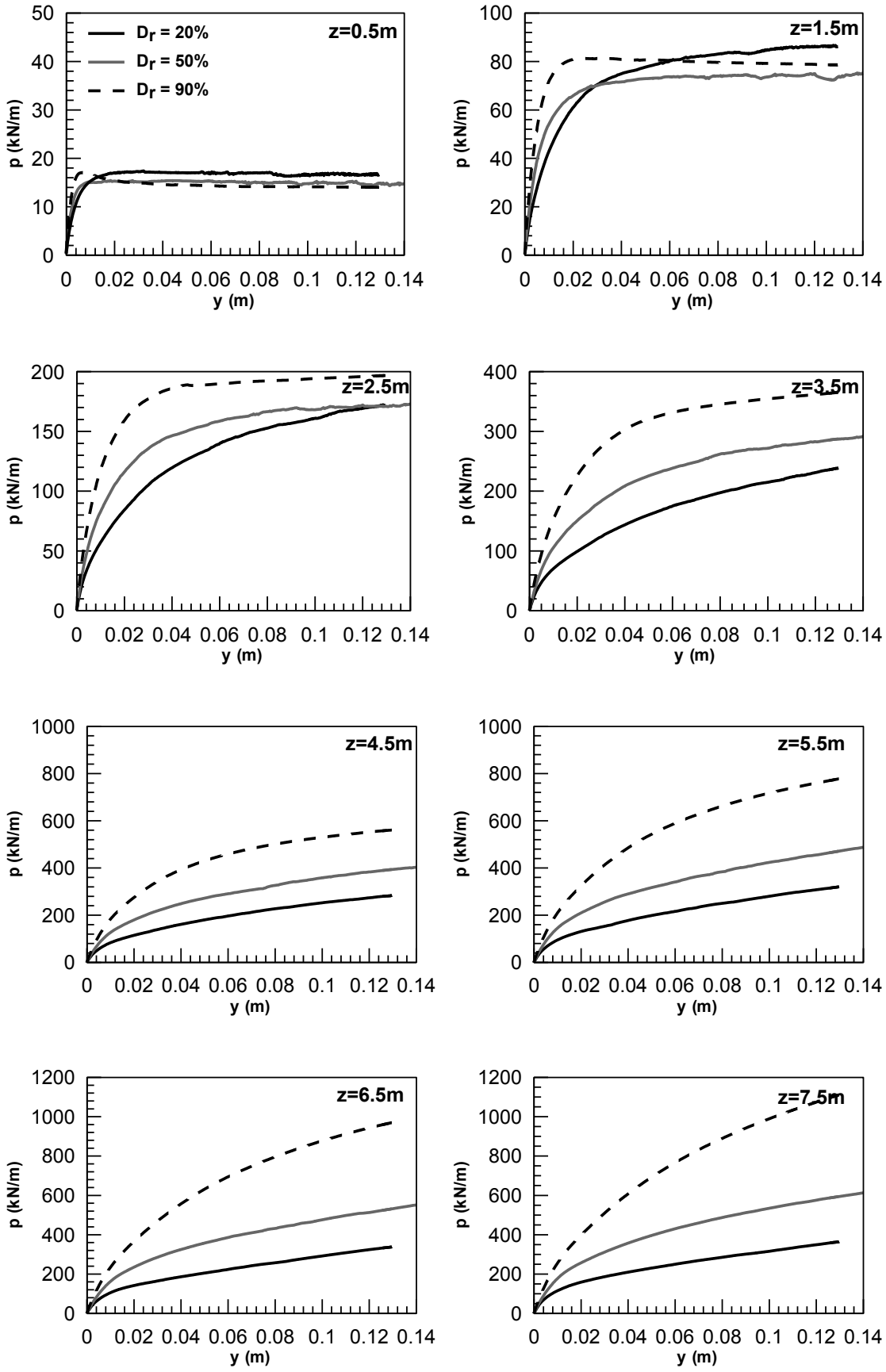

Figure 5.4: Numerical p-y curves for D_r=20,50,90% and various depths along the pile (D=0.60m, d_{cav}=0)

It can be observed that, for large depths (z>2.5m), the increase in soil Relative Density causes the ultimate resistance of the soil to increase as well. However, the response is not similar for depths less than 2.5m, where larger ultimate resistance values develop for more loose soils. This contradiction can be explained in terms of deformation mechanisms and depth in which the mode of failure changes.

Namely, **Figure 5.5** shows displacement vectors for each one of the three analyses with D_r=20, 50 and 90%. The direction of displacement vectors indicates that the depth at which transition between the wedge and the plane strain failure mechanism occurs, increases with relative density. Namely for D_r=20, 50 and 90%, this depth is approximately equal to 4, 6 and 10 diameters respectively. This means that for the depth of z=1.5m, for instance, ultimate resistance is determined based on a plane strain mechanism for D_r=20% and a wedge-type mechanism for D_r=90%. The former yields a larger p_{ult} than the latter, despite the large difference in the value of D_r, leading to the response shown in **Figure 5.4**.

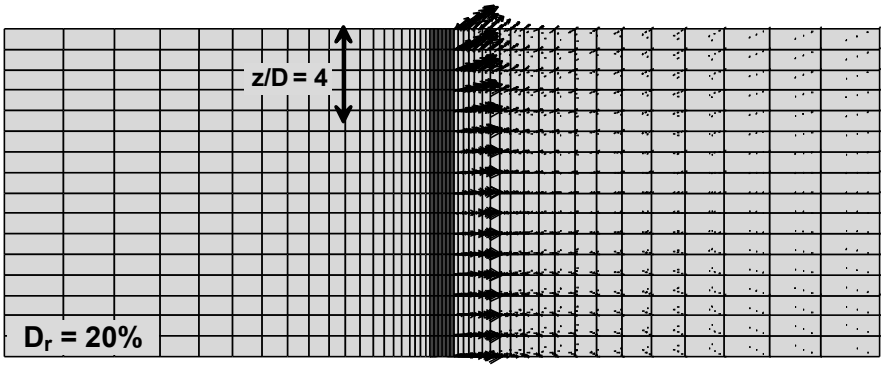

Figure 5.5a: Displacement vectors from the analyses with different Relative D_r=20%)

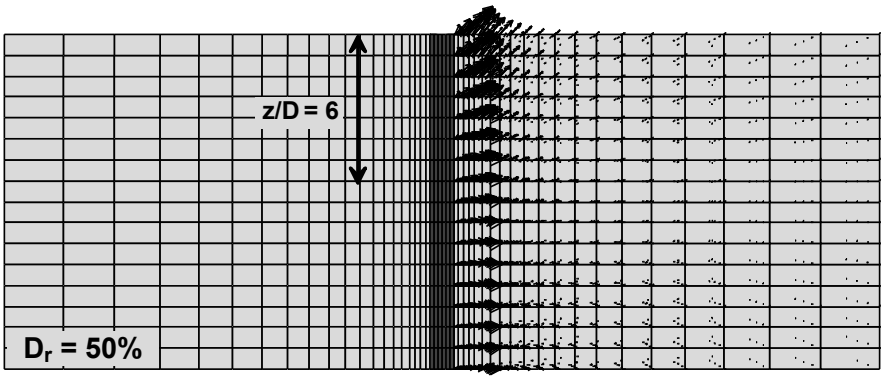

Figure 5.5b: Displacement vectors from the analyses with different Relative D_r=50%)

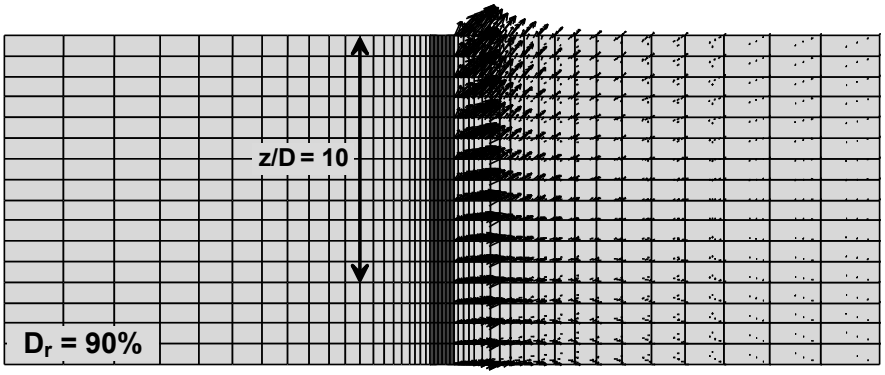

Figure 5.5c: Displacement vectors from the analyses with different Relative D_r=90%)

In **Figure 5.6** the different values for the critical depth are plotted versus the relative density of the soil. Note that $(z/D)_{cr}$ values are normalized with the corresponding value for D_r=50%. It can be observed that the variation can be expressed mathematically as follows:

$$z/D_{cr} = z/D_{cr,D_r=50\%} \cdot \left(\frac{D_r}{50\%}\right)^{0.6} \tag{5.4}$$

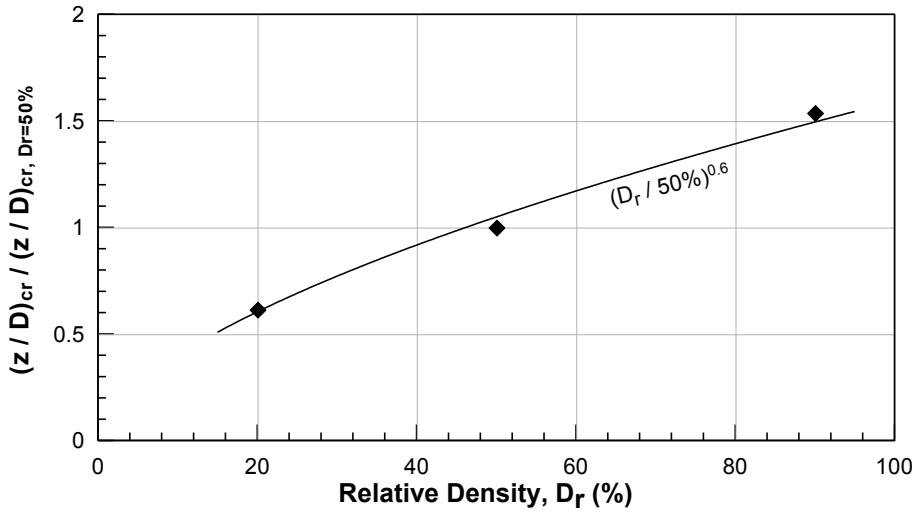

Figure 5.6: Variation of critical depth with Relative Density

These deformation patterns are reflected in the estimation of the initial subgrade modulus coefficient and the ultimate soil resistance, shown in **Figure 5.7a** and **b** respectively. Note that comparison between numerical and analytical k_{ini} and D_r values will be performed in subsequent figures separately for each D_r. The first thing

to observe is that critical depth increases with Relative Density. The former can be estimated to $(z/D)_{cr}$=4, 7 and 11 for D_r=20,50 and 90%. Again, $(z/D)_{cr}$ is very close to the depth at which the failure mode changes. Furthermore, **Figure 5.7a** shows that k_{ini} increases with relative density, while the variation with depth is practically the same for all three cases (k_{ini} increases until z_{cr} and remains constant thereafter). Similarly, for the normalized p_{ult}, **Figure 5.7b** shows that, irrespective of D_r, it increases approximately linearly with depth until $z=z_{cr}$, where it reaches an ultimate value. As for the relative effect of D_r, for small depths, it is shown that p_{ult} values are close with each other. This is a result of different failure mechanisms, as explained previously. However, for large depths, where the soil fails in plane strain mode in all cases (z/D>10), results clearly indicate that p_{ult} increases with D_r.

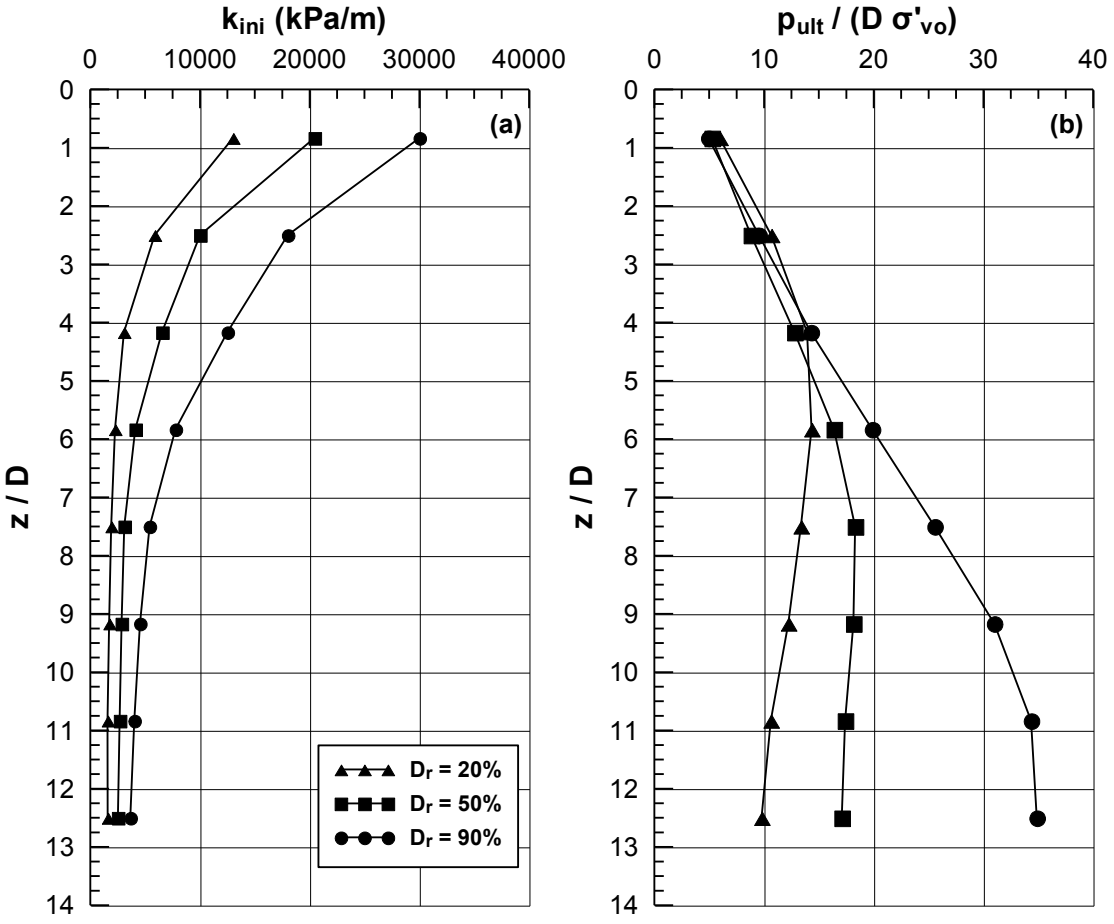

Figure 5.7: Variation of (a) coefficient of initial subgrade reaction, k_{ini}, and (b) normalized ultimate resistance with depth, $p_{ult}/D\sigma'_{vo}$ from numerical analyses with D_r=20,50 and 90%.

Comparison between the numerical and the analytical k_{ini} predictions is shown in **Figure 5.8a** and **b**. Note that the various analytical p_{ult} methods were applied for soil friction φ=31 °, 33 ° and 37° for D_r=20, 50 ,90% respectively, based on the results of numerical triaxial tests described in Chapter 2. For D_r=20%, **Figure 5.8a** indicates that for large depths, numerical values are better approximated with Terzaghi's recommendations, while for small depths k_{ini} increases significantly and reaches values well above the suggestions by Reese or API. Similarly, for D_r=90% k_{ini} values are close and slightly larger to Terzaghi, while, for small depths, they fall within the range suggested by Reese. Note that for this high D_r value, API's values were estimated through extrapolation, since the guidelines do not provide k_{ini} estimates for D_r larger than 80%, and hence should be used with caution.

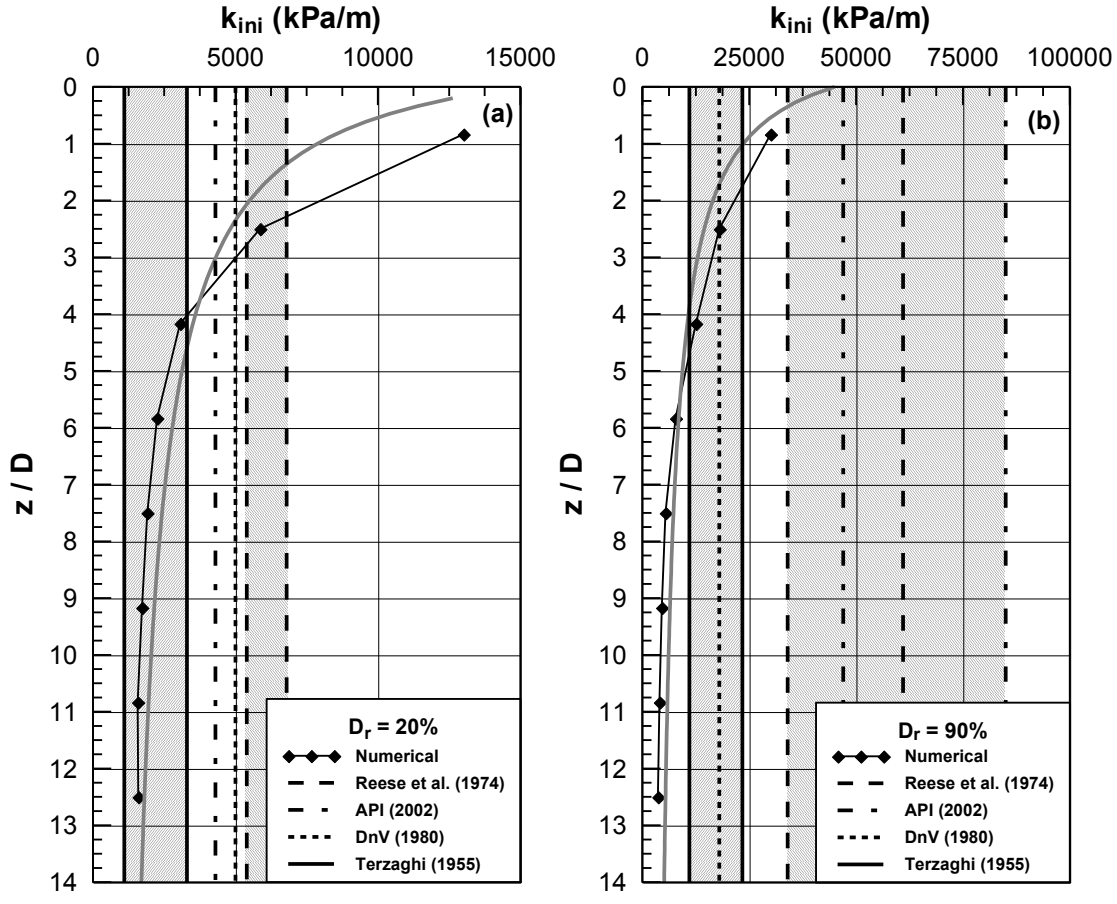

Figure 5.8: Comparison between numerical and analytical values of the coefficient of initial subgrade modulus k_{ini} (a) D_r=20% (b) D_r=90%

In a similar fashion, results for ultimate soil resistance are summarized in **Figure 5.9**. For both cases (D_r=20 and 90%) the response is qualitatively very similar with the

basic analysis presented previously. For D_r=20%, shown in **Figure 5.9a**, it can be observed that for $z<z_{cr}$, p_{ult} is slightly larger compared to Reese's or Hansen's expressions, while for $z>z_{cr}$, it is better approximated by the values recommended by DnV or Hansen.

For D_r=90%, shown in **Figure 5.9b**, numerical data are slightly below Reese's recommendations for $z<z_{cr}$ and deviate significantly as depth increases. As for the other two (2) methods, they seem to overestimate p_{ult} for small depths (~5D), and underestimate it thereafter. However, Hansen's method, which takes into account the variation of normalized p_{ult} with depth, provides an overall better approximation of the numerical results for all depths.

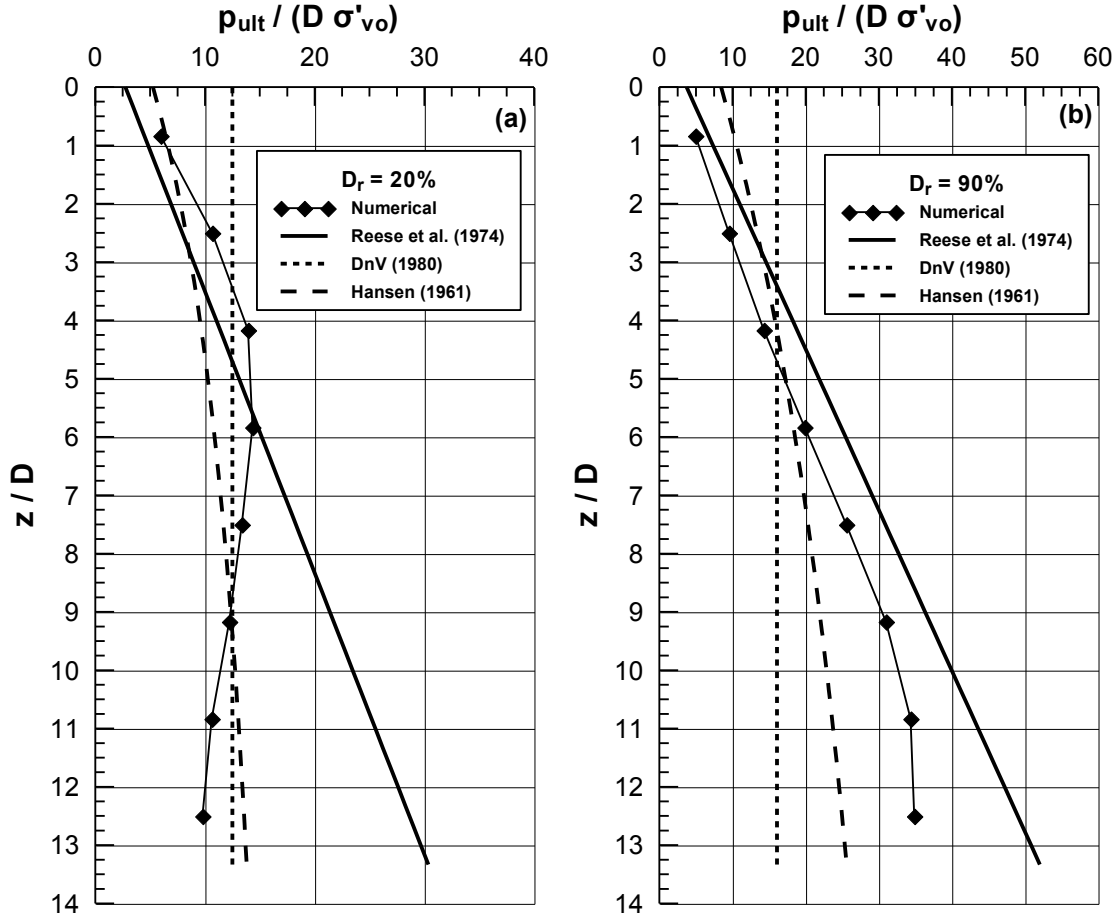

Figure 5.9: Comparison between numerical and analytical values of the ultimate soil resistance p_{ult} (a) D_r=20% (b) D_r=90%

In order to demonstrate the relative effect of D_r on k_{ini} and p_{ult}, and investigate how accurately it is captured by analytical methodologies, the plots shown in **Figure 5.10** were drawn. Namely, the black symbols in the figure correspond to numerical k_{ini} or p_{ult} values for three different depths along the pile. Note that numerical values are normalized against the respective values for D_r=50%, for the relative effect to be more clear. Similarly, normalized trends based on analytical recommendations are plotted. It can be observed that in terms of k_{ini} all the analytical methodologies presented can capture the relative effect of D_r, with the suggestions by DnV yielding a much better quantitative agreement. The trends observed in this figure, in combination with the observation from the baseline analysis can yield the recommendations shown in **Table 5.2** for the estimation of k_{ini} at the ground surface with respect to the relative density of the soil.

Table 5.2: Variation of initial subgrade modulus coefficient at the ground surface ($k_{ini,0}$) with relative density

Relative Density	**Loose**	**Medium**	**Dense**
$k_{ini,0}$ (kPa/m)	18000	30000	45000

As far as p_{ult} is concerned, this comparison indicates that the effect of D_r can be captured consistently by all three (3) methods only for intermediate depths. For large depths, analytical methods appear to underestimate the effect of D_r (for small D_r analytical values are larger than numerical, while for large D_r analytical values are smaller than numerical). Finally, for small depths, all three (3) methods predict increase in soil resistance with D_r, and do not capture the mechanism of different failure modes, described above, that yields the inversed trend followed by the numerical results.

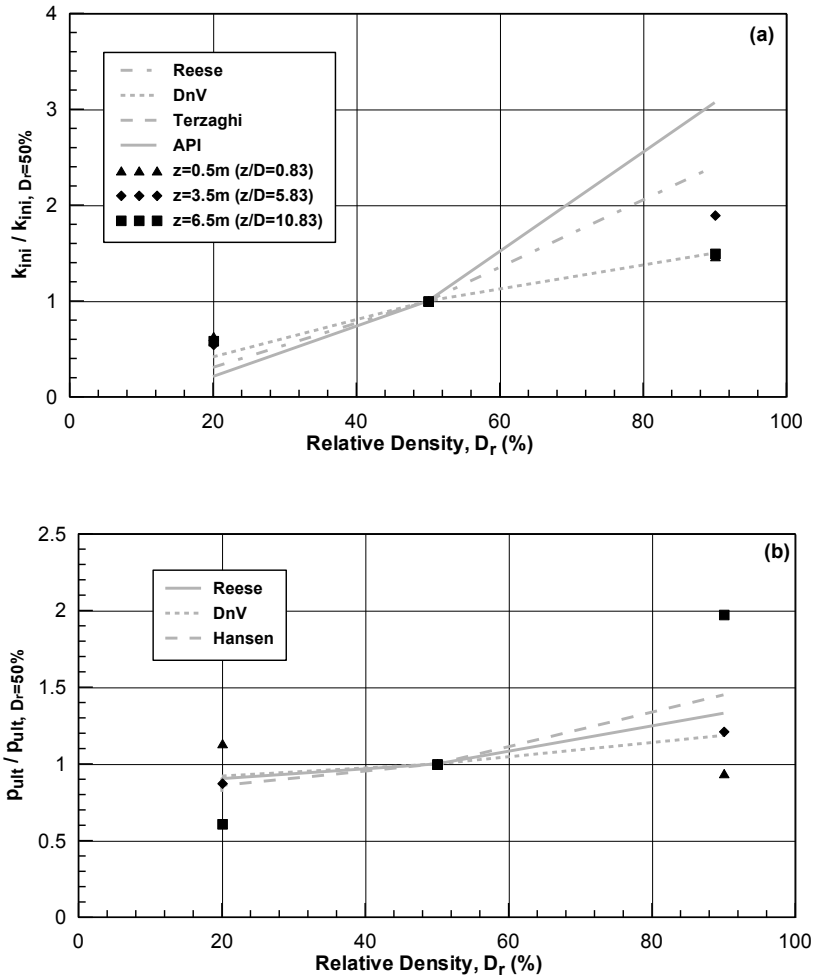

Figure 5.10: Evaluation of relative effect of D_r based on analytical recommendations in terms of (a) initial subgrade modulus coefficient and (b) ultimate soil resistance

5.5 Effect of Pile Diameter, D

As described at the beginning of this chapter, the effect of pile diameter was examined through a set of three (3) analyses, for D=0.40, 0.60 and 1.0m. Note that, in order to eliminate boundary effects, the size of the mesh used in each analysis was scaled according to the diameter. As a result, for the D=0.40m case all three mesh dimensions were reduced by 0.4/0.6=67% compared to the D=0.60m case. Similarly, for the D=1.0m analysis, the mesh was 66.7% larger. Comparison in terms of p-y curves is shown in **Figure 5.11**. Note that for D=0.40m, mesh resizing reduced the height of the model to 5.0m, and hence p-y curves are not presented for depths larger than that. Based on these curves it can be observed that pile diameter mainly affects the ultimate resistance of the soil, as most analytical methods suggest, but also has a

non-negligible effect on the initial stiffness of the curve, an effect which is not included in existing methodologies.

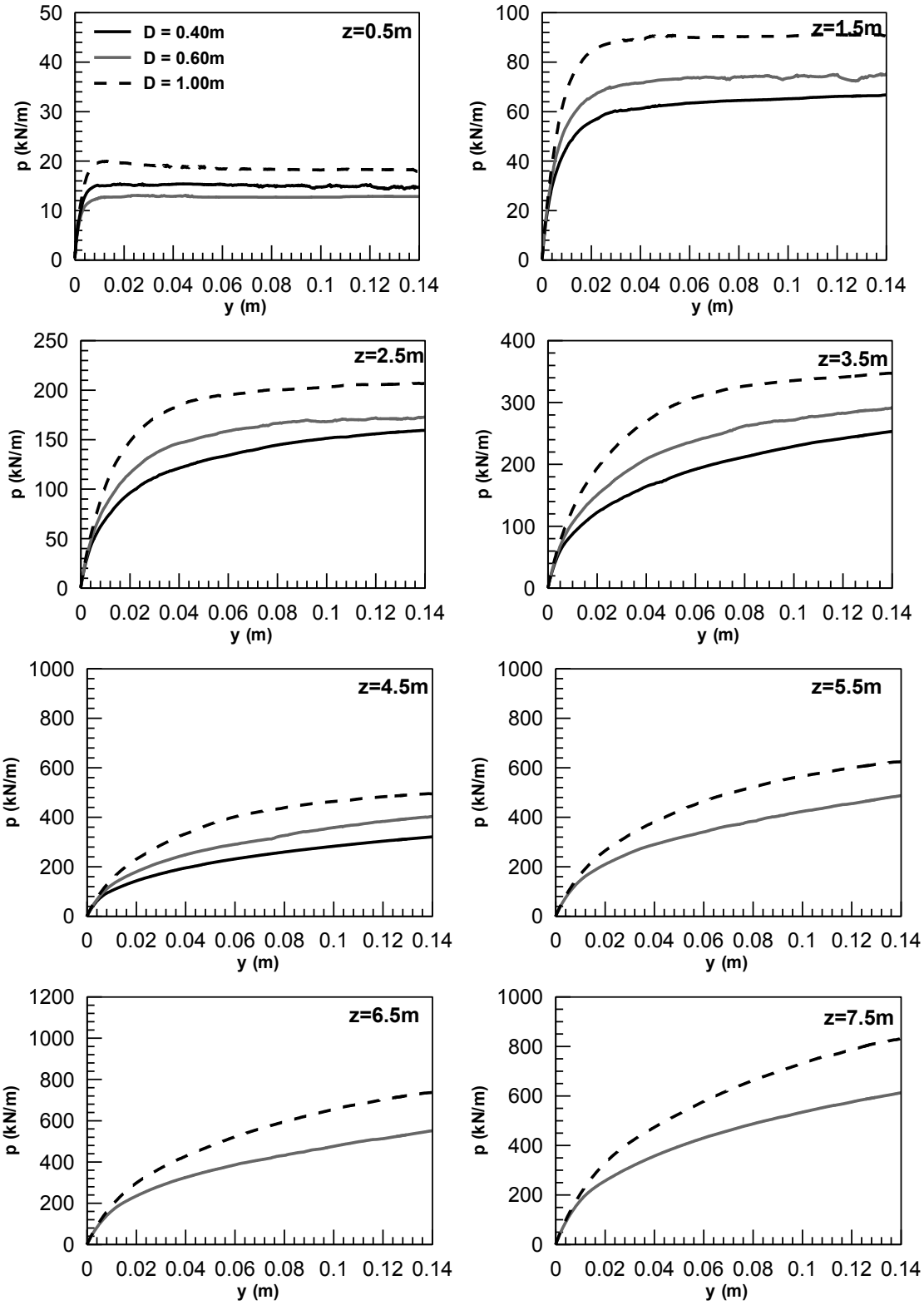

Figure 5.11: P-y curves for different pile diameters and various depths

A more thorough investigation on the influence of pile diameter is performed in **Figure 5.12** which shows values of the initial subgrade modulus, k_{ini}, as a variation with depth (**Figure 5.12a** for absolute and **Figure 5.12b** for normalized depth). Also plotted are the analytical recommendations, which are identical for all three (3) cases, since existing recommendations do not account for diameter effects. Variation with depth for all three (3) cases follows the trend already observed in previous analyses, i.e. a decreasing initial section followed by one in which k_{ini} remains constant. During the second part k_{ini} is not affected by diameter. However, during the initial decreasing part, larger diameters result in larger stiffnesses (a trend which is more clear in **Figure 5.12a)**. This type of response comes in contrast with analytical methodologies which, in their majority, assume no effect of pile diameter on k_{ini}. In any case it should be noted that effects of pile diameter on k_{ini} have been a subject of investigation in many studies (Vesic, 1961; Ashford and Juirnarongrit, 2006; Fan and Long, 2005; Carter, 1984; Ling, 1988; Lesly and Wiemann, 2006), which, however, do not end up to a common conclusion. Namely the three (3) first predict negligible influence, while the others predict a strong dependence.

Finally, the depth at which response changes also depends on the diameter, namely it is approximately equal to 9, 7 and 5 pile diameters for D=0.4, 0.6 and 1.0m. As far as analytical suggestions are concerned, numerical values are closer to the lower value of Terzaghi's recommendation for $z>z_{cr}$, while for small depths they approach the values proposed by Reese and API.

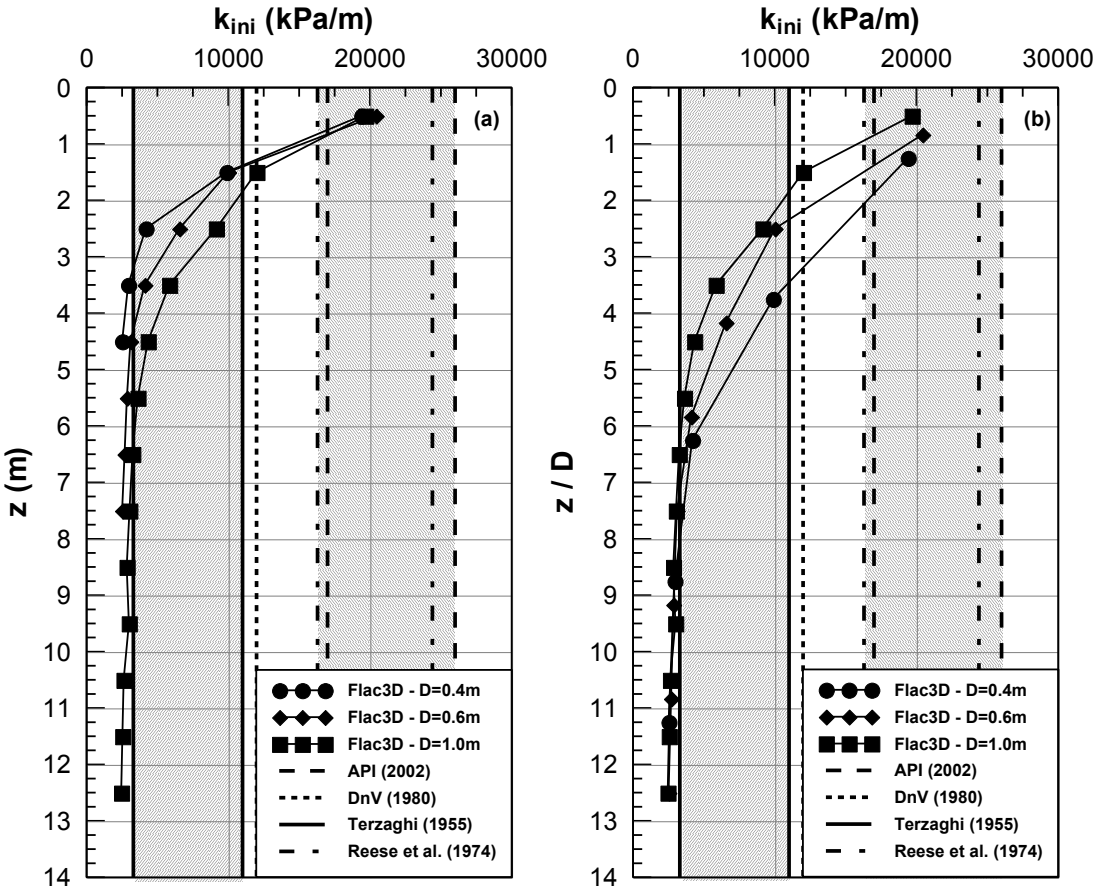

Figure 5.12: Effect of Pile diameter on p-y response: Initial Subgrade Modulus with (a) depth and (b) normalized depth for D=0.4, 0.6 and 1.0m

As discussed earlier, pile diameter also affects ultimate resistance of the soil. **Figure 5.13a** shows absolute p_{ult} values as a function of depth, where it can be concluded that soil resistance increases with diameter, although this effect cannot be clearly evaluated especially for small depths. To clear the view p_{ult} is normalized in **Figure 5.13b** against the diameter (D) and the in-situ vertical stress (σ'_{vo}), while depth is normalized against D. Again two response patterns can be identified: Initially p_{ult} increases linearly with depth, while after the critical depth is reached, it stabilizes to an ultimate value. These critical depth values can be easily estimated from the curves in **Figure 5.13b** as $(z/D)_{cr}$ = 9,7 and 5 for D=0.4, 0.6 and 1.0m respectively. This variation is graphically presented in **Figure 5.14**, where it can be observed that it can be expressed by an equation of the following form:

$$z/D_{cr} = z/D_{cr,D=0.6m} \cdot \left(\frac{D}{0.6m}\right)^{-0.64} \qquad (5.5)$$

Note that these estimates are consistent with the depth values at which response changes in terms of k_{ini}, as discussed in the previous paragraph. Finally, as for the relative effect of the pile diameter, it can be considered small, or even negligible, for depths lower than the critical, and more pronounced for larger depths. Note that, since analytical recommendations vary with pile diameter, it is not possible to include them in the same figure.

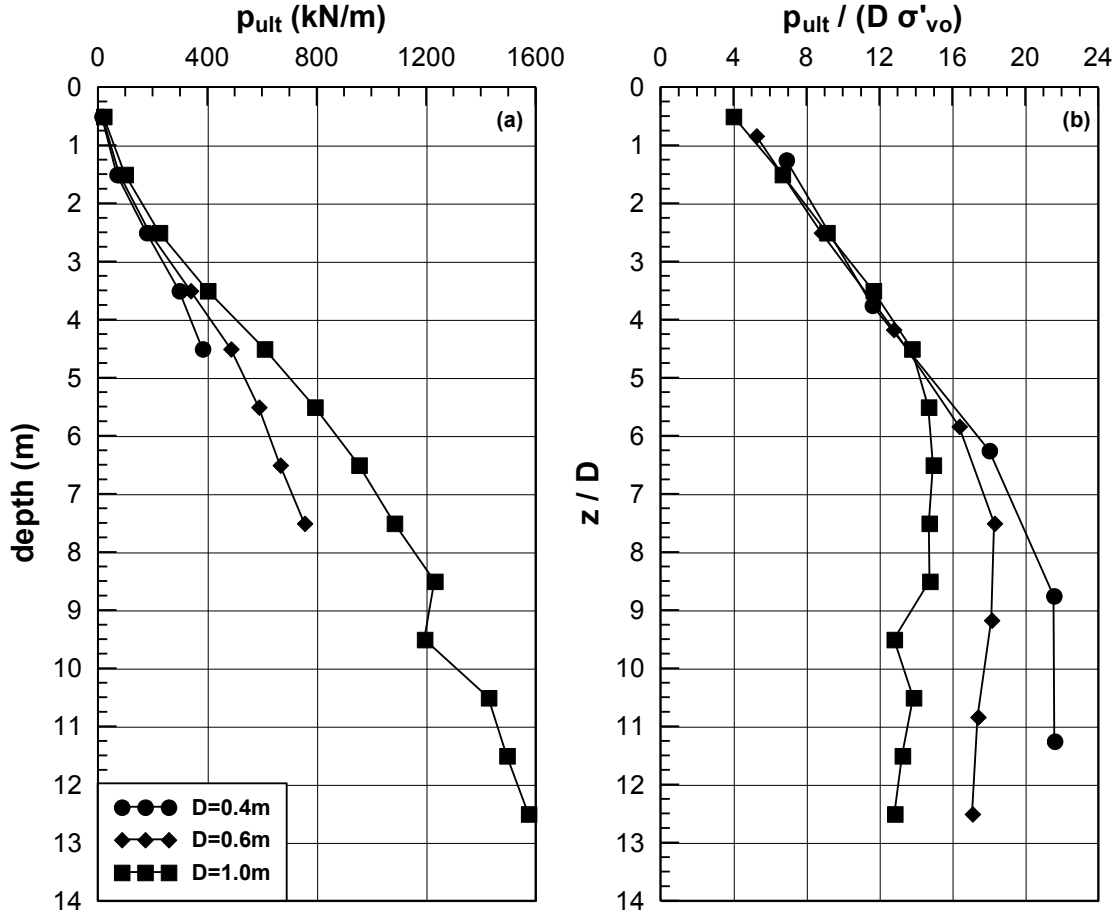

Figure 5.13: Effect of pile diameter on p-y response: (a) Ultimate resistance with depth and (b) Normalized resistance with normalized depth for D=0.4, 0.6 and 1.0m

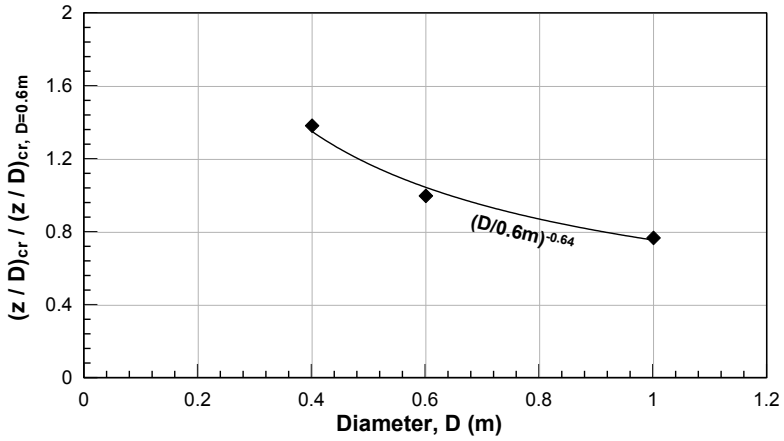

Figure 5.14: Variation of critical depth with pile diameter

Hence, comparison between numerical and analytical estimates is performed separately in **Figure 5.15a** and **Figure 5.15b** for D=0.40m and D=1.0m respectively. A first conclusion from both figures is that none of the analytical methods differentiates between the two (2) different response patterns, predicted from the numerical results. At this point it should be mentioned that Reese's method does predict two (2) different deformation patterns, a wedge-shaped pattern with linear $p_{ult}/D\sigma'_{vo}$ variation with depth and a plane strain in which the variation of $p_{ult}/D\sigma'_{vo}$ is constant. However, transition between the two (2) mechanisms occurs at much larger depths compared to the limits of the figure, and hence is not visible. Furthermore, the two (2) figures indicate that numerical results fall below analytical predictions for small depths, while they outreach them as depth increases. The only exception to this is Reese's method which, for D=0.40m, lays constantly above the numerical predictions. Overall it can be concluded that numerical results can be better approximated again using Hansen's methodology.

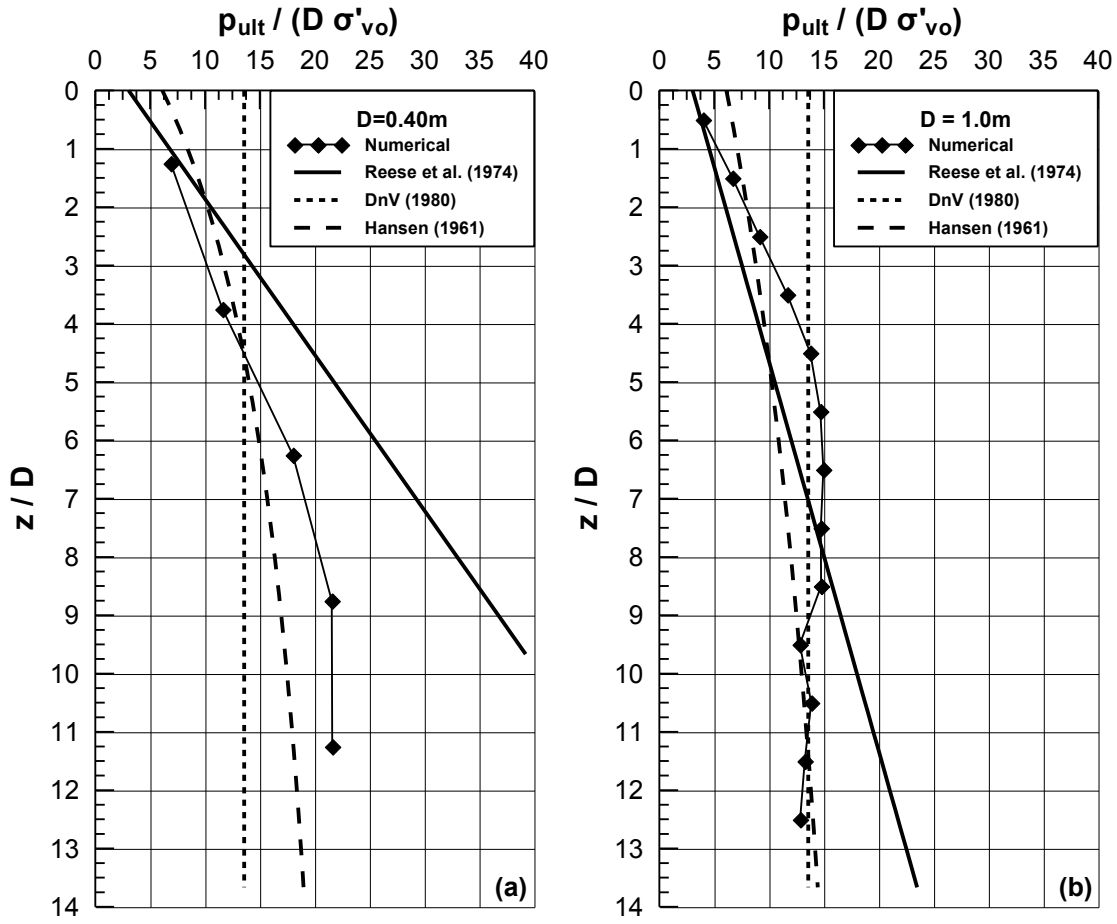

Figure 5.15: Effect of Pile diameter: Comparison between numerical and analytical ultimate soil resistance values (p_{ult}) for (a) D=0.40m and (b) D=1.0m.

In addition, evaluation of the relative effect of pile diameter is shown in **Figure 5.16a** and **b** for the initial subgrade modulus coefficient and the ultimate soil resistance respectively. Similarly to **Figure 5.10** numerical results are normalized against the D=0.60m baseline case, while the three (3) different symbols correspond to three (3) different depths (z=0.5, 2.5 and 4.5m). As for analytical predictions, they are presented with a straight line, for k_{ini}, as none of them accounts for diameter effects; while for p_{ult} each methodology is shown in terms of a range that is associated to the depths shown from the numerical analyses. As for k_{ini} it can be observed that the assumption of no pile diameter effect on soil stiffness is oversimplifying. Namely, comparison shows the relative effect ranges between 0-20% both for D=0.4m and for D=1.0m. As shown in the figure, this effect can be expressed mathematically with the following equation:

$$k_{ini} = k_{ini,D=0.6m} \cdot \left(\frac{D}{0.6m} \right)^{-0.35} \tag{5.6}$$

As for p_{ult} both numerical and analytical solutions yield a relative pile diameter effect which is more pronounced as depth increases. Furthermore, comparison between the two (2) indicates that analytical solutions can capture the relative effect consistently, with the methods of Reese et al and Hansen being more realistic.

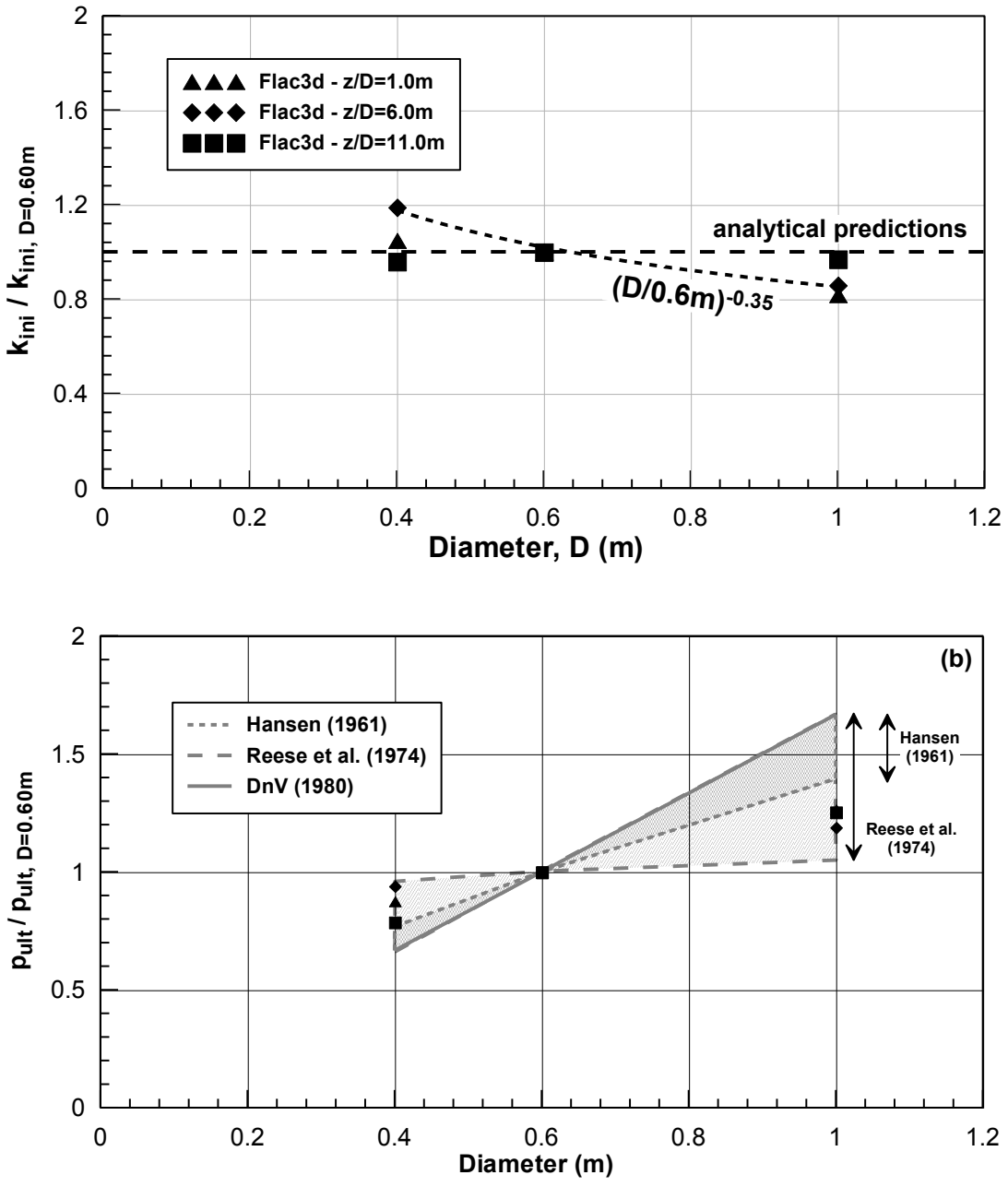

Figure 5.16: Effect of Pile diameter: Evaluation of relative effect and comparison with analytical methodologies (a) initial subgrade modulus, k_{ini} (b) ultimate soil resistance p_{ult}.

Finally it is interesting to investigate whether the z_{cr} values as estimated from k_{ini} and p_{ult} distribution with depth in previous figures, are correlated with the depth at which transition between the two (2) failure mechanisms occurs. For this purpose, **Figure 5.17** shows development of displacement vectors for the D=0.4m and D=1.0m case. In the same figure the critical depths estimated previously are also noted. It can be observed that for both cases $(z/D)_{cr}$ approaches with good agreement the depth at which displacement vectors become horizontal indicating plane strain response.

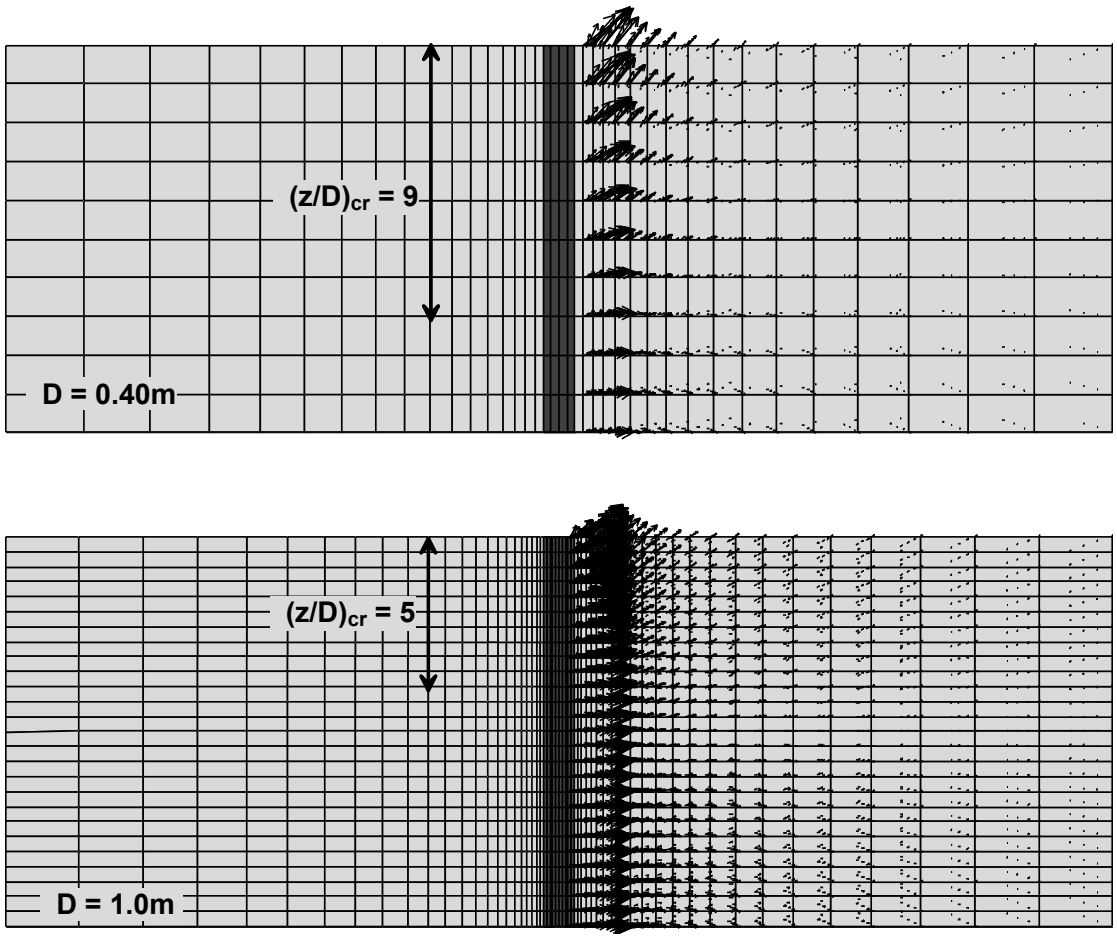

Figure 5.17: Effect of Pile Diameter: Deformation mechanisms and transition from the wedge shape to the plane strain failure mechanism for D=0.40m and D=1.0m

5.6 Effect of Pile Installation

Installation of nondisplacement piles was modeled by manually implementing in the mesh the stresses that result from expansion of a cylindrical cavity, according to the procedure described in the previous chapter. The effect was investigated for piles of various wall thicknesses (d_{cav}) and different diameters (D=0.4 and 0.6m). The

inclusion of pile diameter in the investigation was necessary in order to examine whether a normalization of d_{cav} with D is possible. The exact set of analyses performed is given in **Table 5.1**, at the beginning of this chapter.

The effect of pile installation on the initial subgrade modulus coefficient of the soil is shown in **Figure 5.18** for D=0.60m and D=0.40m (**Figure 5.18a** and **b** respectively). Values of k_{ini} are plotted as a function of depth for the different values of pile wall thickness examined. The results indicate that initial soil stiffness is largely affected from pile installation. Namely, for D=0.60m, k_{ini} appears to be approximately three (3) times larger for the case of a close ended pile (d_{cav}=30cm) compared to the case of nondisplacement piles. For the case D=0.40m, the corresponding increase is about 2-2.5. A second observation is that, for both cases this increase in k_{ini} is grossly uniform with depth. Finally, it should be noted that analytical predictions, also plotted in the figure, do not account for pile installation effects.

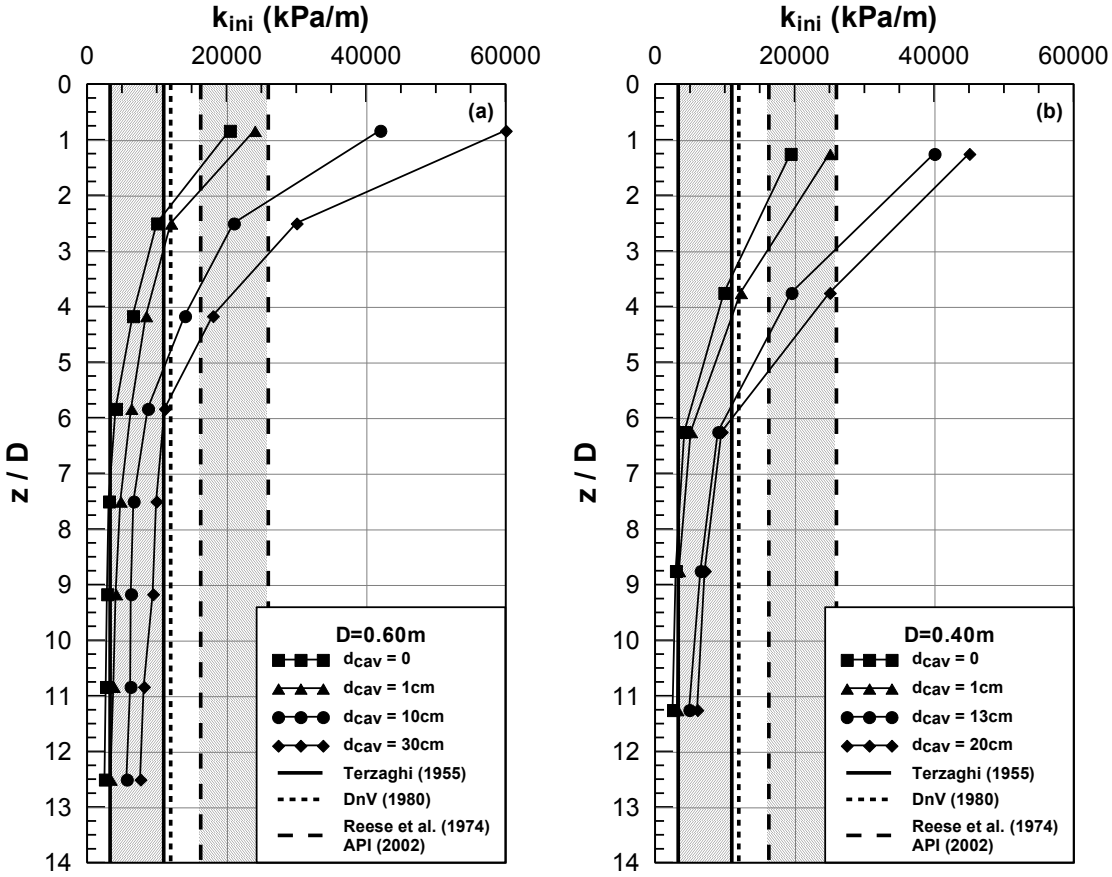

Figure 5.18: Effect of pile installation: Variation of initial subgrade modulus coefficient with depth for various pile wall thicknesses and (a) D=0.60m and (b) D=0.40m

In order to evaluate quantitatively pile installation effects, the kini/$k_{ini,o}$ ratio is plotted in **Figure 5.19** against the normalized pile wall thickness d_{cav}/D, where $k_{ini,o}$ is the value for the nondisplacement pile. The black symbols correspond to the D=0.60m case, while the gray to the D=0.40m case. The various points for each d_{cav} case correspond to different depths along the pile. Firstly, it is observed that these points form a very narrow band, which indicates that the effect of pile installation is uniform along the depth of the pile. Furthermore, the following expression can be introduced to quantify the effect of installation:

$$\frac{k_{ini,d_{cav}}}{k_{ini,d_{cav=0}}} = 1 + 3\sqrt{\frac{d_{cav}}{D}} \tag{5.7}$$

where:

$k_{ini,dcav}$: Coefficient of subgrade reaction modulus for displacement pile

$k_{ini,dcav=0}$: Coefficient of subgrade reaction modulus for nondisplacement pile

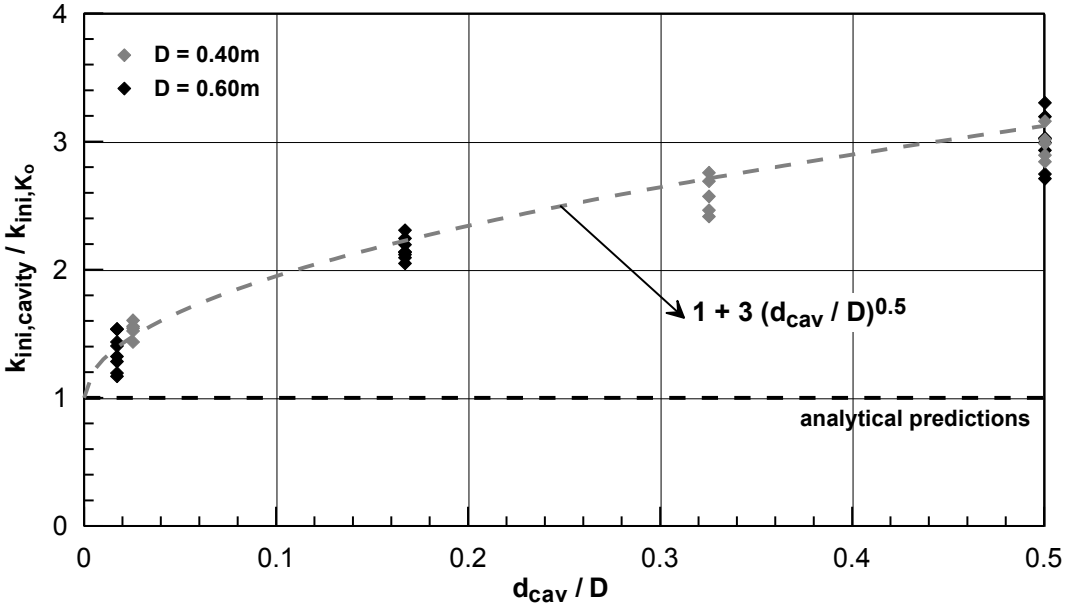

Figure 5.19: Evaluation of pile installation effects on initial subgrade modulus coefficient.

Note that this correlation emanates from the cavity expansion theory, in which the size of the plastic zone depends on the ratio of applied displacement over the final radius of the cavity, as indicated by the following equation (for further details see Chapter 4):

$$R_p / r_o = I_{rr} \sec\varphi^{1/2} \left(1 - \frac{r_i^2}{r_o^2} + \Delta\right)^{1/2} \quad (5.8)$$

where:

R_p: Radius of plastic zone

I_{rr}: Reduced Rigidity Index

φ: Soil friction angle

Δ: Average volumetric strain in plastic zone

r_i: Initial radius of cavity

r_o: Final radius of cavity

The effect of pile installation on the ultimate resistance of the p-y curve (p_{ult}) is illustrated in **Figure 5.20** for D=0.60m and D=0.40m. This comparison clearly shows that pile installation only has a minor effect on p_{ult} which can be practically ignored. This trend, observed in the numerical analyses, agrees with the predictions of the analytical methodologies, also plotted in the figure, which do not account for any installation effects on p_{ult}. This conclusion can be more clearly observed with the aid of **Figure 5.21**, where the ratio of ultimate resistance of displacement piles over nondisplacement piles for all cases investigated and all depths along the pile is plotted against the normalized wall thickness. It is clear that for all cases the ratio remains close to unity, and hence it is rational to assume that pile installation has negligible effect on p_{ult}.

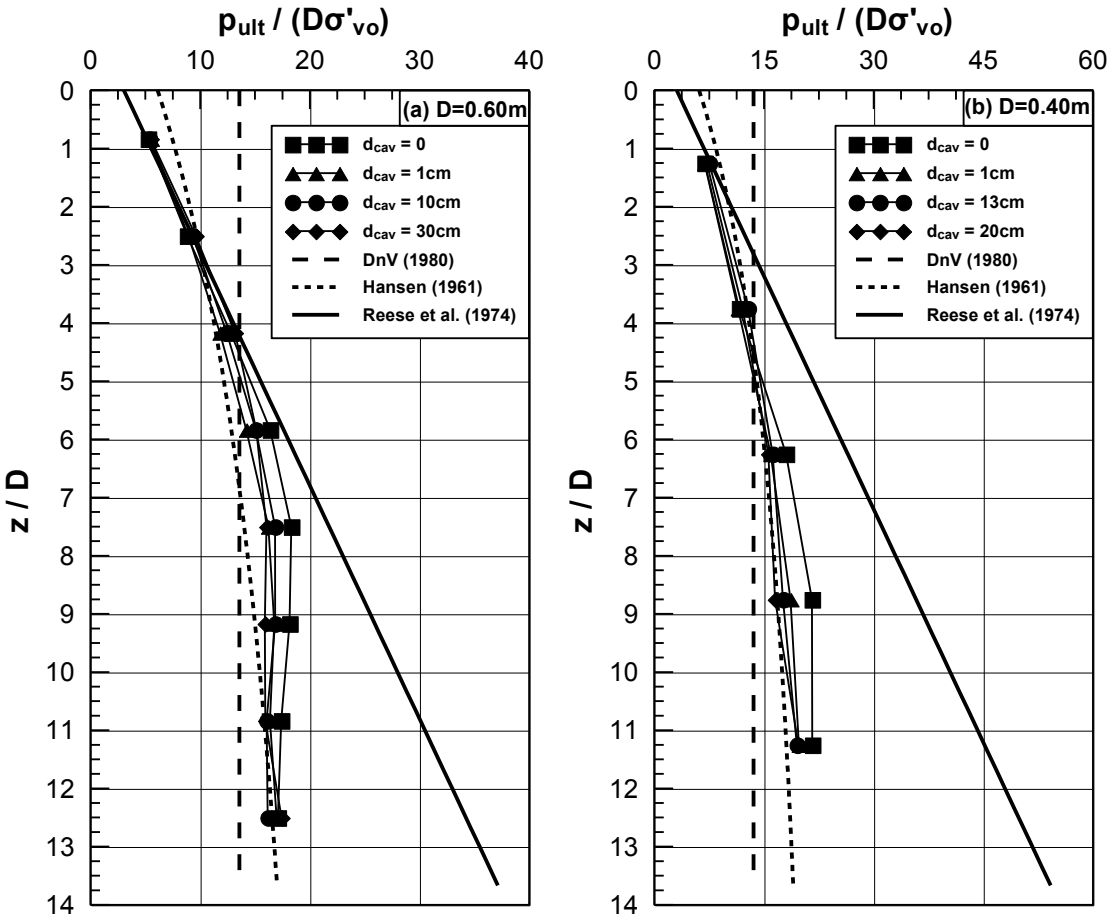

Figure 5.20: Effect of pile installation on the ultimate resistance of the p-y curve

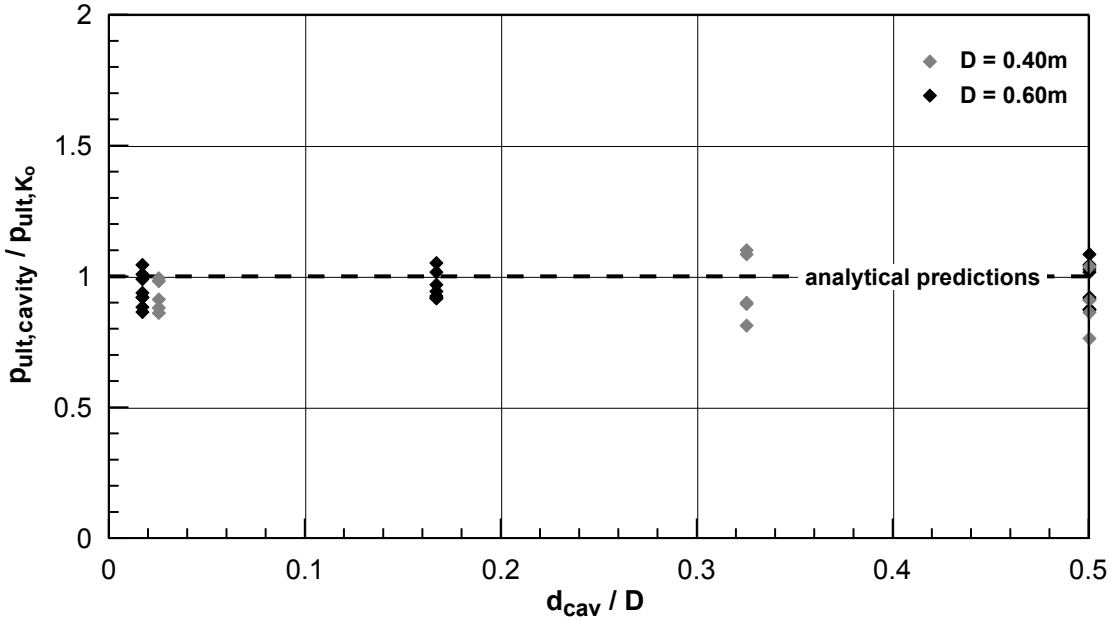

Figure 5.21: Evaluation of pile installation effects on ultimate resistance of p-y curve

5.7 Effect of loading type

The last parameter examined in the current investigation is the effect of loading type. All analyses presented so far involved a uniform lateral displacement of the pile which causes no shearing between soil layers. Note that this assumption is also adopted in the formulation of the p-y method, since the p-y spring of a specific layer is not affected by the deformation of the layer below and above. Inclusion of these effects in the development of a p-y curve is expected to increase both the stiffness and the ultimate resistance of the curve, due to contribution of the shear stiffness of the soil.

In order to investigate those effects two (2) additional analyses were performed in which only pile head was subjected to a lateral displacement, resulting in a non-uniform displacement variation with depth. In the first of the two (2) analyses the head of the pile was free to rotate, while in the second it was not. Note that numerical simulation of this type of problem is more tedious compared to the case where the pile is uniformly displaced. As described in Chapter 3, FLAC3D is making use of a mass scaling procedure, by which the gridpoint masses are increased according to the stiffnesses so that the timestep is equal to one. In the case where the pile is uniformly displaced the pile gridpoints are fixed and, consequently, their stiffness is not included in the mass scaling process. This is not the case for the head displacement analyses, where pile gridpoints are free to displace. As a result, pile's large stiffness leads to large mass readjustments which in turn produce significant instabilities (mass is included in equation of motion and hence increases the acceleration of the gridpoint). In order to eliminate the latter, the displacement should be applied in very small increments causing the time of the analysis to increase significantly.

Figure 5.22 shows the deformed shape of the two (2) models. The displacement at the head of the pile is equal to 30cm for both cases. It can be initially observed that the soil is seriously deformed only for a few pile diameters below the ground surface. Therefore, it is of no value to calculate and interpret p-y response for depths in which the lateral displacement is very small.

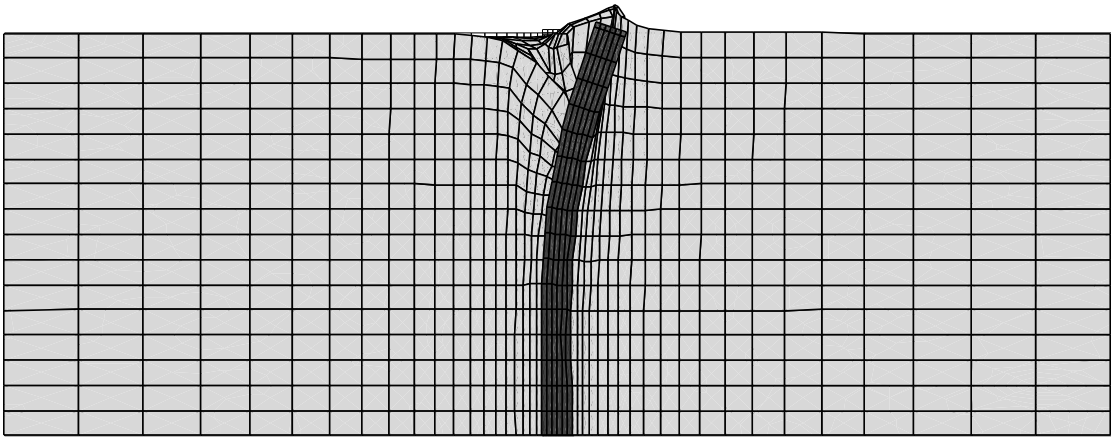

(a) free-head

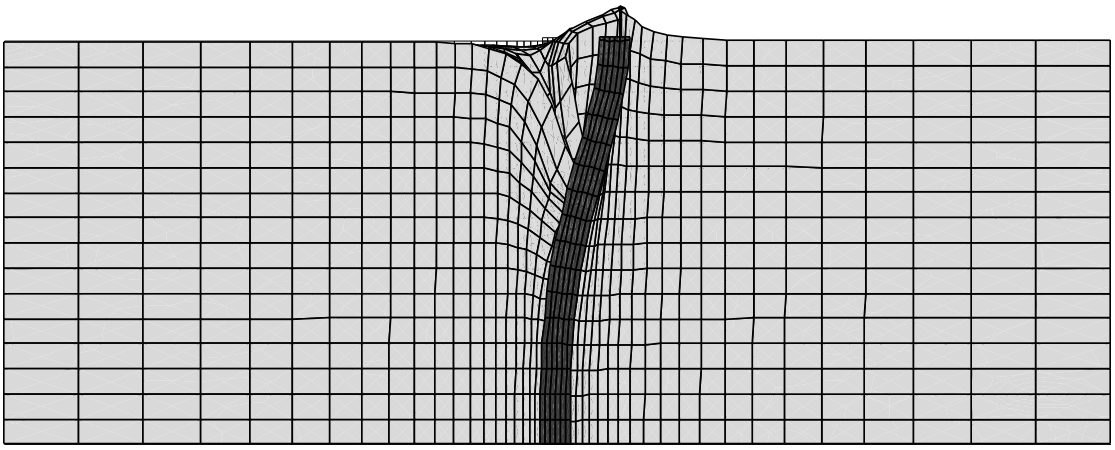

(b) fixed-head

Figure 5.22: Deformed shape for the case of lateral displacement applied at the head of the pile (a) free rotational constraint (b) fixed rotational constraint

This is further demonstrated in **Figure 5.23** which shows the distribution of lateral pile displacement with depth for the two (2) cases of pile head displacement. It is observed that displacement becomes less than one (1) centimeter at an approximate depth of four (4) meters (~6.6 pile diameters) for the free-head case and of five (5) meters (~8.3 pile diameters) for the fixed-head case. Hence, no p-y curves will be presented for depths larger than four (4) meters. Note that this value of one centimeter was selected based on experience from the previous analyses, with uniform lateral displacement, which revealed that for displacements less than this value, interpretation of p-y curves can lead to misleading results.

Another thing to observe both from **Figure 5.22** and **Figure 5.23** is that for the case of rotational constraint on pile head, the distribution is more uniform close to the head

of the pile. As a result, effects of shear stiffness are expected to be less pronounced at this area for this case.

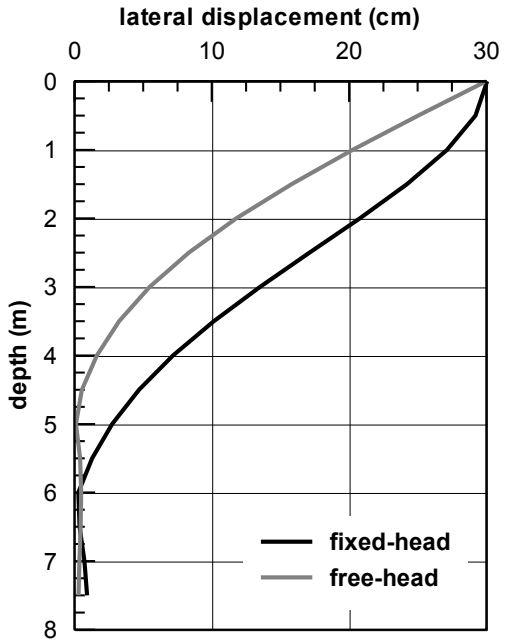

Figure 5.23: Distribution of lateral pile displacement with depth

The numerically estimated p-y curves are shown in **Figure 5.24** for depths up to 4.5m. Also plotted in these figures are the curves for uniform displacement applied at the whole length of the pile. Namely the black and grey continuous lines correspond to the cases of applied pile head displacement with and without head rotation constraint respectively, while the gray dashed line refers to the case of uniform lateral displacement along the pile. As expected, the analyses for pile head displacement yield significantly larger values for the ultimate resistance of the soil, while initial stiffness appears not to be largely affected. Those effects weaken with depth, while comparison indicates that at the depth of 4.5m the curves for pile head and uniform pile displacement coincide. As for the comparison between the free and fixed rotational head constraint case it is observed that the former results in slightly larger soil capacity and stiffness. As noted earlier, this is attributed to the fact that in the case of the fixed head, displacement distribution near the head is more uniform, and as a result shearing effects are limited.

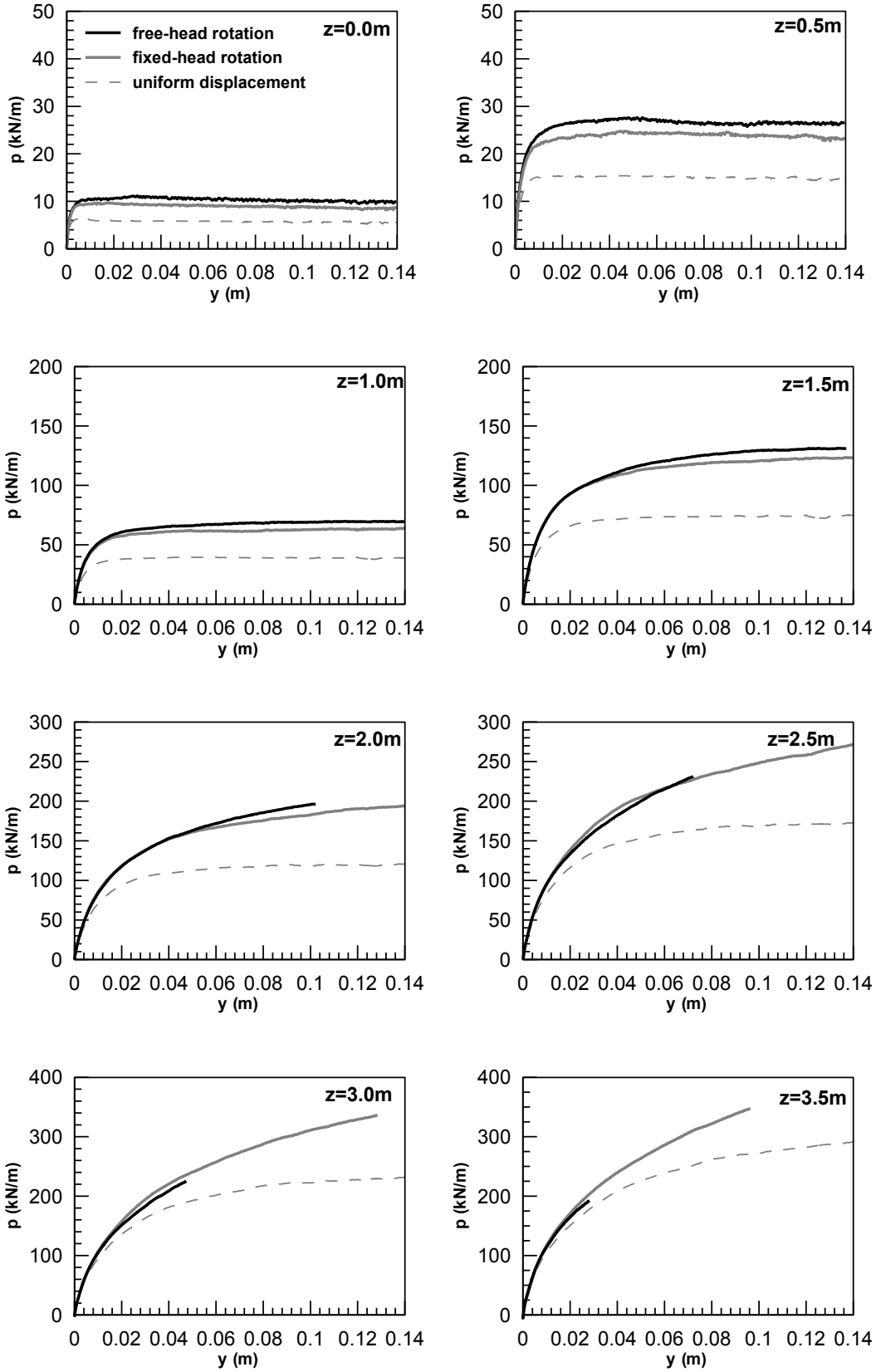

Figure 5.22a: Numerical p-y curves for various depths and boundary conditions (head displacement with and without rotation and uniform lateral displacement)

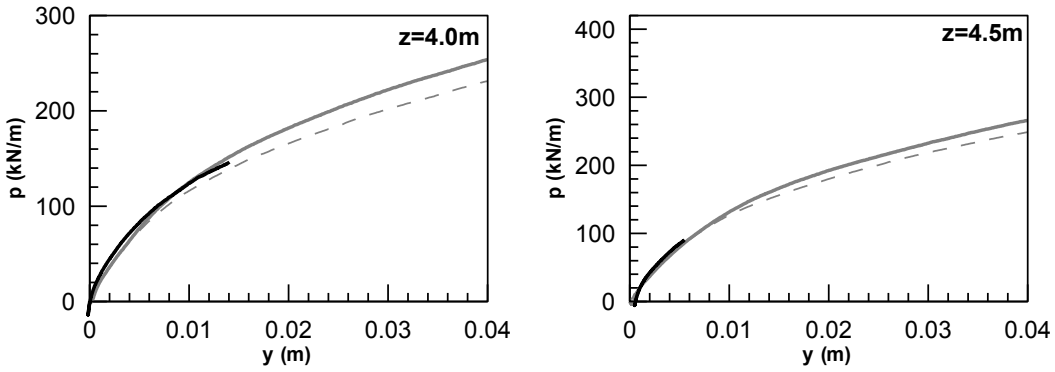

Figure 5.24b: Numerical p-y curves for various depths and boundary conditions (head displacement with and without rotation and uniform lateral displacement)

In order to quantify the above observations, as well as to compare numerical and analytical predictions, numerical values of p_{ult} and k_{ini} were determined by fitting a hyperbolic curve to the numerical curves, as described in paragraph 5.2. Results in terms of initial subgrade modulus coefficient, k_{ini}, are summarized in **Figure 5.25**. Namely, **Figure 5.25a** shows the variation of k_{ini} with depth for the three (3) different cases, i.e. uniform pile displacement, as well as pile head displacement with and without rotational constraint. Also plotted in the same figure are the analytical predictions which do not account for different loading types and hence they yield the same results for all three (3) cases. Finally, in order to demonstrate the relative effect of loading type, in **Figure 5.25b** values of k_{ini} from the analyses with pile head loading are divided with k_{ini} from the analyses with uniform applied displacement.

This figure indicates that head loading causes a slight increase of the initial stiffness of the pile. This increase is approximately equal to 10-20% and is uniform along the length of the pile. As for the effect of rotational constraint, it is observed that it causes a slight decrease (approximately 10%) in k_{ini} near the ground surface. This variation can be explained by the fact that rotational constraint causes displacement distribution near the pile head to be more uniform, and hence contribution of shearing stiffness is prevented to some extent. Finally, as far as comparison with analytical methods is concerned the observations stated in paragraph 5.3 also apply here, i.e. the numerical predictions can be better approximated using either Reese's or API's recommendations for shallow depths and Terzaghi's values for large depths.

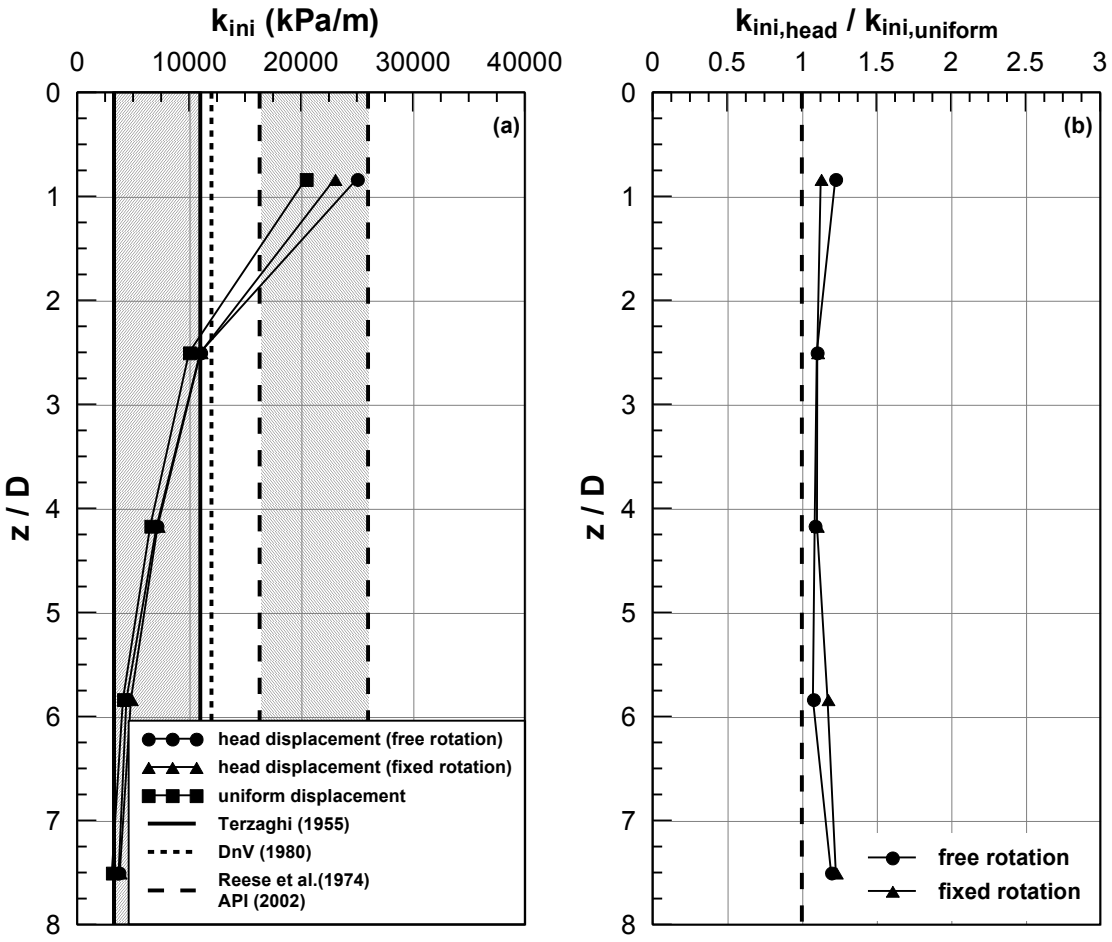

Figure 5.25: Effect of loading type on the initial stiffness of the p-y curve: (a) Coefficient of initial subgrade modulus with depth and (b) Ratio of k_{ini} values for head over uniform loading

The effect of loading type on ultimate soil resistance is demonstrated in **Figure 5.26**. Namely, **Figure 5.26a** shows the variation of p_{ult} with depth, as estimated from the numerical analyses, and compares it to analytical predictions. Note that in the comparison shown in the figure, Reese's expression was applied without taking into account the empirical coefficient A. Though not mentioned clearly in Reese's 1974 paper or in subsequent studies, coefficient A is assumed to account for the effects of shearing force between soil layers, which are not included in the formula for the evaluation of p_{ult} as a result of a wedge-shaped failure mechanism. Therefore, Reese's expressions are evaluated for A=0.9 and are assumed to correspond to the case where the pile is pushed laterally with a uniform displacement. Finally, **Figure 5.26b** demonstrates the relative effect of loading type on p_{ult} by dividing p_{ult} from analyses for pile head displacement with p_{ult} from analyses for uniform pile displacement. The resulting distributions with depth are compared with the two (2) recommendations

for the empirical coefficient A found in the literature. The first was proposed by Reese et al. (1974) and API (2002) and the second by Georgiadis et al. (1992), and can be calculated as follows:

$$A = \left(3.0 - 0.8\frac{z}{D} \right) \geq 0.9 \text{ (Reese et al. 1974; API, 2002)} \quad (5.9)$$

$$A = \left(2.0 - \frac{1}{3}\frac{z}{D} \right) \geq 1.0 \text{ (Georgiadis et al., 1992)} \quad (5.10)$$

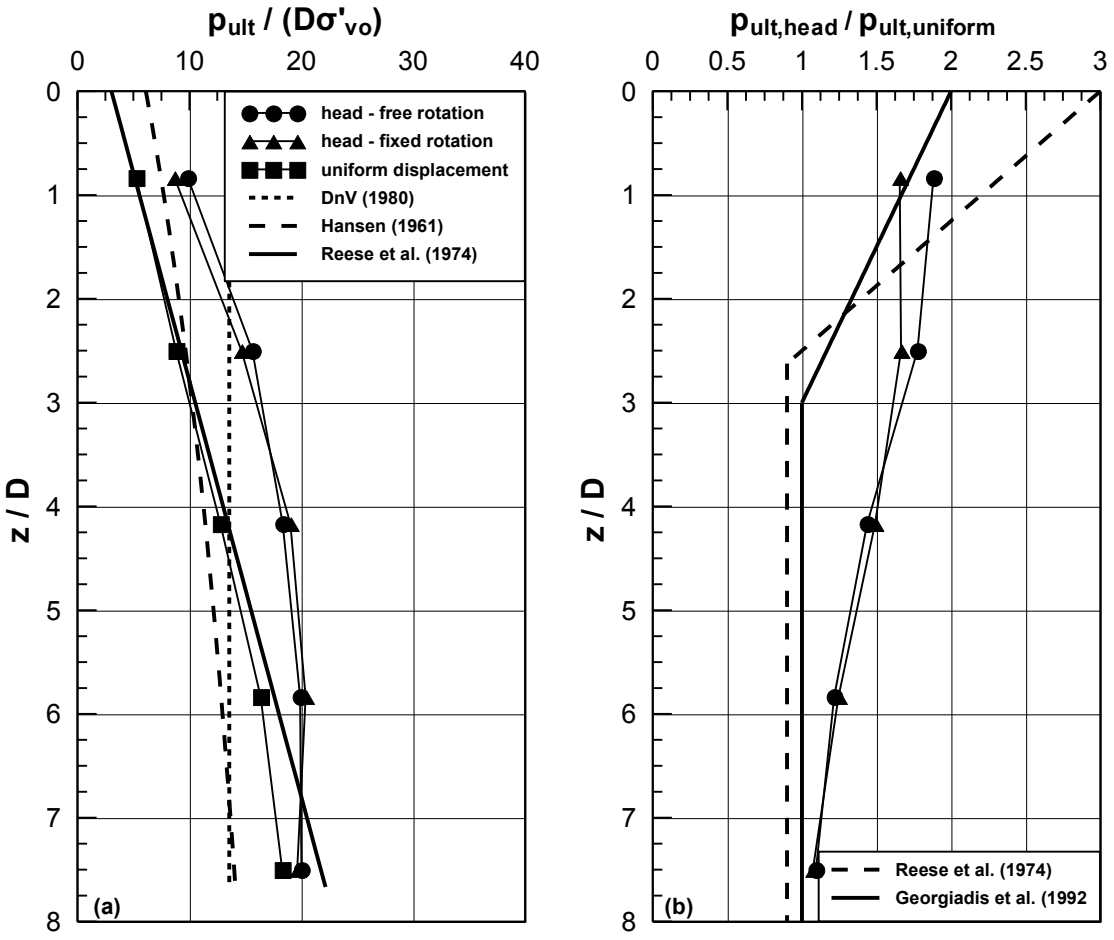

Figure 5.26: Effect of loading type on ultimate soil resistance: (a) Variation of p_{ult} with depth and (b) Ratio of p_{ult} from head displacement analyses over uniform displacement analyses

Focusing first on **Figure 5.26a** it is observed that variation with depth also follows the bilinear shape, i.e. a linearly increasing segment followed by a part of constant p_{ult}. However, in the case of head loading two (2) major differences are observed:

- Ultimate soil resistance during the linearly increasing phase (wedge-shaped failure mechanism) is significantly larger
- Transition between wedge-shaped to plane strain failure mechanism occurs at shallower depths. Namely, for the case of head loading results indicate a transition depth of approximately four (4) pile diameters, while in the case of uniform loading transition occurs approximately at 6-7 diameters.

The first of these two (2) discrepancies is attributed to the additional resistance due to the shearing that occurs in the soil as a result of the non-uniform lateral displacement distribution with depth. In order to further investigate and verify the second observation, **Figure 5.27** shows the variation of vertical displacements in front of the pile. Displacements are normalized with maximum vertical displacement that occurs at the ground surface. Positive values indicate upward ground movement. The distribution shown in this figure verifies that indeed upward movement, typical of a wedge-shaped failure mechanism, becomes zero at a depth of approximately two (2) meters for the head loading case. On the other hand, for the uniformly pushed pile, upward displacements become very small at a depth of about five (5) meters. In other words, the plane strain failure mode becomes critical at much smaller depths.

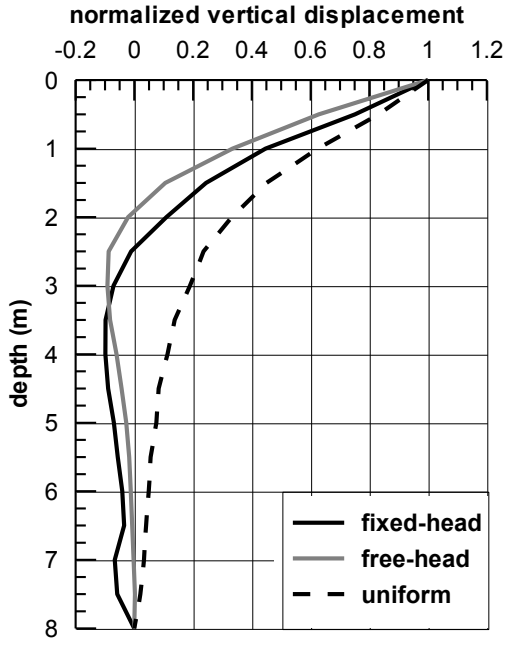

Figure 5.27: Distribution of vertical displacement with depth indicating the transition from wedge-shaped to plane strain failure mode

In this context, the variation of p_{ult} for pile head loading over p_{ult} for uniform loading, shown in **Figure 5.27b**, can be explained as follows:

- For depths smaller than two (2) pile diameters, where soil in both cases fails according to a wedge-shaped mechanism, difference in p_{ult} is attributed solely to the additional shear resistance. The latter causes p_{ult} to increase by approximately 60-70%, a variation that is captured satisfactorily from both analytical correlations.
- For depths larger than 7-8 pile diameters both models fail in a plane strain mode, which yields approximately equal values for the ultimate resistance.
- Finally, for intermediate depths, increased p_{ult} values are mainly the result of different failure mechanisms, i.e. plane strain for head displacement and wedge for uniform displacement. This causes an increase in p_{ult} that diminishes with depth, as the response for the case of uniform loading gradually becomes more plane strain.

As discussed earlier, coefficient A was most probably introduced in the analytical methodologies to account for effects of additional shearing and does not account for different critical depths of transition between the wedge and the plane strain failure. As a result, coefficient A yieldσ satisfactory results for shallow depths, where both models fail in the wedge mode, while it does not capture the p_{ult} variation in intermediate depths.

Finally, as for the effect of head constraint, the comparison shows that only the region close to the pile head is affected. Namely, restriction of head rotation causes both k_{ini} and p_{ult} to slightly decrease (approximately by 10%). As already argued, this variation is due to the more uniform distribution of displacements near the head which reduces the contribution of interlayer soil shear stiffness.

5.8 Conclusions

In the present chapter, the results of thirteen (13) numerical analyses were presented which investigated the effects or Relative Density (D_r), Pile diameter (D), Pile installation and type of loading on the p-y response of the soil, as a result of the lateral movement of a pile. The main conclusions from the parametric study are the following:

5.8.1 Shape of p-y curves

It was found that the nonlinear shape of the numerical p-y curve can be fairly described with a hyperbolic function, as follows:

$$p = \frac{y}{\frac{1}{k_{ini} z} + \frac{y}{p_{ult}}} \tag{5.11}$$

where:

y: pile lateral displacement

p: soil reaction for lateral displacement y

z: depth

The hyperbolic function is defined by means of two (2) parameters:

- Coefficient of initial subgrade modulus, k_{ini}
- Ultimate soil resistance, p_{ult}

Secondly, numerical analyses revealed the existence of a critical depth, $(z/D)_{cr}$, which delineates two (2) response patterns for the soil. Namely:

- For $z/D < z/D_{cr}$ soil fails by forming a wedge-shaped mechanism. For this range of depths, k_{ini} decreases with depth and $p_{ult}/D\sigma'_{vo}$ (D: pile diameter, σ'_{vo}: in-situ vertical effective stress) increases linearly.
- For $z/D > z/D_{cr}$ soil fails by forming a plane strain mechanism. In this region both k_{ini} and $p_{ult}/D\sigma'_{vo}$ remain constant.

It should be noted that the critical depth concept is also suggested by Reese et al. (1974) in their analytical methodology. However, as thoroughly discussed in Chapter 3, numerical analyses estimate the critical depth of transition between the two (2) mechanisms to be significantly smaller than that proposed by Reese et al.

Given the hyperbolic shape of the curve, our efforts were consequently focused on investigating the parameters that affect k_{ini} and p_{ult}, as well as evaluate the efficiency of existing analytical methods to capture those effects. In the following sections major conclusions with regard to k_{ini} and p_{ult} based on observations from numerical analyses are summarized.

5.8.2 Typical response characteristics for k_{ini} and p_{ult}

Based on the basic analysis with D_r=50%, D=0.60m, uniform pile displacement and no installation effects accounted, the following basic response characteristics were identified with regard to k_{ini} and p_{ult}:

- Above critical depth, k_{ini} decreases with depth, and does not remain constant as predicted by most analytical methodologies.
- Below critical depth, k_{ini} remains practically constant
- For small depths k_{ini} is better approximated with Reese's et al (1974) or API's (2002) recommendations, while for large depths k_{ini} is closer to the values proposed by Terzaghi (1955).
- Overall, variation of k_{ini} with depth can be described with the following analytical expression:

$$k_{ini,z} = k_{ini,0}\left(1 - \frac{z/D}{1+z/D}\right) \qquad (5.12)$$

where:

$k_{ini,z}$: Value of k_{ini} at desired depth

$k_{ini,0}$: Value of k_{ini} at ground surface (close to Reese's or API's recommendations)

- Above critical depth, $p_{ult}/D\sigma'_{vo}$ increases linearly with depth yielding good agreement with Reese's analytical predictions for wedge-shaped failure mechanisms.
- Below critical depth, $p_{ult}/D\sigma'_{vo}$, remains constant, a response that agrees with DNV's methodology, as well all methods based on passive earth pressure theory. Note that this type or response also agrees with Reese's plane strain failure formulas, with the latter, however, becoming critical for significantly larger depths.
- Overall, for the whole range of depths, numerical values can be better approximated using the relations proposed by Hansen (1961).

5.8.3 Effect of Relative Density, D_r

Apart from the basic conclusions noted previously, the following can be added with regard to the effect of D_r:

- As D_r increases the critical depth $(z/D)_{cr}$ also increases causing loose models to develop plane strain failure mechanisms at much lower depths compared to more dense models. As a result, loose soils for relatively shallow depths develop larger ultimate loads compared to soils with large D_r (a plane strain mechanism for loose soil can give larger p_{ult} than a wedge mechanism for a dense soil). In all cases, the critical depth, remains well below Reese's estimates.
- Initial subgrade modulus coefficient increases with D_r, with the increase being uniform and irrespective of depth.
- Qualitatively, all existing analytical methods for k_{ini} are able to predict consistently the relative effect of D_r on k_{ini}, with better quantitative agreement by the recommendations found in DnV's (1980) guidelines.
- For D_r=20% and the above critical depth, $p_{ult}/D\sigma'_{vo}$ is slightly above analytical methods, while below critical depth the ultimate $p_{ult}/D\sigma'_{vo}$ value can be well predicted by both DnV and Hansen's methods.
- For D_r=90% and the above critical depth, the methods of DnV or Hansen can be used as a fair approximation of numerical values. For depths below the critical, numerical estimates appear to diverge from existing methods.

5.8.4 Effect of Pile diameter, D

Pile diameter effect was investigated by performing two (2) additional analyses with D=0.4m and D=1.0m. The effect on the p-y response can be summarized on the following:

- The critical depth ratio, $(z/D)_{cr}$, decreases with pile diameter. However, it is observed that this decrease is mainly attributed to the increase of pile diameter. The absolute critical depth, z_{cr}, which for this case is a more perceptible parameter, appears to slightly increase with D.
- Pile diameter affects initial stiffness for depths above the critical, given that k_{ini} increases with pile diameter. On the other hand k_{ini} remains unaffected for $z/D>(z/D)_{cr}$.

- Analytical solutions do not account for pile diameter effects on soil stiffness, however the latter appear to have a non negligible effect of up to 30% for D=0.40m and up to 50% for D=1.0m.
- Normalized ultimate resistance, $p_{ult}/D\sigma'_{vo}$, is not affected by pile diameter for depths smaller than the critical. For larger depths, though, the $p_{ult}/D\sigma'_{vo}$ ratio is decreased with pile diameter. It is observed that ratio of decrease is approximately equal to the diameter ratio.
- As for analytical methodologies, in general they capture the effect of diameter on p_{ult}, as analytical predictions are in good agreement with numerical values. The consistency is more fair for depths larger than the critical, while divergence is observed for smaller depths, where, depending on the diameter and the depth, numerical values are either over- or under-estimated

With regard to k_{ini} it should be noted that most of the existing analytical methodologies (Reese et al., API, DnV e.t.c) do not account for diameter effects and determine initial stiffness according to the relative density of the soil. This assumption has neither been confirmed nor inverted in the literature. Namely Vesic (1963), Ashford and Juirnarongrit (2005) and Fan and Long (2005) based on experimental and numerical studies argue that pile diameter has a negligible effect on k_{ini}. On the other hand, Carter (1984), Ling (1988) and Lesny and Wiennan (2006) observed significant influence of the pile diameter on k_{ini}, which appeared to increase linearly with depth. The present study is aligned with the second opinion, while observation of the relative effect confirms an approximately linear dependence of k_{ini} from D.

5.8.5 Effect of pile installation

Effects of pile installation were modeled by manually implementing in the mesh the stresses caused by the installation of open- and close ended piles of various wall thicknesses (d_{cav}) and diameters. For this purpose, Vesic's analytical method for cavity expansion was calibrated and implemented in the numerical model, as thoroughly described in the previous chapter. Major observations from this part of the study can be summarized to the following:

- Pile installation does not affect ultimate resistance of the soil.

- Initial stiffness of the soil increases significantly, but uniformly with depth, with the wall thickness of the pile. Indicatively, for a close-ended pile, increase is of the order of 200%.
- Following the logic of the cavity expansion theory, where the size of the plastic zone depends on the ratio of the initial over the final thickness, it was found that the relative effect of installation on k_{ini} can be expressed as a function of the ratio d_{cav}/D as follows:

$$\frac{k_{ini,d_{cav}}}{k_{ini,d_{cav=0}}} = 1 + 3\sqrt{\frac{d_{cav}}{D}} \tag{5.13}$$

  where $k_{ini,dcav}$ and $k_{ini,dcav=0}$ the stiffness for the displacement and the nondisplacement pile respectively.

- Finally, all the analytical methods invoked in the present investigation do not account for installation effects neither for p_{ult} nor for k_{ini}.

5.8.6 Effect of type of loading

All the analyses presented so far, were performed by applying a uniform lateral displacement at the whole length of the pile. In this final step of investigation two (2) additional analyses were performed in which a lateral displacement was applied at the head of the pile. In the first case it was assumed that the pile head is free to rotate, while in the second it was assumed fixed. In the case of head loading, soil response is significantly affected by an additional shear force that is developed due to the non-uniform distribution of lateral displacements. Comparison between analyses with head and uniform displacement indicate the following:

- Head loading causes the critical depth to decrease approximately in half.
- Below a depth of approximately 7-8 pile diameters soil is not affected by the loading on pile head, as lateral displacements become practically negligible.
- Initial subgrade modulus shows a slight increase of approximately 10-20%, due to shear stiffness contribution. Despite the small increases numerical values agree with Reese's and Terzaghi's recommendations for small and large depths respectively.

- As for ultimate soil resistance in general pile head analyses yield larger p_{ult} values. The relative effect, however, varies with depth and depends on the depth of the point in question with respect to the critical depth of the head as well as the uniform analysis. Namely:
  - For $z/D < z/D_{cr,head} < z/D_{cr,uniform}$ both models fail with the wedge-shaped mechanism. For this case p_{ult} is larger for the head analysis as a result of additional shearing forces.
  - For $z/D_{cr,head} < z/D < z/D_{cr,uniform}$ analysis with head displacement fails with the plane strain mechanism, while the analyses with the uniform applied displacement according to the wedge. As a result the former yields larger ultimate resistance which decreases from 60 to 20% as depth increases. This reduction is due to the fact that the uniform model progressively enters in the plane strain mode, causing his p_{ult} to increase.
  - Finally, for $z/D > z/D_{cr,head} > z/D_{cr,uniform}$ both models fail in the plane strain mode, and as a result differences in soil resistance are small.
- As for analytical methods, they only account for additional resistance due to shear through coefficient A. Hence, they yield good agreement only for shallow depths where both models fail in the wedge mechanism and for very large depths where both models fail in the plane strain mode. For intermediate depths, analytical methods assume wedge failure and, therefore, cannot capture the increase of p_{ult} due to different deformation mechanisms.
- Finally, as for the effect of rotational constraint on pile head, differences are limited only in the region close to the pile head. In the case where rotational constraints are applied both k_{ini} and p_{ult} are slightly smaller (in the order of 10%), due to more uniform displacement distribution and, hence, less pronounced shearing effects.

5.9 Analytical estimation of p-y curves in nonliquefied soils

The observations from the numerical results along with the preceding discussion, can be further processed to form a complete analytical methodology for the estimation of p-y curves in nonliquefied sandy soils and for piles undergoing kinematic loads:

Nonlinear shape

The nonlinear shape of the p-y curve is described by the following hyperbolic function:

$$p = \frac{y}{\frac{1}{k_{ini} z} + \frac{y}{p_{ult}}} \tag{5.14}$$

Coefficient of Initial Subgrade Modulus, k_{ini}

The coefficient of initial subgrade modulus is calculated as follows:

$$k_{ini} = k_{ini,0} \cdot \left(1 - \frac{z/D}{1 + z/D}\right) \cdot \left(\frac{D}{0.6m}\right)^{-0.35} \cdot \left(1 + 3\sqrt{\frac{d_{cav}}{D}}\right) \tag{5.15}$$

where:

$k_{ini,0}$: Subgrade modulus coefficient at the ground surface

z: Depth from the ground surface for which the p-y curve is estimated

D: Pile diameter

d_{cav}: Pile wall thickness for nondisplacement piles

Values of $k_{ini,0}$ can be estimated based on the relative density of the soil according to **Table 5.3**.

Table 5.3: Variation of initial subgrade modulus coefficient at the ground surface ($k_{ini,0}$) with relative density

Relative Density	**Loose**	**Medium**	**Dense**
$k_{ini,0}$ (kPa/m)	18000	30000	45000

Ultimate Soil Resistance, k_{ini}

The ultimate soil resistance of the soil, normalized with pile diameter and vertical effective stress is estimated as follows:

$$\frac{p_{ult}}{\sigma'_{vo} D} = \begin{cases} \text{Reese et al (1974) - API (2002)}, & z/D < z/D_{cr} \\ \text{σταθερό}, & z/D > z/D_{cr} \end{cases} \tag{5.16}$$

where $(z/D)_{cr}$ corresponds to the depth at which the mode of failure changes from wedge-type to plane strain, and can be evaluated as follows:

$$z/D\ _{cr} = (6-7)\cdot\left(\frac{D_r}{50\%}\right)\cdot\left(\frac{D}{0.6m}\right)^{-0.64} \tag{5.17}$$

Finally, it is reminded that according to API's methodology the ultimate resistance is calculated as follows:

$$\frac{p_{ult}}{\sigma'_{vo}D} = \min\begin{cases} C_1\cdot z/D + C_2 \\ C_3 \end{cases} \tag{5.18}$$

where C_1, C_2 and C_3 given by:

$$\begin{aligned} C_1 &= 0.115\cdot 10^{0.0405\cdot\varphi} \\ C_2 &= 0.571\cdot 10^{0.022\cdot\varphi} \\ C_3 &= 0.646\cdot 10^{0.0555\cdot\varphi} \end{aligned} \tag{5.19}$$

where φ is the friction angle of the soil.

The predictions of the above methodology are compared with numerical estimates in **Figure 5.28a** and **b** in terms of k_{ini} and $p_{ult}/(\sigma'_{vo}D)$ respectively. In both cases, it can be observed that the analytical methodology can predict accurately the numerical results.

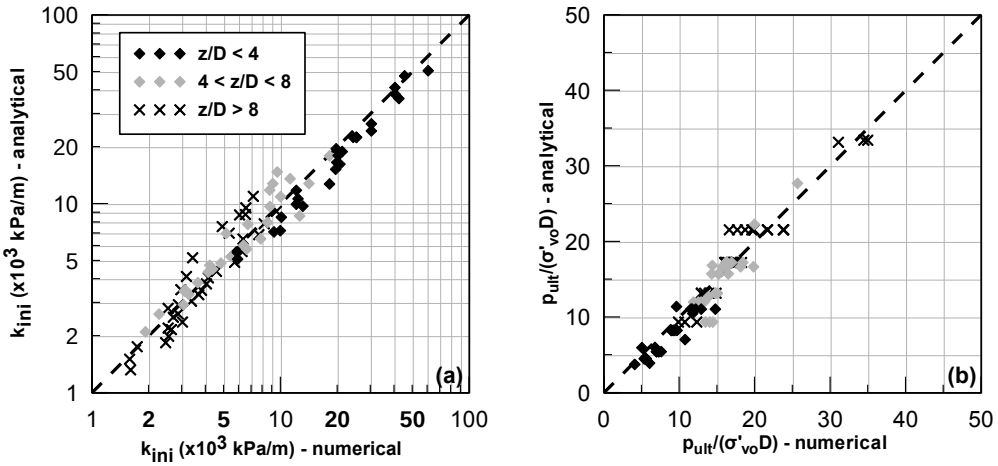

Figure 5.28: Comparison between numerical and analytical prediction (a) for the initial subgrade modulus, k_{ini} and (b) the ultimate soil resistance $(p_{ult}/(\sigma'_{vo}D)$.

6

Numerical Simulation of Piles in Laterally Spreading Soils

6.1 General

The present, as well as subsequent chapters, investigate the problem of a single pile undergoing large kinematic loads due to liquefaction and lateral spreading of the surrounding soil. The main objective of the investigation is to evaluate the degraded p-y response of the liquefied soil relatively to the curves for nonliquefied soils described previously for sound sand deposits, through a series of parametric analyses. The present chapter thoroughly describes the numerical model built to simulate the problem.

Note that the numerical model used for the analyses for the nonliquefied soil was used as origin. However, proper modifications were necessary, that arise from the fact that the geometry examined herein is inclined, and the load applied is dynamic.

6.2 Problem Statement and Basic Input Parameters

The problem simulated is schematically illustrated in **Figure 6.1**. In the basic analysis presented herein, the pile is 8m long, with a diameter D=0.60m and bending stiffness EI=1300000kNm^2. The soil is 8m thick and consists of a uniform, saturated Nevada sand layer with D_r=50% Relative Density. The soil layer is inclined by an angle $\theta=2^o$ and the groundwater surface is located at an average height of 1m above the ground surface. The base of the model is excited by a horizontal sinusoidal motion which causes the soil to liquefy and develop large lateral displacements. The Nevada sand properties are listed in **Table 6.1** (Arulmoli et al., 1992), while **Table 6.2** summarizes basic soil, pile and input motion characteristics.

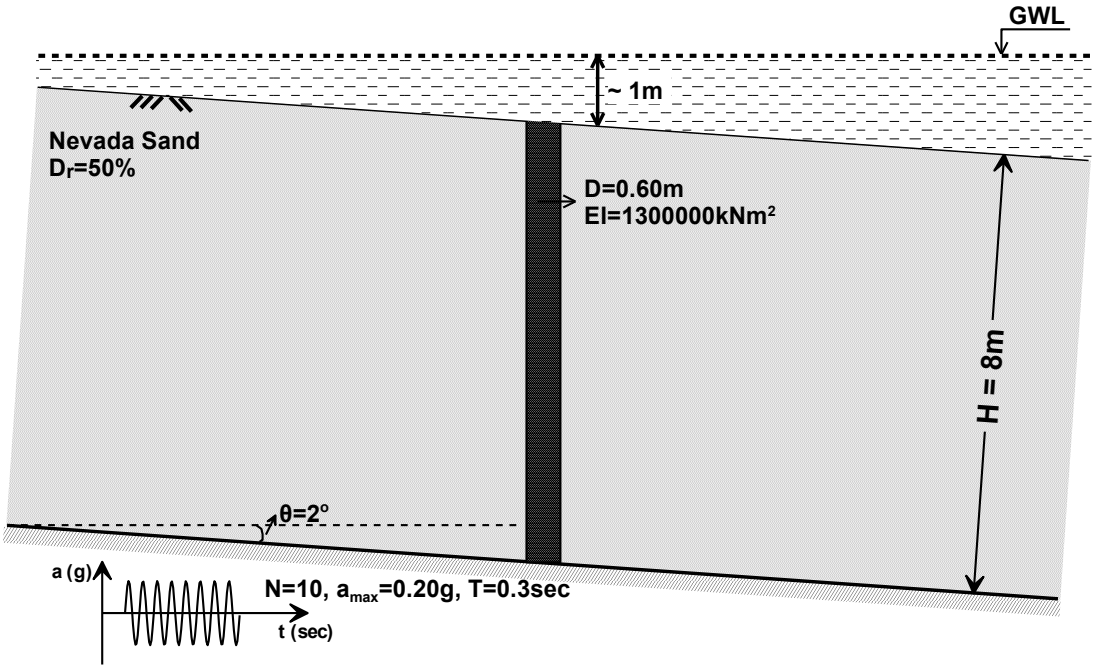

Figure 6.1: Layout and basic parameters of the problem analyzed

Table 6.1: Summary of Nevada Sand properties (Arulmoli et al., 1992)

Density of grains, ρ_s (Mgr/m^3)	2.67
Maximum void ratio, e_{max}	0.887
Minimum void ratio, e_{min}	0.511
Mean Grain Size, D_{50} (mm)	0.1
Coefficient of Uniformity, C_u	1.41

Table 6.2: Summary of basic soil, pile and input motion properties for the basic analysis

Soil Properties		**Pile Properties**		**Excitation**	
Relative Density, Dr (%)	50	Length, L (m)	8.0	Number of cycles, N	14
Density, ρ (Mgr/m3)	1.543	Diameter, D (m)	0.60	Period, T (sec)	0.30
Permeability, k (m/sec)	6.1x10-5	Bending Stiffness, EI (kNm²)	1300000	Amplitude, a_{max} (g)	0.20

The numerical analysis aims at estimating the kinematic loads, in the form of p-y curves, imposed on the pile due to ground displacement. The analysis is performed in three (3) stages:

- Stage 1: Generation of the proper static stress field for the infinite slope

- Step 2: Pile installation
- Stage 3: Application of dynamic loading at the base of the model

6.3 Stage 1: Generation of the proper stress field for the infinite slope

The stress field of an infinite slope is differentiated from level ground conditions mainly due to the development of an additional shear stress required to equilibrate the gravitational force parallel to ground surface. In general, there are three (3) main patterns that characterize the stress field of an infinite slope:

- Shear stresses required to balance the gravitational force parallel to ground surface.
- Perpendicular and parallel to the ground surface normal stresses do not balance the whole gravitational force, but only the component which is perpendicular to the ground surface.
- All cross sections perpendicular to ground surface should be equivalent, i.e. characterized by the same normal and shear effective stress.

In the present simulation, proper stress values that correspond to the infinite slope equilibrium are assigned manually in the mesh through analytical expressions that are developed based on the equilibrium of the infinite slope. The accuracy of the above expressions, as well as the performance of this semi-analytical approach, is further evaluated through numerical analysis.

6.3.1 Analytical computation of static stress field

In order to develop analytical expressions for the stress distribution in an infinite slope, the equilibrium of the infinitesimal slice of inclined soil, shown in **Figure 6.2**, was considered. The angle of inclination is θ, while the unit weight of the soil is equal to γ'. At the left end of the slice the normal stress is equal to σ'_x and the shear τ_{zx}. At the right end, the normal and shear stresses are equal to $\sigma'_x + \partial\sigma'_x/\partial x \; dx$ and $\tau_{zx} + \partial\tau_{zx}/\partial x \; dx$ respectively. Similarly, no stresses develop at the ground surface, which is a free boundary, while the normal and shear stress at the bottom boundary are equal to $\partial\sigma'_z/\partial z \; dz$ and $\partial\tau_{xz}/\partial z \; dz$ respectively.

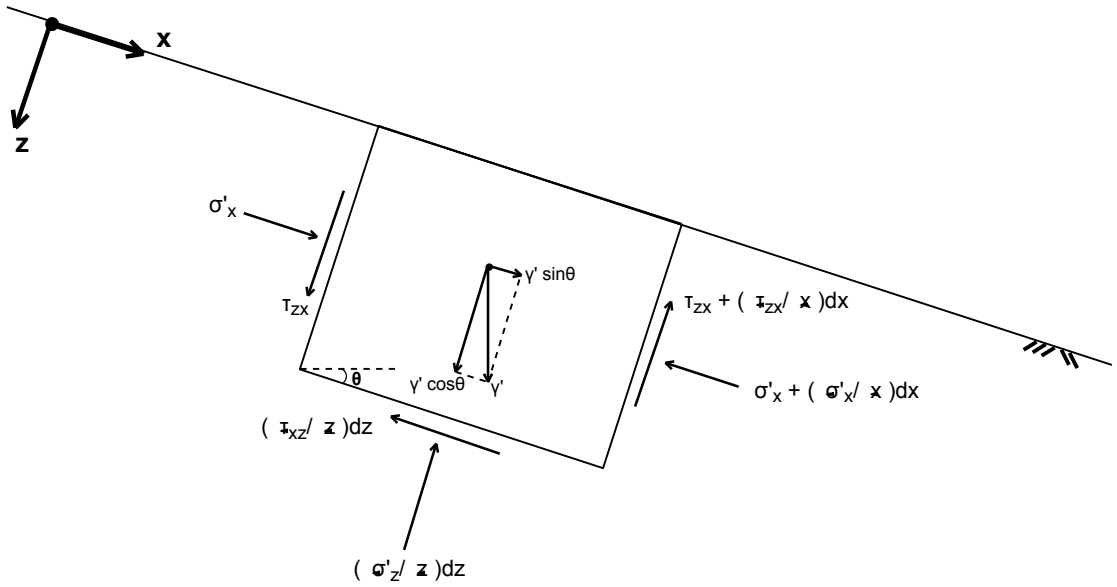

Figure 6.2: Stress variation across an infinitesimal slice of inclined soil of unit weight γ'.

The equilibrium of the infinite slope requires that all cross-sectional planes perpendicular to the ground surface (along the z-axis) are identical, i.e. characterized by the same normal (σ'_x) and shear (τ_{zx}) stress. In other words, no variation of σ'_x and τ_{zx} takes place along the x axis, and consequently:

$$\frac{\partial \sigma'_x}{\partial x} = 0 \tag{6.1}$$

$$\frac{\partial \tau_{zx}}{\partial x} = 0 \tag{6.2}$$

Furthermore, assuming that the slice examined is 1m wide in the direction perpendicular to the x-z coordinate system, force equilibrium in the x direction is written as follows:

$$\Sigma F_x = 0 \Rightarrow \gamma' \cdot \sin\theta \cdot dx \cdot dz \cdot 1 - \frac{\partial \sigma'_x}{\partial x} dx \cdot dz \cdot 1 - \frac{\partial \tau_{xz}}{\partial z} dz \cdot dx \cdot 1 = 0 \tag{6.3}$$

which, in combination with (6.1), yields:

$$\frac{\partial \tau_{xz}}{\partial z} = \gamma' \sin\theta \tag{6.4}$$

Similarly equilibrium in the z direction is expressed as follows:

$$\Sigma F_z = 0 \Rightarrow \gamma' \cdot \cos\theta \cdot dx \cdot dz \cdot 1 - \frac{\partial \sigma'_z}{\partial z} dz \cdot dx \cdot 1 - \frac{\partial \tau_{zx}}{\partial x} dz \cdot dx \cdot 1 = 0 \qquad (6.5)$$

which, based on (6.2), becomes:

$$\frac{\partial \sigma'_z}{\partial z} = \gamma' \cos\theta \qquad (6.6)$$

Equations (6.4)and (6.6) represent the variation of shear and vertical effective stresses with depth that balance the x- and z- gravitational forces respectively. These equations can be used to calculate analytically the distribution of all stress components in a slightly inclined soil profile.

For this purpose, the inclined soil profile, shown in **Figure 6.3a**, is considered. As shown in the figure, the profile has a thickness H, and is inclined by an angle θ. Assuming that the gravity vector is rotated by θ, an equivalent level ground profile is created, in which soil inclination is simulated in terms of both a horizontal and a vertical gravitational component (**Figure 6.3b**). The latter can be calculated based on θ as follows:

$$\begin{aligned} g_x &= g \cdot \sin\theta \\ g_z &= g \cdot \cos\theta \end{aligned} \qquad (6.7)$$

where:

g_x: horizontal component of gravity vector

g_z: vertical component of gravity vector

g: gravitational acceleration (=9.81m/s^2)

θ: angle of soil inclination

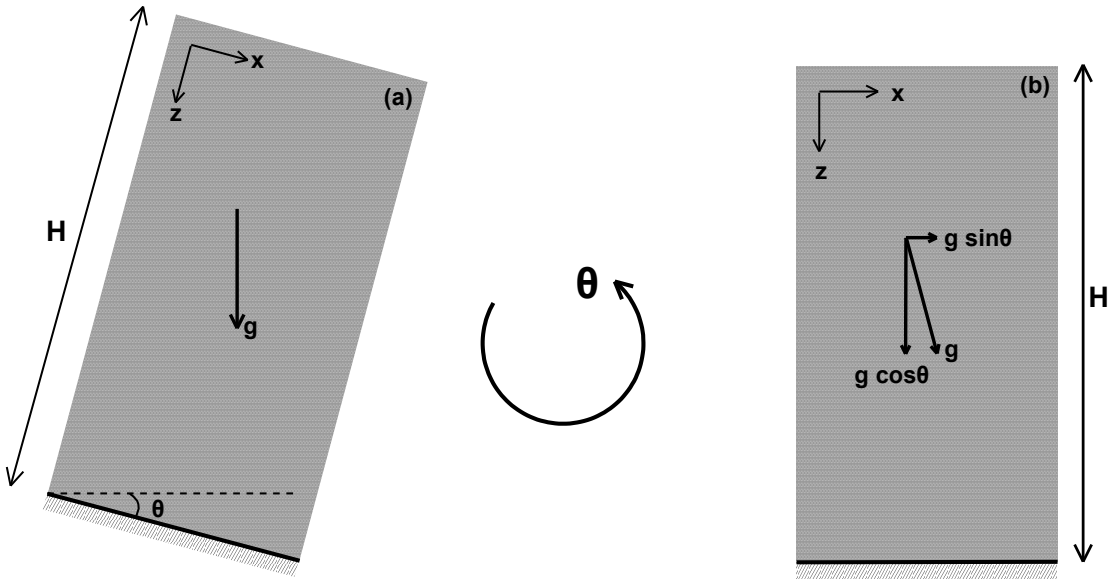

Figure 6.3: Rotation of inclined soil profile and calculation of equivalent horizontal and vertical gravitational components.

Therefore, it is possible to perform the numerical analysis assuming a horizontal mesh, and simulating soil inclination with both a horizontal and vertical gravitational component. This logic is beneficial mainly for numerical reasons, as in general, analyses with inclined meshes cause some sort of inconvenience in the simulation. For example, they do not allow the use of rectangular elements (which are considered more efficient numerically), they complicate the application of boundary constraints (especially tied nodes), as well as the separation of the mesh in groups and assignment of zone properties, and overall the management of the analysis is much more inefficient. However, the major drawback with the level-ground formulation is that it has to simulate a pile which is also inclined, but considering the small values of inclination, these effects are expected to be insignificant.

According to equations (6.4) and (6.6), the effective stresses at the base of the equivalent level ground profile, shown in **Figure 6.4**, can be calculated as follows:

$$\begin{aligned} \sigma'_z &= \gamma' \mathrm{H} \cos\theta \\ \sigma'_x &= \sigma'_y = K_o \sigma'_z \\ \tau_{xz} &= \gamma' \mathrm{H} \sin\theta \\ \tau_{xy} &= 0 \end{aligned} \qquad (6.8)$$

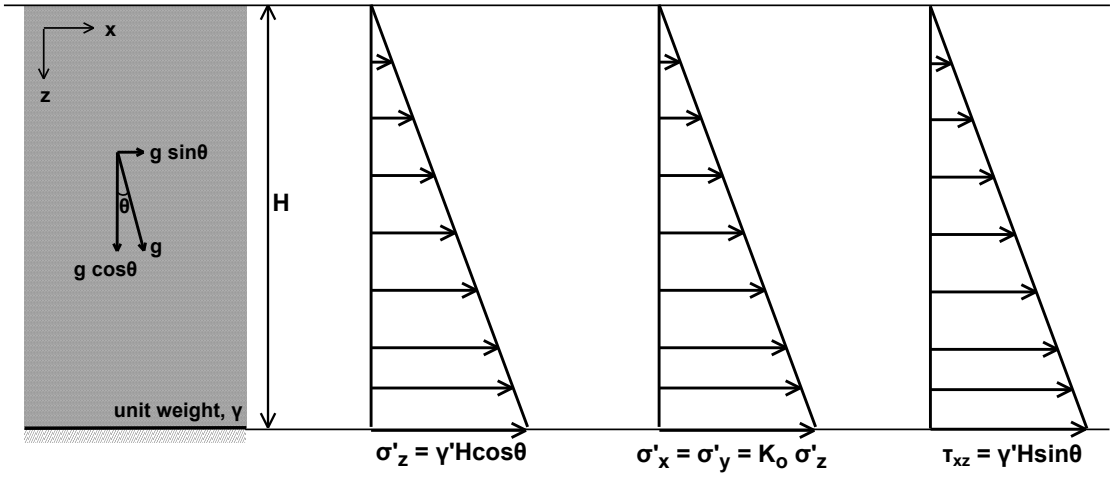

Figure 6.4: Effective stress distribution in an infinite slope inclined by an angle θ.

The mesh built for the analysis is shown in **Figure 6.5**. The dimensions and discretization, which are also shown in the figure, are the same with the mesh used in the static p-y analyses described in the preceding chapters. Namely, the height of the model is 8m, while the length and the width are 22m and 5m respectively. Similarly to the static analysis the vertical plane through the pile axis is a plane of symmetry for the problem. The tip of the pile is located at x=y=z=0. As for discretization, the width of the zone adjacent to the pile is 0.10m, while zone size gradually increases with radial distance from the pile. At this point it should be noted that the mesh from the static analyses is only used herein as an origin. Given that the type of problem analyzed is significantly modified compared to the static case (dynamic loading, inclined soil e.t.c.), the adequacy of the mesh will be again verified later.

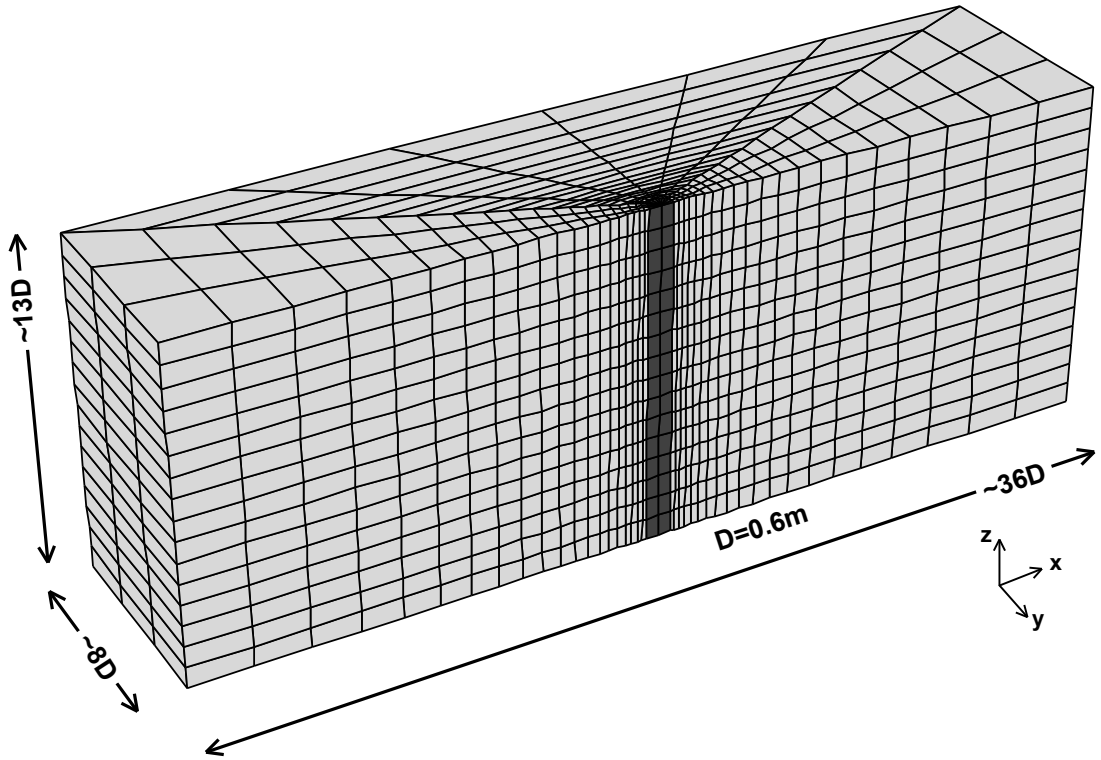

Figure 6.5: Numerical model layout and boundary constraints during initialization of stresses for static infinite slope equilibrium

At this first stage of the analysis, soil properties are assigned to all model zones. Sand response was simulated with the advanced constitutive model also used in the static analyses described in the previous chapters. Model parameters were the ones corresponding to the behavior of Nevada sand, while the initial void ratio was set to e=0.699 corresponding to a Relative Density of D_r=50%. Soil permeability was set to k=6.1x10^{-5}m/sec, a value which is based on measurements from constant-head permeability tests on Nevada sand specimens (Arulmoli et al., 1992). Typical permeability values for various relative densities of Nevada Sand are summarized in **Table 6.3**.

Table 6.3: Permeability coefficient of Nevada Sand (Arulmoli et al., 1992)

Relative Density, Dr (%)	Coefficient of Permeability, k (m/sec)
40	6.6x10-5
60	5.6x10-5
91	2.3x10-5

Displacements at the y-direction were constrained for all gridpoints with y=0 and y=5m. For the rest of the boundaries (|x|=11m and z=0m) horizontal and vertical joints were used necessary to balance the shear stress developed due to the inclination.

In a first approach, the analytical expressions were applied for a dry soil profile with unit weight equal to the buoyant unit weight of the soil ($\gamma' \approx 10kN/m^3$). After proper stress values are manually assigned to each zone, based on the zone's location in the mesh, the model is allowed to attain equilibrium. As expected, only a very few number of steps is required to reach convergence, as stress values have been properly specified, so that the model is already in equilibrium. The numerically computed distribution of shear and horizontal effective stress are shown in **Figure 6.6a** and **b** respectively. As it can be easily observed in the figure, resulting stresses are totally compatible with the stress patterns observed in infinite slopes, as both stress components increase with depth, while all cross-sections vertical to the ground surface are identical.

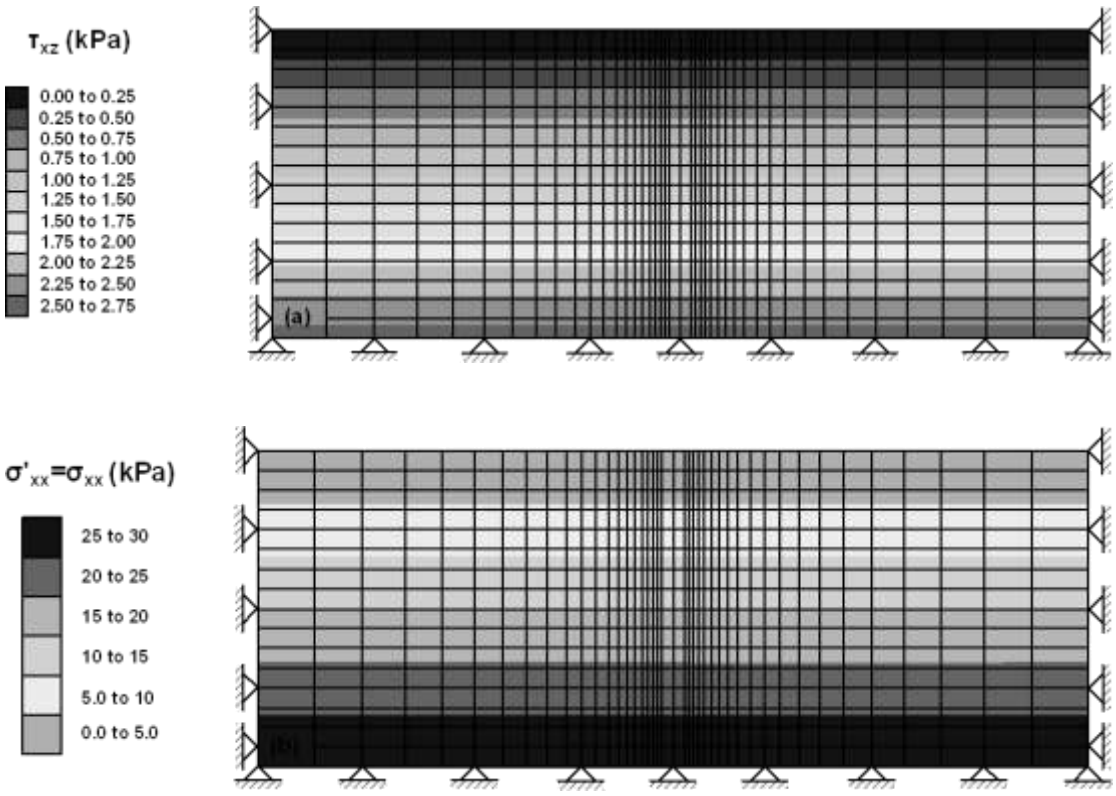

Figure 6.6: Distribution of (a) shear and (b) horizontal stresses after manually implementing in the mesh the analytical relationships

In a second stage, the same procedure was repeated, but this time for the case where the slope is submerged into water. Namely, it was assumed that water elevation at the left boundary of the model is equal to 1m above ground surface. The logic of a submerged slope is adopted in the current simulation to ensure that the model will remain saturated throughout the dynamic shaking. The submerged inclined profile, as well as the equivalent level-ground, is schematically illustrated in **Figure 6.7**.

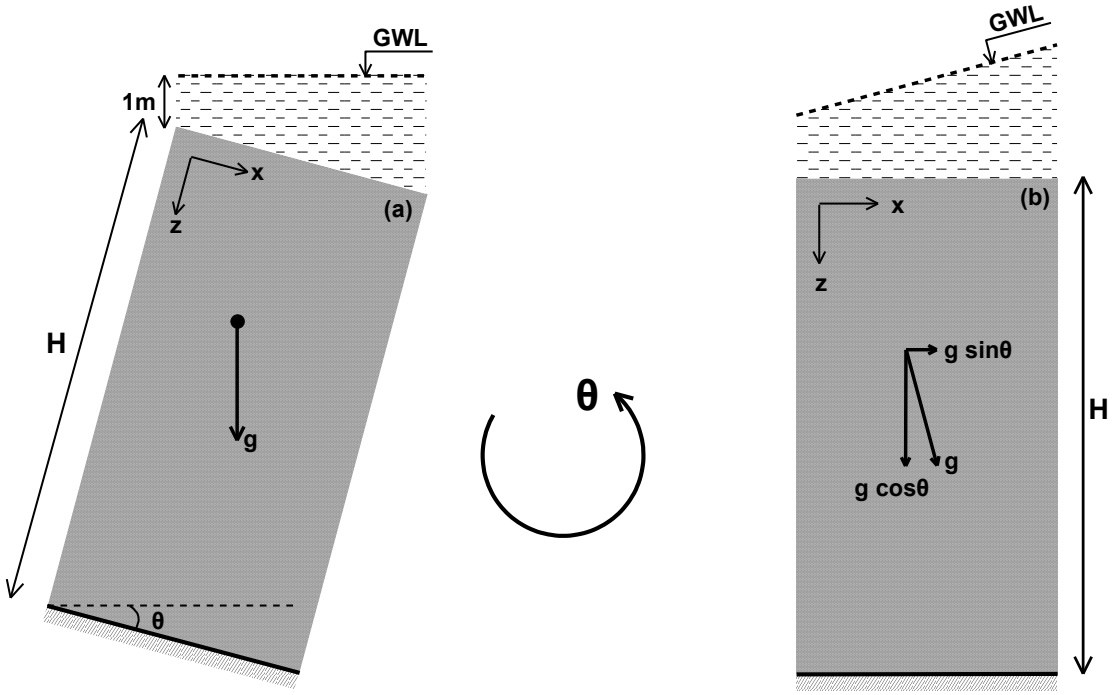

Figure 6.7: Equivalent level ground profile for the case of the submerged infinite slope

Since the gravity vector is rotated to simulate soil inclination, the water table should also be rotated so that no water flow occurs along the horizontal component of the gravity vector. This results in the inclined pore pressure distribution, as shown in **Figure 6.8**. Similarly with stresses, pore pressures are initialized manually in the mesh before the model is allowed to reach static equilibrium. For this case, the analytical expressions (6.4) and (6.6) are used to initialize effective stresses, with their distribution being identical with the one shown in **Figure 6.6**. The latter do not vary horizontally but, in combination with the "inclined pore pressure distribution", the resulting total stress field is inclined as well. As it will be explained later in the chapter, this observation is critical for the numerical establishment of static stress field.

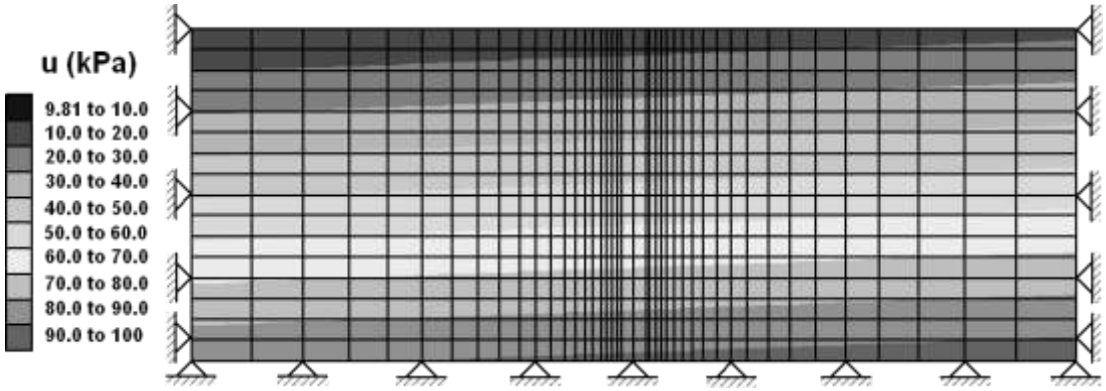

Figure 6.8: Inclined pore pressure distribution for the case of the submerged infinite slope.

6.3.2 Numerical generation of static stress field

The semi-analytical procedure described above for the establishment of static stress equilibrium is verified both for the case of the dry and the submerged slope. The investigation also reveals that establishment of stress equilibrium numerically is a rather tedious task, as it is highly depended on the fixity conditions at the boundaries of the model. As it will be described onwards, typical boundary types like rollers or joints are not adequate, and more advanced boundaries should be incorporated, but only after proper modifications, so that they take into account the kinematics of the problem.

Dry Slopes.- The numerical simulation for this case follows the same steps as in the semi-analytical procedure described previously. However, stress values are not manually assigned at the zones of the model, while different types of fixity conditions are tested at the boundaries of the model ($|x|$=11m and z=0). As for the other lateral boundary (y=0 and y=5m), only y- displacements were constrained. Also, since the current simulation deals with a dry slope, the buoyant unit weight of the soil was assigned in all zones. Following the mesh creation and the application of appropriate boundaries, the model is allowed to reach equilibrium and the stress distribution is obtained numerically. The three (3) different boundary conditions considered were the following:

- Horizontal and vertical rollers at the bottom and side boundaries of the model respectively (**Figure 6.10a**).

- Horizontal and vertical joints at the bottom and side boundaries of the model respectively (**Figure 6.10b**).
- Tied node boundary conditions at the sides of the model which impose the same horizontal and vertical displacement at the gridpoints of the same elevation. Also for the bottom boundary horizontal joints were considered (**Figure 6.10c**).

The last have been widely used in many simulations found in the literature (e.g. Ghosh and Madabhushi, 2003; Elgamal et al., 2005; Popescu et al., 2006), and practically correspond to the kinematic response of the laminar boxes used in centrifuge and shaking table experiments yielding equal horizontal and vertical displacements at each side of the model. In dynamic problems, their main drawback is that waves that propagate near the boundaries might get reflected, and consequently they may affect the numerical results. However, for the highly non-linear problem examined herein, the large portion of hysteretic damping developed, absorbs most of the energy transmitted through reflected waves.

In the numerical analysis, the tied-node boundary conditions and the kinematic response of the laminar box are achieved through a special function written in FLAC's built-in programming language (FISH). The function is executed during each solution step and its formulation can be described with the aid of **Figure 6.9**, which shows a typical horizontal cross section of the mesh used in the analysis and schematically illustrates the application of the tied-node function. Namely:

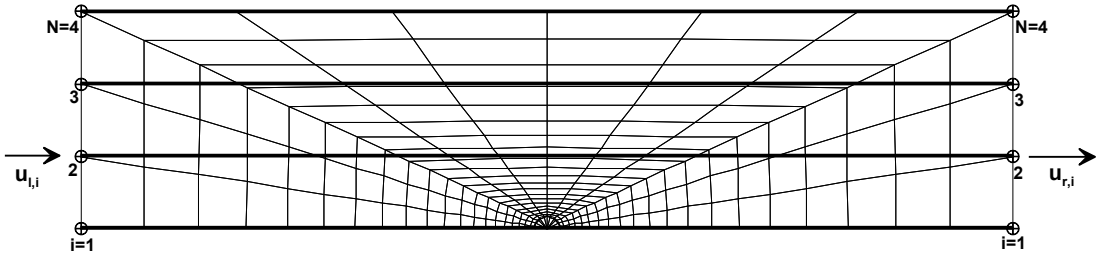

Figure 6.9: Typical horizontal cross-section of the mesh illustrating the application of the tied-node formulation at an arbitrary elevation.

- At the beginning of the calculation cycle, velocities $u_{l,i}$ and $u_{r,i}$, at the left (upward) and right (downward) side of the mesh respectively, are calculated

by FLAC based on the stress state of the zones surrounding the specific gridpoints.

- At that point of the solution algorithm (see Chapter 3), the tied-node function is called and assigns an average, common velocity at all lateral gridpoints of the same elevation. This velocity is calculated as follows:

$$u_{av} = \frac{\sum u_{l,i} + u_{r,i}}{2N} \tag{6.9}$$

where 2N is the number of upward and downward gridpoints (in the case of **Figure 6.9**, 2N=8).

- Finally, velocities $u_{l,I}$ and $u_{r,I}$ are overwritten and the new common velocity u_{av} is assigned to all gridpoints
- The calculation step is completed with the calculation of strains (based on the velocities) and new stresses (based on the strains and the constitutive law adopted).

All three (3) boundary cases considered are schematically illustrated in **Figure 6.10**. Namely, each figure shows the boundary conditions applied, as well as distribution of shear stresses after the model has been brought to equilibrium. The three (3) figures indicate that the resulting initial stress field highly depends on the boundary constraint assumptions. Specifically, the use of rollers at the bottom and side boundaries (**Figure 6.10a**) causes zero stresses at the boundaries, while stress values progressively increase near the center of the mesh. In the case of horizontal and vertical joints along all model boundaries (**Figure 6.10b**), the picture is reversed: large nonzero stresses develop near the boundaries and decrease at the inner part of the model. In any case, both of these formulations do not generate a stress field compatible with the infinite slope logic, as they do not yield a uniform shear stress distribution in the direction parallel to ground surface.

Finally, **Figure 6.10c** shows shear stress distribution as obtained from the numerical analysis when tied nodes were adopted as model boundaries. The resulting distribution is much more realistic and compatible with the basic principles of the infinite slope theory:

- Shear stress remains equal in the horizontal direction, i.e. all vertical cross sections are equivalent
- Shear stress increases with depth, as the horizontal component of the soil mass that needs to be equilibrated is also increased.

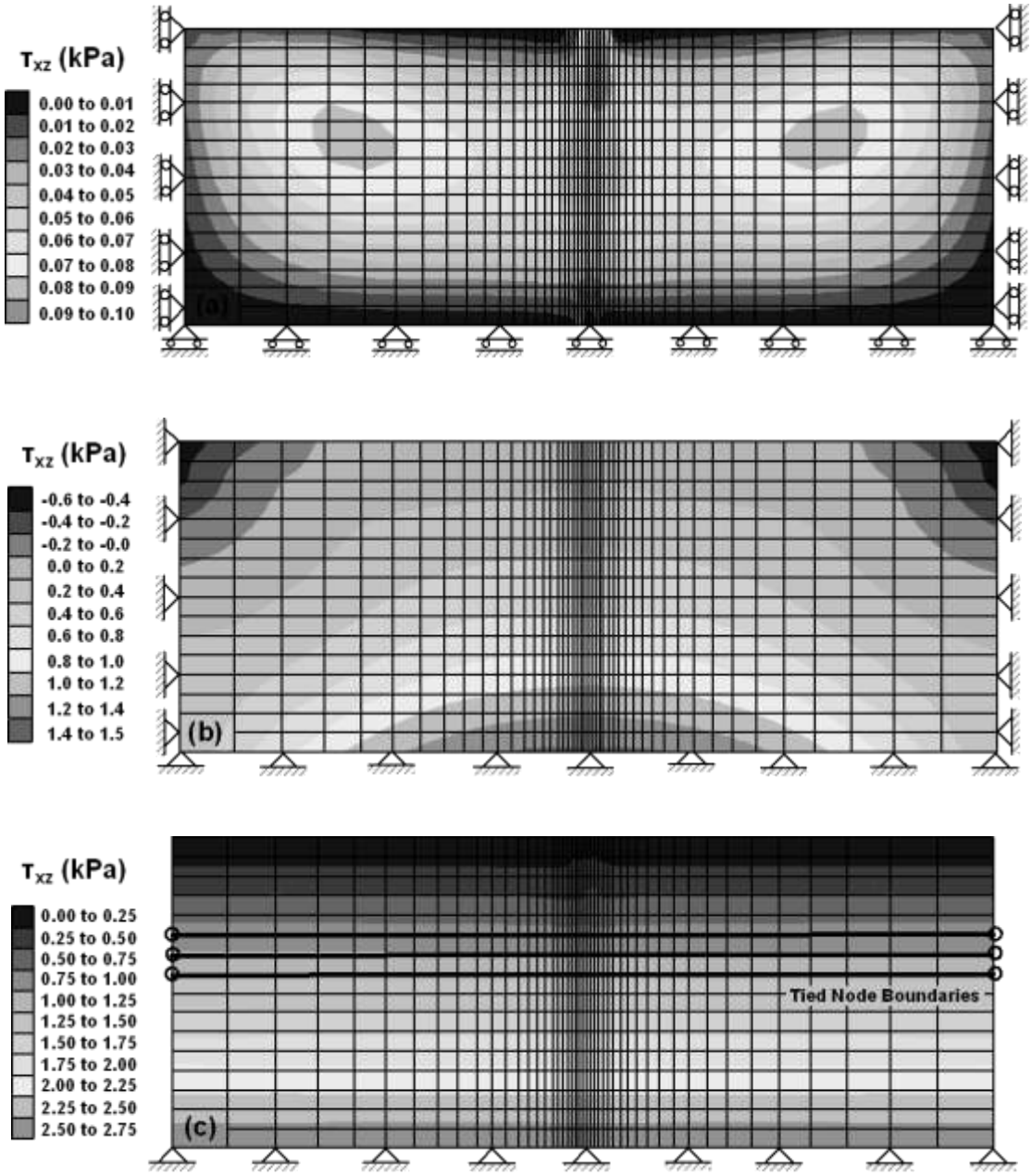

Figure 6.10: Infinite slope shear stresses distribution after numerical equilibrium of the three (3) models examined: (a) Horizontal rollers at the bottom and vertical rollers at the sides (b) Horizontal and vertical joints at the bottom and side boundaries (c) Tied node boundaries at the side boundaries and joints at the bottom

Similar patterns are also observed for the case of effective (or total) horizontal stresses, plotted in **Figure 6.11**. Overall, the above investigation indicates that the only way to eliminate boundary effects and generate a stress field compatible with the basic patterns of infinite slope response, is the use of consistent tied node boundaries at the sides of the model. In all other cases the simulation is practically more close to that of a slope of finite and not infinite width.

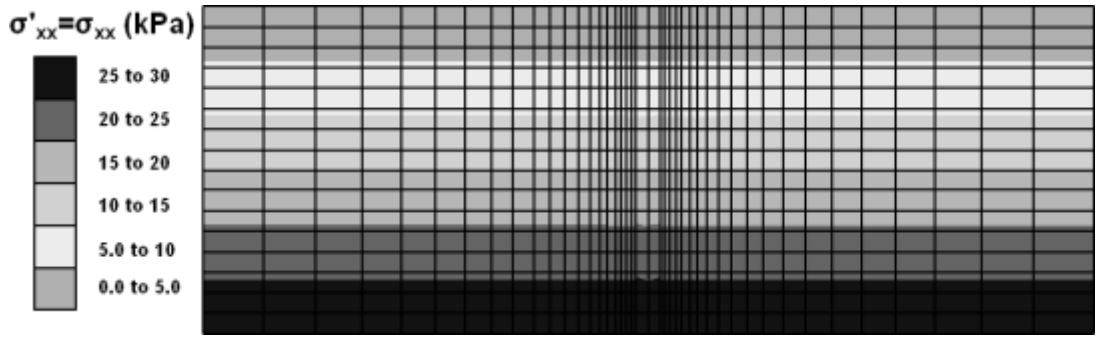

Figure 6.11: Total and effective horizontal stress distribution for the dry infinite slope

Saturated, Submerged Slopes.- For the case presented in this paragraph, only the model with the tied-node boundary constraints is considered. However, analysis shows that application of tied-nodes with the formulation described in the previous paragraph is not adequate and not compatible with the kinematics of the problem. As a result, a modified version of tied-node boundaries had to be introduced.

Before the model is stepped down to equilibrium, the pore pressure distribution is specified manually. As discussed earlier, in order to avoid water flow, the phreatic surface is rotated, yielding the inclined pore pressure distribution shown in **Figure 6.8**. Resulting stress distributions after equilibrium, are shown in **Figure 6.12a**, **b** and **c** in terms of τ_{xz}, σ'_{xx} and σ_{xx} respectively.

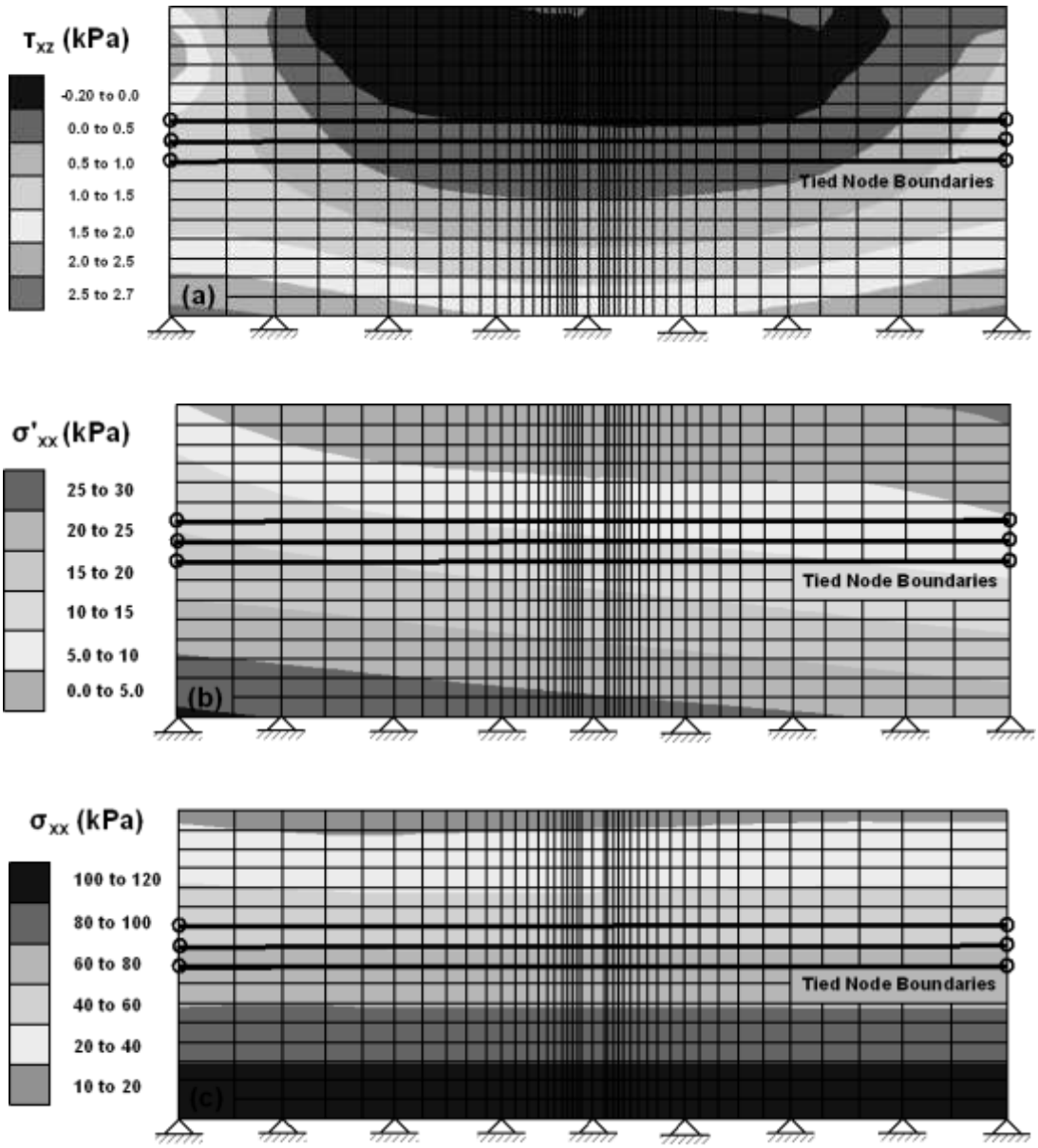

Figure 6.12: Distribution of (a) shear (b) horizontal effective and (c) horizontal total stresses after equilibrium of the submerged slope with the conventional tied-node boundaries.

Based on the stress patterns shown in the figures, the following can be observed:

- Shear stress are neither uniformly distributed along the horizontal direction nor they increase with depth. In general, it can be said that they follow a rather irregular pattern. However, the distribution at the center of the mesh appears to be in good agreement with the stresses from the analysis with the dry profile (**Figure 6.10c**)
- Similarly, horizontal effective stresses distribution is inclined, with larger σ'_{xx} values appearing at the right lateral boundary. Again, the stresses at the mid

cross section of the mesh are in good agreement with the dry profile (**Figure 6.11**).

- Finally, rotation of the effective horizontal stress distribution yields a stress field for the total stresses which is practically horizontal.

The above observations clearly indicate that the current simulation cannot produce a stress field compatible with the kinematics of saturated infinite slopes. In addition, rotation of the effective horizontal stress field and reduction of σ'_{xx} at the right lateral boundary, indicates that the model has a tendency to move to the right, i.e. develop a permanent downward displacement. This is confirmed in **Figure 6.13** where displacement vectors after static equilibrium are plotted. In other words, the model is pushed downwards by a resultant force, which, for the given boundary constraints, is equilibrated only when the total stresses at the two (2) lateral boundaries become equal (**Figure 6.12c**). Of course, since pore pressures remain unchanged, making the total stress distribution horizontal causes the effective stresses to rotate in the direction opposite to the pore pressures. No need to note that this response is not realistic, since infinite slopes in nature do not move downwards. The cause of this downward displacement, as well as the role of the boundaries in the resulting stress field can be clearly explained, when the equilibrium after the use of the analytical expressions developed earlier is considered.

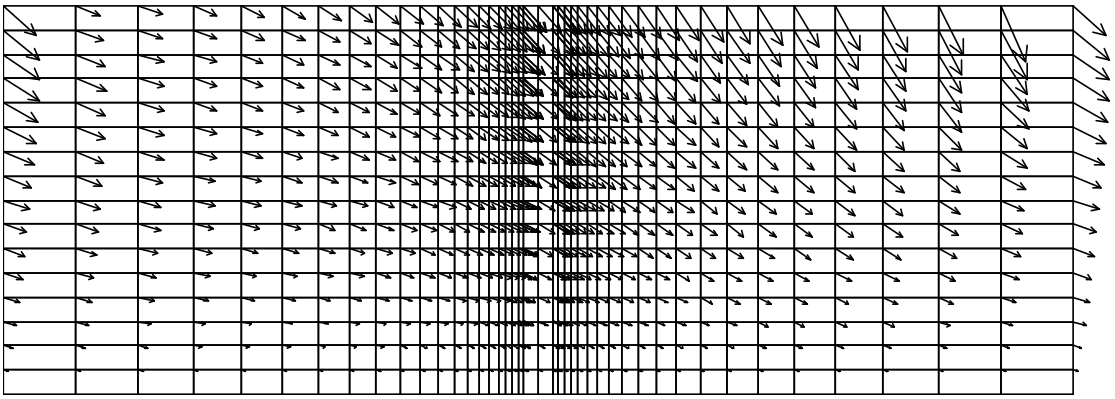

Figure 6.13: Development of permanent downward displacements in a submerged infinite slope after equilibrium with the conventional tied nodes.

Namely, **Figure 6.14a** shows the inclined pore pressure distribution, as a result of the rotated water table, while **Figure 6.14b,** shows the variation of horizontal effective stresses. In the above figures the pore pressure distribution can be calculated based

on the inclination of the slope, while the effective stress field is estimated based on the analytical expressions described earlier. Finally, **Figure 6.14c** shows distribution of total horizontal stresses, which, due to the inclined pore pressures and the horizontal effective stresses, is also rotated relative to the horizontal. This rotation in the total stress field generates the permanent downward velocity, as it can be easily shown after examining the equilibrium of a slice of soil around gridpoints A and B (**Figure 6.14c**).

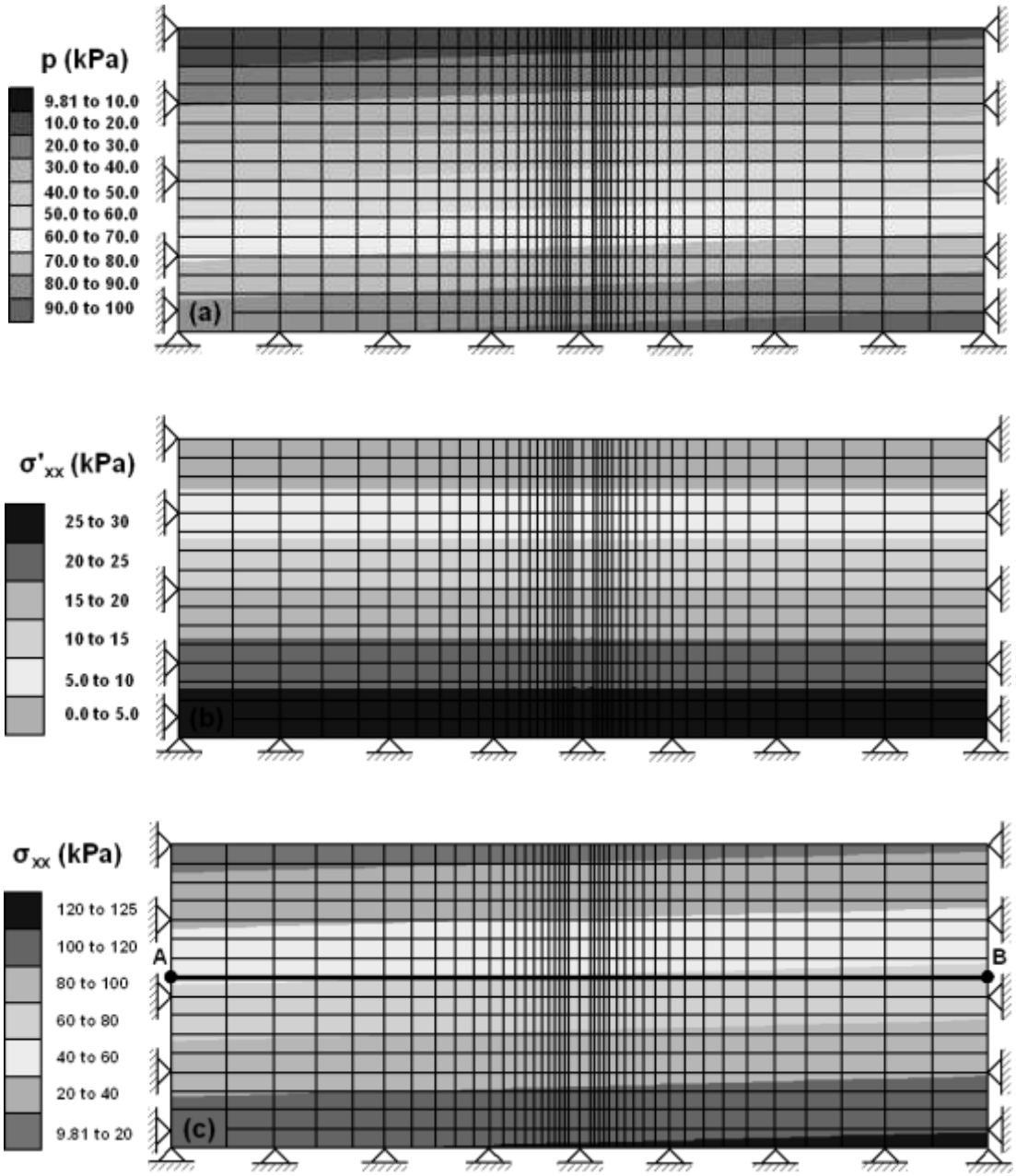

Figure 6.14: Distribution of (a) pore pressures (b) horizontal effective and (c) horizontal total stresses in a submerged slope after stress initialization using the analytical expressions

The equilibrium of the slice is shown in **Figure 6.15**. Considering FLAC's solution algorithm, described in Chapter 3, based on the average total horizontal stress from the zones surrounding gridpoints A and B, a total horizontal force is calculated as follows:

$$F_A = \sigma_{xx,A} \cdot A_s$$
$$F_B = \sigma_{xx,B} \cdot A_s \qquad (6.10)$$

where:

F_A, F_B: Horizontal force at gridpoints A and B.

$\sigma_{xx,A}$, $\sigma_{xx,B}$: Average horizontal total stress from zones surrounding gridpoints A and B

A_s: Area corresponding to gridpoints A and B (for the mesh adopted in the simulation all gridpoints with the same x- and y- coordinate have the same corresponding area).

For the specific problem examined herein, since the total horizontal stress at B is larger than in A, the resulting force at B will also be larger, i.e.:

$$\sigma_{xx,B} > \sigma_{xx,A} \Rightarrow F_B > F_A \qquad (6.11)$$

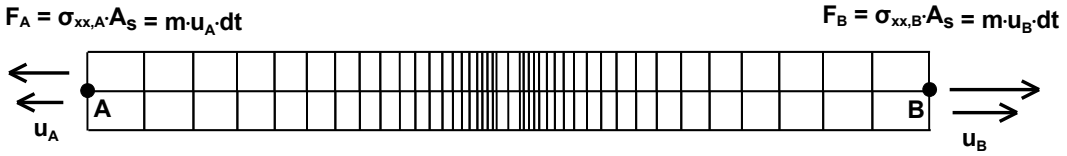

Figure 6.15: Equilibrium of an infinitesimal slice of soil around gridpoints A and B.

At the next step of the computational cycle, the equations of motion are invoked and an acceleration is calculated for each gridpoint based on the total force estimated previously (assuming no damping is specified):

$$a_A = F_A / m$$
$$a_B = F_B / m \qquad (6.12)$$

where:

α_A, α_B: Acceleration at gridpoints A and B respectively

m: mass corresponding to the gridpoint (for the mesh adopted in the simulation all gridpoints with the same x- and y- coordinate have the same corresponding mash)

Based on the preceding values of the acceleration, corresponding velocities can be calculated for each gridpoint given the timestep of the analysis:

$$\begin{aligned} u_A &= a_A \cdot dt = F_A / m \cdot dt \\ u_B &= a_B \cdot dt = F_B / m \cdot dt \end{aligned} \tag{6.13}$$

where:

u_A, u_B: gridpoint velocities at A and B

dt: analysis timestep

Of course, given that $F_B > F_A$, then

$$u_B > u_A \tag{6.14}$$

Note that equation (6.14) refers to the magnitude of the velocities, while it is obvious that u_A and u_B also have opposite signs, as shown in **Figure 6.15**. At that point of the solution algorithm, the tied-node function is called to modify the velocities at the boundary gridpoints as follows (the formulation of the function was described earlier in the chapter):

- An average velocity value is estimated from u_A and u_B:

$$u_{av} = \frac{u_A + u_B}{2} \neq 0 \tag{6.15}$$

- The velocities at gridpoints A and B are updated and assigned the common velocity u_{av}, while u_A and u_B are overwritten.
- The tied-node function is terminated, and the numerical solution progresses with the calculation of strains (based on u_{av}) and new stresses (based on the constitutive law adopted).

Given (6.14), despite the fact that the slope is in equilibrium, the current tied-node formulation will generate a downslope velocity, which will disrupt the stresses.

In other words, the difference in total stresses between corresponding points of the same elevation is the one that generates this permanent downward velocity. Therefore, equilibrium can only be achieved when the total stresses at the two (2) boundaries become equal. For this reason, the total stress field, shown in **Figure 6.12c**, has become practically horizontal after equilibrium. In a clear physics context, this phenomenon is absolutely normal, as, according to Newton's 2nd law of motion, the acceleration of a mass depends on the total force applied on it. Therefore, despite the fact that effective stresses are horizontal, the inclined total stresses cause the soil mass to move.

However, the inclined total stress distribution cannot be avoided, as it emanates from the need to rotate the water table, so that no water flow occurs. In addition, as shown for the case of the dry profile, no other boundary conditions, but tied-nodes, can properly simulate the infinite slope using a model with finite boundaries. Therefore, a new, modified version of the tied-node concept had to be introduced, compatible with these particular kinematic characteristics of the specific problem. The modified tied-node formulation is based on the idea that an upward velocity should be applied at the lateral boundaries of the model, so that the static stress equilibrium is not disturbed.

Based on the preceding analysis [equations (6.10) through (6.14)], the upward velocity, u_{up}, necessary to stabilize the slope will be equal to:

$$u_{up} = u_B - u_A \tag{6.16}$$

From the above equation it is clearly indicated that estimation of u_{up} requires the knowledge of u_A and u_B. The latter can only be calculated once the proper stress field is established, since they depend on the stresses of the zones surrounding the specific gridpoints. This leads to the conclusion that the upward velocity, u_{up}, requires the a priori establishment of the correct stress-field in the model, and hence, static equilibrium cannot be achieved numerically, but only with the use of the analytical relations. However, examining more carefully the preceding equations, it can be observed that while u_A and u_B depend on the total stress values, their difference is not. Namely, combining equations (6.10), (6.13) and (6.16) we get:

$$u_{up} = u_B - u_A = \left(\frac{F_B}{m}\right)\cdot dt - \left(\frac{F_A}{m}\right)\cdot dt = \left(\frac{\sigma_{xx,B}\cdot A_s}{m}\right)\cdot dt - \left(\frac{\sigma_{xx,A}\cdot A_s}{m}\right)\cdot dt = \\ = \frac{A_s\cdot dt}{m}\ \sigma_{xx,B} - \sigma_{xx,A} \tag{6.17}$$

Furthermore, considering the effective stress principle the difference $\sigma_{xx,B} - \sigma_{xx,A}$ becomes:

$$\sigma_{xx,B} - \sigma_{xx,A} = \sigma'_{xx,B} + p_B - \sigma'_{xx,A} - p_A \tag{6.18}$$

where:

$\sigma'_{xx,A}$ and $\sigma'_{xx,B}$: Effective stresses at gridpoints A and B

p_A, p_B: Pore pressures at gridpoints A and B

However, the basic infinite slope feature that requires all planes vertical to the surface to be identical yields:

$$\sigma'_{xx,B} = \sigma'_{xx,A} \tag{6.19}$$

Therefore, the difference in total stresses is equal to the difference in pore pressures:

$$\sigma_{xx,B} - \sigma_{xx,A} = p_B - p_A \tag{6.20}$$

However, pore pressure distribution and hence pore pressure values at each point of the grid are known prior to static equilibrium based on the inclination of the slope (see paragraph 6.3.1 and **Figure 6.8**).

Based on the above, the modified formulation of the tied-node boundaries, which is also illustrated in **Figure 6.16**, for an arbitrary elevation, can be described as follows:

- For each set of gridpoints with same y- and z- and opposite x- coordinates (i=1-4 in the figure), values of $A_{s,i}$, m_i, $p_{l,i}$ and $p_{r,i}$ are accessed through appropriate FISH variables, where:

  $p_{l,i}$, $p_{r,i}$: Pore pressure at the left (upward) and right (downward) gridpoint respectively

  $A_{s,i}$: Area corresponding to gridpoint

m_i: Mass corresponding to gridpoint

Note that for the specific mesh created for the problem, all gridpoints with the same y- and z- coordinate have the same mass and area.

- For each set of gridpoints (i=1-4 in the figure) the corresponding upward velocity can be calculated as follows:

$$u_{up,i} = \frac{A_{s,i} \cdot dt}{m_i} \; p_{l,i} - p_{r,i} \tag{6.21}$$

where dt is the timestep of the analysis, common for the whole mesh.

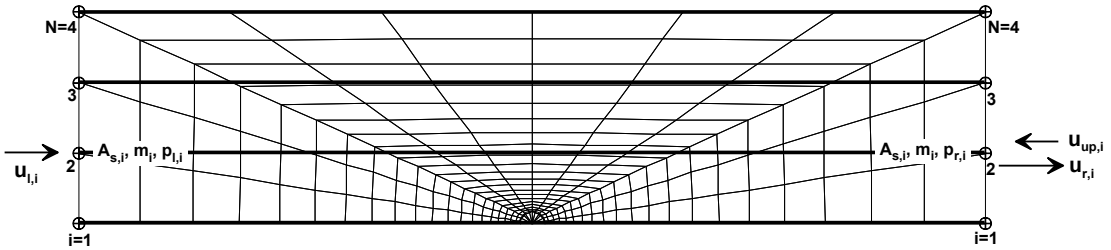

Figure 6.16: Typical horizontal cross-section of the mesh illustrating the application of the modified tied-node formulation at an arbitrary elevation.

Note that the two (2) previous steps are executed only once, after assignment of pore pressures to zones, and prior to stepping. Hence, the computational cost from these calculations is practically negligible. During stepping, the function works as follows:

- At the beginning of FLAC's calculation cycle, velocities $u_{l,i}$ and $u_{r,i}$, at the left (upward) and right (downward) side of the mesh respectively, are calculated based on the stress state of the zones surrounding the specific gridpoints.
- At that point of the solution algorithm (see Chapter 3), the tied-node function is called and assigns an average, common velocity at all lateral gridpoints of the same elevation. This velocity is calculated as follows:

$$u_{av} = \frac{\sum \; u_{l,i} + u_{r,i} - u_{up,i}}{2N} \tag{6.22}$$

- Finally, velocities $u_{l,i}$ and $u_{r,i}$ are overwritten and the new common velocity u_{av} is assigned to all gridpoints

- The computation circle is completed with the calculation of strains (based on velocities) and the calculation of the new stresses (according to the constitutive law adopted)

The performance of the modified tied-node function, as well as an overall comparison of the different methods used to obtain the static stress field of a submerged infinite slope, is demonstrated in **Figure 6.17** and **Figure 6.18**, for the shear and the horizontal effective stresses respectively. Namely, each figure shows the stress distribution obtained from the analytical relationships (**Figure 6.17a** and **Figure 6.18a**), the conventional tied-node formulation (**Figure 6.17b** and **Figure 6.18b**) and the modified tied-nodes (**Figure 6.17c** and **Figure 6.18c**)

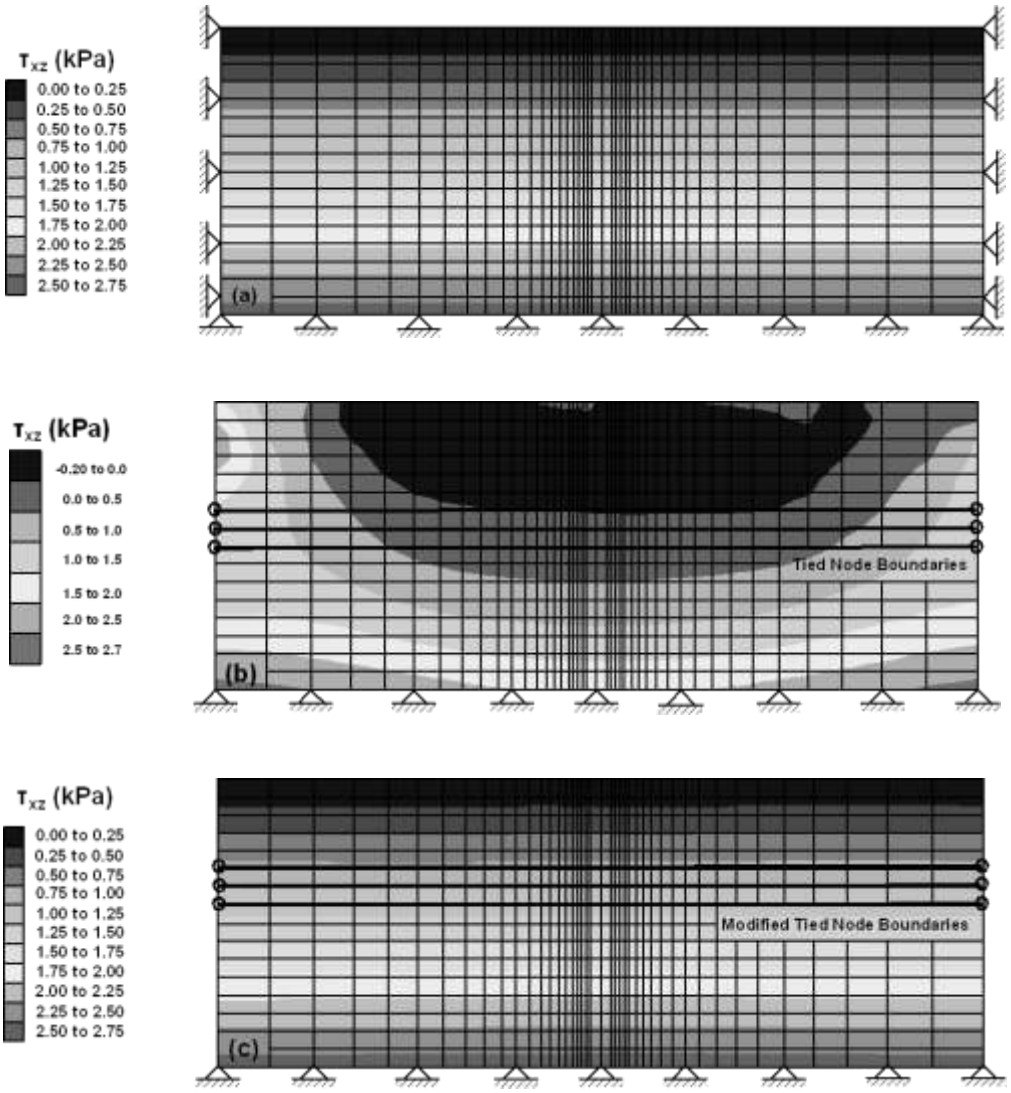

Figure 6.17: Establishment of static shear stress distribution based on three (3) different approaches (a) analytically (b) numerically with classic tied-nodes (c) numerically with the modified tied-nodes

The comparison from both shear and horizontal stresses shows that the analytical expressions agree with the numerical, only when the modified tied-nodes are used. On the other hand, when the conventional tied-node formulation is used, the stress field developed is not largely differentiated qualitatively, but in terms of distribution shape, it definitely does not reflect the stress conditions as they would appear in actual slopes.

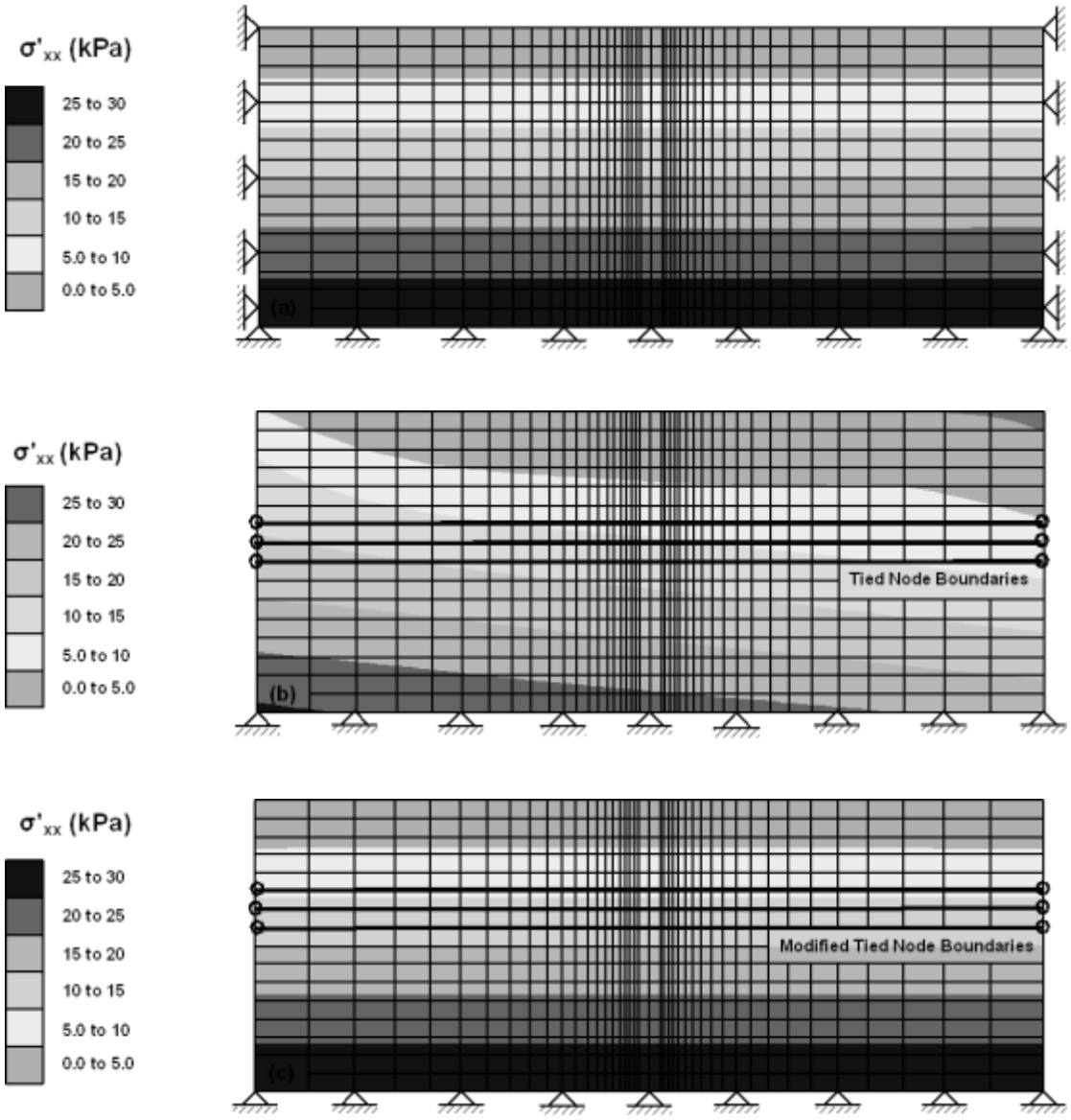

Figure 6.18: Establishment of static horizontal effective stress distribution based on three (3) different approaches (a) analytically (b) numerically with classic tied-nodes (c) numerically with the modified tied-nodes

At this point it should be noted that all the preceding analysis and the development of the modified tied-node concept does not only apply for the stage of static stress

equilibrium, but in the dynamic part as well. In the latter, as it will be thoroughly described later, tied-node boundaries are used, and hence, the use of the conventional tied nodes, and the induced permanent velocity that they cause, could affect the dynamic response of the system. In any case, the performance of the modified boundaries compared to the old will be further analyzed later in the chapter. This last investigation and comparison becomes more essential, taking into account that the conventional tied-node formulation reflects the boundary conditions as applied in the laminar boxes, which are widely used in centrifuge and shaking table tests.

6.4 Stage 2: Pile installation

This stage simulates the installation of the pile in the soil. Numerically this is performed by assigning pile properties to the corresponding zones in the mesh, as well as creating interface elements between the soil and the pile to simulate sliding and/or separation. Pile is simulated using an elastic model, assuming that no plastic hinges will develop. This type of response for the pile was intentionally assumed on the basis that plastic pile response is not usually an allowable design scenario. Plastic hinges due to large kinematic loads remain open after the end of shaking constituting foundation failure. In addition, accessing and repairing damaged parts of pile foundations is a rather tedious, and in many cases an impossible task.

The properties of the interface elements are assigned similarly to the static analyses, i.e. large stiffness to avoid straining of the interface and friction angle equal to ½ of the friction angle of the soil.

Furthermore, this stage simulates stress changes that occur in the surrounding soil during installation of open and close ended driven piles. The method of numerical simulation of these effects has been thoroughly described in Chapter 5 of the present thesis. In short, it models installation as the expansion of a cylindrical cavity. The new stresses are calculated using Vesic's analytical solution of the specific problem and implemented manually in the mesh using a FISH (the in-built flac3d programming language) function.

6.5 Stage 3: Seismic Shaking

At this stage of the analysis a horizontal sinusoidal dynamic motion is applied at the base of the model and the response of the pile-soil system is investigated mainly in the form of p-y curves. Similarly to the static analyses, soil pressures are numerically calculated through the stresses that develop at the interface gridpoints, hence yielding the net soil reaction. For this purpose, as described in Chapter 3, a function in FLAC's programming language, FISH, was programmed and executed during the analysis. Also, for the case where both the pile and the soil develop lateral displacements, displacement y is defined as the difference between the free-field displacement of the soil and the pile displacement. The former is calculated as the displacement at the left boundary of the model (which is equal to the one at the right given the tied-node boundaries), and the latter as the displacement at the axis of the pile, i.e.:

$$y = y_{ff} - y_p \tag{6.23}$$

where:

y_p: Horizontal displacement at the pile axis

y_{ff}: Horizontal displacement at the boundary of the model

However, since the presence of the pile is known to affect soil displacements at the area close to pile ("pinning effects"), it should be verified that the lateral boundary is far enough so that displacements are not affected by the pile and are equal to the actual free field displacements. Satisfaction of this requirement will be demonstrated later along with the investigation of the appropriate mesh size.

As far as the boundary conditions are concerned, the dynamic excitation is directly applied at the base of the model simulating rigid bedrock conditions. Furthermore, the lateral boundaries at y=0 and y=+5m were only fixed in the y-direction and free to move in the x- and z- direction. For the lateral boundaries at the direction of shaking (|x|=11), the modified tied-node conditions described earlier, were considered. As noted earlier, the overall performance of the modified tied-node formulation in a fully coupled dynamic problem will be further evaluated in the following paragraphs.

6.6 Comparative evaluation of the modified tied nodes formulation

In the present section the performance of the modified formulation of tied nodes is evaluated with respect to two (2) different problems involving dynamic loading of infinite slopes:

- Lateral spreading of a uniform sand layer
- Single pile in laterally spreading soil

6.6.1 Lateral spreading of uniform sand layer

The problem of a laterally spreading uniform sand layer is simulated using two (2) different approaches, in order to evaluate the performance of the modified formulation of tied nodes, described in 0, during the dynamic excitation. In the first approach, the numerical methodology described previously (for the analysis without the pile) is adopted. The second approach simulates the conditions prevailing in actual laminar boxes used to investigate the specific problem experimentally. Namely, the "laminar box" simulation is performed as follows:

- Stage 1: Geostatic stress field for level ground conditions is obtained (only the vertical gravitational component is specified).
- Stage 2: The model is rotated by specifying a horizontal gravitational component and an inclined pore pressure distribution. Then the model is stepped to equilibrium and the static stress field of the slope is obtained. The two (2) lateral sides of the model are tied using the typical (prior to modification) tied nodes.
- Stage 3: The dynamic excitation is applied at the base of the model keeping the same tied-node boundaries as before.

The basic differences between the two (2) simulations are summarized in **Table 6.4**. Note that the geometry of the model, as well as the soil and excitation properties are the same as described in 6.2, with the only difference being in the period of the excitation, which for the comparison shown here was T=0.35sec and not 0.30sec as in the analyses shown earlier. Also, given that the objective of the present investigation is only to assess the relative differences between the two (2) simulations, a more sparse mesh with only square elements with size 1x1x1m was used in order to reduce the computational time.

Table 6.4: Basic aspects of the two (2) different models used to simulate lateral spreading

Simulation	Stage 1: Static Equilibrium	Stage 2: Dynamic Excitation
(1) Typical ("laminar box")	a) Geostatic stress field for level-ground conditions b) Rotation of the model and infinite slope equilibrium using the **typical** tied-node formulation	Application of dynamic loading at the base of the model using the **typical** tied-node formulation
(2) Modified ("free-field")	a) Geostatic stress field for level-ground conditions b) Rotation of the model and infinite slope equilibrium using the **modified** tied-node formulation	Application of dynamic loading at the base of the model using the **modified** tied-node formulation

6.6.1.1 Static stress equilibrium

Resulting stress distributions after static equilibrium are demonstrated in **Figure 6.19** and **Figure 6.20** in terms of shear stress and horizontal effective stress respectively. The major deficiencies of the typical tied-node formulation (the "laminar box" model) have already been discussed in 0. In short:

- Shear stresses are not uniformly developed, but show a rather irregular shape.
- The inclined pore pressure distribution in combination with the kinematic requirement for equal total stresses at the two (2) lateral sides of the model (see paragraph 0), yields the inverted horizontal effective stress distribution shown in **Figure 6.20b**.
- Overall, the static stress field developed with the "laminar box" simulation is not typical of an actual infinite slope found in nature.
- However, it should be noted that stress values at the mid-section of the model with the typical tied-nodes are in good agreement with the ones from the model with the modified tied-nodes.

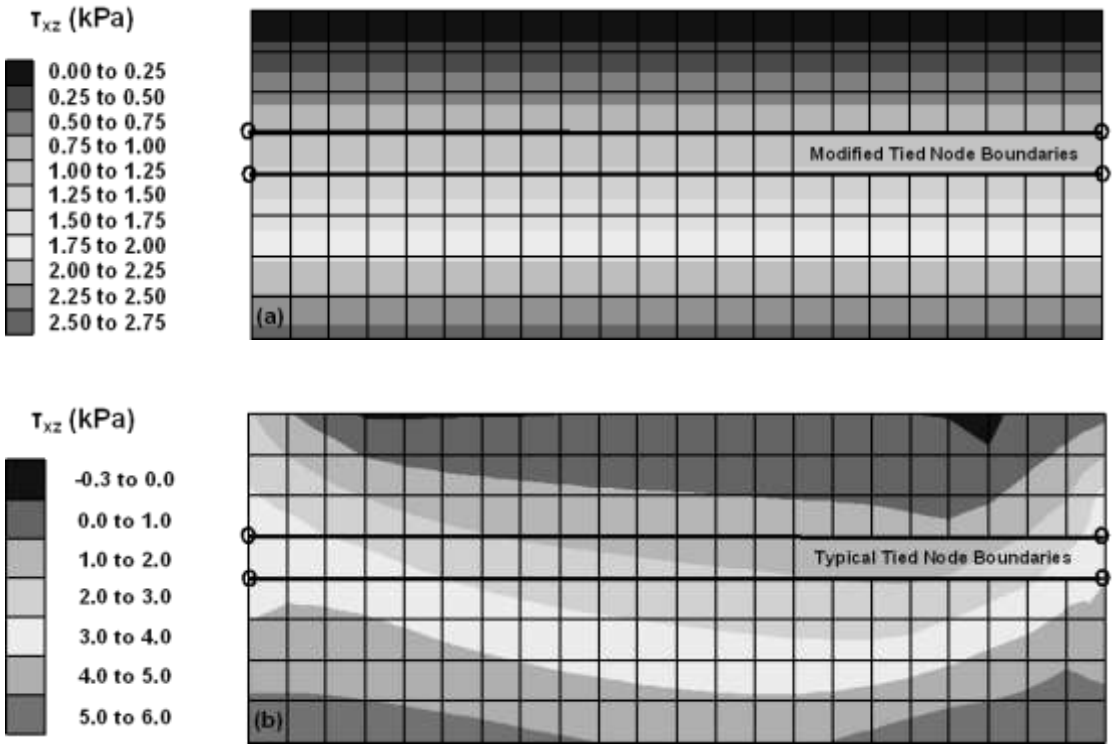

Figure 6.19: Shear stress distribution after applying the (a) modified tied-nodes and the (b) typical tied-nodes model

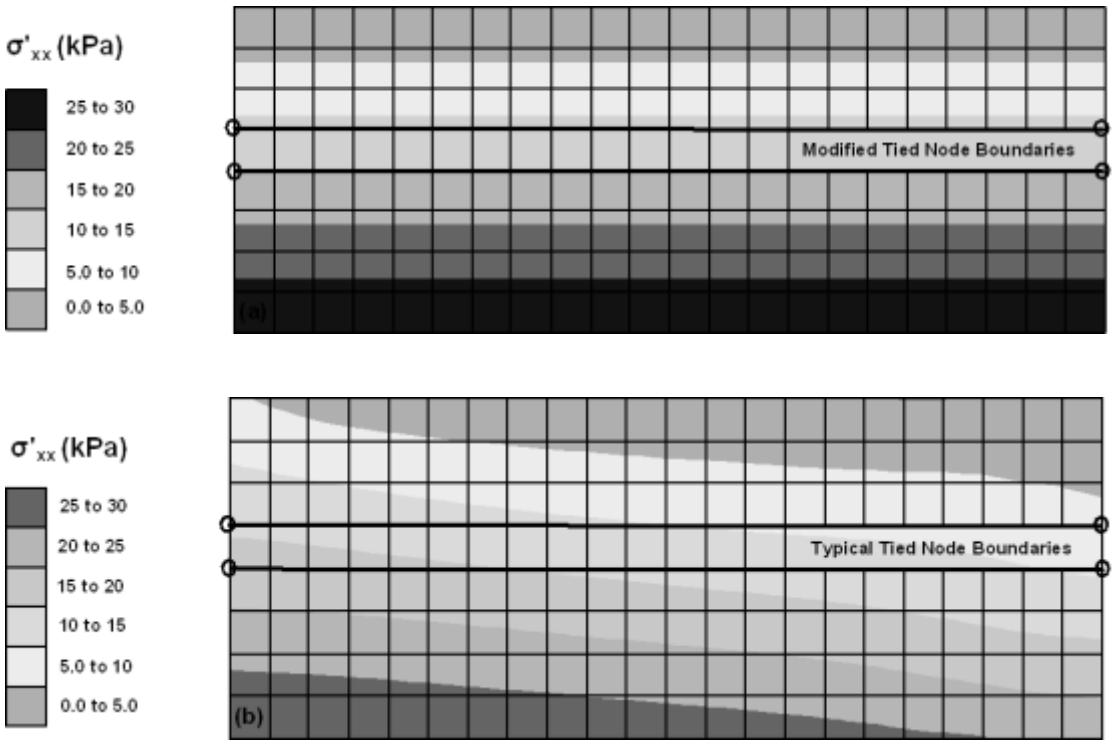

Figure 6.20: Horizontal effective stress distribution after applying the (a) modified tied-nodes and the (b) typical tied-nodes model

The above differences are further demonstrated in **Figure 6.21a** and **b** which show the variation with depth of shear and horizontal effective stresses. In these figures, the black line corresponds to the typical ("laminar box") simulation and the grey to the modified. In addition, for both simulations variation is shown for three (3) different vertical cross sections. One at the center of the mesh (continuous line) and two (2) at each lateral boundary (dashed lines). For the modified model all three (3) cross sections are identical, as they yield the same shear and horizontal effective stresses. However, this is not the case for the typical-laminar box model, where stress values appear to be increased at the left boundary and decrease at the downstream side. In any case, it can be observed that the values at the mid-cross section are in relatively good agreement with the modified model, especially in terms of σ'_{xx}.

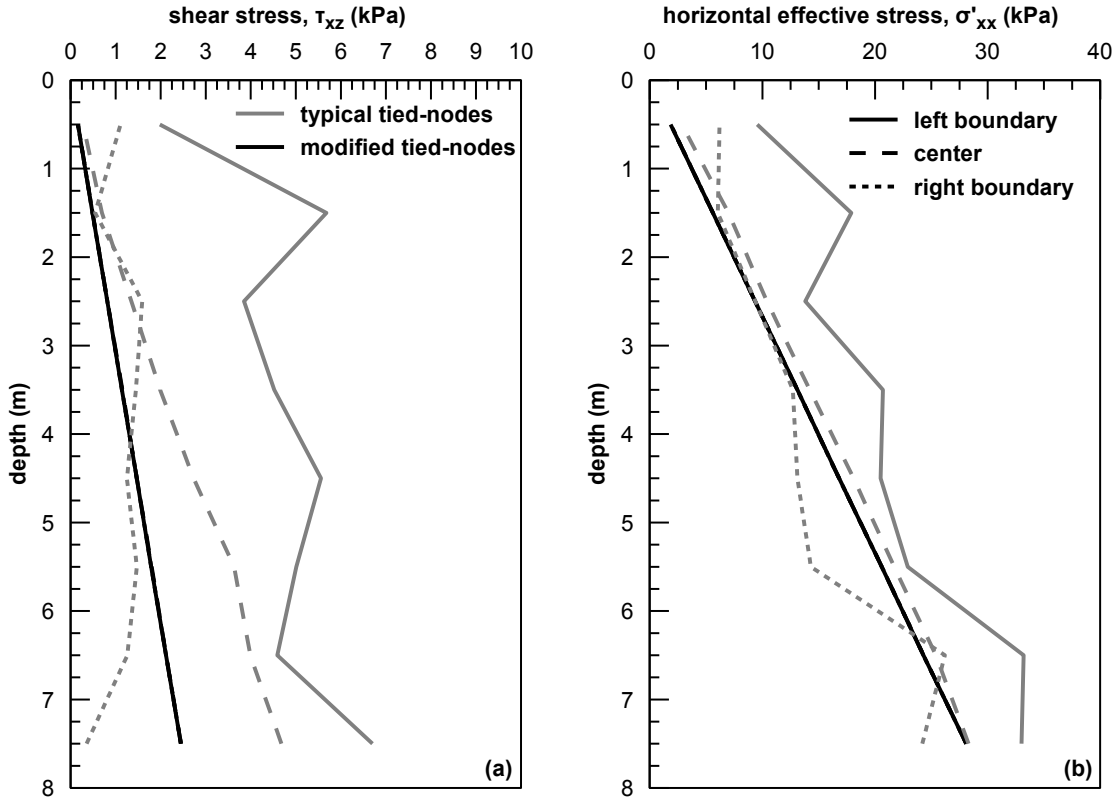

Figure 6.21: Variation of (a) shear and (b) horizontal effective stress with depth at the two lateral boundaries and at the center of the model using the two different simulations

6.6.1.2 Response after dynamic loading

Following static equilibrium, a sinusoidal excitation is applied at the bottom of the mesh. The deformed mesh and the contours of horizontal displacements are shown

in **Figure 6.22a** and **b**, for the modified and the typical tied-node simulation respectively. The two (2) figures indicate that the maximum accumulated displacements are similar for the two (2) models (with the "laminar box" model yielding slightly larger values). However, large differences are observed between the two (2) models as far as the distribution of displacements along the x- and the z- axes is concerned. Namely, the modified tied-nodes model yields a response which is practically equivalent for all cross sections along the x- axis. On the other hand, this does not appear to be the case for the model with the typical tied-nodes. For small depths, displacements at the center are slightly smaller and increase close to the boundaries. However, as depth increases, displacements near the boundaries become larger than at the center. In general, displacement distribution with depth does not appear to be equivalent along the horizontal direction.

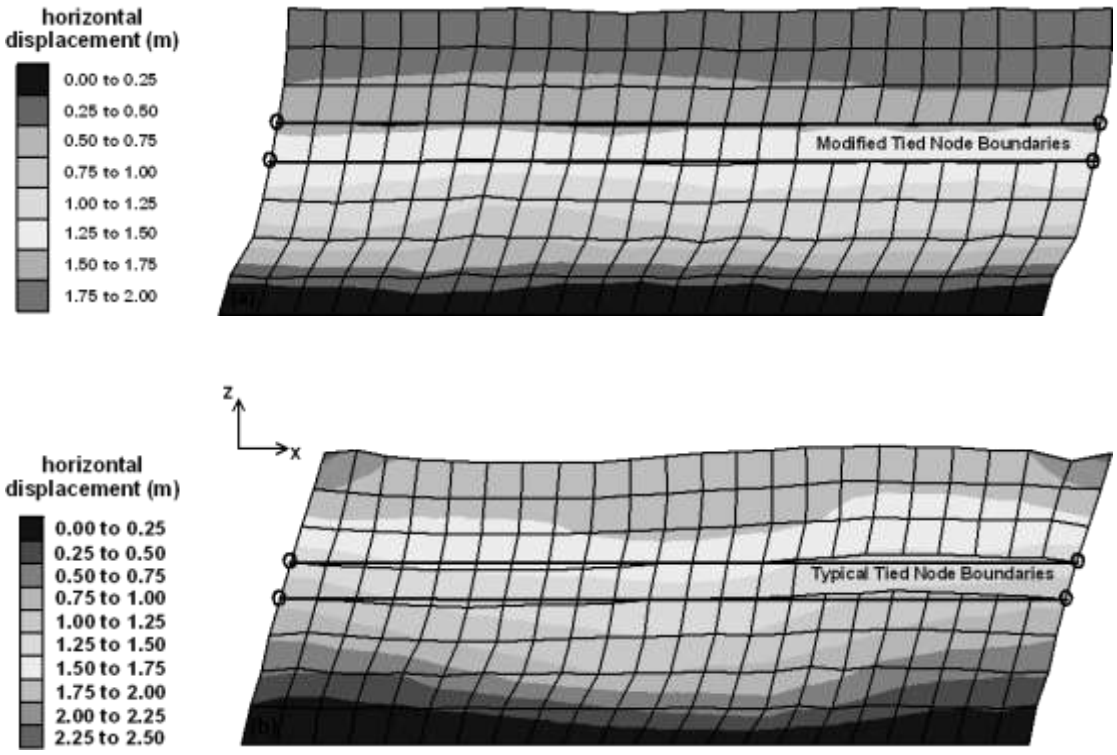

Figure 6.22: Deformed mesh and contours of lateral soil displacement at the end of shaking for the (a) modified tied-nodes and the (b) typical tied-nodes model

In order to further investigate these differences, **Figure 6.23** illustrates displacement profiles with depth for the two (2) models at different locations in the grid. Namely,

the black lines correspond to the modified tied-node formulation, while the grey lines correspond to the "laminar box" formulation. In addition the continuous lines show displacement variation at the center of the model, and the dashed lines show displacement variation at the two (2) lateral boundaries. For the model with the modified tied-nodes, the three (3) black lines practically coincide, indicating very similar response along the whole width of the model. In addition variation with depth has the well-known sinusoidal shape. Displacements at ground surface are approximately equal to 20cm. On the other hand, the picture is not the same, for the "laminar box" model, where the response at the center and the boundaries is different. Namely, at the center of the mesh both the maximum displacement, as well as variation with depth is very close to the ones estimated from the modified model. The two (2) boundaries, however, respond totally differently, as they yield larger displacements at the top, while the overall distribution with depth has a linear rather than a sinusoidal shape.

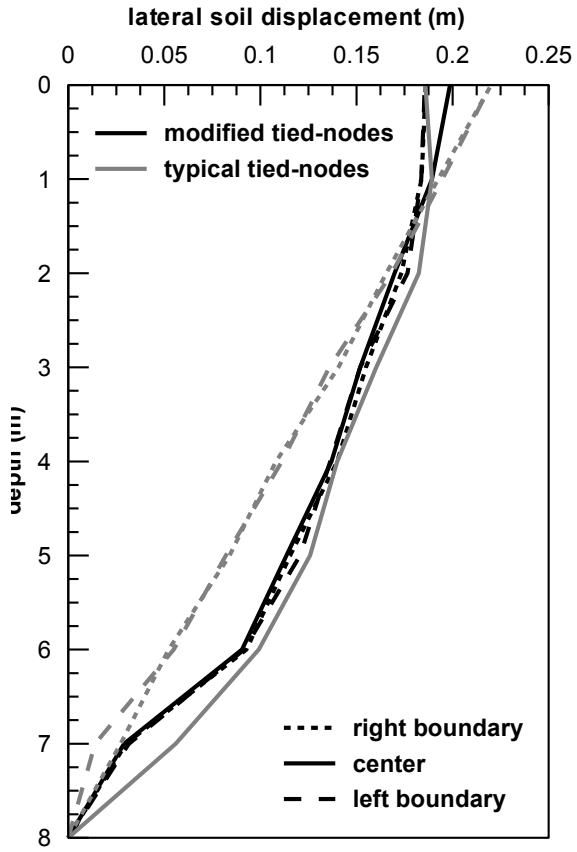

Figure 6.23: Variation of lateral displacements at the center and the two lateral boundaries of the grid using the modified and the typical tied-node formulation

Based on the above, the following can be concluded with regard to the performance of the modified tied-nodes formulation:

- The new concept yields a response which is not differentiated along the horizontal axis of the model, both in terms of static equilibrium and lateral displacement after dynamic loading. This type of response is undoubtedly more compatible with the actual response of infinite slopes in nature.
- Displacements at the center of the model are very similar between the two (2) simulations. Hence, for cases where the numerical evaluation of lateral spreading displacements is investigated, the "laminar box" model can properly estimate the response, given that displacements are measured at the center of the grid.
- Displacements at the boundaries of the model are very different between the two (2) simulations both in terms of absolute values and variation with depth. Hence, for cases, where displacement estimates at the boundaries of the grid are necessary (i.e. "free-field" displacements for the evaluation of p-y curves in models involving piles), the lateral displacements and the overall response can be underestimated.

6.6.2 Single pile in laterally spreading soil

Similarly to the case of the laterally spreading soil, two (2) different simulations are considered, the "free-field" simulation, in which the modified tied-node formulation is adopted, and the "laminar box" simulation, which makes use of the typical tied-nodes. The "free-field" simulation is applied exactly as described in the previous paragraphs of this chapter (6.3-6.5). For the "laminar box" simulation the procedure described for the case of laterally spreading soil is repeated (6.6.1). However, between stages 1 and 2 (prior to specifying the horizontal gravitational component), the zones that correspond to the pile are assigned pile properties, and also interface elements are installed between the soil and the pile.

The stress field after static equilibrium is not affected by the presence of the pile, hence the comparison between the two (2) simulations at this stage of the analysis is not differentiated. Hence, in the current section comparison focuses only on the response after dynamic loading.

In this context **Figure 6.24a** and **b** show the deformed shape and the distribution of horizontal displacements for the "free-field" and the "laminar box" simulation respectively, at the end of shaking. For the "free-field" analysis, it can be observed that soil displacements are smaller close to the center of the model, and gradually increase with distance from the pile, while, after a certain point, variation with depth becomes practically uniform. It can be suggested that this deformation pattern reflects the actual field conditions, i.e. close to the pile displacements are small, as a result of "pinning effects", but as distance from the pile increases free field conditions are established (response is equivalent along the horizontal direction).

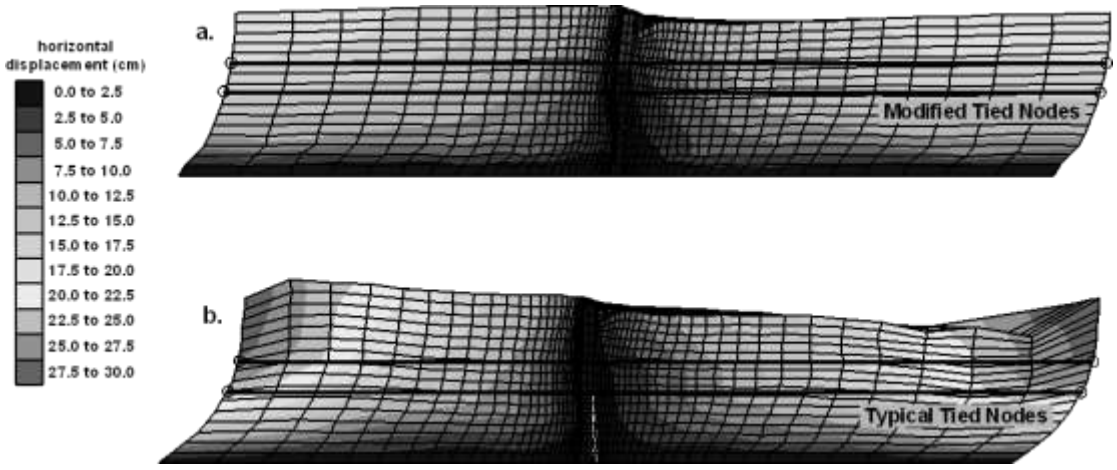

Figure 6.24: Deformed mesh and contours of later displacement at the end of shaking for the (a) modified tied-nodes and the (b) typical tied-nodes

The case does not appear to be the same for the case of the "laminar box" analysis. More specifically, soil displacements are again smaller close to the pile, and gradually increase with distance from the pile. However, variation with depth never becomes uniform, as displacements become unnaturally large close to the boundaries. Furthermore, configuration leads to the development of vertical displacements as well. The above observations indicate that the typical tied-node formulation cannot capture correctly the kinematics of the problem.

In order to evaluate the deficiency of the "laminar box" analysis qualitatively, **Figure 6.25** shows variation of pile and free field displacements (displacements at the lateral boundaries of the model) at the end of shaking. Large differences are observed both for the pile and the free field. Namely, with the "laminar box" formulation pile

displacements are underestimated by approximately 72.2%, and free field displacements are overestimated by approximately 66.7%.

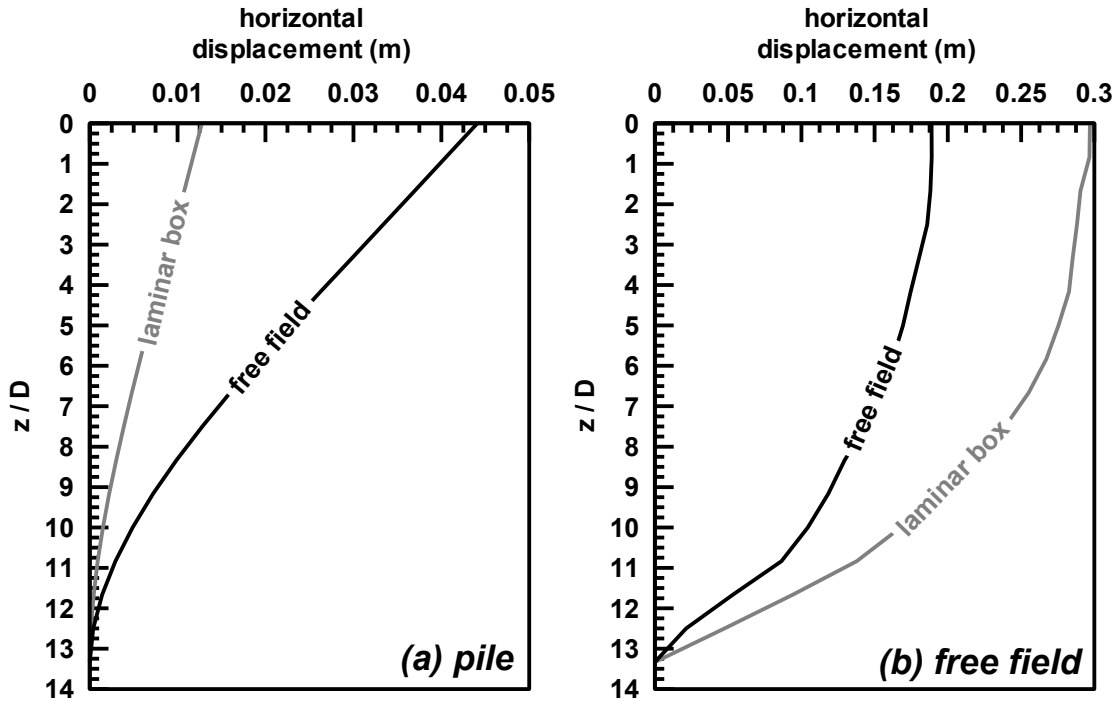

Figure 6.25: Comparison between the "free-field" and the "laminar box" simulation in terms of lateral displacements at the (a) pile and at the (b) free field

Finally, **Figure 6.26** demonstrates the comparison in terms of p-y curves at various depths along the pile. It can be observed that the typical formulation of the "laminar box" leads to unconservative estimates of the loads imposed at the pile. The effect is more intense at swallow depths, while differences elapse as depth increases. For instance at z=1.5m, soil pressures are underestimated by approximately 35%.

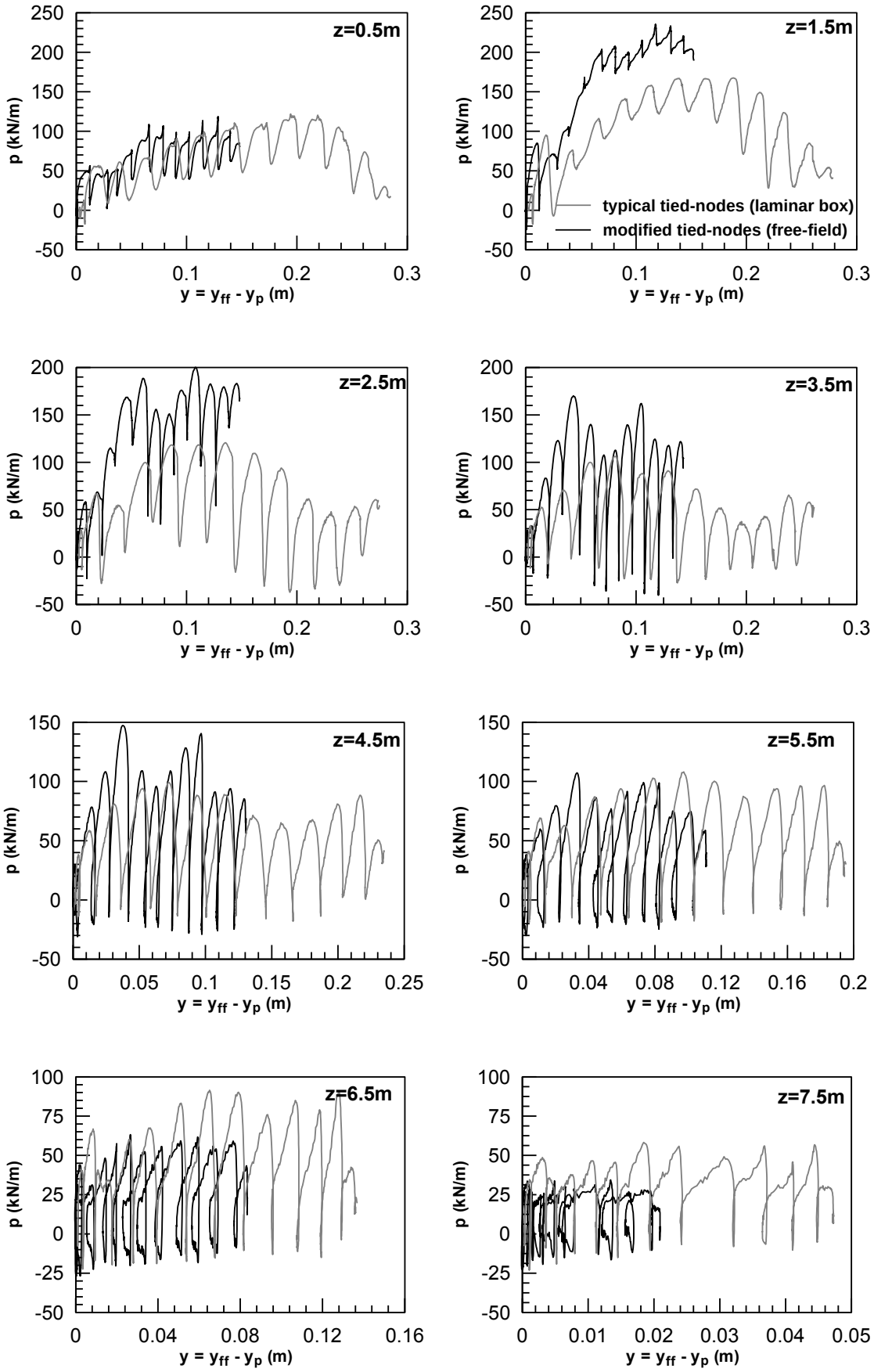

Figure 6.26: Comparison of p-y curves at various depths for the case of modified and typical tied node formulation

6.7 Concluding Remarks

In the present chapter, the numerical model built to simulate the problem of a pile installed in laterally spreading ground was thoroughly described. During development of the model two (2) critical aspects with regard to the numerical simulation were revealed:

- Numerical initialization of the static stress field in infinite slopes is highly dependent on the type of fixities at the boundaries of the model. It was found that the only way to eliminate boundary effects and generate a stress field compatible with the mechanics of infinite slopes is with the use of tied-nodes at the lateral boundaries of the model. In all other cases (rollers and joints) the resulting field was close to that of a finite and not an infinite slope, yielding also downslope movement.
- Inclined pore pressure distribution (in order to avoid flow in the direction parallel to the slope) generates a downward permanent velocity. In order to avoid this type of movement (which affects both the static and the dynamic response of the slope), it was necessary to modify the typical tied-node formulation, by introducing in the function a constant upward velocity equilibrating the one produced by the difference in pore pressures.
- The performance of the modified vs. typical tied-node formulation was firstly evaluated for the simple case of an infinite slope undergoing lateral spreading. It was found that the two (2) different approaches yield similar results at the central part of the mesh. However, as the distance from the center increases, the response with the typical formulation is significantly differentiated.
- Secondly, for the case of a single pile undergoing loads from laterally spreading ground, large differences were observed between the two (2) formulations. Namely, the typical tied node formulation yielded significantly smaller pile displacements, as well as soil pressures, hence, being in the unconservative direction.
- Typical tied-node formulation reflects the boundary conditions of the laminar boxes used in experimental tests. Hence, the above observations raise concerns with regard to displacements, as well as the soil pressures measured at the experimental models.

All the above indicate that the numerical model developed is capable enough to capture the basic mechanisms of the problem investigated, and produce p-y curves which can be used to evaluate the degradation due to liquefaction. In the following chapters a series of parametric analyses will be performed to investigate the effect of the various parameters involved more systematically. However, prior to this, the numerical methodology will be further verified based on the results of a centrifuge test.

7

Numerical Methodology Verification

7.1 General

The numerical methodology described in the previous chapter is applied herein to simulate the tests performed by Gonzalez et al. (2009) in the centrifuge facilities at RPI. The tests involved the response of pile foundations built in liquefiable and gently sloping grounds. From the specific experimental program, models 1x1-w and 1x1-v, which involve the response of single piles, are considered. These models were identical except from the viscosity of the pore fluid which was changed, in order to simulate the effects of fluids of different permeability.

In the present chapter, emphasis will be given in the simulation of test 1x1-v, which is more close to the actual field conditions. The purpose of the simulation is three-fold:

- To verify the methodology's capacity to capture the basic response patterns observed in the experiments.
- To calibrate the methodology in terms of in situ soil permeability, a controversial parameter which is extensively discussed in the literature.
- To explore the effect of boundary conditions (conventional vs. modified tied nodes) and consequently comment on the accuracy of the current centrifuge practice using of laminar boxes to represent actual field conditions.

In the following, the setup of the tests, as well as the assumptions of the numerical model, are thoroughly described, before coming to the comparison between the numerical predictions and the experimental results.

7.2 Description of the Centrifuge Test

The centrifuge tests used to verify and calibrate the numerical methodology were conducted on the 150 g-ton Rensselaer Polytechnic Institute (RPI) centrifuge facility and are thoroughly described in Gonzalez (2005), Gonzalez et al. (2006) and Gonzalez et al. (2009). The tests were performed in a large laminar box which has a total weight of 80kg and internal dimensions of 35.5cm (width) x 71cm (length) x 35.5cm (height). The box consists of a stack of up to 38 rectangular rings (in the present experiment 20 of the rings were used), each of 9.35 mm height, while a maximum relative displacement of 3.13mm between adjacent rings is possible. As a result of the latter, the maximum allowable shear distortion of the box is about 33% (=3.13/9.35). This limit is reasonable for non-liquefied soils, or for liquefiable soils at level ground conditions, but it may prove inadequate for lateral spreading simulations, as it is discussed in following sections.

The setup of the model, as well as the instrumentation used, are shown in **Figure 7.1** and **Figure 7.2**. Namely, the first figure shows the front view of the model, while the second shows the, transversal and horizontal cross sections A-A and B-B respectively. Note that all dimensions, times and measurements in the figures, as well as in the rest of the chapter, are presented in prototype scale. The tests were performed under a 50g centrifugal acceleration.

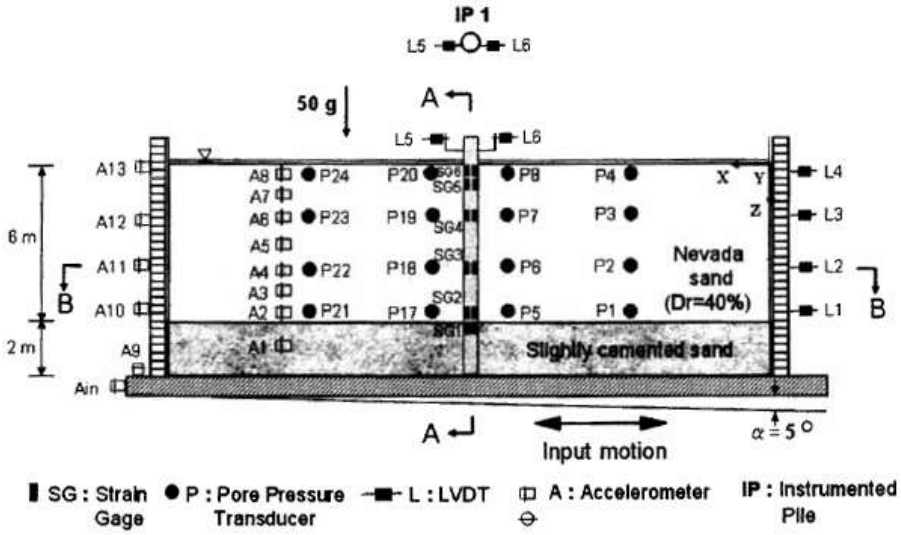

Figure 7.1: Setup and Instrumentation used in models 1x1-w and 1x1-v (prototype units).

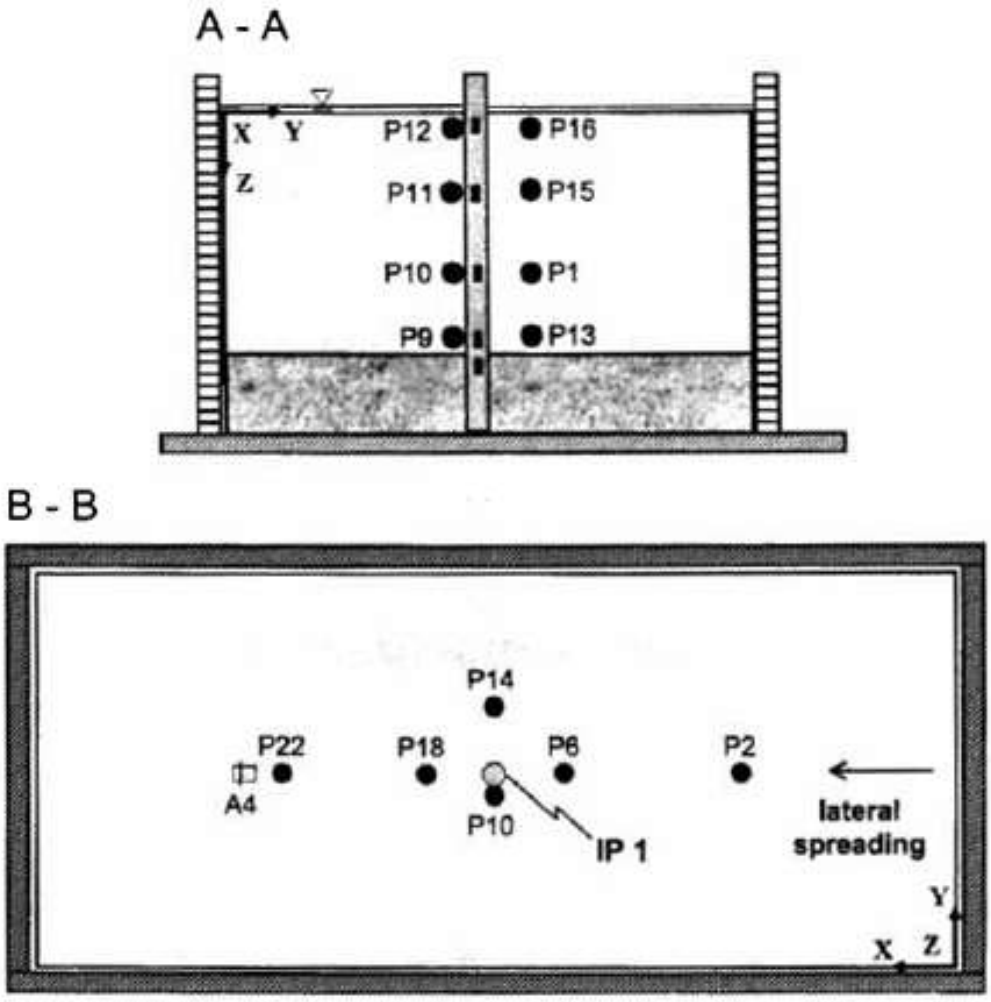

Figure 7.2: Transversal and horizontal sections of models 1x1-w and 1x1-v

The soil is in total 8m thick, and consists of a 6m thick layer of Nevada sand overlying a 2m thick nonliquefiable layer of slightly cemented sand. The box was inclined at an angle of five (5) degrees relative to the horizontal, in order to simulate an infinite mild ground slope. Basic Nevada sand properties, as determined from lab tests performed in RPI (Arulmoli et al., 1992), are summarized in **Table 7.1**. In the specific models the sand was placed at a relative density of D_r=40%. As noted earlier, the two (2) models only differed in terms of the fluid used to saturate the voids. Taking into account that under 1g conditions Nevada sand (D_r=40%) permeability is approximately k=6.6x10^{-5}m/s, model 1x1-w which was saturated with water, yields a permeability k=3.3x10^{-3}m/s. On the other hand, model 1x1-v was saturated with a methylcellulose-water mixture (metulose) which had a viscosity approximately 50 times lower than that of water, hence being theoretically equivalent to a water-

saturated sand layer ($k \approx 6.6 \times 10^{-5}$m/s) under the 50g acceleration. Note that the above values of sand permeability are proposed by the authors based on results from constant head permeability tests. However, these values may be differentiated as a result of the large centrifugal acceleration, the dynamic nature of the problem and the development of liquefaction. These effects are taken into account in the numerical simulation, as it will be discussed later. Finally, the nonliquefiable cemented sand layer consisted of a dry mixture of Nevada sand and quick-setting cement, with the latter being 10% by weight of the clean Nevada sand.

Table 7.1: Properties of Nevada Sand No. 120 (Arulmoli et al., 1992)

Property	**Value**
d_{10}	0.09mm
d_{50}	0.15mm
Specific Gravity, G_s	2.67
Maximum void ratio, e_{max}	0.887
Minimum void ratio, e_{min}	0.511
Maximum dry unit weight, γ_{max}	17.33kN/m^3
Minimum dry unit weight, γ_{min}	13.87kN/m^3
Permeability at 50g for D_r=40%, k	
Model saturated with water (1x1-w)	3.3×10^{-3} m/sec
Model saturated with water (1x1-v)	6.6×10^{-3} m/sec

For the simulation of the pile, a polyetherimide rod was used, with prototype diameter and bending stiffness D=0.60m and EI=9000kN/m respectively. Also, it should be noted that the pile, which is 8m long, was placed in the model before pluviation of the soil, so that minimal disturbance is caused. Hence it can be assumed that the tests refer to a drilled pile that does not affect the stress and volumetric state of the surrounding soil. In addition, the piles were placed in the model without any kinematic constraints being imposed at their ends. Hence, it can be assumed that the base of the pile is free to rotate. In addition, after placement of strain gauges, the pile was covered with a thin layer of wax and a soft shrink tube, while sand grains were glued at the sides. As a result, adequate roughness between the pile and the soil was developed, representing the interface between the soil and the pile. Finally, as far as excitation is concerned, it consisted of 30 sinusoidal cycles with period T=0.5sec and peak acceleration a_{max}=0.3g (**Figure 7.3**).

As far as instrumentation is concerned this included (**Figure 7.1**):

- *Strain gauges (SG)* placed at different locations around the pile to measure bending moments. In total, five (5) pairs of gauges were used, four (4) along the part of the pile within the sand, and one (1) within the cemented bedrock.
- *Pore Pressure Transducers (P)* placed at different locations in the box (far field, near field and adjacent to the pile both upstream and downstream of the pile).
- *Accelerometers (A)* at various depths in the far field upstream side
- *Linear Variable Differential Transducers (LVDTs)* placed at the head of the pile and at various depths, along the downstream boundary of the model, for the lateral displacements measurement.

Free field acceleration recordings for both 1x1-w and 1x1-v models are shown in **Figure 7.3**, at the bottom, at the middle and at the top of the sand layer (accelerometers A_{in}, A4 and A8 respectively). It is observed that positive acceleration components, which correspond to downward movement of the soil, are nearly zero, while negative spikes are generated as a result of soil dilation, when soil moves at the upward direction. These spikes are slightly larger for the water saturated model (1x1-w). However, the response between the two (2) models is very similar indicating that soil acceleration at the free field is not affected by soil permeability.

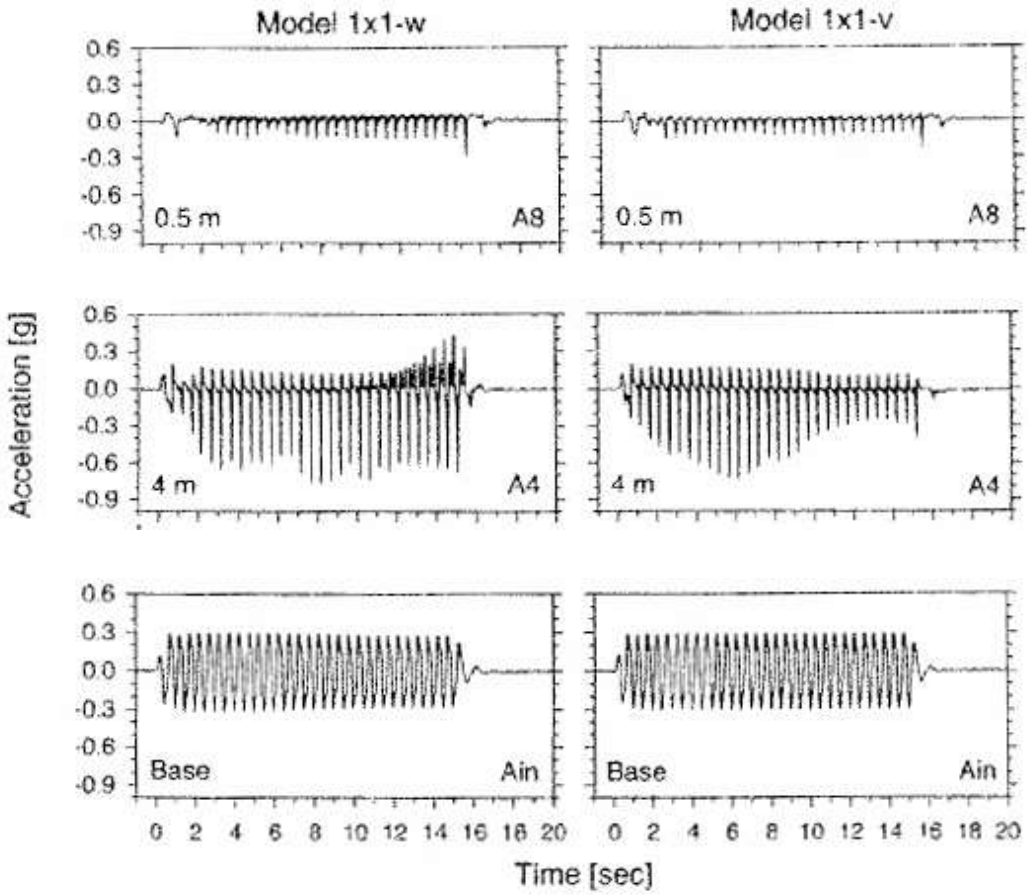

Figure 7.3: Soil acceleration at various depths for the models saturated with water (1x1-w) and metulose (1x1-v)

Recorded excess pore pressures are shown in **Figure 7.4**, for both models (model 1x1-w with black dashed line and model 1x1-v with gray continuous line) and two (2) locations: at the free-field and next to the pile. The figures correspond to locations near the surface (P4), around the middle height of the pile (P2 and P3) and near the bottom of the liquefiable layer (P1). As for the response in the free-field (**Figure 7.4a**), it can be observed that both models did liquefy after about one or two cycles of shaking, with the two (2) models exhibiting very similar response during shaking. As expected, the dissipation process evolved much faster for the model saturated with water, after but also during seismic shaking.

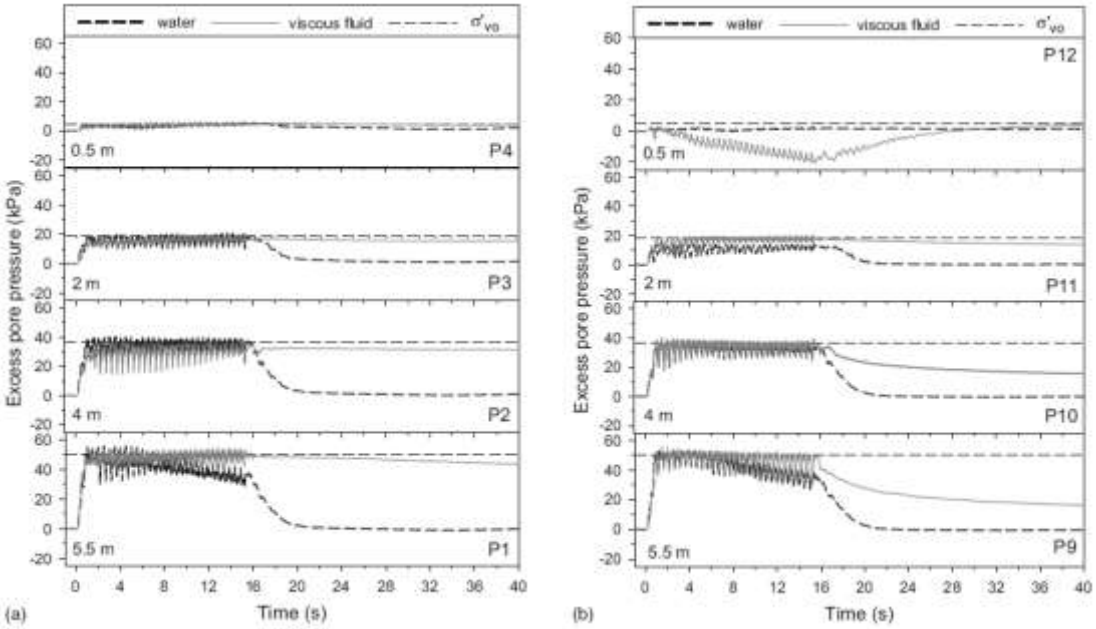

Figure 7.4: Excess pore pressure measurements (a) in the free field and (b) close to the pile, for models 1x1-w and 1x1-v.

For the area close to the pile (**Figure 7.4b**), it can be observed that at deeper elevations, soil liquefies early during shaking, independent of soil permeability. However, for shallow depths, the soil in 1x1-v model exhibits a tendency to dilate. Gonzalez et al (2009) speculate that this type of response is a result of large straining and unloading. For 1x1-w model dilation effects are not so much pronounced since water rapidly flows from deeper elevations and far field regions, thus dissipating the negative excess pore pressures. Fluid flow is much slower for model 1x1-v, thus resulting in the development of a nonliquefied zone around the pile. After examining measurements from pore pressure transducers, the authors concluded that this negative pore pressure zone has the shape of an inverted cone.

Recorded time histories of soil and pile head lateral displacement are illustrated in **Figure 7.5a** and **Figure 7.5b** for models 1x1-w and 1x1-v respectively. Observe that soil permeability has a significant effect on the displacements developed at the head of the pile. Namely in the water-saturated model, pile displacement reaches a maximum value, shortly after the start of the shaking, and bounces back afterwards. The authors attribute this response to the fact that the liquefied soil flows around the pile, since it has become very weak and cannot drag the pile along. On the other hand, in the small permeability model, pile displacement constantly increases during

shaking and never bounces back. In this case, the soil around the pile is rather stiff, as a result of large negative pressures, and hence the pile is forced to its movement.

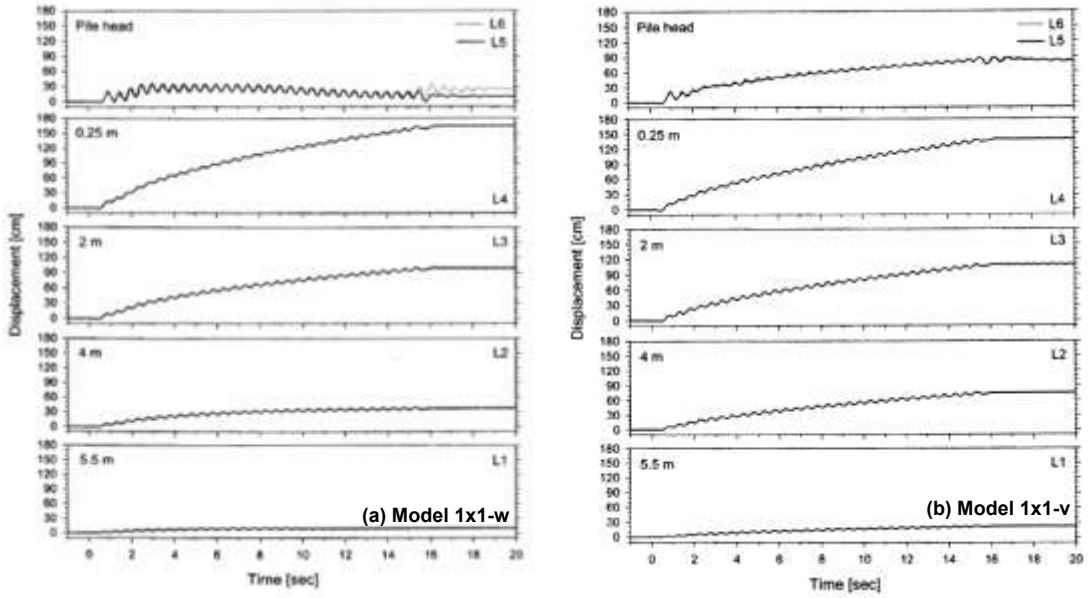

Figure 7.5: Comparison of pile head and free field lateral soil displacements in models (a) 1x1-w and (b) 1x1-v

In addition, **Figure 7.6a** and **b** show lateral displacement distribution with depth at various time instances. These figures indicate that the free-field response is not largely affected by permeability. The only difference is that the model saturated with metulose develops slightly smaller displacements near the ground surface, and slightly larger at deeper elevations.

However, as described in the following, these measurements might be affected by the displacement capacity of the box. Namely, also plotted in the figure (with heavy dashed) line is the capacity of the laminar box, i.e. the maximum lateral displacement that can be developed by the walls of the box before the maximum relative displacement between the rings is reached. In theory, this line is readily estimated based on the thickness of soil layers, the height of the rings (9.35mm) and the maximum relative displacement between rings (3.13mm). However, given the uncertainties involved, e.g. number of rings used to cover the cemented layer (for the given geometry they might be 4 or 5) e.t.c., this is an approximate estimate, and the exact line might be slightly displaced to the right or left.

In any case, **Figure 7.6b** indicates that, for model 1x1-v, the ultimate displacement capacity of the box is reached at t=3sec at the depth of z=5.5m and at approximately t=9sec for the depth of z=4m. This aspect of the experiment is expected to significantly affect the displacement measurements at the free field, and through them, the overall response of the system. This is not the case for the water-saturated model (**Figure 7.6b**), as experimental values are systematically below the line of maximum displacement. However, **Figure 7.6b** indicates that the rate of free field displacement accumulation is constantly decreasing with time, while variation with depth at the lower part of the pile does not follow the usual sinusoidal shape (also observed in test 1x1-v), but it is parallel to the maximum capacity line. These observations, in conjunction to the fact that the exact location of the line could not have been accurately estimated, lead to the conclusion that the displacement capacity of the box might have been reached in the case of 1x1-w model as well.

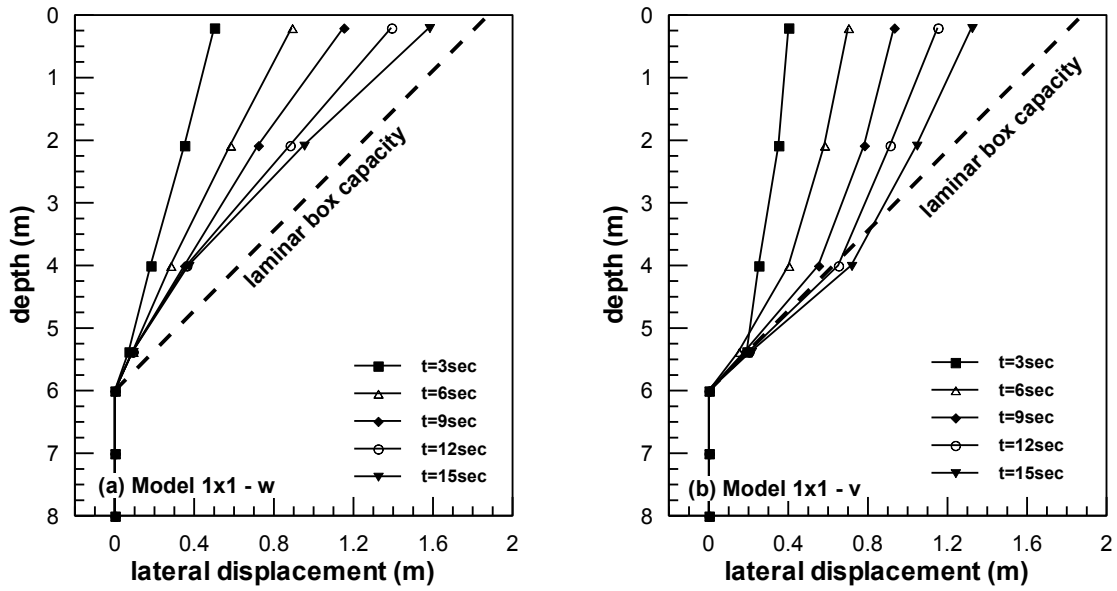

Figure 7.6: Lateral displacement at the boundary of the (a) water and (b) metulose saturated model at various time instances.

Bending moment profiles are plotted in **Figure 7.7a** and **b**, for the water and metulose model respectively. Note that the variations shown in the above figure have been obtained from strain gauges measurements after filtering out the cyclic component. In all, five (5) pairs of strain gauges along the length of the pile were used for that purpose. In both cases it can be observed that in both cases maximum values occur at the interface between the liquefiable and the nonliquefiable layer.

Furthermore, for the water saturated model the maximum bending moment takes place approximately at t=6sec, i.e. when the displacement of the pile head also reaches a local maximum, and decreases thereafter following the displacement of the pile which bounces back. On the other hand, the bending moment in the viscous model (**Figure 7.7b**) increases steadily with time (similarly to pile head displacement) and reaches a maximum value at the end of shaking.

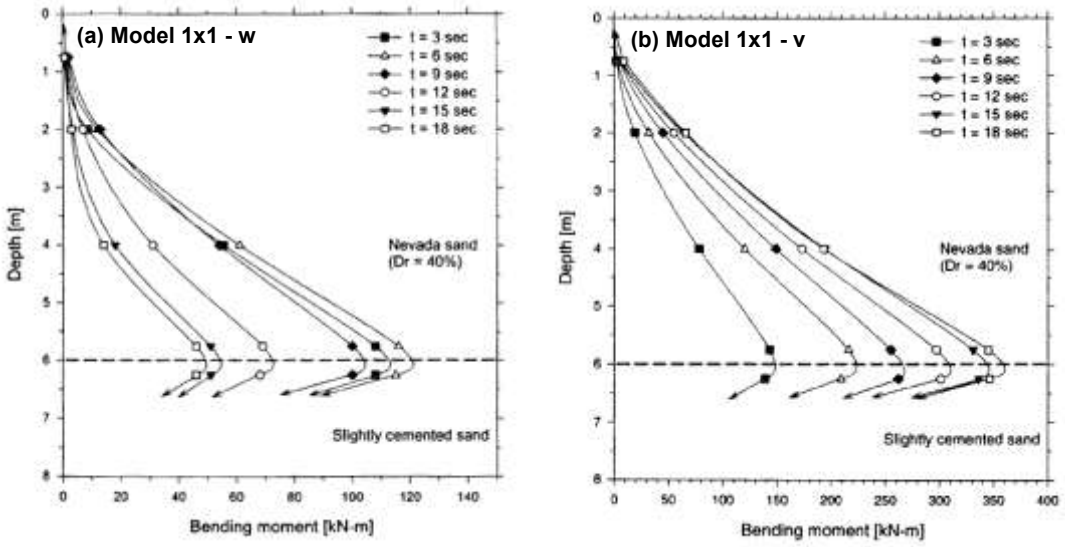

Figure 7.7: Bending moment distributions at various time instances for (a) the water saturated and the (b) metulose saturated model.

Finally, both models were used to obtain estimates of the p-y response of the pile at different depths. This was achieved by fitting a cubic spline to the discrete bending moment measurements, obtained from the strain gauges. Hence, soil pressures (p) were calculated by double differentiation of the cubic spline as follows:

$$p\ \ z\ = \frac{\partial^2 M\ \ z}{\partial z^2} \tag{7.1}$$

where:

p(z): Soil pressure variation with depth (along the pile)

M(z): Bending moment distribution with depth (along the pile)

The Authors acknowledge that the use of the cubic spline, which is the simplest curve to be differentiated twice, in combination with the rather small number of strain gauges used, can only yield approximate values for soil pressure (p).

The pile displacement profile with depth $y_p(h)$, was first estimated by double integration of the corresponding bending moment profile as follows:

$$y_p(z) = \frac{1}{EI}\iint M(z)\,dz \tag{7.2}$$

where:

y_p: Lateral pile displacement

EI: Bending stiffness of pile

However, this procedure yielded displacements at the pile head which were smaller compared to the LVDT measurements, a difference attributed to the rotation stiffness of the cemented sand layer. The latter was back calculated by subtracting the estimates from equation (7.2) from the LVDT measurements, and dividing the remainder with the thickness of the liquefiable sand. It was thus found that a good approximation for the rotational stiffness of the cemented sand is the value of K_r= 8000kN/rad. Consequently, the final $y_p(h)$ profile was obtained by adding the deformations due to curvature [Eq. (7.2)] to the ones from rotation. Finally, the profiles of relative lateral displacement, used to describe the p-y curves, were obtained as follows:

$$y(z) = y_g(z) - y_p(z) \tag{7.3}$$

where:

y(z): Relative free field-pile displacement

$y_g(z)$: Free field displacement after filtering the cyclic component from the LVDT measurements

$y_p(z)$: Pile displacement

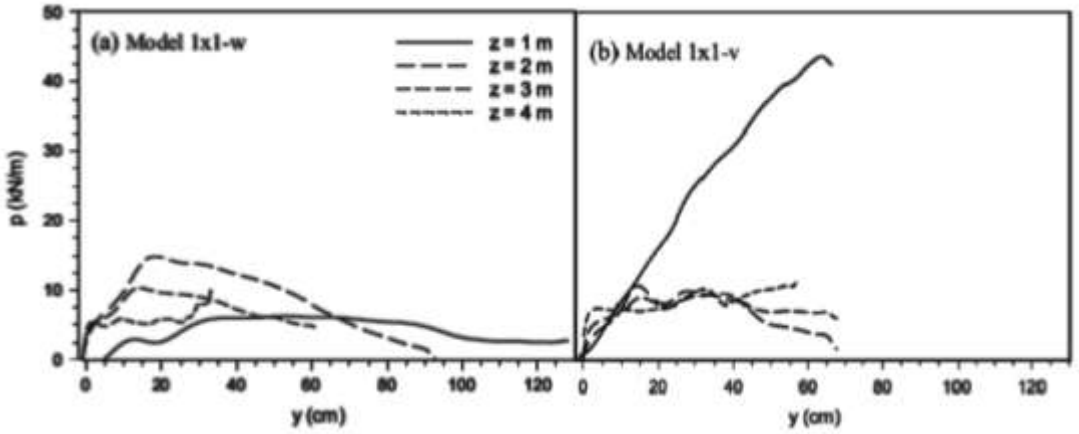

Figure 7.8: Back-calculated p-y curves for models (a) 1x1-w and (b) 1x1-v

The p-y curves obtained with the previous procedure are shown in **Figure 7.8**. In the water-saturated model (**Figure 7.8a**) soil pressure applied on the pile initially increases reaching values that range between 7-15kPa/m depending on depth. However, as shaking progresses, soil cannot sustain this load and reaction practically becomes zero. Response in the metulose-saturated model (**Figure 7.8b**) is quite similar for depths larger than two (2) meters. However, for swallow elevations soil reaction gradually increases throughout the shaking, a response that can be correlated to the large dilation that takes place at these elevations.

7.3 Numerical Simulation of metulose saturated model (1x1-v)

In the present section the numerical model built to simulate the low permeability test (1x1-v as identified previously) is thoroughly described. As noted at the beginning of the chapter, the present simulation places more emphasis on the verification of the low permeability test (1x1-v), since it is closer to the actual field conditions. Apart from evaluating the efficiency of the numerical model, this section also focuses on the effect of parameters which remain uncertain during the formulation, such as the permeability of the sand and the properties of the interface between the soil and the pile.

7.3.1 Numerical model description

The mesh created to simulate the test is shown in **Figure 7.9**. Following the geometry of the laminar box, the grid is 35.5m long, 9m wide and 8m tall. With reference to the coordinate system shown in the figure, the vertical x-z plane that passes through the axis of the pile is a plane of symmetry for the problem and hence half of the width of

the box has to be simulated. Along the z-axis, the mesh is divided into 16 zones of 0.5m height each. As for discretization, the thickness of the zone adjacent to the pile is 0.30m, while zone size progressively increases with the distance from the pile.

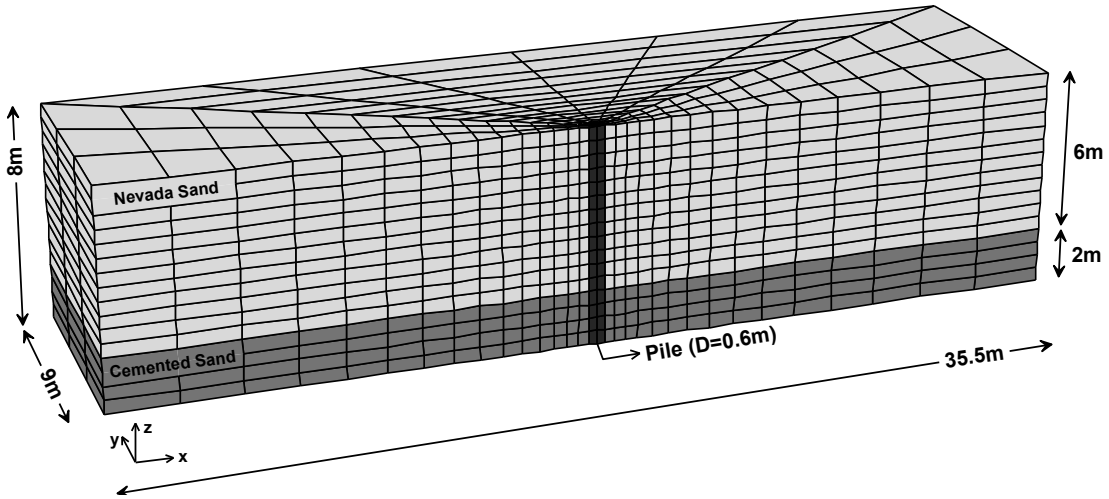

Figure 7.9: Finite Difference mesh created to simulate the centrifuge experiment.

The liquefiable Nevada Sand response was simulated with the NTUA_Sand model (Andrianopoulos et al. 2010), already discussed and used in previous chapters, whose parameters have been calibrated for the specific type of sand. The only parameter of the model that needs to be adjusted is the void ratio, which was set equal to e=0.7366 corresponding to D_r=40% Relative Density.

As described at the beginning, one of the main goals of the chapter is the calibration of the model with respect to the permeability of the Nevada sand. In the study of Gonzalez et al. (2009), this parameter is defined as k=6.6x10^{-5}m/sec. This will be referred as *static* permeability, as it has been determined from constant head tests, under 1g gravitational acceleration (Arulmoli et al., 1992). However, given the nature of the problem at hand, two (2) additional values were considered, based on previous recommendations reported in literature:

- *Dynamic* Permeability: k=2.1x10^{-5}m/sec (Liu and Dobry, 1997)
- *Variable* Permeability: k=f(r_u) (Shahir et al., 2012)

The second case above, referred as *dynamic* permeability, takes into account the effect of both the large centrifugal acceleration and the dynamic nature of the loading,

which causes the flow to constantly change direction. These special conditions deviate from the basic assumptions of 1g gravity and flow in one direction, under which Darcy's law was developed. As a result, estimates from constant head tests, which are based on Darcy's law, should be properly re-adjusted. The specific value of $k=2.1x10^{-5}m/s$ was suggested by Liu and Dobry (1997), who studied the response of surface footings on sands through centrifuge testing.

The first two permeability values above (*static* and *dynamic* permeability) refer to the value of permeability for the case of no significant pore pressure build-up. However, the latter is known to significantly increase the permeability, as excess pore pressures cause the soil particles to lose full contact and, hence, creating additional flow paths. So far, this phenomenon has been treated numerically in the literature either by applying an increased (compared to the static) permeability (Arulanandan and Sybico, 1993; Balakrishnan, 2000; Taeibat et al., 2007) or by assuming that permeability varies with time (Manzari and Arulanandan, 1994; Andrianopoulos, 2006). However, in a more recent study, Shahir et al. (2011) suggest that it is more reasonable to relate the permeability coefficient to the excess pore pressure ratio r_u:

$$r_u = \frac{\Delta u}{\sigma'_{vo}} \tag{7.4}$$

where:

Δu: excess pore pressures

σ'_{vo}: initial vertical effective stress

In order to develop such a relationship, they back-analyzed experiments where they recorded the development of excess pore pressures and settlements during 1-D shaking of liquefied free field level ground. The experiment was reproduced numerically, by assuming various scenarios for the evolution of permeability. It was thus observed that the best agreement between numerical and experimental results was obtained when permeability was modeled as a function of excess pore pressure ratio r_u, of the form:

$$\frac{k_b}{k_{ini}} = 1 + \left(a - 1\right) r_u^{\beta} \tag{7.5}$$

where:

k_b: Permeability coefficient during pore-pressure build-up

k_{ini}: Permeability coefficient before shaking (r_u=0)

α: Positive constant defining the ratio of permeability for r_u=1.0 over permeability for r_u=0 $a = k_{r_u=1} / k_{r_u=0}$

β: Positive constant defining the rate of permeability increase during the pore pressure increase phase.

The above concept was implemented to the present numerical analysis through a FISH (FLAC's inbuilt programming language) function. Namely, for each zone in the mesh and for each timestep, the value of excess pore pressure ratio is calculated. Then, equation (7.5) is employed and the updated value of permeability coefficient at the specific zone is assigned. As a result, permeability is constantly updated both in time and space. Calibration of constants α and β, as well as k_{ini}, was based on the following considerations:

- For constant β, which defines the rate of permeability increase, the recommendations by Shahir et al., who assume linear increase (i.e. β=1.0).
- For constant α, which expresses the ratio of the permeability of liquefied soil ($k_{ru=1}$) over the permeability of non-liquefied soil ($k_{ru=0}$), Shahir et al. propose the value of α=20. However, their study involved a level ground deposit where full liquefaction took place early during shaking, and r_u remained close to unity throughout shaking. On the contrary, in the problem simulated herein, the existence of an initial static stress causes the development of large dilation spikes, and hence the effects of excess pore pressure development on the permeability are not expected to be so pronounced. In addition, various studies on the permeability of liquefied soil (Arulanandan and Sybico, 1992; Balakrishnan, 2000; Taiebat et al., 2007) suggest values for α that range between 3.67 and 10. Based on all the above, it was finally decided to assign α=10.
- As for the permeability of the non-liquefied soil, k_{ini}, given that the analysis simulates a centrifuge test involving dynamic loading under large

gravitational acceleration, the *dynamic* value was adopted i.e. $k_{ini}=2.1x10^{-5}$ m/sec, following the recommendations of Liu and Dobry (1997).

The cemented sand was assumed to behave as a linearly elastic material. As for the elastic parameters, Poisson's ratio was taken as v=0.33, while a value of G_o=120000kPa was adopted for the shear modulus, which corresponds to the stiffness of clean Nevada sand at the same Relative Density and confining stress levels, multiplied by a factor of two (2). This approach for the modulus definition of the cemented soil is based on various studies (Acar and El-Tahir, 1986; Saxena et al., 1988; Sharma and Fahey, 2003; Schnaid et al, 2001) which suggest that cementation increases the stiffness compared to the uncemented soil.

Furthermore, a key factor in the simulation of the cemented crust is to ensure that it provides the appropriate rotational stiffness K_r=8000kNm/rad, as it was back-calculated from the test results. For this purpose, a region around the tip of the pile was appropriately softened, and the appropriate shear modulus was defined parametrically through a total of six (6) analyses. A detail of the mesh in the area under consideration is shown in **Figure 7.10**.

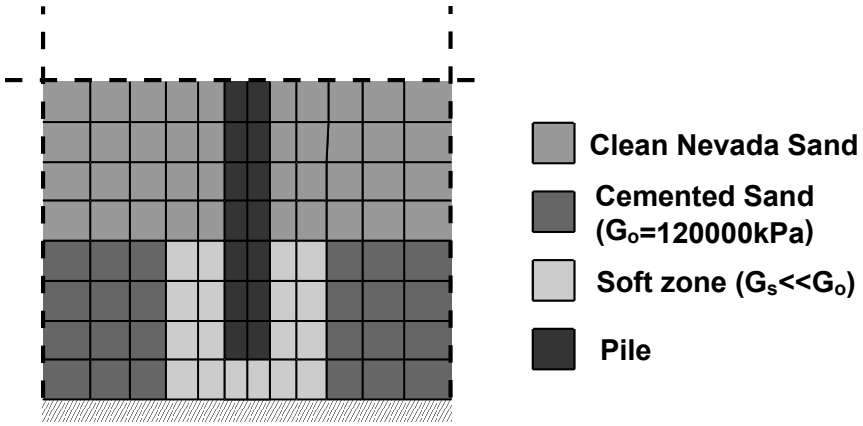

Figure 7.10: Detail of the grid showing the softening of a small area around the pile in order to achieve the appropriate rotational flexibility.

Finally, an elastic model was also adopted for the pile, as no plastic response of the pile is reported in the study. The elastic properties were selected so as to yield a flexural stiffness EI=9000kNm^2. Interface elements were placed between the pile and the soil to allow for slip and separation. Interfaces were assumed to have zero cohesion, while for the friction angle δ, two (2) cases were considered, δ=1/2φ and

δ=φ, where φ is the friction angle of the soil. The first case is more representative of steel, and the second of concrete piles. As mentioned earlier in the Chapter, sand grains were glued to the outer part of the pile, so that the friction of the interface is expected to be closer to the friction of the sand (δ=φ). However, it was decided to examine both scenarios, in order to reduce the uncertainty with regard to δ, and also investigate its effect on the model response.

Given the above objective uncertainties with regard to soil permeability, rotational stiffness of the cemented sand and friction angle of the interface, a total of eleven (11) analyses had to be performed in order to fit experimental results in a rational way. The basic input parameters of each analysis are summarized in **Table 7.2**. The first six (6) analyses aim at specifying the appropriate stiffness so that the condition K_r=8000kNm/rad is satisfied, while the remaining aim at investigating the effects on the numerical simulation of soil permeability and interface friction.

Table 7.2: Summary of analyses performed for the verification of the numerical methodology

α/α	Permeability, k (x10^{-5} m/sec)	Interface friction (δ/φ)*	Stiffness of cemented sand around pile (G_s/G_o)**
1	6.6	0.5	1.0
2	6.6	0.5	0.02
3	6.6	0.5	0.01
4	6.6	0.5	0.002
5	6.6	0.5	0.0005
6	6.6	0.5	0.0001
7	6.6	1.0	0.0005
8	2.1	0.5	0.0005
9	2.1	1.0	0.0005
10	$2.1\cdot\ 1+9r_u$ ***	0.5	0.0005
11	$2.1\cdot\ 1+9r_u$ ***	1.0	0.0005

*(δ/φ): Ratio of interface friction over soil friction angle

**(G_s/G_o): Shear modulus of softened zone around pile over shear modulus of cemented sand

***Variable permeability with excess pore pressure ratio, r_u

Each analysis was performed in two (2) steps which represent the process by which the test was actually carried out in the laminar box:

- Step 1: The model in **Figure 7.9** was inclined at five (5) degrees relative to the horizontal and stress equilibrium under static conditions was established.

- Step 2: Dynamic loading was applied to the base of the model.

For the first step, initially the geostatic stress field for level ground conditions is established manually. Next, inclination is modeled by applying a horizontal gravity vector component, with simultaneous rotation of the phreatic surface, while the model is stepped to equilibrium numerically. This procedure directly reflects the process by which inclination is applied in the laminar box. In order to be compatible with the kinematic constraints of the laminar box, the conventional formulation of tied nodes is adopted (see previous chapter) as boundary conditions. Obviously the base of the model is fixed both in the vertical and in the horizontal direction.

After the model has attained equilibrium, a sinusoidal motion of N=30 cycles, period T=0.50sec and amplitude a_{max}=0.30g, is applied at the base of the model, while the same tied-node configuration is retained at the boundaries of the model. Acceleration, excess pore pressure and displacement time histories are kept in memory at the exact same locations where recording instruments were placed in the experimental model. Additionally, time histories of soil subgrade reaction are saved at various depths along the length of the pile, in order to calculate the corresponding p-y curves. As already discussed in previous chapters, soil pressures are estimated through the stresses at the interface nodes through a properly programmed FISH function.

Since the numerical analysis does not provide directly the pile bending moments, these are estimated indirectly, from the soil pressure time histories. The latter are calculated every 0.5m along the pile, providing a quite accurate pressure distribution, which can be used to derive bending moments reliably. As mentioned previously, the bending moments presented in the work by Gonzalez et al. (**Figure 7.7**), correspond to the strain gauges measurements, after the cyclic component has been removed. Thus, in order for the experimental and the numerical bending moments to be comparable, the cyclic component was filtered out from the numerical data, as well. A typical example of non filtered and filtered pressure time history is shown in **Figure 7.11** for one of the analyses and a random depth.

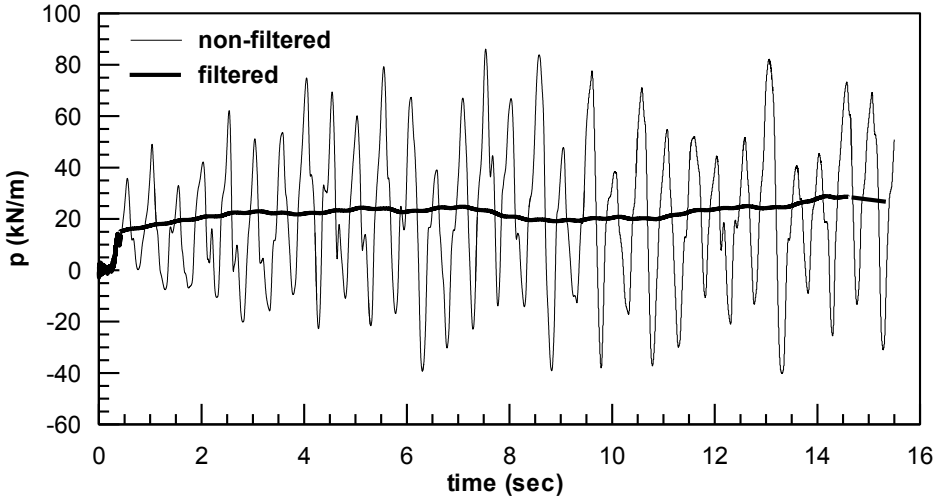

Figure 7.11: Typical shape of non-filtered and filtered soil reaction time history used for the calculation of pile bending moment

In the following, numerical predictions are compared to the experimental results in terms of:

- Rotational Stiffness of the cemented sand, K_r
- Acceleration time histories
- Excess Pore Pressure time histories
- Free-field displacements
- Pile displacements
- P-y curves
- Pile bending moments

Note that, prior to performing the analyses shown in **Table 7.2**, the basic analysis was repeated by using a more dense mesh. The width of the zone next to the pile for the refined mesh was 0.10m. In the following three (3) figures the effect of this 3:1 refinement is evaluated in terms of predicted soil displacements and pile bending moments at the end of shaking (**Figure 7.12**), pile head displacement (**Figure 7.13**) and excess pore pressures in the free field and close to the pile (**Figure 7.14**). In general, it can be observed that the "sparse" mesh (**Figure 7.9**) captures quite accurately the system response in all cases, without need for further refinement.

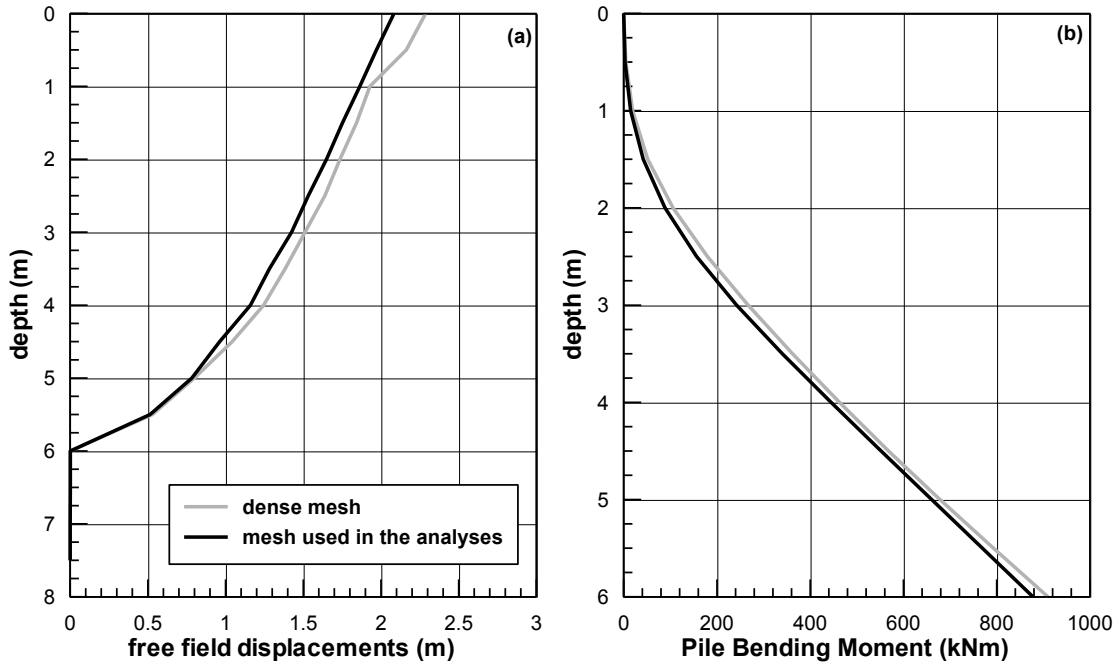

Figure 7.12: Comparison between the mesh used in the analyses and a more dense mesh in terms of (a) Free field displacement (b) pile bending moments at the end of shaking

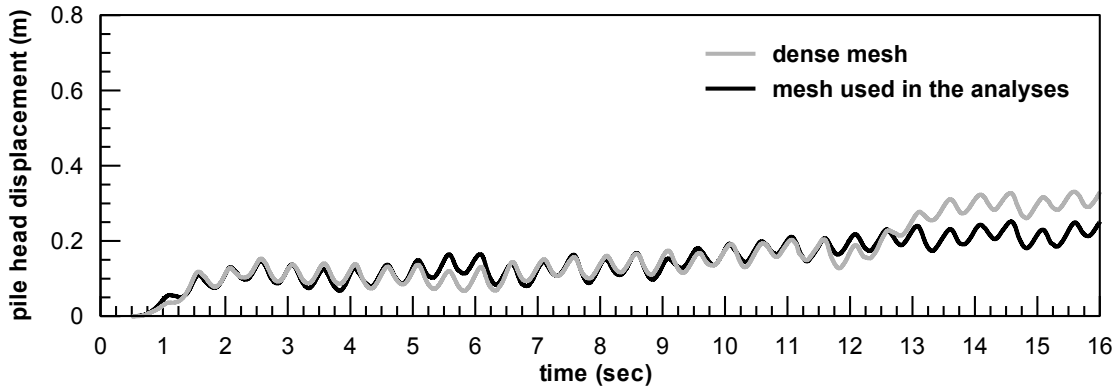

Figure 7.13: Time histories of pile head displacement for the mesh used in the analyses and the dense mesh

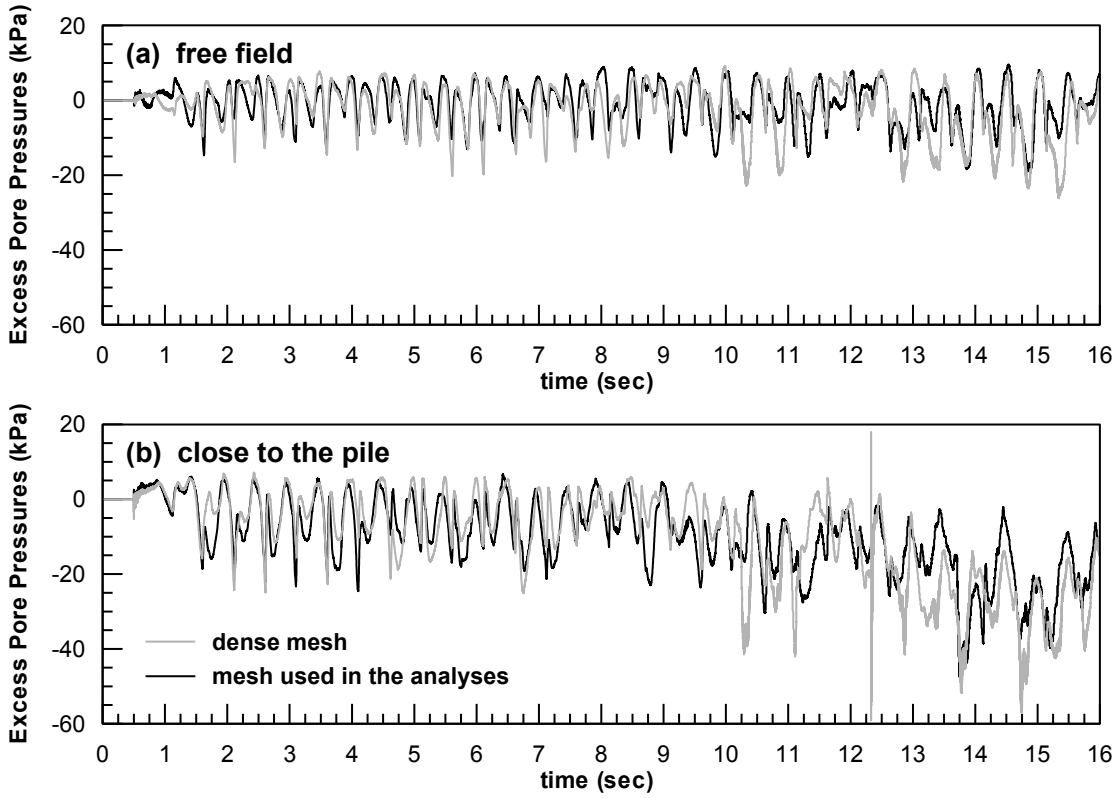

Figure 7.14: Time histories of excess pore pressures for the mesh used in the analyses and the dense mesh in the (a) free field and (b) near the pile

7.3.2 Rotational Stiffness of Cemented Sand, K_r

As described previously, in order to obtain the back-calculated rotational stiffness K_r=8000kNm/rad a soft zone of low stiffness was considered around the pile (**Figure 7.10**). The appropriate stiffness of this zone that yields K_r=8000kNm/rad, was determined through a set of six (6) parametric analyses (analyses 1-6 in **Table 7.2**), where the G_s/G_o ratio (G_s is the modulus of the softened area and G_o the modulus of the cemented sand) varied from 1 to 10^{-4}. For each analysis, a value for K_r was estimated as:

$$K_r = \frac{M_{\max}}{\theta} \tag{7.6}$$

where:

M_{max}: Pile bending moment at the interface between liquefiable sand and cemented crust at the end of shaking (this elevation coincides with the location of maximum moment along the pile)

θ (rad): Rotation of pile cross section at the interface between sand and cemented crust at the end of shaking

Rotation angle θ can be easily estimated based on the displacements that correspond to the pile cross section at the specific elevation, while M_{max} was obtained based on the procedure described previously. Results of this parametric investigation are summarized in **Figure 7.15**. In the horizontal axis of the figure the different values of G_s/G_o that were investigated are shown, while the vertical axis shows the corresponding values for the rotational stiffness. All values in the figure correspond to the end of shaking.

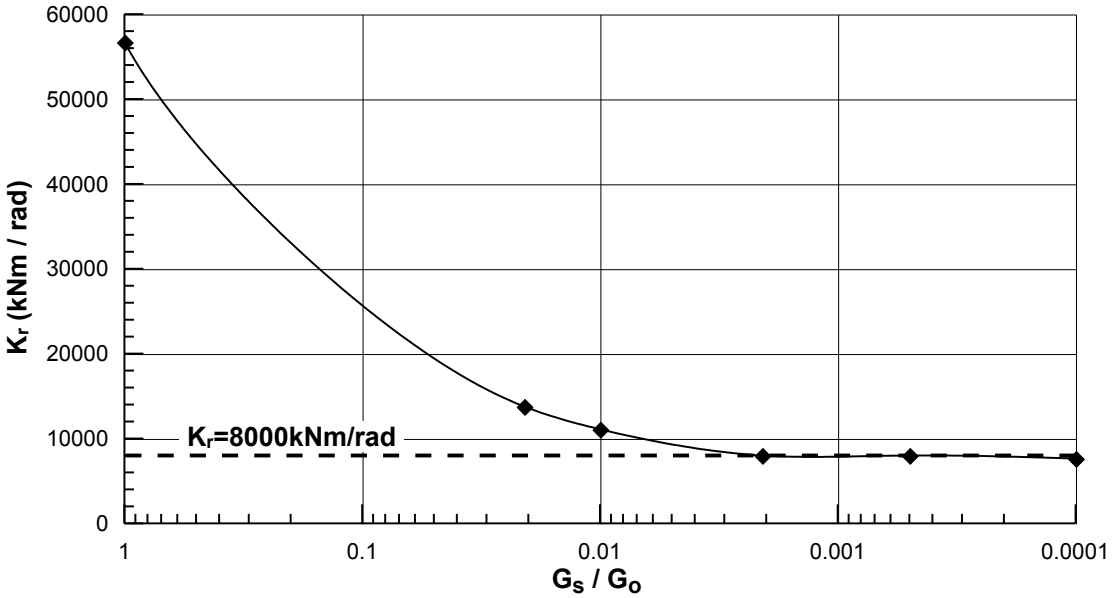

Figure 7.15: Variation of rotational stiffness, K_r provided by the cemented sand versus the degradation of elastic modulus in the area surrounding the pile tip.

The figure clearly indicates that no softening of the cemented crust around the pile tip results in very large values for the rotational stiffness, which for the case examined herein reach K_r=57000kNm/rad. However, once the softened zone is created the value of K_r decreases dramatically. Namely for G_s/G_o=0.02 the rotational stiffness decreases from 57000kNm/rad to 14000kNm/rad. From that point on, further decreases of G_s/G_o does not affect K_r largely, even though a small additional reduction is observed. Finally, as indicated in the figure, for ratios G_s/G_o<0.002, K_r appears to obtain a residual value which is approximately 8000kNm/rad. Hence, for

the needs of the present simulation, the ratio G_s/G_o=0.0005 was adopted, which corresponds to a shear modulus for the softened area of G_s=60kPa.

7.3.3 Soil acceleration

Experimental and numerical acceleration time histories within the sand layer are shown in **Figure 7.16** to **Figure 7.18** for the three (3) different permeability assumptions. Namely, **Figure 7.16** corresponds to the static permeability case ($k=6.6x10^{-5}$m/sec), **Figure 7.17** to the dynamic ($k=2.1x10^{-5}$m/sec) and **Figure 7.18** for the case where permeability varies with excess pore pressure ratio at equation (7.5). Each Figure shows the time histories at the base, as well as four (4) different depths in the free-field (accelerometers A_{in}, A2, A4, A6 and A8 as identified in **Figure 7.1**). The thick black line in the figures corresponds to the experimentally recorded time history, the dark gray to the numerical with interface friction angle $\delta=1/2\ \varphi$, and the light gray to the numerical with $\delta=\varphi$.

The first thing to observe is that the numerical predictions are not significantly affected either by the permeability or by the friction angle of the interface. It is only noted that, for the case of variable permeability, it appears that the magnitude of dilation spikes is slightly smaller compared to the cases where the permeability coefficient is constant.

Secondly, the overall comparison between experimental predictions and numerical results is fairly good. Namely, both sets of data exhibit a significant negative component (corresponding to upward soil movement) which can be attributed to the large shear straining and the initial static stress. The magnitude of these negative dilation spikes is slightly larger in the experiment, for middle to large depths, and significantly larger in the numerical analyses near the ground surface. On the other hand, the numerical predictions exhibit a larger positive acceleration component (corresponding to downward movement), with the difference being more pronounced at small depths.

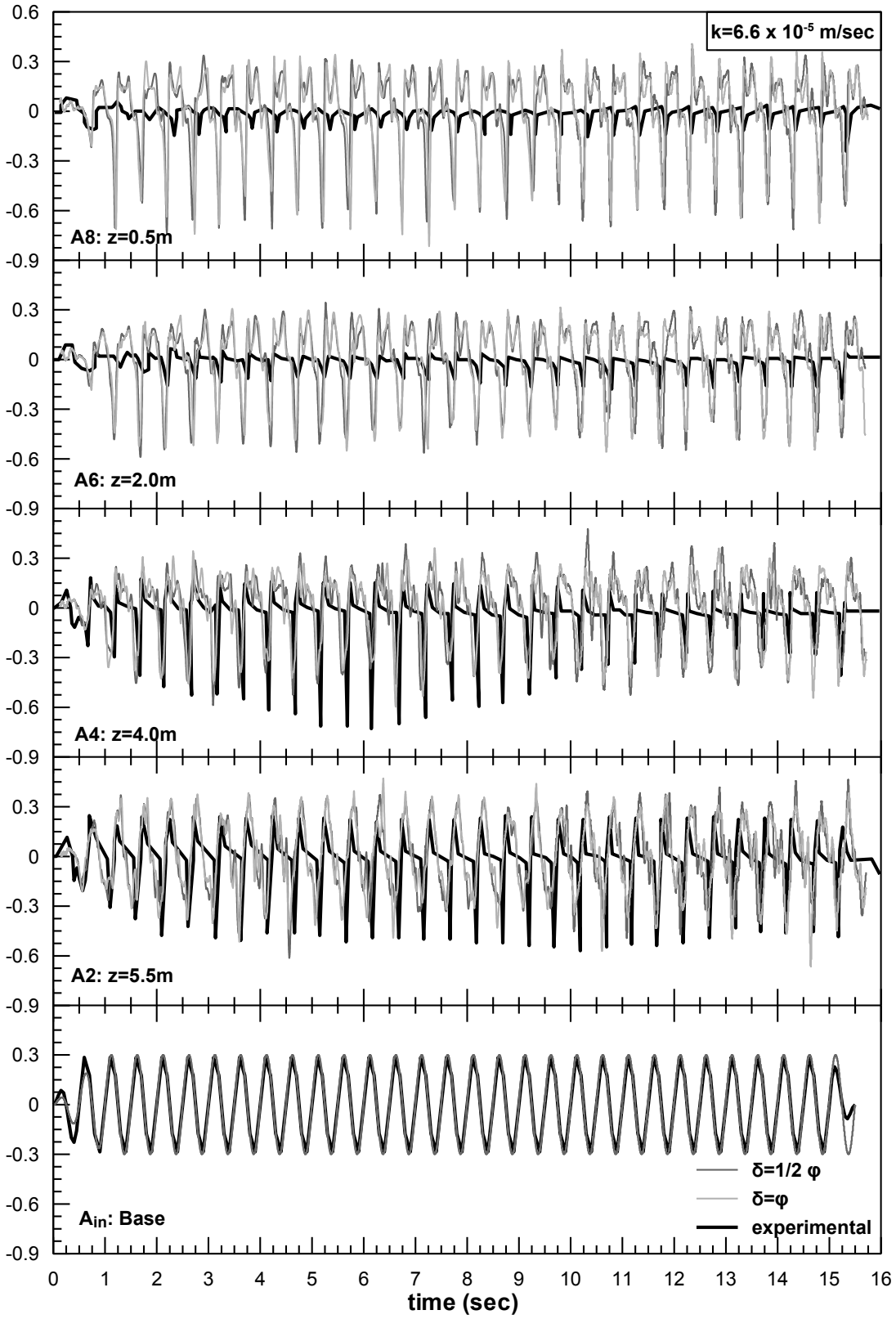

Figure 7.16: Soil acceleration time histories at various depths in the sand for soil permeability k=6.6x10^{-5}m/sec

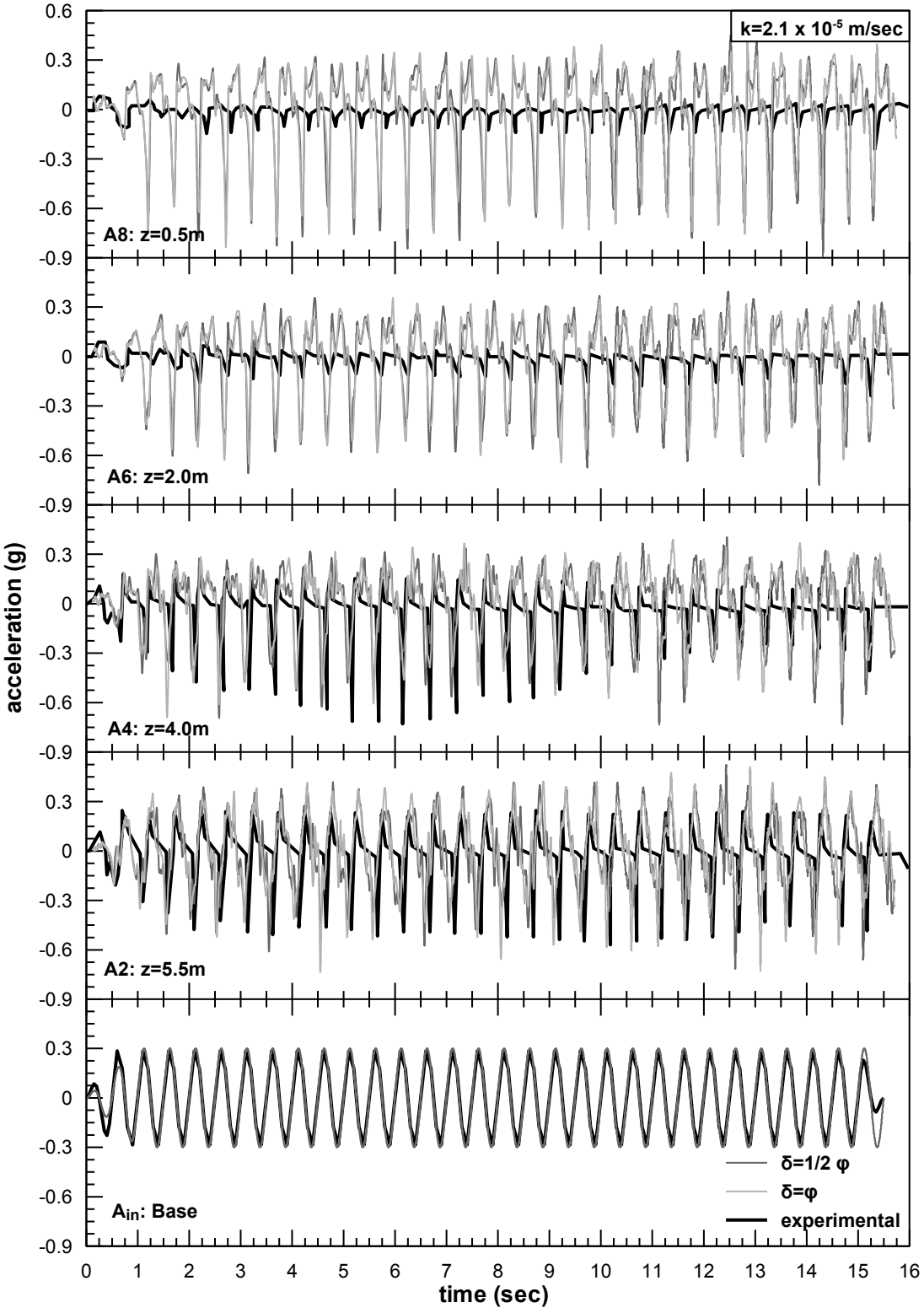

Figure 7.17: Soil acceleration time histories at various depths in the sand for soil permeability k=2.1x10^{-5}m/sec

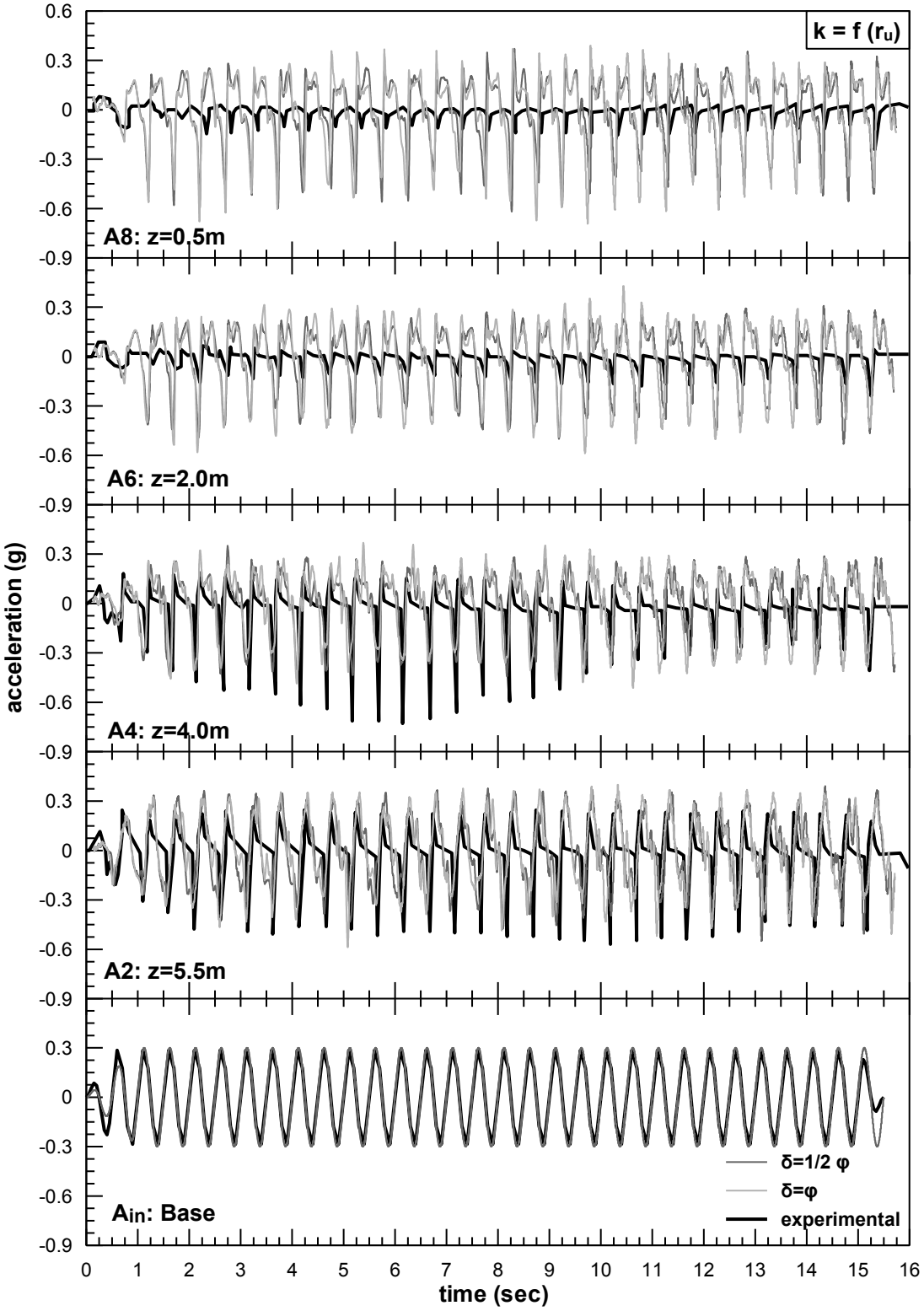

Figure 7.18: Soil acceleration time histories at various depths in the sand for the case of variable soil permeability k=f(r_u)

7.3.4 Pore pressures in the free-field (P1-P4)

The evolution of excess pore pressures in the free field is shown in **Figure 7.19** through **Figure 7.21**. Similarly to the acceleration time histories shown previously, each one of the figures corresponds to a different permeability scenario. Thus, **Figure 7.19** is for $k=6.6x10^{-5}$m/sec, **Figure 7.20** for $k=2.1x10^{-5}$m/sec and **Figure 7.21** for the $k=f(r_u)$ case. In each figure, experimental data and numerical results are shown for four (4) different depths from ground surface (PPTs P1, P2, P3 and P4 in **Figure 7.1**). The continuous black line corresponds to the experiment, the dark gray to the numerical with $\delta=1/2\varphi$, and the light gray to the numerical with $\delta=\varphi$. Along with the evolution of excess pore pressures, the initial vertical effective stress is also shown with a black dashed line.

The overall agreement between experimental measurements and numerical predictions is satisfactory, judging from the fact that both sets of data predict:

- The onset of liquefaction at the early stages of shaking (i.e. after 1-2 cycles)
- Negative (dilation) excess pore pressure spikes due to the presence of initial static shear stresses and lateral spreading.

However, the dilation spikes mentioned above increase with depth for the numerical predictions, while they seem to remain practically constant with depth for the experimental measurements.

The above observations are practically common to all figures, implying that the exact value of permeability has a minor effect on the numerical predictions. Still, it is worth noting that assuming the lowest permeability value, $k=2.1x10^{-5}$ m/s, exaggerates the observed difference between experimental and numerical dilation spikes.

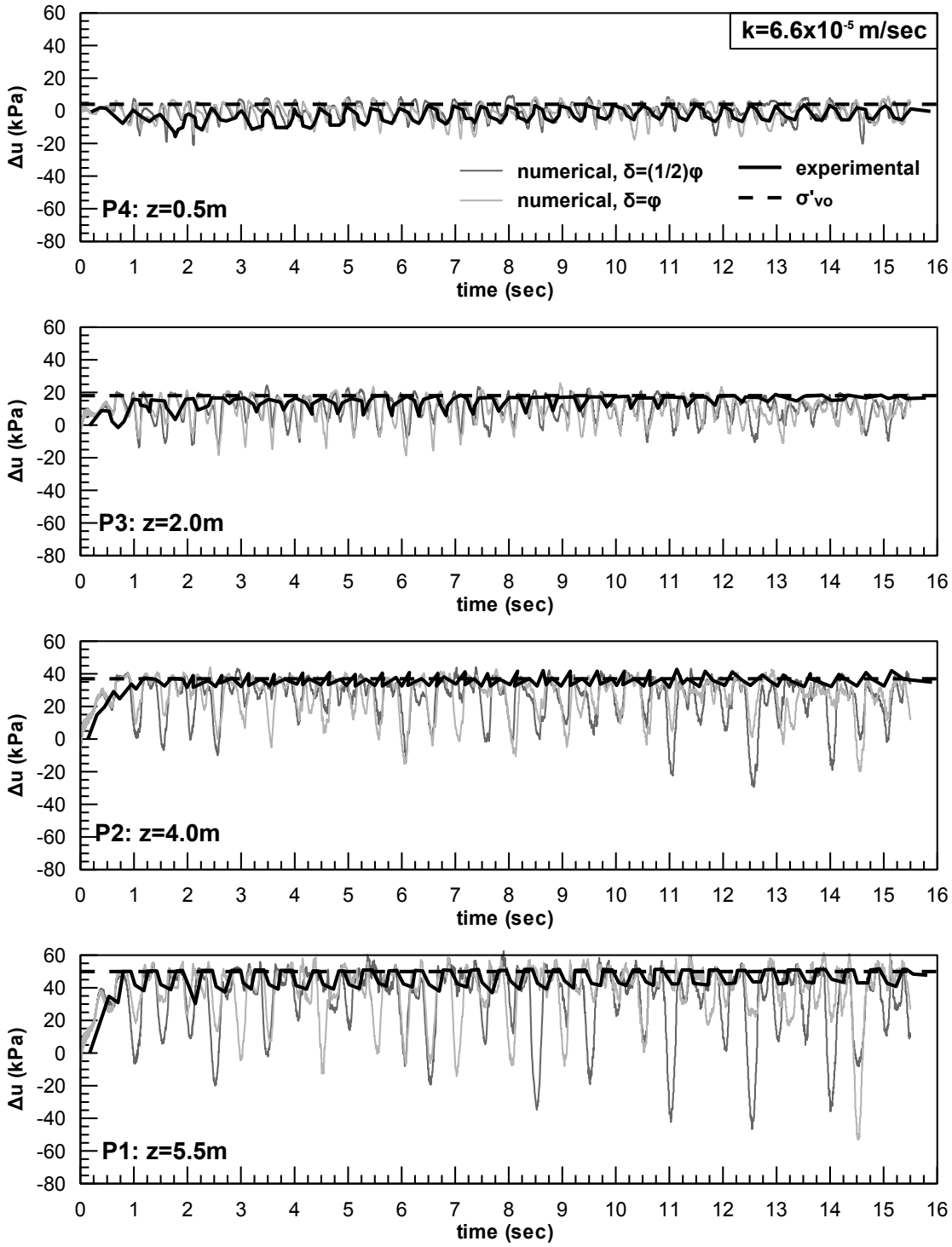

Figure 7.19: Experimental and numerical excess pore pressures for PPTs P1, P2, P3 and P4 and k=6.6x10^{-5}m/sec

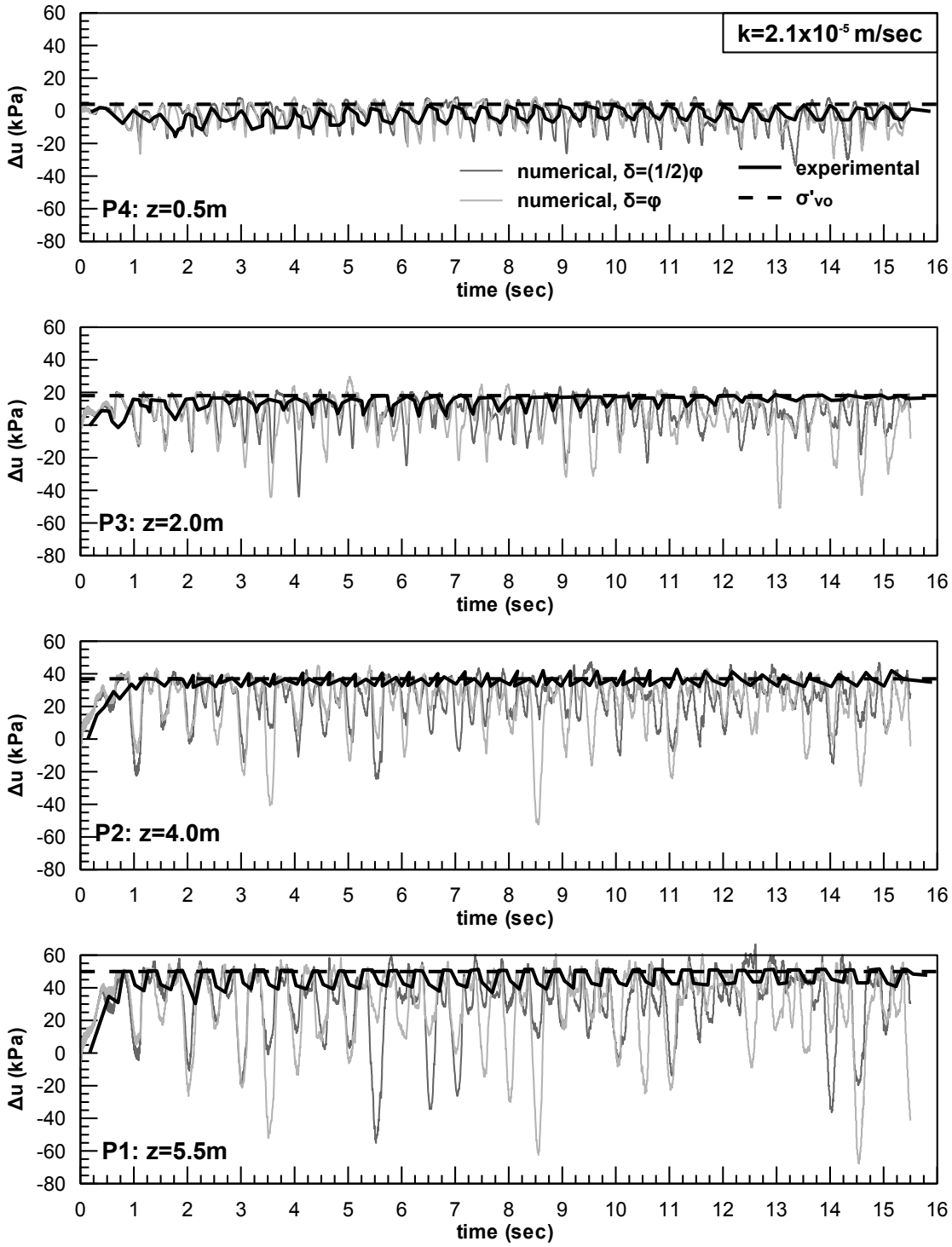

Figure 7.20: Experimental and numerical excess pore pressures for PPTs P1, P2, P3 and P4 and k=2.1x10^{-5}m/sec

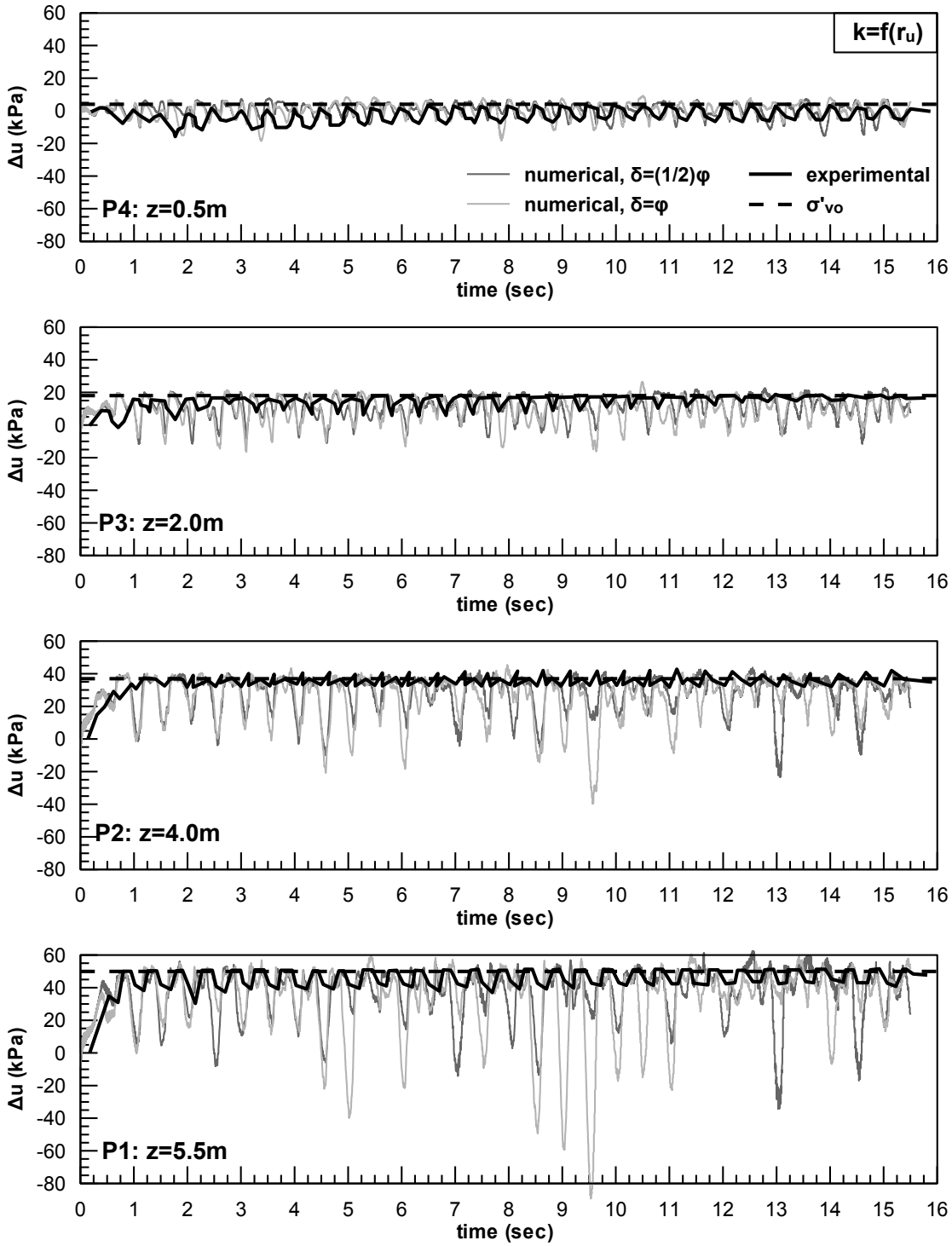

Figure 7.21: Experimental and numerical excess pore pressures for PPTs P1, P2, P3 and P4 and k=f(r_u)

7.3.5 Pore pressures in the near field and close to the pile (P5-P12)

Development of pore pressures in the area close to the pile was recorded in the test though pore pressure transducers P5 to P12, as shown in **Figure 7.1**. More specifically, transducers P5 to P8 were placed at a distance of 1.75m (approximately three diameters) away from the pile, at four different depths that range from 0.5m to 5.5m from ground surface. Transducers P9 to P12 were placed right next to the pile at the same four (4) depths with P5 to P9. Test recordings as well as numerical results are shown in **Figure 7.22** through **Figure 7.24** for the P5 to P9 transducers and in **Figure 7.25** through **Figure 7.27** for P9 to P12 transducers. Similarly to the response in the free field, comparison is shown separately for each permeability scenario considered. Thus, comparisons for P5 to P8 are shown in **Figure 7.22**, **Figure 7.23** and **Figure 7.24** for $k=6.6x10^{-5}m/sec$, $k=2.1x10^{-5}m/sec$ and $k=f(r_u)$ respectively. In a similar fashion, comparisons for P9 to P12 are shown in **Figure 7.25**, **Figure 7.26** and **Figure 7.27** for $k=6.6x10^{-5}m/sec$, $k=2.1x10^{-5}m/sec$ and $k=f(r_u)$ respectively. In each of the figures, experimental data are shown with the black continuous line, and numerical with the dark gray for $\delta=1/2\varphi$, and light gray for $\delta=\varphi$. Also plotted, with the black dashed line, is the initial vertical effective stress. Comparison between the experiment and the numerical analysis shows the following:

- For medium to large depths (z>2m) both in the test and the analysis the pore pressures developed are practically equal to the initial effective stress indicating liquefaction. Again, however, the analysis contains dilation spikes which are hardly visible in the test results.
- Near the surface, the negative pore pressures observed in the test, are very well predicted by the analysis, as shown in the comparisons for transducers P8 and P12 (z=0.5m). Note that according to Gonzalez et al. dilation and negative pore pressures near the surface is a dominant factor for the overall response of the system.
- As for the interface friction angle, the various comparisons indicate that its effect is practically negligible. However, near the ground surface, and especially for transducers P12, the $\delta=1/2\varphi$ case exhibits slightly larger dilation, yielding better agreement with the test.
- Similarly, no significant effect is observed with permeability variation. The only differences are related to the magnitude of dilation spikes in large

depths. Namely, numerical results indicate that for the variable permeability case [$k=f(r_u)$], dilation spikes are reduced compared to the case of dynamic permeability ($k=2.1x10^{-5}$m/sec), while the static permeability case ($k=6.6x10^{-5}$m/sec) yields results that fall approximately in the middle of the other two. Near the ground surface, the differences are minor, however, the best overall comparison is observed for the $k=2.1x10^{-5}$ case.

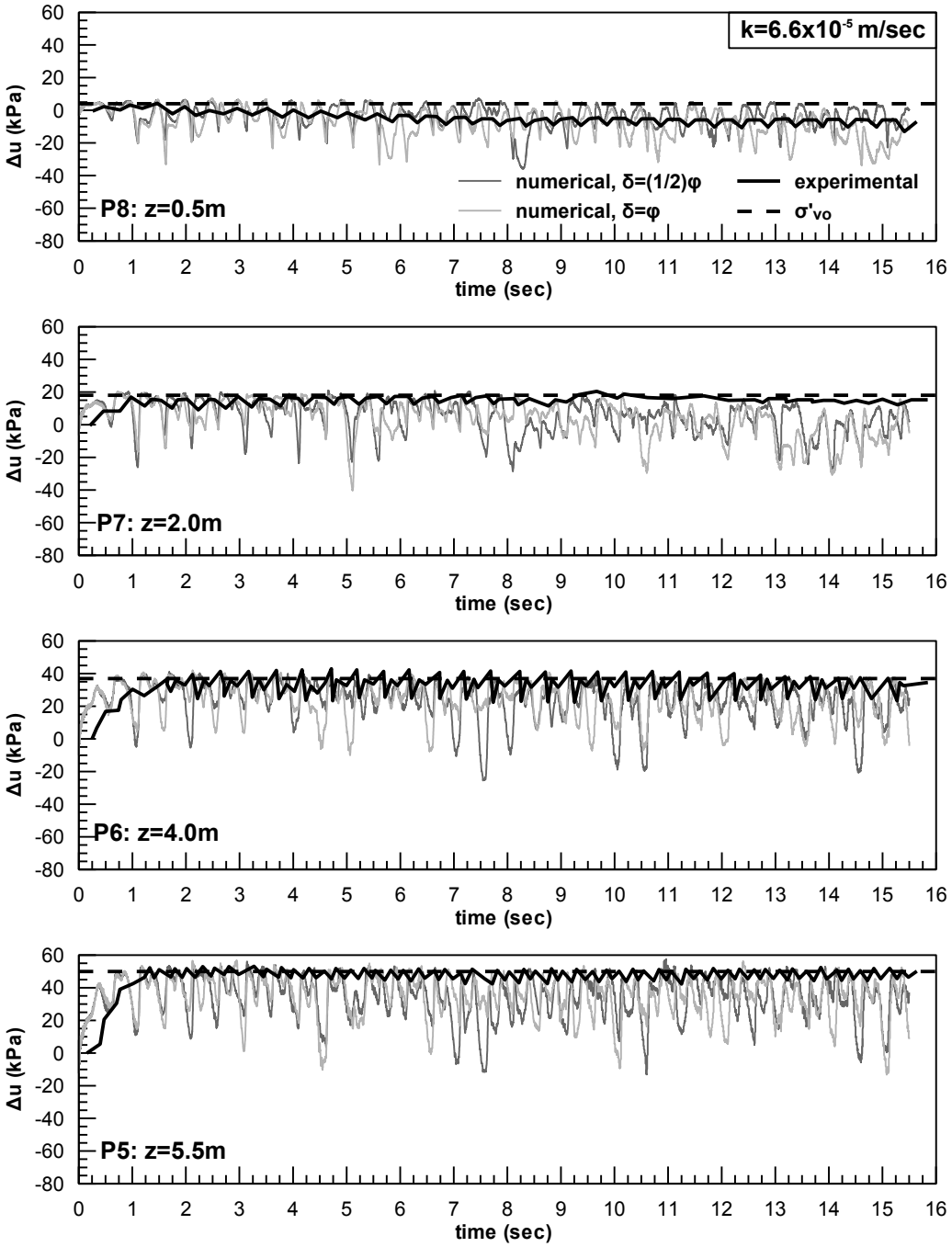

Figure 7.22: Experimental and numerical excess pore pressures for PPTs P5, P6, P7 and P8 and $k=6.6x10^{-5}$m/sec

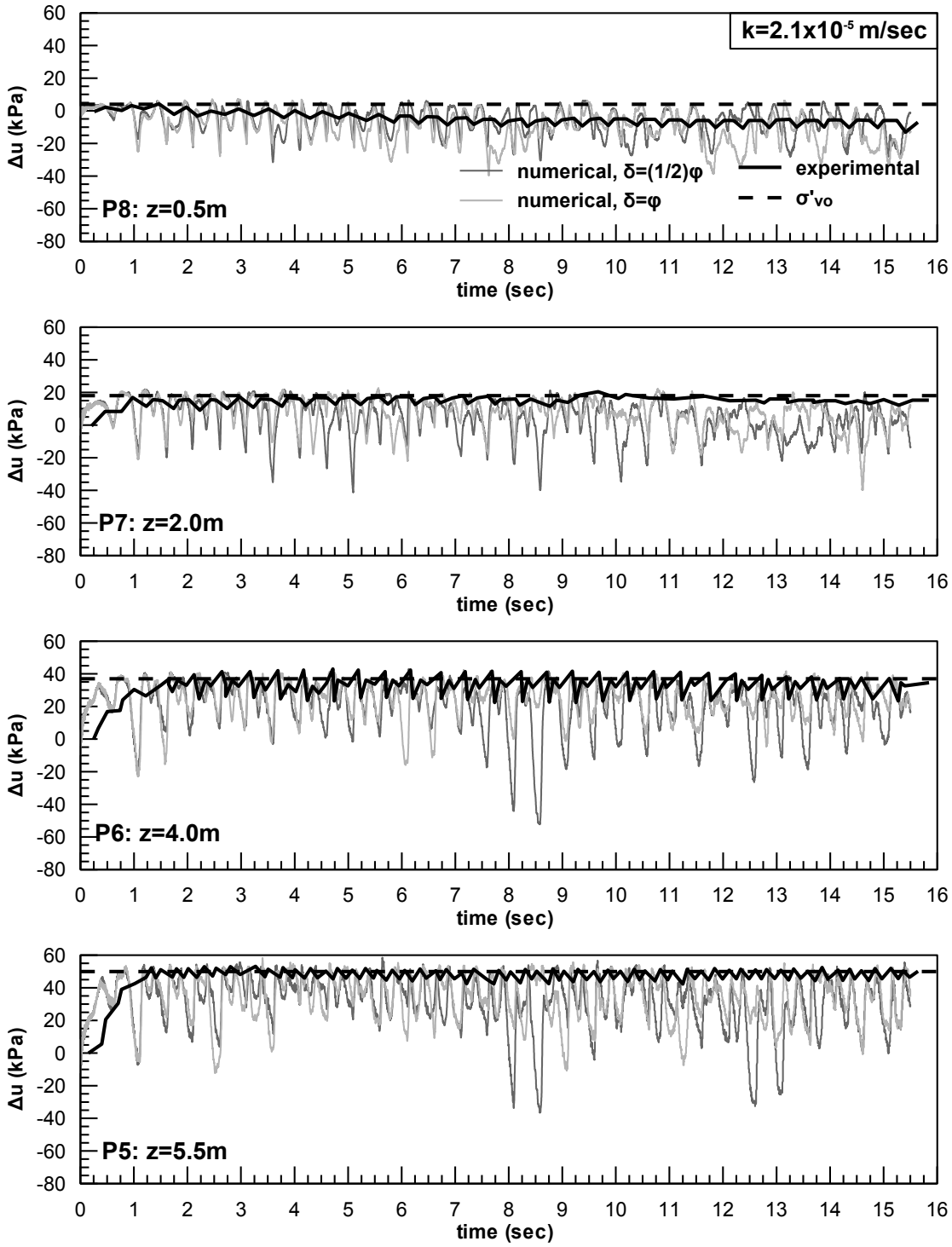

Figure 7.23: Experimental and numerical excess pore pressures for PPTs P5, P6, P7 and P8 and k=2.1x10^{-5}m/sec

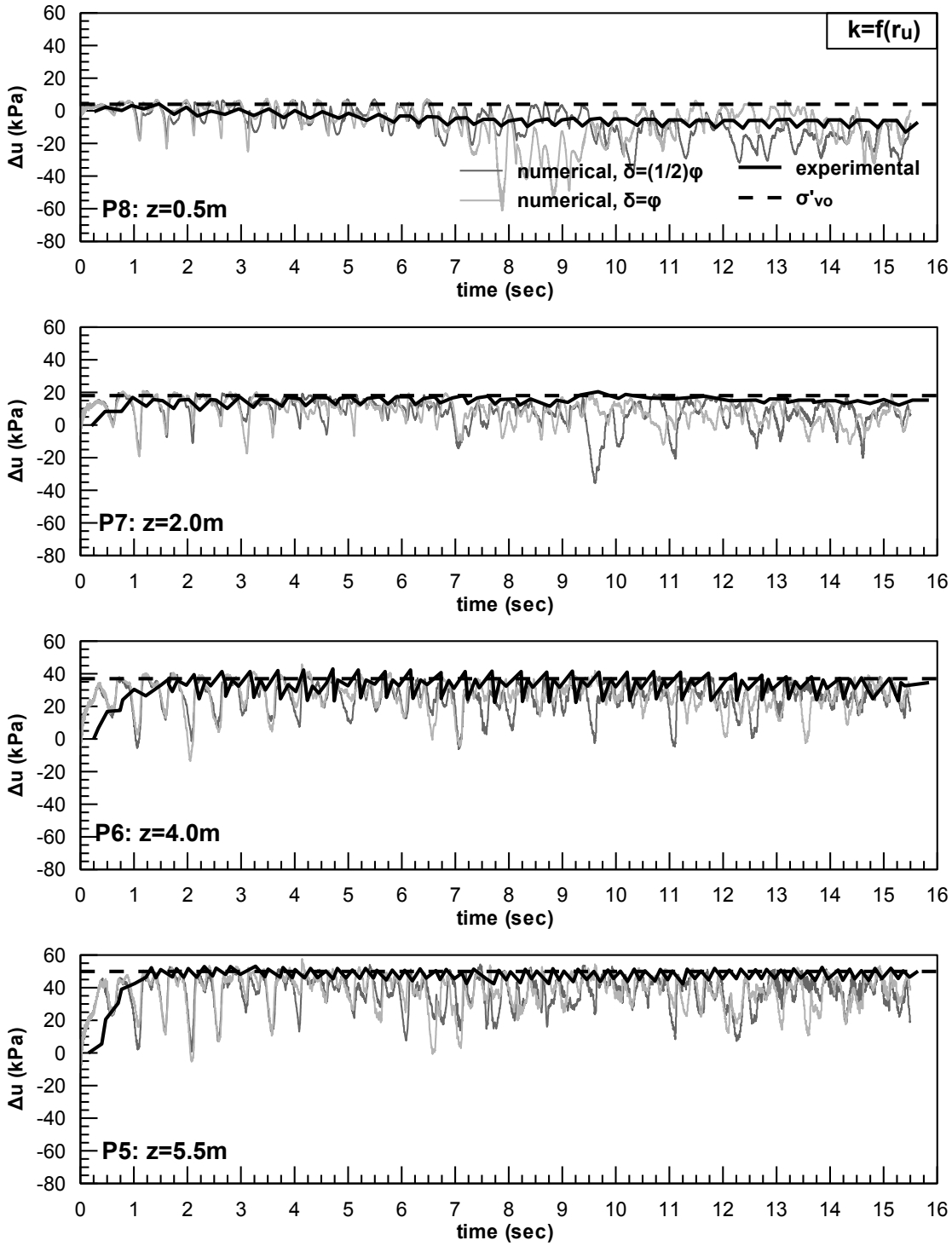

Figure 7.24: Experimental and numerical excess pore pressures for PPTs P5, P6, P7 and P8 and k=f(r_u)

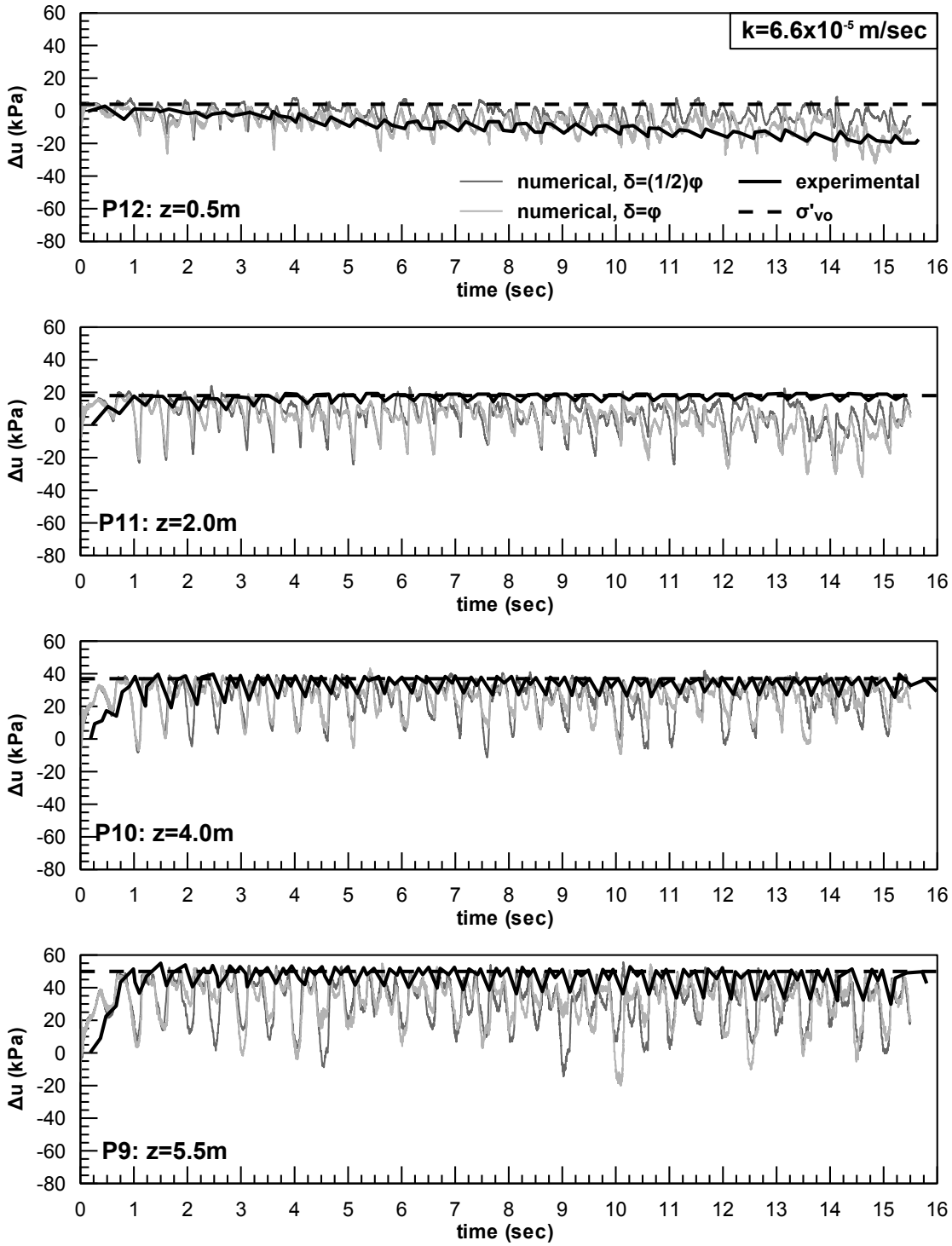

Figure 7.25: Experimental and numerical excess pore pressures for PPTs P9, P10, P11 and P12 and k=6.6x10^{-5}m/sec

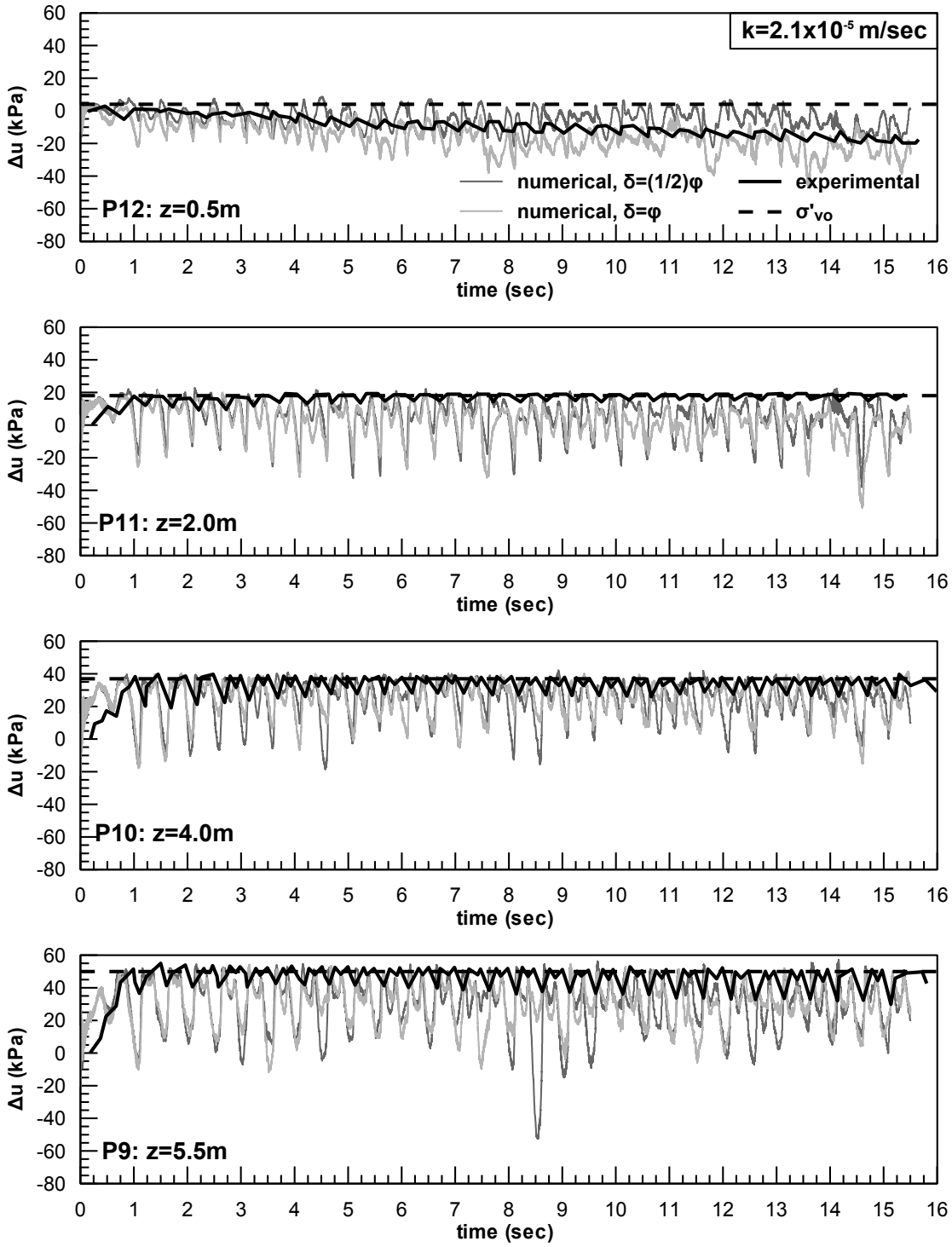

Figure 7.26: Experimental and numerical excess pore pressures for PPTs P9, P10, P11 and P12 and k=2.1x10^{-5}m/sec

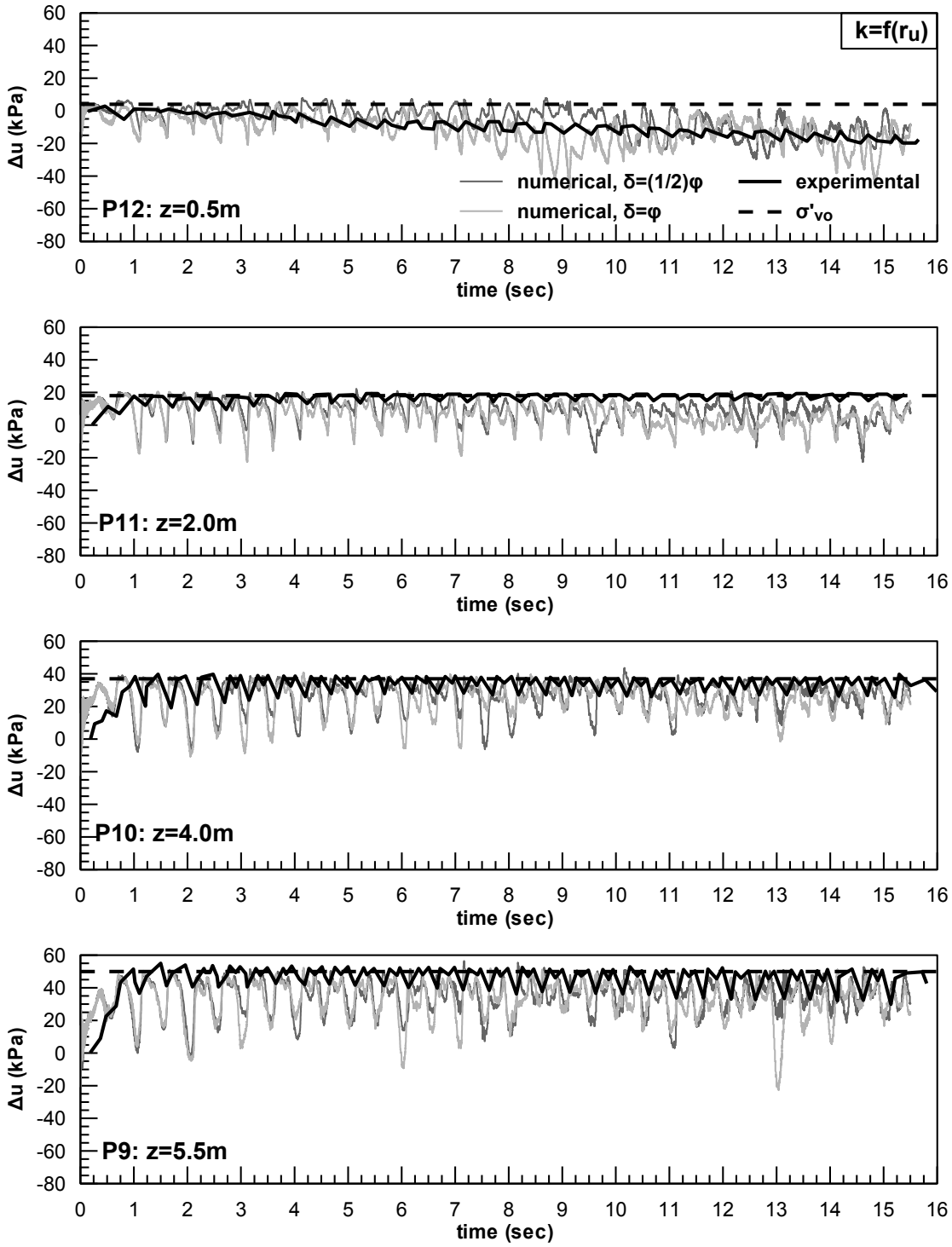

Figure 7.27: Experimental and numerical excess pore pressures for PPTs P9, P10, P11 and P12 and k=f(r_u)

With respect to the k=f(r_u) case presented above, it should be noted that despite the fact that the differences in excess pore pressure development are minor between the δ=1/2φ and δ=φ case, the evolution of permeability is expected to be affected both in time and space. For example, **Figure 7.28** shows permeability evolution with time at

two (2) different depths near the pile (**Figure 7.28a**) and at the free field (**Figure 7.28b**). Mainly from **Figure 7.28a**, and for the depth of z=2m, it can be observed that even small differences in the magnitude of dilation spikes can cause significant differences in the permeability. Hence, any differences observed between the analyses with $\delta=1/2\varphi$ and $\delta=\varphi$ in the $k=f(r_u)$ case, cannot only be attributed to the difference in interface friction, but they include permeability effects as well.

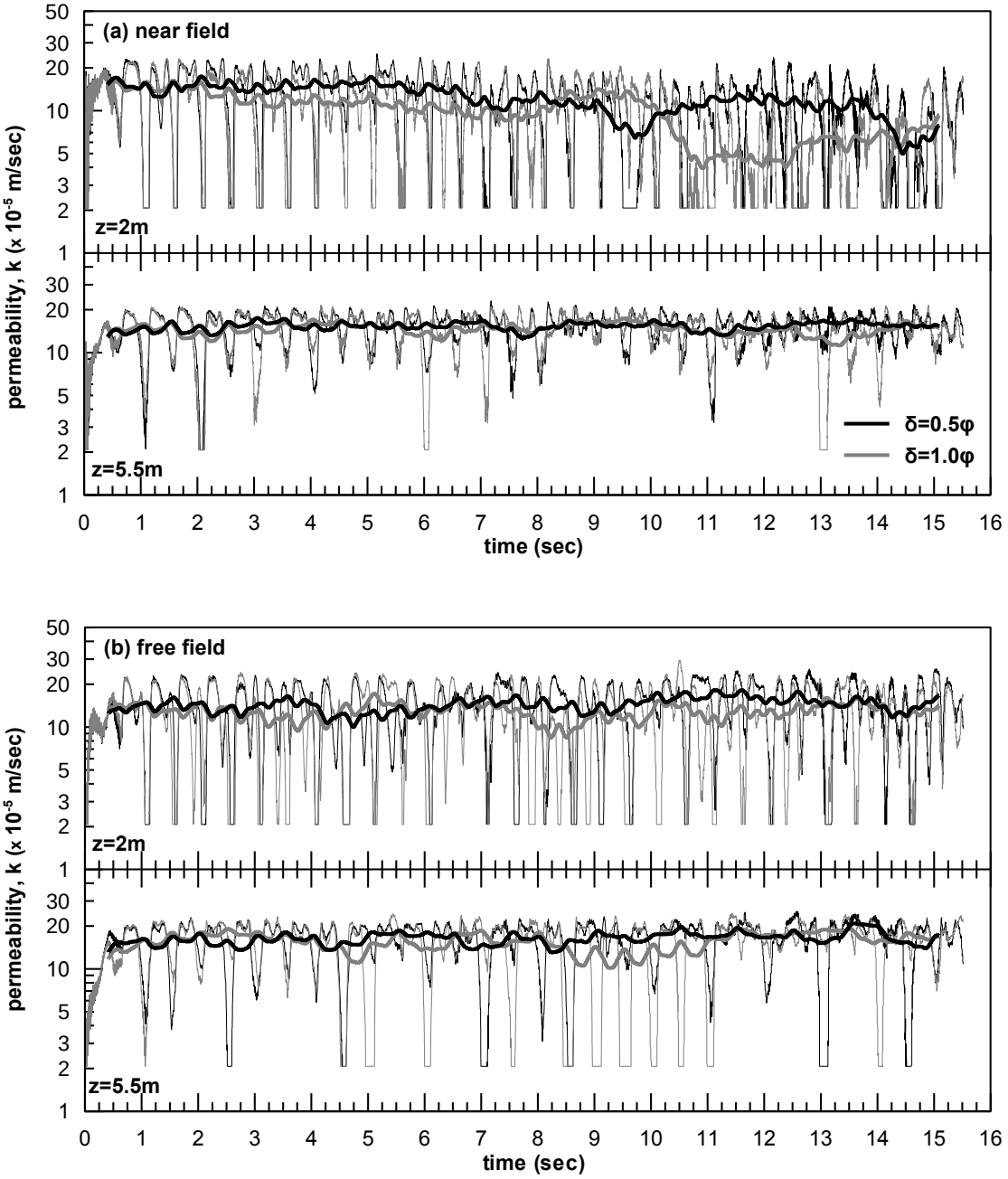

Figure 7.28: Permeability evolution with time for the $k=f(r_u)$ case at two different depths (a) close to the pile and (b) at the free field.

7.3.6 Free field soil displacements

Soil displacements at the free field were recorded in the test through four (4) LVDTs which were placed at the boundary of the box, as shown in **Figure 7.1**. Comparison between test recordings and numerical results is illustrated in **Figure 7.29** through **Figure 7.32**. The first three (3) figures show displacement time histories as measured by the LVDTs, and as estimated numerically, while the fourth compares the profiles of soil displacement with depth at the end of shaking. In all figures, experimental data are shown with the black continuous line, while numerical with dark gray for $\delta=1/2\varphi$ and light gray for $\delta=\varphi$. Finally, in **Figure 7.32**, the black dashed line corresponds to the ultimate, in terms of horizontal displacement, capacity of the box.

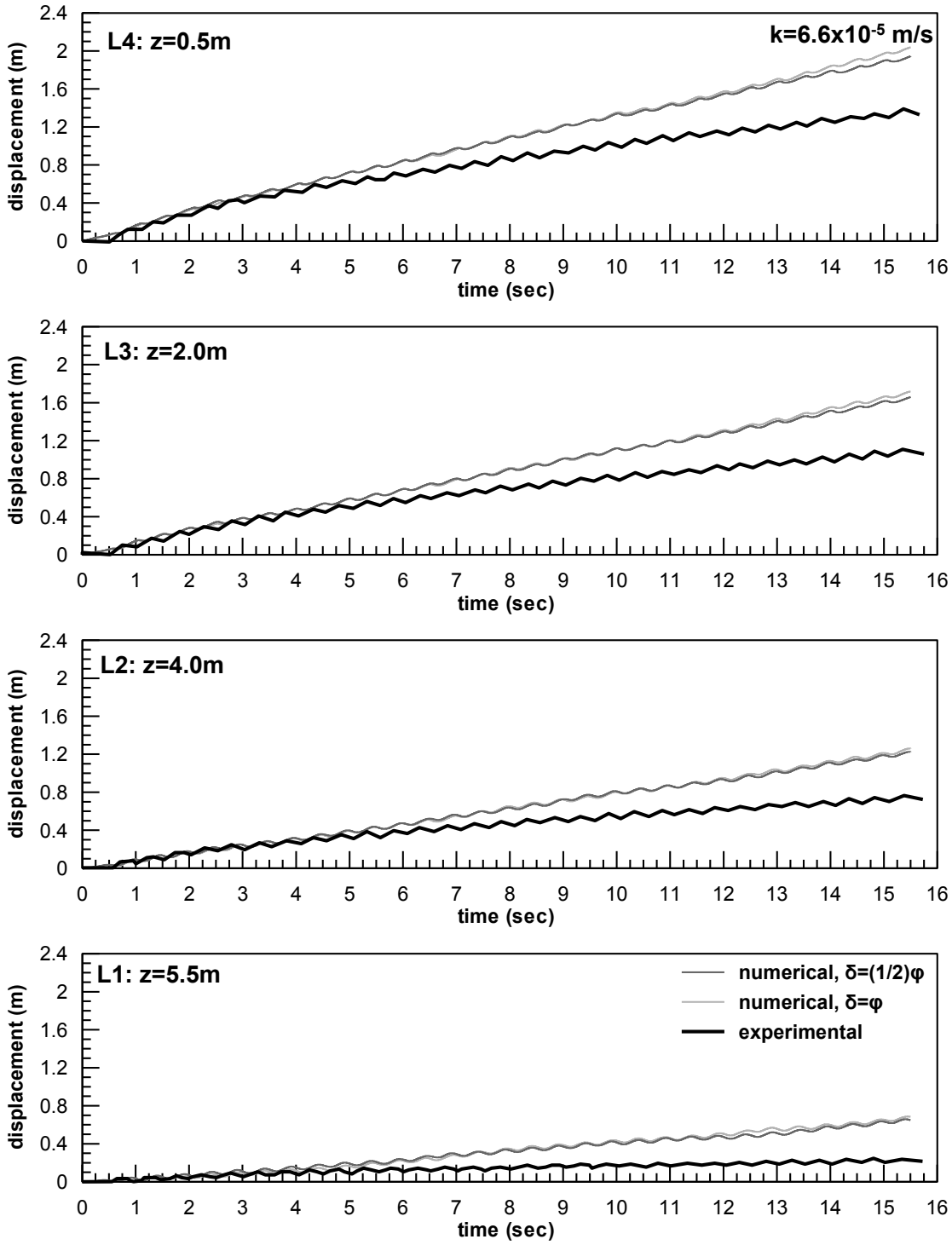

Figure 7.29: Experimental and numerical free-field lateral displacement time histories for LVDTs L1, L2, L3 and L4 for k=6.6x10^{-5} m/s

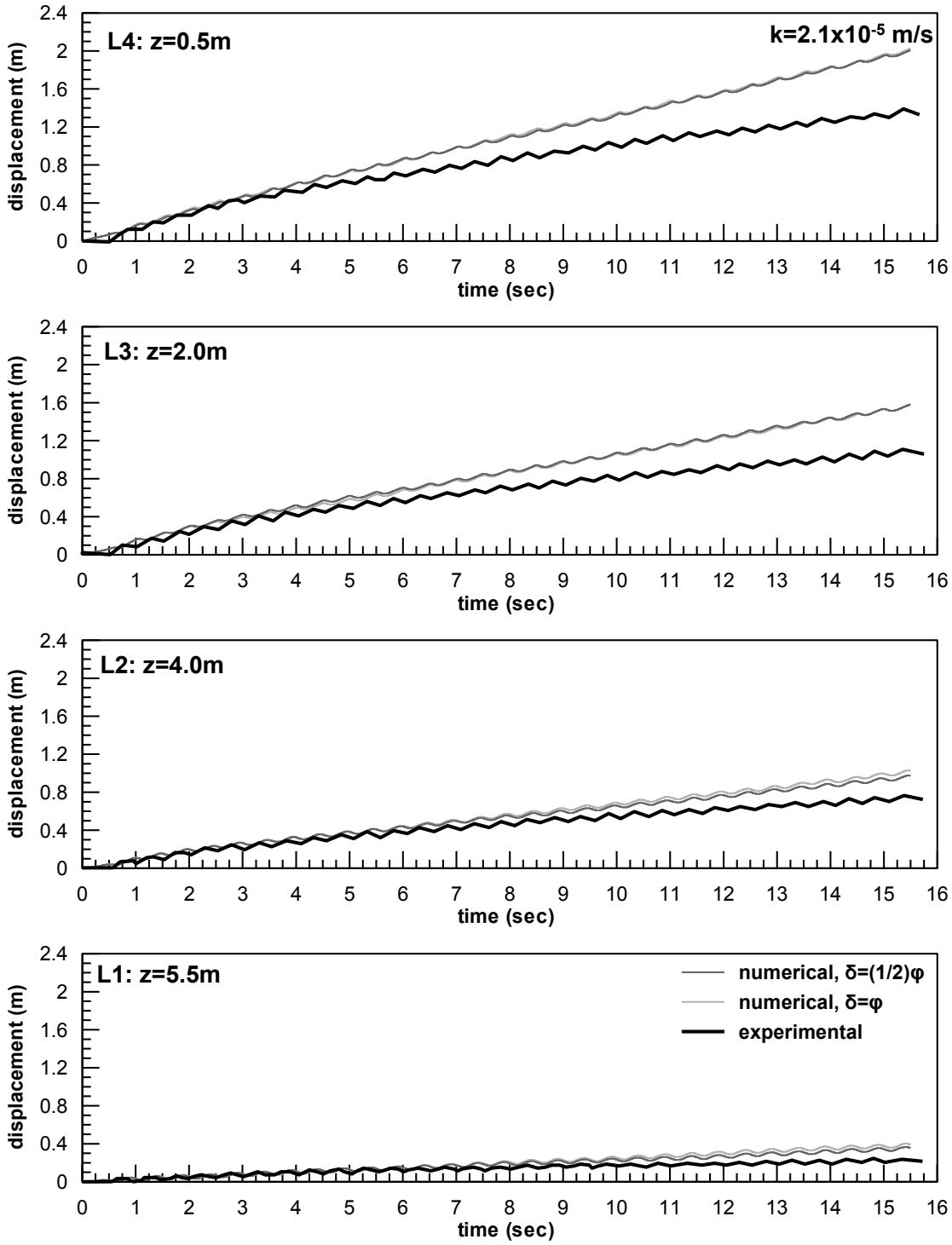

Figure 7.30: Experimental and numerical free-field lateral displacement time histories for LVDTs L1, L2, L3 and L4 for k=2.1x10^{-5} m/s

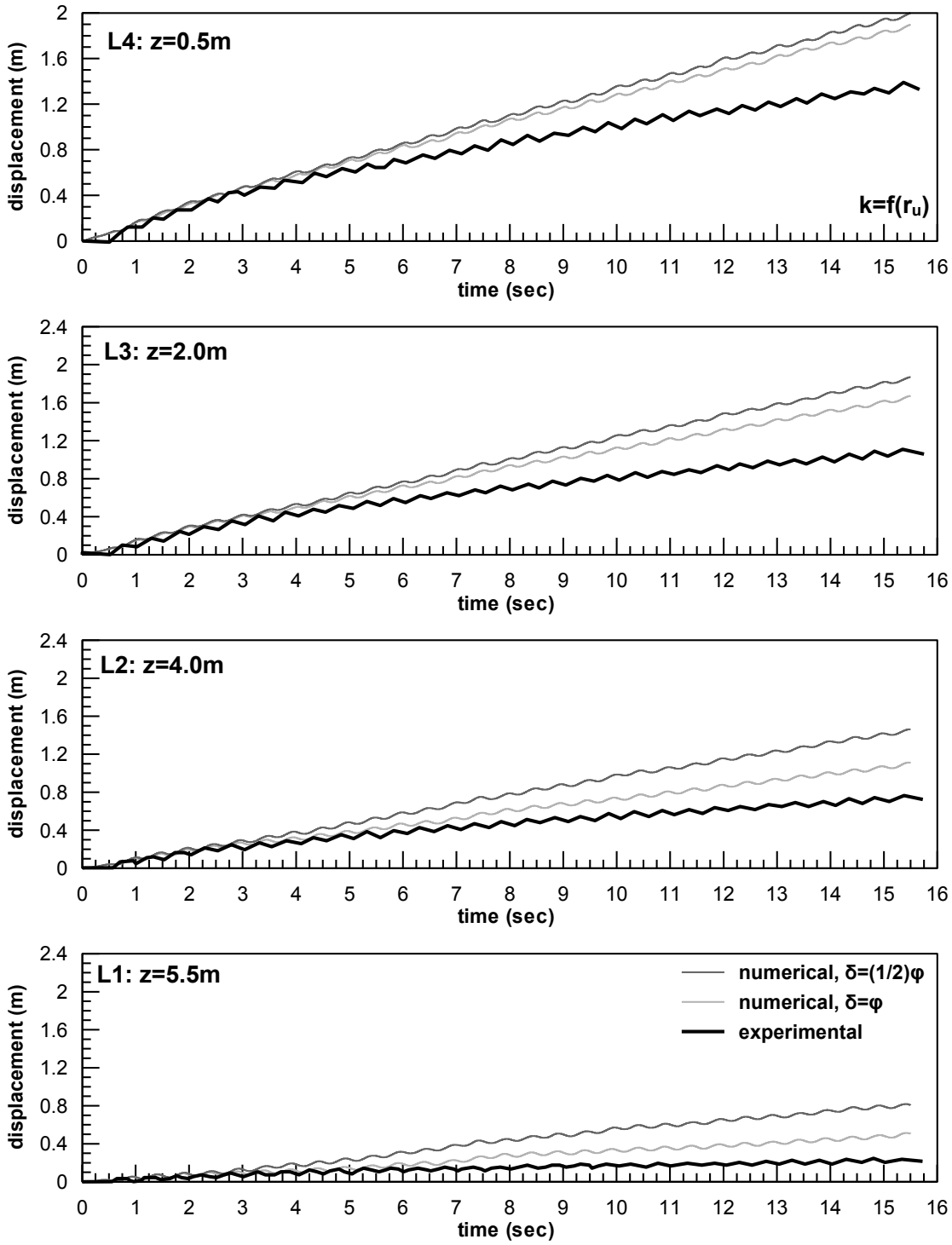

Figure 7.31: Experimental and numerical free-field lateral displacement time histories for LVDTs L1, L2, L3 and L4 for $k=f(r_u)$

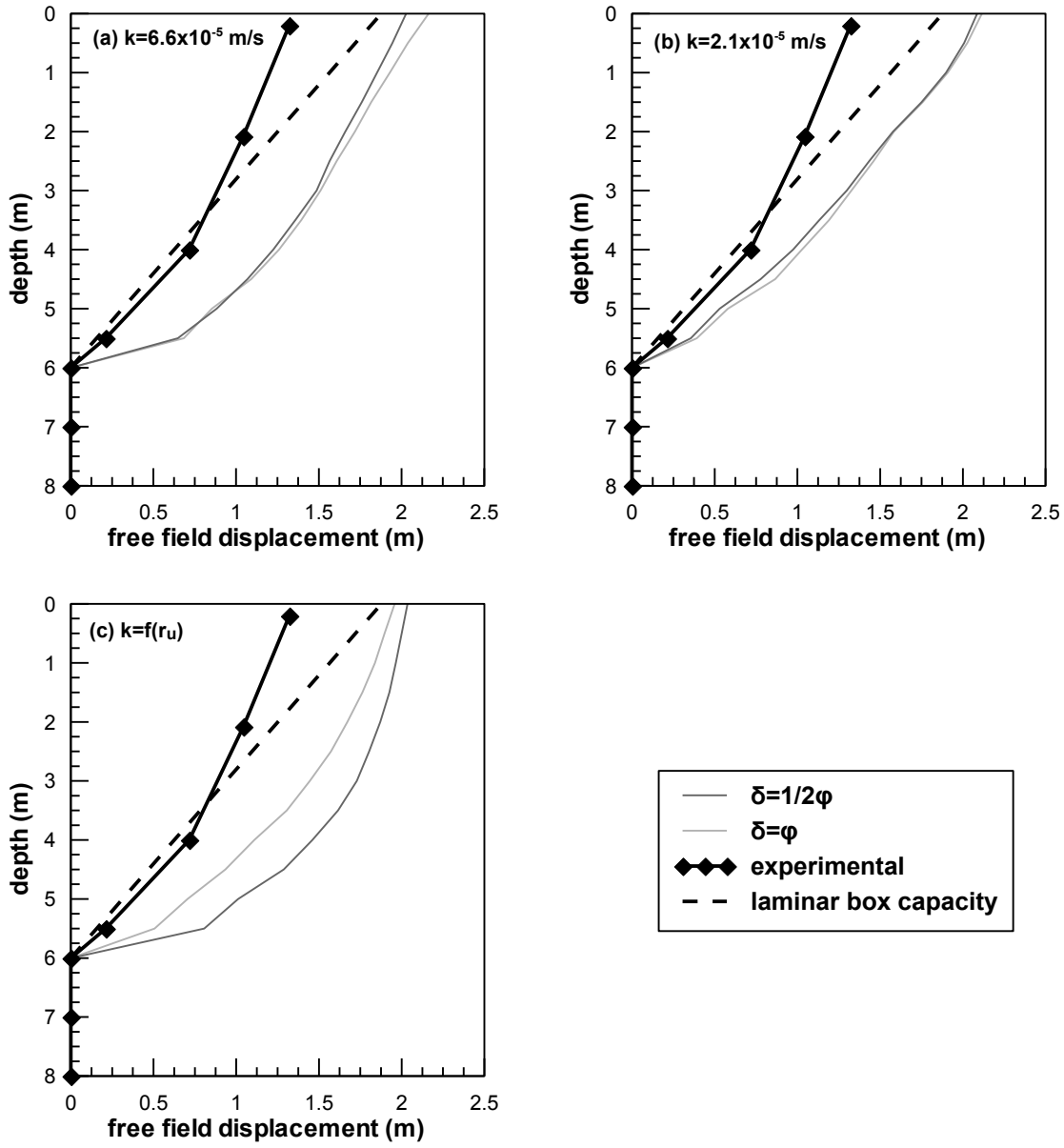

Figure 7.32: Experimental and numerical free-field displacement profiles with depth at the end of shaking for (a) k=6.6x10^{-5} m/s, (b) k=2.1x10^{-5} m/s and (c) k=f(r_u).

The time histories, shown in **Figure 7.29** through **Figure 7.31**, indicate that numerical analyses significantly overpredict the displacements at the free field in all depths. However, comparison between the experimentally obtained soil displacement profile and the displacement capacity of the laminar box (continuous and dashed black lines in **Figure 7.32**) shows that, for depths z=4.0m and 5.5m, the capacity of the box is reached. In addition, a more detailed observation of the time histories shows that during the first loading cycles, the numerical and the experimental lines are in good agreement. In order to further investigate the influence of the laminar box's capacity

on the above comparison, **Figure 7.33** shows displacement soil profiles at various instances during shaking. Note that numerical results are only plotted for the analysis with $k=6.6x10^{-5}m/sec$ and $\delta=1/2\varphi$, but the relevant conclusions apply to all other cases as well.

For t=3sec (**Figure 7.33a**) numerical and experimental data practically coincide. However, the displacement at z=5.5m is almost equal to the maximum displacement the box can undertake at that depth. This is reflected in the displacement distribution for t=6sec (**Figure 7.33b**), where the numerical displacement for this particular depth is larger than the experimental. Of course, the kinematic constraint imposed by the box at this depth affects the response along the whole layer, and hence the numerical analysis yields overall larger displacements. For t=9sec (**Figure 7.33c**), the deviation between numerical and experimental estimates has become larger, while for z=4.0m soil displacement is almost equal to the capacity of the box. As a result, for t=12sec and t=15sec (**Figure 7.33d** and **e**), the difference between numerical and experimental measurements is even larger, with the former yielding a displacement at the ground surface of approximately 2m, and the latter around 1.35m.

The preceding analysis shows a possible deficiency of the experimental setup to capture the full deformation of the free field. This deficiency should be taken into account when examining other aspects of the response, such as pile head displacements, the p-y curves and the bending moments developing along the pile.

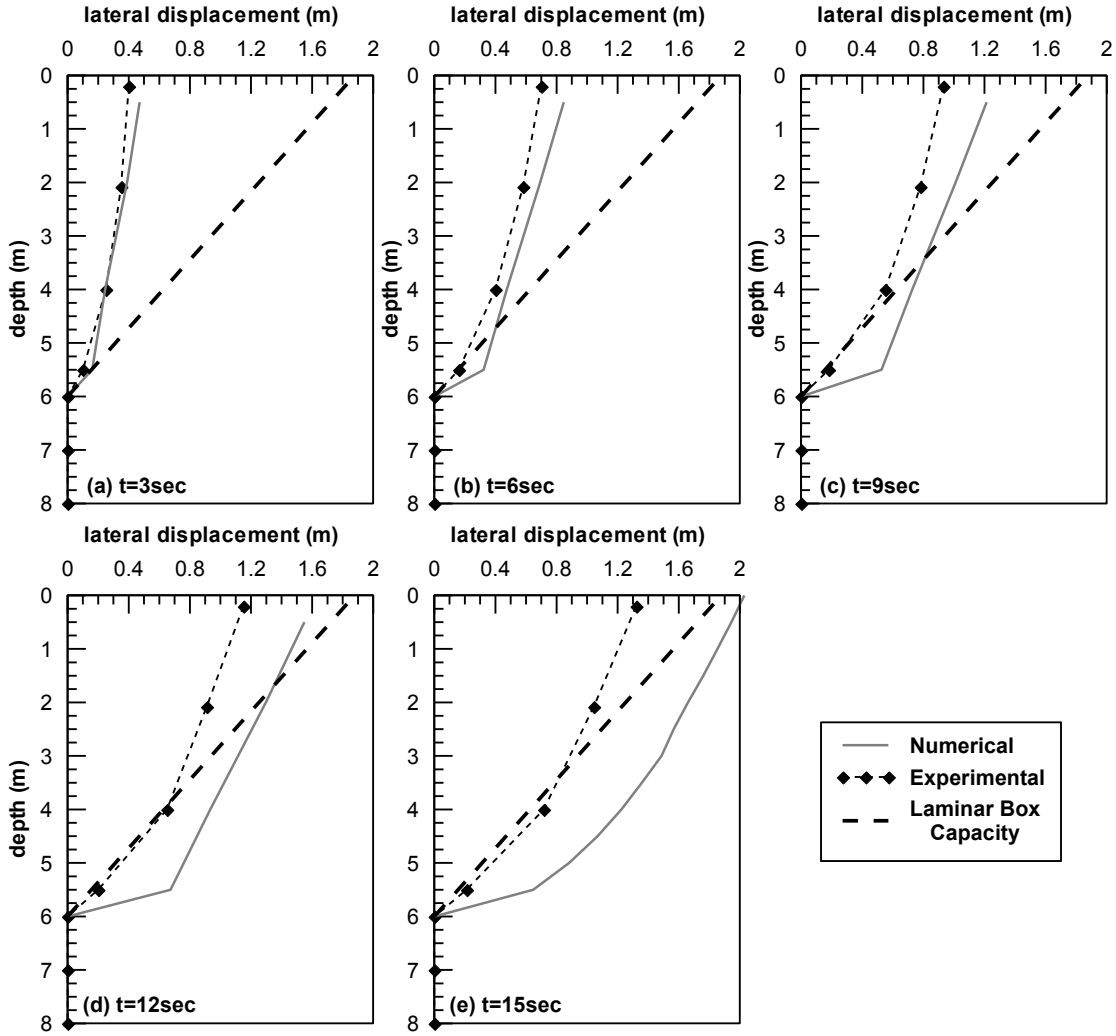

Figure 7.33: Free field soil displacement versus depth for various instances during shaking relatively to the displacement capacity of the laminar box

In order to eliminate this objective deficiency of the experiment and make the comparison more clear, numerical predictions were modified based on the following simple relation:

$$y_{ff}\ h = \int_0^h \gamma\ h \cdot dh \qquad (7.7)$$

where:

h: height above the bottom of the liquefiable layer

y_{ff} (h): free field soil displacement at h

γ (h): Shear strain at h (obtained numerically)

In order to account for ultimate laminar box capacity, γ(h) in the above equation cannot exceed the maximum shear strain that can be developed in the box, i.e.:

$$\gamma\ h\ \leq \gamma_{ult} \approx 33\% \tag{7.8}$$

Hence, comparisons shown in **Figure 7.29** through **Figure 7.32** are repeated in **Figure 7.34** through **Figure 7.37**, with the corrected numerical displacements being plotted as well with the dashed line. The comparison further verifies that the differences observed previously were a result of the insufficient capacity of the laminar box, while the agreement between experimental data and corrected numerical predictions is remarkable.

Finally, the following can be observed with respect to the effect of permeability and interface friction:

- In general the friction angle of the interface has a negligible effect on the displacements at the free field. Only, for the k=f(r_u) case, the analyses with δ=1/2φ and δ=φ yield displacements that differ at a certain amount, especially at large elevations.
- As for permeability, it appears that the best agreement is achieved for the k=6.6x10^{-5} m/s and k=f(r_u) case, while displacements are slightly overestimated when the k=2.1x10^{-5} m/s value is applied.

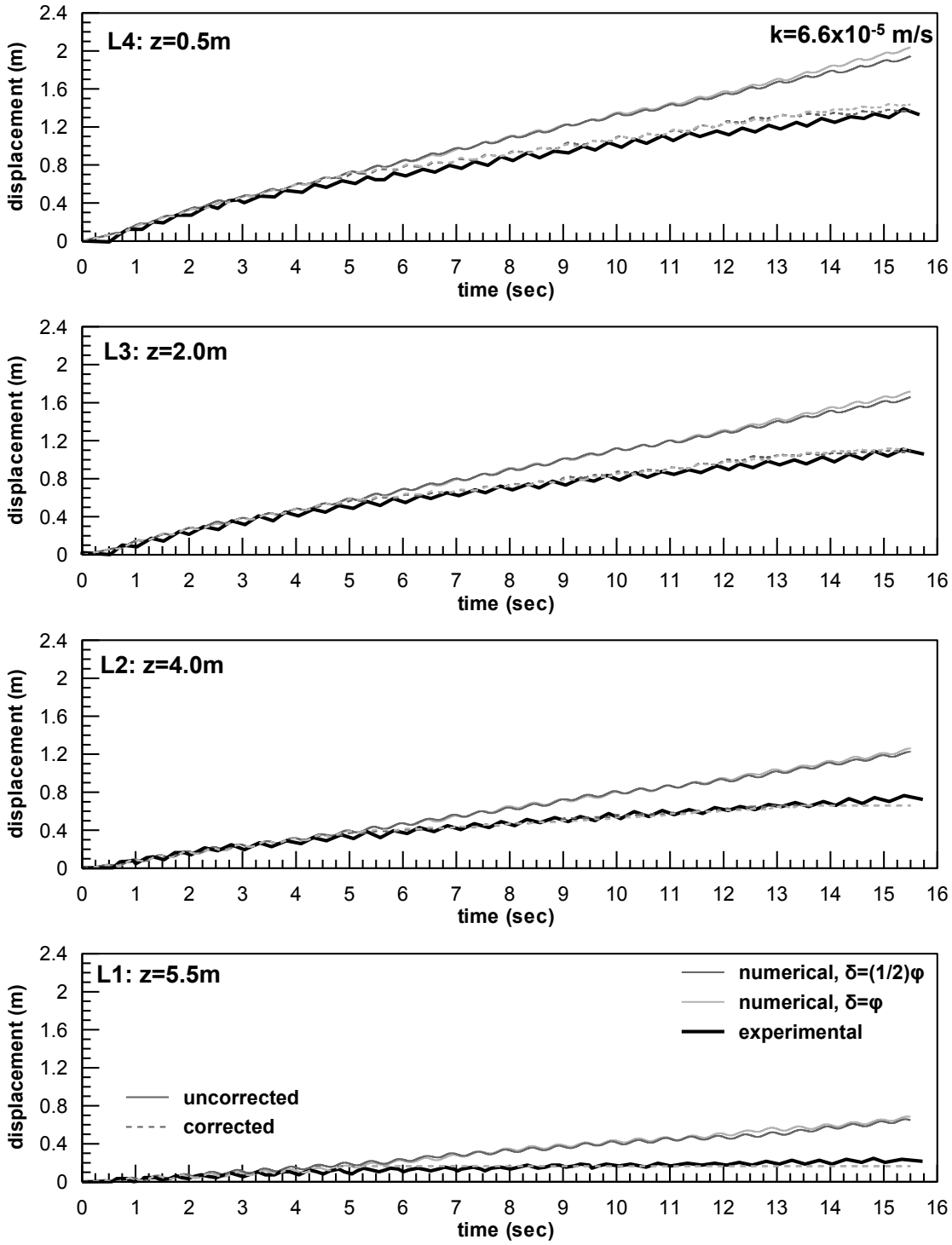

Figure 7.34: Experimental and numerical free-field lateral displacement time histories for LVDTs L1, L2, L3 and L4 for k=6.6x10^{-5} m/s before and after correction

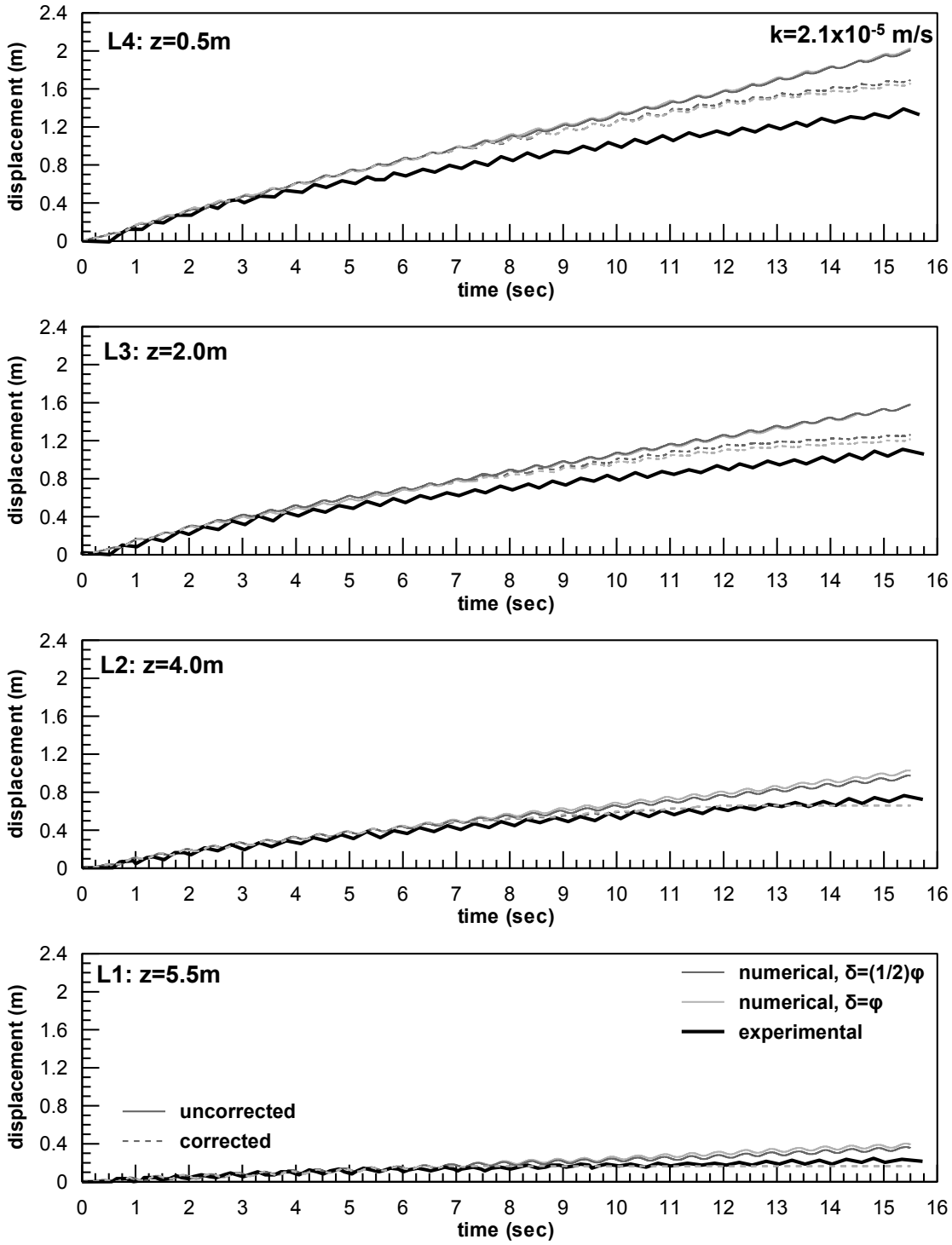

Figure 7.35: Experimental and numerical free-field lateral displacement time histories for LVDTs L1, L2, L3 and L4 for k=2.1x10^{-5} m/s before and after correction

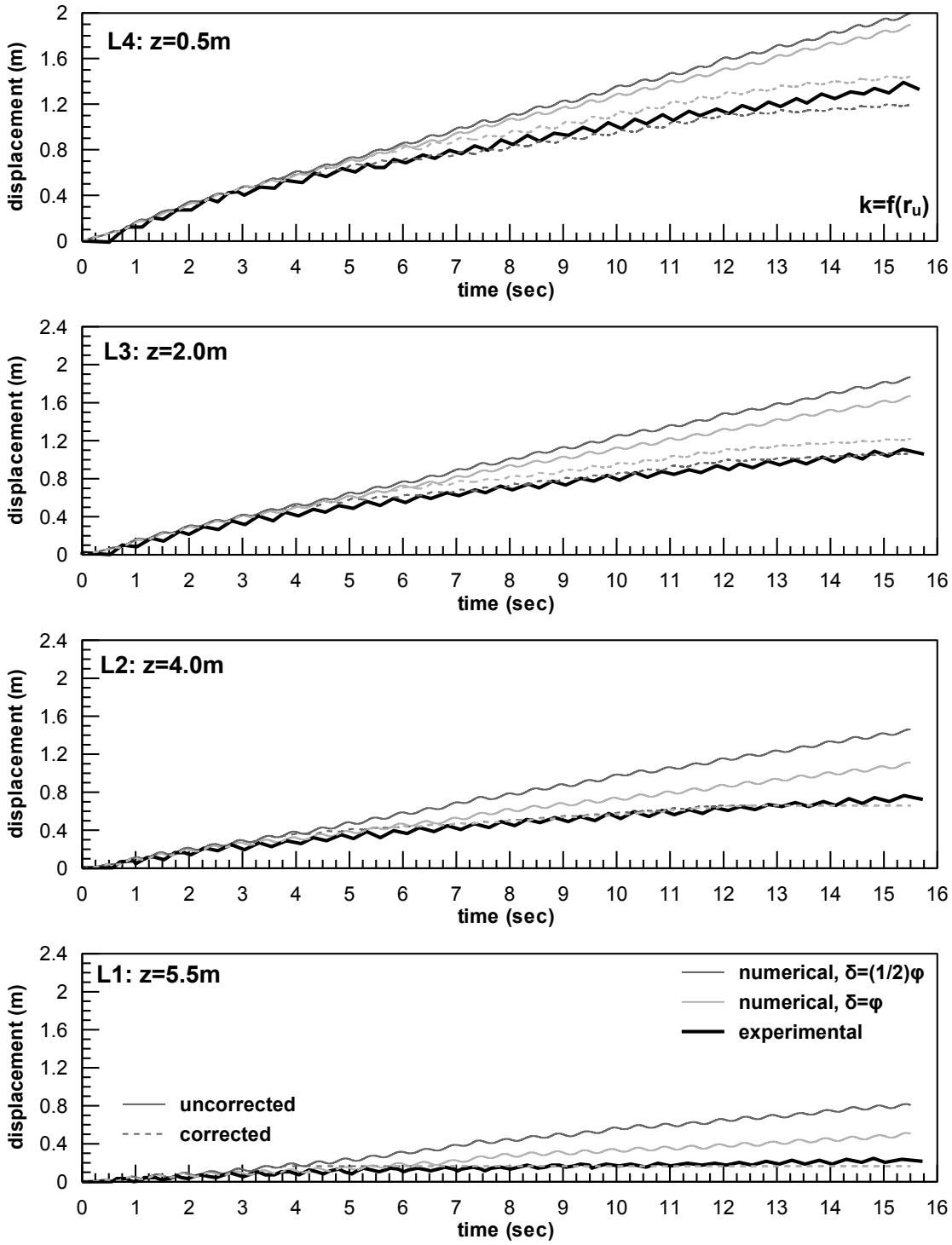

Figure 7.36: Experimental and numerical free-field lateral displacement time histories for LVDTs L1, L2, L3 and L4 for $k=f(r_u)$ before and after correction

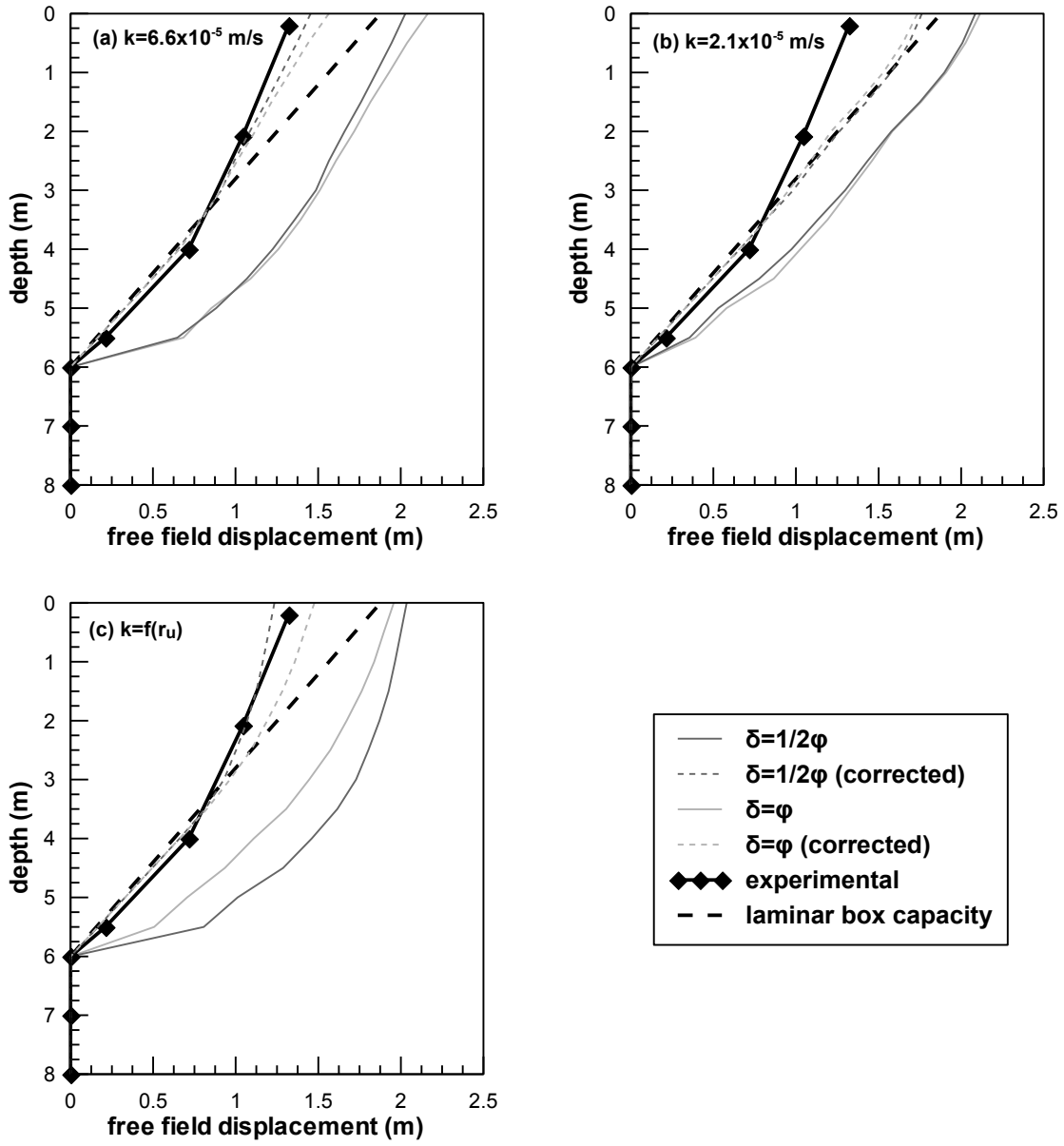

Figure 7.37: Experimental and numerical free-field displacement profiles with depth at the end of shaking for (a) k=6.6x10^{-5} m/s, (b) k=2.1x10^{-5} m/s and (c) k=f(r_u) before and after correction

7.3.7 Pile head displacements

The displacement of the head of the pile was recorded through two (2) LVDTs (L5 and L6) as shown in **Figure 7.1**. However, the respective recordings are practically identical and consequently, in the following comparisons, only data from LVDT L5 will be presented. **Figure 7.38** summarizes test recordings and numerical results for k=6.6x10^{-5} m/sec (**Figure 7.38a**), k=2.1x10^{-5} m/sec (**Figure 7.38b**) and k=f(r_u) (**Figure 7.38c**). Also plotted in each figure is the δ=0.5φ case (dark gray line) and the δ=φ case (light gray line). Experimental data are plotted with the black continuous line.

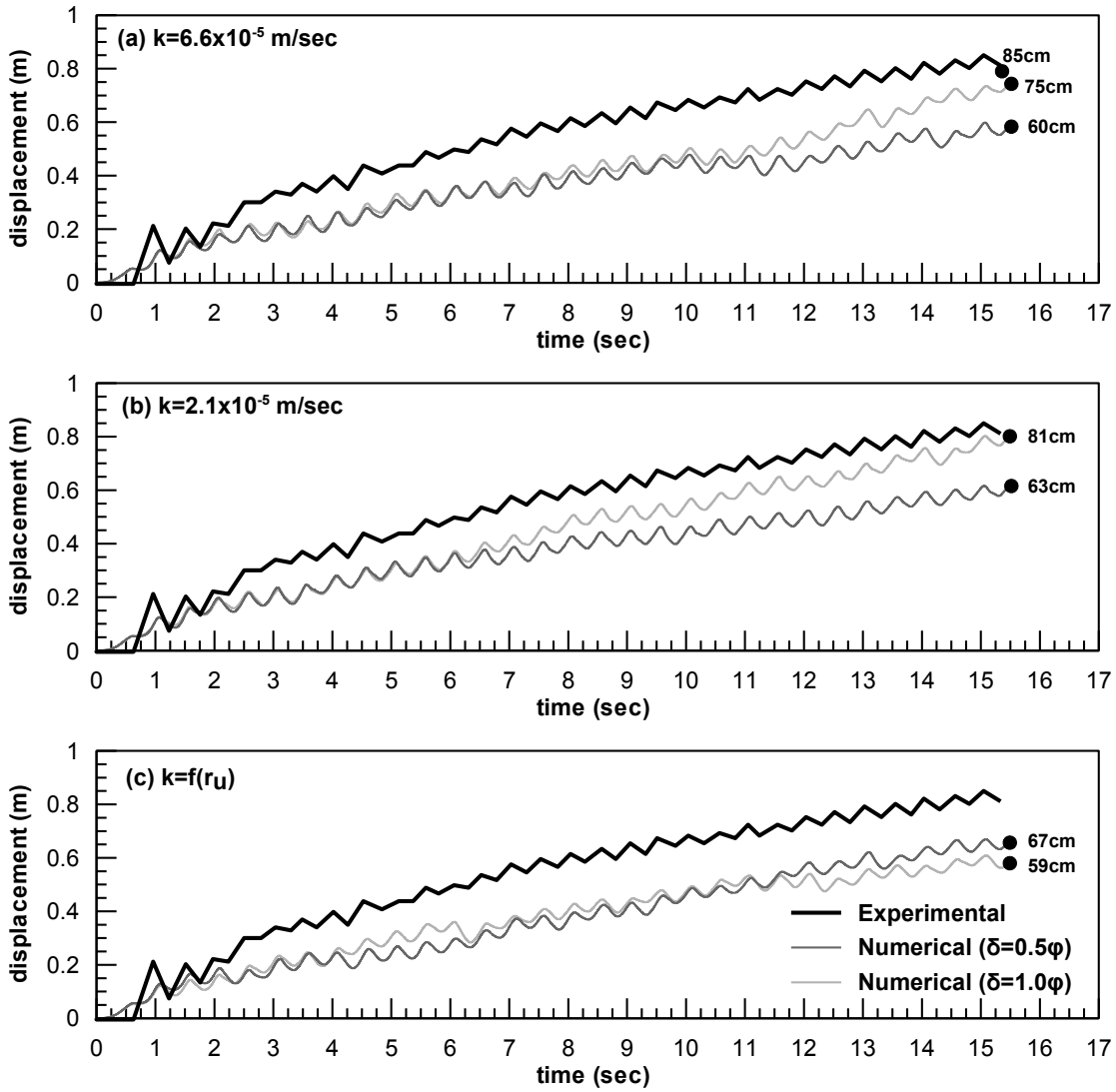

Figure 7.38: Experimental and numerical pile head displacements for the three permeability cases considered (a) k=6.6x10^{-5} m/sec (b) k=2.1x10^{-5} m/sec and (c) k=f(r_u)

The figures indicate the following:

- In all cases the displacement of the pile is lower in the analyses compared to the test. Namely, numerical estimates range from 60 to 81cm, while the measured value was 85cm.
- For constant permeability values, pile head displacements are consistently affected by the friction angle of the interface. More specifically, increase in the interface friction angle from 1/2φ to 1.0φ caused the final displacement of the pile to increase by 25-30%.
- The effect of permeability on pile displacement is much less significant. Numerical results indicate that as permeability decreases from 6.6x10^{-5} m/sec

to 2.1x10^{-5} m/sec head displacement increases by approximately 5-8%. Still, the k=2.1x10^{-5} m/s case yields the overall better comparison.

- Finally, the more detailed simulation with the variable permeability yields displacements which are closer to the k=6.6x10^{-5} m/sec case, while the friction of the interface has an overall negligible effect.

7.3.8 P-y curves

As described earlier, experimental p-y curves were back-calculated from the bending moments after the cyclic component was filtered out. On the other hand, in the numerical analysis, p-y curves are directly estimated through the normal and shear stress at the node of the interface element, and hence both the transient and permanent component can be obtained. As a result, in the following figures, experimental curves are plotted only in terms of the permanent component, while numerical curves are shown both before and after the cyclic component is filtered out. Namely, **Figure 7.39** through **Figure 7.41** compare experimental and numerical p-y curves for k=6.6x10^{-5} m/s, k=2.1x10^{-5} m/s and k=f(r_u) respectively. In each figure, numerical curves for the various permeability and interface friction cases are shown separately. Experimental data are plotted with the black line, numerical prior to filtering with a gray thin line, and numerical after filtering with a thick gray. Finally, as far as displacements are concerned, similarly to the experiment, the curves are shown in terms of the relative displacement y, which is the difference between the free field minus the pile displacement. The former are measured at the downward boundary of the mesh (like in the test), and the latter at the vertical axis of the pile. The comparisons indicate the following:

- Numerical curves reach relative displacement values which are significantly larger compared to the experimental. For the reasons explained in 7.3.6, this discrepancy is attributed to the fact that numerical analyses estimate much larger free field soil displacements.
- The response patterns observed in the test are correctly predicted in the analyses. Namely, soil pressures are larger near the surface (due to soil dilation), while at deeper elevations they obtain a residual value which remains approximately constant with depth.

- In all cases the experimental curves fall within the range defined by the cyclic and permanent component of the numerical curve.
- The comparison in terms of average numerical p-y curves, shows in general good agreement. Namely, for z>2m, numerical analyses appear to slightly overpredict the ultimate resistance, as they yield maximum loads around 15-20kN/m, while the corresponding experimental values range around 10kN/m. On the other hand, for z=1m, the various assumptions produce different numerical predictions. More specifically, for $k=6.6x10^{-5}$ m/sec and $k=f(r_u)$, both for $\delta=1/2\varphi$ and $\delta=\varphi$, numerical curves fall below the experimental data, while for $k=2.1x10^{-5}$m/sec the two (2) numerical curves ($\delta=1/2\varphi$ and $\delta=\varphi$), are very close to them.
- The effect of permeability is negligible at large depths where and all approaches result in approximately the same value of residual soil resistance. On the other hand, near the surface (e.g. for z=1m), numerical results indicate that soil resistance decreases with increased permeability. This is reasonable as larger pressures near the surface are attributed to soil dilation and the associated negative pore pressures. Therefore, when permeability increases water can flow faster towards the area of large dilation suppressing the negative pressures and hence reducing the soil pressure.
- The effect of interface friction is again negligible for large depths it is negligible where the liquefied soil quickly reaches a residual strength. However, near the surface, analyses with $\delta=\varphi$, yield slightly larger resistance values.

Overall, and given the approximate way the experimental p-y curves were estimated, it can be concluded that the numerical model can accurately capture the p-y response of the liquefied soil.

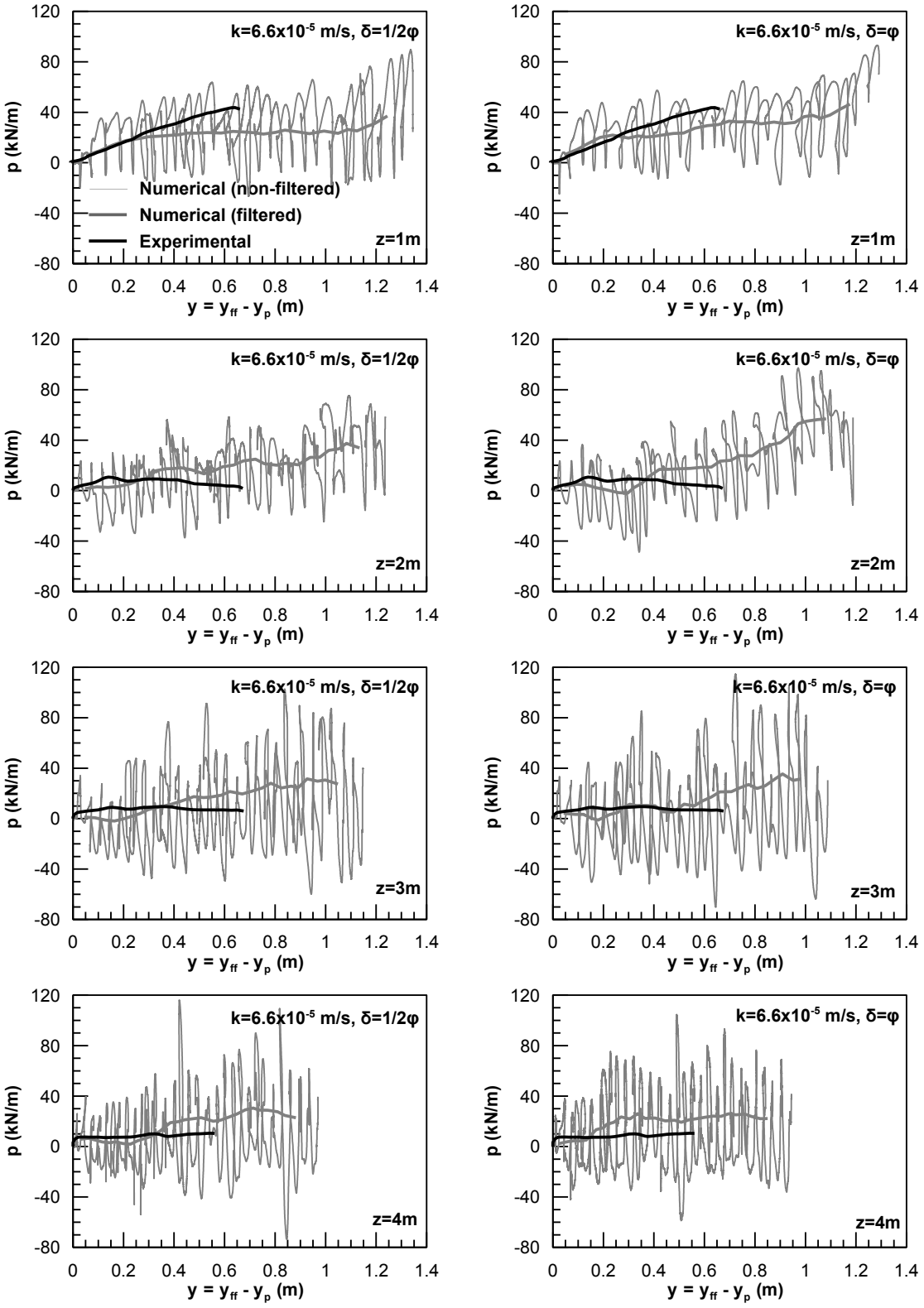

Figure 7.39: Experimental and numerical p-y curves for k=6.6x10^{-5} m/s

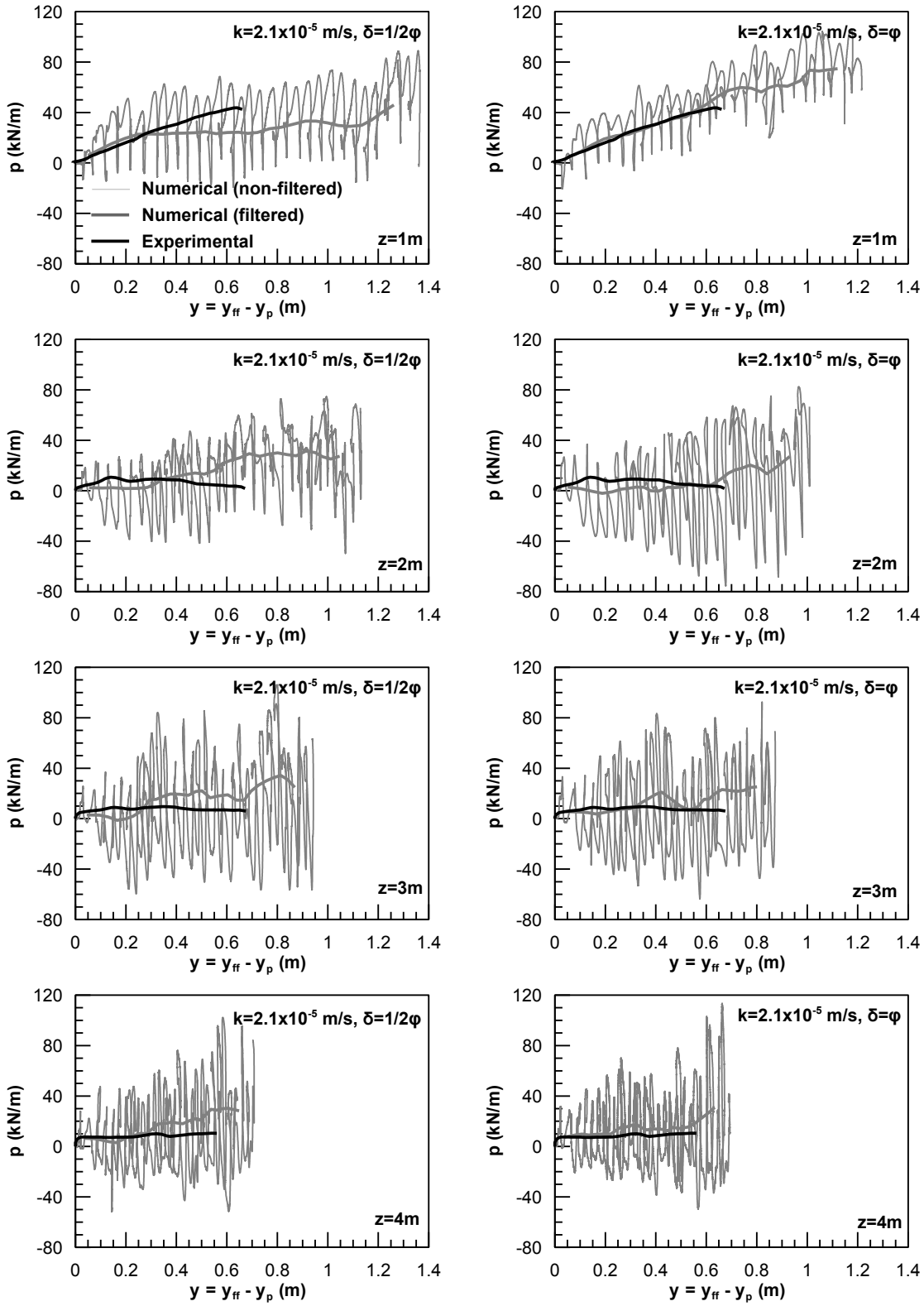

Figure 7.40: Experimental and numerical p-y curves for k=2.1x10-5 m/s

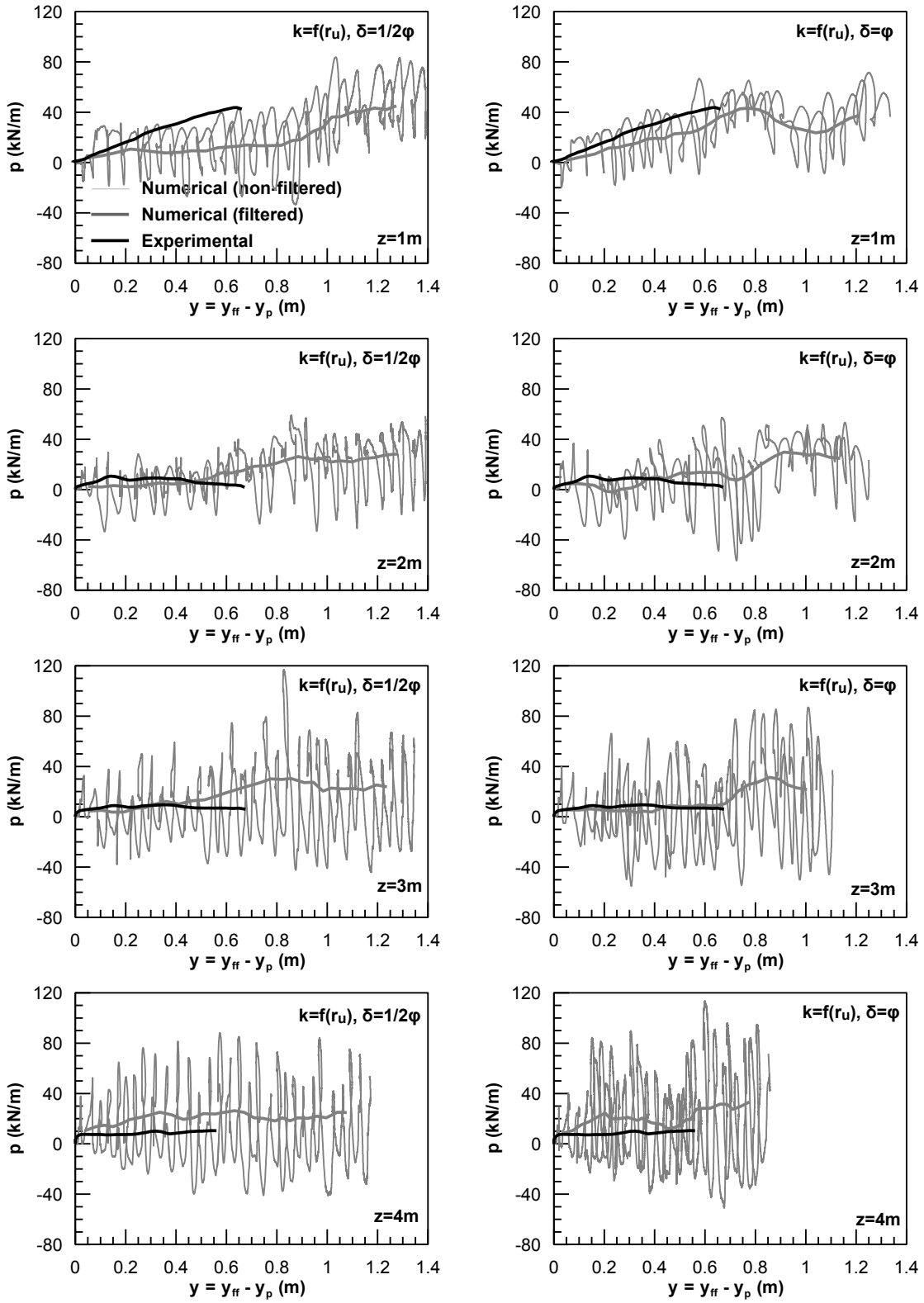

Figure 7.41: Experimental and numerical p-y curves for k=f(r_u)

7.3.9 Pile Bending Moments

The comparison between experimental and numerical bending moments is illustrated in **Figure 7.42**, **Figure 7.43** and **Figure 7.44** for k=6.6x10^{-5} m/s, k=2.1x10^{-5} m/s and k=f(r_u) respectively. As shown earlier, at the end of shaking displacements at the free field are significantly larger in the analysis than in the test, because the displacement capacity of the laminar box is locally reached below 3m depth. In addition the effect of this discrepancy on the response of the pile cannot be easily prescribed. Hence, it was decided to compare pile bending moments at various moments during shaking. More specifically, each figure shows comparisons of both free-field displacements and bending moments at five (5) different instances during shaking (t=3, 6, 9, 12 and 15 sec). The following can be observed:

- Soil displacements at the free field seem to affect the bending moments developed along the pile, as in all cases, numerical and experimental bending moments are in good agreement as long as numerical and experimental free-field displacements remain close.
- More specifically, numerical and experimental bending moments are in good agreement at the initial stages of loading and approximately up to 9 seconds of shaking.
- As shaking progresses, the rate of displacement accumulation in the experiment decreases, and the same applies to the associated rate of bending moment increase. As a result, numerically predicted bending moments start to diverge from the experimental, and end up being significantly larger and at the end of shaking.
- The effect of soil permeability is not very significant, although, smaller permeability results in slightly larger bending moments. In any case, the comparison is satisfactory for all cases considered, with the k=6.6x10^{-5} m/sec case giving an overall better match.
- Except for the case of variable permeability, analyses with larger interface friction result in slightly larger moments.

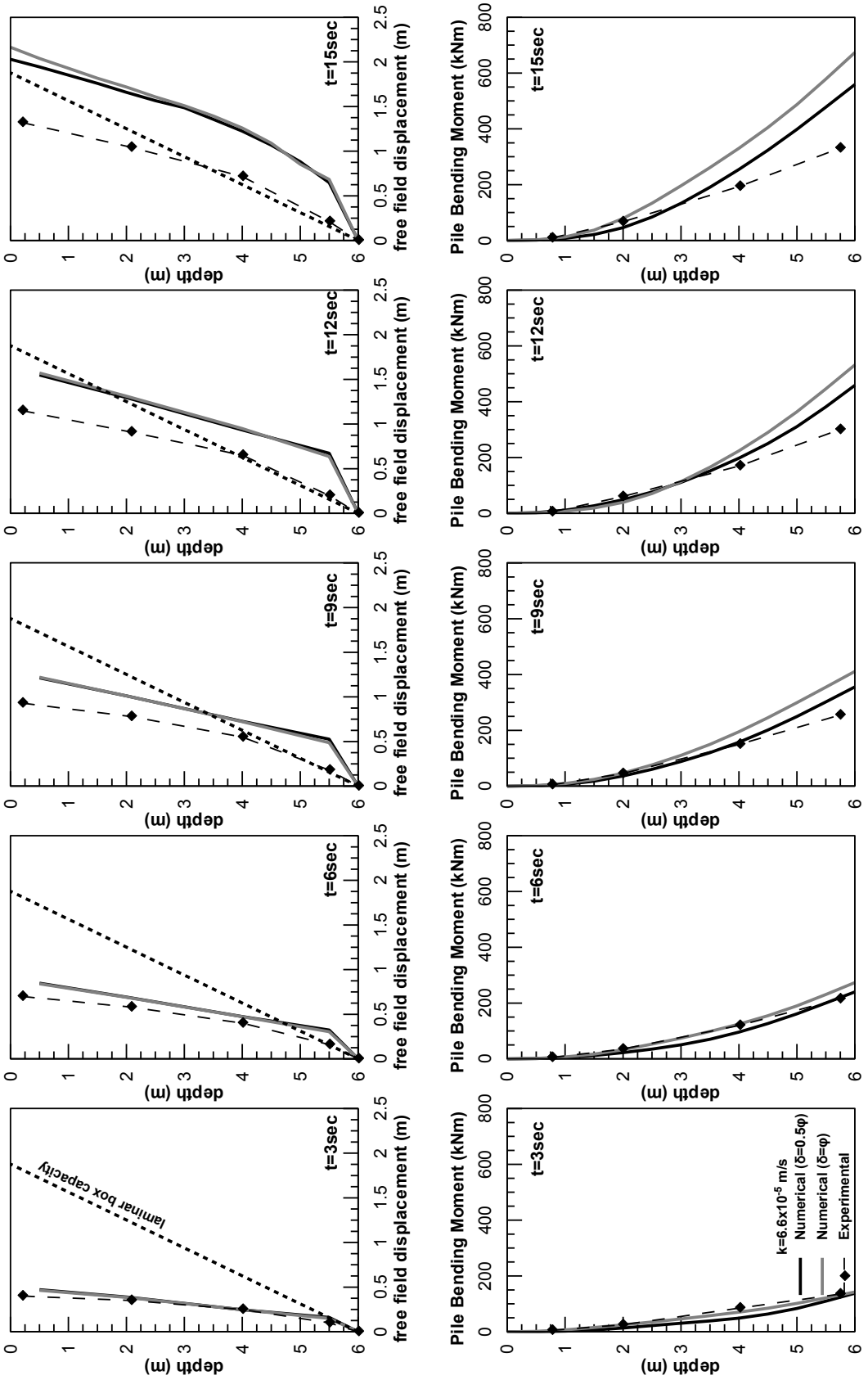

Figure 7.42: Experimental and Numerical pile bending moments at various instances during shaking for $k=6.6\times10^{-5}$ m/s and $\delta=0.5$ and $\delta=\varphi$.

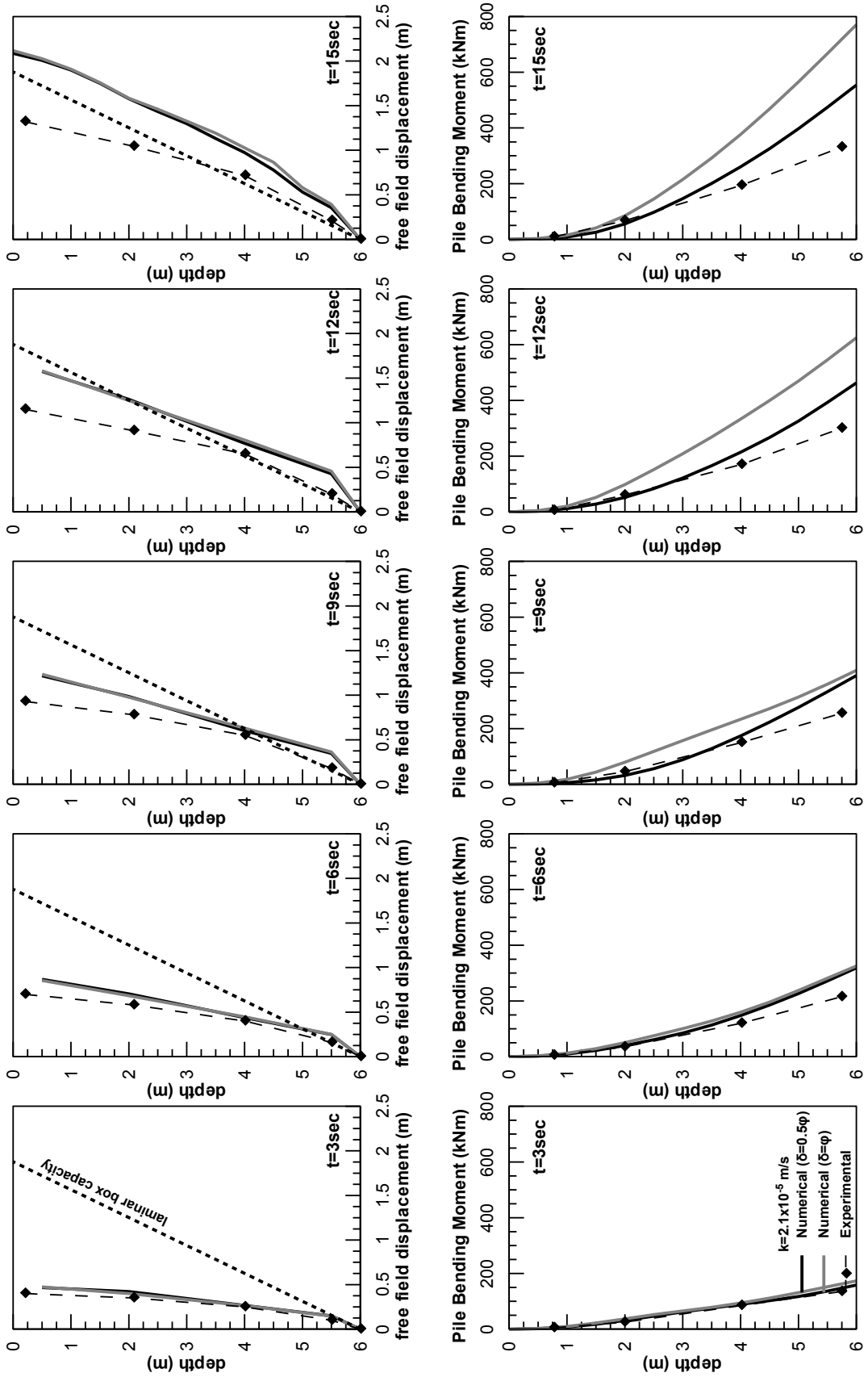

Figure 7.43: Experimental and Numerical pile bending moments at various instances during shaking for k=2.1x10^{-5} m/s and δ=0.5 and δ=φ.

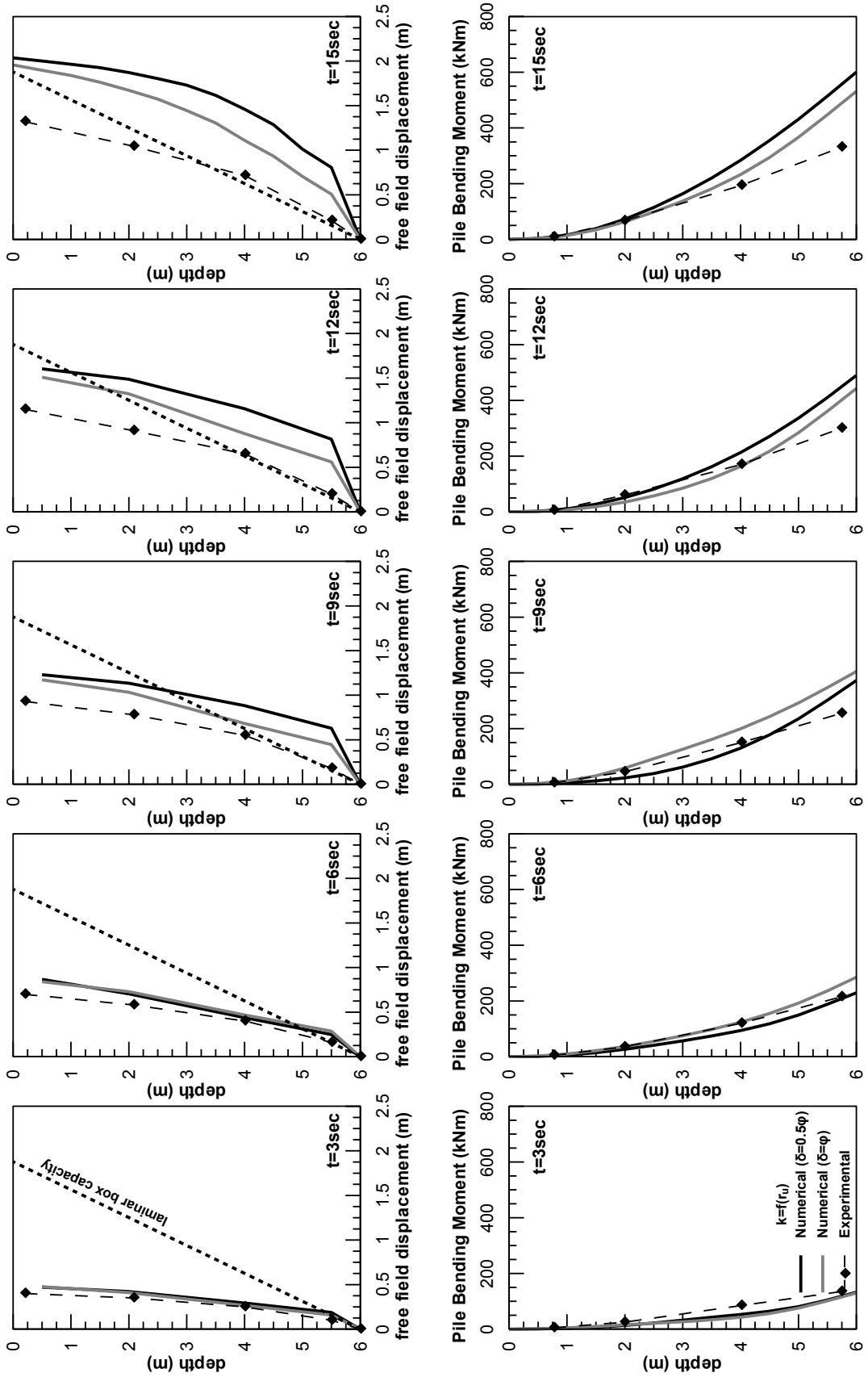

Figure 7.44: Experimental and Numerical pile bending moments at various instances during shaking for $k=f(r_u)$ and $\delta=0.5$ and $\delta=\varphi$.

7.4 Numerical Simulation of water saturated model (1x1-w)

The methodology described previously is used in the present section to simulate the second experiment in which water instead of metulose is used in pore fluids, resulting in a significantly larger permeability. For the simulation of this test, two (2) analyses are performed, one for δ=1/2φ and one for δ=φ. All other model parameters retain the same values as before, except from the permeability, which is set fifty (50) times larger than the static value, i.e.:

$$k = 50 \cdot k_{static} = 50 \cdot 6.6x10^{-5} m/\sec \Rightarrow k = 3.3x10^{-3} m/\sec \qquad (7.9)$$

At this point it should be noted that the purpose of these set of analyses is not to quantitatively capture the experimental results, like for the case of the metulose saturated model. This would require a larger number of parametric analyses in order to account for the various experimental uncertainties discussed in the previous section. In addition, since the numerical methodology is already verified quantitatively for one of the tests, repeating the same procedure would be unnecessarily time-consuming. Hence, emphasis is now placed on the numerical methodology's efficiency to capture the relative effect of the very large permeability compared to the small, as observed in the test. Therefore, the comparisons refer to the numerical predictions for the 1x1-w and 1x1-v tests and not to the relevant experimental results which have already been presented in section 7.2.

The following figures illustrate the comparison in terms of excess pore pressures, pile and free-field displacements, p-y curves and pile bending moments. Namely, **Figure 7.45** and **Figure 7.46** show excess pore pressure time histories at the free field and close to the pile respectively. Furthermore, **Figure 7.47** and **Figure 7.48** compare displacements at the free field and at the pile head respectively. The former are shown as a function of depth at the end of shaking and the latter as a function of time. Finally, in **Figure 7.49** and **Figure 7.50** compare p-y curves and end of shaking pile bending moments. In all cases, the comparisons are demonstrated separately for δ=1/2φ and δ=φ, while in all figures the black line corresponds to $k=6.6.10^{-5}$m/s (metulose saturated model), and the gray line to the $k=3.3x10^{-5}$ m/s (water saturated model).

Overall, it is observed that the numerical methodology captures qualitatively all basic differences observed in the high and low permeability experiments. Namely, the following common response patterns are observed in the test results and in the numerical predictions:

Excess pore pressures

- Along the free field the magnitude of dilation spikes, mostly observed at large depths, is significantly smaller in the water saturated model
- Near the pile, the overall dilation observed at small depths when metulose is used as pore fluid, is now suppressed as a result of faster water flow from the surrounding liquefied area.

Displacements

- At the free field (**Figure 7.47**) displacements are slightly larger for the case of the water saturated model. Near the ground surface, this increase was approximately equal to 20% in the test, and 40% in the numerical prediction.
- Pile head displacements (**Figure 7.48**) are smaller in the case of the water saturated model. The decrease is approximately 67% in the test, and 40% in the analysis. However, it should also be noted that the analysis does not capture the bouncing back of the pile after the maximum displacement value is reached.

P-y curves (**Figure 7.49**)

- Due to larger soil and smaller pile displacements, p-y curves extend to a much larger displacement range. The same trend is observed in the experimental results also.
- For large depths, the two (2) pore fluids yield very similar curves, with a residual value close to 10kN/m for the tests results, and 15-20kN/m for the numerical predictions.
- For small depths, soil pressures are much smaller for the case of the water saturated model as a result of the non-dilative response. Both in the test data and the numerical predictions, soil pressures near the surface become approximately equal to the ones at larger depths.
- Finally, the cyclic component of the p-y curves is drastically reduced in the case of the water saturated model.

Pile bending moments (**Figure 7.50**)

- Pile bending moments are reduced in the case of water saturation, as a result of the associated smaller soil pressures which develop near the surface. Both in the test and in the analyses, maximum pile bending moments are reduced by approximately 200kNm.

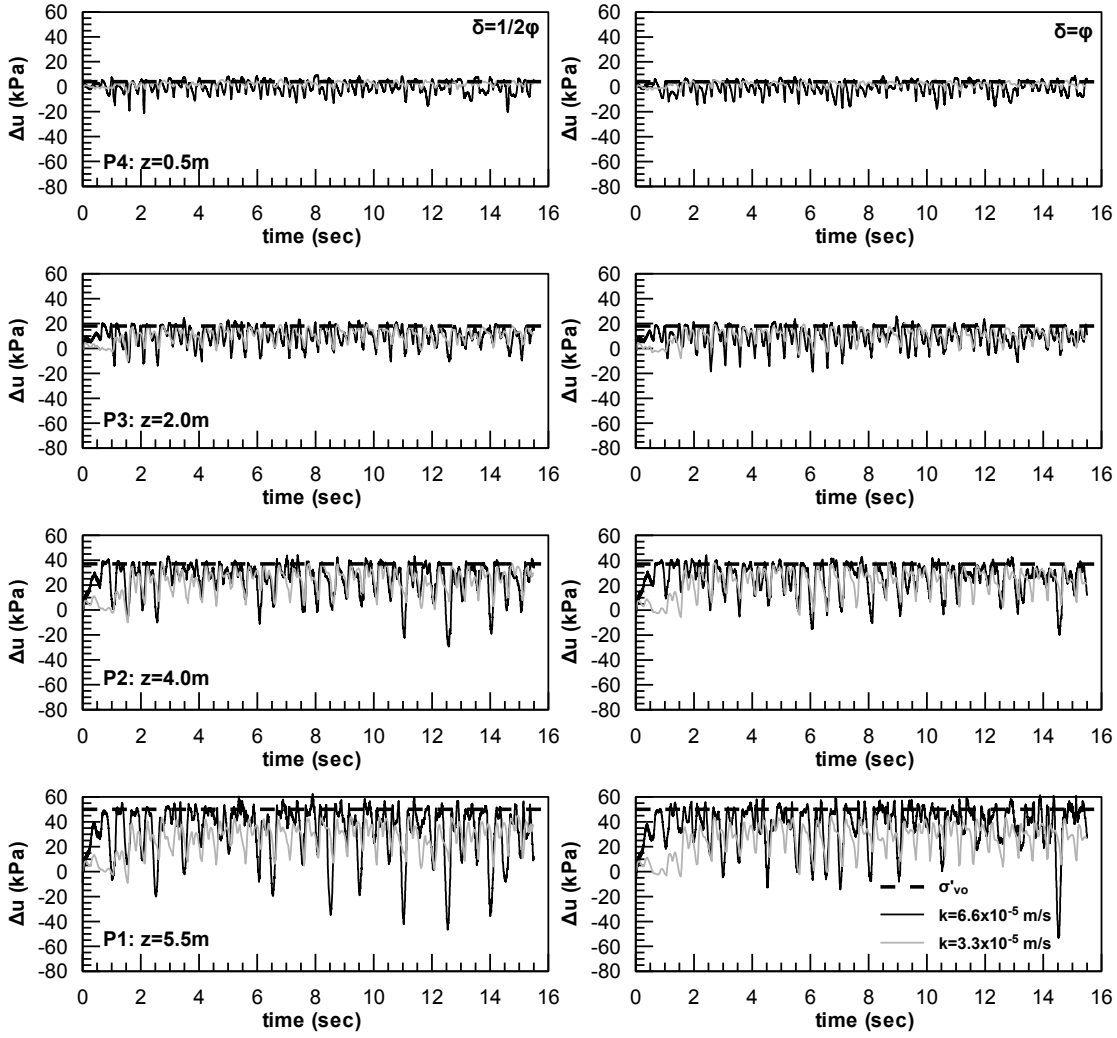

Figure 7.45: Comparison of excess pore pressures at the free field between the $k=6.6x10^{-5}$ m/s and the $k=3.3x10^{-3}$ m/s model

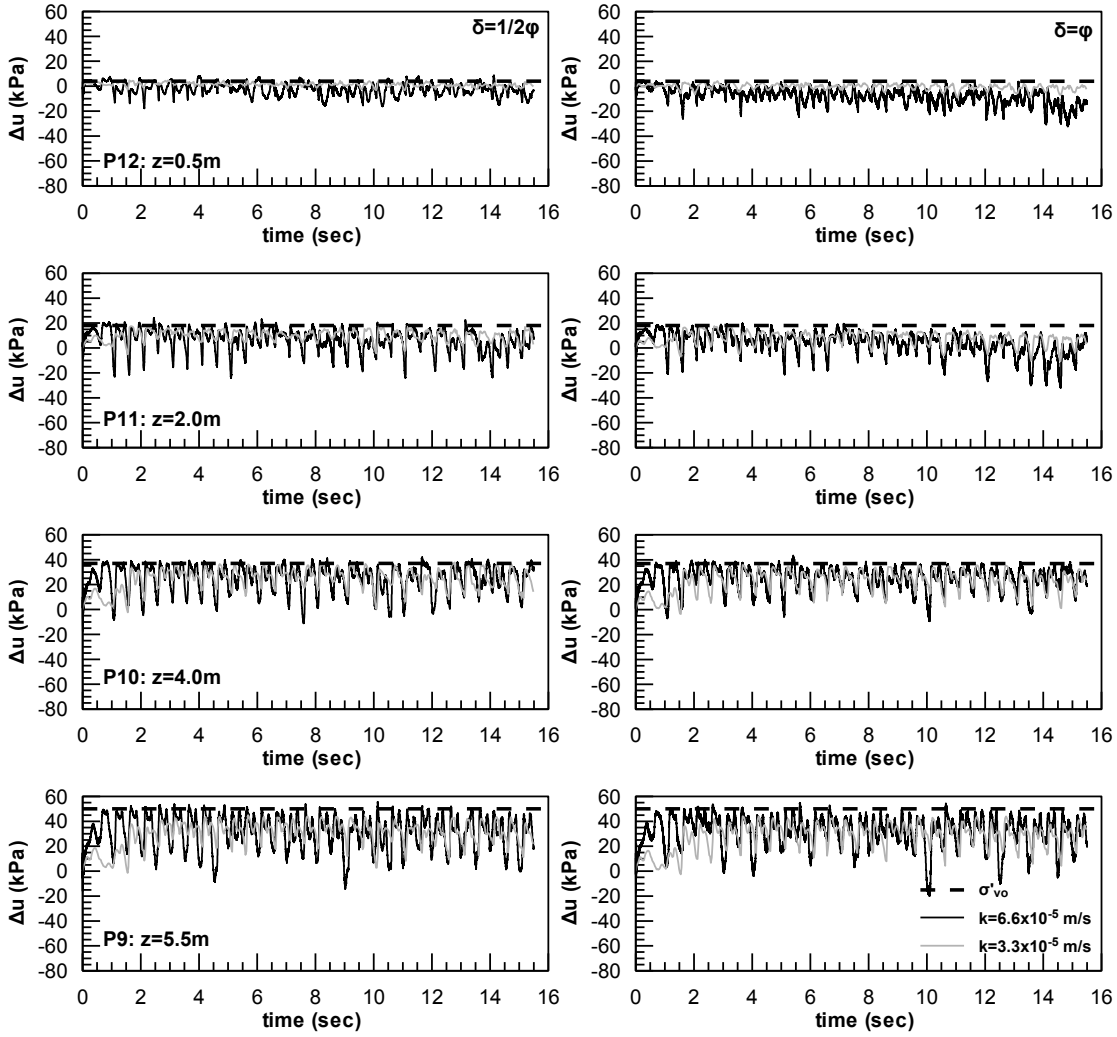

Figure 7.46: Comparison of excess pore pressures near the pile between the k= 6.6×10^{-5} m/s and the k=3.3×10^{-3} m/s model

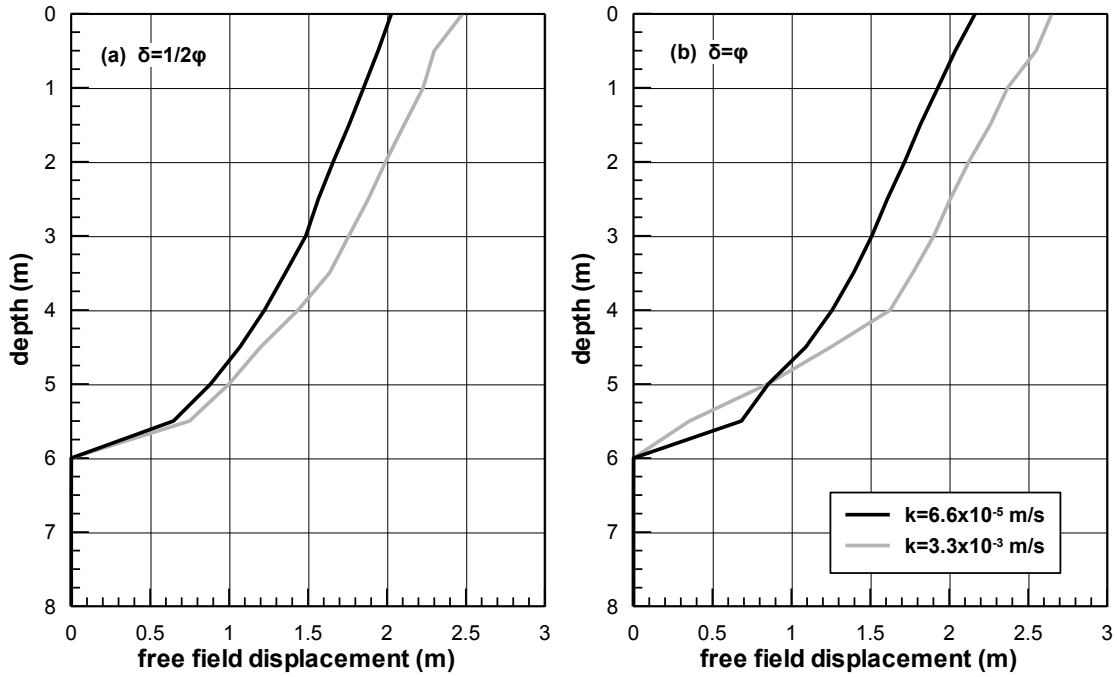

Figure 7.47: Variation of free field soil displacements with depths for (a) δ=1/2φ and (b) δ=φ

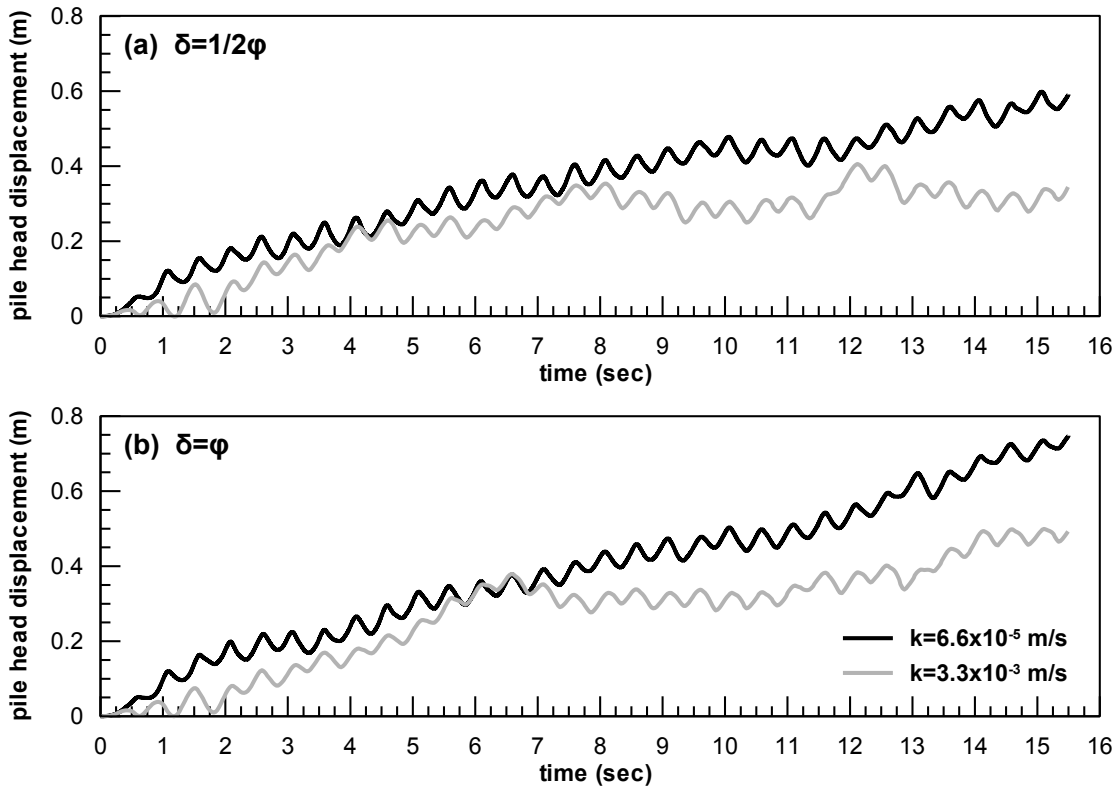

Figure 7.48: Development of pile head displacement with time for (a) δ=1/2φ and (b) δ=φ

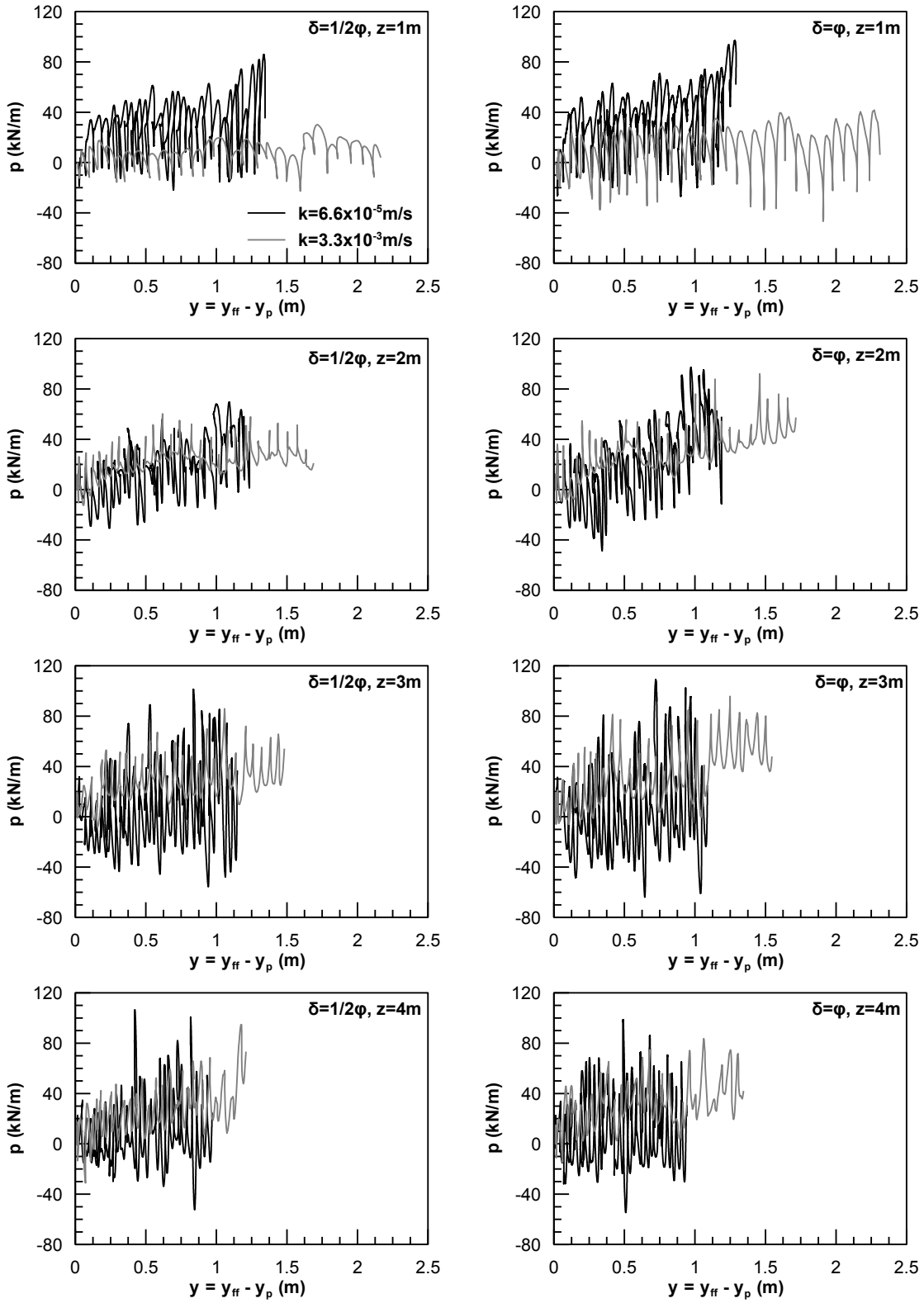

Figure 7.49: Comparison of p-y curves between k=6.6x10^{-5} m/s and k=3.3x10^{-3} m/s

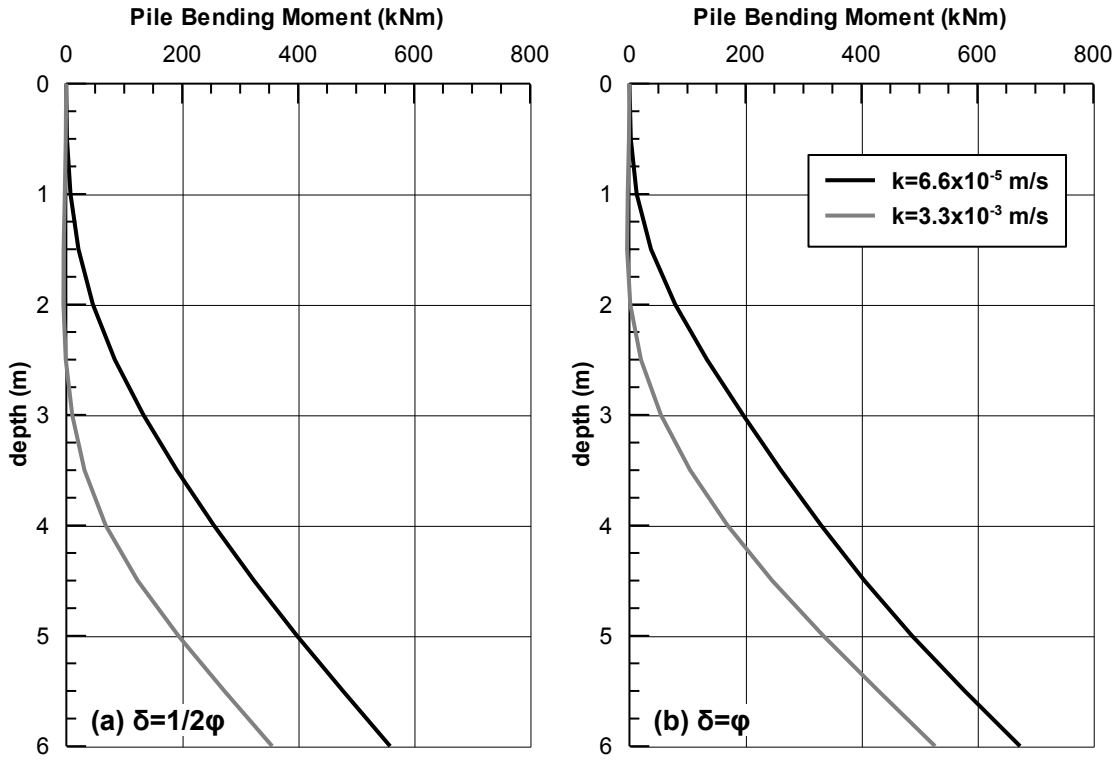

Figure 7.50: Comparison between pile bending moments for $k=6.6x10^{-5}$ m/s and $k=3.3x10^{-3}$ m/s for (a) $\delta=1/2\varphi$ and (b) $\delta=\varphi$.

7.5 Free Field vs. Laminar Box Simulation

In the previous chapter, it was demonstrated that laminar boxes do not reflect the kinematic constraints that are imposed in actual infinite slopes. Furthermore, a modified formulation of tied-node boundary conditions was introduced capable of reproducing the actual field conditions, as compared to the typical tied-node formulation, also discussed in the previous chapter, which corresponds to the conditions of the laminar box. The present section attempts to investigate the effects of the aforementioned different boundary conditions on the overall response of pile-soil systems, and thus evaluate the efficiency of laminar boxes as a means to simulate such problems.

So far, all the analyses were performed with the typical tied-node formulation, since their purpose was to simulate an experiment carried out in a laminar box. In order to explore the effects of boundary conditions and compare the response between the field and the laminar box, two (2) additional analyses were performed by using the modified tied-node boundaries. Apart from the different boundary conditions, the

configuration of these analyses was the same as described in section 7.3.1, with the permeability being set to $k=6.6 \times 10^{-5}$ m/s, and the interface friction $\delta=0.5\varphi$ and $\delta=\varphi$.

Excess Pore Pressure build-up

The effects of boundaries on excess pore pressure build up are examined in **Figure 7.51** through **Figure 7.53**, for three distinct locations: free field (i.e. P1, P2, P3 and P4 in **Figure 7.1**), near field (i.e. P5, P6, P7 and P8 in **Figure 7.1**) and next to the pile (i.e. P9, P10, P11 and P12 in **Figure 7.1**). In all three (3) figures, the black line corresponds to the laminar box analysis and the gray to the field analysis. **Figure 7.51** shows that pore pressure build up in the free field is practically not affected by the boundary conditions, as excess pore pressures become equal to the initial vertical effective stress early in the shaking.

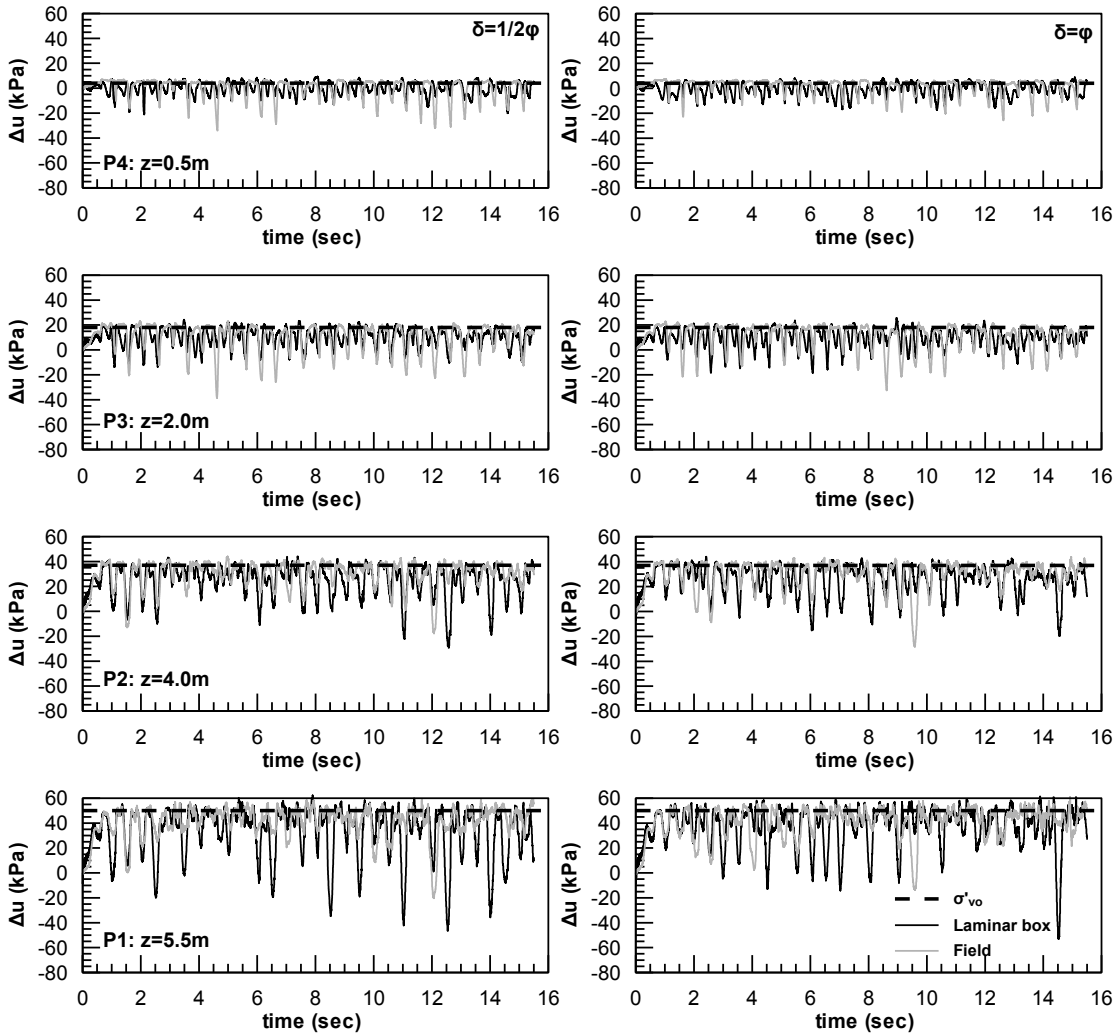

Figure 7.51: Excess pore pressures at the free field in the laminar box and under field conditions

However, the response changes drastically in the areas close and next to the pile. Both **Figure 7.52** and **Figure 7.53** indicate that the field analysis exhibits much more intense dilation compared to the laminar box. For large depths (z>4m), the more dilative response is suggested by the significantly larger (almost double) magnitude of dilation spikes. For elevations near the ground surface (z<2m), the negative excess pore pressures observed in the laminar box, are much more pronounced in the field. Namely, while in the laminar box negative excess pore pressures reached a value of approximately -10kPa at the end of shaking, in the field analysis they range from -20 to -60kPa depending on the depth and the assumption for the interface friction. In addition, in the field analysis, the area of dilative response is much more extended compared to the laminar box. Namely, in the latter negative pore pressures are observed only at the depth of z=0.5m, where in the field negative pore pressures are observed for z=0.5m and z=2m. Finally, in the field analysis, the depth of maximum dilation is not near the surface, as in the laminar box, but slightly deeper, at approximately z=2m. Given that pore pressure build-up near the pile is one of the most crucial factors with regard to the characteristics of the p-y curves, the differences observed herein are expected to cause further differences in the overall pile-soil interaction response.

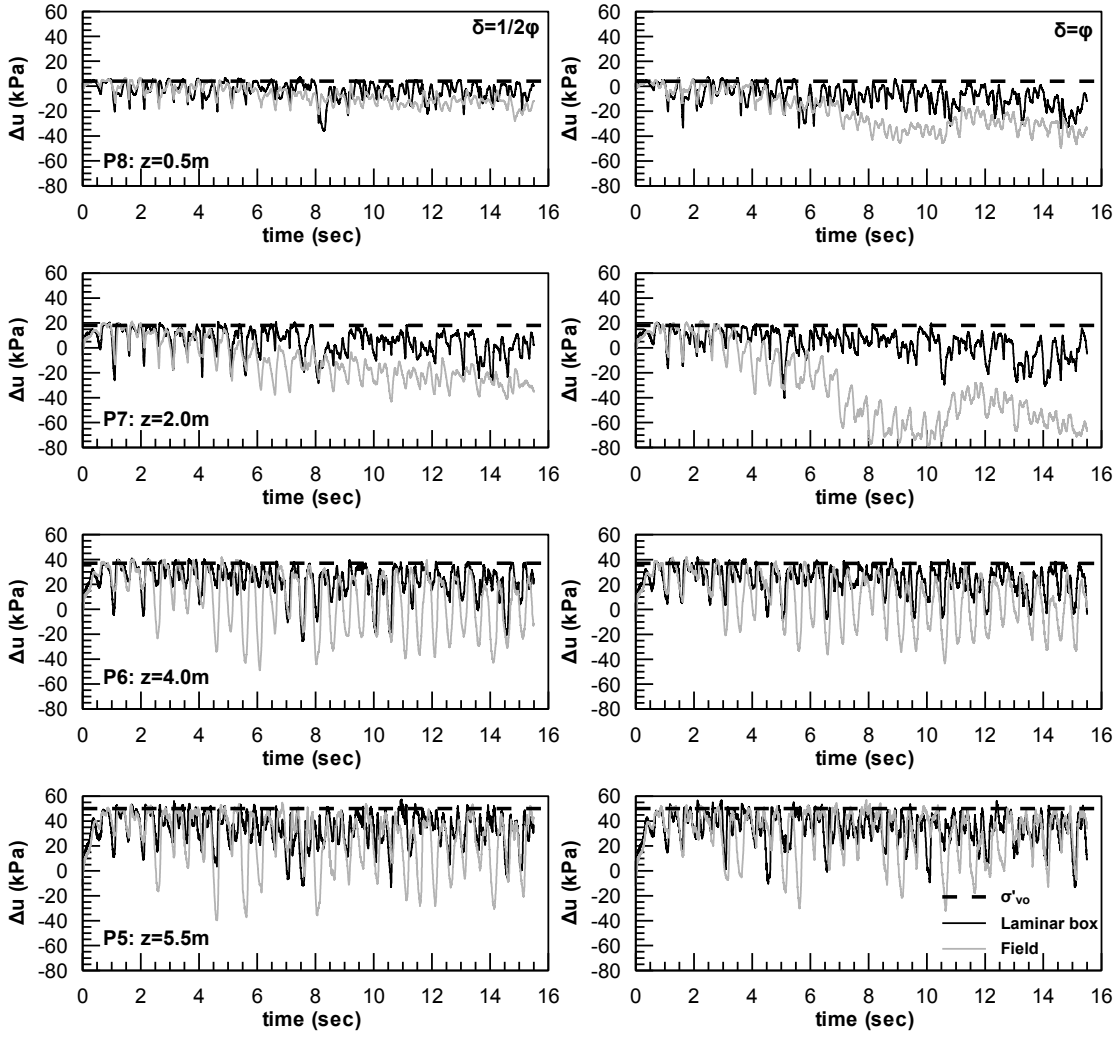

Figure 7.52: Excess pore pressures near the pile in the laminar and under field conditions

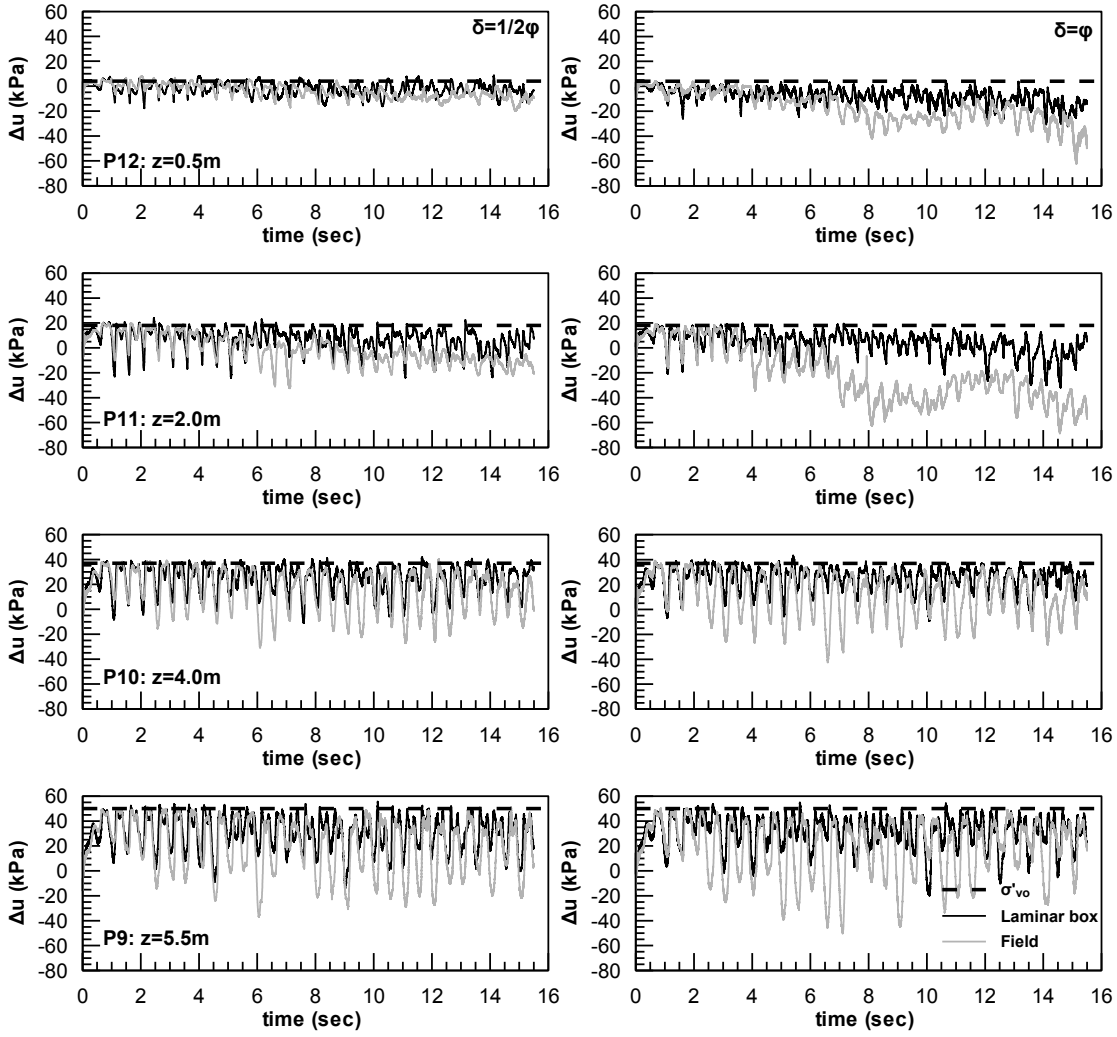

Figure 7.53: Excess pore pressures next to the pile in the laminar box and under field conditions

Free field Soil Displacements

Boundary effects on the accumulation of soil displacements at the free field are explored in **Figure 7.54** and **Figure 7.55**. More specifically, the first figure shows contours of horizontal displacement, as well as the deformed shape of the model, at the end of shaking, while the second figure shows displacements profiles with depth at the right boundary of the model. The following can be observed:

- In the laminar box, significant vertical displacements are developed, resulting in a deformed shape which does not reflect the deformation in the field. These vertical displacements are the consequence of the permanent downward velocity component, a parasitic (side) effect has been thoroughly described in the previous chapter.

- In the field analysis, displacement contours near the boundaries become practically horizontal, suggesting a uniform variation of displacements with depth in that area. On the other hand, the shape of contours in the laminar box is rather irregular, leading to the conclusion that free-field soil response is not captured correctly.
- The previous observation is also verified when examining the displacement profiles with depth, shown in **Figure 7.55**. The field analysis suggests a nearly sinusoidal distribution, reported in literature. On the other hand the distribution in the laminar box is practically bi-linear.
- Finally, as far as quantitative prediction of free field displacements is concerned, the laminar box analysis yields larger displacements, with the maximum differences observed near the surface and the bottom of the liquefied layer. Namely, ground surface displacements in the laminar box are overpredicted by approximately 15-20%.

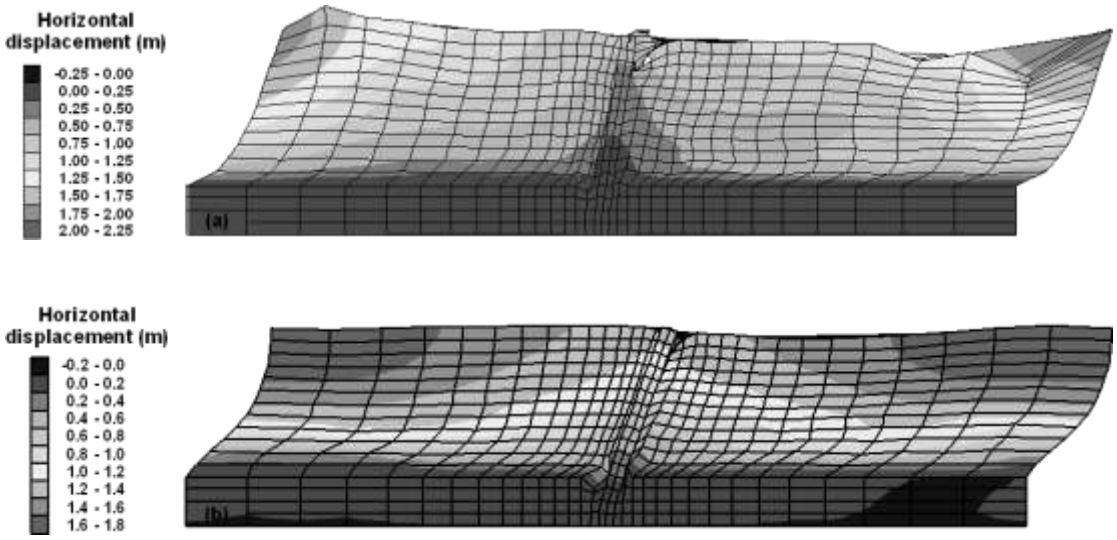

Figure 7.54: Contours of horizontal displacement and deformed shape of the model at the end of shaking (a) laminar box (b) field conditions.

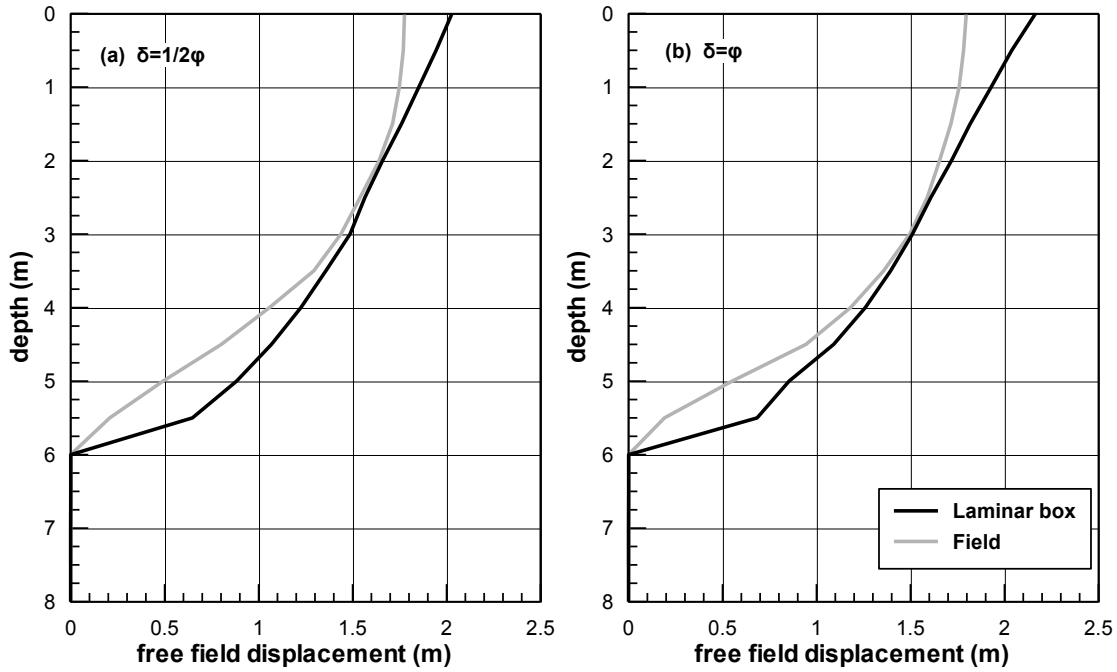

Figure 7.55: Free field displacements at the end of shaking in the laminar box and under field conditions for (a) δ=1/2φ and (b) δ=φ

Pile Displacements

The two (2) simulations yield large differences in predicted displacements. This is shown in **Figure 7.56** which compares predicted accumulation of pile head displacement with time, for the field and laminar box analyses. Displacements for field conditions are 120% and 104% larger for δ=1/2φ and δ=φ respectively. This difference can be due to various reasons. For example soil displacement around the head of the pile in the field analysis are larger compared to the laminar box (as shown in **Figure 7.54**), hence the pile, as being pulled and pushed by the soil, develops larger displacements. Also, as discussed earlier, dilation is more extensive in the field, thus the more stiff soil does not flow around the pile but enforces it to follow the ground movement.

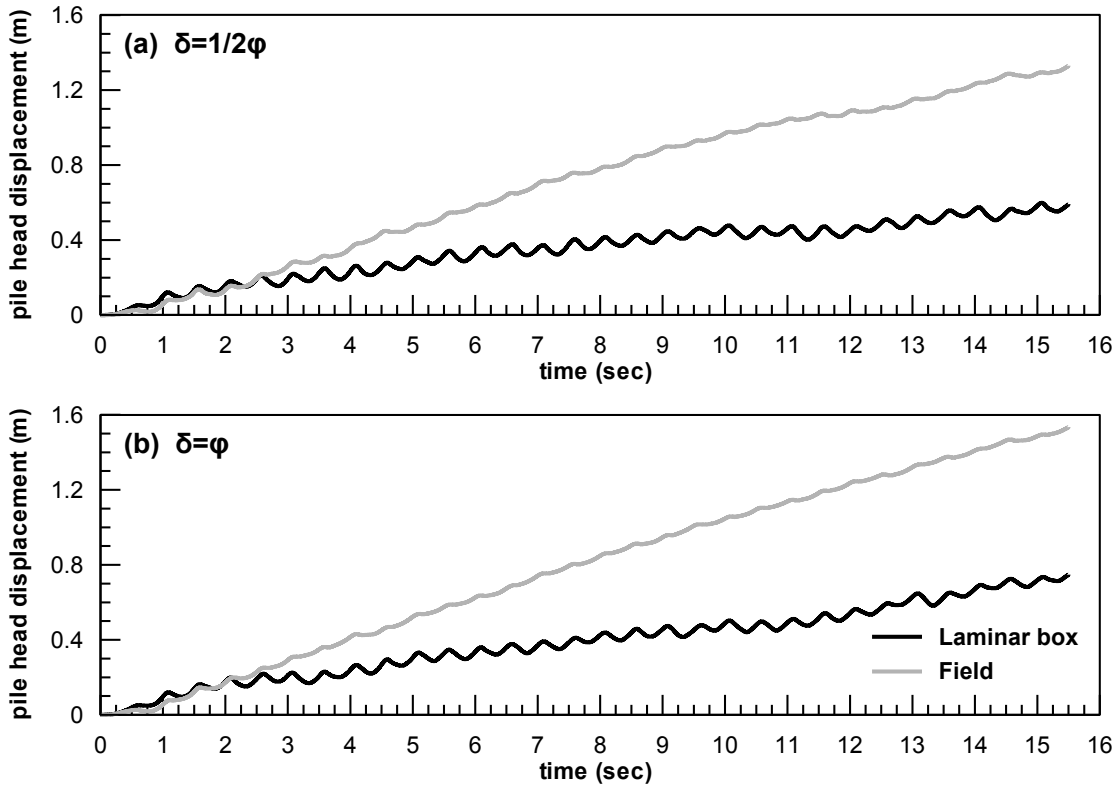

Figure 7.56: Time histories of pile head displacement in the laminar box and under field conditions for (a) δ=1/2φ and (b) δ=φ

P-y Response

Figure 7.57 shows the comparison of p-y curves for four (4) different depths along the pile and δ=1/2φ and δ=φ. Comparisons can be summarized to the following:

- In all cases, p-y curves from the laminar box reach much larger displacement levels, mainly due to the much smaller pile displacements.
- Near the ground surface, i.e. for z=1m, where pore pressure build up is similar, the resulting p-y curves for field and laminar box conditions are similar.
- However, for z=2 and 3m, where liquefaction occurs in the laminar box, and dilation in the field, the curves from the first case are much lower compared to the curves from the second. Namely, the average residual value under field condition is approximately 100-150kN/m for δ=1/2φ, and 150-200kN/m for δ=φ. For comparison, the corresponding values in the laminar box are approximately 25-50kN/m.

- Finally, for z=4m, where liquefaction is observed in both cases, p-y curves yield similar residual values for the soil reaction. However, the cyclic component under field conditions is much larger, a response that can be attributed to the larger magnitude of dilation spikes at the specific depth.

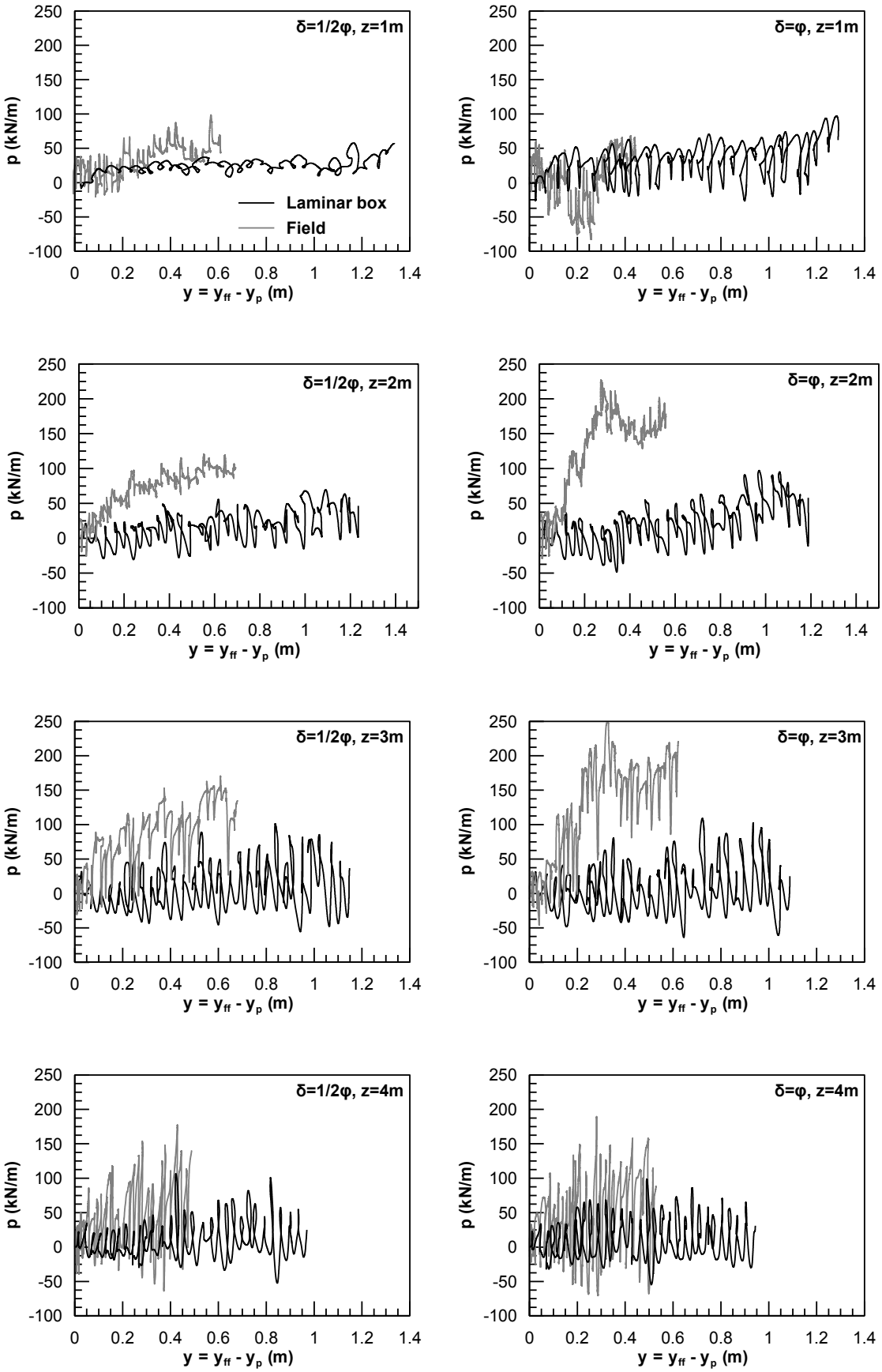

Figure 7.57: P-y curves in the laminar box and under field conditions

Bending Moments

The previous differences in excess pore pressure build-up and p-y response are also reflected on the bending moments of the pile. The relevant comparison is shown in **Figure 7.58**, for δ=1/2φ and δ=φ. Near the surface, where soil pressures are similar, the two (2) curves are in good agreement. However, due to the fact that for medium depths soil pressures at the field are much larger than in the laminar box, the pile under field conditions sustains significantly larger moments. The comparison shows that the maximum bending moment in the field is approximately double of that in the laminar box.

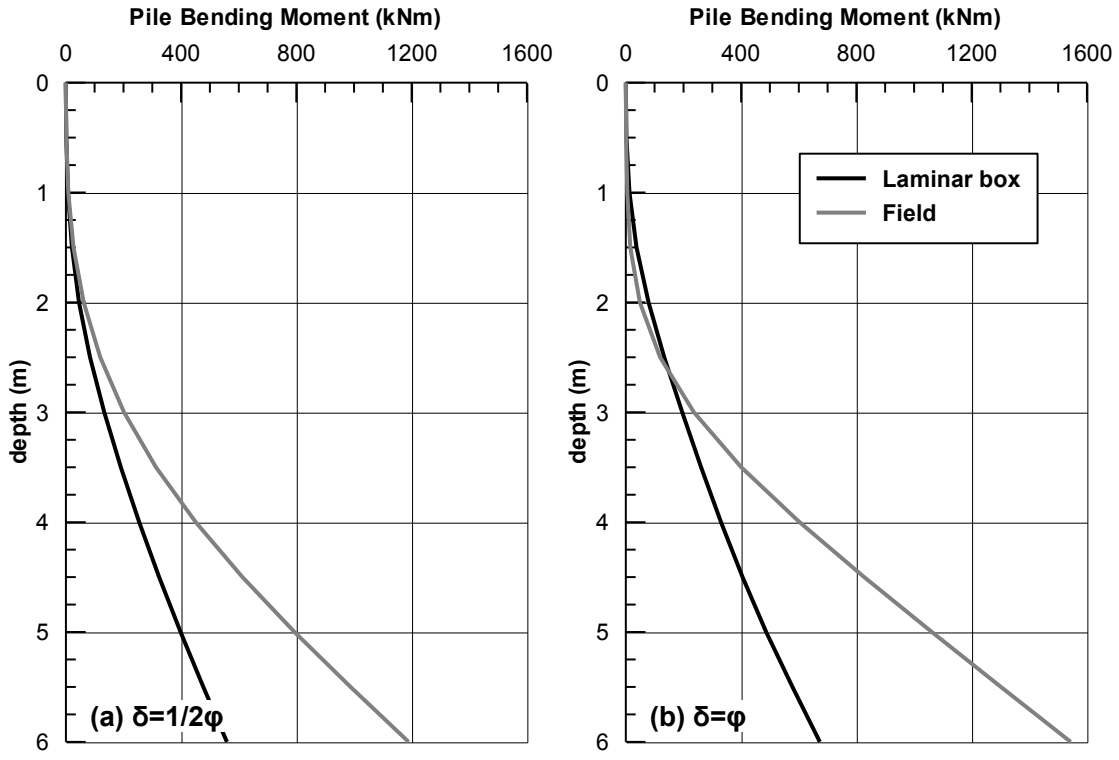

Figure 7.58: Pile bending moments in the laminar box and under field conditions for (a) δ=1/2φ and (b) δ=φ.

7.6 Concluding Remarks

In the present chapter, the numerical methodology for the evaluation of pile response in liquefiable soils was used to simulate two (2) centrifuge experiments. Apart from verification of the methodology, investigation also focused on calibrating the model in terms of soil permeability, and evaluate the potential effects on the pile-

soil response of the interface friction and the side boundaries of the model. The following concluding remarks refer to each of these issues separately.

Methodology Verification

Numerical predictions were in remarkably good overall agreement with experimental measurements for both centrifuge tests. Note that all predictions were based exclusively on the reported soil, pile and excitation parameters, with only one exception: the stiffness of the cemented bedrock which was not reported and had to be back-calculated from the reported rotational stiffness of the pile at the sand-bedrock interface.

Objective limitations were faced when simulating the free field ground displacements, due to the limited angular distortion capacity of the laminar box that was used in the tests. Nevertheless, this deficiency of the tests had a relatively minor effect on the response of the pile and the soil surrounding it and did not blur the intended evaluation of the numerical methodology.

Soil Permeability and Interface Friction

The potential effects of these two (2) analysis parameters were examined together, for two (2) main reasons:

- Both were not known with certainty, as they had not been directly measured in the tests.
- The associated effects on the pile response are coupled since the skin friction of the pile depends not only on the interface friction angle (δ), but also on the excess pore pressures developing at the interface, and, in extent, on the correct value of soil permeability.

To quantify the overall performance of the numerical predictions with respect to these two (2) parameters, **Error! Reference source not found.** through **Table 7.5** provide a personal evaluation of the respective parametric analyses depending on their accuracy for predicting the experimental measurements. The first two (2) tables evaluate the performance in terms of soil and pile response respectively, while **Table 7.5** summarizes the performance from the previous Tables and concludes on the

overall performance of each analyses. The applied rating of each analysis is made in proportion to the most successful one for the specific measurement.

Table 7.3: Summary of performance of numerical predictions in terms of soil response

α/α	k (x10^{-5} m/s)	δ/φ	Accel.	Excess Pore Pressures			Free field disp.	Soil Response
				FF*	NF**	Pile		
1	6.6	1/2	9***	10	8.5	8.5	10	**9.2**
7	6.6	1	9	10	8.5	8.5	10	**9.2**
8	2.1	1/2	9	8.5	7.5	7.5	8	**8.1**
9	2.1	1	9	8.5	7.5	7.5	8	**8.1**
10	f(r_u)	1/2	10	10	10	10	10	**10**
11	f(r_u)	1	10	8.5	9.5	10	9	**9.4**

*FF: Free field
**NF: Near Field
***Rating is performed in a scale from 1 to 10

Table 7.4: Summary of performance of numerical predictions in terms of pile response

α/α	k (x10^{-5} m/s)	δ/φ	Pile disp.	P-y	Bending Moments	Pile Response
1	6.6	1/2	7.5*	7.5	9.5	**8.2**
7	6.6	1	9.5	7.5	10	**9**
8	2.1	1/2	8	7.5	8.5	**8**
9	2.1	1	10	9	8.5	**9.2**
10	f(r_u)	1/2	8.5	9	9.5	**9**
11	f(r_u)	1	7.5	10	10	**9.2**

*Rating is performed in a scale from 1 to 10

Table 7.5: Overall evaluation of performance of numerical predictions

α/α	k (x10^{-5} m/s)	δ/φ	Soil Response	Pile Response	Overall Response
1	6.6	1/2	9.2	8.2	**8.7**
7	6.6	1	9.2	9	**9.1**
8	2.1	1/2	8.1	8	**8.05**
9	2.1	1	8.1	9.2	**8.6**
10	f(r_u)	1/2	10	9	**9.5**
11	f(r_u)	1	9.4	9.2	**9.3**

The first thing to observe in these Tables is that the assumption regarding soil permeability and interface friction have a distinguishable but not crucial effect on the response. For instance, the individual ratings range between 7.5/10 and 10/10, while the overall ratings range between 8/10 and 9.3/10.

Secondly, the specific experiments were better fitted assuming that $\delta=\varphi$, a conclusion which is consistent with the description of pile preparation with sand grains glued on its outer face. It is worth noting that this value of interface friction angle was chosen on the basis only of pile response predictions (pile displacements, p-y curves and bending moments), as it had practically no effect on the predicted soil response (accelerations and excess pore pressures). In any case, δ is a function of the pile material and consequently the parametric investigation at the liquefied pile response should be performed for both $\delta=1/2\varphi$ (steel piles) and $\delta=\varphi$ (concrete piles).

Finally, it should be acknowledged that the assumption of variable soil permeability coefficient had a systematic head over the assumption of constant permeability coefficient in nearly all aspects of soil and pile response. Second, at close distance, comes the assumption of constant permeability coefficient $k=6.6x10^{-5}$ m/s, while the assumption of constant dynamic permeability, $k=2.1x10^{-5}$ m/s, gave the least favorable agreement with the experiments.

Field vs. Laminar box boundaries

The present analyses verified concerns that centrifuge experiments with an inclined laminar box may not simulate accurately lateral spreading in the field. They have also shown that the laminar box simulation is not conservative and provided gross estimates of the anticipated differences in predicted soil and pile response. Namely:

- Extent of dilation near the pile is underestimated in the laminar box
- Free field displacements are slightly overestimated in the laminar box, while their variation with depth deviates from the sinusoidal shape.
- Soil pressures can be up to three (3) times larger in the field
- Pile head displacements are more than 100% larger under field conditions
- Maximum pile bending moments are approximately double under field conditions

The above findings are disturbing as they imply that the design guidelines for piles in laterally spreading ground may underestimate the soil pressures applied on the pile by the liquefied ground and consequently the resulting pile head displacements and maximum bending moments.

8

Parametric Investigation of the p-y Pile Response in Laterally Spreading Soils

8.1 General

The numerical methodology described and evaluated in the previous chapter, is used herein to investigate, through a series of parametric analyses, the p-y response of laterally spreading soils. Based on recent experimental findings (Gonzalez et al, 2009), which were readily verified by the numerical analyses in the previous chapter, the selection of the soil and pile parameters that were investigated was guided by the fact that ultimate soil resistance is unequivocally related to the excess pore pressure ratio developed in the soil surrounding the pile. Hence, eighteen (18) analyses were performed, which investigated the effects of the following groups of soil and pile properties:

- In-situ soil conditions (Relative Density, Confining Stress, Installation Effects)
- Drainage (Soil Permeability, Excitation Period)
- Imposed shear straining (Pile displacement, and thus Bending Stiffness, Diameter, Head Constraint, Installation)

The results of the numerical analyses were first used to validate the corner-stone assumption of Gonzalez et al. (2009), through a direct correlation of the normalized ultimate pile resistance $p_{ult,liq}/(\sigma'_{vo}D)$ against the excess pore pressure ratio $r_u=\Delta u/\sigma'_{vo}$. In the sequel, analytical relationships are developed for the estimation of the p-y response of liquefied soils, in terms of readily available pile and soil properties. Finally, the proposed relationships are evaluated against existing empirical methodologies developed mostly upon the experimental results of centrifuge and large shaking table tests. Emphasis is given to the prediction of the

detrimental effects of excessive negative pore pressures that may develop in the upper part of the pile, thus increasing lateral pile loads and associated bending moments and deflections.

8.2 Outline of parametric analyses

The pile and soil discretization (mesh) that was used for the analyses is shown in **Figure 8.1**. It is 46m long, 10m wide and 8m high. Also plotted in the figure are the values of the soil-pile-excitation characteristics that were adopted for the basic analysis. Namely, the pile is 8m long, it has a diameter D=0.6m and a bending stiffness EI=1300000kNm^2. No displacement constraints are applied at the head of the pile. The surrounding soil consists of a 8m thick Nevada Sand layer of Relative Density D_r=50% and permeability k=6.1e-5 m/s. The value of the permeability was selected based on the results of the investigation performed in the previous chapter with regard to the centrifuge experiment. At the base of the model a harmonic excitation of amplitude a_{max}=0.20g, period T=0.30sec and N=14 cycles is applied.

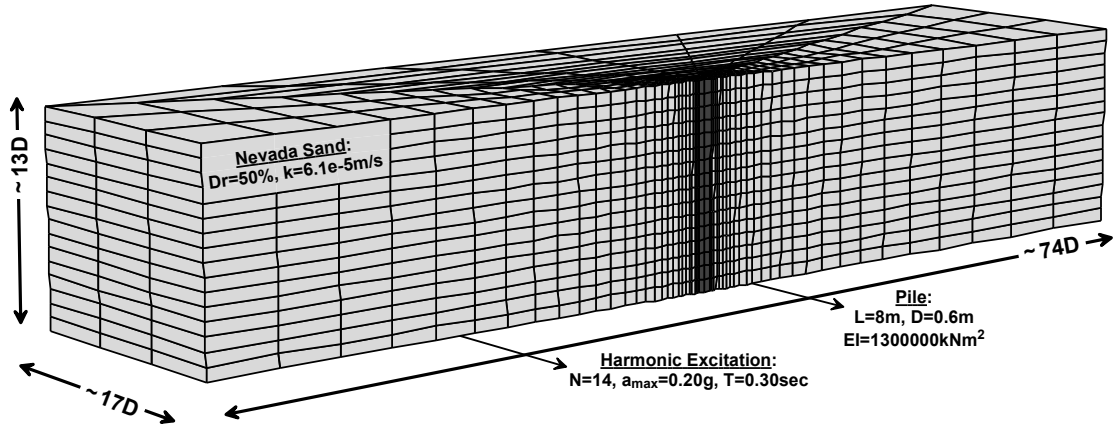

Figure 8.1: Mesh built for the parametric analyses and values of basic input parameters

As mentioned earlier, a total of eighteen (24) analyses were performed for the following values of soil, pile and excitation properties:

Soil Properties

- Relative Density: D_r=25, 35, 50, 60, 70%
- Permeability: k=1.8e-5, 6.1e-5, 1.8e-4, 6.1e-4, 1.8e-3 m/sec

Pile Properties

- Diameter: D=0.4, 0.6, 1.0m
- Bending Stiffness: EI=1.3, 2.5, 3.25, 6.0, 9.1, 13.0, 20.0, 97.5 ($x10^5$ kNm^2)
- Pile Type: Drilled and Driven
- Head Constraint: Free head, Fixed head, No Head Rotation

Excitation Properties

- Period: T=0.20, 0.30, 0.40, 0.50 sec

Note that the range of values for soil permeability considered above is typical for very fine to coarse sands (e.g. Craig, 1997). The analysis with a driven pile was performed using the numerical techniques described in previous chapters for computing initial soils stresses, by assuming that the pile tip is perfectly plugged during driving (i.e. close-ended pile). Also, the analyses exploring the effects of diameter were performed by scaling proportionally all mesh dimensions in **Figure 8.1**. The basic input parameters for each analysis are summarized in **Table 8.1**.

Table 8.1: Outline of parametric analyses – basic input parameters

α/α	Soil Properties		Pile Properties				Excitation Properties
	k (m/sec)	Dr (%)	D (m)	EI (kNm^2)	Head Constraint	Pile Type	T (sec)
1	6.1e-5	50	0.60	1300000	free	drilled	0.30
2	6.1e-5	25	0.60	1300000	free	drilled	0.30
3	6.1e-5	35	0.60	1300000	free	drilled	0.30
4	6.1e-5	60	0.60	1300000	free	drilled	0.30
5	6.1e-5	70	0.60	1300000	free	drilled	0.30
6	1.8e-5	50	0.60	1300000	free	drilled	0.30
7	1.8e-4	50	0.60	1300000	free	drilled	0.30
8	6.1e-4	50	0.60	1300000	free	drilled	0.30
9	1.8e-3	50	0.60	1300000	free	drilled	0.30
10	6.1e-5	50	0.40	1300000	free	drilled	0.30
11	6.1e-5	50	1.0	1300000	free	drilled	0.30
12	6.1e-5	50	0.60	130000	free	drilled	0.30
13	6.1e-5	50	0.60	250000	free	drilled	0.30
14	6.1e-5	50	0.60	325000	free	drilled	0.30
15	6.1e-5	50	1.0	630000	free	drilled	0.30
16	6.1e-5	50	1.0	910000	free	drilled	0.30
17	6.1e-5	50	1.0	2000000	free	drilled	0.30
18	6.1e-5	50	1.0	9750000	free	drilled	0.30
19	6.1e-5	50	1.0	1300000	free	driven	0.30
20	6.1e-5	50	1.0	1300000	fixed	driven	0.30
21	6.1e-5	50	1.0	1300000	no rotation	driven	0.30
22	6.1e-5	50	1.0	1300000	free	driven	0.20
23	6.1e-5	50	1.0	1300000	free	driven	0.40
24	6.1e-5	50	1.0	1300000	free	driven	0.50

Although not relevant to the accuracy of the study, it is worth to note that the average time required to perform each of the analyses was approximately twenty (20) hours using a quad-core i7 processor with frequency 3.20GHz and 6.0GB of RAM.

8.3 Mesh size verification

In order to ensure that boundary effects are effectively eliminated, a series of analyses was performed prior to the parametric investigation, involving meshes of different size. Namely, three (3) different meshes were analyzed, of total length L=22, 44 and 66m each. The comparison is shown in **Figure 8.2**, in terms of p-y curves for various depths below ground surface. It can be observed that the curves calculated with the narrow mesh (L=22m) significantly underestimate soil resistance, especially near the ground surface. As for the other two (2) cases, results appear to be in good agreement, indicating that the 44m long mesh suffices for our analyses.

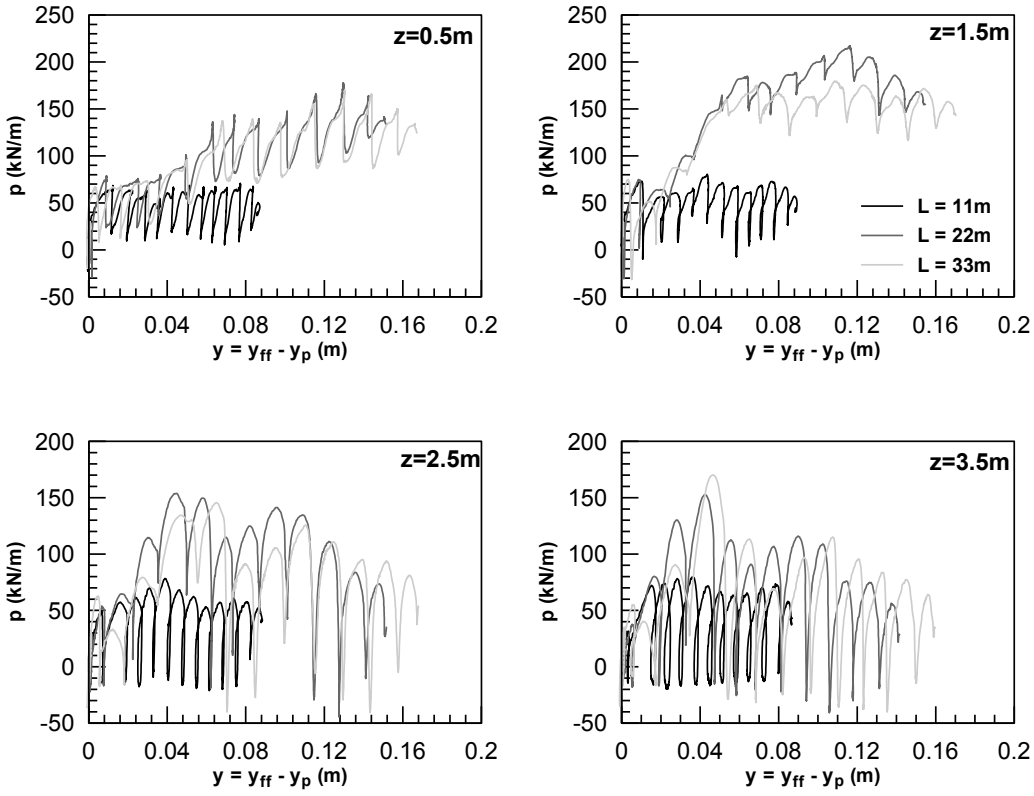

Figure 8.2a: P-y curves along the pile for different mesh dimensions

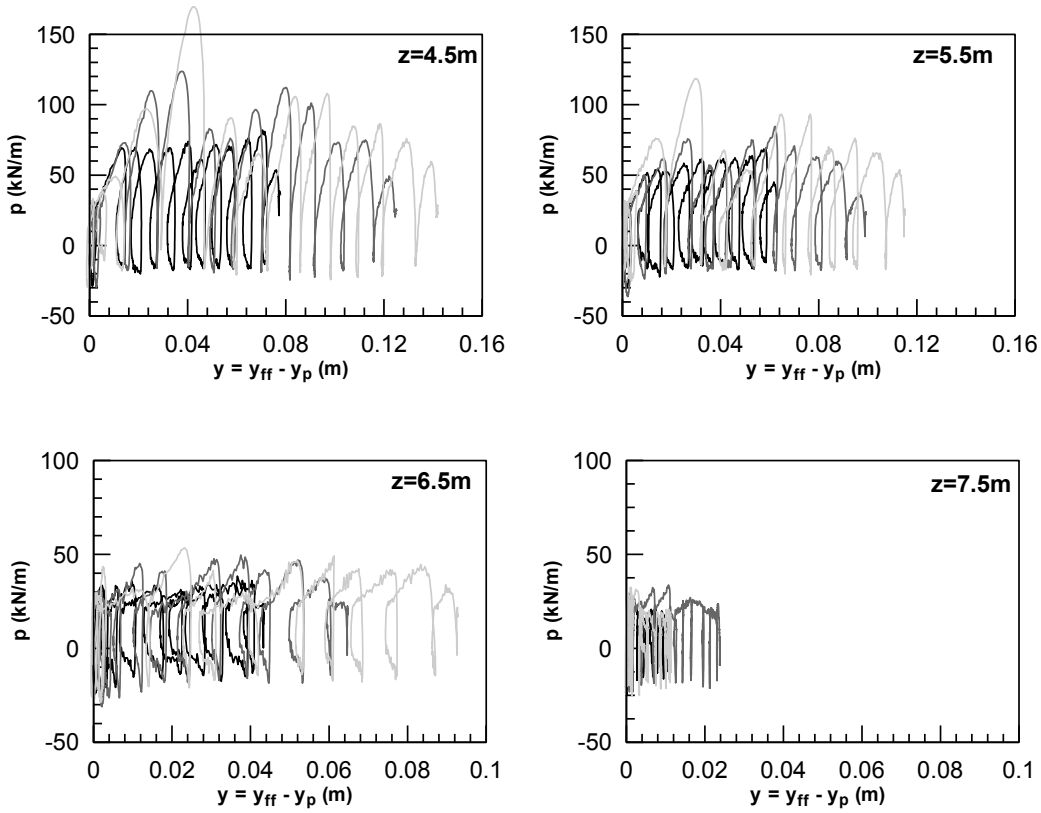

Figure 8.2b: P-y curves along the pile for different mesh dimensions

In addition, the finally selected mesh was checked against possible "pinning" effects from the pile itself. More specifically, according to the definition of p-y curves, the relative displacement, y, is defined as follows:

$$y_{rel} = y_{ff} - y_p \tag{8.1}$$

where,

y_{rel}: Relative displacement

y_{ff}: Soil displacement at the free field

y_p: Pile displacement

In the numerical analysis, the quantity y_{ff} is taken as the value of the horizontal displacement at the lateral boundary of the mesh. However, the presence of the pile is known to affect soil displacements in the area close to the pile ("pinning effects"). Therefore it has to be ensured that the lateral boundaries of the model are far enough so that soil displacements are the actual displacements at the free field. For this purpose, an additional analysis was performed, in which the pile was excluded and the pile zones were assigned with soil properties. Comparison with the analysis including a pile is shown in **Figure 8.3**, in terms of lateral displacement versus depth

at the end of shaking. It can be observed that the displacements estimated from the analysis with the pile correspond to the actual free field displacements.

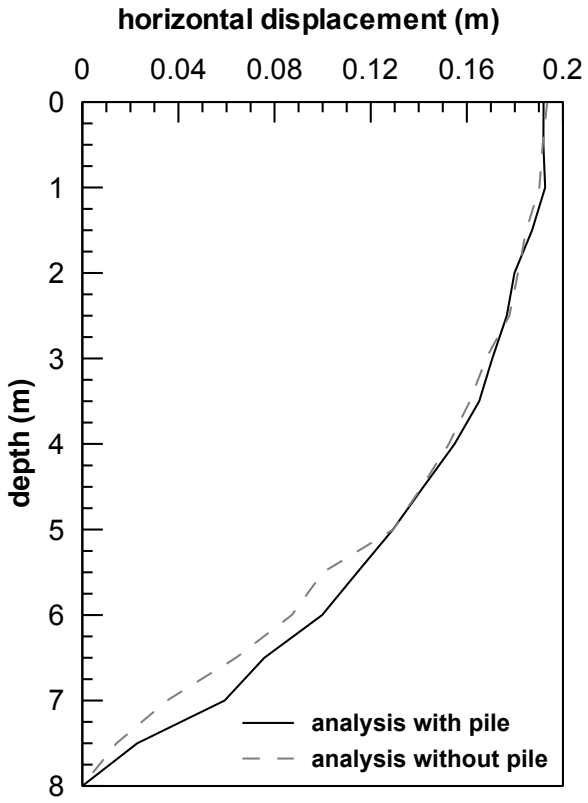

Figure 8.3: Displacements at the lateral boundary of an analysis with and an analysis without a pile.

8.4 Typical numerical predictions

In the current section, typical results from the basic analysis are presented, in terms of soil acceleration, pore pressure build-up, displacement accumulation, soil reaction development and p-y curves. In general, it is noted in advance that numerical results agree well with observations and response patterns as they are identified in centrifuge and shaking table tests.

8.4.1 Near and far field Soil Acceleration

Acceleration time histories at the surface, both in the near and the far field, are plotted in **Figure 8.4**. Namely, **Figure 8.4a** shows the response at the free-field, as it is calculated from the analyses with and without the pile. In the first case, free-field response is defined as the response at a distance far away from the pile (for the specific case this distance is approximately equal to 15D, where D is the pile

diameter). For the second case, all surface grid points are practically equivalent, while for the purpose of the figure the gridpoint at the center of the mesh is considered. Furthermore, **Figure 8.4b** shows the response right next to the pile. Finally, in both figures the excitation applied at the base of the model is also plotted in the background.

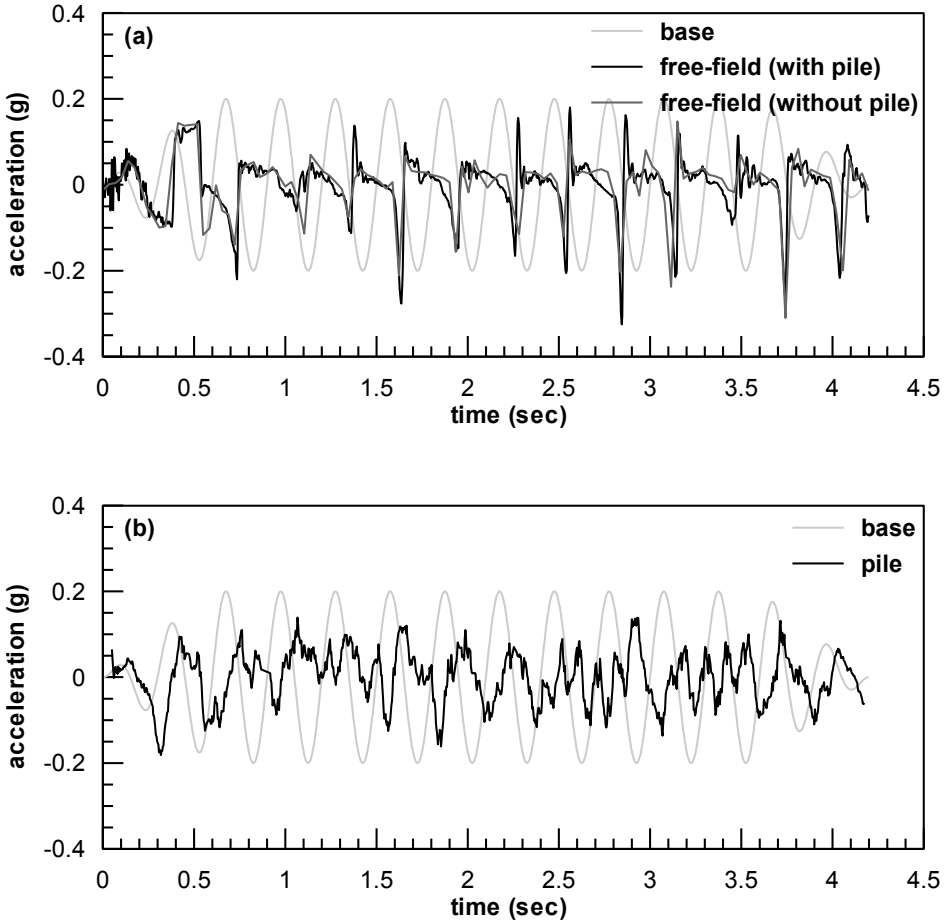

Figure 8.4: Acceleration time histories in the (a) free-field and in the (b) near field

The following typical trends are observed with regard to in the response of a laterally spreading soil appear:

- Positive (downslope) accelerations are practically vanished in early stages of shaking (after the first 1-2 loading cycles) as a result of seismic isolation effects due to liquefaction. Liquefaction effects are less pronounced in the time history that corresponds to the acceleration near the pile, in which some positive peaks are observed as well. These peaks can be attributed to pile

vibration which is not seismically isolated, and also to the fact that the area close to the pile is not liquefied, as it will be demonstrated afterwards.

- Negative (upslope) accelerations exhibit large spikes, as a result of dilative response of the sand during lateral spreading. This mechanism will be further described in the following.
- In terms of the seismic acceleration, the dynamic analysis with the pile captures with great accuracy the actual free-field response, as estimated from the analysis without the pile.

8.4.2 Development of Excess Pore Pressures

Pore pressure build-up at the end of shaking is illustrated in **Figure 8.5a** and **Figure 8.5b,** in terms of excess pore pressure and excess pore pressure ratio

$$r_u = \frac{\Delta u}{\sigma'_{vo}} \tag{8.2}$$

contours respectively, where:

r_u: Excess Pore Pressure ratio

Δu: Excess Pore Pressures

σ'_{vo}: Vertical Effective Stress

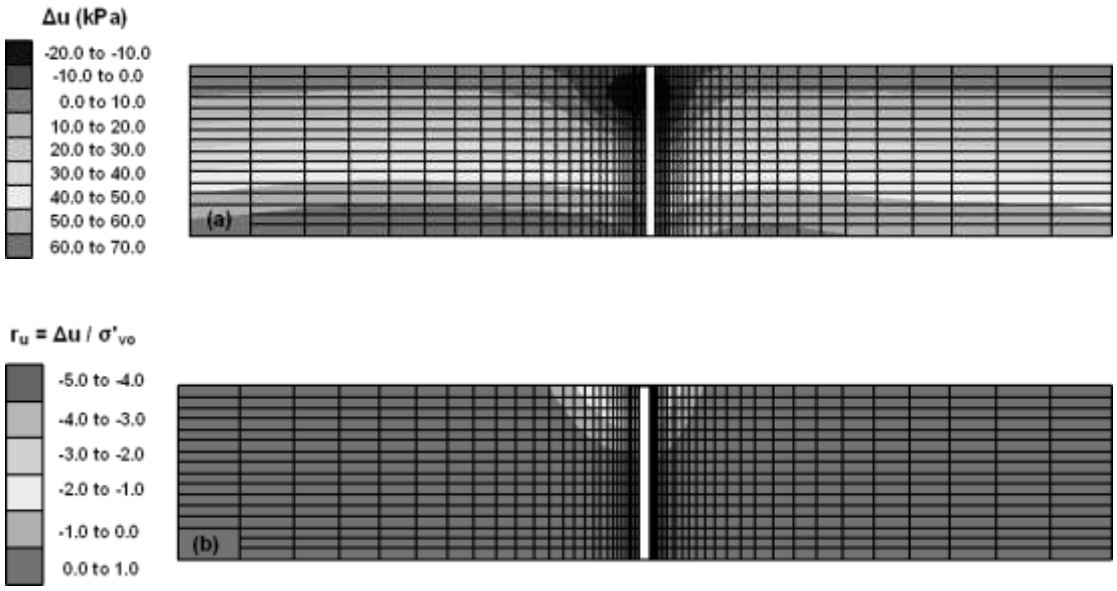

Figure 8.5: (a) Excess Pore Pressures and (b) Excess Pore Pressure ratio at the end of shaking

Figure 8.5a shows that excess pore pressures are significantly smaller in the region around the pile, where they obtain significant negative values. In addition, the distribution is roughly uniform near the boundaries, indicating that no boundary effects are present. Similar patterns are observed in **Figure 8.5b** showing the distribution of r_u. Namely, near the boundaries of the model r_u reaches values that are more or less close to unity. However, near the pile, r_u is much smaller taking even negative values, indicating dilation. More specifically, r_u takes values from -5.0 near the surface to 0.75 at the bottom. Note that dilative response in the area surrounding the pile has been widely observed in many centrifuge tests including the one by Gonzalez et al. (2009) analyzed in the previous chapter. Furthermore, this study also confirmed the inverted cone shape of the zone with extensive dilation, as it appears in **Figure 8.5b**

Pore pressure build-up is further demonstrated in **Figure 8.6**, where r_u - time histories are plotted for various locations in the mesh, from the analyses both with and without the pile. The upper row of the figures corresponds to the lower depths (z=0.75m), the middle row corresponds to intermediate depths (z=3.25m) and the third row corresponds to large depths (z=6.25m). The response in the free-field is shown in the second column of figures, (d) through (f), both from the analyses with the pile (black line), as well as from the analysis without the pile (grey line).

These figures reveal liquefaction of the soil early during shaking (after 1-2 cycles), while all time histories exhibit large dilation spikes. The latter appear when large straining occurs in soil elements that possess an initial static shear stress (as in the case of an infinite slope). They take place when the soil moves upwards relative to the base and are more pronounced near the surface, where the tendency of the soil to dilate is in general larger, due to the small confining stress. Finally, comparison between the two (2) types of analyses (with and without the pile) indicate that the analysis with the pile captures accurately the free-field response, with the only difference being that in the analysis without the pile the dilation spikes are somewhat larger.

The response in the area close to the pile is demonstrated in figures (a) through (c), both for the upstream side (grey line) and for the downstream side (black line). Observe that the pore pressure response at the upstream and downstream sides are

practically identical, while they are distinctly different compared to the free-field. Namely, near the ground surface large dilation occurs as excess pore pressures attain negative values. The dilative response, which will be further investigated later in the chapter, is attributed to the small confining stress, as well as to the large shearing imposed to the soil as a result of its displacement relative to the pile.

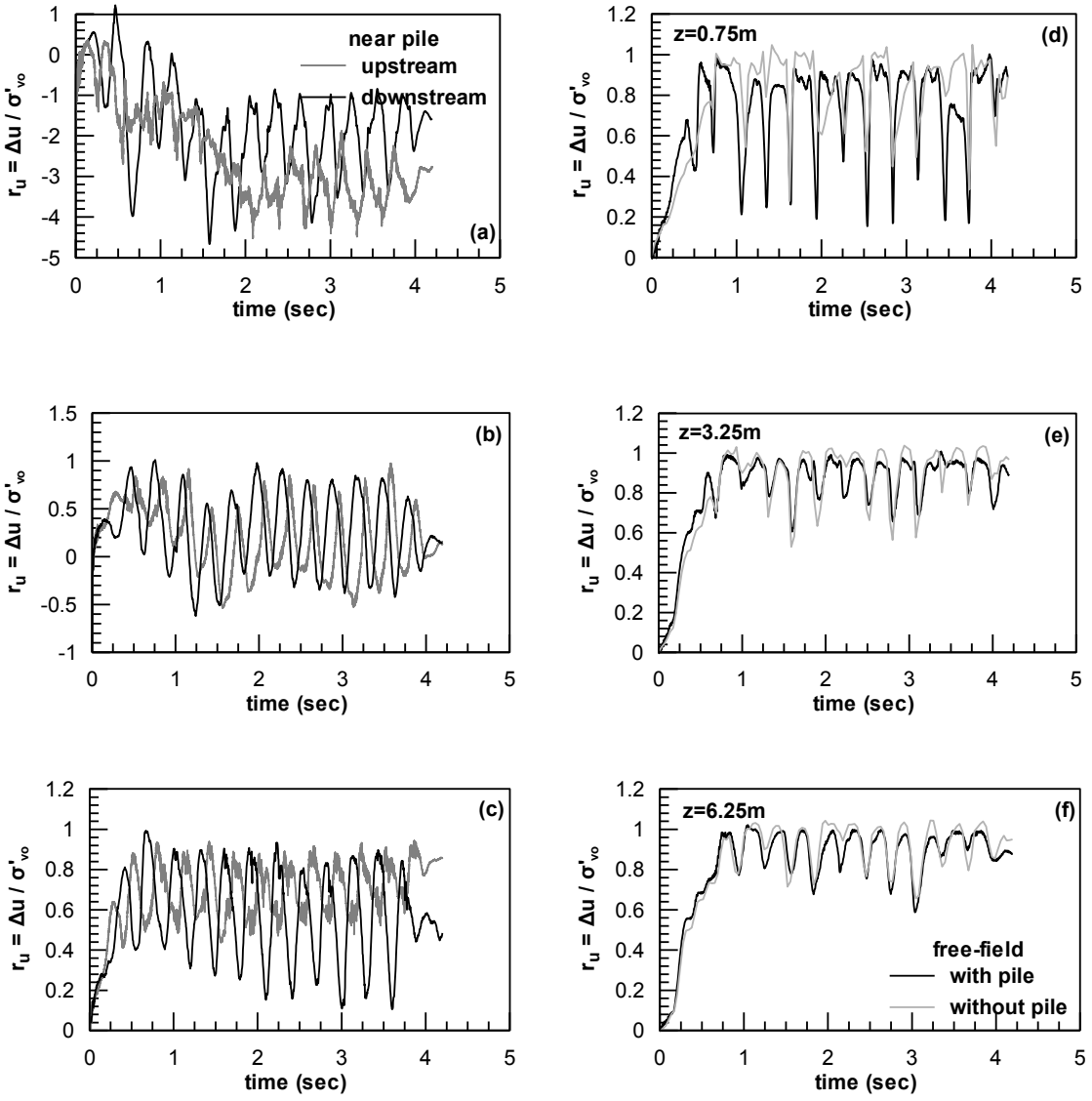

Figure 8.6: Pore pressure ratio time histories near the pile [figures (a) through (c)] and in the free field [figures (d) through (f)]

It is also important to note that excess pore pressures reach an ultimate negative value and afterwards they remain constant. It is speculated that this is because the soil has reached the critical state, given the large magnitude of displacements in that area. As depth increases, dilation effects are less pronounced probably due to the

lower shear strains and the higher confining stresses. However, even for large depths, pore pressure ratio never becomes equal to one (1.00). The algebraically maximum value is about $r_u \approx 0.75$, indicating small or large dilation effects prevent complete liquefaction near the pile.

8.4.3 Soil and Pile Lateral Displacements

Figure 8.7 shows the deformed mesh as well as the contours of horizontal displacements at the end of shaking. Furthermore, **Figure 8.8a** and **8.8b** show the displacement time histories at ground surface and their variation with depth at the end of shaking respectively. In each figure, two (2) different displacements are plotted: the black line corresponds to the displacement of the pile (horizontal displacement at the axis of the pile) and the grey to the free-field displacement.

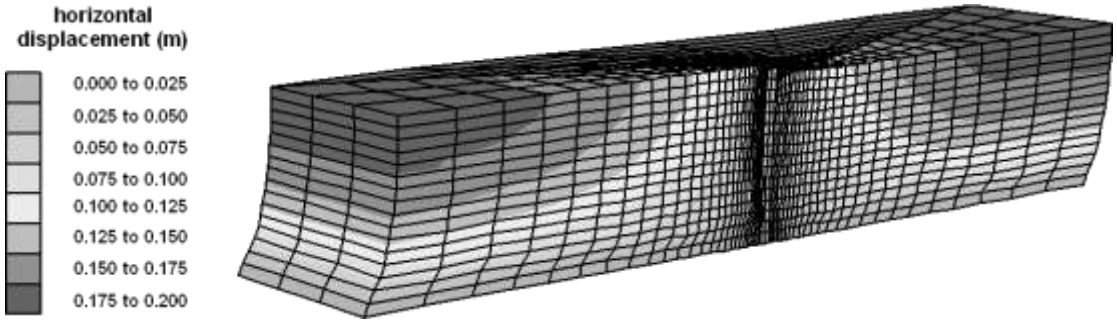

Figure 8.7: Deformed mesh and Contours of lateral displacement at the end of shaking

As shown in **Figure 8.8a**, displacement accumulation with time follows the typical "slip-stick" mechanism, which suggests that the rate of displacement accumulation is not constant during each cycle. Namely, the largest amount of displacement is accumulated when the soil moves downwards. On the other hand, when the soil moves upwards, dilation spikes cause the negative accelerations, observed in **Figure 8.4**. These accelerations cause the velocity to decrease resulting in much less displacement accumulation, or, in some cases, even small displacement decrease. Finally, Figure 8.8a shows that pile displacements increase at the early stages of loading but eventually stabilize to a constant value. Apparently, at that stage, the pile resists the soil movement without any further deflection, while the soil continues to flow around the pile.

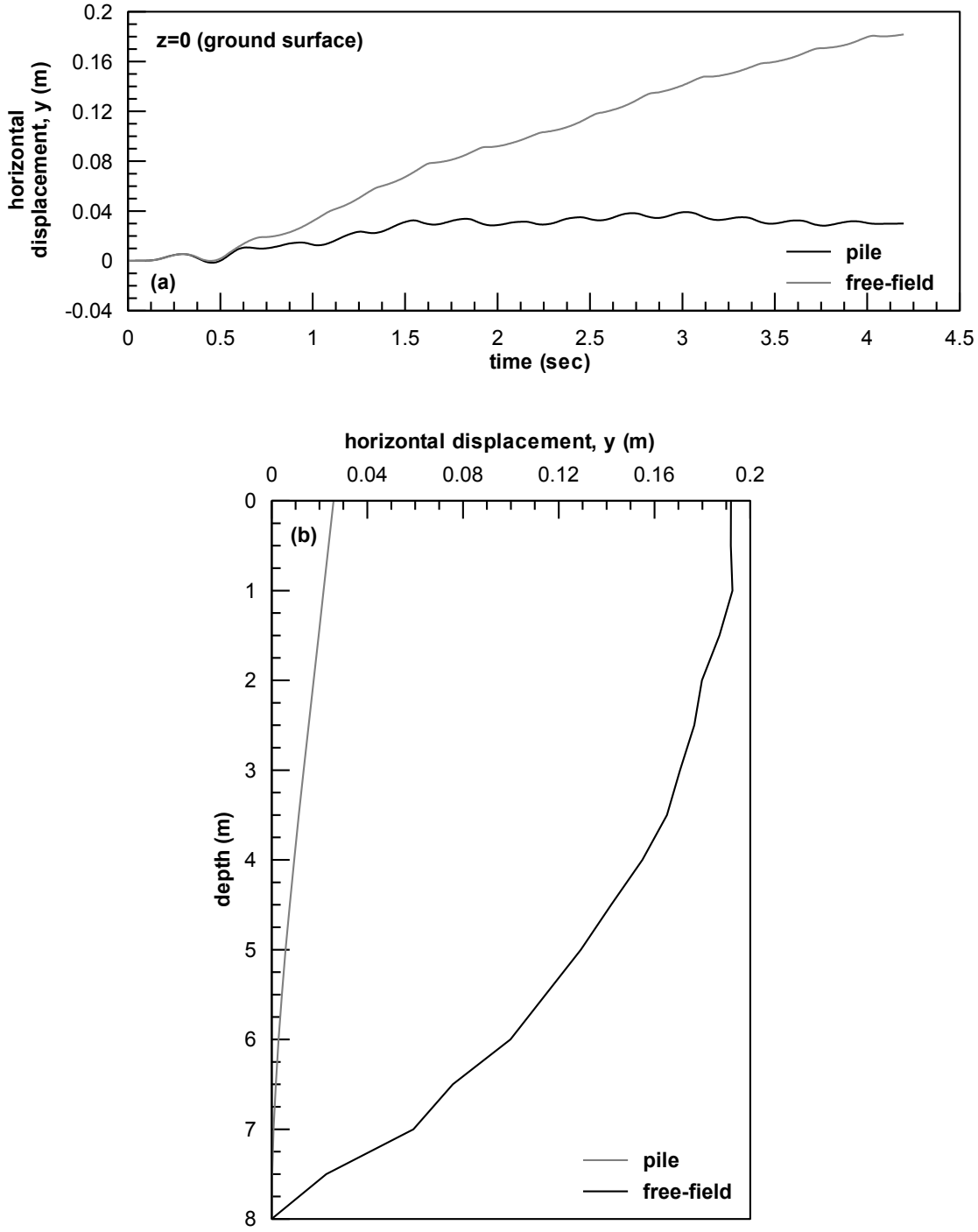

Figure 8.8: Development of soil and pile lateral displacements (a) variation with time at ground surface (b) variation with depth at the end of shaking

8.4.4 Development of soil reaction

The development of soil subgrade reaction is illustrated in **Figure 8.9a** and **8.9b**, for shallow (z=0.5m) and large depths (z=6.5m) respectively. Also plotted in each figure are the corresponding time histories of excess pore pressure ratio, as well as the relative pile-soil displacement, as well as the displacement of the pile. The latter are

recalled in order to investigate the possible inter-relation between soil reaction on one hand and pore pressure build-up and applied displacement on the other hand.

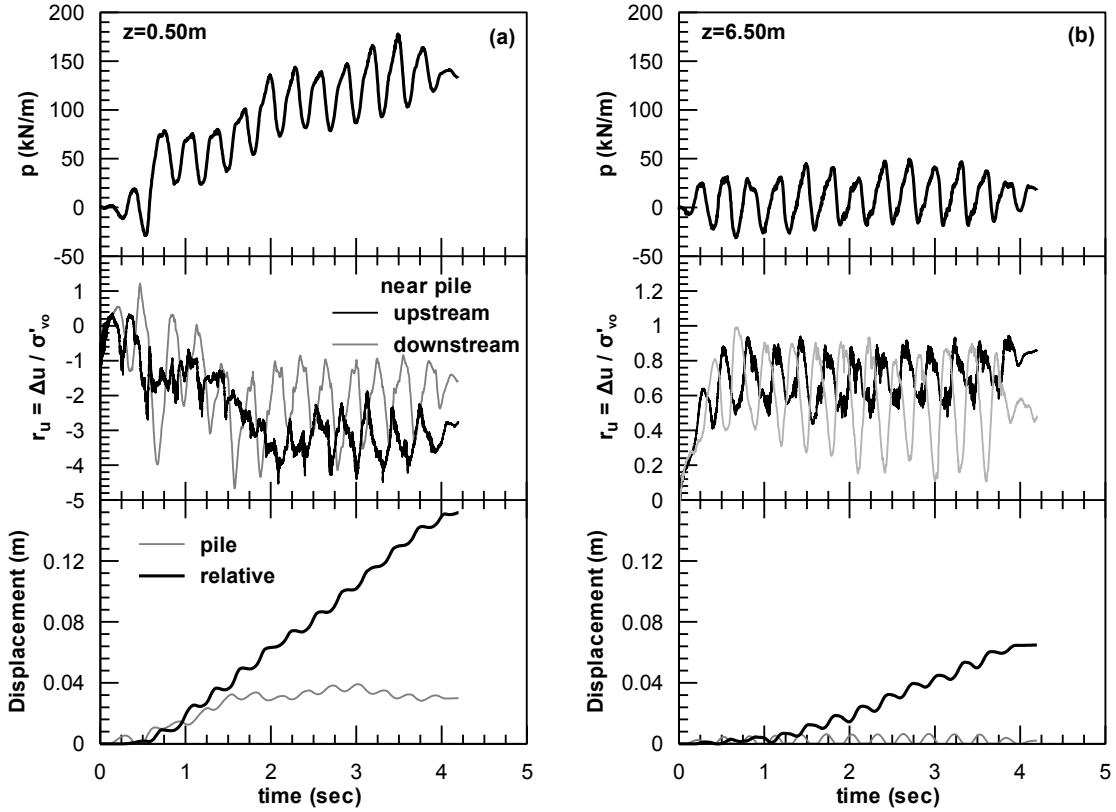

Figure 8.9: Soil subgrade reaction time histories in connection with pore-pressure build-up and displacement accumulation for (a) z=0.5m and (b) z=6.5m from ground surface

The following can be observed with regard to the soil reaction:

- Development of soil reaction is characterized by a transient (due to the cyclic nature of the loading) and a permanent (due to the accumulated displacement) component.
- As shown in both figures, the transient component is directly correlated to the evolution of pore pressures, as soil reaction fluctuations coincide with the development of dilation spikes.
- In addition to the transient, the permanent component of soil reaction is also related to excess pore pressure build up. Namely, for large depths, where r_u values are positive high ($r_u \approx 0.6$-0.8), soil resistance is small. On the other hand, soil reaction obtains very large values near the surface where significant negative excess pore pressures develop.

- Finally, it appears that the large negative excess pore pressure values are not only a result of the in-situ soil conditions (relative density and confining stress), but also of the pile-soil displacements and the associated shearing of the soil around the pile. Namely, near the ground surface, pore pressure become more and more negative as long as pile displacement increases. After the latter stabilizes, pore pressures stabilize as well. On the other hand, at large depths, where pile displacement is very small, dilation effects are very limited.
- The above reveal that development of soil reaction is definitely associated with pore –pressure build-up and dissipation in the area around the pile, hence the parameters that control soil reaction should be the same that control pore-pressures at this region. This scenario will be quantitatively documents in the following, based on the results of the parametric analyses.

8.4.5 P-y curves

Typical p-y curves for eight (8) different depths are shown in **Figure 8.10**. In all cases the pile displaces less than the soil, resulting in significant amount of accumulated relative displacement. In addition, no matter how weird it may sound in the context of current practice, soil reaction obtains larger values near the ground surface, and decreases with depth. To explain this, one may refer to **Figure 8.5**, which shows excess pore pressures distribution at the end of shaking. It is thus observed that the larger reaction values are associated with extensive soil dilation and negative excess pore pressure build up near the pile.

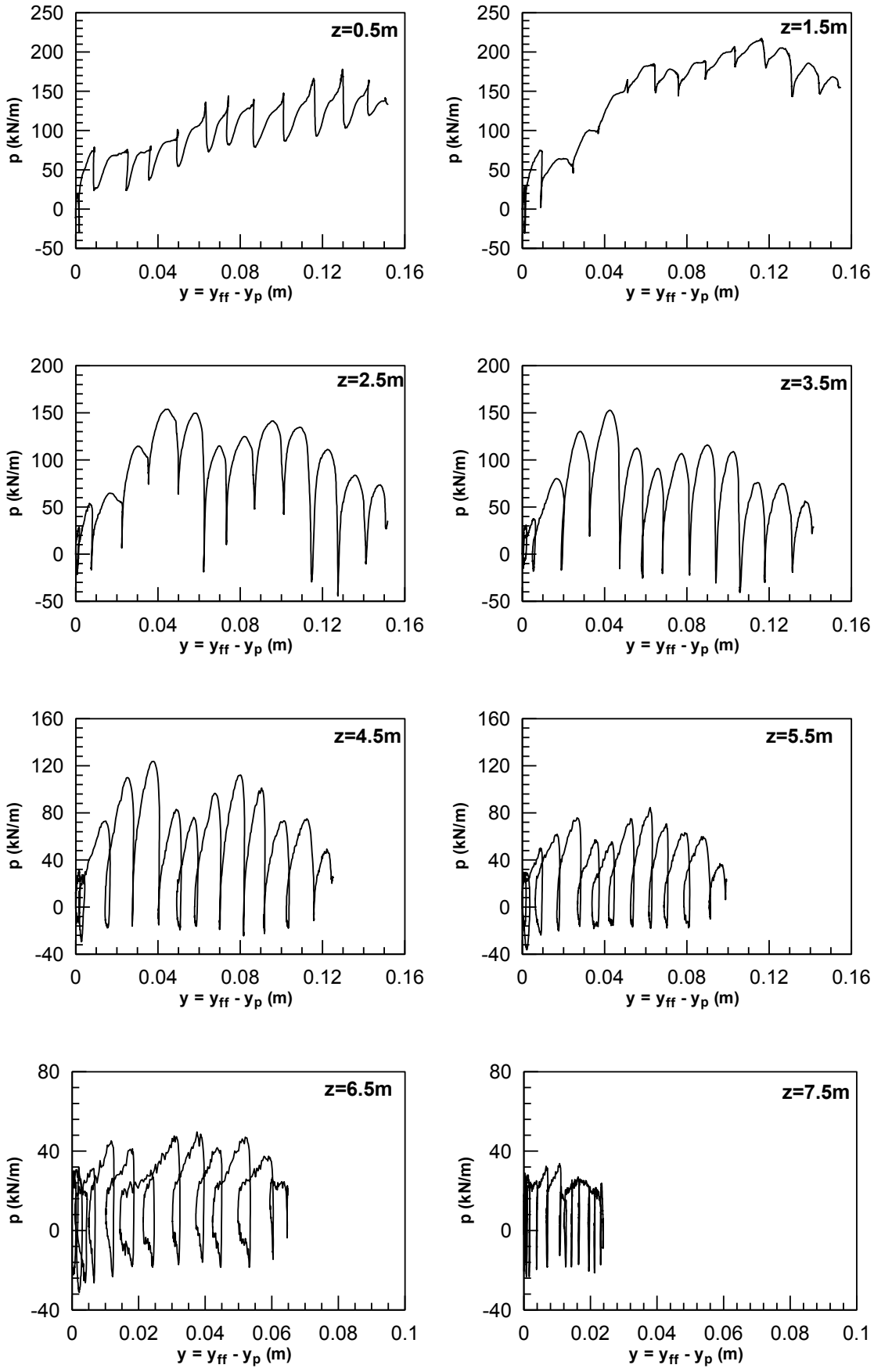

Figure 8.10: Typical p-y curves for various depths.

8.5 Evaluation of liquefied soil subgrade reaction

8.5.1 Interpretation of numerical p-y predictions

As described in previous chapters, there are three (3) basic elements that are needed in order to define a p-y curve:

- An analytical (nonlinear) p-y function
- The initial Stiffness. dp/dy for y=0
- Ultimate Resistance, $p_{ult,liq}$ for $y \rightarrow \infty$

For the case of laterally spreading soils (and in general problems involving cyclic loading), defining the above elements is a rather tedious and not clear task. For example ultimate resistance can be defined by considering either the maximum or the average values of soil pressure during each cycle. In the present thesis, the criterion for establishing practice oriented p-y curves is to obtain an overall best average fitting of the numerical predictions.

For this purpose, as well as for compatibility with the procedure followed in the case of firm soils, the numerically obtained p-y curves were described by means of a hyperbolic function, mathematically expressed as:

$$p = \frac{y_{rel}}{\frac{1}{k_{ini,liq} z} + \frac{y_{rel}}{p_{ult,liq}}} \tag{8.3}$$

where:

p: Soil reaction [kN/m]

y_{rel}: Relative displacement between the pile and the soil at the free field [m]

$k_{ini,liq}$: Gradient of Initial Subgrade Modulus of the laterally spreading soil [kN/m^3]

$p_{ult,liq}$: Ultimate soil resistance of the laterally spreading soil [kN/m]

To obtain a best average fitting, the following methods were consequently tried for the estimation of $k_{ini,liq}$ and $p_{ult,liq}$:

Method 1: In this case $k_{ini,liq}$ was estimated from the first peak of the p-y curve, as:

$$k_{ini,liq} = \frac{p_{\max,1} / 2}{y_{rel,1}} \tag{8.4}$$

where:

$p_{max,1}$: Maximum value of soil pressure during the first loading cycle

$y_{rel,1}$: Value of relative displacement at which $p_{max,1}$ occurs

In the above equation $p_{max,1}$ is divided by two (2) given that an average fit is desired. After $k_{ini,liq}$ is estimated, equation (8.3) is adjusted in the numerical curve to calculate a best-fit value for $p_{ult,liq}$.

Method 2: In this case, $k_{ini,liq}$ is also obtained numerically, however this time by considering the average value of p for the first 0.5cm of relative displacement:

$$k_{ini,liq} = \frac{p_{av\ \ y_{rel}=0\rightarrow 0.5cm}}{0.005} \tag{8.5}$$

where:

$p_{av\ \ y_{rel}=0\rightarrow 0.5cm}$: Average value of soil pressure during the first 0.5cm of relative displacement

The value of 0.5cm was selected after a trial and error procedure and corresponds to the minimum displacement beyond which calculation of $k_{ini,liq}$ is not affected by numerical instabilities. Similarly to the previous case after the stiffness has been estimated, $p_{ult,liq}$ is obtained by fitting the hyperbola of equation (8.3) to the numerically predicted p-y curves.

Method 3: In this case $k_{ini,liq}$ is assumed to be equal to the value of initial stiffness for the firm soil, i.e.:

$$k_{ini,liq} = k_{ini,firm} \tag{8.6}$$

where $k_{ini,firm}$ values are obtained from the static p-y analyses described in the previous chapters.

Method 4: The exact same procedure with "Method 3" above is followed, with the difference that $k_{ini,liq}$ is taken equal to one half of the value for the firm soil, given that pore pressure build-up is expected to cause degradation of the soil stiffness:

$$k_{ini,liq} = \frac{1}{2} \cdot k_{ini,firm} \tag{8.7}$$

For both 3 and 4 methods above, after $k_{ini,liq}$ has been determined, the hyperbolic function is adjusted on the numerical curve to calculate $p_{ult,liq}$. Methods 3 and 4 are based on the logic that ultimate resistance is reached relatively early during loading, so that estimation of initial stiffness is not crucial for the overall fitting procedure.

Method 5: Finally, in this case, the values of k_{ini} and p_{ult} for the firm soil are considered, and equation (8.3) is adjusted on the curve, by fitting a common load multiplier m_p:

$$p = m_p \cdot \left(\frac{y_{rel}}{\frac{1}{k_{ini,\,firm}} + \frac{y_{rel}}{p_{ult,\,firm}}} \right) \tag{8.8}$$

This approach is based on the concept of load multipliers m_p that assume that k_{ini} and p_{ult} are equally reduced as a result of liquefaction.

Application of all above methods is demonstrated in **Figure 8.11a** and **8.11b** for two (2) typical p-y curves obtained from the basic analysis. The two (2) curves correspond to depths z=2.5m and z=6.5m from the ground surface respectively. It can be observed that all approaches produce curves which provide an overall accurate description of the average p-y response of the soil. However, "Method 5" (the m_p multiplier scenario) appears to overestimate the stiffness and slightly underestimate soil resistance for small depths, while this trend reverses for large depths. The differences between the other three (3) cases are practically negligible, with "methods 1, 2 and 4" yielding the best comparison, while "method 3" is slightly less accurate. Finally, given that estimation of $k_{ini,liq}$ based on the numerical results for every depth and every analysis is a rather tedious and time consuming task, while it slightly improves the overall accuracy of the fitting, it was finally decided to adopt "method 4", in which it is assumed that $k_{ini,liq}$ is equal to the half of the value corresponding static value.

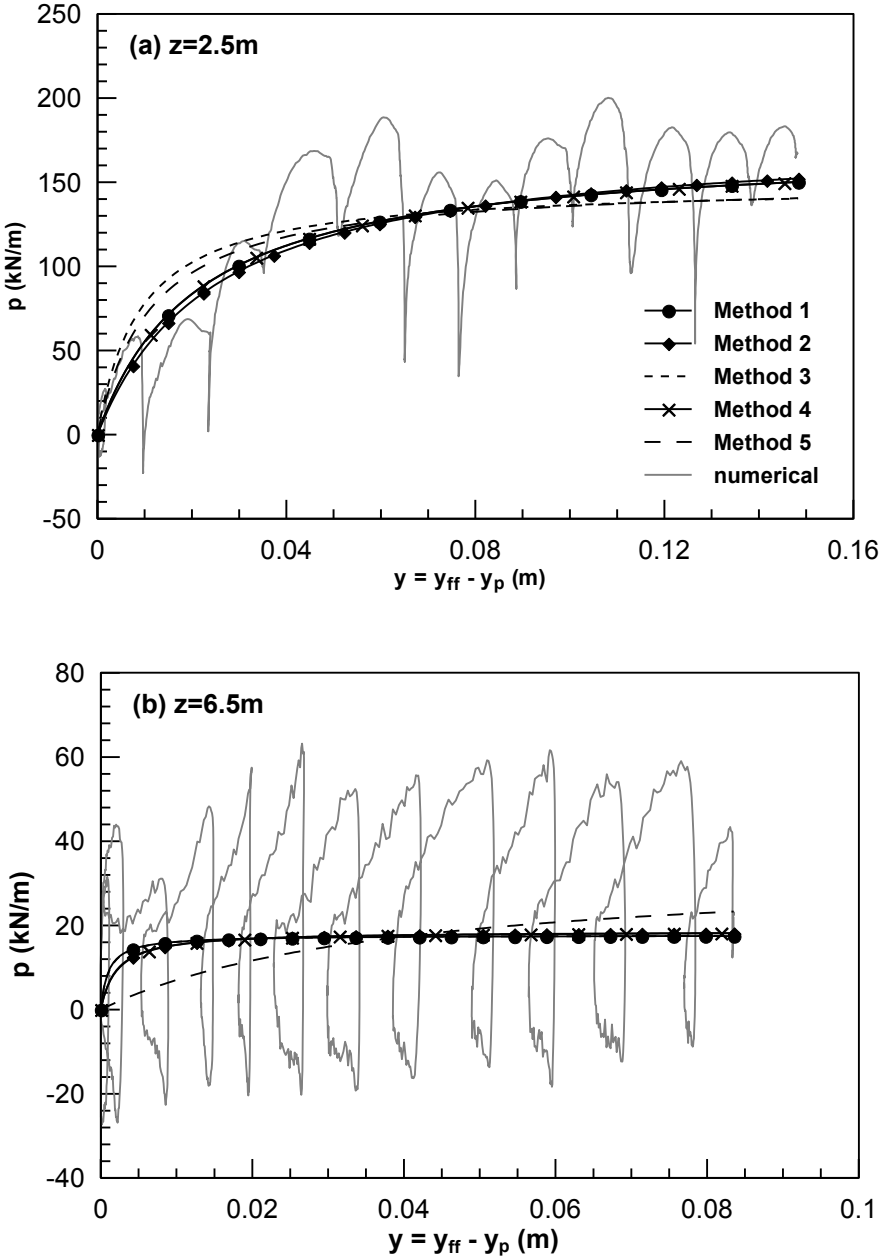

Figure 8.11: Application of the different ways to adjust a hyperbolic curve on the numerical p-y curves obtained from the basic analysis for (a) z=1.5m and (b) z=6.5m from ground surface

This procedure was consequently applied to all eighteen (18) analyses listed in **Table 8.1**. For each analysis, $k_{ini,liq}$ and $p_{ult,liq}$ values were obtained for eight (8) different depths along the pile. The results will be presented and discussed in the following.

8.5.2 Mechanisms affecting the Ultimate p-y Resistance

Based on the procedure described previously, best fit values for the ultimate resistance of the liquefied soil, $p_{ult,liq}$, were estimated for all eighteen (18) analyses

listed in **Table 8.1**, and eight (8) different depths per analysis (i.e. a total of 144 $p_{ult,liq}$ values). **Figure 8.12a** shows the variation of $p_{ult,liq}$ with normalized depth as obtained from the results of the basic analysis. Also plotted in **Figure 8.12b** is the variation of excess pore pressures in the area close to the pile (Δu_{pile}) at the end of shaking. Namely, the distribution shown was obtained directly from the numerical analysis by averaging the excess pore pressures of the zones right next to the pile, at the upstream and the downstream sides.

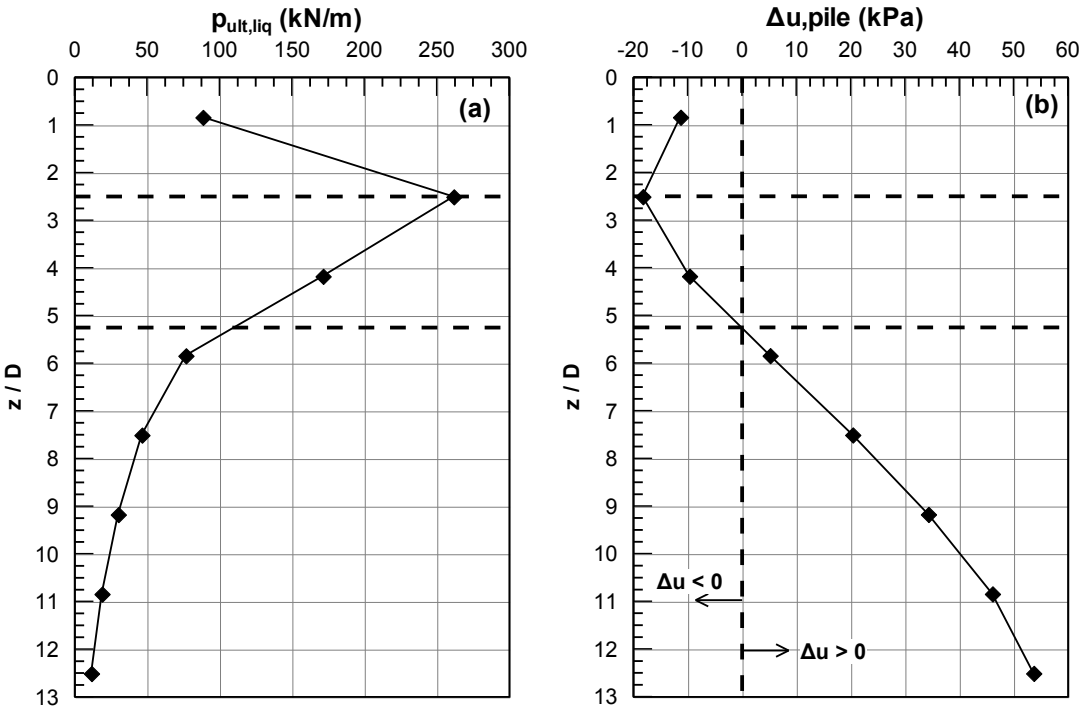

Figure 8.12: Variation of (a) ultimate soil resistance, $p_{ult,liq}$ (b) excess pore pressures, next to the pile, Δu,pile with depth

Following the discussion in paragraph 8.4.4, this comparison leaves little doubt that the ultimate soil resistance is directly related to the development of pore pressures close to the pile. Namely:

- At the upper part of the pile ($0<z/D<2.5$) excess pore pressures are negative and decrease algebraically (increase in absolute values) with depth reaching a peak value at z=2.5D. The dilative response of the soil at this area can be attributed to the small stresses, as well as the large relative pile-soil displacements. The fact that maximum dilation does not occur right at the ground surface, where geostatic stresses are minimum, is due to drainage and dissipation of the excess pore pressures towards the free surface. As shown in

Figure 8.12a, along this length, the ultimate soil resistance increases with depth following the evolution of negative excess pore pressures. Eventually, $p_{ult,liq}$ reaches a maximum value at z=2.5D, i.e. at the same depth of the negative peak of Δu_{pile}.

- Below the depth of z=2.5D dilation gradually turns to contraction and excess pore pressures become positive. Thus, Δu becomes zero at z=5.25D, and keeps increasing algebraically to positive values thereafter. Following the algebraic increase of Δu_{pile} along this length, $p_{ult,liq}$ gradually decreases with a constantly decreasing rate. However, it never reaches a constant value, such as proposed by Brandenberg et al., 2007, at least for the range of depth examined herein.

The results of **Figure 8.12** are plotted again in **Figure 8.13** using a different format: $p_{ult,liq}$ is normalized with respect to the vertical effective stress and the pile diameter, while excess pore pressures are normalized against the vertical effective stress. These new plots practically confirm the observations discussed previously. Namely, the excess pore pressure ratio $r_{u,pile}$ is large close to the surface and gradually increases with depth, reaching an almost constant value of $r_{u,pile}\approx 0.70\text{-}0.75$. Except from dilation effects, this observation indicates that complete liquefaction never occurs near the pile. Similarly, the normalized ultimate soil resistance $p_{ult,liq}/(\sigma'_{vo}D)$ is large close to the ground surface and gradually decreases with depth. It is also interesting to note that there is an upper limit to the dilation-induced large values of normalized soil resistance, which are observed close to the ground surface, so that the value of $p_{ult,liq}/(\sigma'_{vo}D)$ is practically constant with depth for the first few pile diameters. This observation for $p_{ult,liq}/(\sigma'_{vo}D)$ will be useful later in this chapter for the development of an analytical expression for $p_{ult,liq}/(\sigma'_{vo}D)$. It should be finally noted that, in qualitative terms, the response patterns discussed herein for the basic numerical analysis are representative for all other parametric analyses as well.

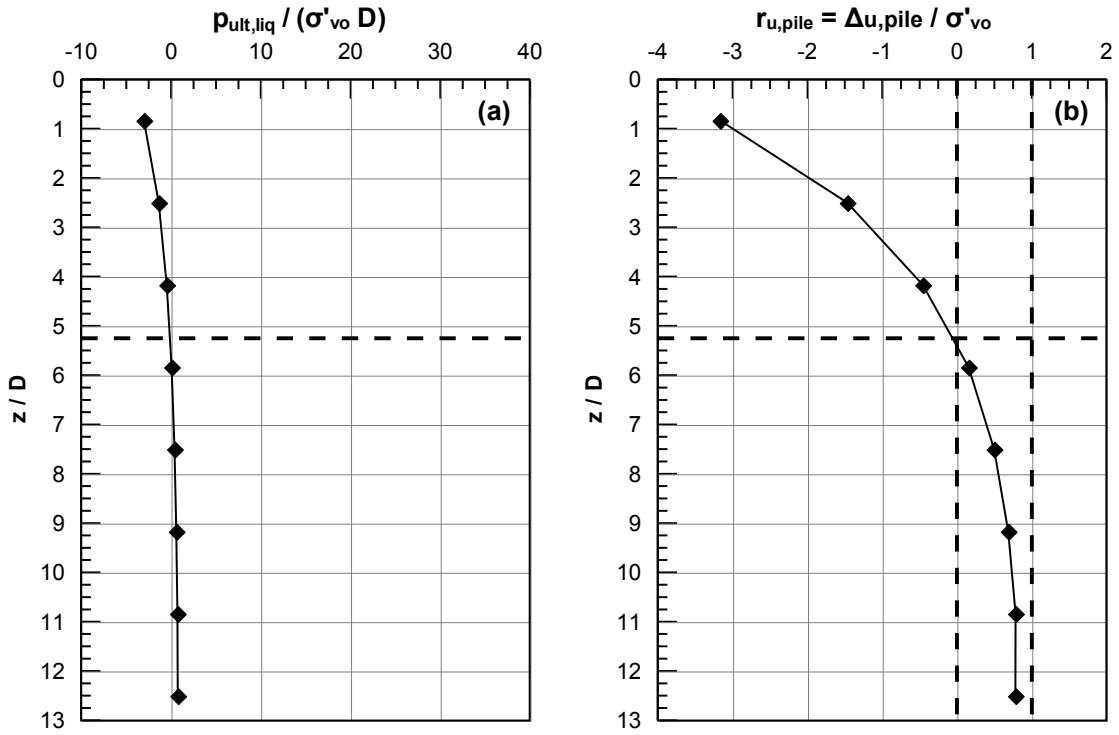

Figure 8.13: Variation of (a) normalized ultimate soil resistance $p_{ult,liq}/(\sigma'_{vo}D)$ and (b) excess pore pressure ratio near the pile, $r_{u,pile}$ with depth.

To further investigate the correlation between ultimate resistance and pore pressure development near the pile **Figure 8.14** through **Figure 8.16** plot the $p_{ult,liq}/(\sigma'_{vo}D)$ values against $1\text{-}r_{u,pile}$, for the whole set of numerical analyses performed herein. Note that the term $1\text{-}r_{u,pile}$ is preferred instead of $r_{u,pile}$ for two (2) reasons:

- To avoid negative $r_{u,pile}$ values that would make a possible analytical correlation more difficult (e.g. exclude a "power" type correlation).
- To be consistent with critical state theory, where stress changes due to undrained shearing are not proportional to r_u but to $1\text{-}r_u$, (e.g. see later sections of this chapter).

In **Figure 8.14**, the comparison is shown with reference to the basic parameters that are associated to pile characteristics, i.e. Bending Stiffness (Figure 8.14a), Pile Diameter (Figure 8.14b), Head Constraint (Figure 8.14c) and Pile Type (Figure 8.14d). Similarly, in **Figure 8.15**, the correlation is shown with reference to the basic parameters that are related to the soil and excitation characteristics, i.e. Relative Density (Figure 8.15a), Soil Permeability (Figure 8.15b) and Excitation Period (Figure 8.15c).

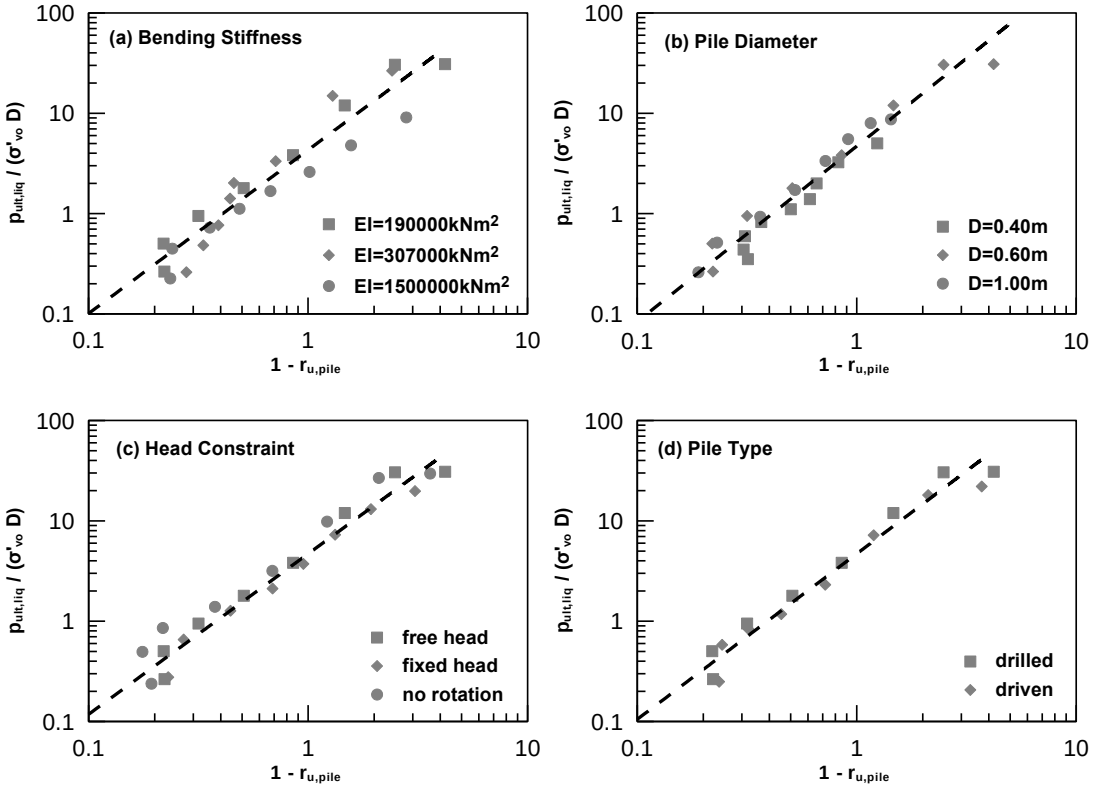

Figure 8.14: Correlation between ultimate soil resistance and excess pore pressure ratio near the pile for the various pile characteristics

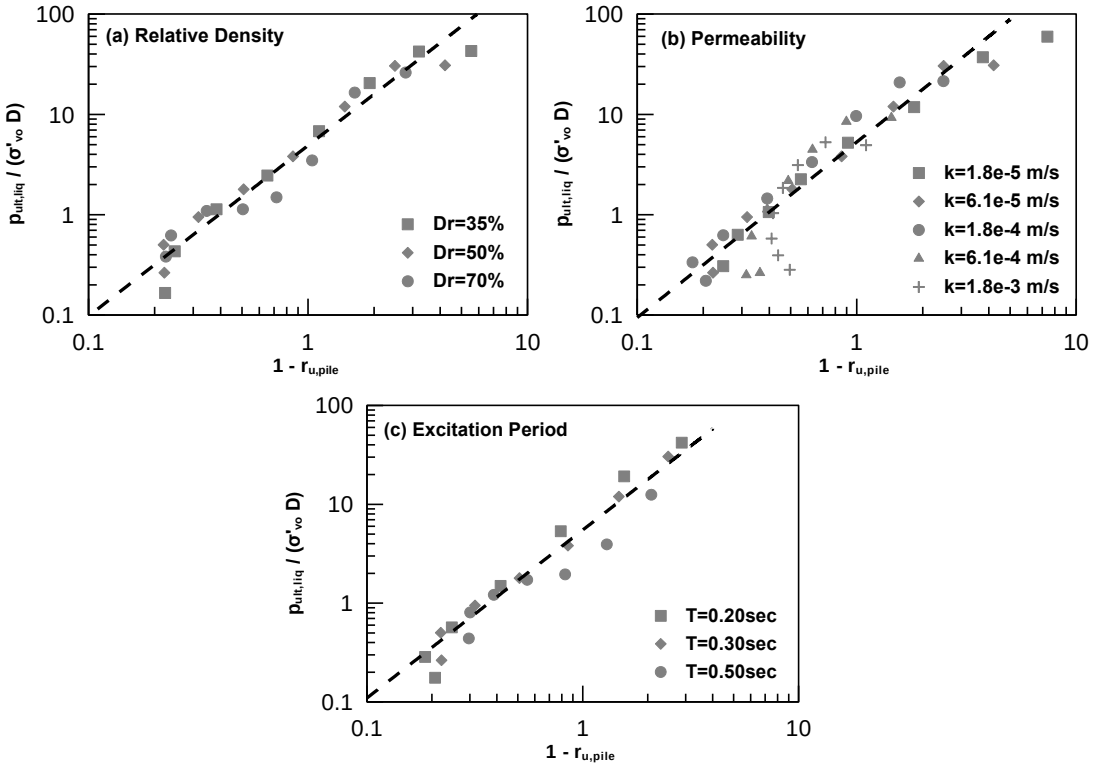

Figure 8.15: Correlation between ultimate soil resistance and excess pore pressure ratio near the pile for the various soil properties and excitation characteristics

Observe that, for all pile and soil parameters, the relation between $p_{ult,liq}$ and $1\text{-}r_{u,pile}$ is unique and not affected by the specific value of the parameter examined. In other words, each parameter affects directly the development of excess pore pressures near the pile and indirectly the ultimate soil resistance, only as a function of the former.

In view of the above finding, **Figure 8.16** shows the same comparison, but for all pile and soil parameters. All data points form a unique, remarkably narrow band which can be readily fitted by the following analytical expression:

$$\frac{p_{ult,liq}}{\sigma'_{vo} D} = 5.0 \cdot \left(1 - r_{u,pile}\right)^{1.75} \tag{8.9}$$

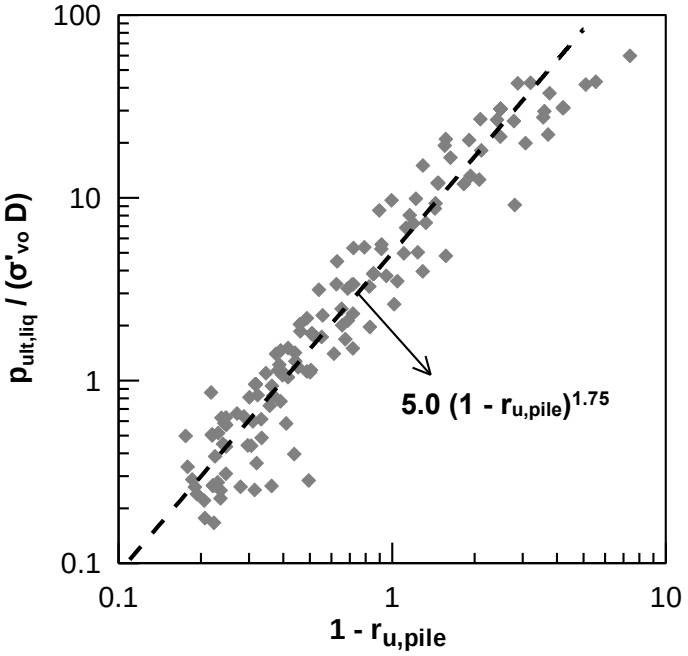

Figure 8.16: Relation between normalized ultimate resistance and excess pore pressure ratio next to the pile

8.5.3 Simplified Pile-Soil Interaction Model

The above relationship, along with all the preceding discussion, verifies that the normalized ultimate resistance is a unique function of the excess pore pressure ratio near the pile. Thus, identification of the pile and soil parameters which govern the development of ultimate resistance, is essentially equivalent to the identification of the parameters that affect pore pressure build-up near the pile.

Along this line of thought, it was subsequently assumed that the development of soil reaction is described by the simple elastoplastic curve shown in **Figure 8.17a**. In this case the evolution of excess pore pressure ratio will have the form shown in **Figure 8.17b** and in **Figure 8.17c** in terms of r_u and $1\text{-}r_u$ respectively. Namely, r_u initially increases with applied displacement, during the elastic phase of loading, while it subsequently decreases until it reaches an ultimate value $r_{u,ult}$, which corresponds to the critical state. Similarly, $1\text{-}r_u$ initially decreases (to a minimum value $1\text{-}r_{u,min}$) and then increases linearly, according to a slope α (which will be defined later), until the ultimate value $1\text{-}r_{u,ult}$.

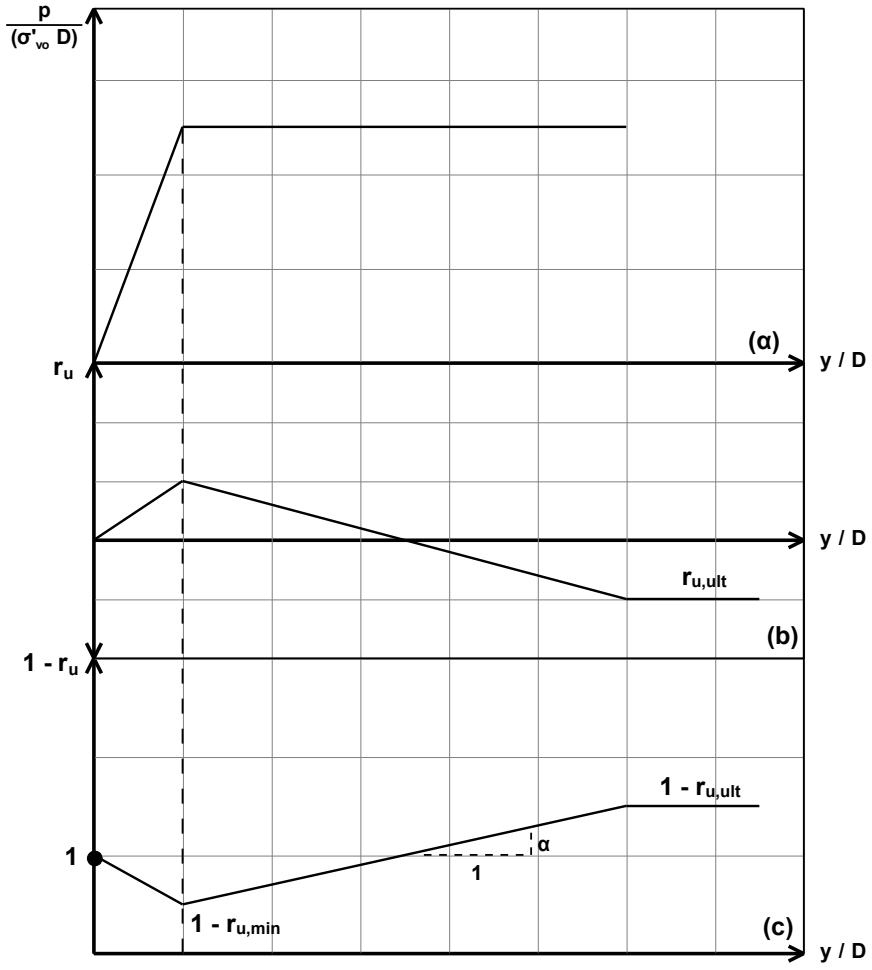

Figure 8.17: Simple elastoplastic model to investigate pore pressure build-up (a) Soil resistance (b) Excess Pore Pressure Ratio, r_u and (c) $1\text{-}r_u$ versus normalized displacement.

In order to determine the ultimate value of excess pore pressures ratio $r_{u,ult}$, the Critical State Theory is employed, as shown in **Figure 8.18**. Assume that the Critical State Line is described by the following equation:

$$e = e_a - \lambda \ln\left(\frac{p_f}{p_a}\right) \tag{8.10}$$

where:

e_a: void ratio at critical state for $p=p_a$

p_a: atmospheric pressure (=98.1kPa)

λ: slope of Critical State Line (CSL) in the e-lnp space

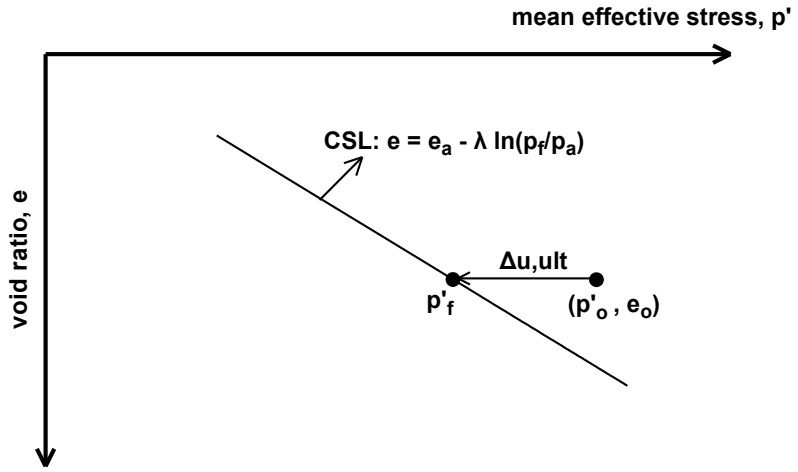

Figure 8.18: Calculation of Excess Pore Pressures during undrained loading according to Critical State Theory.

Consider next the undrained loading of a soil element with initial mean effective stress p'_o and void ratio e_o. At the critical state, the mean effective stress of the element will be equal to:

$$\frac{p_f}{p_a} = \exp\left(\frac{e_a - e_o}{\lambda}\right) \tag{8.11}$$

while the corresponding excess pore pressure $\Delta u_{,ult}$ will be:

$$\Delta u, ult = p'_o - p'_f \tag{8.12}$$

As a result,

$$r_{u,ult} = 1 - \frac{p'_f}{p'_o} \tag{8.13}$$

and

$$1 - r_{u,ult} = \frac{p'_f}{p'_o} \tag{8.14}$$

Combining (8.11) with (8.14) we obtain the following expression for the excess pore pressure ratio at the critical state:

$$1 - r_{u,ult} = \frac{1}{p'_o / p_a} \cdot \exp\left(\frac{e_a - e_o}{\lambda} \right) \tag{8.15}$$

Given 1-$r_{u,ult}$, slope α in **Figure 8.17c** can be approximated as follows:

$$a \approx \frac{1 - r_{u,ult}}{y / D_{ult}} = k \frac{1}{p'_o / p_a} \cdot \exp\left(\frac{e_a - e_o}{\lambda} \right) \tag{8.16}$$

where $(y/D)_{ult}$ is the displacement at which the critical state is reached and k is a constant.

Finally, based on the above, excess pore pressure ratio build-up can be expressed as follows:

$$\begin{aligned} (1 - r_u) &= (1 - r_{u,\min}) + a \cdot \ y / D \ \Rightarrow \\ 1 - r_u \ &- \ 1 - r_{u,\min} \ = k \frac{1}{p'_o / p_a} \cdot \exp\left(\frac{e_a - e_o}{\lambda} \right) \cdot \ y / D \end{aligned} \tag{8.17}$$

The above equation indicates that pore pressure build-up depends on the in-situ stress and volumetric conditions (the exponential term can be considered as a dependence to Relative Density D_r), as well as displacement y. For the problem examined herein, displacement y most probably refers to the relative pile-soil displacement of the pile (y_{rel}), as it is the one that controls the magnitude of shearing imposed in the surrounding soil. Also, it should be noted that in the above analysis, it was assumed that the loading of the soil was undrained, hence factors related to drainage (permeability and excitation period) are also expected to affect r_u.

To this extent, it can be concluded that the parameters that determine pore pressure build-up during the kinematic loading of a pile as result of lateral spreading are the following:

- In-situ soil conditions (Relative Density, confining stress, pile installation)
- Drainage Conditions (soil Permeability, excitation Period)
- Imposed Shear Strain (relative pile displacement, or else pile diameter, bending stiffness and pile head constraints)

Furthermore, although simplified, the pile-soil model analyzed herein explains fairly well the response patterns observed in the analysis with regard to pore pressure build-up. Namely:

- Near the surface large, dilation occurs as a result of small confining stress and large displacements. The latter cause the soil to reach the critical state, and hence negative excess pore pressures obtain an ultimate value (as indicated by the time history shown in **Figure 8.6**)
- At large depths, dilation effects are much less pronounced, however complete liquefaction is not reached as a result of the shear stress offset imposed by the pile.

8.6 Concluding Remarks

In the present chapter the results of a series of parametric analyses investigating the response of piles in laterally spreading ground, were presented. The analyses investigated the effects of various parameters related to soil (Relative Density, Soil Permeability), pile (Diameter, Bending Stiffness, Installation, Head Constraint) and excitation (Period) characteristics. Emphasis was placed on the prediction of the p-y response and mainly on the factors affecting the ultimate resistance of the soil. In this context the following were concluded:

a. As a result of the dynamic nature of the problem, numerical p-y curves are characterized by a cyclic and residual component. The average response can be captured by applying the well-established hyperbolic formula

$$p = \frac{y}{\frac{1}{k_{ini,liq} z} + \frac{y}{p_{ult,liq}}} \tag{8.18}$$

b. The initial stiffness modulus coefficient, $k_{ini,liq}$, can be fairly approximated by considering the half of the corresponding value for firm soil:

$$k_{ini,liq} = \frac{1}{2} k_{ini,static} \tag{8.19}$$

c. However, a much more interesting conclusion was raised with regard to the development of ultimate soil resistance. Namely, it was found that $p_{ult,liq}$ is directly correlated to the development of excess pore pressures near the pile, irrespectively of the value of the various parameters involved. Mathematically, this unequivocal relation can be described as follows:

$$\frac{p_{ult,liq}}{\sigma'_{vo} D} = 5.0 \cdot \left(1 - r_{u,pile}\right)^{1.75} \tag{8.20}$$

d. Based on the above, the development of excess pore pressures near the pile was further investigated. It was observed that response near the pile is characterized by the development of negative excess pore pressures. Dilation phenomena are more intense close to the surface and diminish with depth. Similarly to recent experimental results, the contours of excess pore pressure ratio indicated that the soil mass undergoing dilation is of inverted conical shape. Finally, based on the results of the analyses, and a simplified pile-soil interaction model that was considered, it was concluded that excess pore pressure development near the pile is controlled by the following mechanisms:

- In-situ soil conditions (Relative Density, Confining Stress)
- Drainage Conditions (Soil Permeability, Excitation Period)
- Imposed Shear Strain (Relative pile-soil displacement)

9

Analytical Calculation of Ultimate Soil Resistance in Laterally Spreading Soils

9.1 Identification of main problem parameters

The discussion in the previous chapter provided valuable insight to the development of soil reaction in laterally spreading soils. Furthermore, it suggests that the development of an empirical relationship for the prediction of ultimate soil resistance in practice could proceed in two (2) steps:

- Calculation of excess pore pressure ratio near the pile ($1-r_{u,pile}$) as a function of the various soil, pile and excitation properties that control pore pressure build-up.
- Calculation of ultimate soil resistance ($p_{ult,liq}$) as a function of $1-r_{u,pile}$ based on the correlation developed in the previous chapter.

Nevertheless, this approach requires the development of two (2) empirical correlations, one for $1-r_{u,pile}$ versus the various parameters and one for $p_{ult,liq}$ versus $1-r_{u,pile}$, and would inevitably increase the scatter of the predictions. Therefore, it was decided to correlate directly $p_{ult,liq}$ with the various parameters that affect $r_{u,pile}$, avoiding the objective limitations of the two separate empirical relationships.

Based on the preceding discussion, the calculation of ultimate resistance should account for in-situ soil conditions, drainage as well as magnitude of imposed shear straining. Obviously, the latter is best represented by the relative pile-soil displacement. However, including this parameter to the p-y relations would lead to a non-linear system of equations that can only be solved iteratively. Therefore, two (2) different types of correlations were attempted:

- The first, in terms of basic soil (D_r, permeability coefficient), pile (EI, D, Head Constraint, Pile Type) and excitation parameters (T) which are known a priori.
- The second, in terms of basic soil and excitation parameters, as well as the relative pile-soil displacement.

9.2 Empirical relations in terms of pile, soil and excitation characteristics

The variation of normalized ultimate resistance illustrated in **Figure 9.1a** shows that $p_{ult,liq}/(\sigma'_{vo}D)$ attains a constant peak value for the top few pile diameters, near the ground surface, and decreases with depth beyond that elevation. To capture this response pattern, which is characteristic for all parametric analyses, **Figure 9.1b** shows values of $[p_{ult,liq}/(\sigma'_{vo}D)]$ plotted against $[1/(\sigma'_{vo}/p_a)]$ for the basic analysis.

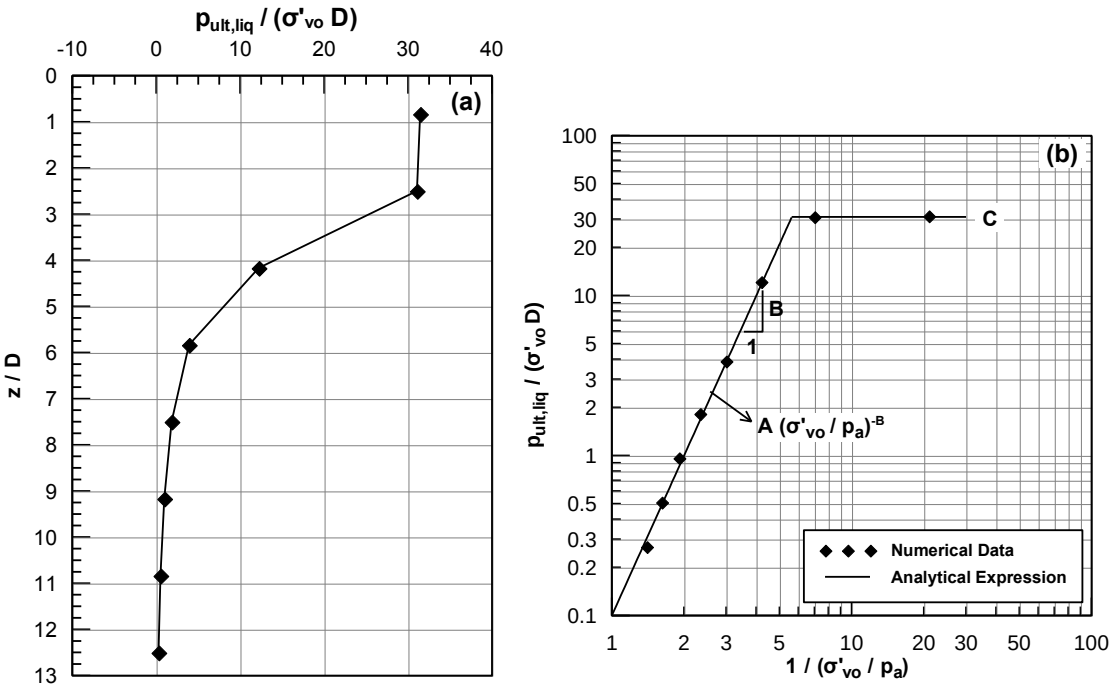

Figure 9.1: Variation of normalized ultimate resistance, $p_{ult,liq}/(\sigma'_{vo}D)$ with (a) normalized depth and (b) the inverse of normalized vertical effective stress, $1/(\sigma'_{vo}/p_a)$ for the basic analysis.

This figure indicates that, in a log-log diagram, ultimate resistance increases linearly with the inverse of vertical effective stress, until it reaches a constant peak value. Analytically, this pattern can be expressed as:

$$\frac{p_{ult,liq}}{\sigma'_{vo} D} = A\left(\frac{\sigma'_{vo}}{p_a}\right)^{-B} \leq C \quad (9.1)$$

where σ'_{vo} is the vertical effective stress and A, B and C constants.

The following can be noted with regard to the physical meaning of parameters A, B and C:

- Parameter A corresponds to the value of normalized resistance at a vertical effective stress of 1atm. In other words, it is representative of soil resistance at relatively large depths, where the response is contractive, characterized by values of excess pore pressure ratio close to unity and accordingly relatively small ultimate resistance values.
- On the other hand, parameter C is representative of soil resistance at small depths, where large dilation occurs, resulting in large soil resistance values. As observed in the figure, parameter C is an upper bound value for soil resistance, meaning that soil resistance at small depths remains more or less constant. This stabilization can be attributed to water drainage towards the free surface, which effectively suppresses dilation-induced negative excess pore pressures.
- Finally, parameter B represents the transition from the state of compression, positive excess pore pressures and small resistance values ($p_{ult,liq}\approx A$) to that dilation, negative excess pore pressures and large soil resistance values ($p_{ult,liq}\approx C$).

Hence, as a first step for the development of an analytical expression for $p_{ult,liq}$, parameters A, B and C were computed from fitting equation (9.1) to the results of each numerical analysis. The resulting values for A, B and C are summarized in **Table 9.1**. It can be observed that all three (3) constants may vary significantly from one parametric analysis to the other. This is expectable, as equation (9.1) above accounts directly only for the effects of confining stress, while the analysis in the previous chapter has shown that $p_{ult,liq}$ practically depends on a number of other parameters as well, to the extent that they affect pore pressure build-up near the pile. The effect of these parameters should be consequently incorporated to constants A, B and C and is independently evaluated for each constant in the following.

Table 9.1: Values of constants A, B and C determined from the results of the numerical analyses

α/α	Soil Properties		Pile Properties				Excitation Properties	Fitting		
	k (m/sec)	Dr (%)	D (m)	EI (kNm²)	Head Constraint	Pile Type	T (sec)	A	B	C
1	6.1e-5	50	0.60	1300000	free	drilled	0.30	0.10	3.32	31.0
2	6.1e-5	25	0.60	1300000	free	drilled	0.30	0.04	5.00	50.0
3	6.1e-5	35	0.60	1300000	free	drilled	0.30	0.06	4.12	42.0
4	6.1e-5	60	0.60	1300000	free	drilled	0.30	0.11	2.90	25.0
5	6.1e-5	70	0.60	1300000	free	drilled	0.30	0.12	2.60	22.0
6	1.8e-5	50	0.60	1300000	free	drilled	0.30	0.12	3.10	50.0
7	1.8e-4	50	0.60	1300000	free	drilled	0.30	0.08	3.10	21.0
8	6.1e-4	50	0.60	1300000	free	drilled	0.30	0.09	2.92	9.0
9	1.8e-3	50	0.60	1300000	free	drilled	0.30	0.14	2.20	5.1
10	6.1e-5	50	0.40	1300000	free	drilled	0.30	0.04	2.20	19.0
11	6.1e-5	50	1.0	1300000	free	drilled	0.30	0.90	6.00	51.0
12	6.1e-5	50	0.60	130000	free	drilled	0.30	0.18	2.00	8.0
13	6.1e-5	50	0.60	250000	free	drilled	0.30	0.10	2.80	14.0
14	6.1e-5	50	0.60	325000	free	drilled	0.30	0.11	2.70	15.0
15	6.1e-5	50	1.0	600000	free	drilled	0.30	0.10	2.85	21.0
16	6.1e-5	50	1.0	910000	free	drilled	0.30	0.12	2.62	25.0
17	6.1e-5	50	1.0	2000000	free	drilled	0.30	0.12	2.5	21.0
18	6.1e-5	50	1.0	9750000	free	drilled	0.30	0.12	2.06	7.0
19	6.1e-5	50	1.0	1300000	free	driven	0.30	0.12	2.86	20.0
20	6.1e-5	50	1.0	1300000	fixed	drilled	0.30	0.12	3.22	17.0
21	6.1e-5	50	1.0	1300000	no rotation	drilled	0.30	0.10	3.32	29.0
22	6.1e-5	50	1.0	1300000	free	drilled	0.20	0.04	4.36	41.0
23	6.1e-5	50	1.0	1300000	free	drilled	0.40	0.18	2.60	30.0
24	6.1e-5	50	1.0	1300000	free	drilled	0.50	0.25	2.03	25.0

The effect of relative density D_r is illustrated in **Figure 9.4**; the following can be observed:

- Parameter A increases with D_r. This is because the resistance of liquefied soils is larger for more dense soils. Hence, A also increases with D_r, as it reflects ultimate pressure for large positive values of r_u,
- Parameter C decreases with D_r. As D_r increases, liquefaction induced lateral ground displacements, and consequently the relative displacement between the pile and the soil, also decrease. However, for lower displacement levels, dilation phenomena are less severe. As a result soil resistance is reduced. Of course, one may argue that more dense soils are more dilative as well. However, it appears that the mechanism of negative excess pore pressure accumulation due to large displacements and straining prevails.

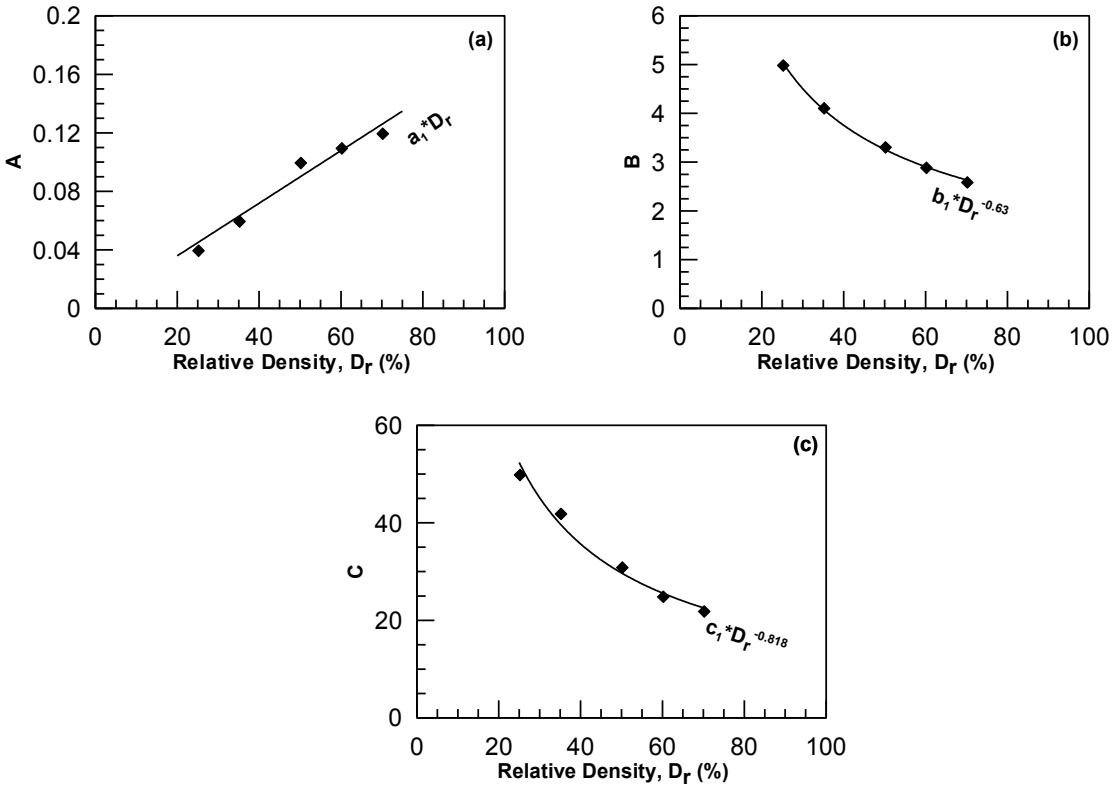

Figure 9.2: Variation of parameters A, B and C with Relative Density, D_r.

The effect of soil permeability k is demonstrated in **Figure 9.3**; observe that :

- Parameter A is relatively less affected by soil permeability up to k=2e-4 m/s. A appears to increase for larger k values, as excess pore water pressures at the pile tip decrease due to flow towards the negative excess pore pressures at the pile head.
- Parameter C drastically decreases with k, as pore water flows faster towards the area around the pile head that exhibits dilation, hence suppressing the associated negative excess pore pressures and decreasing ultimate soil resistance.

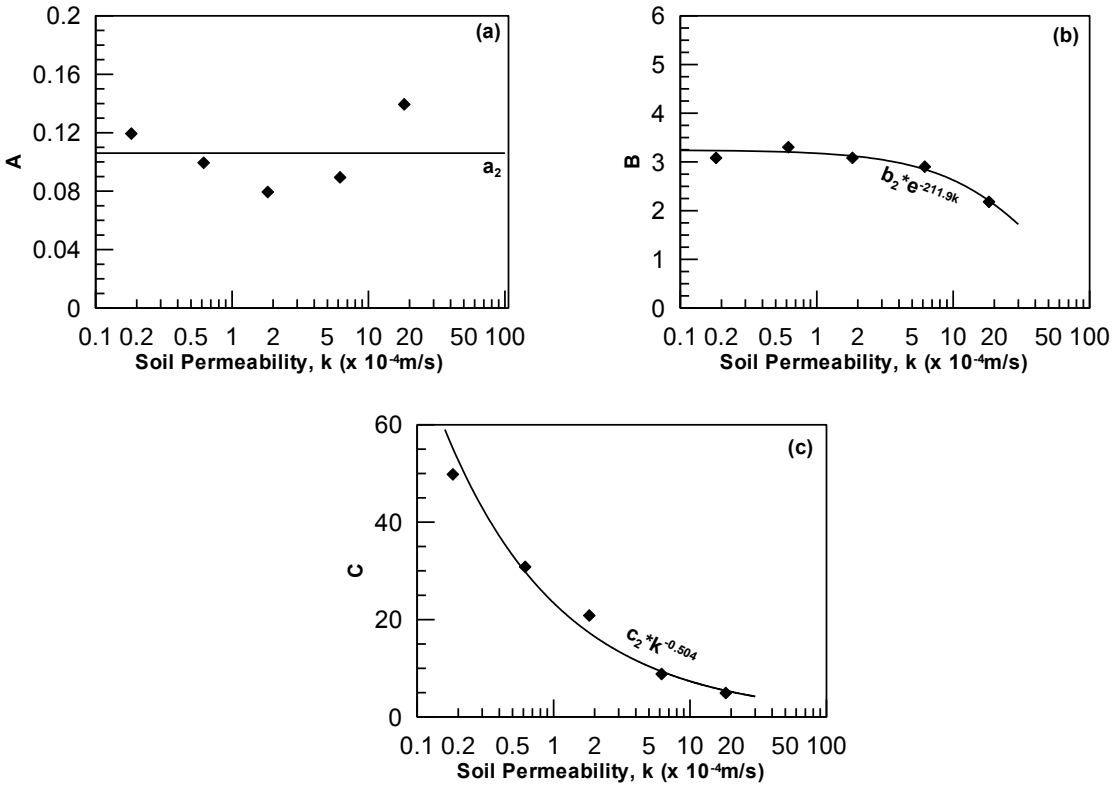

Figure 9.3: Variation of parameters A, B and C with soil permeability.

The **effect of excitation period T** is shown in **Figure 9.4**. It can be observed that this effect resembles grossly the effect of soil permeability, as both T and k affect the response in terms of drainage conditions. Namely:

- Parameter A increases with T. For liquefied soils, residual strength is not a function of excitation period. However as the latter increases, water has more time to flow towards the ground surface and the pile head during each loading cycle, hence excess pore pressures are dissipated more rapidly causing soil resistance to increase.
- Parameter C decreases with T. Similarly to soil permeability, as the excitation period increases, water has more time to flow towards the area near the pile with large dilation, suppressing the corresponding large negative excess pore pressures. As a result soil pressures are decreased.

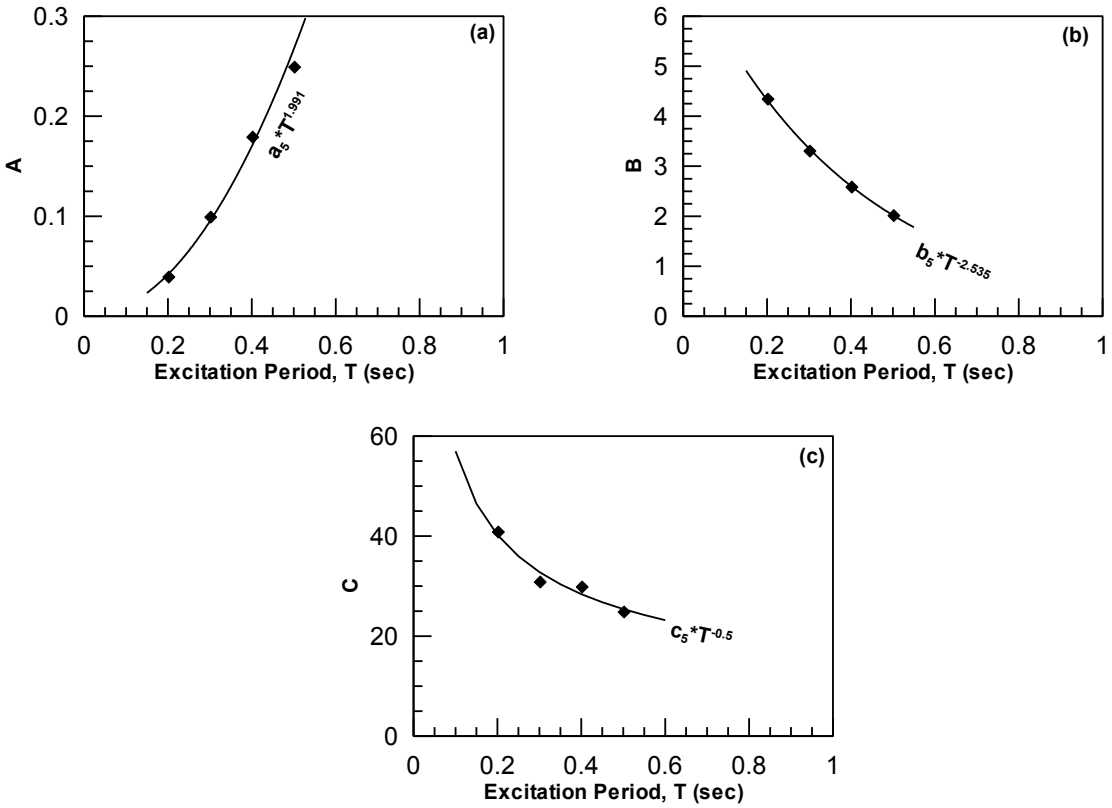

Figure 9.4: Variation of parameters A, B and C with excitation period, T.

The **effect of pile bending stiffness EI** is illustrated in **Figure 9.5,** where the following can be observed:

- Parameter A is not affected by EI. The residual strength of liquefied soils is obviously not influenced by the bending stiffness of the pile, as the relative pile – soil movement is minimized at the base of liquefied soil layer.
- The effect on parameter C is ambiguous. Following strictly the data points in this figure, it is observed that soil resistance near the surface initially increases with EI but subsequently decreases after reaching a peak value. The following can be speculated with regard to this effect: (a) Very flexible piles practically follow the movement of the soil, yielding small relative pile-soil displacements, and, hence small dilation and small soil resistance. (b) As the flexural stiffness of the pile increases, pile-soil relative displacements increases leading to the development of negative excess pore pressures and increased soil resistance. (c) After a certain EI value, i.e. for very stiff piles, relative displacement are again is reduced due to "pinning effects" causing the soil pressure to decrease again.

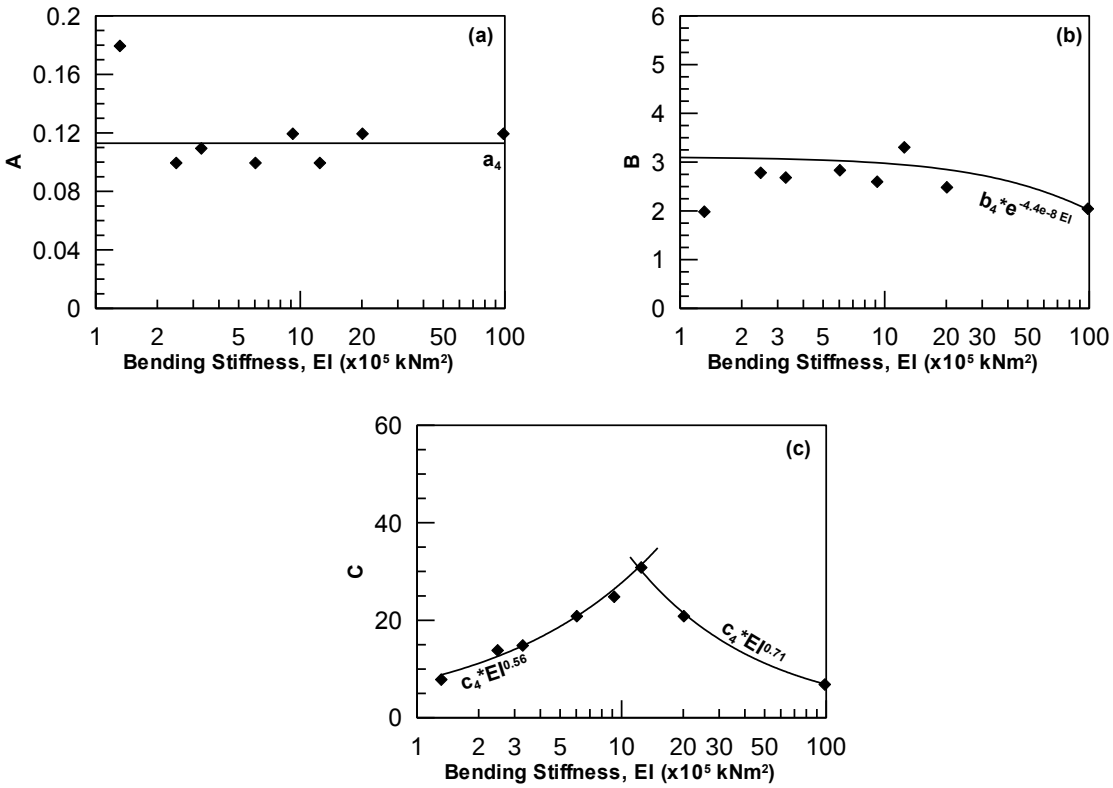

Figure 9.5: Variation of parameters A, B and C with bending stiffness, EI.

The **effect of pile diameter D** is illustrated in **Figure 9.6**. Note that this effect is not easy to interpret, as it is well known that pile diameter is associated with scale effects and may affect soil pressures even in dry soils. Namely:

- Parameter A appears to increase with pile diameter. The variation is not very significant between the D=0.4 and D=0.6m case, but A obtains a much higher value for D=1.0m. In order to explain this response it is necessary to go back to the physical meaning attributed to A. By definition, A corresponds to the normalized resistance at σ'_{vo}=98.1kPa, i.e. at a depth of about z≈5.0m. For all analyses presented so far, at the specific depth of z=5.2m (z/D = 8.67 ÷ 13.00) soil response was contractive, with values of excess pore pressure ratio close to unity. Hence, the physical meaning attributed to A was that of soil's residual strength at a state of liquefaction. As shown in **Figure 9.7**, this is not the case for the analysis with D=1.0m. More specifically, this figure shows the variation of excess pore pressure ratio with depth for all three (3) pile diameters. Note that the three (3) curves end up at different depths, as the analyses were performed by scaling all mesh dimensions according to the variation of the diameter. It can be observed that at the depth of z=5.12m

(corresponding to σ'_{vo}=1atm) where A is obtained, the excess pore pressure ratio r_u for the D=0.4m and D=0.6m case is indeed close to unity and consequently A reflects the residual strength of the liquefied soil. However, for the D=1.0m case, r_u is well below zero, indicating that at the specific depth response is still dilative. For this case, A does not correspond to the residual strength of the liquefied soil, but to the strength at a state of dilation and negative excess pore pressures development, thus explaining why A for D=1.0m is significantly increased.

- Parameter C also increases with pile diameter, D. Again, this trend may be readily explained observing **Figure 9.7**. Namely, as diameter increases dilation phenomena become more intense, with excess pore pressures becoming more negative near the pile head. This response causes soil resistance to increase. However, the reasons for this more dilative response cannot be easily clarified, and a possible explanation cannot only be based on speculation. For instance, as diameter increases the length of drainage paths also increases, causing the dissipation of pore pressures to evolve much more slowly. Also, the increase in the thickness of the sand layer (as described earlier, all mesh dimensions were scaled based on the change in diameter), resulted in larger free field displacements and possibly larger pile-soil relative displacements. This increase in relative displacement could explain a more dilative response of the soil. In any case, the effect of pile diameter, as well as scale effects in general, deserve further studied.

Finally, it should be noted that the above observations agree with the experimental data by Rollins et al. (2007) who report that liquefied soil pressure increased with pile diameter.

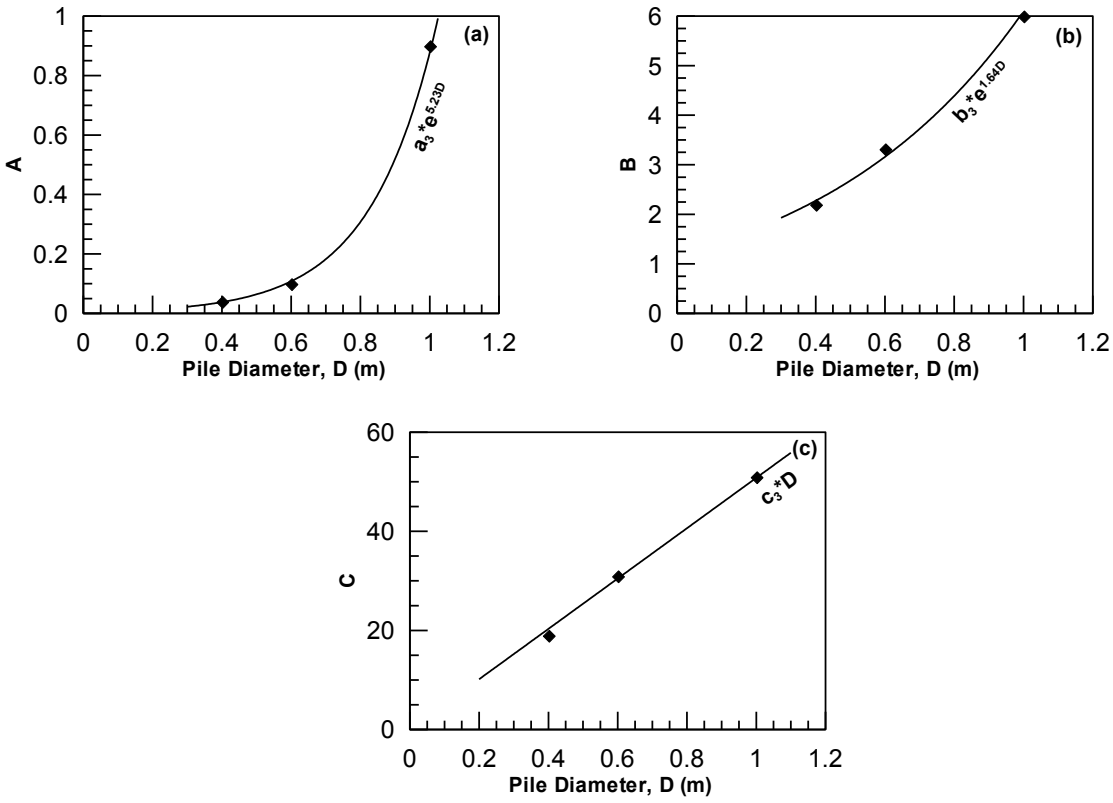

Figure 9.6: Variation of parameters A, B and C with pile diameter, D.

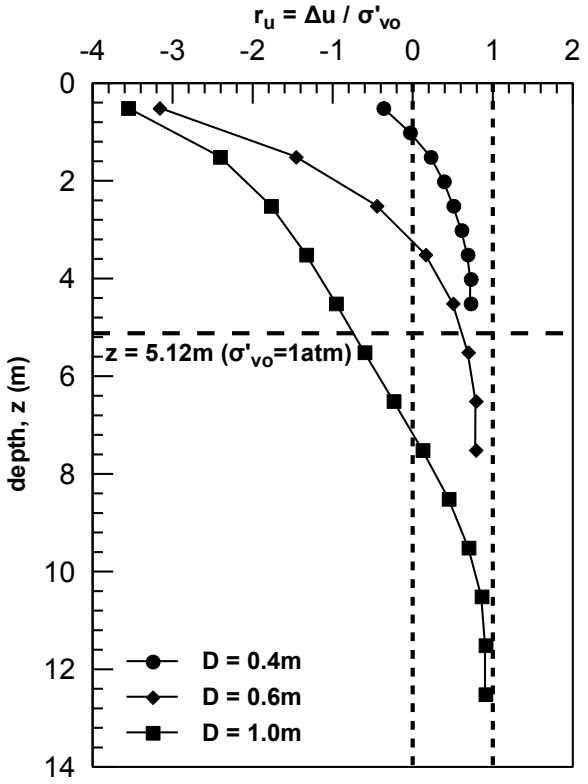

Figure 9.7: Variation of excess pore pressure ratio, r_u, with depth for the analyses with different diameters.

Finally, it was investigated whether the effect of the parameters that control drainage conditions can be combined in a single parameter. For this purpose, in **Figure 9.8** variation of A, B and C is plotted with respect to the composite nondimensional term (kT/D). The figure indicates that no specific trend is observed for parameters A and B. However, for the case of parameter C, i.e. the maximum value of soil pressure near the ground surface as a result of dilation and negative excess pore pressure generation, it is clearly shown that as kT/D increases the value of C drastically decreases, while the data form a narrow band which can be expressed by means of a power relationship.

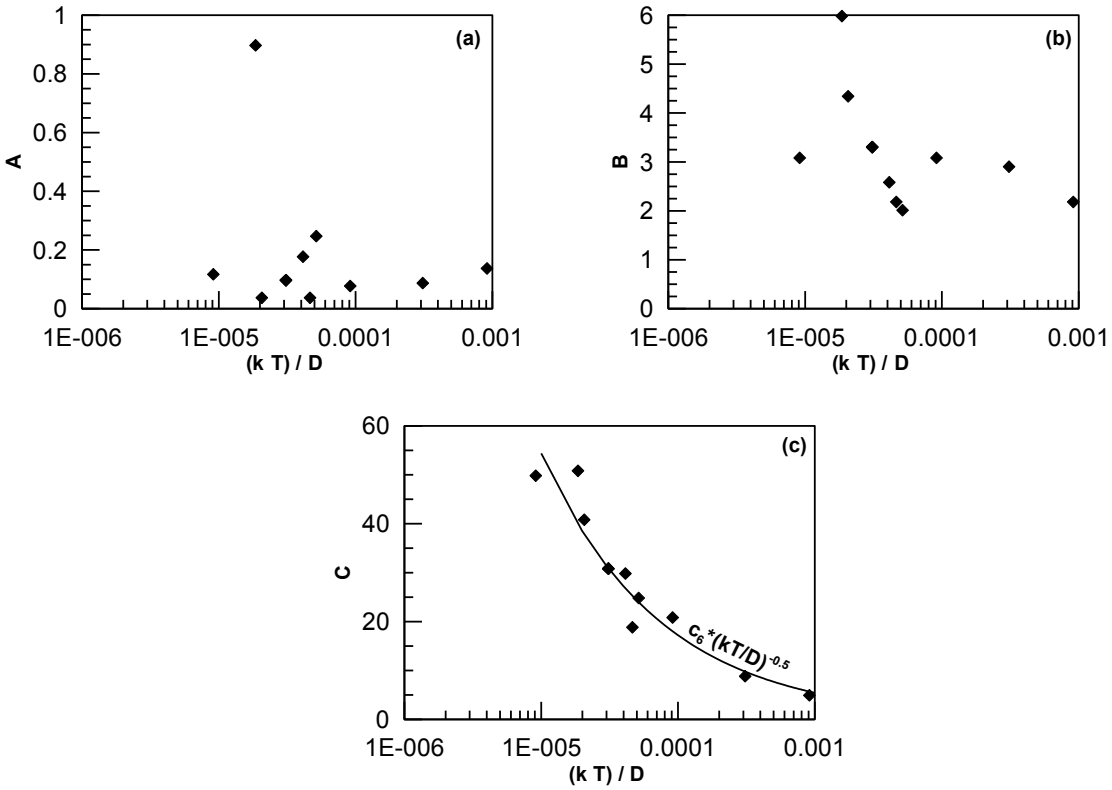

Figure 9.8: Variation of parameters A, B and C with the composite parameter (kT/D) that accounts for drainage effects.

Empirical expressions for A, B and C were subsequently obtained following an extensive multivariable statistical analysis of the data in Table 9.1. The resulting relations for free head - drilled piles are the following:

$$A = 0.0013 \cdot D_r \cdot e^{5.2D} \cdot T^2 \tag{9.2}$$

$$B = 27 \cdot D_r^{-0.6} \cdot e^{1.6D} \cdot \mathrm{e}^{-4.4 \cdot 10^{-8} \cdot EI} \cdot e^{-2.5T} \cdot e^{-212k} \tag{9.3}$$

$$C = 0.9 \cdot D_r^{-0.8} \cdot \min\left[\ EI \cdot 10^{-5} \ ^{0.6}, 24.1 \cdot \ EI \cdot 10^{-5} \ ^{-0.7} \right] \cdot \left(\frac{k \cdot T}{D} \right)^{-0.5} \qquad (9.4)$$

where:

D_r: Relative Density (%)

D: Pile Diameter (m)

T: Excitation Period (sec)

EI: Bending Stiffness (kNm^2)

k: Soil Permeability (m/sec)

The following corrections apply for driven piles, as well as for piles with displacement or rotation constrained heads:

$$\begin{aligned} A_{fixed-head} &= A_{no-rotation} = A_{free-head} \\ A_{driven} &= A_{drilled} \end{aligned} \qquad (9.5)$$

$$\begin{aligned} B_{fixed-head} &= B_{no-rotation} = B_{free-head} \\ B_{driven} &= 0.86 \cdot B_{drilled} \end{aligned} \qquad (9.6)$$

$$\begin{aligned} C_{fixed-head} &= 0.5 \cdot C_{free-head} \\ C_{no-rotation} &= C_{free-head} \\ C_{driven} &= 0.67 \cdot C_{drilled} \end{aligned} \qquad (9.7)$$

Equations (9.1) through (9.7) provide a complete set of empirical relations for the estimation of ultimate soil resistance in laterally spreading soils, which accounts for all major soil, pile and excitation characteristics. The overall accuracy of these relations is evaluated in **Figure 9.9a** where analytical predictions are compared to numerical predictions from all parametric analyses. Furthermore, **Figure 9.9b** presents the corresponding relative error, expressed as the ratio numerical over empirical prediction of $p_{ult,liq}/(\sigma'_{vo}D)$.

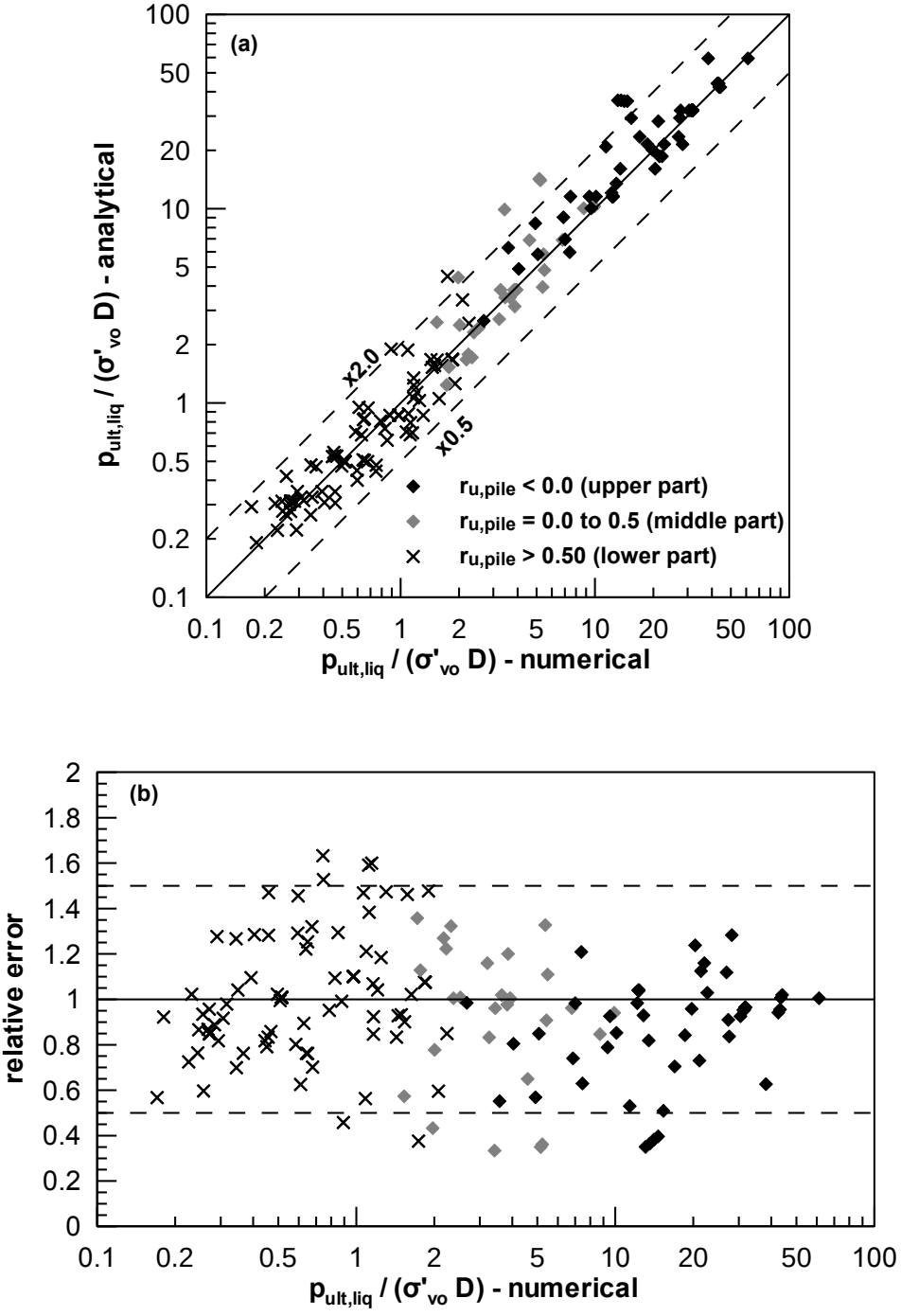

Figure 9.9: Comparison between numerical results and analytical predictions in terms of normalized ultimate soil resistance, $p_{ult,liq}/(\sigma'_{vo}D)$.

As shown in the figures, comparison is demonstrated separately for areas with large dilation ($r_{u,pile}<0$), which takes place at the upper part of the pile, areas of partial liquefaction ($0<r_{u,pile}<0.5$), which takes place at middle elevations, and, finally, areas where significant pore pressure build-up occurs ($r_{u,pile}>0.50$), which takes place at the lower part of the pile. The agreement between empirical and numerical predictions is

consistent for the entire range of the data, while the relative error for approximately 95% of the data points is less than 50%.

9.3 Soil resistance in terms of relative soil-pile displacement

Given the accuracy and simplicity (no iterative procedure for pile displacement estimation is required) of the methodology developed so far, the attempt for a second correlation between soil resistance and relative pile displacement, as described in the beginning of the paragraph, is of little practical interest. However, it is of significant theoretical interest, as it will further verify the basic mechanisms that control excess pore pressure generation and, in extent, ultimate soil resistance.

In order to introduce the relative displacement to the empirical relations, the y_{rel}/L was related in **Figure 9.10** with the same pile and soil parameters as the ultimate soil resistance. Following the same procedure as for A, B and C, the resulting expression for y_{rel}/L becomes:

$$\begin{aligned} y_{rel,\max}/L &= 50.95 \cdot D_r^{-1.375} \cdot e^{-1.28D} \cdot e^{5.78e-8 \cdot EI} \cdot T^{1.51} \cdot k^{0.03} \\ y_{rel,\max}/L &= 50.95 \cdot D_r^{-1.375} \cdot e^{-1.28D} \cdot e^{5.78e-8 \cdot EI} \cdot e^{4.51T} \cdot e^{62.66k} \end{aligned} \quad (9.8)$$

where:

$y_{rel,max}$: Maximum relative displacement of the pile

L: Length of the pile

The equation for y_{rel} is presented in two (2) alternative forms, which are differentiated with regard to the correlation for soil permeability and excitation period. In the first form, a power equation is employed, while in the second an exponential. This is necessary only for mathematical purposes, as the specific parameters are correlated with constants B and C with exponential and power functions respectively. Therefore, in order to introduce y_{rel} in both equations for B and C, two (2) different expressions should be developed. For the same reason an exponential function is used to describe the relation between y_{rel} and EI, despite the fact that a much more accurate equation (e.g. power) could be employed.

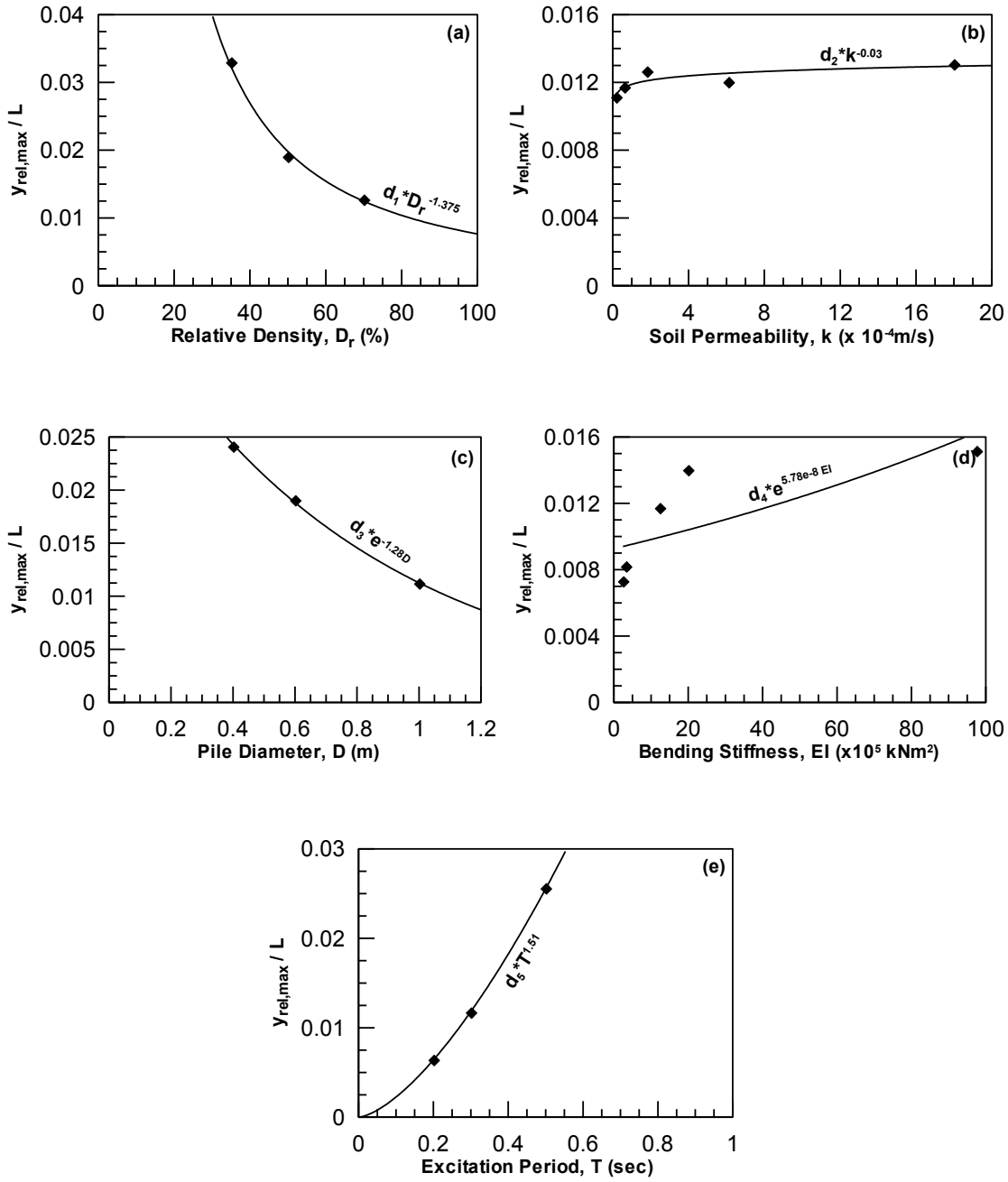

Figure 9.10: Variation of maximum pile displacement normalized by pile length ($y_{p,max}$/L) with (a) Relative Density, (b) Soil Permeability, (c) Pile Diameter, (d) Pile Bending Stiffness and (e) Excitation Period.

As a next step, y_{rel} is introduced into the expressions for A, B and C based on the following logic: Among the various parameters examined, the only one that affects relative displacement without influencing any other of the pore pressure generation mechanisms is the bending stiffness of the pile. For instance, relative density influences both displacement and dilative response of the soil, pile diameter affects both pile displacement and length of drainage paths. Hence, EI in the empirical

relationships was replaced in terms of y_{rel}/L and the following expressions were finally derived for parameters B and C:

$$B = 53.53 \cdot D_r^{-1.71} \cdot e^{0.67D} \cdot e^{0.895T} \cdot e^{-164.3k} \cdot \left(y_{rel,\max} / L \right)^{-0.76} \quad (9.9)$$

$$C = 4760 \cdot D_r^{-3.782} \cdot e^{-1.072D} \cdot T^{2.343} \cdot k^{-0.444k} \cdot \left(y_{rel,\max} / L \right)^{-2.076} \quad (9.10)$$

Equation (9.2) for parameter A, does not involve EI, hence it remains unaffected.

The comparison between numerical results and analytical predictions with equations (9.2), (9.9) and (9.10) is shown in **Figure 9.10a** for the whole set of numerical analyses. Also plotted, in **Figure 9.10b**, is the relative error in relation to the analytically predicted values of $p_{ult,liq}/(\sigma'_{vo}D)$. Note that equations (9.9) and (9.10) were applied by using the relative displacement values obtained from the numerical analyses.

It may be observed that the new empirical relations, in terms of the relative pile displacement, are equally accurate, with 94% of the data points exhibiting less than 50% relative error. In addition, and possibly more important, this fairly good agreement verifies the hypotheses stated earlier with regard to the mechanisms which control the ultimate pile resistance, i.e.:

- Ultimate soil resistance is controlled by all parameters that affect excess pore pressure build-up near the pile.
- The latter is largely influenced by the shear strain imposed to the soil as a result of the relative pile–soil displacement. This causes the soil to exhibit dilative response, especially near the surface, where significant negative excess pore pressures and large values of ultimate soil resistance develop.

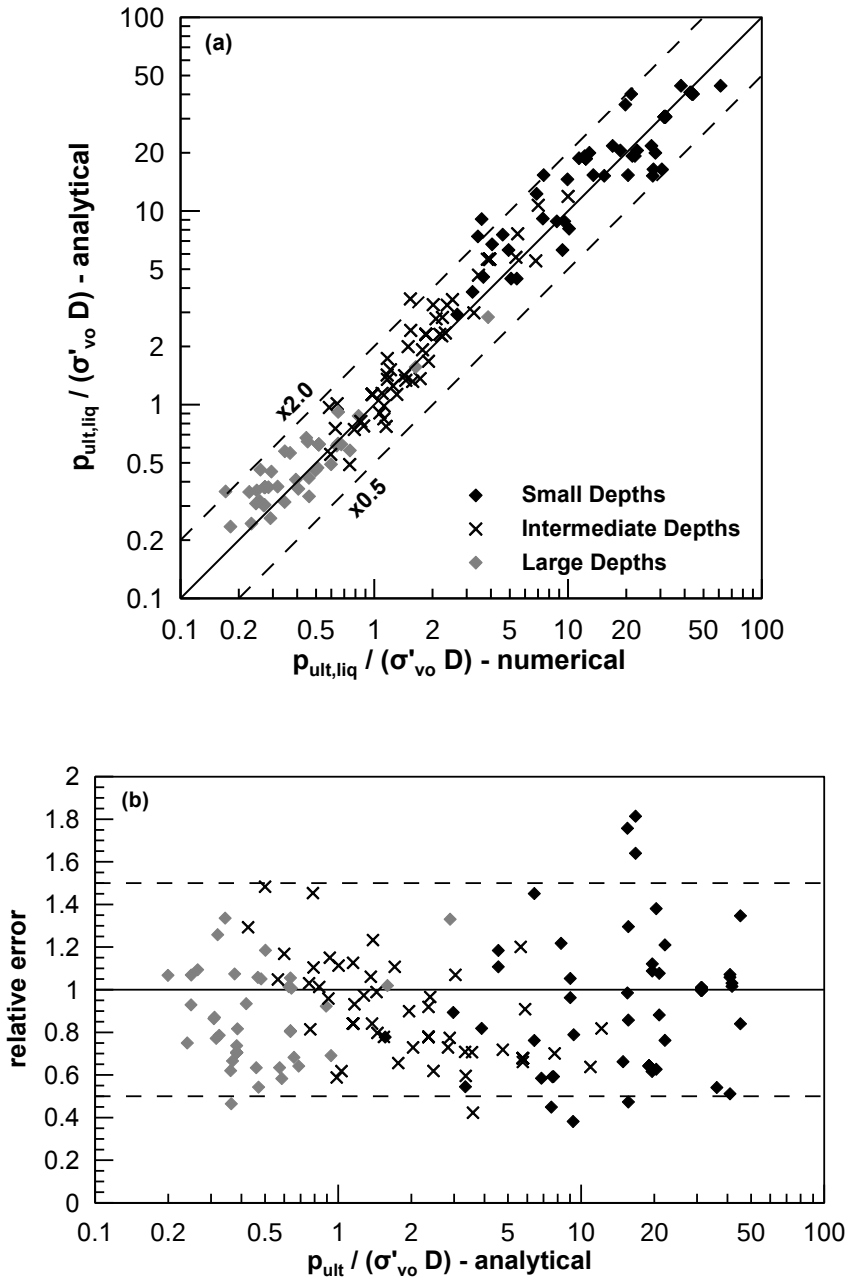

Figure 9.11: Comparison between numerical results and analytical predictions in terms of normalized ultimate soil resistance, $p_{ult,liq}/(\sigma'_{vo}D)$.

9.4 Comparison against existing empirical relations

9.4.1 Overview of existing empirical relations

The previously proposed empirical relations for ultimate soil resistance are evaluated with respect to existing empirical relations (guidelines, as well as, recent recommendations) by various researchers. The methodologies considered have been already thoroughly described in Chapter 2. However, their basic assumptions and equations are also repeated herein for convenience.

Brandenberg et al. (2007) performed pseudo-static p-y analyses to back-analyze the results of a set of dynamic centrifuge tests (Brandenberg et al. 2005). The tests involved single piles and pile groups embedded in inclined soil formations, which included both liquefiable and non-liquefiable layers. It should also be noted that in all centrifuge tests water was used as pore fluid.

The response of the liquefied sand was modeled using the p-y curves included in the API (1993) guidelines multiplied with a reduction factor to account for liquefaction effects:

$$p = m_p \tanh\left(\frac{k_{ini} z}{p_{ult}} y_{rel}\right) \tag{9.11}$$

where:

p: Soil Reaction

y_{rel}: Relative displacement between the soil at the free field and the pile

z: Depth from ground surface

k_{ini}: Gradient of initial subgrade modulus

p_{ult}: Ultimate soil resistance for firm soil

m_p: p-multiplier to account for liquefaction effects

From the above quantities, p_{ult} is calculated, in terms of pile diameter D, buoyant weight of the soil γ' and friction angle φ, as follows:

$$p_{ult} = A \cdot \min\begin{cases} C_1 z + C_2 D \ \gamma' z \\ C_3 D \gamma' z \end{cases} \tag{9.12}$$

where:

$$\begin{aligned} C_1 &= 0.115 \cdot 10^{0.0405\varphi} \\ C_2 &= 0.571 \cdot 10^{0.022\varphi} \\ C_3 &= 0.646 \cdot 10^{0.0555\varphi} \end{aligned} \tag{9.13}$$

Furthermore, parameter A is expressed as:

$$A = \begin{cases} 3 - 0.8\dfrac{z}{D} \geq 0.9 & \text{for static loading} \\ 0.9 & \text{for dynamic loading} \end{cases} \tag{9.14}$$

The gradient of initial subgrade modulus, k_{ini}, is calculated through the graph shown in **Figure 9.12**, as a function of the Relative Density or the friction angle of the soil, while in the API (1993) it is assumed that it remains constant with depth. However, in their work, Brandenberg et al. (2007), argue that this assumption results in overestimated values of k_{ini} especially for large depths, and propose the following correction:

$$k_{ini}^{*} = k_{ini}\sqrt{\frac{\sigma'_{ref}}{\sigma'_{v}}} \tag{9.15}$$

where:

k^{*}_{ini}: Corrected gradient of initial subgrade modulus

σ'_{ref}: Reference state at which k_{ini} was calibrated, taken as 50kPa

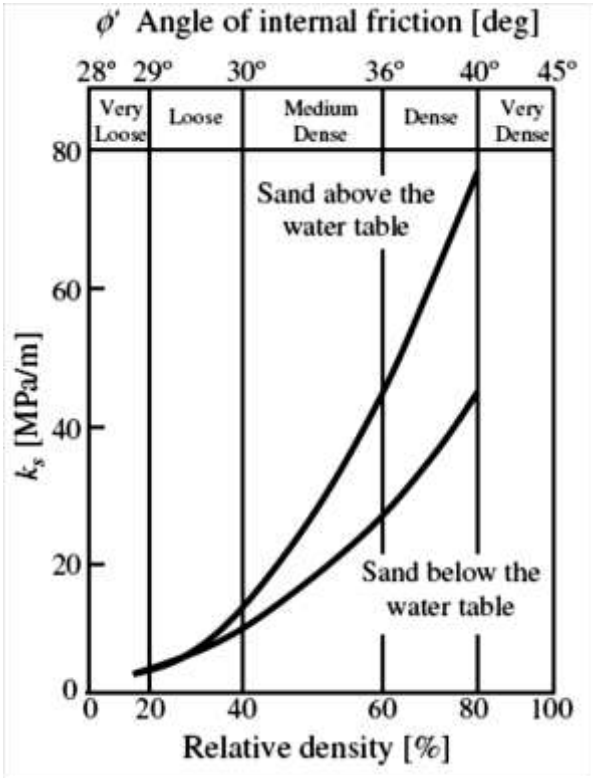

Figure 9.12: Calculation of gradient of initial subgrade modulus according to API (1993)

Finally, the reduction multiplier, m_p, is estimated from **Figure 9.13**, in terms of the SPT blow count for clean sands, $(N_1)_{60\text{-cs}}$. An average value for m_p, shown with the dashed line in the figure can be obtained by the following empirical equation:

$$m_p = 0.00036 \cdot \left[N_{1\ 60-cs} \right]^2 + 0.0009 \cdot N_{1\ 60-cs} + 0.05 \tag{9.16}$$

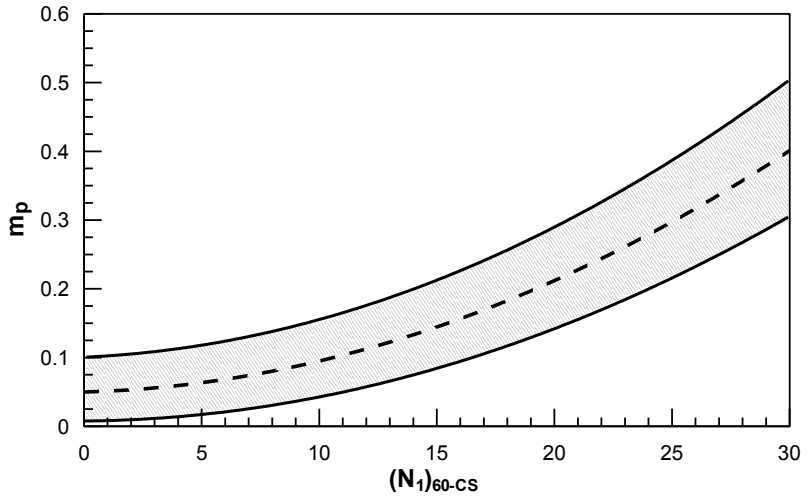

Figure 9.13: Reduction multiplier after Brandenberg et al. (2007)

Cubrinovski and Ishihara (2004, 2007) based on the results of large shaking table tests proposed a bilinear model for the p-y response of liquefied soil, expressed as follows:

$$p = \beta_2 \cdot k_2 \cdot D \cdot y_{rel} \le p_{ult} \tag{9.17}$$

where:

k_2: Subgrade reaction coefficient

β_2: Stiffness degradation factor

For the subgrade reaction coefficient k_2, the Authors adopt the expression incorporated in the recommendations for Design of Building Foundations (AIJ, 2001) calculated as follows:

$$k_2 = 56000 \ N_{1\ 60-CS} \ D^{-3/4} \tag{9.18}$$

Note that in the above expression k_2 is in kN/m^3 and the pile diameter is in cm. Degradation factor β_2 is evaluated through the diagram shown in **Figure 9.14** as a function of the lateral ground displacement at the top of the liquefied layer.

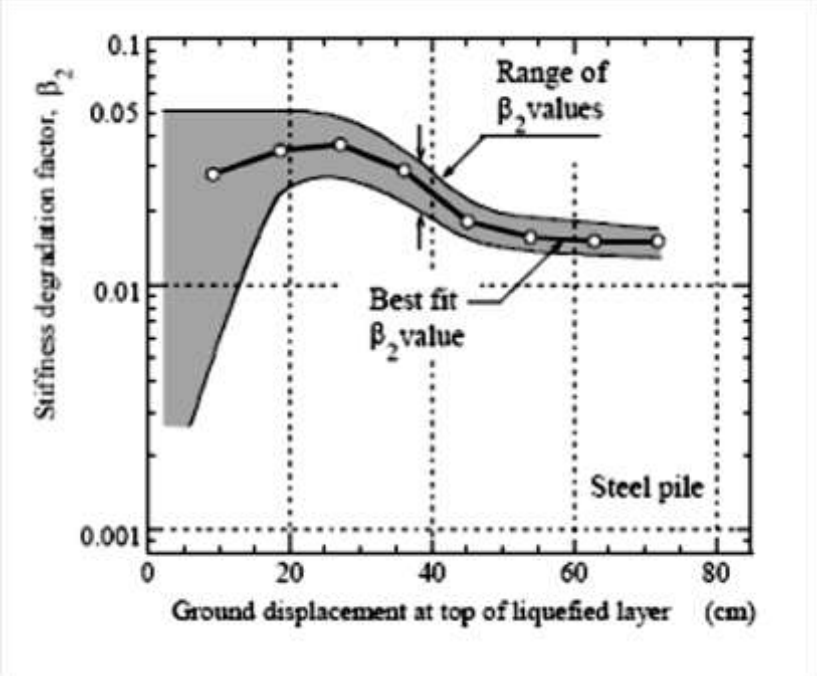

Figure 9.14: Degradation of stiffness in liquefied soils undergoing lateral spreading (Cubrinovski and Ishihara, 2007)

Finally, the ultimate resistance is expressed in terms of the residual shear strength, $S_{u,res}$ of the liquefied soil:

$$p_{ult} = S_{u,res} D \tag{9.19}$$

Among the various expressions for $S_{u,res}$, the authors recommend that proposed by Seed and Harder (1991):

$$S_{u,res} = 0.14 \cdot \left[N_{1\ 60-cs} \right]^2 \tag{9.20}$$

Tokimatsu and Suzuki (2009), following the observations from full scale shaking table tests on piles subjected to lateral spreading displacements, proposed the following assumptions for the p-y response of liquefied sands:

$$p = \frac{2 \cdot \beta \cdot k_{ho}}{1 + |y_{rel} / y_l|} \cdot D \cdot y_{rel} \qquad (9.21)$$

where:

k_{ho}: Reference value for coefficient of subgrade reaction calculated according to equation (9.18)

β: Stiffness degradation factor

y_l: Reference value of y_{rel}

For the estimation of scaling factor β, the authors adopt the recommendations included in the guidelines of the Design of Building Foundations (AIJ, 2001), in which β is related to the SPT blow count of the soil and the depth, as shown in **Figure 9.15**.

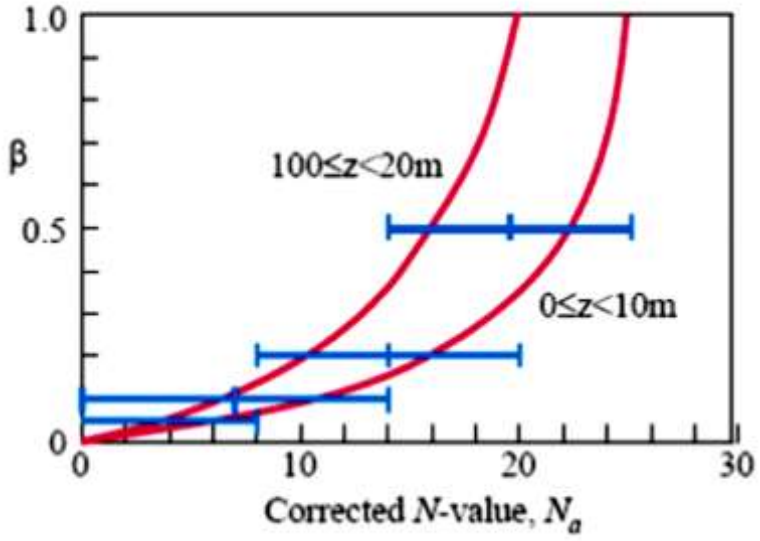

Figure 9.15: Scaling factor for the initial stiffness and the ultimate soil resistance of liquefied soils (AIJ, 2001)

For very large values of y_{rel}, equation (9.21) yields an ultimate maximum value, p_{max} that is equal to:

$$p_{ult} = 2 \cdot \beta \cdot k_{ho} \cdot D \cdot y_l \qquad (9.22)$$

In addition, the authors adopt the assumption that the ultimate soil resistance of the liquefied soil can be calculated using Brom's equation for firm soil multiplied by β:

$$p_{ult} = \beta \cdot 3 \cdot K_p \cdot \sigma'_{vo} \cdot D \tag{9.23}$$

Combining equations (9.22) and (9.23) the following expression can be obtained for y_1:

$$y_l = \frac{3 \cdot K_p \cdot \sigma'_{vo}}{2 \cdot k_{ho}} \tag{9.24}$$

Gonzalez et al. (2009) performed centrifuge experiments which were thoroughly described in previous chapters, as part of the evaluation of the numerical methodology. In short six (6) tests were performed, two (2) of which involved single piles in laterally spreading soil. In both tests a L=8m long and of D=0.6m diameter pile of EI=9000kNm^2 was considered built in a 6m thick Nevada Sand liquefiable layer, overlaying a 2m thick layer of cemented sand. In the first test the pore fluids were saturated with water resulting in high permeability values, while in the second with metulose yielding low permeability.

Based on the results of the tests the authors back-calculated the value of the limit pressure imposed on the pile by the surrounding soil. It was concluded that a good approximation for the limit pressure for both tests was a value of p_{lim}=11.5kPa, uniform along the pile. For the case of the high permeability test, it was assumed that this pressure is applied on the foundation, as shown in **Figure 9.16a**. However, for the low permeability test this pressure was assumed to act on a wider area (shown in **Figure 9.16b**), which has the shape of an inverted cone and includes both the foundation and part of the soil surrounding it. This is to account for the large dilation and the soil stiffening observed in that area.

Expressing the above limit pressure in terms of load per unit length of the pile (so that it can be compared to all previous methodologies), and considering piles of uniform diameter (the effect of dilation is taken into account by increasing the value of limit pressure), the following expressions for ultimate resistance are obtained:

$$p_{ult} = 6.9kN/m \text{ for the high permeability model} \tag{9.25}$$

$$p_{ult} = \begin{cases} 52.9 - 23z, & 0 \le z \le 2m \\ 6.9, & z \ge 2m \end{cases} \text{ for the low permeability model} \tag{9.26}$$

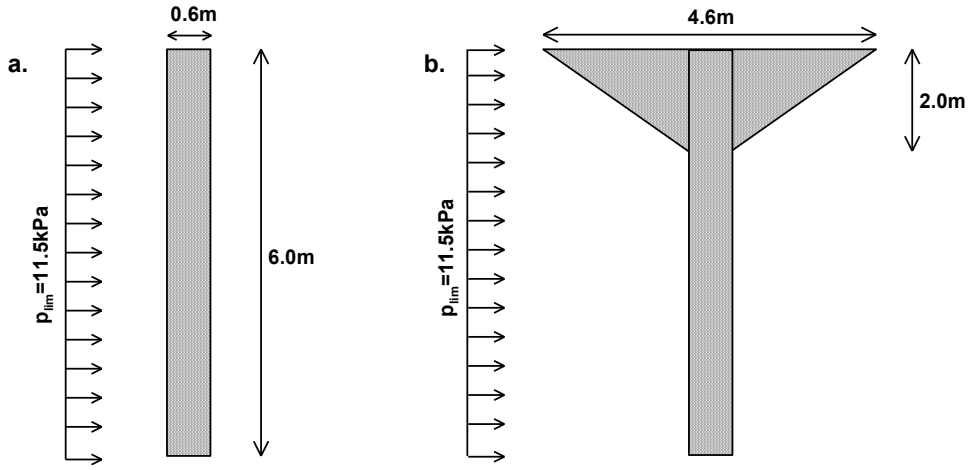

Figure 9.16: Limit pressures on piles built in laterally spreading soils: (a) High permeability test (b) Low permeability test (Gonzalez et al., 2009)

However, it should be noted that, compared to the methodologies presented previously, the above predictions by Gonzalez et al. (2009) are based on tests where the Relative Density of the soil was constant and equal to D_r=40%. Hence, their generalization to other relative densities is questionable.

9.4.2 Comparison of proposed and existing empirical relations

From the previous qualitative comparison between the proposed and the existing empirical relations and guidelines for subgrade p-y reaction of liquefied soils, it becomes evident that existing means for pile design overlook the possible increase in ultimate soil pressure close to the ground surface, due to the dilation of the liquefied ground. To evaluate the consequences of this omission on the bending moments and the pile displacements, all previous methodologies were applied to a reference case, which involves an L=8m long and D=0.6m diameter concrete pile, with bending stiffness EI=190000kNm^2. It is installed within an 8m thick uniform Nevada sand layer with a relative density of D_r=50%. The friction angle of the soil was taken equal to φ=33^o and the buoyant weight as γ'=9.81kN/m^3. Two (2) values were considered for the permeability coefficient of the sand:

- k=6.1e-5 m/s
- k=3.05e-3 m/s

In the first case, typical of a fine sand or silt-sand mixture, dilation effects are expected to be significant, since dissipation of excess pore pressures progresses slowly. In the second case, typical of a coarse sand or sand-gravel mixtures, excess

pore pressures are quickly dissipated, and hence, dilation effects are expected to be minimal. In addition, it was assumed that the excitation has a period T=0.30sec. Finally, the equivalent SPT blow count for this soil was estimated as $(N_1)_{60\text{-}cs}$=11 based on the empirical relation by Tokimatsu and Seed (1987):

$$N_{1\ 60-cs} = 44 \cdot D_r^2 \tag{9.27}$$

At first, the predictions of the various methodologies are compared in terms of normalized ultimate resistance with depth in **Figure 9.17**. Note that all existing methodologies do not account for permeability effects, hence predictions do not differentiate for small and large values of k. For the recommendations by Gonzalez et al. (2009), which are also included in the figure, it should be further stressed that they concern different pile and soil properties (i.e. D_r=40%, EI=9000kN^2, T=0.50sec) and may not be directly relevant to the example case study. In addition, two (2) curves have been drawn for the method proposed by Brandenberg et al.: one for the lower and the other for the upper bound value of m_p=0.050 and 0.165 respectively. Finally, for Suzuki and Tokimatsu, the degradation factor β was taken equal to β=0.097 based on **Figure 9.15**.

A careful inspection of existing empirical relations reveals the following differences:

- Brandenberg et al. assume that ultimate load increases with depth, hence their method yields small loads near the surface and large at the lower parts of the pile.
- Cubrinovski and Ishihara assume that soil resistance decreases with depth, hence they yield larges loads near the surface. This approach seems to agree with the experimental findings by Gonzalez et al., however, as stated earlier, the latter correspond to specific pile and soil properties and cannot be generalized.
- Finally, Suzuki and Tokimatsu assume that $p_{ult,liq}$/ (σ'_{vo} D) does not vary with depth, while their predictions appear to lay around the middle of the other analytical predictions.

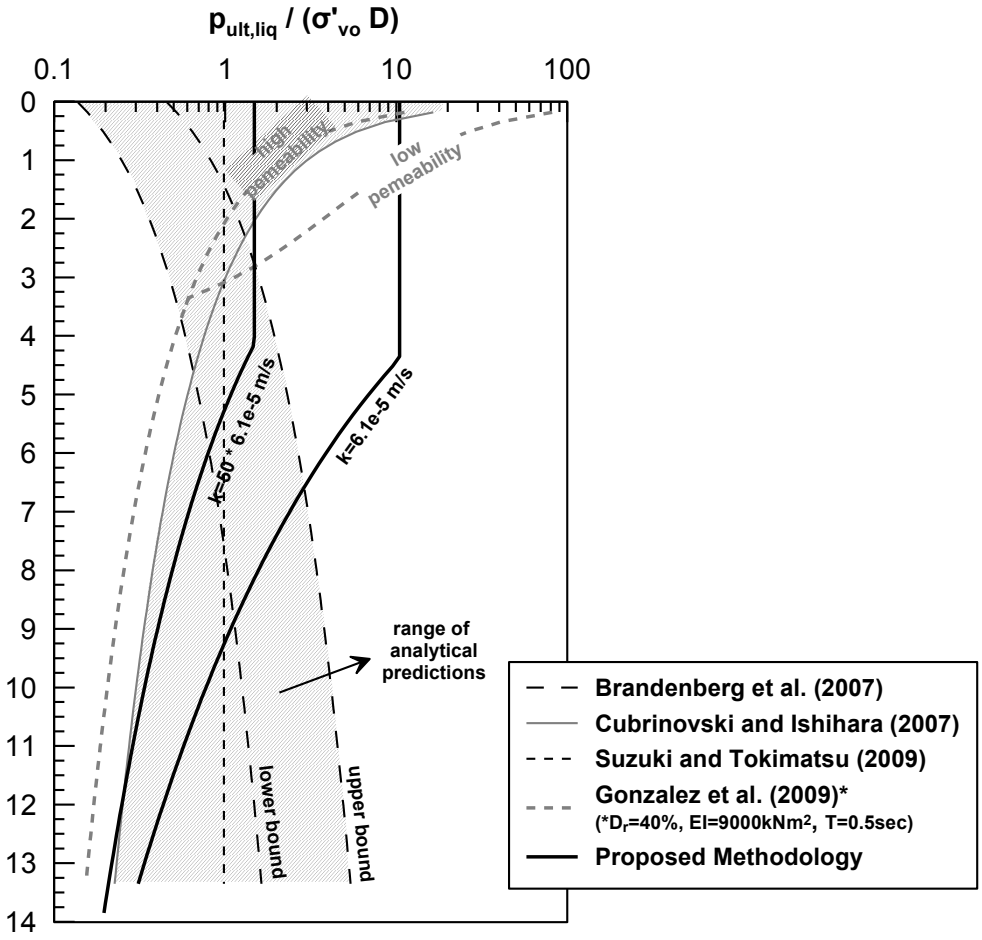

Figure 9.17: Comparison between various methodologies of the normalized ultimate soil resistance with depth for low and high soil permeability.

In addition, the following may be observed with regard to the suggestions by Gonzalez et al.:

- They agree well with the above methods only when dilation phenomena do not take place, i.e. for: (a) large depths and (b) the case where the permeability of the soil is large.
- For the low permeability soil, their loads are significantly larger and fall out of the range produced by the existing methods. The differences are very large close to the surface, where dilation phenomena are more intense.
- As for the load distribution with depth, they suggest that it decreases with depth, being in line with the recommendations by Cubrinovski and Ishihara

However, it should be reminded that these observations are only indicative of the gross response, as they concern very specific pile and soil properties.

Coming next to the proposed methodology, the following can be concluded:

- For cases where large dilation is not expected to occur (medium and large depths, large permeability), predictions with the proposed methodology fall within the range of existing methodologies.
- However, for the case of severe dilation (small depths and low permeability), loads imposed on the pile drastically increase and approximately become ten (10) times larger.

In short, the comparison for the reference case presented herein reveals that existing methods are in good terms with the proposed only for the case where large dilation phenomena do not occur. In the opposite case, where large negative pore pressures develop near the ground surface, existing methods significantly underestimate the loads imposed on the pile by the soil.

In order to investigate whether the above statement can be generalized to a much wider range of soil, pile and excitation properties, **Figure 9.18** shows an one-to-one comparison between all results of the numerical analyses and the corresponding analytical predictions after applying the method by Cubrinovski and Ishihara. The latter was selected among the existing, as it is the only one that predicts decrease of ultimate resistance with depth, i.e. a trend that coincides with the numerical estimates. Since all numerical results are included in the figure, comparison covers a very wide range of pile and soil characteristics. Again the data points are divided in three (3) groups depending on the development of excess pore pressure near the pile, as obtained from the numerical analyses:

- $r_{u,pile} < 0$, which occurs at the upper part of the pile
- $r_{u,pile} = 0.0$ to 0.5, which occurs at the middle part of the pile
- $r_{u,pile} > 0.5$, which occurs at the lower part of the pile.

The comparison shown in this figure further supports the statement drawn previously, i.e. that existing methodologies are in good agreement with the numerical results and the proposed equations only for cases where the response of the soil is not dilative. More specifically, the analytical predictions are close to the numerical ones only at the $r_{u,pile}>0.5$ area, where the soil is close to liquefaction. As the response gradually becomes more dilative ($r_{u,pile}$ = 0.0 to 0.50), analytical predictions yield smaller loads compared to the numerical analyses. Finally, the deviation is maximum when large dilation ($r_{u,pile} < 0$) takes place, i.e. at the upper part of the pile.

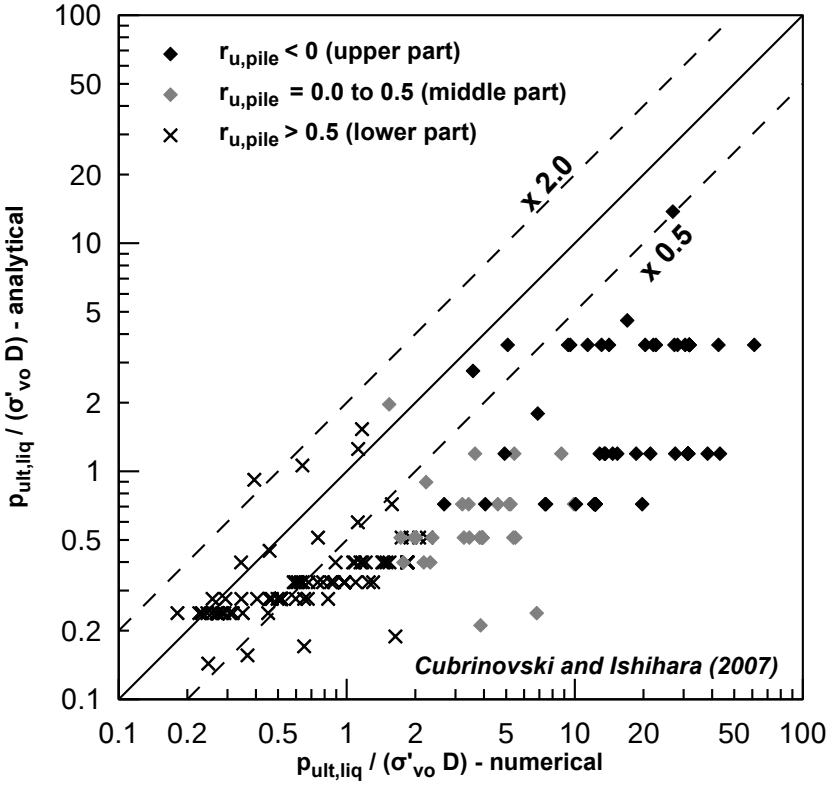

Figure 9.18: Comparison between numerical results and the analytical predictions by Cubrinovski et al. (2007)

In order to evaluate the effects of dilation on the response of the pile, the reference case was analyzed by means of a pseudo-static p-y analysis. The analysis was performed with the finite element code ANSYS v.13. The 8m long pile was modeled with sixteen (16) linear elastic beam elements, assigned a diameter D=0.60m and the elastic properties of concrete, i.e. Young's modulus E=30GPa and Poisson's ratio v=0.20, yielding a flexural stiffness EI=190000kNm^2. The base of the model was rigidly supported, i.e. all translational and rotational degrees of freedom were constrained.

Soil-structure interaction was modeled with horizontal nonlinear p-y springs attached along the pile. The springs were attached on the beam elements on one end, and fixed on the other. Their response was determined based on the four (4) analytical methodologies described before. The input parameters for each methodology have been defined previously. Note that for the method by Cubrinovski and Ishihara (2007) three (3) analyses were performed for values of the stiffness degradation factor β_2=0.02, 0.035 and 0.05. However, in all three (3) cases the

ultimate soil resistance was reached early during loading, and hence the results of the different analyses coincide.

Finally, demands from the laterally spreading soil were presented by imposing free-field displacements at the fixed end of the springs. For the purpose of the present analysis, the displacements imposed were the ones obtained from the basic numerical analysis with FLAC3D. As shown in **Figure 9.1**, the maximum applied displacement at the soil surface is approximately 20cm and decreases with depth following grossly a sinusoidal shape.

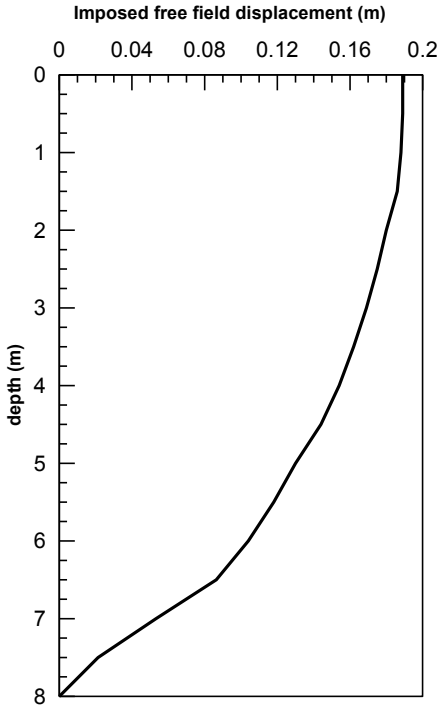

Figure 9.19: Displacement variation applied at the fixed ends of the soil springs for the p-y analysis.

The results from these analyses are shown in **Figure 9.20a** and **Figure 9.20b,** in terms of pile displacements and bending moments respectively. The comparison between the various methodologies leads to the following observations:

- All existing methodologies are in fairly good agreement as the range of their predictions is relatively small. Namely, maximum pile displacement ranges between 3 and 8cm, and maximum bending moment from 300 to 1300kNm.
- For the case of high permeability (negligible dilation), the predictions with the proposed methodology are similar to the predictions with the existing

methodologies. Namely, the maximum displacement and bending moment of the pile is 3.5cm and 300kNm respectively.

- For the case of low permeability (large dilation phenomena), existing methods appear to underestimate pile response, as both displacements and bending moments significantly increase, yielding values which are approximately 5.0 to 5.5 times larger.

Overall, the pseudo-static analysis reveals that existing methodologies do not capture the effects of dilation, which can be detrimental on the response of the pile and should not be neglected in the design.

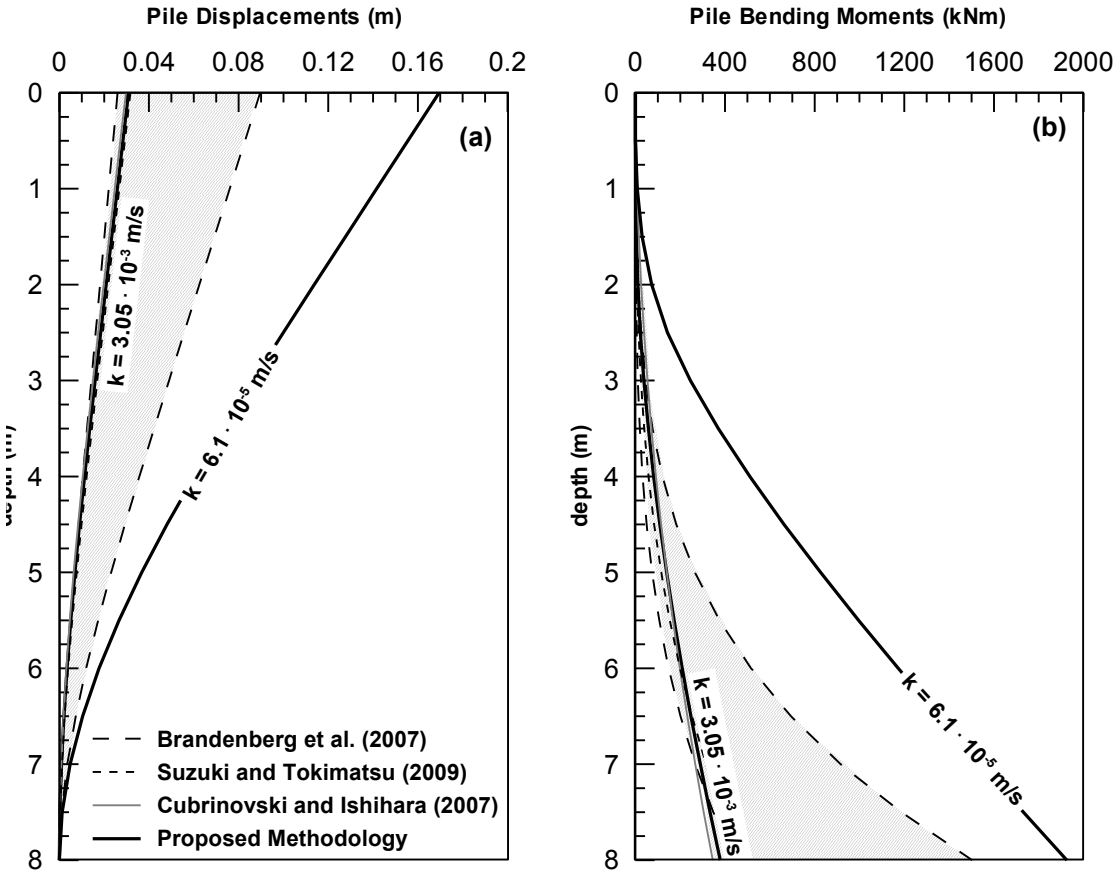

Figure 9.20: (a) Pile Displacements and (b) Bending Moments for different p-y methodologies as obtained from the pseudo-static analysis.

10

Conclusions

10.1 Summary of main points

As posed in the introduction, the scope of the present Thesis was to develop a consistent and rational methodology for the design of piles in cohesionless soils, undergoing lateral ground movements. Both the case of non-liquefied (dry) and liquefied soil was considered. Towards this direction, two (2) main objectives were pursued. The first was to develop and verify a three-dimensional numerical methodology for the simulation of pile response in cohesionless soils undergoing horizontal kinematic loads, with emphasis upon large kinematic loads due to ground lateral spreading. The second objective was to use this methodology for the parametric investigation of the mechanisms that govern the interaction between the pile and the liquefied soil, and also to develop simple relationships for the p-y curves of the laterally moving ground required in a BNWF analysis of the pile response.

Both these objectives were achieved. Namely:

a. A numerical methodology was developed for the simulation of drilled piles in cohesionless non-liquefied soils, under horizontal kinematic loading. The methodology is based on the implementation by Karamitros (2010) of the bounding surface model NTUA_Sand (Papadimitriou and Bouckovalas, 2002; Andrianopoulos et al., 2010) in the finite difference code FLAC3D. The methodology incorporates all the necessary numerical features required to capture the basic response patterns of the problem, such as slip and separation interface elements, as well as a special subroutine written in FLAC's built-in programming language FISH, which allows for the direct numerical calculation of p-y curves. Sensitivity analyses were performed in order to verify the various assumptions adopted in the analysis (mesh size and discretization, interface

properties, e.t.c.), while the overall accuracy of the proposed methodology was ensured through comparison against results from centrifuge tests, as well as existing empirical relationships.

b. The aforementioned methodology was further extended in order to capture the changes that occur to the stress state of the soil as a result of open-end or close-end pile driving, namely the formation of a passive wedge at small depths and the expansion of a cylindrical cavity at medium to large depths.

   In order to capture these patterns, Vesic's analytical methodology for the problem of cylindrical cavity expansion was programmed and implemented in the analysis through a FISH function, thus, allowing for the manual implementation of the modified stresses due to pile driving. The various parameters included in Vesic's equations (mainly the volumetric response of the soil) were calibrated through a series of parametric analyses that examined the cylindrical cavity expansion of the various soil slices along the pile. After the FISH function is called (just before the execution of the p-y analysis) the kinematic inconsistency at the surface (passive wedge vs. cavity expansion) is identified by the code, leading to the development of upward displacements and the formation of the passive wedge in order to establish equilibrium.

   The accuracy of this semi-analytical procedure was verified based on results from numerical analyses that fully simulated the problem of pile installation in sands. It was observed that the proposed methodology decreases drastically the computational cost, with negligible effects on the accuracy of the predictions.

c. Before focusing upon the kinematic interaction between the pile and the laterally spreading liquefied ground, an extensive parametric investigation was performed regarding the kinematic interaction between the pile and the dry non-liquefiable soil. The investigation concerned the effects of soil relative density, pile diameter and pile type and led to the development of specific design recommendations for the estimation of the p-y curves for piles in cohesionless soils subjected to horizontal ground movements. The proposed recommendations suggest that additional parameters, such as the type of the pile (drilled or driven) may affect the response and should not be neglected in the pile design. Furthermore, they present specific deviations from currently available and widely used similar empirical approaches. Based on a limited number of

additional analyses that considered the case of external static loads applied on the pile head, it was found that these deviations are mainly due to the fact that existing methods have been developed for the latter loading case, and not for kinematic loads due to ground displacements.

d. The aforementioned numerical methodology was then extended in order to simulate pile response to large ground displacements due to liquefaction-induced lateral spreading. A major innovation that had to be introduced to the methodology was the development of a new type of free field boundary conditions for inclined ground. The new concept is based on the well-known tied known formulation, but is properly adjusted in order to account for the hydrostatic pore pressure surplus that is created at the downslope free field boundary of the infinite slope.

   Numerical predictions were evaluated through comparison with well-documented recent centrifuge experiments. The agreement was remarkable and verified the accuracy of the applied methodology both in quantitative terms, as well as, in terms of response patterns and mechanisms.

e. The numerical model was consequently utilized for the extensive parametric investigation of piles undergoing large kinematic loads from laterally spreading ground. Initially the results of the analyses were used to gain insight to the physical mechanisms that govern the response, with special emphasis placed on the development of the limiting (ultimate) soil reaction. It was thus found that the latter is a unique function of the average excess pore pressure ratio ($r_{u,pile}$) developed around the pile. Namely, for typical pile, soil and excitation conditions, large negative excess pore pressure ratios may develop near the ground surface, as a result of dilation of the liquefied soil that flows around the pile. Excess pore pressure ratios increase algebraically with depth, reaching unity at large depths where the relative ground-to-pile movement is negligible and field liquefaction prevails over soil dilation. As a result, effective stresses and soil pressures may become large close to the ground surface and decrease with depth.

f. No matter how fundamental is the excess pore pressure development for the pile response, its identification is of little practical importance since $r_{u,pile}$ is rather difficult to predict by simple means. This is because it does not coincide with the excess pore pressure ratio of the liquefied free field soil (i.e. $r_{u,ff} \approx 1.0$), but it is

strongly affected by three at least complex mechanisms: (a) The in situ stress and volumetric state, (b) drainage conditions and (c) magnitude of imposed shearing due to the relative ground-to-pile displacement. In view of the above objective limitation in the estimation of $r_{u,pile}$, interpretation of the results led to the development of empirical relationships for the direct estimation of ultimate soil resistance in terms of soil, pile and excitation parameters. The basic characteristic of the proposed equations is that they capture the effects of soil dilation and negative excess pore pressure generation at small depths near the pile, which result in increased values for the soil pressure. These effects are not predicted by any of the existing empirical methodologies, despite that they lead to significantly increased pile displacements and bending moments and cannot be overlooked by any design practice.

10.2 Recommendations for future research

This Thesis draws upon a robust numerical methodology that has been developed over the last decade in the Geotechnical Division of NTUA that allows to approach and thoroughly investigate complicated geotechnical problems involving static or dynamic loading, large displacements and earthquake-induced liquefaction. Numerous verifications against element and model tests, including the ones presented in this Thesis, has shown that this methodology offers qualitative as well quantitative accuracy, at a readily affordable computational cost, so that we can now plan for "numerical experiments" (as opposed to laboratory or field experiments).

In this context, the present Thesis examined the problem of single, laterally loaded piles in cohesionless soil, and drew conclusions both of theoretical and practical interest that have been overlooked in a number of previous elaborate experimental investigations. It is worth to continue in the same direction, considering the following new topics of practical interest:

a. The response of **pile groups** subjected to lateral ground movements of dry soil is an issue that deserves to be further addressed, for dry as well as for liquefied soil conditions. Research could focus on two (2) objectives:
   - Many studies point out that a critical head-to-head distance exists, above which no interaction between the piles occurs. Hence, at a first stage, a series

of analyses should be performed, in order to provide an accurate estimate for this critical distance.

- Furthermore, for close-spaced piles soil resistance is reduced as a result of "shadowing" effects, a term used to describe the overlapping of shear zones from neighboring piles. Hence, at a second stage a systematic investigation should be performed to quantify these "shadowing effects" for different pile group formations, and pile head constraints.

b. The problem of single pile response should be re-examined for the case where a **non-liquefiable layer (e.g. clay crust)** lays on top of the liquefiable sand. This case, which is very commonly met in practice, has been investigated in the past through centrifuge experiments, which have provided valuable insight mainly on the loads imposed on the pile by the crust. Therefore, it is of particular importance to focus on the p-y response of the sand and on whether the mechanisms observed for the case of not overlying crust, still apply (e.g. intense dilation and large loads at the upper level of the sand layer).

c. **Superstructure effects** (e.g. from a bridge pier) should be evaluated through fully coupled dynamic analyses of the combined pile-soil-structure system. The analysis should primarily focus on the response of the structure (i.e. the loads transmitted to the structure as a result of both pore pressure build-up in the soil and pile-soil interaction), as well as, on how the reaction of the liquefied soil is affected by the presence of the structure. Emphasis should also be placed on the critical combination of inertial and kinematic loads that should be considered in a pseudo-static analysis of the structure.

d. Finally, another topic that may be seen as extension of this Thesis, is the simulation of the pile-soil-structure interaction by means of a **dynamic p-y relationship**. Development of such relationships is essential for the analysis of pile-soil interaction in cases of firm or liquefied level ground formations where the nature of loading is purely cyclic, contrary to the case of laterally moving ground where the permanent component of displacement prevails over the transient.

   In dynamic p-y methods pile-soil interaction should be modeled using macro-elements which include spring, dashpot and, when necessary (e.g. presence of clay layers), gap elements. Only a very limited number of such studies has been published so far with respect to the formulation of the soil and the dashpot

element. In general, a monotonic p-y curve is considered for the soil springs, in combination with a hysteretic parameter to capture the cyclic response, while the common practice is to implement existing theories for radiation damping for computing the characteristics of the dashpots.

It is therefore evident that, for firm soils, formulation of soil springs incorporates all the uncertainties involved in p-y curves for non-liquefied soils. The same applies to liquefied soils, where the research with respect to the p-y response for level ground conditions is very limited. Also, calibration of the hysteretic parameter should be based on experimental data and/or relevant numerical analyses, which for the time being are also very limited. Finally, while the assumption for radiation damping seems rational for firm soils, this might not be the case for the case of liquefaction, where the mechanisms of energy absorption might be different.

11

References

Abdoun, T., Dobry, R., O'Rourke, T. D., and Goh, S. H. (2003). "Pile response to lateral spreads: Centrifuge modeling." *Journal of Geotechnical and Geoenvironmental Engineering*, Dept. of Civil Engineering, Rensselaer Polytechnic Institute, Troy, NY 12180-3590, United States, 129(10), pp. 869-878.

Abdoun, T., and Dobry, R. (2002). "Evaluation of pile foundation response to lateral spreading." *Soil Dynamics and Earthquake Engineering*, Department of Civil Engineering, Rensselaer Polytechnic Institute, Troy, NY 12180, United States, 22(9-12), pp. 1051-1058.

Acar, Y. B., and El-Tahir, E.-T. A. (1986). "LOW STRAIN DYNAMIC PROPERTIES OF ARTIFICIALLY CEMENTED SAND." *Journal of geotechnical engineering*, Louisiana State Univ, Baton Rouge,, LA, USA, Louisiana State Univ, Baton Rouge, LA, USA, 112(11), pp. 1001-1015.

American Petroleum Institute. (2007). *Recommended Practice for Planning, Designing and Constructing Fixed Offshore Platforms - Working Stress Design*. Washington, D.C.

Andrianopoulos, K. I. (2006). "Numerical Modeling of Static and Dynamic Behavior of Elastoplastic Soils." PhD Thesis, Dept of Civil Engineering, NTUA, Athens.

Andrianopoulos, K. I., Papadimitriou, A. G., and Bouckovalas, G. D. (2010). "Explicit integration of bounding surface model for the analysis of earthquake soil liquefaction." *International Journal for Numerical and Analytical Methods in Geomechanics*, Geotechnical Department, School of Civil Engineering, National Technical University of Athens, Athens, Greece, 34(15), pp. 1586-1614.

Andrianopoulos, K. I., Papadimitriou, A. G., and Bouckovalas, G. D. (2010). "Bounding surface plasticity model for the seismic liquefaction analysis of geostructures." *Soil Dynamics and Earthquake Engineering*, Department of Geotechnical Engineering, School of Civil Engineering, National Technical University of Athens, Greece, 30(10), pp. 895-911.

Arulanandan, K., and Sybico Jr, J. (1993). "Post-liquefaction settlement of sands." *Predictive soil mechanics. Proc. of the Wroth memorial symposium, Oxford, 1992*, (H. G.T. and S. A.N., eds.), Thomas Telford, pp. 94-110.

Arulmoli, K., Muraleetharan, K. K., Hossain, M. M., and Fruth, L. S. (1992). "VELACS: verification of liquefaction analyses by centrifuge studies; Laboratory Testing Program – Soil Data Report." *Research Report, The Earth. Technology Corporation*.

Ashford, S. A., Juirnarongrit, T., Sugano, T., and Hamada, M. (2006). "Soil-pile response to blast-induced lateral spreading. I: Field test." *Journal of Geotechnical and Geoenvironmental Engineering*, Department of Structural Engineering, University of California, La Jolla, CA 92093-0085, United States, 132(2), pp. 152-162.

Ashour, M., and Norris, G. (2000). "Modeling lateral soil-pile response based on soil-pile interaction." *Journal of Geotechnical and Geoenvironmental Engineering*, ASCE, ASCE, 126(5), pp. 420-428.

Ashour, M., and Norris, G. (2003). "Lateral loaded pile response in liquefiable soil." *Journal of Geotechnical and Geoenvironmental Engineering*, Civil Engineering Dept., Univ. of Nevada, Reno, NV 89557, United States, 129(5), pp. 404-414.

Assimaki, D., and Varun, V. (2009). "Nonlinear macroelements for performance-based design of pile-supported waterfront structures in liquefiable sites." *Computational Methods in Structural Dynamics and Earthquake Engineering*, M. Papadrakakis, N. D. Lagaros, and M. Fragiadakis, eds., Rhodes, Greece.

Badoni, D., and Makris, N. (1996). "Nonlinear response of single piles under lateral inertial and seismic loads." *Soil Dynamics and Earthquake Engineering*, Dept. of Civ. Eng. and Geol. Sci., University of Notre Dame, Notre Dame, IN 46556, United States, 15(1), pp. 29-43.

Balakrishnan, A. (2000). "Liquefaction remediation at a bridge site." PhD dissertation. Davis: University of California.

Basu, P., Loukidis, D., Prezzi, M., and Salgado, R. (2011). "Analysis of shaft resistance of jacked piles in sands." *International Journal for Numerical and Analytical Methods in Geomechanics*, Department of Civil and Environmental Engineering, Pennsylvania State University, University Park, PA 16802, United States, 35(15), pp. 1605-1635.

Berger, E., Lysmer, J., and Seed, H. B. (1975). *ALUSH, a computer program for seismic response of axisymmetric soil-structure systems*. EERC, University of California Berkeley.

Bigoni, D., and Laudiero, F. (1989). "The quasi-static finite cavity expansion in a non-standard elastoplastic medium." *International Journal of Mechanical Sciences*, 31(11), pp. 825-837.

Bouc, R. (1971). "Modele mathematique d' hysteresis." *Acustica*, 21, pp. 16-25.

Bouckovalas, G. D. (1981). "Prediction Methods for stresses around piles." MSc Thesis, Massachusetts Institute of Technology.

Boulanger, R. W., Chang, D., Brandenberg, S. J., Armstrong, R. J., and Kutter, B. L. (2007). "Seismic design of pile foundations for liquefaction effects." *Earthquake Geotechnical Engineering*, K. Pitilakis, ed., Springer, pp. 277-302.

Boulanger, R. W., Chang, D., Gulerce, U., Brandenberg, S. J., and Kutter, B. L. (2006). "Evaluating pile pinning effects on abutments over liquefied ground." *Geotechnical Special Publication*, B. R.W. and T. K., eds., ASCE, United States, pp. 306-318.

Boulanger, R. W., Curras, C. J., Kutter, B. L., Wilson, D. W., and Abghari, A. (1999). "Seismic soil-pile-structure interaction experiments and analyses." *Journal of Geotechnical and Geoenvironmental Engineering*, ASCE, Dept. of Civ. and Envir. Engrg., Univ. of California, Davis, CA 95616, United States, 125(9), pp. 750-759.

Bowles, J. K. (1995). *Foundation Analysis and Design*. McGraw-Hill Science/Engineering/Math.

Brandenberg, S. J., Boulanger, R. W., Kutter, B. L., and Chang, D. (2005). "Behavior of pile foundations in laterally spreading ground during centrifuge tests." *Journal of Geotechnical and Geoenvironmental Engineering*, Dept. of Civil and Environmental Engineering, Univ. of California, Davis, CA 95616, United States, 131(11), pp. 1378-1391.

Brandenberg, S. J., Boulanger, R. W., Kutter, B. L., and Chang, D. (2006). "Observations and analysis of pile groups in liquefied and laterally spreading ground in centrifuge tests." *Geotechnical Special Publication*, B. R.W. and T. K., eds., ASCE, United States, pp. 161-172.

Brandenberg, S. J., Boulanger, R. W., Kutter, B. L., and Chang, D. (2007). "Static pushover analyses of pile groups in liquefied and laterally spreading ground in centrifuge tests." *Journal of Geotechnical and Geoenvironmental Engineering*, Dept. of Civil and Environmental Engineering, Univ. of California at Los Angeles, Los Angeles, CA 90095, United States, 133(9), pp. 1055-1066.

Brandenberg, S. J., Boulanger, R. W., Kutter, B. L., and Chang, D. (2007). "Liquefaction-induced softening of load transfer between pile groups and laterally spreading crusts." *Journal of Geotechnical and Geoenvironmental Engineering*, Dept. of Civil and Environmental Engineering, Univ. of California at Los Angeles, Los Angeles, CA 90095-1593, United States, 133(1), pp. 91-103.

Bransby, M. F. (1996). "The difference between load transfer relationships for laterally loaded pile groups: Active p-y or passive p-delta." *Journal of Geotechnical and Geoenvironmental Engineering*, 122(12), pp. 1015-1033.

Brinch-Hansen, J. (1961). "The Ultimate Resistance of Rigid Piles Against Transversal Forces." *Bulletin No. 12, Geoteknisk Institut (The Danish Geotechnical Institute)*, pp. 5-9.

Broms, B. B. (1964). "The Lateral Resistance of Piles in Cohesive Soils." *ASCE Journal of the Soil Mechanics and Foundations DivisionsJournal of the Soil Mechanics and Foundations Divisions1*, 90(3), pp. 27-63.

Broms, B. B. (1964). "Lateral Resistance of Piles in Cihesionless Soils." *ASCE Journal of the Soil Mechanics and Foundations DivisionsJournal of the Soil Mechanics and Foundations Divisions*, 90(3), pp. 126-156.

Brødbæk, K. T., Møller, M., and Sørensen, S. P. H. (2009). *Review of p-y relationships in cohesionless soil*.

Butterfield, R., and Banerjee, P. K. (1970). "The effect of pore water pressures on the ultimate bearing capacity of driven piles." *2nd South East Asian Conference on Soil Engineering*, Bangkok, pp. 385-394.

Carter, D. P. (1984). "A Non-Linear Soil Model for Predicting Lateral Pile Response." *Report No. 359*, Univ. of Auckland, New Zealand.

Carter, J. P., Booker, R. J., and Yeung, S. K. (1986). "Cavity Expansion in cohesive frictional soils." *Géotechnique*, 36(3), pp. 349-358.

Chopra, A. K. (2007). *Dynamics of Structures: Theory and Applications to Earthquake Engineering*. Pearson/Prentice Hall.

Chopra, M. B., and Dargush, G. F. (1992). "Finite-element analysis of time-dependent large-deformation problems." *International Journal for Numerical & Analytical Methods in Geomechanics*, Dept. of Civil Eng., State Univ. of New York at Buffalo, Buffalo, NY 14260, USA, 16(2), pp. 101-130.

Clark, J. I., and Meyerhof, G. G. (1972). "The Behavior of Piles Driven in Clay. I. An Investigation of Soil Stress and Pore Water Pressure as Related to Soil Properties." *Canadian Geotechnical Journal*, NRC Research Press, 9(4), pp. 351-373.

Collins, I. F., Pender, M. J., and Yan, W. (1992). "Cavity expansion in sands under drained loading conditions." *International Journal for Numerical & Analytical Methods in Geomechanics*, 16, pp. 3-23.

Constantinou, M. C., and Adnane, M. A. (1987). "Evaluation of two models for yielding systems." *Report to NSF*, Dept. Civil Engineering, Drexler University.

Cooke, R. W., and Price, G. (1973). "Strains and Displacements around friction piles." *8th I.C.S.M.F.E.*, Moscow, pp. 53-60.

Cox, W. R., Reese, L. C., and Grubbs, B. R. (1974). "Field Testing of Laterally Loaded Piles In Sand." *Offshore Technology Conference, 6-8 May , Houston, Texas*, Offshore Technology Conference.

Cubrinovski, M., Kokusho, T., and Ishihara, K. (2006). "Interpretation from large-scale shake table tests on piles undergoing lateral spreading in liquefied soils." *Soil Dynamics and Earthquake Engineering*, 26(2-4 SPEC. ISS.), pp. 275-286.

Cubrinovski, M., and Ishihara, K. (2004). "Simplified method for analysis of piles undergoing lateral spreading in liquefied soils." *Soils and Foundations*, Kiso-Jiban Consultants Co., Ltd., 1-11-5 Kudan-kita, Chiyoda-ku, Tokyo 102-8220, Japan, 44(5), pp. 119-133.

Cubrinovski, M., and Ishihara, K. (2006). "Assessment of pile group response to lateral spreading by single pile analysis." *Geotechnical Special Publication*, B. R.W. and T. K., eds., ASCE, Japan, pp. 242-254.

Cubrinovski, M., and Ishihara, K. (2007). "Simplified Analysis of Piles Subjected to Lateral Spreading: Parameters and Uncertainties." *4th International Conference on Earthquake Geotechnical Engineering*, K. Pittilakis, ed., Thessaloniki, Greece.

De Alba, P., Seed, H. B., and Chan, C. K. (1976). "Sand Liquefaction in Large-Scale Simple Shear Tests." *ASCE J Geotech Eng Div*, 102(9), pp. 909-927.

Desai, C. S. (1978). "EFFECTS OF DRIVING AND SUBSEQUENT CONSOLIDATION ON BEHAVIOUR OF DRIVEN PILES." *International Journal for Numerical and Analytical Methods in Geomechanics*, 2(3), pp. 283-301.

Dobry, R., Abdoun, T., O'Rourke, T. D., and Goh, S. H. (2003). "Single piles in lateral spreads: Field bending moment evaluation." *Journal of Geotechnical and Geoenvironmental Engineering*, Dept. of Civil Engineering, Rensselaer Polytechnic Institute, Troy, NY 12180-3590, United States, 129(10), pp. 879-889.

Dobry, R., Taboada, V., and Liu, L. (1995). "Centrifuge Modeling of Liquefaction Effects During Earthquakes." *1st Intlernational Conference on Earthquake Geotechnical Engineering*, K. Ishihara, ed., Tokyo, Japan, pp. 1291-1324.

Dobry, R., and Gazetas, G. (1988). "Simple method for dynamic stiffness and damping of floating pile groups." *Geotechnique*, Rensselaer Polytechnic Inst, United States, 38(4), pp. 557-574.

Dungca, J. R., Kuwano, J., Takahashi, A., Saruwatari, T., Izawa, J., Suzuki, H., and Tokimatsu, K. (2006). "Shaking table tests on the lateral response of a pile buried in liquefied sand." *Soil Dynamics and Earthquake Engineering*, Department of Civil Engineering, Tokyo Institute of Technology, Tokyo, Japan, 26(2-4 SPEC. ISS.), pp. 287-295.

Dunnavant, W. T., and O'Neill, M. W. (1986). "Evaluation of design-oriented methods for analysis of vertical pile groups subjected to lateral loads." *Numerical Methods in Offshore Piling: 3rd International Conference, Institute Francais du Petrole, Laboratoire Central de Ponts et Chaussees, Nantes, France*, Nantes, France, pp. 303-316.

Elgamal, A., Lu, J., and Yang, Z. (2005). "Liquefaction-induced settlement of shallow foundations and remediation: 3D numerical simulation." *Journal of Earthquake Engineering*, Department of Structural Engineering, University of California, San Diego, San Diego, CA 92093, United States, 9(SPEC. ISS.), pp. 17-45.

Ersig, M. I., and Kirby, R. C. (1977). "Initial Development of a General Effective Stress Method for the Prediction of Axial Capacity for Driven Piles." *OTC, Paper No. 2942*.

Fan, C. C., and Long, J. H. (2005). "Assessment of existing methods for predicting soil response of laterally loaded piles in sand." *Computers and Geotechnics*, 32, pp. 274-289.

Fleming, W. G. K., Weltman, A. J., Randolph, M. F., and Elson, W. K. (1992). *Piling Engineering*. *Surrey University Press*, London.

Gazetas, G., and Dobry, R. (1984). "Simple Radiation Damping Model for Piles and Footings." *Journal of Engineering Mechanics*, 110(6), pp. 937-956.

Georgiadis, M., Anagnostopoulos, C., and Saflekou, S. (1992). "Centrifugal testing of laterally loaded piles in sand." *Canadian Geotechnical Journal*, NRC Research Press, 29(2), pp. 208-216.

Gerolymos, N., Escoffier, S., Gazetas, G., and Garnier, J. (2009). "Numerical modeling of centrifuge cyclic lateral pile load experiments." *Earthquake Engineering and Engineering Vibration*, Civil Engineering, National Technical University, Athens, Greece, 8(1), pp. 61-76.

Ghosh, B., and Madabhushi, S. P. G. (2003). "A numerical investigation into effects of single and multiple frequency earthquake motions." *Soil Dynamics and Earthquake Engineering*, Geotechnical Research Group, Department of Engineering, University of Cambridge, Cambridge, United Kingdom, 23(8), pp. 691-704.

Goh, S. H., and O'Rourke, T. D. (1999). "Limit State Model for Soil-Pile Interaction During Lateral Spread." *7th U.S.-Japan Workshop on Earthquake Resistant Design of Lifeline Facilities and Countermeasures Against Soil Liquefaction, Seattle, WA, August 15-17*, MCEER-99-0019, Multidisciplinary Center for Earthquake Engineering Research, University at Buffalo.

González, L. (2005). "Centrifuge modeling of permeability and pinning reinforcement effects on pile response to lateral spreading." PhD thesis, Dept. of Civil and Environmental Engineering, Rensselaer Polytechnic Institute,Troy, NY, USA.

González, L., Abdoun, T., and Dobry, R. (2006). "Effect of soil permeability on centrifuge modeling of pile response to latehal spreading." *Geotechnical Special Publication*, B. R.W. and T. K., eds., Rensselaer Polytechnic Institute, Troy, NY, United States, pp. 50-60.

González, L., Abdoun, T., and Dobry, R. (2009). "Effect of soil permeability on centrifuge modeling of pile response to lateral spreading." *Journal of Geotechnical and Geoenvironmental Engineering*, Dept. of Civil Engineering, Univ. of Chile, Avda. Blanco Encalada 2002, Santiago, Chile, 135(1), pp. 62-73.

Graig, R. F. (1999). *Soil Mechanics*. E & FN Spon.

H, D., Maotian, L., Bo, L., and Rong, C. (2010). "Numerical analysis of cylindrical cavity expansion in sand considering particle crushing and intermediate principal stress." *Transactions of Tianjin University*, 16(1), pp. 68-74.

Haigh, S. K. (2002). "Effects of Liquefaction on Pile Foundations in Sloping Ground." Cambridge.

Haigh, S. K., and Madabhushi, S. P. G. (2005). "The effects of pile flexibility on pile-loading in laterally spreading slopes." *Seismic Performance and Simulation of Pile Foundations in Liquefied and Laterally Spreading Ground*, R. W. Boulanger and K. Tokimatsu, eds., University of California, Davis, CA, pp. 24-37.

Hamada, M. (1999). "Similitude law for liquefied-ground flow." *7th U.S.-Japan Workshop on Earthquake Resistant Design of Lifeline Facilities and Countermeasures Against Soil Liquefaction, Seattle, WA, August 15-17*, pp. 191-205.

Han, J. T., Kim, S. R., Hwang, J. I., and Kim, M. M. (2007). "Evaluation of the dynamic characteristics of soil-pile system in liquefiable ground by shaking table tests." *4th International Conference on Earthquake Geotechnical Engineering*, K. Pittilakis, ed., Thessaloniki, Greece.

Hardin, B. O., and Drnevich, V. P. (1972). "SHEAR MODULUS AND DAMPING IN SOILS: MEASUREMENT AND PARAMETER EFFECTS." *ASCE J Soil Mech Found Div*, 98(SM6), pp. 603-624.

He, L., Elgamal, A., Abdoun, T., Abe, A., Dobry, R., Hamada, M., Menses, J., Sato, M., Shantz, T., and Tokimatsu, K. (2009). "Liquefaction-induced lateral load on pile in a medium dr sand layer." *Journal of Earthquake Engineering*, AMEC Geomatrix, Newport Beach, CA, United States, 13(7), pp. 916-938.

Iai, S. (1991). "A strain space multiple mechanism model for cyclic behavior of sand and its application." *Earthquake Engineering Research Note No. 43*, Port and Harbor Researh Institute, Ministry of Transport, Japan.

Imamura, S., Hagiwara, T., Tsukamoto, Y., and Ishihara, K. (2004). "Response of pile groups against seismically induced lateral flow in centrifuge model tests." *Soils and Foundations*, Research Institute, Nishimatsu Construction Co., Ltd., Japan, 44(3), pp. 39-55.

Juirnarongrit, T., and Ashford, S. A. (2006). "Soil-pile response to blast-induced lateral spreading. II: Analysis and assessment of the p-y method." *Journal of Geotechnical and Geoenvironmental Engineering*, Department of Structural

Engineering, University of California, La Jolla, CA 92093-0085, United States, 132(2), pp. 163-172.

Kagawa, T., Taji, Y., Sato, M., and Minowa, C. (1997). "Soil-pile-structure interaction in liquefying sand from large-scale shaking-table tests and centrifuge tests." *Geotechnical Special Publication*, Department of Civil Engineering, Wayne State University, Detroit, MI 48202, United States, (70), pp. 69-84.

Karamitros, D. K. (n.d.). "Development of a Numerical Algorithm for The Dynamic Elastoplastic Analysis of Geotechnical Structures in Two and Three Dimensions." PhD Thesis, Dept of Civil Engineering, NTUA, Athens.

Kaynia, A. M. (1988). "Dynamic Interaction of Single Piles under lateral and seismic loads." *Esteghlal Journal of Engineering*, 6, pp. 5-26.

Kim, B. T., Kim, N.-K., Lee, W. J., and Kim, Y. S. (2004). "Experimental load-transfer curves of laterally loaded piles in Nak-Dong River sand." *Journal of Geotechnical and Geoenvironmental Engineering*, Coastal/Harbor Engineering Division, KORDI, P.O. Box 29, Ansan, Kyunggi-do, South Korea, 130(4), pp. 416-425.

Kirby, R. C., and Wroth, C. P. (n.d.). "APPLICATION OF CRITICAL STATE SOIL MECHANICS TO THE PREDICTION OF AXIAL CAPACITY FOR DRIVEN PILES IN CLAY." *Proceedings of the Annual Offshore Technology Conference*, Houston, TX, USA, 3, pp. 483-494.

Kodner, R. L. (1963). "Hyperbolic Stress-Strain Response: cohesive soils." *ASCE Journal of the Soil Mechanics and Foundations DivisionsJournal of the Soil Mechanics and Foundations Divisions*, 89(1), pp. 115-143.

Kulhawy, F. H., O'Rourke, T. D., and Landers, P. G. (1983). "GEOTECHNICAL PLANNING FOR TRANSMISSION STRUCTURES." Canadian Geotechnical Soc, Cornell Univ, Sch of Civil &, Environmental Engineering, Ithaca,, NY, USA, Cornell Univ, Sch of Civil & Environmental Engineering, Ithaca, NY, USA, pp. 135-145.

Kulhawy, F. H., Trautmann, C. H., Beech, J. F., O'Rourke, T. D., and McGuire, W. (1983). "TRANSMISSION LINE STRUCTURE FOUNDATIONS FOR UPLIFT-COMPRESSION LOADING." *Electric Power Research Institute, (Report) EPRI EL*.

Kulhawy, F. H., Trautmann, C. H., and O'Rourke, T. D. (1991). "Soil-rock boundary. What is it and where is it?" *Geotechnical Special Publication*, Publ by ASCE, Cornell Univ, Ithaca, United States, pp. 1-15.

Lee, J., Salgado, R., and Paik, K. (2003). "Estimation of load capacity of pipe piles in sand based on cone penetration test results." *Journal of Geotechnical and Geoenvironmental Engineering*, School of Civil/Environ. Engineering, Yonsei Univ., Seoul, South Korea, 129(5), pp. 391-403.

Lesny, K., and Wiemann, J. (2006). "Finite Element Modeling of Large Diameter Monopiles for Offshore Wind Energy Converters." *Geo Congress, 2006*, Atlanta, GA, USA.

Lin, S. S., Tseng, Y. J., Liao, J. C., Wang, C. H., and Lee, W. F. (2007). "Uncoupled Numerical Analysis for Ground Lateral Spread Effects on Single Pile." *4th International Conference on Earthquake Geotechnical Engineering*.

Ling, L. F. (1988). "Back Analysis of Lateral Load Test on Piles." *Report No. 460*, Univ. of Auckland, New Zealand.

Liu, L., and Dobry, R. (1997). "Seismic response of shallow foundation on liquefiable sand." *Journal of Geotechnical and Geoenvironmental Engineering*, ASCE, 123(6), pp. 557-566.

Liyanapathirana, D. S., and Poulos, H. G. (2005). "Pseudostatic approach for seismic analysis of piles in liquefying soil." *Journal of Geotechnical and Geoenvironmental Engineering*, Dept. of Civil, Mining and Environmental Engineering, Univ. Wollongong, Northfields Ave., Wollongong, NSW 2522, Australia, 131(12), pp. 1480-1487.

Liyanapathirana, D. S., and Poulos, H. G. (2005). "Seismic lateral response of piles in liquefying soil." *Journal of Geotechnical and Geoenvironmental Engineering*, Dept. of Civil, Mining and Environmental Engineering, Univ. of Wollongong, Northfields Ave, Wollongong, NSW 2522, Australia, 131(12), pp. 1466-1479.

Loukidis, D., and Salgado, R. (2008). "Analysis of the shaft resistance of non-displacement piles in sand." *Geotechnique*, School of Civil Engineering, Purdue University, W. Lafayette, United States, 58(4), pp. 283-296.

Mabsout, M. E., Sadek, S. M., and Smayra, T. E. (1999). "Pile driving by numerical cavity expansion." *International Journal for Numerical and Analytical Methods in Geomechanics*, John Wiley & Sons Ltd, Dept. of Civ. and Environ. Eng., American University of Beirut, Beirut, Lebanon, 23(11), pp. 1121-1140.

Manjari, M. T., and Arulanandan, K. (1994). "Numerical Predictions for Model No. 1." *Int. Conf. on Verification of numerical procedures for the analysis of soil liquefaction problems*, Davis, CA, Vol. 1, pp. 179-185.

Matlock, H. (1970). "CORRELATIONS FOR DESIGN OF LATERALLY LOADED PILES IN SOFT CLAY." Houston, TX, USA, 1, pp. 577-594.

Matlock, H., Foo, S. H. C., and Bryant, L. M. (1978). "SIMULATION OF LATERAL PILE BEHAVIOR UNDER EARTHQUAKE MOTION." ASCE, Pasadena, Calif, v(2), pp. 600-619.

Meyerhof, G. G., Mathur, S. K., and Valsangkar, A. J. (1981). "The bearing capacity of rigid piles and pile groups under inclined loads in layered sand." *Canadian Geotechnical Journal*, 18(4), pp. 514-519.

Mokwa, R. L. (1999). "Investigation of the resistance of pile caps to lateral spreading." PhD Thesis, Virginia Poltechnic Institute and State University, Blacksburg, Va.

Mokwa, R. L., and Duncan, J. M. (2003). "Rotational restraint of pile caps during lateral loading." *Journal of Geotechnical and Geoenvironmental Engineering*, Dept. of Civil Engineering, Montana State Univ., 205 Cobleigh Hall, Bozeman, MT 59717, United States, 129(9), pp. 829-837.

Murchison, J. M., and O'Neill, M. W. (1984). "Evaluation of P-Y Relationships in Cohesionless Soils." *Analysis and Design of Pile Foundations*, J. R. Meyer, ed., ASCE, San Francisco, California, October 1-5, 1984, pp. 174-191.

NAVFAC. (1986). "DM7-02: Foundations and Earth Structures." Naval Facilities Engineering Command 200 Stovall Street Alexandria, Virginia 22332-2300.

Det Norske Veritas. (1980). *Rules for the design, construction and inspection of offshore structures. Appendix F: Foundations*. Hovik, Norway.

Pamuk, A., and Zimmie, F. (2007). "Behavior of Floating Piles in Liquefiable Soils." *4th International Conference on Earthquake Geotechnical Engineering*, K. Pittilakis, ed.

Papadimitriou, A. G. (1999). "Elastoplastic Modeling of Monotonic and Dynamic Behavior of Soils." PhD Thesis, Dept of Civil Engineering, NTUA, Athens.

Papadimitriou, A. G., Bouckovalas, G. D., and Dafalias, Y. F. (2001). "Plasticity model for sand under small and large cyclic strains." *Journal of Geotechnical and Geoenvironmental Engineering*, ASCE, 127(11), pp. 973-983.

Papadimitriou, A. G., and Bouckovalas, G. D. (2002). "Plasticity model for sand under small and large cyclic strains: A multiaxial formulation." *Soil Dynamics and Earthquake Engineering*, Department of Geotechnical Engineering, Faculty of Civil Engineering, National Technical University of Athens, 42 Patission Street, 10682 Athens, Greece, 22(3), pp. 191-204.

Papadopoulos, V. (2010). "3-D Numerical Simulation of Laterally Loaded Piles in Cohesionless Soil." Diploma Thesis, NTUA, Athens.

Popescu, R., Prevost, J. H., Deodatis, G., and Chakrabortty, P. (2006). "Dynamics of nonlinear porous media with applications to soil liquefaction." *Soil Dynamics and Earthquake Engineering*, Faculty of Engineering and Applied Science, Memorial University, St. John's, Nfld. A1B 3X5, Canada, 26(6-7), pp. 648-665.

Potyondy, J. G. (1961). "Skin Friction between Various Soils and Construction Materials." *Geotechnique*, 11(4), pp. 339-353.

Poulos, H. G. (1995). "Design of reinforcing piles to increase slope stability." *Canadian Geotechnical Journal*, 32(5), pp. 808-818.

Prasad, Y. V. S. N., and Chari, T. R. (1999). "Lateral capacity of model rigid piles in cohesionless soils." *Soils and Foundations*, 39(2), pp. 21-29.

Randolph, M. F., Carter, J. P., and Wroth, C. P. (1979). "DRIVEN PILES IN CLAY - THE EFFECTS OF INSTALLATION AND SUBSEQUENT CONSOLIDATION." *Geotechnique*, 29(4), pp. 361-393.

Randolph, M. F., and Murphy, B. S. (1985). "Shaft capacity of driven piles in clay." *IN: OTC '85, PROC. SEVENTEENTH ANNUAL OFFSHORE TECHNOLOGY CONF. (HOUSTON, U.S.A.: MAY 6-9, 1985)*, OffshoreTechnol. Conf, 1 , Richar, pp. 371-378.

Randolph, M. F., and Murphy, B. S. (1985). *SHAFT CAPACITY OF DRIVEN PILES IN CLAY. Cambridge University, Engineering Department, (Technical Report) CUED/D-Soils*.

Reese, L. C., Cox, W. R., and Koop, F. D. (1974). "Analysis of Laterally Loaded Piles in Sand." *Offshore Technology Conference, 6-8 May , Houston, Texas*, Offshore Technology Conference.

Reese, L. C., Isenhower, W. M., and Wang, S.-T. (2005). *Analysis and Design of Shallow and Deep Foundations*. John Wiley.

Reese, L. C., Wright, S. G., Wang, S.-T., and Walsh, M. A. (1989). "Analysis of drilled shafts in a deep fill." Publ by ASCE, Univ of Texas, United States, pp. 1366-1380.

Reese, L. C., and Van Impe, W. F. (2001). *Single Piles and Pile Groups Under Lateral Loading*. Taylor & Francis.

Rollins, K. M., Bowles, S., Brown, D., and Ashford, S. A. (2007). "Lateral Load Testing of Large Drilled Shafts after Blast-Induced Liquefaction." *4th International Conference on Earthquake Geotechnical Engineering*, K. Pittilakis, ed., Thessaloniki, Greece.

Rollins, K. M., Gerber, T. M., Lane, J. D., and Ashford, S. A. (2005). "Lateral resistance of a full-scale pile group in liquefied sand." *Journal of Geotechnical and Geoenvironmental Engineering*, Dept. of Civil/Environ. Engineering, Brigham Young Univ., 368 CB, Provo, UT 84602, United States, 131(1), pp. 115-125.

Rollins, K. M., and Sparks, A. (2002). "Lateral resistance of full-scale pile cap with gravel backfill." *Journal of Geotechnical and Geoenvironmental Engineering*, ASCE, 128(9), pp. 711-723.

Roy, M., Michaud, D., Tavenas, F. A., Lerolueil, S., and LaRochelle, P. (1975). "The Interpretation of Static Cone Penetration Tests in Sensitive Clays." *European Symposium of Penetration Testing*, Stockholm, Vol. 2.1, pp. 323-331.

Salgado, R. (2008). *The Engineering of Foundations*. McGraw-Hill, New York, NY.

Salgado, R., and Randolph, M. F. (2001). "Analysis of Cavity Expansion in Sand." *International Journal of Geomechanics*, 1(2), pp. 175-192.

Saxena, S. K., Avramidis, A. S., and Reddy, K. R. (1988). "Dynamic moduli and damping ratios for cemented sands at low strains." *Canadian Geotechnical Journal*, Department of Civil Engineering, Illinois Institute of Technology, Chicago, IL 60616, USA, 25(2), pp. 353-368.

Schnaid, F., Prietto, P. D. M., and Consoli, N. C. (2001). "Characterization of cemented sand in triaxial compression." *Journal of Geotechnical and Geoenvironmental Engineering*, Dept. of Civ. Engrg., Fed. Univ. of Rio Grande do Sul, Av. Osvaldo Aranha, 99, 3. andar, Rio Grande do Sul 90035-190, Brazil, 127(10), pp. 857-868.

Seed, R. B., Cetin, K. O., Moss, R. E. S., Kammerer, A. M., Wu, J., Pestana, J. M., Riemer, M. F., Sancio, R. B., Bray, J. D., Kayen, R. E., and Faris, A. (2003). "Recent Advances in Soil Liquefaction Engineering: A Unified and Consistent Framework." *REPORT NO.EERC 2003-06*, University of California, Berkeley, CA.

Seed, R. B., and Harder, L. F. (1990). "SPT-based Analysis of Cyclic Pore Pressure Generation and Undrained Residual Strength." *H. Bolton Seed Memorial Symposium*, University of Berkeley, California, pp. 351-376.

Sesov, V., Towhata, I., and Gonzalez, M. (2005). "Performance of pile foundation in multi-layered liquefied soil." *16th Int. Conf. Soil Mechanics and Geotechnical Engineering*, Ozaka, Japan, pp. 2183-2186.

Shahir, H., Pak, A., Taiebat, M., and Jeremić, B. (2012). "Evaluation of variation of permeability in liquefiable soil under earthquake loading." *Computers and Geotechnics*, Department of Engineering, Tarbiat Moallem University, P.O. Box 31979-37551, Karaj, Iran, 40, pp. 74-88.

Shamoto, Y., Zhang, J.-M., and Tokimatsu, K. (1998). "New charts for predicting large residual post-liquefaction ground deformation." *Soil Dynamics and Earthquake Engineering*, Elsevier Sci Ltd, Institute of Technology, Shimizu Corp., 4-17, Etchujima 3-C., Tokyo, Japan, 17(7-8), pp. 427-438.

Sharma, S. S., and Fahey, M. (2003). "Degradation of stiffness of cemented calcareous soil in cyclic triaxial tests." *Journal of Geotechnical and Geoenvironmental Engineering*, Ctr. for Offshore Foundation Systems, The Univ. of Western Australia, 35 Stirling Highway, Crawley, WA 6009, Australia, 129(7), pp. 619-629.

Sharma, S. S., and Fahey, M. (2003). "Evaluation of cyclic shear strength of two cemented calcareous soils." *Journal of Geotechnical and Geoenvironmental Engineering*, Ctr. for Offshore Foundation Systems, The Univ. of Western Australia, 35 Stirling Highway, Crawley, WA 6009, Australia, 129(7), pp. 608-618.

Sharma, S. S., and Fahey, M. (2004). "Deformation characteristics of two cemented calcareous soils." *Canadian Geotechnical Journal*, Ctr. for Offshore Foundation Systems, School of Civil/Resource Engineering, The University of Western Australia, 35 Stirling Highway, Crawley, WA 6009, Australia, 41(6), pp. 1139-1151.

Soderberg, L. O. (1962). "Consolidation Theory Applied to Foundation Pile Time Effects." *Géotechnique*, 12(3), pp. 217-225.

Stewart, D. P. (2000). "User Manual PYGMY." University West Australia.

Suzuki, H., Tokimatsu, K., Sato, M., and Abe, A. (2005). "Factor Affecting Horizontal Subgrade Reaction of Piles During Soil Liquefactions and Lataral Spreading." *Seismic Performance and Simulation of Pile Foundations in Liquefied and Laterally Spreading Ground*, R. W. Boulanger and K. Tokimatsu, eds., University of California, Davis, CA, pp. 1-10.

Tabesh, A., and Poulos, H. G. (2001). "The effects of soil yielding on seismic response of single piles." *Soils and Foundations*, Department of Civil Engineering, University of Sydney, Sydney, NSW 2006, Australia, 41(3), pp. 1-16.

Taiebat, M., Shahir, H., and Pak, A. (2007). "Study of pore pressure variation during liquefaction using two constitutive models for sand." *Soil Dynamics and Earthquake Engineering*, Department of Civil and Environmental Engineering, University of California, Davis, One Shields Avenue, Davis, CA 95616, United States, 27(1), pp. 60-72.

Terzaghi, K. (1955). "Evalution of Conefficients of Subgrade Reaction." *Géotechnique*, 5(4), pp. 297-326.

Tokimatsu, K., Suzuki, H., and Sato, M. (2005). "Effects of inertial and kinematic interaction on seismic behavior of pile with embedded foundation." *Soil Dynamics and Earthquake Engineering*, Department of Architecture and Building Engineering, Tokyo Institute of Technology, 2-12-1 O-okayama, Meguro-ku, Tokyo 152-8552, Japan, 25(7-10), pp. 753-762.

Tokimatsu, K., and Asaka, Y. (1998). "Effects of Liquefaction-Induced ground displacements on Pile Performance in the 1995 Hyogoken-Nambu Earthquake." *Soils and Foundations*, Special Is, pp. 163-177.

Tokimatsu, K., and Seed, H. B. (1987). "Evaluation of Settlement in Sands due to Earthquake Shaking." *Journal of geotechnical engineering*, Tokyo Inst of Technology, Tokyo, Jpn, Tokyo Inst of Technology, Tokyo, Jpn, 113(8), pp. 861-878.

Tokimatsu, K., and Suzuki, H. (2009). "Seismic soil-pile-structure interaction based on large shaking table tests." *Performance-Based Design in Earthquake Geotechnical Engineering*, T. Kokusho, Y. Tsukamoto, and M. Yoshimine, eds., Taylor & Francis.

Towhata, I., Sesov, V., Motamed, R., and Gonzalez, M. (2006). "Model Tests on Lateral Earth Pressure on Large Group Pile Exerted by Horizontal Displacement of Liquefied Sandy Ground." *8th U.S. National Conference on Earthquake Engineering, April 18-22, 2006*, San Francisco, California, USA.

Towhata, I., and Ishihara, K. (1985). "Modeling Soil Behavior under principal axes rotation." *5th International Conference on Numerical Methods in Geomechanics*, Nagoya, Japan, pp. 523-530.

Uchida, A., and Tokimatsu, K. (2006). "Comparison of current Japanese design specifications for pile foundations in liquefiable and laterally spreading ground." *Geotechnical Special Publication*, T. K. Boulanger R.W., ed., Davis, CA, pp. 61-70.

Ueng, T. S., Chen, C. H., and Tseng, Y. C. (2009). "Shaking Table Tests on model piles in liquefiable sand." *17th International Conference on Soil Mechanics and Geotechnical Engineering*, M. Hamza et al., ed.

Uzuoka, R., Sento, N., and Kazama, M. (2005). "Numerical Analysis of Rate-Dependent Reaction of Pile in Saturated or Liquefied Soil." *Seismic Performance and Simulation of Pile Foundations in Liquefied and Laterally Spreading Ground*, R. W. Boulanger and K. Tokimatsu, eds., University of California, Davis, CA, pp. 204-217.

Valsamis, A. I. (2008). "Numerical Investigation of Liquefaction Induced Lateral Spreading Effects on Piles." PhD Thesis, Dept. of Civil Engineering, NTUA, Athens.

Valsamis, A. I., Bouckovalas, G. D., and Chaloulos, Y. K. (2012). "Parametric analysis of single pile response in laterally spreading ground." *Soil Dynamics and Earthquake Engineering*, Department of Geotechnical Engineering, School of Civil Engineering, National Technical University of Athens, 9 Heroon Polytechneiou str., 15780 Zografou, Greece, 34(1), pp. 99-110.

Valsamis, A. I., Bouckovalas, G. D., and Papadimitriou, A. G. (2010). "Parametric investigation of lateral spreading of gently sloping liquefied ground." *Soil Dynamics and Earthquake Engineering*, Geotechnical Department, School of Civil Engineering, National Technical University of Athens, 9 Iroon Polytechniou Street, 15780 Zographou, Greece, 30(6), pp. 490-508.

Vesic, A. S. (1961). "Beam on Elastic Subgrade and the Winkler's Hypothesis." *5th International Conference on Soil Mechanics and Foundation Engineering*, pp. 845-850.

Vesic, A. S. (1972). "Expansion of cavities in infinite soil mass." *ASCE J Soil Mech Found Div*, 98(SM3), pp. 265-290.

Wen, Y.-K. (1976). "Method for random vibration of hysteretic systems." *ASCE J Eng Mech Div*, 102(2), pp. 249-263.

Wilson, D. W., Boulanger, R. W., and Kutter, B. L. (1998). "Signal Processing for analyses of dynamic soil-pile-interaction experiments." *ISSMFE Centrifuge '98*, T. Kimura, O. Kusakabe, and J. Takemura, eds., Rotterdam, The Netherlands.

Wilson, D. W., Boulanger, R. W., and Kutter, B. L. (1999). "Lateral resistance of piles in liquefying sand." *Geotechnical Special Publication*, Department of Civil Engineering, University of California at Davis, One Shields Avenue, Davis, CA 95616, United States, (88), pp. 165-179.

Yang, Z., and Jeremić, B. (2002). "Numerical analysis of pile behaviour under lateral loads in layered elastic-plastic soils." *International Journal for Numerical and Analytical Methods in Geomechanics*, Department of Civil and Environmental Engineering, University of California, Davis, CA 95616, United States, 26(14), pp. 1385-1406.

Youd, T. L., Hansen, C. M., and Bartlett, S. F. (2002). "Revised multilinear regression equations for prediction of lateral spread displacement." *Journal of Geotechnical and Geoenvironmental Engineering*, Civil Engineering Dept., Brigham Young Univ., Provo, UT 84602-4081, United States, 128(12), pp. 1007-1017.

Yu, H. S., and Houlsby, G. T. (1991). "Finite cavity expansion in dilatant soils: loading analysis." *Géotechnique*, 41(2), pp. 173-183.

Zhang, J.-M., Shamoto, Y., and Tokimatsu, K. (1998). "Evaluation of earth pressure under any lateral deformation." *Soils and Foundations*, Institute of Technology, Shimizu Corporation, 4-17, Etchujima 3-chome, Koto-ku, Tokyo 135-0044, 38(1), pp.15-33.